TESIS DE LA UNIVERSIDAD DE ZARAGOZA

2015

80

Ignacio Julián Burillo

Fluidodinámica de un reactor de lecho fluidizado de dos zonas con cambio de sección y su aplicación usando membrana permeoselectiva

Departamento

Ingeniería Química y Tecnologías del Medio Ambiente

Director/es

Herguido Huerta, Javier

Menéndez Sastre, Miguel

ISSN 2254-7606

Prensas de la Universidad Universidad Zaragoza

ISSN 2254-7606

Universidad Zaragoza
1542

Tesis Doctoral

FLUIDODINÁMICA DE UN REACTOR DE LECHO FLUIDIZADO DE DOS ZONAS CON CAMBIO DE SECCIÓN Y SU APLICACIÓN USANDO MEMBRANA PERMEOSELECTIVA

Autor

Ignacio Julián Burillo

Director/es

Herguido Huerta, Javier

Menéndez Sastre, Miguel

UNIVERSIDAD DE ZARAGOZA

Ingeniería Química y Tecnologías del Medio Ambiente

2015

Tesis Doctoral

Universidad de Zaragoza

Escuela de
Ingeniería y Arquitectura
Universidad Zaragoza

FLUIDODINÁMICA DE UN REACTOR DE LECHO FLUIDIZADO DE DOS ZONAS CON CAMBIO DE SECCIÓN Y SU APLICACIÓN USANDO MEMBRANA PERMEOSELECTIVA

Autor:

Ignacio Julián Burillo

Directores:

Javier Herguido Huerta

Miguel Menéndez Sastre

Departamento de Ingeniería Química

y Tecnologías del Medio Ambiente (IQTMA)

Instituto de Investigación en Ingeniería de Aragón (I3A)

Departamento de Ingeniería
Química y Tecnologías
del Medio Ambiente
Universidad Zaragoza

Instituto Universitario de Investigación
en Ingeniería de Aragón
Universidad Zaragoza

Dr. D. Javier Herguido Huerta, Catedrático de Universidad, y

Dr. D. Miguel Menéndez Sastre, Catedrático de Universidad

ambos pertenecientes al Departamento de Ingeniería Química y Tecnologías del Medio Ambiente (IQTMA) y al grupo de Catálisis, separaciones moleculares e ingeniería de reactores (CREG) y al Instituto Universitario de Investigación en Ingeniería de Aragón (I3A) de la Universidad de Zaragoza,

CERTIFICAN

que la presente Memoria titulada

Fluidodinámica de un Reactor de Lecho Fluidizado de Dos Zonas con Cambio de Sección y su aplicación usando membrana permeoselectiva

ha sido realizada bajo nuestra dirección en el Departamento de Ingeniería Química y Tecnologías del Medio Ambiente y en el Instituto Universitario de Investigación en Ingeniería de Aragón (I3A) por D. Ignacio Julián Burillo, autorizando su presentación como compendio de publicaciones.

Y para que así conste, firmamos este certificado en Zaragoza a 09 de Junio de 2015.

Fdo. Prof. Dr. D. Javier Herguido Huerta Fdo. Prof. Dr. D. Miguel Menéndez Sastre

Con estas líneas deseo mostrar mi agradecimiento a todas las personas que, de una manera u otra, han contribuido a que la presente Tesis Doctoral vea la luz.

En primer lugar agradezco la labor de mis directores, los doctores Javier Herguido y Miguel Menéndez por confiar en mí para llevar a cabo este proyecto. Sus sabios consejos y decisiones me han ayudado a superar todas las dificultades que la Tesis ha ido planteando.

A mis mentores en las estancias de tesis, los doctores Fausto Gallucci y Martin van Sint Annaland, por compartir conmigo sus inmensos conocimientos en fluidodinámica de lechos fluidizados y estar siempre dispuestos a colaborar y orientarme en mi investigación.

A mis compañeros de laboratorio, especialmente a Javi, Miriam, Paúl y Jorge quienes han vivido conmigo este periplo desde el primer día y se han entregado desinteresadamente para ayudarme y apoyarme en todos los ámbitos.

A toda la gente que ha ido pasando por el laboratorio en estos últimos cuatro años por su sincera amistad y su calidad humana. ¡Gracias a todos! En especial a José Antonio, Marian y Héctor, a quienes tuve el placer de dirigir el Proyecto Fin de Carrera, y de los cuáles aprendí mucho. Gracias también a los compañeros del CREG-INA y GPT con quienes he compartido buenos momentos.

Igualmente debo expresar mi gratitud por el soporte financiero al Ministerio de Economía y Competitividad (MINECO) por concederme la beca FPI (ref. BES-2011-043703) asociada al proyecto de investigación del MINECO ref. CTQ2 010-15568, cofinanciada por el Fondo Social Europeo.

Esta tesis ha constituido un enorme reto para mí, tanto a nivel intelectual como personal. Cuando me sumergí en la *"fluidodinámica de reactores multifásicos"*, constaté que era un perfecto ignorante en temas como la *programación de algoritmos de cálculo computacional*, el *tratamiento digital de imagen* o el *uso de simuladores CFD*, poco afines a un perfil de ingeniero químico "al uso". Cuatro años después, aunque estos tecnicismos ya no me son ajenos, sigo teniendo dificultades para tratar de explicar a familiares y amigos en qué consiste mi trabajo...

He alternado días de euforia y pasión por la investigación con momentos de grandes dudas y desánimo. Durante todos esos días he tenido la gran suerte de contar mis padres, mis hermanas y Elisa, a quienes he aburrido narrando mis pequeños logros y preocupado con mis agobios. Representan para mí un pilar fundamental sin el cuál esta Tesis no habría sido posible.

A mis padres, Jesús y María Pilar, quienes han hecho de mí todo lo que soy con mis virtudes y mis defectos. Gracias a ellos he llegado hasta aquí. Espero que estén tan orgullosos de mí como yo lo estoy de ellos.

Elisa, por tu paciencia infinita, por compartir conmigo cada momento, por tus consejos, por tu apoyo, por no dejarme caer, por todo: ¡GRACIAS!

“The arrival time of a space probe travelling to Saturn can be predicted more accurately than the behavior of a fluidized bed chemical reactor!”

D. Geldart (1986)

SUMARIO

La presente Tesis Doctoral, que lleva por título "Fluidodinámica de un Reactor de Lecho Fluidizado de Dos Zonas con Cambio de Sección y su aplicación usando membrana permeoselectiva", realizada por D. Ignacio Julián Burillo y dirigida por los doctores D. Javier Herguido Huerta y D. Miguel Menéndez Sastre se presenta en la modalidad de compendio de publicaciones con mención internacional.

La memoria de la tesis constituye un resumen del trabajo de investigación realizado, el cuál se detalla en los ocho artículos científicos previamente publicados que conforman el compendio. Adicionalmente, se ha considerado la inclusión de tres trabajos pendientes de publicación (y relacionados directamente con la unidad temática de la tesis) a fin de cohesionar los contenidos presentados en la memoria.

De acuerdo con la normativa vigente relativa a la obtención de la mención internacional en el título de doctor, se anexa un resumen de la tesis en inglés.

La relación de publicaciones que compendian la presente tesis doctoral se detalla a continuación.

I. I. Julián, J. Herguido, M. Menéndez, *Particle Mixing in a Two-Section Two-Zone Fluidized Bed Reactor. Experimental Technique and Counter-Current Back-Mixing Model Validation*, Ind. Eng. Chem. Res. 52 (2013) 13587 – 13596.

II. I. Julián, F. Gallucci, M. v. Sint Annaland, J. Herguido, M. Menéndez, *Coupled PIV/DIA for fluid dynamic studies on a Two-Section Two-Zone Fluidized Bed Reactor*, Chem. Eng. J. 207 – 208 (2012) 122 – 132.

III. I. Julián, J. Herguido, M. Menéndez, *A non-parametric bubble size correlation for a Two-Section Two-Zone Fluidized Bed Reactor (TS-TZFBR),* Powder Technol. 256 (2014) 146-157.

IV. I. Julián, J. Herguido, M. Menéndez, *CFD model prediction of a Two-Section Two-Zone Fluidized Bed Reactor (TS-TZFBR) hydrodynamics,* Chem. Eng. J. 248 (2014) 352-362.

V. I. Julián, F. Gallucci, M. v. Sint Annaland, J. Herguido, M. Menéndez, *Hydrodynamic study of a Two-Section Two-Zone Fluidized Bed Reactor with an immersed tube bank via PIV/DIA,* Chem. Eng. Sci. 134 (2015) 238-250.

VI. I. Julián, J. Herguido, M. Menéndez, *Experimental and simulated solids mixing and bubbling behaviour in a scaled Two-Section Two-Zone Fluidized Bed Reactor,* Chem. Eng. Sci. (2015) *Enviado*.

VII. I. Julián, J. Herguido, M. Menéndez, *Gas permeation effect on the Two-Section Two-Zone Fluidized Bed Membrane Reactor (TS-TZFBMR) fluid dynamics: a CFD simulation study,* Chem. Eng. J. (2015) *Enviado*.

VIII. I. Julián, J. Herguido, M. Menéndez, *On the use of α–shapes for the measurement of 3D bubbles in fluidized beds from Two-Fluid Model simulations,* Powder Technol. (2015) *Enviado*.

IX. J.A. Medrano, I. Julián, J. Herguido, M. Menéndez, *Pd-Ag membrane coupled to a Two-Zone Fluidized Bed Reactor (TZFBR) for propane dehydrogenation on a Pt-Sn/$MgAl_2O_4$ catalyst,* Membranes 3 (2013) 69 – 86.

X. J.A. Medrano, I. Julián, F. García, K. Li, J. Herguido, M. Menéndez, *Two-Zone Fluidized Bed Reactor (TZFBR) with palladium membrane for catalytic propane dehydrogenation: experimental performance assessment,* Ind. Eng. Chem. Res. 52 (2013) 3723 – 3731.

XI. H. Montesinos, I. Julián, J. Herguido, M. Menéndez, *Effect of the presence of light hydrocarbon mixtures on the hydrogen permeation through Pd-Ag alloyed membranes,* Int. J. Hydrogen. Energ. 40 (2015) 3462-3471.

Lo que se hace constar en cumplimiento del Reglamento sobre Tesis Doctorales de la Universidad de Zaragoza (artículo 20, apartado a), aprobado según el acuerdo de 20 de diciembre de 2013 del Consejo de Gobierno de la Universidad.

NOMENCLATURA

Acrónimos

AR	Relación de aspecto (*Aspect Ratio*), (-)
BET	Brunauer – Elmett – Teller
CCBM	Retromezcla a contracorriente (*Counter-Current Back-Mixing*)
CFD	Fluidodinámica computacional (*Computational Fluid Dynamics*)
CREG	Grupo de Catálisis, Separaciones moleculares e Ingeniería de Reactores
DH	Correlación de Davidson y Harrison
DIA	Análisis de imágenes digitales (*Digital Image Analysis*)
DPM	Modelo de partículas discretas (*Discrete Particle Model*)
FCC	Craqueo catalítico de petróleo (Fluid Catalytic Cracking)
GC	Cromatografía de gases (*Gas Chromatography*)
HD	Alta definición (*High Definition*)
I3A	Instituto de Investigación en Ingeniería de Aragón
IM	Índice de Mezcla, (-)
JHM	Modelo Julián-Herguido-Menéndez
KTGF	Teoría cinética de Flujo Granular (*Kinetic Theory of Granular Flow*)
MBP	Membrana de pared
MBT	Membrana tubular
MW	Correlación de Mori y Wen
PDH	Deshidrogenación catalítica de propano (*Propane dehydrogenation*)
PDr	Probabilidad de distribución radial, (%)
PIV	Velocimetría de partículas (*Particle Image Velocimetry*)
PSD	Distribución de probabilidad de tamaños (*Probability Size Distribution*)
RGB	Colores primarios de imagen (*Red – Green – Blue*)
RMS	Media cuadrática (*Root Mean Square*)
RLF	Reactor de lecho fluidizado
RLFDZ	Reactor de lecho fluidizado de dos zonas
RLFDZ-CS	RLFDZ con cambio de sección
RLFDZ-CS+MB	RLFDZ-CS con membrana permeoselectiva
SMR	Grupo de Reactores Multifásicos (*Multiphase Reactors Group*)
TFM	Modelo de dos fluidos (*Two-Fluid Model*)
TUe	Universidad Tecnológica de Eindhoven
XRD	Difracción de rayos X (*X-Ray Diffraction*)

Símbolos

A	Parámetro de la correlación ε_{3D} (ε_{2D}), (-)
A_i	Área frontal proyectada de la burbuja i en la imagen, (píxeles)
B	Parámetro de la correlación ε_{3D} (ε_{2D}), (-)
b_{CoM}	Centro de masas de una burbuja tridimensional, (cm)
b_h	Fracción volumétrica de burbujas en el lecho, (%)
C_D	Coeficiente de arrastre, (-)

C_1	Concentración de trazador en la fase ascendente (estela), (-)
C_2	Concentración de trazador en la fase descendente (emulsión), (-)
C_∞	Concentración de trazador a tiempo infinito, (-)
d_b	Diámetro de burbuja equivalente, (cm)
$d_{b(área)}$	Formulación superficial del diámetro de burbuja equivalente, (cm)
$d_{b(vol)}$	Formulación volumétrica del diámetro de burbuja equivalente, (cm)
$d_{b,orif}$	Diámetro de burbuja para las burbujas del distribuidor inmerso, (cm)
$d_{b,m}$	Diámetro de burbuja máximo teórico, (cm)
D_{down}	Diámetro del lecho en la zona inferior del RLFDZ-CS, (cm)
d_{orif}	Diámetro interno de los orificio del distribuidor inmerso, (mm)
D_{up}	Diámetro del lecho en la zona superior del RLFDZ-CS, (cm)
d_p	Diámetro de partícula, (m)
e	Coeficiente de restitución, (-)
E_m	Eficiencia de membrana, (-)
f_1	Fracción volumétrica de la fase sólida ascendente, (-)
F_{C3H8}	Flujo volumétrico de propano alimentado al RLFDZ-CS+MB, (cm^3/min)
F_s	Flujo axial de sólidos, (kg/m^2s)
f_w	Fracción de la burbuja ocupada por la estela, (-)
g	Aceleración debida a la gravedad, (m/s^2)
g_0	Función de distribución radial, (-)
h_{fb}	Posición axial de la superficie libre o *freeboard*, (cm)
$H_{lecho\ fijo}$	Altura de lecho fijo, (cm)
h_{min}	Altura mínima a la cual comienza la mezcla axial de sólidos, (cm)
$\bar{\bar{I}}$	Tensor de esfuerzos, (-)
I_{umb}	Gradiente de intensidad umbral, (píxeles)
K	Parámetro de correlación de Davidson y Harrison, (-)
K_{gs}	Coeficiente de transferencia de momento en la interfase, (kg/m^3s)
k_w	Coeficiente de transferencia de material entre estela y emulsión, (s^{-1})
L_1	Anchura de la zona inferior del lecho, (cm)
L_{bed}	Profundidad del lecho pseudo-2D, (mm)
L_{cs}	Anchura de la zona de cambio de sección en un RLFDZ-CS, (cm)
L_{lecho}	Perímetro del lecho, (cm)
n_b	Número de burbujas en una región del lecho, (-)
n_i	Coordenada i de nodo en la malla del dominio computacional, (cm)
P	Presión, (Pa)
Q_b	Caudal volumétrico de burbujas (cm^3/min)
Q_{C3H8}	Caudal volumétrico de propano alimentado (cm^3/min)
Q_{gas}	Caudal volumétrico de gas alimentado (cm^3/min)
r^2	Coeficiente de regresión, (-)
R_{C3H6}	Rendimiento a propileno, (%)
Re	Número adimensional de Reynolds, (-)
rf	resolución del fotograma, (píxeles/cm)
S_e	Sección transversal equivalente limitada por región defluidizada, [cm^2]
S_0	Sección transversal de la zona inferior del RLFDZ-CS, [cm^2]
S_1	Sección transversal de la zona inferior del RLFDZ-CS, [cm^2]

S_{BET}	Superficie específica del catalizador, (m^2/g)
S_{lecho}	Sección transversal del lecho, (cm^2)
t	Tiempo, (min)
t_c	Tiempo de circulación promedio de partículas en RLFDZ-CS, (min)
u_1	Velocidad ascensional de la fase estela, [cm/s]
u_b	Velocidad ascensional de burbuja, (cm/s)
u_{br}	Velocidad de burbujas, (cm/s)
u_{gas}	Velocidad de gas, (cm/s)
u_{mf}	Velocidad de mínima fluidización, (cm^3_{STP}/cm^2s)
u_{mf}^*	Velocidad de mínima fluidización aparente, (cm^3_{STP}/cm^2s)
$u_{r,inf}$	Velocidad relativa de gas (u_{gas}/u_{mf}) en la sección inferior del lecho, (-)
$u_{r,reac}$	Velocidad relativa de gas en la zona de reacción del RLFDZ, (-)
$u_{r,reg}$	Velocidad relativa de gas en la zona de regeneración del RLFDZ, (-)
$u_{r,sup}$	Velocidad relativa de gas (u_{gas}/u_{mf}) en la sección superior del lecho, (-)
u_s	Velocidad de sólidos (m/s)
$\vec{v}$	Velocidad local de partículas, (m/s)
V_b	Volumen ocupado por una burbuja, (cm^3)
v_p	Volumen de poro, (cm^3)
v_z	Velocidad axial de sólidos, (cm/s)
W_{cat}	Peso de catalizador en el lecho, (g)
w_{lecho}	Anchura del lecho, (cm)
x_{C3H8}	Conversión catalítica de propano, (-)
Y_{C3H6}^*	Rendimiento a propileno normalizado, (-)
z_{dis}	Posición axial del distribuidor inmerso en el lecho, (cm)
z_{fb}	Altura de la superficie libre del lecho, (cm)
z_{ilum}	Altura de la zona inicialmente iluminada en el RLFDZ-CS, (cm)
z_{max}	Altura máxima alcanzada por el lecho en régimen de fluidización, (cm)
z_{sc}	Posición axial del cambio de sección en un reactor RLFDZ-CS, (cm)

Símbolos griegos

α	Ángulo de cambio de sección, (º)
α_{3D}	Distancia umbral de discretización para burbujas 3D, (cm)
β	Ángulo de defluidización, (º)
δ	Fracción volumétrica de burbujas en el lecho, (%)
ε_i	Fracción volumétrica de la fase i, (-)
θ	Temperatura granular, (m^2/s^2)
λ	Viscosidad, (kg/(m·s))
μ	Viscosidad dinámica, (kg/(m·s))
μ_{col}	Contribución colisional de la viscosidad dinámica, (kg/(m·s))
ρ_{bulk}	Densidad de lecho empaquetado, [kg/m^3]
ρ_s	Densidad de partícula, [kg/m^3]
$\bar{\bar{\tau}}$	Tensor de esfuerzo tangencial, ($kg/(m\cdot s^2)$)

Subíndices

i	Fase i, sólida o fluida

g	Fase fluida (gas)
s	Fase sólida
0	Inicial
1x	Reactor a pequeña escala
2x	Reactor escalado

ÍNDICE

1 INTRODUCCIÓN Y OBJETIVOS

1.1 Contexto de la investigación
1.2 Alcance y objetivos

1. INTRODUCCIÓN Y OBJETIVOS

1.1 Contexto de la investigación

La intensificación de procesos en ingeniería química tiene como propósito el ahorro en costes energéticos y de capital así como en medidas de seguridad, optimizando los beneficios derivados de procesos industriales en base a la reducción del tamaño en las plantas químicas (1). En este contexto, el Reactor de Lecho Fluidizado de Dos Zonas (RLFDZ) representa un sistema con un elevado potencial en el campo de la catálisis heterogénea, debido a su capacidad de integrar diversos procesos catalíticos de manera simultánea en un único equipo. En particular, la tecnología RLFDZ ha resultado efectiva en aquellas reacciones gas-sólido catalíticas en las que el catalizador sufre una rápida desactivación por deposición de coque y en oxidaciones catalíticas en las que el catalizador puede ser utilizado como un transportador de oxígeno (2).

Tradicionalmente, los procesos que involucran la reducción catalítica y su posterior regeneración (oxidación) se llevan a cabo en etapas consecutivas en una o varias unidades. Esta es la base de los lechos fluidizados circulantes implementados a escala industrial para craqueo catalítico de petróleo, deshidrogenación de alcanos ligeros u oxidación catalítica de butano (2). En otros casos, como en el proceso comercial Houdry Catadiene^{TM}, la oxidación y la reducción del catalizador se llevan a cabo en el mismo reactor de modo discontinuo (3). Entre las ventajas de separar las etapas redox del catalizador se encuentra la mejora de la selectividad y un mejor control del grado de oxidación catalítica. Además, se mejora la seguridad del proceso reduciendo el riesgo de explosión que podría tener lugar al mezclarse hidrocarburo y oxígeno en una misma unidad de proceso. Asimismo, se evitan reacciones indeseadas promovidas por la eventual presencia de oxígeno en la unidad de reducción del proceso. Por el contrario, la gran desventaja del uso de lechos circulantes radica en la dificultad para controlar el flujo de sólidos entre las distintas unidades de proceso. El transporte de sólidos es costoso y puede dar lugar a problemas de operación.

Con el objetivo de ofrecer procesos alternativos que preserven las ventajas de los tradicionales, permitan una operación en continuo y minimicen recursos, reduciendo el tamaño de las unidades de proceso, el grupo de Catálisis, Separaciones Moleculares e Ingeniería de Reactores (CREG) ha desarrollado durante las dos últimas décadas el llamado Reactor de Lecho Fluidizado de Dos Zonas (RLFDZ).

El reactor RLFDZ, propuesto y ampliamente estudiado por la Universidad de Zaragoza, fue concebido con el propósito de integrar los procesos de reacción catalítica heterogénea y regeneración del catalizador (2). La regeneración in-situ del catalizador cobra especial interés en aquellas reacciones en las que intervienen hidrocarburos a alta temperatura. En muchas de estas reacciones gas-sólido catalíticas se genera un residuo carbonoso altamente deshidrogenado (coque), que se deposita sobre la superficie activa del catalizador desactivándolo (2). Como consecuencia, la conversión del gas reactivo se ve disminuida en función del grado de cubrimiento por coque del catalizador. En función de las condiciones de operación, esta desactivación puede tener lugar tras unos días, horas o incluso segundos (4, 5). Un claro ejemplo es el proceso de craqueo catalítico de petróleo (FCC) en el cuál el catalizador se desactiva en fracciones de segundo y debe ser regenerado en continuo para mantener constante la actividad del mismo. En el caso del RLFDZ, la regeneración en continuo tiene lugar en un único lecho fluidizado, con el consiguiente ahorro en equipamiento, materiales y energía que supone un sistema más compacto.

El fundamento del reactor radica en la alimentación fraccionada de gas en el lecho. Por un punto intermedio de éste se introduce una corriente de gas reactivo, mientras que por la parte inferior del mismo se alimenta una corriente de gas oxidante. De este modo se inducen dos zonas con atmósferas diferentes en un mismo lecho fluidizado (reductora y oxidante) y la circulación de partículas de catalizador entre ambas zonas del lecho permite mantener una actividad catalítica constante a lo largo del tiempo. En la zona superior del lecho tiene lugar la reacción catalítica que genera, como subproducto, un depósito carbonoso (coque) sobre la superficie activa del catalizador mientras que en la zona inferior del lecho se produce la combustión de dicho coque obteniéndose partículas de catalizador regeneradas y nuevamente activas para desarrollar la actividad catalítica en la zona superior.

Con el fin de ganar en versatilidad y poder mantener el régimen de fluidización (la velocidad del gas) entre ambas zonas del lecho, aún trabajando con caudales muy diferentes de corriente reactiva y de regeneración, el diseño original del RLFDZ se modificó añadiendo un cambio de sección (Figura 1.b), resultando un nuevo Reactor de Lecho Fluidizado de Dos Zonas con Cambio de Sección (RLFDZ-CS) que fue objeto de patente española por la Universidad de Zaragoza en el año 2009 (PCT/ES2009/070241). En dicha patente se recoge, asimismo, la inclusión de membranas para la retirada selectiva de productos de reacción. La integración de una membrana permeoselectiva a H_2 en el RLFDZ-CS con el fin de desplazar el equilibrio termodinámico en reacciones limitadas por éste, como la deshidrogenación de alcanos (6-11) (Figura 1.c), es uno de los objetos de estudio de la presente tesis. De este modo, el reactor de lecho fluidizado de dos zonas con cambio de sección y membrana permeoselectiva (RLFDZ-CS+MB) sería capaz de integrar, bajo ciertas condiciones de operación, tres procesos diferentes en un único lecho fluidizado: reacción, regeneración catalítica y separación.

El RLFDZ se ha utilizado con éxito para llevar a cabo diversas reacciones gas-sólido catalíticas fuertemente limitadas por la rápida desactivación del catalizador, como son: deshidrogenación de alcanos (6, 9, 11-13), aromatización de metano (14), reformado oxidativo de etanol y reformado de glicerol con vapor de agua. Un uso alternativo de este reactor en reacciones de oxidación catalítica selectiva está basado en utilizar el catalizador para transportar oxígeno

entre las dos zonas, oxidándolo en la zona inferior y reduciéndolo en la zona superior, donde se cede el oxígeno para la reacción deseada. De esta forma se ha usado el RLFDZ en acoplamiento oxidativo de metano (15, 16), deshidrogenación oxidativa de alcanos y oxidación de butano a anhídrido maleico.

La tasa de circulación axial de sólidos entre las distintas regiones del lecho fluidizado, así como las cinéticas catalíticas de reacción y regeneración, determinan la eficiencia de la integración de procesos en un RLFDZ-CS. Precisamente, una mezcla axial de sólidos apropiada conlleva la posibilidad de alcanzar una actividad catalítica constante en el proceso: las partículas parcialmente coquizadas por efecto de la reacción química circularían hacia la zona inferior del lecho donde una corriente oxidante quemaría el coque depositado recuperando la actividad inicial del catalizador (2). Las partículas regeneradas ascenderían a la zona superior, volviendo a actuar como sustancias activas en la reacción catalítica, cerrando así el ciclo de reacción (2).

Si bien el comportamiento fluidodinámico de lechos fluidizados gas-sólido ha sido ampliamente estudiado desde hace más de cinco décadas (17-21), únicamente algunos trabajos recientes se centran en el estudio fluidodinámico experimental (22-24) y simulado (25-28) de lechos con cambio de sección gradual, múltiples entradas de gas (29-32) o acoplamiento de membranas permeoselectivas para la adición o extracción de gas (33-36). El uso de membranas también ha revivido el interés por estudiar el efecto de elementos internos en el lecho (37-39).

Ante la inexistencia de estudios previos sobre el efecto simultáneo de la alimentación fraccionada de gas, cambio de sección localizado en un punto intermedio del lecho y extracción selectiva de gas en el comportamiento fluidodinámico de un RLFDZ, la presente tesis constituye una primera aproximación al análisis fluidodinámico de este tipo de reactores multifuncionales RLFDZ-CS+MB. Como producto del estudio, se pretende mitigar las limitaciones hidrodinámicas del reactor así como establecer una ventana de operación que permita un adecuado comportamiento del sistema en función de los caudales de gas alimentados, la geometría del reactor y el tipo de partículas utilizado. Adicionalmente, se ensayará el RLFDZ-CS+MB para la producción de propileno a partir de deshidrogenación catalítica de propano (PDH).

El estudio fluidodinámico del RLFDZ-CS+MB se ha llevado a cabo en varias fases, tratando de caracterizar simultáneamente el comportamiento de las burbujas y el lecho particulado en función de las condiciones de operación tanto experimentalmente como a través de modelos fluidodinámicos.

Por un lado, se han realizado mediciones de burbujeo en frío en RLFDZ-CS pseudo-bidimensionales. Mediante análisis digital de imágenes (DIA), no invasivo, se ha cuantificado el tamaño, la posición y la forma de las burbujas de gas en el lecho así como su velocidad ascensional en función de distintas variables de operación (velocidad de gas de fluidización, geometría del reactor o posición relativa del distribuidor de gas superior respecto a la región cónica del lecho). De entre las técnicas de análisis no invasivas (40, 41), se ha elegido el tratamiento digital de imágenes DIA debido a su simplicidad de implementación y la gran cantidad de información que es posible extraer a partir de los fotogramas de fluidización en

lechos pseudo-2D (42, 43). Los resultados relacionados con la variación axial del tamaño de burbuja han permitido desarrollar un modelo matemático capaz de predecir la evolución del diámetro de burbuja equivalente promedio con la altura en el lecho en función del caudal de gas alimentado, tipo de partícula, pendiente de la sección inclinada o posición axial del distribuidor de gas superior.

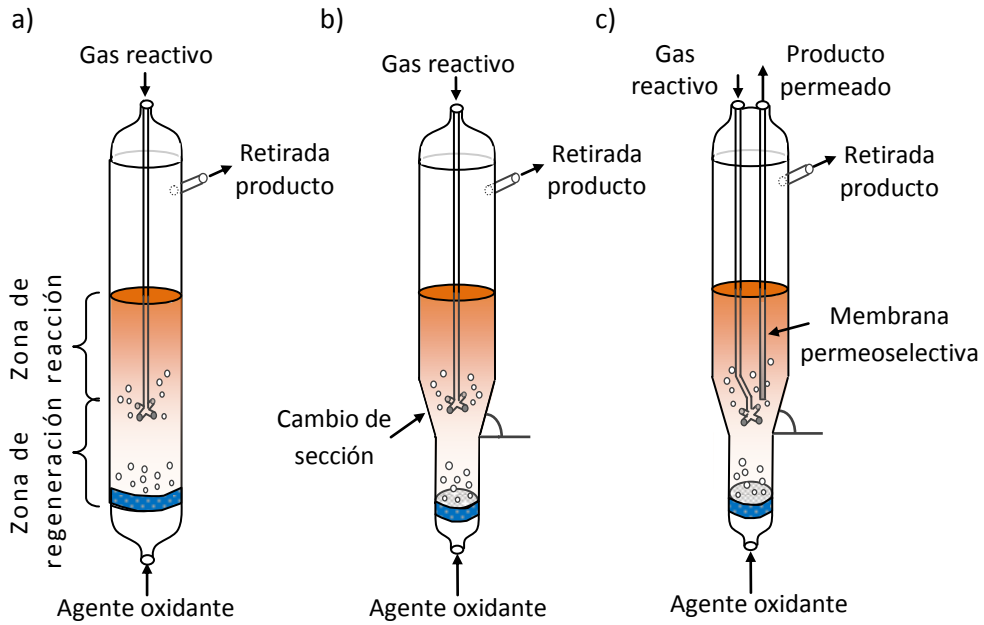

Figura 1. a) RLFDZ, b) RLFDZ-CS, c) RLFDZ-CS+MB

Por otro lado, se ha estudiado la mezcla axial de sólidos entre las dos zonas del lecho haciendo uso de partículas fosforescentes a modo de trazadores ópticos. Los resultados experimentales han servido para validar el modelo de retromezcla a contracorriente (*Countercurrent Backmixing*, CCBM) y medir el grado de mezcla entre partículas inicialmente segregadas en función de las condiciones de operación.

Además, se ha utilizado la técnica no intrusiva de velocimetría de partículas (*Particle Image Velocimetry,* PIV) haciendo uso del software comercial DaVis (LaVision®), a fin de cuantificar el movimiento de partículas discretas en el lecho, generando mapas de circulación de sólido y perfiles de velocidad. La técnica PIV está basada en la correlación espacial de dos imágenes consecutivas para obtener diagramas de flujo instantáneos a lo largo del área fotografiada. Cada imagen se divide en áreas de sección constante en las cuales se evalúa el desplazamiento de las partículas entre fotogramas. Haciendo uso del procesado digital de imágenes (*Digital Image Analysis*, DIA) ha sido posible estimar la fracción ocupada por sólidos en cada punto del lecho y acoplar los mapas de porosidad a los resultados de velocimetría para determinar los flujos másicos de sólidos en la dirección vertical en el lecho.

El trabajo experimental se ha completado con la realización de simulaciones fluidodinámicas en Ansys-CFX y Ansys-Fluent, dos programas comerciales de fluidodinámica computacional (CFD). Dichas simulaciones, basadas en la resolución de ecuaciones diferenciales no lineales de Navier-Stokes según el modelo de dos fluidos (*Two-Fluid Model*, TFM), permiten estimar a

cada paso temporal la fracción volumétrica ocupada por el gas (ε_{gas}) y por el sólido disperso (ε_{lecho}) y su velocidad en función de la posición en el reactor. La identificación de burbujas de gas a partir de simulaciones fluidodinámicas requiere la definición de una porosidad de lecho umbral de modo que si ésta se supera en una determinada región del lecho, dicha región se considera volumen hueco o burbuja (44). De esta forma, es posible llevar a cabo el estudio comparativo entre las propiedades de burbuja experimentales, simuladas y modeladas a partir de la correlación de tamaños de burbuja propuesta.

La respuesta fluidodinámica del RLFDZ-CS+MB se ha evaluado en función de las siguientes variables de operación: velocidad de gas alimentado (u_{gas}), tipología de partícula (u_{mf}, ρ_{bulk}), posición del distribuidor superior (z_{dis}), altura de la zona inferior cilíndrica del lecho (z_{cs}) e inclinación del ángulo de cambio de sección (α). Se ha estudiado, además, el efecto de otro tipo de variables sobre el comportamiento fluidodinámico del lecho como son: cambio de escala, inclusión de elementos internos al lecho (*internals*) para favorecer la ruptura de burbujas o extracción de gas a través de membranas permeoselectivas.

En principio, el uso de un reactor pseudo-bidimensional puede considerarse representativo del comportamiento de una rodaja aislada de un lecho cilíndrico tridimensional, sin entrar a valorar el efecto de las paredes frontal y trasera sobre la hidrodinámica del lecho. Para evaluar la validez de la suposición, se ha simulado por último el régimen de burbujeo en geometría cilíndrica y se ha comparado con los resultados obtenidos en reactores pseudo-2D.

Una vez el comportamiento fluidodinámico del lecho ha sido caracterizado experimentalmente y mediante modelos de flujo de fluidos, se ha estudiado la viabilidad del reactor para integrar los procesos de reacción, regeneración y separación en un proceso catalítico real: la deshidrogenación catalítica de propano (PDH).

Las principales limitaciones de la PDH son su elevada endotermicidad, la existencia de reacciones secundarias a las temperaturas típicas de trabajo, la existencia de un equilibrio termodinámico que limita la conversión del reactivo y la tendencia a la formación de depósitos carbonosos (coque) sobre el catalizador, que lo desactivan a lo largo del tiempo.

El concepto de reactor del RLFDZ-CS+MB es, en principio, ideal para tratar de mitigar las limitaciones del proceso PDH, el cuál resulta de gran interés en la industria química debido al bajo precio del propano y a la demanda creciente de propileno (45, 46).

Por un lado, el uso de un catalizador muy activo y selectivo permite alcanzar conversiones cercanas a las del equilibrio, limitando la existencia de reacciones secundarias. De entre los catalizadores utilizados en literatura para llevar a cabo la deshidrogenación catalítica de propano (zeolita MWW/Ga_2O_3 (47), CrO_x/SiO_2 (48), Pt-Sn/γ-Al_2O_3 (49), Pt-Sn-K/γ-Al_2O_3 (50, 51), Sr-V-Mo/ γ-Al_2O_3 (52), Pt-Sn/SAPO-34 (53), Pt-Sn/$MgAl_2O_4$ (11)), el catalizador basado en platino y estaño soportado sobre aluminato de magnesio, Pt-Sn/$MgAl_2O_4$, es el que conduce a los mejores resultados en deshidrogenación catalítica de alcanos ligeros (11). El catalizador cuenta, como soporte, con una espinela que conserva la elevada superficie específica de los soportes de Al_2O_3 (favoreciendo la dispersión de centros activos), pero lo mejora reduciendo su acidez por adición de Mg, lo que limita la deposición de residuos carbonosos. El platino, aun en bajas cantidades, es muy activo catalíticamente y el estaño estabiliza el catalizador, mejora

la relación deshidrogenación/craqueo y disminuye la capacidad de hidrogenólisis del Pt, reduciendo su sinterización (11).

Por otro, la extracción selectiva de un producto de reacción (hidrógeno, en este caso, a través de membranas densas basadas en paladio), desplaza el equilibrio termodinámico hacia la formación del producto de interés. Además, la desactivación catalítica por deposición de coque puede ser mitigada por el uso de oxígeno en la zona de regeneración del RLFDZ-CS+MB, el cual no solo actúa regenerando la superficie activa del catalizador sino que también compensa parcialmente las necesidades energéticas de la PDH, pudiéndose alcanzar un régimen autotérmico en el sistema bajo ciertas condiciones de operación.

1.2 Alcance y objetivos

El objetivo principal de la presente tesis es caracterizar el comportamiento fluidodinámico de un reactor de lecho fluidizado de dos zonas con cambio de sección y membrana permeoselectiva (RLFDZ-CS+MB) determinando el comportamiento de las fases presentes en el mismo a fin de establecer unas condiciones de trabajo que garanticen el buen comportamiento de la fluidización en dicho reactor y detectar las posibles limitaciones del sistema. Se pretende también caracterizar experimentalmente la deshidrogenación catalítica de propano en RLFDZ-CS con retirada selectiva de hidrógeno a través de membranas densas de paladio, a la que es aplicable la información proveniente del estudio fluidodinámico. Para alcanzar el objetivo principal se presenta una relación de tareas parciales:

1º) Estudiar el grado de mezcla axial de la fase sólida entre las dos zonas del lecho con diferentes atmósferas, en función de las variables de operación que afectan al comportamiento fluidodinámico del reactor. Determinar perfiles de concentración axial de trazadores, haciendo uso de partículas fosforescentes y validar un modelo de mezcla axial, *Countercurrent Backmixing model* (CCBM), para la predicción del grado de mezcla a partir de correlaciones hidrodinámicas (Artículo I).

2º) Implementar la técnica de velocimetría de partículas, PIV, para la medición de flujos densamente cargados de partículas como son los lechos fluidizados. Acoplar el tratamiento digital de imágenes, DIA, con algoritmos PIV para generar mapas de circulación de sólidos y obtener información detallada sobre el comportamiento fluidodinámico del lecho bajo diversas condiciones experimentales (Artículos II y V).

3º) Caracterizar el régimen hidrodinámico de la fase gas a través de la medición de las propiedades características de las burbujas de gas como tamaño, forma, velocidad, frecuencia de aparición, etc. en función de distintas condiciones de operación (Artículos II, III, IV, V, VI, VII y VIII). Implementar un modelo matemático capaz de predecir la evolución axial del tamaño y la velocidad de burbuja en un RLFDZ-CS bajo la influencia de una alimentación de gas adicional y una variación en el tamaño de la sección transversal del lecho (Artículo III).

4º) Validar un modelo computacional multifásico capaz de simular el comportamiento fluidodinámico del RLFDZ-CS en presencia (Artículo VIII) y en ausencia de extracción localizada de gas (Artículos IV, VI y VII).

5º) Estudiar el efecto del ángulo de cambio de sección en la generación de regiones de lecho parcialmente defluidizadas y establecer una geometría de reactor con un grado de inclinación mínima entre las dos zonas del RLFDZ-CS para evitar la aparición de zonas muertas (Artículos I, II, III, IV, VI y VII).

6º) Comparar las características de burbuja en lechos tridimensionales, obtenidas a partir de simulaciones fluidodinámicas, y la proyección frontal de las burbujas observadas en lechos pseudo-bidimensionales. Establecer criterios para adaptar los resultados de burbujeo a reactores tubulares reales (Artículo VIII).

7º) Evaluar el comportamiento fluidodinámico del lecho en presencia de elementos internos (Artículo V) o membranas extractivas (Artículo VII), así como estudiar la afección del cambio de escala en el movimiento de los sólidos y en las características de las burbujas de gas (Artículo VI).

8ª) Estudiar la reacción de deshidrogenación catalítica de propano en un reactor RLFDZ-CS+MB en presencia de un catalizador activo y selectivo a PDH (Pt-Sn/$MgAl_2O_4$) y membranas densas de Pd (Artículo IX) o aleaciones Pd-Ag (Artículo X).

9ª) Aplicar la caracterización fluidodinámica adquirida para esta configuración de reactor. Establecer un rango de temperaturas de operación y fracciones de agente oxidante en la alimentación óptimos para maximizar la producción estacionaria de propileno (Artículos IX y X).

10º) Estudiar el efecto de la presencia de propileno en el ensuciamiento y pérdida de eficacia de la membrana densa por deposición de coque. Cuantificar la reducción de la tasa de permeación en función del contenido en hidrocarburos ligeros (propano y propileno) de la corriente reactiva (Artículo XI).

2 METODOLOGÍA EXPERIMENTAL

2. METODOLOGÍA EXPERIMENTAL

En este capítulo se describen las instalaciones experimentales utilizadas así como la metodología de trabajo seguida para la realización de los experimentos que conforman la presente tesis. La mayor parte del estudio experimental se ha llevado a cabo en los laboratorios del Grupo de Catálisis, Separaciones Moleculares e Ingeniería de Reactores (CREG) en el Instituto Universitario de Investigación en Ingeniería de Aragón (I3A). Sin embargo, la fase experimental relativa al uso de la técnica de velocimetría de partículas, PIV, ha sido realizada en las instalaciones del Grupo de Reactores Multifásicos (SMR) perteneciente a la Universidad Tecnológica de Eindhoven (TUe) en los Países Bajos.

En esencia se han utilizado tres instalaciones diferentes a lo largo de esta tesis: la relativa a los estudios de mezcla axial de sólidos y medidas de burbujeo, la utilizada en el estudio de velocimetría de partículas y la instalación reactiva para llevar a cabo la deshidrogenación catalítica de propano en RLFDZ-CS+MB. Si bien, debido a la diferente disposición del sistema de iluminación y metodología experimental utilizada en los estudios de mezcla axial de sólidos y medidas de burbujeo, se van a describir las dos configuraciones de esta instalación por separado.

2.1 Mezcla axial de sólidos en un RLFDZ-CS

La experimentación se ha llevado a cabo en reactores RLFDZ-CS pseudo-bidimensionales construidos en polimetacrilato Perspex® con las siguientes dimensiones: 300 mm x 40 mm x 8 mm (altura x anchura máxima x profundidad). Los reactores constan de una entrada inferior de gas a través de una placa de vidrio poroso (tamaño de poro: 40 – 75 µm) y una varilla distribuidora de altura variable inmersa en el lecho. Esta varilla, posicionada radialmente en el centro del reactor, alimenta gas al lecho a través de dos orificios (2 mm diámetro) practicados en su base en forma de T, de anchura 10 mm, como se aprecia en la Figura 2.1 (a). La anchura del reactor varía entre las zonas inferior (2 cm) y superior (4 cm) a través de un cambio de sección gradual localizado a 8 cm de altura desde la base del reactor, z_{cs} = 8 cm. Se dispone de varios reactores con distinta inclinación de la sección cónica que conecta ambas zonas del lecho o *ángulo de cambio de sección*, α.

Los experimentos de mezcla se llevan a cabo a temperatura ambiente utilizando aire comprimido como gas de fluidización.

Los sólidos utilizados son partículas fosforescentes, a modo de trazadores ópticos, basadas en aluminato de estroncio dopado con Eu y Dy, suministradas por Materiales Inteligentes S.L. Se

trata de sólidos tipo B en la clasificación de Geldart (54), cuyos tamaño de partícula, densidad y velocidad de mínima fluidización con aire son, respectivamente: d_p = 100 – 320 µm, ρ_{bulk} = 1,5 g/cm^3 y $u_{mf,\ aire\ (25^oC)}$ = 10,1 cm/s.

Dado que el grado de mezcla se va a determinar en función de la intensidad de luz emitida por los trazadores ópticos en la oscuridad, los reactores se encuentran en el interior de una caja negra evitando cualquier entrada de luz externa (Figura 2.1 (b)).

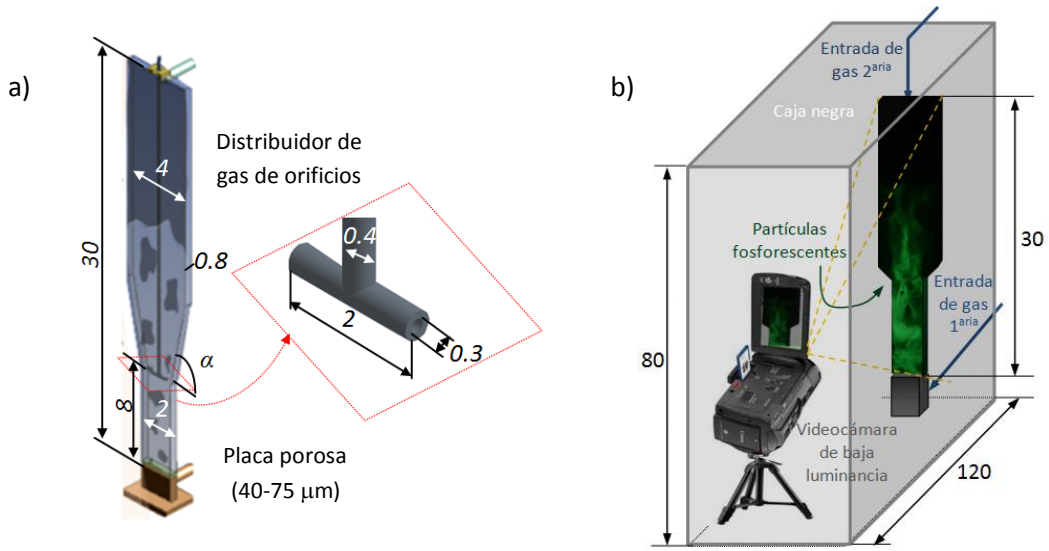

Figura 2.1. a) Esquema del RLFDZ-CS pseudo-2D, b) Instalación experimental para la medición de la mezcla axial de sólidos

El sistema de adquisición de datos consta de una cámara Canon Legria HF R106 Full HD de baja luminancia, capaz de grabar con alta resolución en la oscuridad, conectada a un ordenador para el procesado de imágenes en Matlab® 2010a.

En el presente estudio se ha trabajado con lechos fluidizados con cinco ángulos de cambio de sección: α = 0º, 45º, 60º, 80º, 85º y se ha variado la posición axial de la varilla distribuidora, z_{dis}, desde la base de la sección cónica del lecho (z_{cs}) hasta z_{dis} = 10 cm. Asimismo, se ha realizado un barrido de velocidades de gas, u_{gas}/u_{mf} = 1,5 – 3,5. Así pues, el grado de mezcla axial de trazadores ópticos ha sido analizado bajo el efecto de tres variables: la velocidad relativa de gas alimentado, la posición relativa del distribuidor secundario respecto al cambio de sección y la inclinación de la región cónica del lecho. Los estudios relativos a la determinación de regiones defluidizadas en el lecho se han realizado con la geometría de reactor α = 0º.

Los experimentos parten de un estado de lecho fijo en el cuál se excitan con luz blanca las partículas de la pared frontal ubicadas en la zona inferior del lecho. Tras unos segundos, cesa la excitación y comienza a alimentarse gas. En ese instante comienza la grabación que recoge la evolución de la mezcla axial entre partículas fosforescentes excitadas y no excitadas, inicialmente segregadas en las zons inferior y superior del lecho, respectivamente.

El algoritmo de tratamiento de imágenes implementado en Matlab® R2010a con la ayuda de su herramienta de procesado de imágenes (*Image Processing Toolbox®*) permite obtener perfiles axiales de concentración de trazador a lo largo del tiempo. Para cada sección transversal de 1 cm de altura en la que se divide cada imagen transitoria de mezcla en el lecho se obtiene el histograma en escala de grises en el rango de intensidades: 0 – 255 (Figura 2.2).

El valor medio de intensidad en cada "rodaja" de lecho se relaciona con la concentración axial de trazador, una vez normalizada respecto a las intensidades máxima y mínima correspondientes a las iniciales en las zonas inferior y superior del lecho, respectivamente. Por último, para tener en cuenta el decaimiento sucesivo de la intensidad de luz emitida por el trazador, se fuerza el área bajo la curva de concentración de trazador, $C_t(z)$, a permanecer constante a lo largo del tiempo corrigiendo las concentraciones normalizadas. Este post-procesado de imágenes de mezcla es similar al método usado por Grasa y Abanades (55). En el Anexo A.1 se detalla el código Matlab desarrollado para la obtención de perfiles axiales de concentración de trazador.

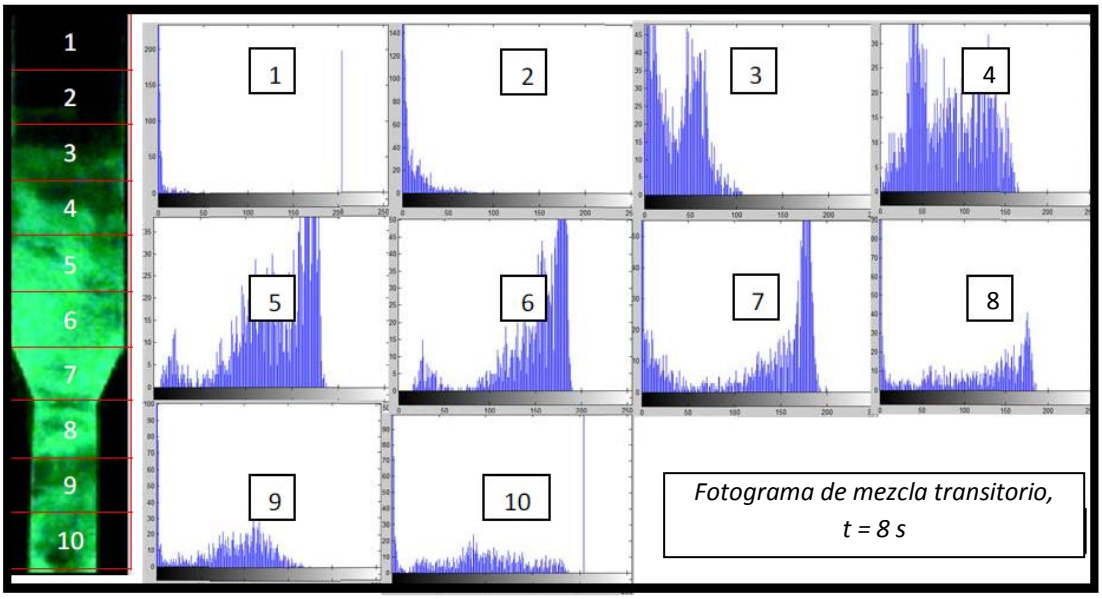

Figura 2.2 Histograma de cada "rodaja" de lecho para un fotograma de mezcla transitorio

Una vez se dispone de los perfiles axiales de concentración de trazador a lo largo del tiempo de mezcla es posible determinar el grado de mezcla o *Índice de Mezcla* (*IM*) entre partículas iluminadas y no iluminadas, inicialmente segregadas. *IM* puede tener valores en el rango [0 – 1] (de segregación total a mezcla completa) aunque, eventualmente, podría superar el valor 1 si la concentración de trazador llegase a ser mayor en la zona superior del lecho que en la inferior. La descripción matemática de *IM* se muestra en la ecuación 1, siendo z_{max} la altura máxima del lecho, z_{ilum} la altura inicialmente iluminada y $C(z,t)$ la concentración de trazador a una altura z y tiempo *t*. C_∞ representa la concentración de trazador a tiempo infinito (mezcla completa).

$$IM = \frac{\int_{z_{ilum}}^{z_{max}} C(z,t) \cdot dz}{(z_{max} - z_{ilum}) C_\infty} \qquad \text{(E.1)}$$

2.2 Medida de burbujeo en un RLFDZ-CS

La instalación experimental, así como la geometría y dimensiones de los reactores, son análogas a las descritas en la Sección 2.1, salvo en la disposición de los equipos y en el método de análisis de imágenes. En este caso, la pared frontal de los reactores es transparente mientras que la pared trasera es traslúcida para evitar una iluminación no homogénea del

lecho, ya que se utiliza una iluminación constante desde la parte trasera del reactor hacia la lente de la cámara para mejorar el contraste de imagen entre las fracciones huecas del lecho o *burbujas* de gas y la fase densa o *emulsión*. La disposición de la instalación se detalla en la Figura 2.3. El gas de fluidización es, igualmente, aire comprimido.

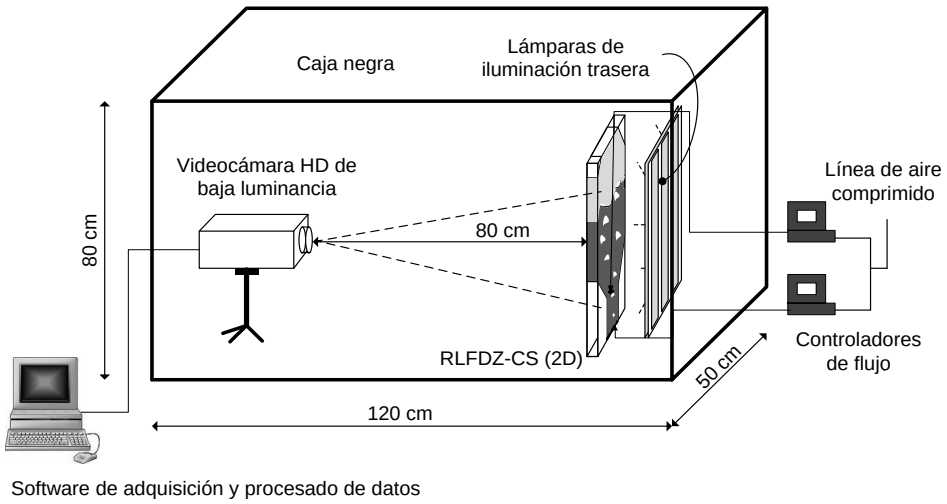

Figura 2.3. Esquema de la instalación experimental para las medidas de burbujeo

Se ha estudiado, igualmente, el efecto de la velocidad de gas, localización del distribuidor secundario y ángulo de cambio de sección en el régimen de burbujeo del RLFDZ-CS pero, además, se ha analizado el efecto del tipo de partícula fluidizada en dicho régimen. Para ello, se han utilizado tanto partículas fosforescentes de distintos tamaños como γ-alúmina (catalizador o soporte catalítico de uso común) y esferas de vidrio, usualmente utilizadas en experimentos fluidodinámicos en frío. Las principales propiedades de cada tipo de partícula se detallan en la Tabla 2.1.

Tabla 2.1 Propiedades de las partículas fluidizadas

	d_p (μm)	ρ_{bulk} (g/cm^3)	ε_{lecho}(-)	$u_{mf,aire\ (25ºC)}$ (cm/s)
Esferas de vidrio	480 ± 60	1,5	0,40	20,5
γ-Al_2O_3	135 ± 30	0,8	0,47	1,2
Part. Fosforesc. A	195 ± 50	1,5	0,58	10,1
Part. Fosforesc. B	680 ± 100	1,3	0,64	48,5

Tanto el reactor como la cámara HD de baja luminancia (la misma descrita anteriormente) se encuentran en el interior de una caja negra para evitar reflexiones de luz en la pared delantera del lecho provenientes de la iluminación del laboratorio.

En todos los casos experimentados se han adquirido datos de burbujeo tales que, al menos, 50 burbujas diferentes hayan atravesado el lecho completamente para asegurar resultados estadísticamente fiables en cuanto a tamaño, velocidad, forma y posición de burbujas (de acuerdo con la estadística clásica, una serie de 30 valores o más permite estimar con suficiente fiabilidad la media poblacional).

Las características de burbuja han sido determinadas a partir de un algoritmo de procesado de imágenes implementado en Matlab para discernir fases burbuja y emulsión a partir del mapa de intensidades de cada imagen (Figura 2.4). El código utilizado a tal efecto se detalla en el Anexo A.2.

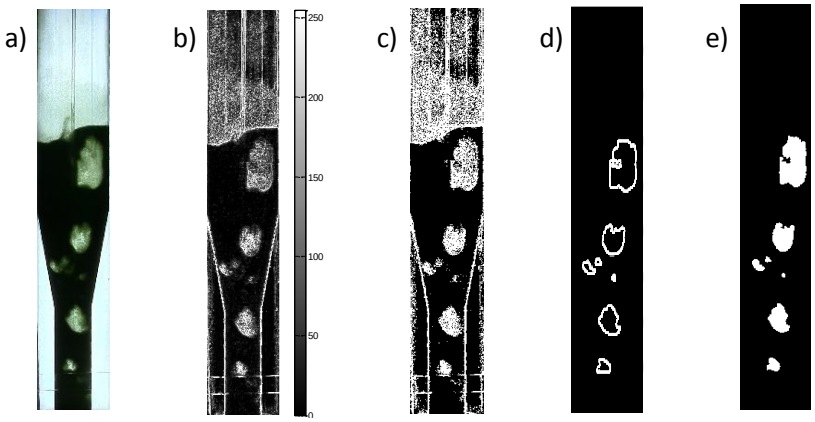

Figura 2.4 Detección de burbujas en experimentos de fluidización en RLFDZ-CS: a) fotograma original, b) gradiente espacial de intensidades, c) suavizado del mapa de gradientes y mejora del contraste, d) filtrado de los límites del lecho y detección del contorno de burbujas, e) imagen binaria

El fotograma RGB original (a) se transforma en escala de grises y se determina su mapa de gradientes de intensidad (b) entre píxeles adyacentes. A fin de obtener el contorno de las burbujas, se suaviza la señal del mapa de gradientes y se mejora su contraste (c) ecualizando el histograma de intensidades. A continuación, se filtran los contornos del reactor así como la superficie libre del lecho y se establece un valor umbral, I_{umb}, de gradiente de intensidad para determinar el contorno de las burbujas (d). Por último, se binariza la imagen (e) de modo que las regiones delimitadas por los contornos de burbuja representan la fase burbuja mientras que las regiones externas a dichos contornos representan la fase emulsión.

La correcta definición del contorno de las burbujas es esencial para obtener resultados representativos. En este trabajo se han descrito los contornos de burbuja como aquellas regiones en las que se alcanzan gradientes de intensidad iguales o superiores al 25% de la amplitud total del rango de intensidades de la imagen (0 – 255).

El diámetro equivalente de burbuja se calcula como el diámetro de una esfera que ocupa el mismo volumen que una burbuja o, por analogía en un sistema bidimensional, el diámetro de una burbuja circular que ocupa la misma área que una burbuja en un lecho pseudo-bidimensional, como muestra la ecuación 2 en la que *rf* representa la resolución del fotograma (cm^2/pixels) y A_i el área de la burbuja i.

$$d_{b,i} = \sqrt{\frac{4\,A_i}{\pi} rf^2} \tag{E.2}$$

$$\overline{d_{b,J}}(z) = \frac{\sum_{i=1}^{n} d_{b,i}(z) \cdot d_{b,i}(z)}{\sum_{i=1}^{n} d_{b,i}(z)} \tag{E.3}$$

Por un lado, desde el punto de vista fluidodinámico, cuanto más grande es una burbuja mayor es su influencia sobre el transporte y la mezcla axial de sólidos. Por otro, desde el punto de

vista de la catálisis heterogénea, las burbujas más grandes representan problemas de contacto entre el gas y el sólido a evitar. Por este motivo, el diámetro de burbuja equivalente promedio ha sido calculado otorgando a cada burbuja un peso proporcional a su tamaño, según describe la ecuación 3.

Por su parte, la velocidad de burbuja se calcula comparando la posición axial del centroide de burbuja entre fotogramas consecutivos. Para identificar burbujas entre fotogramas se utiliza el algoritmo del "vecino más próximo" (*nearest-neighbour algorithm* (56)), minimizando la distancia global entre datos de burbuja relativos a tamaño, posición del centroide y relación de aspecto bajo las siguientes restricciones:

a) La posición axial del centroide de una burbuja no puede ser mayor en el fotograma previo que en el posterior. Esto supone que las velocidades "negativas" no son tenidas en cuenta en el cómputo estadístico de velocidades de burbuja.

b) No se consideran en el estudio estadístico aquellas burbujas cuyo diámetro equivalente cambie más de un 20% entre fotogramas consecutivos (37).

c) Para un fotograma cualquiera cada burbuja debe corresponderse, como máximo, con una burbuja del fotograma previo. Esto evita que los datos estadísticos de velocidad de burbuja queden influenciados por una deficiente identificación de burbujas en caso de coalescencia o ruptura de burbujas.

2.3 Fluidodinámica del lecho

El estudio experimental del movimiento de sólidos en el interior de un RLFDZ-CS se ha llevado a cabo mediante las técnicas de velocimetría de partículas (PIV) y análisis digital de imágenes (DIA), a fin de determinar simultáneamente el campo vectorial de velocidades de sólido y la distribución volumétrica de sólidos en el lecho a lo largo del tiempo. Ambas técnicas se han empleado en ensayos con RLFDZ-CS pseudo-bidimensionales y su fundamento se describe a continuación.

2.3.1 Velocimetría de partículas (PIV)

La técnica de análisis PIV, originalmente desarrollada para visualizar flujos de fluidos utilizando trazadores dispersos, fue adaptada recientemente (57-61) a sistemas gas-sólido densamente cargados de partículas. Entre las ventajas de la técnica destaca su simplicidad, su carácter no intrusivo (esencial cuando se quiere estudiar el comportamiento fluidodinámico de sistemas muy pequeños como el actual) y la detallada información acerca del movimiento de las fases presentes en el reactor con elevada resolución espacial y temporal. El inconveniente es la necesidad de acceso visual al sistema y, por tanto, la restricción del estudio a sistemas pseudo-bidimensionales.

El modo en el que PIV determina campos instantáneos de velocidad a lo largo del lecho se basa en la comparación de los mapas de intensidades para dos fotogramas consecutivos obtenidos con escaso margen temporal. Cada fotograma se divide en pequeñas regiones (*interrogation areas*) y se establece una correlación entre cada región del primer fotograma y su correspondiente región en el siguiente. Así, la velocidad instantánea en cada región del

lecho se obtiene como el cociente entre el desplazamiento promedio más probable del grupo de partículas que integran la región y el paso temporal entre fotogramas consecutivos (Figura 2.5).

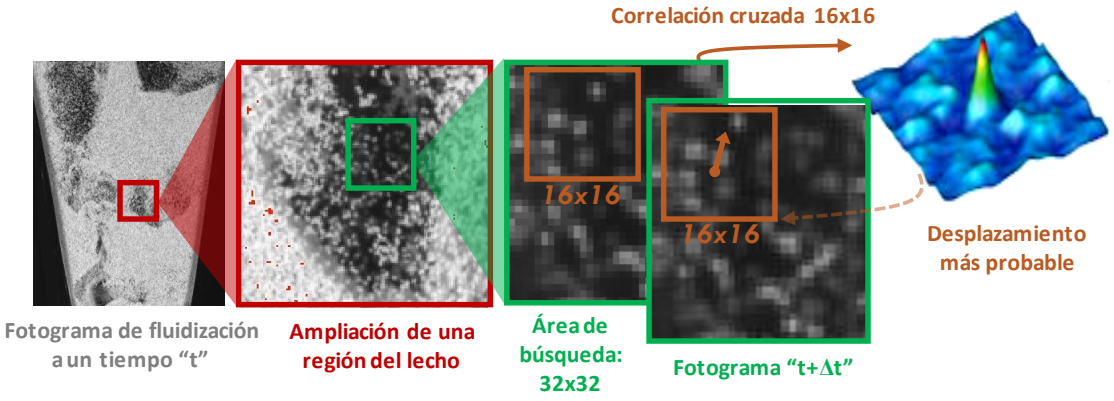

Figura 2.5 Esquema de funcionamiento del algoritmo de velocimetría de partículas (PIV)

En este estudio se ha utilizado un algoritmo de correlación multi-paso con reducción de área, considerando inicialmente un primer paso con *interrogation areas* de 32x32 pixeles y posteriormente dos pasos a 16x16 píxeles. De este modo, se reduce el ruido de la imagen y se incrementa la resolución espacial. Para tener en cuenta aquellas partículas que debido a su desplazamiento entre fotogramas exceden los límites de cada región, se ha considerado un 50% de solapamiento de regiones en todas las direcciones de tal forma que es posible analizar todos y cada uno de los movimientos de partículas que tienen lugar en la pared frontal del lecho.

Los mapas de velocidad obtenidos vía PIV no informan por sí solos del flujo de sólidos, ya que el algoritmo no discrimina zonas densamente cargadas de partículas frente a zonas diluidas. Por tanto, es necesario hacer un tratamiento de imágenes para establecer unos mapas de porosidad tales que sea posible calcular la fracción de sólidos en cada región del lecho y poder acoplar ambos mapas (velocidad y densidad de sólidos) para estimar flujos másicos.

2.3.2 Análisis Digital de Imagen (DIA)

El tratamiento de imágenes o *Digital Image Analysis* (DIA) aplicado a lechos fluidizados fue iniciado hace dos décadas por Agarwal y cols. (62) para detectar burbujas de gas. Posteriormente, Goldschmidt y cols. (63) utilizaron la técnica para detectar partículas. Desde entonces, varios autores han tratado de desarrollar tratamientos de imagen capaces de establecer un mapa de porosidades volumétricas de lecho a partir de imágenes 2D. El algoritmo DIA convencional aplicado a lechos fluidizados es capaz de discriminar burbujas y emulsión en base a la diferencia de intensidad de los pixeles en la imagen. La binarización de la imagen respecto a una intensidad umbral divide el lecho en dos fases: burbuja (libre de sólido) y emulsión (porosidad constante). Dicho algoritmo corrige los mapas de velocidad generados por PIV filtrando aquellas velocidades detectadas en el interior de burbujas de gas. Sin embargo, las variaciones locales de la porosidad no se tienen en cuenta y, además, las intensidades no contienen información de la porosidad interna del lecho, ya que ésta no es visible desde su proyección frontal, por lo que el uso del mapa de intensidades de las

imágenes adquiridas como medida de la fracción volumétrica de sólidos puede introducir errores (64).

Para mejorar la precisión del tratamiento de imágenes convencional y considerar el efecto de la profundidad del lecho en la porosidad del mismo, De Jong y cols. (64) y van Buijtenen y cols. (60) desarrollaron una correlación entre el mapa de intensidades y la fracción volumétrica de sólidos a partir de la reconstrucción artificial de imágenes obtenidas de simulaciones DPM (*Discrete Particle Modeling*). Estos autores encontraron que la porosidad volumétrica aumenta linealmente con la intensidad a bajas intensidades mientras que crece asintóticamente hasta el límite máximo de empaquetamiento del lecho fluidizado a altas intensidades en función de unos parámetros de ajuste *A* y *B* cuyo valor va en función de la relación entre la profundidad del lecho y el tamaño de partícula, $\Delta z/d_p$. La correlación entre intensidad (o porosidad 2D) y fracción volumétrica de sólidos (o porosidad 3D) se muestra en la ecuación 4.

$$\begin{cases} \varepsilon_{s,3D} = \dfrac{\varepsilon_{s,2D}}{1 - \dfrac{\varepsilon_{s,2D}}{B}} A, & for\ \varepsilon_{s,3D} < \varepsilon_{s,3D\ max} \\ \varepsilon_{s,3D} = \varepsilon_{s,3D\ max}, & for\ \varepsilon_{s,3D} \geq \varepsilon_{s,3D\ max} \end{cases} \quad \text{(E.4)}$$

Las imágenes creadas artificialmente con DPM suponen una intensidad frontal homogénea y una caída de intensidad lineal con la profundidad del lecho. La primera premisa rara vez se cumple experimentalmente por lo que la correlación no puede aplicarse directamente a las grabaciones originales. Por tanto, es necesario realizar un procesado de imagen previo al uso de la correlación. Las operaciones a realizar incluyen la eliminación de inhomogeneidades en la iluminación del lecho, el suavizado de la variación local de intensidades y la normalización de las intensidades para homogeneizar la luminosidad de la fase emulsión (tal y como ocurre en las imágenes artificiales obtenidas del análisis DPM). Por último, los parámetros *A* y *B* de la correlación se ajustan de tal modo que se minimice el error en la determinación de la masa total del lecho. La Figura 2.6 ilustra el procesado de imágenes realizado para obtener el mapa de fracciones volumétricas de sólido a partir de las grabaciones originales. En el Anexo A.3 se detalla el algoritmo utilizado para el tratamiento de imágenes.

Por su parte, la Figura 2.7 ilustra de manera esquemática el proceso a seguir para determinar el mapa instantáneo de flujo de sólidos a partir de los datos recogidos por velocimetría de partículas (PIV) y análisis digital de imágenes (DIA).

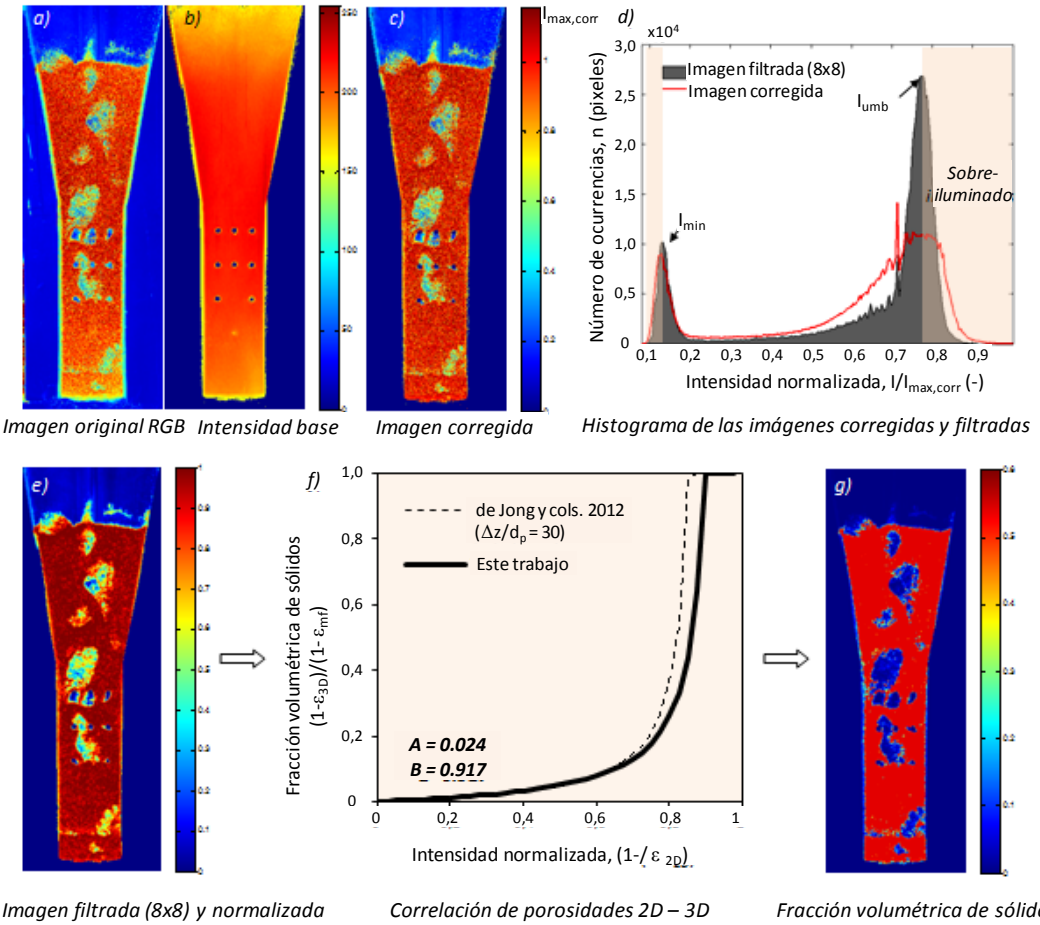

Figura 2.6 Análisis DIA: a) Imagen original, b) Mapa de intensidades de base, c) Imagen corregida, d) Histograma antes y después de aplicar un filtro de imagen (8x8), e) Imagen normalizada en el rango 0-1, f) correlación entre intensidad y fracción volumétrica de sólidos, g) mapa de porosidades 3D

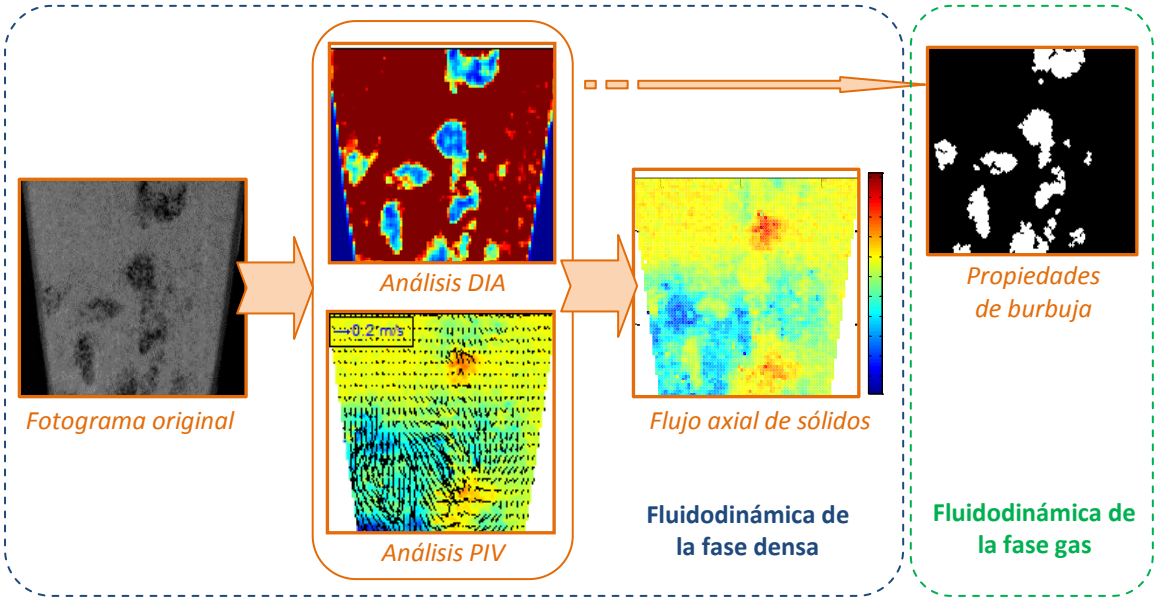

Figura 2.7 Procedimiento para analizar el flujo de sólidos y las propiedades de burbuja en un RLFDZ-CS

2.3.3 Metodología experimental PIV/DIA

En la experimentación PIV, la iluminación del lecho es delantera a base de lámparas LED. La pared trasera del reactor es opaca (negra) y la varilla de vidrio se hace igualmente oscura para aumentar el contraste entre las burbujas de gas y la emulsión, para no producir reflexiones de luz sobre la lente de la cámara ni distorsionar el procesado de imágenes. Además, se utiliza una cámara de ultra-alta frecuencia y alta resolución (*LaVision Imager Pro*) para detectar el movimiento de partículas discretas en detalle y un software de procesado de imagen (*DaVis 8.0.3*) para llevar a cabo el análisis PIV mediante correlación cruzada de imágenes consecutivas tomadas a tiempos muy próximos. La frecuencia de grabación se ajustó a 750 Hz tomando pares de imágenes consecutivas con retardo de 0,3 ms para un tiempo total grabación de 36 segundos. La resolución de imagen se ajustó a 90 pixels/cm o, lo que es lo mismo, entre 2 y 3 píxels por partícula, de acuerdo con los requerimientos de la técnica para un post-procesado de imagen adecuado (58, 64, 65, 71). La frecuencia de grabación o, análogamente, la apertura del obturador se adaptaron a la intensidad de la iluminación del lecho evitando sobreexposición o baja iluminación en las grabaciones.

Como gas de fluidización, se utilizó aire comprimido haciéndolo pasar por un humidificador a fin de controlar su humedad y reducir la carga electrostática entre las partículas sólidas y las paredes del lecho. Las variables objeto de estudio para los ensayos PIV/DIA fueron las ya comentadas en los apartados 2.1 y 2.2 (velocidad de gas, posición del distribuidor inmerso y ángulo de cambio de sección), además del efecto del cambio de escala y la presencia de diversas configuraciones de elementos internos (*internals*) en el comportamiento fluidodinámico del sistema.

2.3.4 Variantes de lecho: concepto de escalado y dimensionado de reactores a escala

La experimentación relacionada con PIV se ha llevado a cabo en reactores RLFDZ-CS de dos tamaños diferentes para estudiar el efecto del escalado en el comportamiento fluidodinámico del lecho.

Tal y como describen Knowlton y cols. (65), el proceso de escalado consiste en aplicar un conjunto de parámetros adimensionales y similitud geométrica (derivado de las ecuaciones hidrodinámicas para flujo multifásico adimensionalizadas) para modificar la escala de un sistema. Los diferentes parámetros adimensionales independientes entre sí conforman el denominado conjunto de Glicksman: número de Reynolds, número de Froude, ratio entre densidades de gas y partícula y longitudes adimensionales (ratio entre tamaño de partícula y tamaño de lecho, cociente entre diámetro y altura de lecho, esfericidad de partículas, distribución de tamaños de partícula) (66, 67).

De acuerdo con el proceso de escalado, los valores físicos del sistema no tienen por qué coincidir entre escalas, pero sí deberían hacerlo los números adimensionales. En la práctica, mantener constantes todos los grupos adimensionales citados anteriormente resulta extremadamente complejo. Di Maio y Di Renzo (68) resumen algunos conjuntos de grupos adimensionales adoptados por diversos autores para llevar a cabo el proceso de escalado de sus respectivos reactores. No obstante, la adopción de leyes de escalado basadas en igualdad de grupos adimensionales no garantiza la reproducibilidad de las condiciones hidrodinámicas entre escalas y, a menudo, resulta inaceptable (65, 69, 70). Basta considerar la adaptación del

tamaño de partícula para mantener constante la ratio d_p/D_{lecho} entre escalas de reactor. En tal caso, puede que el aumento de tamaño de partícula conlleve un cambio de tipo de sólido en la clasificación de Geldart (54) modificándose dramáticamente el comportamiento de la fluidización de las partículas entre escalas. En ese caso, la información recogida de la experimentación puede no ser directamente aplicable al proceso.

Por ello, los reactores a escala utilizados en el presente estudio duplican en tamaño (altura y anchura) a aquellos a pequeña escala, sin modificar las propiedades del lecho: distribución de tamaños de partícula, densidad de sólidos y profundidad del lecho se mantienen constantes.

En concreto, a pequeña escala las dimensiones y geometría de los reactores utilizados coinciden con las descritas en las secciones 2.1 y 2.2. Los reactores construidos a mayor escala poseen las siguientes dimensiones: 65 x 8 x 0,8 cm (altura x anchura máxima x profundidad). La anchura máxima se corresponde con la de la zona superior del lecho. La zona inferior tiene una anchura de 4 cm, una altura de 12 cm y la pendiente de cambio de sección forma 80º con respecto a la posición horizontal (α = 80º). Las dimensiones de la varilla distribuidora inmersa en el lecho así como el tamaño de poro de la placa distribuidora inferior coinciden con los descritos en las secciones previas.

En el caso de los reactores a mayor escala, se han fluidizado sólidos fosforescentes con tamaño de partícula comprendido entre 200-320 μm y densidad y porosidad de lecho, ρ_{bulk} = 1,43 g/cm^3 y ε_{lecho} = 0,58, respectivamente. Respecto a la experimentación descrita en las secciones 2.1 y 2.2, el rango de tamaños de 100-200 μm se ha descartado para adecuar el tamaño de partícula a la resolución de la técnica. La velocidad de mínima fluidización para esta distribución de partículas es de 10,1 cm/s en aire a 25ºC, de acuerdo con la curva de pérdida de carga vs. velocidad de gas llevada a cabo en un reactor cilíndrico.

2.3.5 Variantes de lecho: uso de elementos internos

La disposición de un banco de tubos en el interior de un lecho fluidizado, bien a modo de intercambiadores de calor (72-76), a modo de membranas permeoselectivas para la adición o retirada de gas (35, 36, 61) o como obstáculos internos para la ruptura de burbujas (37, 77-79), normalmente da lugar a una disminución de la mezcla axial de sólidos (ej. (80, 81)). Sin embargo, si el banco de tubos se localiza en una región del lecho en la que normalmente se producen *slugs*, o burbujas lentas de gran tamaño que ocupan la sección transversal del lecho produciendo un cortocircuito en la mezcla axial de sólidos, la ruptura de dichas burbujas podría no solo mejorar el contacto entre el gas y el sólido en el lecho sino también reducir el tiempo de circulación de sólidos.

Para estudiar el efecto del uso de elementos internos en el comportamiento fluidodinámico del RLFDZ-CS, se ha dispuesto un banco de tubos en la zona inferior del lecho escalado con seis configuraciones diferentes. Las dimensiones de los tubos y su localización en el lecho se detallan en la Figura 2.8.

En las configuraciones *3i*, *4i*, *5i* y $6i_s$ los tubos están dispuestos al tresbolillo (alternos), mientras que las configuraciones $6i_h$ y *8i* tienen sus filas de tubos alineadas verticalmente. El objetivo del estudio es evaluar cuál de las configuraciones es más efectiva para reducir el tamaño de burbuja promedio en la zona estrecha del lecho y mejorar así el contacto entre el

gas y el sólido en dicha región. Tomando como referencia la configuración *5i*, la disposición *3i* permite estudiar cómo afecta la ausencia de la primera fila de tubos (z_{1r}) en el perfil axial de tamaños de burbuja, así como la existencia de un tubo central en z_{0r} para la configuración $6i_s$. Se evalúa también la eficacia de la configuración alterna de cuatro tubos (*4i*) frente a la de cinco (*5i*) y, análogamente, se compara la reducción del diámetro de burbuja equivalente entre las configuraciones al tresbolillo y las alineadas.

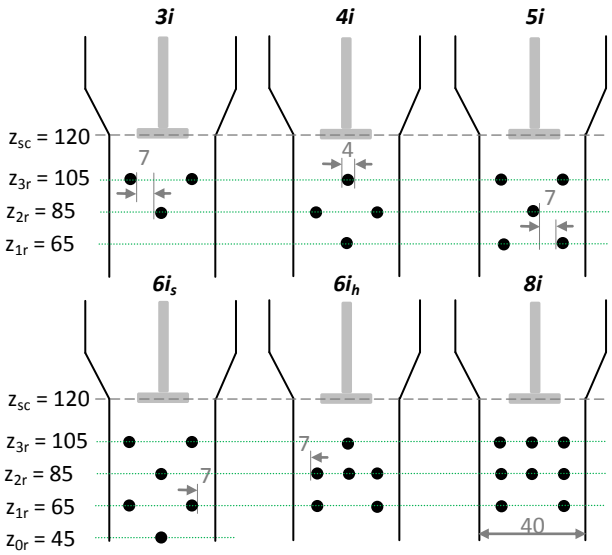

Figura 2.8 Configuraciones de banco de tubos utilizadas en RLFDZ-CS

2.4 Deshidrogenación catalítica de propano: instalación y metodología experimental

2.4.1 Montaje experimental

La planta experimental empleada para la llevar a cabo la deshidrogenación catalítica de propano se puede describir en torno a cuatro secciones diferenciadas: línea de alimentación, sistema de reacción, línea de productos de reacción y línea de gas permeado.

La alimentación consta de las líneas de gases utilizados en reacción: propano (agente reactivo), oxígeno (regenerador del catalizador), argón (inerte para dilución de gases reactivos) e hidrógeno (reductor de los óxidos metálicos del catalizador). Dichas líneas de gas son conducidas hacia el sistema reactivo correspondiente: bien un reactor de lecho fluidizado convencional (RLF), lecho fluidizado de dos zonas con cambio de sección (RLFDZ-CS) o reactor de dos zonas con membrana permeoselectiva (RLFDZ-CS+MB). En los dos primeros casos, el sistema consta de una única salida de gases, que se lleva a un cromatógrafo micro-GC (SRA Instruments, modelo R3000) para analizar su composición. En caso de utilizar la configuración RLFDZ-CS+MB, el reactor consta de una salida de gases adicional para retirar hidrógeno del lecho de manera selectiva por succión a través de una bomba de vacío (Telstar, modelo 2P-3). Esta última configuración es la mostrada en la Figura 2.9.

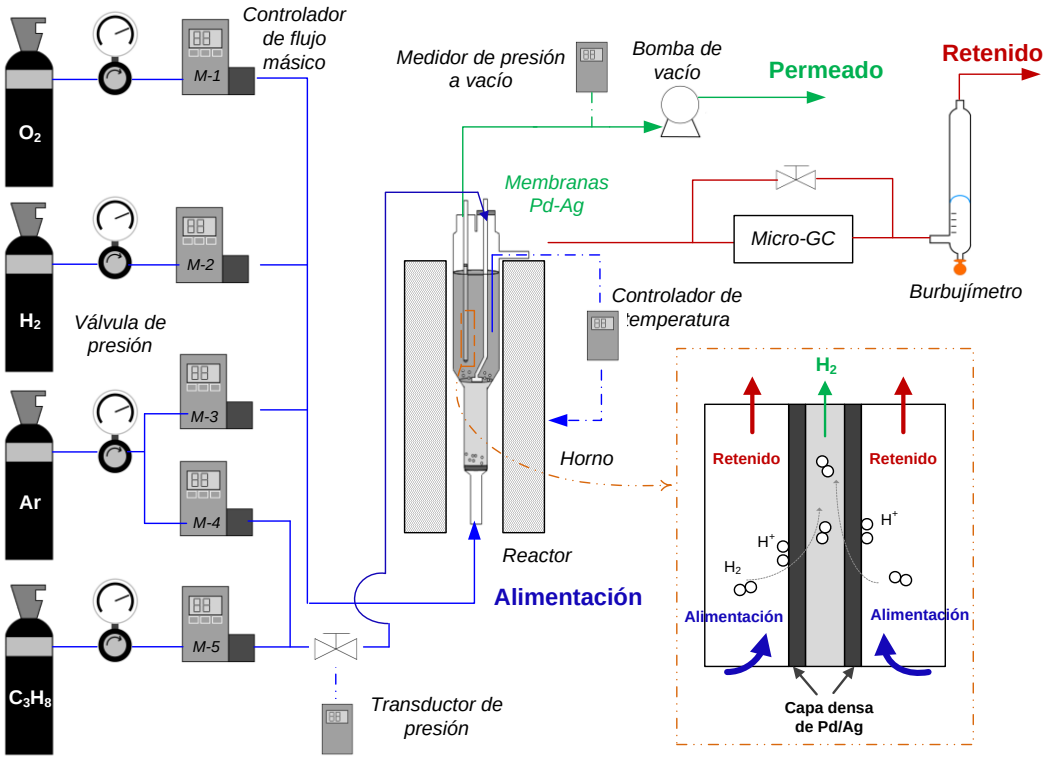

Figura 2.9 Instalación experimental para llevar a cabo la deshidrogenación catalítica de propano en reactor RLFDZ-CS+MB

Como se ilustra en la Figura 2.9, todas las líneas de la sección de la alimentación poseen su manorreductor y medidor de flujo másico correspondiente (Brooks Instruments, modelo 5850TR), con el objetivo de controlar la presión y el flujo de alimentación de cada uno de los gases empleados en el proceso (C_3H_8, Ar, H_2 y O_2). Además, la presión del sistema se controla a través del transductor de presión situado a la entrada del reactor. El reactor está fabricado en cuarzo y se encuentra alojado dentro de un horno eléctrico, cuya temperatura se controla mediante un lazo de control constituido por un termopar en contacto con el lecho y alojado en una vaina de temperatura, controlador de temperatura y resistencias eléctricas. Los gases de salida del reactor se analizan, previa calibración, en el cromatógrafo micro-GC, forzando su entrada con una válvula de aguja situada justo detrás de la entrada del cromatógrafo. El caudal de salida se mide con un medidor de burbuja. La bomba de vacío conectada a la membrana permite retirar el hidrógeno de la zona de reacción, pudiendo medir la presión de esta línea con un medidor de presión a vacío (Vacuubrand, modelo DVR2). Todas las conexiones se han realizado empleando tuberías de nylon y uniones rápidas.

Se han utilizado dos tipos de membrana densa tubular para la permeación selectiva de hidrógeno, basadas en paladio y en aleación Pd-Ag, respectivamente. Las primeras fueron sintetizadas y suministradas por el departamento de Ingeniería Química del Imperial College de Londres. Las segundas son membranas comerciales suministradas por *REB® Research & Consulting*. Las características de ambas se detallan en la Tabla 2.2.

El menor espesor de la capa densa de Pd en la membrana no-comercial favorece la permeación en detrimento de la resistencia a la atrición en contacto con las partículas del

lecho fluidizado. Para acoplar dicha membrana en un RLFDZ-CS es necesario usar una membrana externa a modo de carcasa protectora a fin de evitar el desgaste de la capa de paladio y la pérdida de selectividad a hidrógeno. En el caso de las membranas comerciales, el mayor espesor de capa densa Pd-Ag les confiere una elevada resistencia a la atrición en detrimento del flujo de permeación. Su mayor resistencia mecánica posibilita su uso en contacto directo con el lecho fluidizado sin deteriorar su permeoselectividad.

Tabla 2.2. Características de las membranas permeoselectivas utilizadas

	Membrana Pd (Imperial College)	Membrana 75%Pd-25%Ag (REB® Research & Consulting)
Longitud (mm)	52	153
Diámetro externo (mm)	2	3,17
Superficie permeable (cm^2)	3,2	15,2
Espesor capa densa (μm)	~5	76
Tipo de soporte	Fibra hueca (γ-Al_2O_3)	Acero inoxidable poroso

2.4.2 Síntesis y caracterización del catalizador

Para llevar a cabo la síntesis del catalizador de Pt-Sn/$MgAl_2O_4$, utilizado como material de lecho a lo largo de toda la serie experimental, se ha seguido minuciosamente el método de co-precipitación descrito por Armendáriz y cols. (82). El soporte formado por una espinela de aluminato de magnesio se ha preparado a partir de nitratos de magnesio y aluminio. El Pt y Sn se han adicionado al soporte por impregnación a humedad incipiente con soluciones acuosas de $SnCl_2$ y H_2PtCl_6 hidratados. Se ha realizado la caracterización del soporte de $MgAl_2O_4$ mediante un análisis XRD para corroborar su estructura de espinela, así como un análisis BET para conocer su superficie específica, S_{BET} = 123 m^2/g.

A continuación, se ha realizado un estudio fluidodinámico del catalizador para determinar su velocidad de mínima fluidización, u_{mf} = *0,175 cm^3 (STP)/cm^2s*. Con este ensayo ha sido posible conocer el caudal de gas necesario para asegurar una buena transferencia de sólido entre zonas dentro del reactor. Con el fin de alcanzar unas propiedades catalíticas estables y reproducibles durante reacción, el catalizador se ha sometido, posteriormente, a varios ciclos de reducción-reacción-regeneración en presencia de H_2 diluido, C_3H_8 y O_2 diluido respectivamente, siguiendo el método descrito en el Artículo X del compendio.

2.4.3 Reacción: deshidrogenación de propano (PDH)

El estudio completo del proceso de deshidrogenación, incluyendo el efecto de la temperatura de reacción, caudal de agente regenerante, factor de dilución o retirada selectiva de productos de reacción, se ha llevado a cabo a partir de los experimentos descritos en la Tabla 2.3. Para el diseño de experimentos, algunas variables de operación se han fijado a lo largo de la serie experimental y otras se han variado según los siguientes criterios:

a) El caudal total de gas empleado en todos los experimentos debe coincidir, independientemente de que se trate de un RLF o RLFDZ-CS+MB. Para ello es necesario establecer una velocidad relativa de gas ($u_r = u_{gas}/u_{mf}$) tal que se asegure una buena fluidización en todos los puntos del lecho.

b) El peso de catalizador empleado en cada serie de experimentos se ha de mantener invariable. Esto permite que la relación de alturas de lecho de catalizador entre la zona de reacción y regeneración ($W_{cat,reac}/W_{cat,reg}$) en el RLFDZ-CS+MB sea constante.

c) La deshidrogenación de propano viene limitada por el equilibrio termodinámico. Es por ello que se debe trabajar a temperaturas suficientemente altas, en el rango 500ºC – 600ºC, para alcanzar conversiones aceptables.

d) La temperatura de reacción no puede ser demasiado elevada, ya que puede producirse la sinterización de los componentes activos del catalizador. Además, la temperatura de operación también se encuentra condicionada por el uso de las membranas, que pueden llegar a deteriorarse a temperaturas por encima de 575ºC, de acuerdo con la información facilitada por el fabricante.

e) La proporción de propano en la alimentación se variará entre el 30 y el 70% del caudal total de gas a la entrada, independientemente de tratarse de un RLF convencional (dilución con Ar) o de un RLFDZ-CS+MB (dilución con mezcla Ar-O_2).

En un primer lugar se ha llevado a cabo la reacción de deshidrogenación catalítica de propano en un RLFDZ-CS con ausencia de oxígeno, convirtiéndolo así en un reactor de lecho fluidizado (RLF) convencional. De esta forma se consigue descartar el efecto de la configuración del reactor en la variabilidad de los resultados y se posibilita conocer la desactivación del catalizador por formación de coque, además de analizar la influencia de la temperatura sobre la cantidad de coque formada y la velocidad de la desactivación del catalizador. Posteriormente, se ha llevado a cabo la reacción de deshidrogenación en el RLFDZ-CS barriendo las temperaturas de reacción comprendidas entre 500 y 575ºC. A continuación, se ha realizado la reacción en el RLFDZ-CS+MB bajo las mismas condiciones de operación que en el RLFDZ-CS a las diferentes temperaturas de reacción a fin de comparar el comportamiento de las distintas configuraciones de reactor empleadas. Finalmente, se ha llevado a cabo una nueva tanda de experimentos en el RLFDZ-CS y en el RLFDZ-CS+MB variando la relación $W_{cat}/Q_{C3H8,0}$ a través del cambio del porcentaje de propano en la alimentación, con el objetivo de conocer la influencia que tiene esta variable en el proceso. Por último, se ha realizado un nuevo experimento a 550ºC para comprobar la reproducibilidad de los resultados obtenidos durante la fase experimental.

Tabla 2.3. Condiciones de operación para PDH en RLFDZ-CS+MB

	RLF	RLFDZ-CS	RLFDZ-CS+MB
$T_{reacción}$ (ºC)	500 – 575	500 – 575	500 – 575
$Q_{total,0}$ (cm^3/min)	162	162	162
$C_3H_{8,alimentación}$ (%)	50	30 – 70	30 – 70
$W_{catalizador}$ (g)	70	70	70
$W_{cat}/Q_{C3H8,0}$ (kg·s/cm^3)	0,052	0,086 – 0,037	0,086 – 0,037
$u_{r,reac}$ (-)	1,75	1,75	1,75
$u_{r,reg}$ (-)	2,50	2,50	2,50
$O_{2,0}$ (%)	-	1 – 5	1 – 5

3 MODELADO Y SIMULACIÓN FLUIDODINÁMICA DE RLFDZ-CS+MB

3. MODELADO Y SIMULACIÓN FLUIDODINÁMICA DE UN RLFDZ-CS+MB

En este capítulo se detallan los modelos matemáticos sugeridos para modelar la evolución del tamaño de burbuja con la posición axial en el lecho y la mezcla axial de sólidos así como las ecuaciones del modelo fluidodinámico utilizado para simular el comportamiento del Reactor de Lecho Fluidizado de Dos Zonas con Cambio de Sección y Membrana permeoselectiva (RLFDZ-CS+MB).

En primer lugar, se describirá el modelo de retromezcla a contracorriente (*Countercurrent Backmixing*, CCBM) utilizado para predecir la evolución de la mezcla axial de trazadores ópticos entre las dos zonas del RLFDZ-CS.

A continuación, se presentará el modelo *Julián-Herguido-Menéndez*, JHM, o correlación desarrollada en este estudio para predecir la evolución axial de las características de burbuja (diámetro equivalente, velocidad ascensional) teniendo en cuenta el efecto de la entrada adicional de gas y el ensanchamiento del lecho.

Por último, se detallará el listado de ecuaciones que conforman la aproximación euleriana o modelo de dos fluidos (*Two-Fluid Model*, TFM) para simular el comportamiento fluidodinámico del lecho. Asimismo, se describirán las condiciones de contorno del dominio de computación y los parámetros introducidos en la simulación.

3.1 Modelo de retromezcla a contracorriente (CCBM)

La experimentación y el procesado de imágenes proporcionan una valiosa información sobre el grado de mezcla axial en lechos fluidizados. Sin embargo, son procedimientos costosos en cuanto a tiempo y recursos materiales. Por ello, la implementación de un modelo de mezcla axial capaz de predecir cualitativamente la tasa de mezcla de sólidos bajo determinadas condiciones de operación en un RLFDZ-CS resulta necesaria para ahorrar recursos experimentales.

El transporte de sólidos en el interior de un RLFDZ-CS ha sido modelado con una versión modificada del clásico modelo *Countercurrent Backmixing* (CCBM) para lechos fluidizados. Dicho modelo, originalmente propuesto por van Deemter en 1961 (20) y generalizado por Gwyn y cols. (83), describe el lecho como un sistema trifásico (burbuja – estela – emulsión, Figura 3.1 (a)) en el que la estela o fase sólida ascendente intercambia sólidos con la emulsión o fase sólida descendente (84) de acuerdo con el esquema de circulación propuesto en la Figura 3.1 (b) considerando un elemento diferencial de altura de lecho, *dz*.

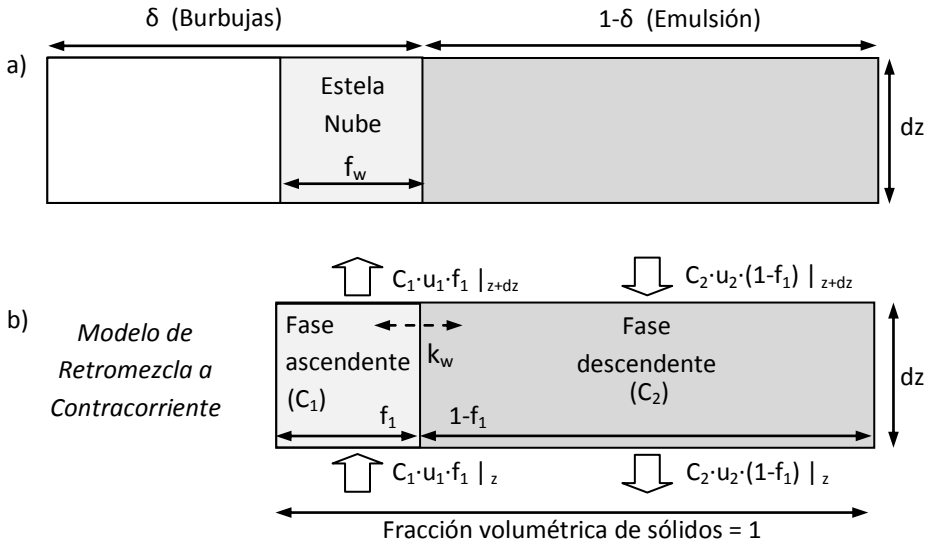

Figura 3.1 a) Modelo clásico de tres fases (burbuja, estela-nube, emulsión), b) Modelo de Retromezcla a Contracorriente (CCBM) para estimar la circulación axial de sólidos en un lecho fluidizado

El balance de materia para estela (o fase ascendente) y emulsión (o fase descendente) está representado por un sistema de ecuaciones en derivadas parciales hiperbólicas (83). Las ecuaciones 5 y 6 representan la evolución temporal de la concentración de trazador en la estela (C_1) y en la emulsión (C_2) en función de la posición axial en el lecho. En estas ecuaciones se define la estela como aquella fracción volumétrica de la fase sólida, f_1, que asciende con una velocidad u_1 intercambiando sólidos la emulsión con una tasa volumétrica k_w. Dicha fase emulsión constituye una fracción volumétrica del sólido total ($1-f_1$) y su velocidad descendente es $u_2 = u_1 f_1 / (1-f_1)$ (55, 85, 86).

$$\frac{\partial C_1}{\partial t} = u_1 \frac{\partial C_1}{\partial z} + K_w (C_1 - C_2) \qquad \text{(E.5)}$$

$$\frac{\partial C_2}{\partial t} = -u_1 \frac{f_1}{1-f_1} \frac{\partial C_2}{\partial z} + K_w \frac{f_1}{1-f_1} (C_2 - C_1) \qquad \text{(E.6)}$$

La resolución a dicho sistema de ecuaciones se ha implementado en *Matlab® 2010a* a partir del método cinemático descrito por Grasa y Abanades (86) consistente en desacoplar las variables espacio (z) y tiempo (t). De este modo, se aproxima el fenómeno de mezcla a partir de la discretización de las fases estela y emulsión en pequeños compartimentos que realizan desplazamientos axiales instantáneos (Δz) tras haber pasado cierto tiempo intercambiando

sólidos con la fase adyacente (Δt). La extensión del desplazamiento axial es el producto de las velocidades de fase respectivas (u_1 o u_2) por el tiempo de intercambio (Δt). En consecuencia, la concentración de trazador en cada posición axial del lecho viene dada por la concentración promedio entre la de la estela y la de la emulsión. La descripción del sistema según el método cinemático se detalla en las ecuaciones 7 a 10. En el Anexo A.4 se detalla el algoritmo de cálculo utilizado.

$$C_1(t+\Delta t) = C_1(t)\left(e^{\frac{-k_w}{(1-f_1)}\Delta t} + f_1\left(1 - e^{\frac{-k_w}{(1-f_1)}\Delta t}\right)\right) + C_2(t)\,(1-f_1)\left(1 - e^{\frac{-k_w}{(1-f_1)}\Delta t}\right) \quad \text{(E.7)}$$

$$C_2(t+\Delta t) = C_1(t)\,(1-f_1)\left(1 - e^{\frac{-k_w}{(1-f_1)}\Delta t}\right) + C_2(t)\left(1 - (1-f_1)\left(1 - e^{\frac{-k_w}{(1-f_1)}\Delta t}\right)\right) \quad \text{(E.8)}$$

$$\Delta z = \overline{u_1}\,\Delta t \quad \text{(E.9)}$$

$$C_i = C_{1,i}\,f_1 + C_{2,i}\,(1-f_1) \quad \text{(E.10)}$$

La estimación de los parámetros del modelo, u_1, f_1 y k_w, se puede realizar a partir de correlaciones empíricas existentes en la literatura. Dichos parámetros representan valores promedio a lo largo del lecho, calculados a partir de la geometría y de las condiciones de operación del RLFDZ-CS.

Según Kunii y Levenspiel (18), el perfil axial de velocidad ascensional de la estela depende de la velocidad de burbuja y de la fracción de burbujas en el lecho, δ. Asimismo, según Davidson y Harrison (19), la velocidad de burbuja depende del exceso de gas y del tamaño de burbuja. La ecuación 11 muestra la correlación que permite determinar $u_1(z)$ en función de $d_b(z)$, $u_{gas}(z)$ y δ, donde la fracción de burbujas en el lecho puede ser estimada a partir de la expansión promedio del lecho y el perfil $d_b(z)$ a partir del modelo JHM (sección 3.2).

$$u_1(z) = (1-\delta)\,u_b(z) = (1-\delta)\left((u_{gas}(z) - u_{mf}) + 0{,}4\left(g\,d_b(z)\right)^{0{,}5}\right) \quad \text{(E.11)}$$

Por otro lado, la fracción del sólido que asciende en forma de estela (f_1) puede ser calculada a partir de un balance de materia a las tres fases presentes en el modelo CCBM. Asumiendo que la fracción volumétrica de las burbujas ocupada por la estela (f_w) supone aproximadamente un 20% independientemente del tamaño de las burbujas y del tipo de sólido, según sugieren algunos autores (87-90), la ecuación 12 muestra la dependencia de f_1 con la fracción de burbujas en el lecho.

$$f_1 = \frac{\delta f_w}{\delta f_w + 1 - \delta} = \frac{0{,}2\,\delta}{1 - 0{,}8\,\delta} \quad \text{(E.12)}$$

Por último, el coeficiente de intercambio estela-emulsión (k_w) ha sido descrito por varios autores (81, 91-93) como un factor proporcional a la velocidad relativa de gas e inversamente proporcional al diámetro de burbuja equivalente. En este trabajo se utilizará la correlación de Lim y cols. (93) para estimar k_w (ecuaciones 13 y 14).

$$k_w = \frac{7{,}5\ (u_r - 1)}{d_b} \quad si \quad u_r \leq 3 \tag{E.13}$$

$$k_w = \frac{15}{d_b} \quad si \quad u_r > 3 \tag{E.14}$$

3.2 Correlación '*Julián-Herguido-Menéndez*' (JHM)

La particular configuración del reactor RLFDZ-CS hace que ninguna de las correlaciones existentes para predecir la evolución de las propiedades de burbuja con la altura del lecho sea capaz de estimar correctamente la tendencia experimental encontrada en este trabajo respecto al crecimiento y velocidad de las burbujas.

De entre las correlaciones propuestas por diversos autores, englobadas en dos revisiones recientes (94, 95), solo algunas de ellas han sido obtenidas para lechos de anchura limitada en los que se tiene en cuenta el efecto de las paredes laterales en el crecimiento de burbujas. Quienes establecieron este tipo de correlaciones, esencialmente Mori y Wen (96), Horio y Nonaka (97) y Agarwal (98), describen un crecimiento de las burbujas asintótico limitado por la anchura del lecho. Los dos últimos autores sugieren correlaciones complejas basadas en numerosos parámetros empíricos mientras Mori y Wen desarrollaron una simple correlación basada en un diámetro de burbuja máximo hipotético en función de la velocidad del gas y el diámetro de la columna, con validez en un amplio rango de condiciones de operación.

La comparación cualitativa entre datos obtenidos en reactores RLFDZ-CS y las predicciones de varias correlaciones clásicas sugiere que el modelo de Mori y Wen (MW) es el que mejor se ajusta a los resultados experimentales de la zona inferior del lecho. Sin embargo, ninguna de las correlaciones es capaz de predecir la evolución del tamaño promedio de burbuja más allá de la zona de cambio de sección con alimentación adicional de gas.

La reducción del diámetro de burbuja equivalente que se ha observado experimentalmente en la zona cónica del lecho puede estar relacionada con dos efectos acoplados. Por un lado, las burbujas provenientes de la parte inferior del lecho intercambian gas con la emulsión (reduciendo su tamaño) para mantener el régimen de mínima fluidización en la fase densa al ensancharse la sección de paso. Por otro lado, las burbujas provenientes del distribuidor inmerso son inicialmente pequeñas, provocando la disminución del tamaño de burbuja promedio en las proximidades del punto de inyección. Los diversos flujos de gas considerados en la región cónica del lecho se muestran en la Figura 3.2.

Para analizar la disminución del tamaño de burbuja en las proximidades de la región cónica para las burbujas provenientes de la sección inferior del lecho, se ha planteado un balance de materia a la fase gas entre dos secciones transversales con distinta área de paso en el lecho, S_0 y S_{1e}. La velocidad relativa en cierta sección de paso S podría expresarse como: $u_{r,s} = Q_{gas,s} / Q_{mf,s}$. Considerando que todo el exceso de gas sobre el de mínima fluidización fluye ascensionalmente en forma de burbujas, que todo el gas cedido por las burbujas se invierte en alcanzar el régimen de mínima fluidización en cualquier punto de la zona cónica y que la velocidad mínima de fluidización es independiente de la sección de paso, se puede relacionar el caudal en burbujas en la sección '*1e*' respecto al de la sección '*0*'. A su vez, el cociente de

caudales de burbuja puede expresarse en función del cociente de diámetros equivalentes al cuadrado. Considerando la geometría del reactor (el ángulo de cambio de sección, α) y profundidad de lecho constante, la ecuación 15 ilustra la reducción axial del tamaño de burbuja a través de la región cónica por intercambio de gas entre burbuja y emulsión.

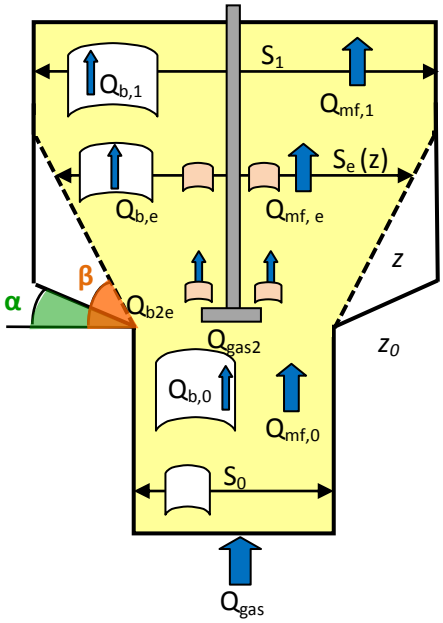

Figura 3.2 Esquema del flujo de gases en la región de transición del RLFDZ-CS

Por otro lado, se ha observado que si el ángulo que forma la pared cónica con la horizontal es demasiado pequeño se produce la defluidización de los sólidos ubicados inmediatamente sobre la pared inclinada. La geometría de las zonas de sólido defluidizadas formadas eventualmente a ambos lados de la región cónica forma, a su vez, un ángulo respecto a la posición horizontal denominado ángulo de zona muerta o *ángulo de defluidización*, β. El ángulo de defluidización, zona muerta o ángulo de talud es característico de cada tipo de partículas y régimen de fluidización (velocidad de gas) utilizado y se ha demostrado que afecta a las propiedades de burbuja a lo largo de la zona cónica. Si las condiciones de operación son tales que $\beta > \alpha$, α debe ser sustituido por β en la ecuación 15.

$$d_{b,1e} = d_{b,0}\sqrt{1+\frac{1}{u_{r,0}-1}\left(1-\frac{S_{1e}}{S_0}\right)} = d_{b,0}\sqrt{1-2\cdot\frac{z_{1e}-z_0}{(u_{r,0}-1)L_0\,tan\,\alpha}} \qquad \text{(E.15)}$$

El intervalo de posiciones axiales en el que tiene validez la ecuación 15 está comprendido entre z_{cs} y $(z_{cs} + tan\,\beta\cdot(L_1-L_{cs})/2)$. En el caso en que $\alpha > \beta$, la posición superior seguiría siendo la altura máxima de la hipotética región defluidizada correspondiente a las condiciones de operación (tipo de partícula y flujo de gas) utilizadas.

En lo que respecta a las burbujas incipientes inyectadas a través del distribuidor de gas inmerso en el lecho, se les considera independientes del flujo de gas proveniente de la zona inferior del lecho y, por tanto, su perfil de tamaño de burbujas se estima directamente con la

correlación de Mori y Wen. Esta aproximación es asumible ya que el tamaño de las burbujas que abandonan el distribuidor secundario es muy pequeño respecto a la anchura del lecho en su zona cónica.

Como resultado, el tamaño de burbuja promedio en la zona de transición puede ser descrito como el resultado de dos contribuciones: las burbujas provenientes del distribuidor inmerso y las que ascienden desde la zona inferior del lecho reduciendo su tamaño. Suponiendo que la frecuencia de aparición de los dos tipos de burbuja es similar, el tamaño medio de burbuja en la región de coexistencia se calcula como el promedio de ambas contribuciones.

Por último, en la parte cilíndrica superior del lecho, la evolución del tamaño se modela con la correlación de Mori y Wen una vez supuesta la unificación de ambas contribuciones de burbujeo. Las ecuaciones 16 a 24 describen la formulación del modelo JHM completo.

- *Zona inferior del lecho*:

$$z < z_0: \qquad d_b(z) = 0{,}65\left(\frac{\pi}{4}{D_{down}}^2\, u_{mf}\,(u_{r,0}-1)\right)^{0,4}\,(1-exp\,(-0{,}3z/D_{down})) \tag{E.16}$$

- *Región cónica*:

· Burbujas provenientes de la zona inferior del lecho (distribuidor primario):

$$z_1 > z > z_0: \qquad d_{b,1e}(z) = d_{b,0}\sqrt{1+\frac{1}{u_{r,0}-1}\left(1-\frac{S_{1e}}{S_0}\right)} = d_{b,0}\sqrt{1-\frac{z-z_0}{(u_{r,0}-1)\,tan\,\beta}} \tag{E.17}$$

· Burbujas incipientes del distribuidor secundario:

$$z_1 > z > z_0: \qquad d_{b,orif}(z) = d_{b,m} - \left(d_{b,m} - d_{b,orif}(z_0)\right) exp\,(-0{,}3z/D_{up}) \tag{E.18}$$

siendo:

$$d_{b,m} = 0{,}65(\pi/4\,{D_{up}}^2\,u_{mf}\,(u_{r,1}-1))^{0,4} \tag{E.19}$$

· Burbuja promedio en la zona de transición:

$$z_1 > z > z_0: \qquad d_b(z) = \frac{d_{b,1e}(z)^2 + d_{b,orif}(z)^2}{d_{b,1e}(z) + d_{b,orif}(z)} \tag{E.20}$$

- *Zona superior del lecho*:

· Burbujas provenientes del distribuidor primario:

$$z > z_1: \qquad d_{b,1}(z) = d_{b,m1} - \left(d_{b,m1} - d_{b,1}(z_1)\right) exp\,(-0{,}3z/D_{up}) \tag{E.21}$$

siendo:

$$d_{b,m1} = 0{,}65(\pi/4\,{D_{up}}^2\,u_{mf}\,(u_{r,0}-1))^{0,4} \tag{E.22}$$

· Burbujas provenientes del distribuidor secundario:

$$z > z_1: \;\; d_{b,orif}(z) = d_{b,m} - \left(d_{b,m} - d_{b,orif}(z_1)\right) exp\,(-0.3z/D_{up}) \tag{E.23}$$

· Burbuja promedio en la zona de transición:

$$z > z_1: \qquad d_b(z) = \frac{d_{b,1}(z)^2 + d_{b,orif}(z)^2}{d_{b,1}(z) + d_{b,orif}(z)} \tag{E.24}$$

Por otro lado, de acuerdo con la correlación de Davidson-Harrison (19) para predecir la velocidad promedio de burbuja, u_b es función del exceso de gas sobre el de mínima fluidización y del tamaño de las burbujas según la ecuación 25.

$$u_b = \left(u_{gas} - u_{mf}\right) + K\sqrt{g\, d_b} \tag{E.25}$$

Estos autores describen el valor del parámetro empírico *K* como 0,4 para lechos pseudo-2D y 0,71 para lechos cilíndricos. Para un RLFDZ-CS, la variación axial del diámetro de burbuja se puede determinar aplicando del modelo JHM. Asimismo, el exceso de gas sobre el de mínima fluidización se puede calcular teniendo en cuenta la geometría del lecho (α) y la ubicación de la entrada adicional de gas. Acoplando las correlaciones de Davidson-Harrison y Mori-Wen al modelo JHM para predecir el comportamiento en la zona cónica del lecho con aporte de gas, es posible realizar la descripción matemática del perfil axial de velocidades de burbuja en un RLFDZ-CS.

3.3 Modelo computacional de dos fluidos (TFM)

De entre los modelos computacionales existentes para describir el comportamiento fluidodinámico de un reactor de lecho fluidizado, el modelo Euleriano-Euleriano o modelo de dos fluidos (*Two-Fluid Model*, TFM) es el preferido para simular lechos de gran tamaño y tamaño medio ya que ofrece un razonable compromiso entre precisión y coste computacional (99-102). La aproximación Euleriana supone la consideración las fases gas y sólida como fases fluidas continuas e interpenetrables, donde el volumen de una fase no puede ser ocupado por otra. De este modo surge el concepto de fracción volumétrica de fase (ε_i), en relación con el concepto experimental de porosidad del lecho. En la presente tesis se han utilizado dos códigos comerciales para resolver los balances de materia y de cantidad de movimiento que se detallan en las ecuaciones 26 a 28 para las dos fases (*i*), gas y sólido, presentes en el sistema: Ansys CFX® y Ansys Fluent®.

$$\frac{\partial}{\partial t}(\varepsilon_i \rho_i) + \nabla \cdot (\varepsilon_i \rho_i \vec{v}_i) = 0 \tag{E.26}$$

$$\frac{\partial}{\partial t}\left(\varepsilon_g \rho_g \vec{v}_g\right) + \nabla \cdot \left(\varepsilon_g \rho_g \vec{v}_g \vec{v}_g\right) = -\varepsilon_g \nabla P + \varepsilon_g \nabla \cdot \bar{\bar{\tau}}_g + \varepsilon_g \rho_g \bar{g} + K_{gs}(\vec{v}_g - \vec{v}_s) \tag{E.27}$$

$$\frac{\partial}{\partial t}(\varepsilon_s \rho_s \vec{v}_s) + \nabla \cdot (\varepsilon_s \rho_s \vec{v}_s \vec{v}_s) = -\varepsilon_s \nabla P - \nabla P_s + \varepsilon_s \nabla \cdot \bar{\bar{\tau}}_s + \varepsilon_s \rho_s \bar{g} + K_{gs}(\vec{v}_s - \vec{v}_g) \tag{E.28}$$

En esencia, ambos simuladores CFD son aptos para estudiar el comportamiento fluidodinámico de sistemas multifásicos. Sin embargo, el modo en el que ambos discretizan el dominio

computacional para resolver el conjunto de ecuaciones en derivadas parciales hiperbólicas y la variedad de modelos y parámetros fluidodinámicos implementados difiere notablemente, como se comentará más adelante. Es por ello que, en función del grado de detalle, tiempo de computación y estabilidad numérica requeridos, sea más adecuado usar uno u otro software para llevar a cabo las simulaciones.

En concreto, las librerías de Fluent contienen un mayor número de modelos y parámetros para simular flujos multifásicos que las de CFX, por lo que proporcionan al usuario más recursos para adaptar el modelo de flujo a las características del sistema a simular. Esto suele redundar en una mayor precisión en los resultados, siempre y cuando los modelos y parámetros seleccionados sean los adecuados. Por el contrario, el algoritmo de cálculo de CFX es más estable y rápido necesitándose, por lo general, menos iteraciones para alcanzar la convergencia (103-105).

Dado que el estudio estadístico de las propiedades de burbuja en un lecho fluidizado requiere una gran cantidad de datos de burbuja debido a su elevada variabilidad espacio-temporal, se ha usado CFX para modelar el régimen de burbujeo, por su menor coste computacional y mayor estabilidad, lo que permite llevar a cabo simulaciones más largas.

Adicionalmente, las simulaciones realizadas en Fluent han servido para validar las anteriores y para extraer una información más precisa del comportamiento fluidodinámico de la fase densa, analizando la variabilidad espacial de la porosidad del lecho y de la velocidad ascensional de sólidos.

En las ecuaciones de conservación del momento para las fases gas y sólido (ecuaciones 27 y 28) la parte izquierda representa los términos de transporte temporal y espacial, mientras que la parte derecha representa el sumatorio de las fuerzas que interactúan en las fases gas y sólido, respectivamente. Estas fuerzas son: flotabilidad, pérdida de carga, esfuerzo viscoso, gravedad y fuerza de arrastre interfacial. K_{gs} representa el coeficiente de transferencia de momento en la interfase y $\bar{\bar{\tau}}_i$ es el tensor del esfuerzo de deformación de la fase *i*. Las fuerzas de sustentación, fuerzas debidas a cuerpos externos, fuerzas másicas virtuales o de lubricación de pared no se consideran significativas frente a las fuerzas de arrastre y no han sido incluidas en el modelo.

La resolución del sistema de ecuaciones diferenciales requiere de ecuaciones extra de cierre para describir la interacción entre las fases presentes. Dichas ecuaciones de cierre, implementadas en cada uno de los códigos comerciales utilizados, están basadas en correlaciones empíricas y determinan la capacidad predictiva del modelo fluidodinámico. En este estudio, el coeficiente de transferencia de momento entre las fases sólido-fluido (K_{gs}) se ha estimado mediante la función de arrastre de Gidaspow. Esta función considera la expresión propuesta por Wen y Yu para regiones diluidas ($\varepsilon_g > 0{,}8$) y la ecuación de Ergun basada en la pérdida de carga en lechos fijos para zonas densamente cargadas en sólidos ($\varepsilon_g \leq 0{,}8$). Para evitar fallos de cálculo, tanto CFX como Fluent modifican el modelo original de Gidaspow por una interpolación lineal entre las correlaciones de Wen y Yu y Ergun (ecuaciones 29 y 30) en el rango de fracciones volumétricas de gas $0{,}7 < \varepsilon_g \leq 0{,}8$.

$$\varepsilon_g \leq 0{,}8 \;\rightarrow\; K_{gs} = 150\frac{\varepsilon_s(1-\varepsilon_g)\mu_g}{\varepsilon_g {d_p}^2} + 1{,}75\frac{\varepsilon_s\rho_g|\vec{v}_s-\vec{v}_g|}{d_p} \tag{E.29}$$

$$\varepsilon_g > 0{,}8 \;\rightarrow\; K_{gs} = \frac{3}{4}C_D\frac{\varepsilon_s\rho_g|\vec{v}_s-\vec{v}_g|}{d_p}{\varepsilon_g}^{-1{,}65} \tag{E.30}$$

Donde el coeficiente de arrastre, C_D, se estima a partir de la correlación de Schiller-Naumann (ecuación 31).

$$C_D = \begin{cases} \frac{24}{\varepsilon_g Re_s}\left[1 + 0{,}15(\varepsilon_g Re_s)^{0{,}687}\right] & Re_s \leq 1000 \\ 0{,}44 & Re_s > 1000 \end{cases} \tag{E.31}$$

siendo Re_s el número de Reynolds de partícula:

$$Re_s = \frac{d_p\rho_g\left|\vec{v}_s - \vec{v}_g\right|}{\mu_g} \tag{E.32}$$

Por otro lado, se supone que el tensor de deformación para la fase *i* (gas o sólido) sigue la relación de deformación newtoniana dada por la ecuación 33:

$$\overline{\overline{\tau}}_i = \varepsilon_i\mu_i\left(\nabla\vec{v_i} + \nabla\vec{v_i}^T\right) + \varepsilon_i(\lambda_i - \frac{2}{3}\mu_i)\nabla\cdot\vec{v_i}\overline{\overline{I}} \tag{E.33}$$

donde λ_i y μ_i representan la viscosidad volumétrica y la dinámica e $\overline{\overline{I}}$ el tensor unidad. La viscosidad volumétrica (*bulk viscosity*) de los sólidos está referida a la resistencia a la compresión o expansión de partículas granulares mientras que la de los gases mediría la diferencia entre presiones termodinámicas y mecánicas. En este trabajo, la viscosidad de la fase sólida ha sido modelada en base a la correlación de Lun y cols. (106) (ecuación 34). Sin embargo, de acuerdo con la suposición de Stoke para fluidos newtonianos, la contribución de la viscosidad del gas no ha sido considerada en el modelo (107).

$$\lambda_s = \frac{4}{3}{\varepsilon_s}^2\rho_s d_p g_0(1+e)\left(\frac{\theta}{\pi}\right)^{1/2} \tag{E.34}$$

En la ecuación 34, g_0 representa la función de distribución radial descrita por Lun y Savage (108), θ la temperatura granular y *e* el coeficiente de restitución de colisiones inelásticas entre partículas. El valor del coeficiente de restitución se ha variado entre simulaciones en el rango 0,90-0,95 mientras que la temperatura granular ha sido determinada de manera algebraica bajo la suposición de equilibrio local en la ecuación de transporte: la energía producida es igual a la disipada. Una descripción más detallada del modelo fluidodinámico del equilibrio algebraico utilizado por el software de simulación, se puede ver en la guía teórica del usuario de CFX-solver (109).

La viscosidad dinámica de la fase sólida (μ_s) se ha modelado en base a la suma de tres contribuciones: colisional, friccional y cinética, de acuerdo con la ecuación 35. Fluent utiliza el modelo de Gidaspow (110) para las viscosidades colisional (ecuación 36) y cinética (ecuación 37), así como el de Schaefer (111) para la viscosidad friccional (ecuación 38) en el cual, el ángulo de fricción interna (φ) se ha fijado en 30º. Por su parte, Ansys CFX omite las

contribuciones friccional y cinética, calculando μ_s como la viscosidad colisional a partir de la correlación de Gidaspow (110).

$$\mu_s = \mu_{s,col} + \mu_{s,fr} + \mu_{s,kin} \tag{E.35}$$

$$\mu_{s,col} = \frac{4}{5}{\varepsilon_s}^2 \rho_s d_p g_0 (1+e)\left(\frac{\theta}{\pi}\right)^{1/2} \tag{E.36}$$

$$\mu_{s,kin} = \frac{5\rho_s d_p \sqrt{\theta\pi}}{48 g_0 (1+e)}\left[1 + \frac{4}{5} g_0 \varepsilon_s (1+e)\right]^2 \tag{E.37}$$

$$\mu_{s,fr} = \frac{P_s \ \sin\varphi}{2\sqrt{I_{2D}}} \tag{E.38}$$

Por último, la presión de la fase sólida se ha modelado de acuerdo a la teoría cinética de los gases adaptada a las colisiones inelásticas entre partículas y al máximo empaquetamiento del lecho (fracción volumétrica máxima de la fase sólida), $\varepsilon_{s,m}$, fijado en 0,65, según se describe en la ecuación 39.

$$P_s = \varepsilon_s \rho_s \theta\left(1 + 2\ \varepsilon_s g_0 (1+e)\right) \tag{E.39}$$

Tanto en CFX como en Fluent, el conjunto de ecuaciones del modelo se ha resuelto por el método de volúmenes finitos para las diferentes geometrías de reactores RLFDZ-CS ilustradas en la Figura 3.3. Según dicho método, el dominio computacional se divide en volúmenes de control, aplicando los principios de conservación de materia y cantidad de movimiento a cada volumen.

La diferencia entre ambas herramientas de cálculo radica en el modo en el que se implementa el método de volúmenes finitos, bien centrado en las celdas delimitadas por los nodos de la malla (Fluent) o bien centrado en los vértices o nodos de la malla (CFX), según se esquematiza en la Figura 3.4.

La aproximación centrada en celdas requiere el uso de métodos de interpolación para aproximar el valor de las variables en el centro de cada celda. La elección del método de interpolación puede suponer un gran impacto en la estabilidad numérica, tasa de convergencia y precisión de los resultados (103). Por su parte, la aproximación centrada en vértices supone la discretización de cada uno de los elementos (caras) que conforman el volumen de control alrededor de cada vértice para resolver el modelo computacional.

En ambos simuladores se ha utilizado un método de resolución “segregado” tal que los campos de presión y velocidad (relacionados en la ecuación de cantidad de movimiento del modelo) no se determinan simultáneamente sino que se resuelven de modo iterativo. Se propone un campo de presiones inicial y se resuelven las ecuaciones de momento obteniéndose un campo de velocidades. Si el campo de velocidades resultante no satisface la ecuación de continuidad se corrige la presión y se resuelve de nuevo la ecuación de cantidad de movimiento, repitiendo el proceso hasta que se satisfagan tanto los balances de materia como de cantidad de movimiento. En ambos casos se utiliza un criterio de convergencia basado en errores

residuales de cierre de balances inferiores a 10^{-3}. El esquema de corrección de presión utilizado en este trabajo es el denominado SIMPLE (*Semi Implicit Method for Pressure Linked Equations*).

La discretización numérica de las ecuaciones del modelo de dos fluidos se ha llevado a cabo mediante diferencias finitas de primer orden (*first-order upwind scheme*) para las fracciones volumétricas de fase en la ecuación de continuidad y de segundo orden (*second-order upwind scheme*) para presiones y velocidades en la ecuación de cantidad de movimiento. Asimismo, los gradientes espaciales se han discretizado por el método de mínimos cuadrados. Para discretizar los términos transitorios se ha usado el método de Euler implícito, siendo de orden 1 (numéricamente más estable) para las simulaciones en Ansys CFX y de segundo orden (más preciso) en Ansys Fluent.

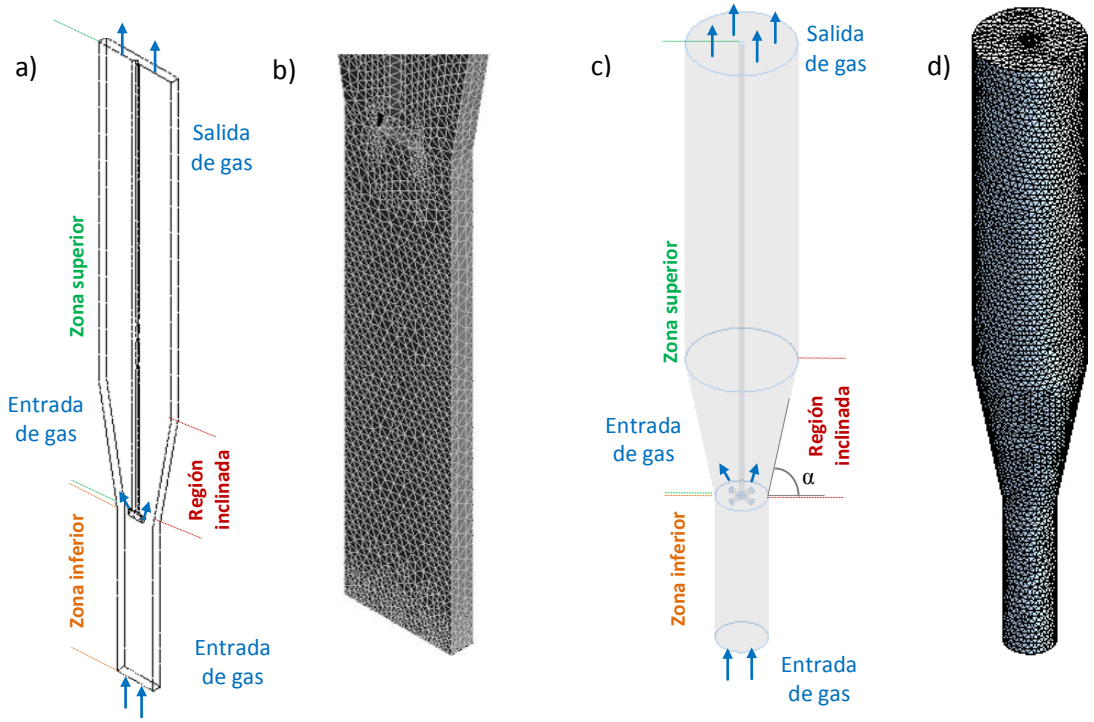

Figura 3.3 RLFDZ-CS pseudo-2D: a) Geometría, b) Detalle de la malla de cálculo. RLFDZ-CS 3D: c) Geometría, d) Malla

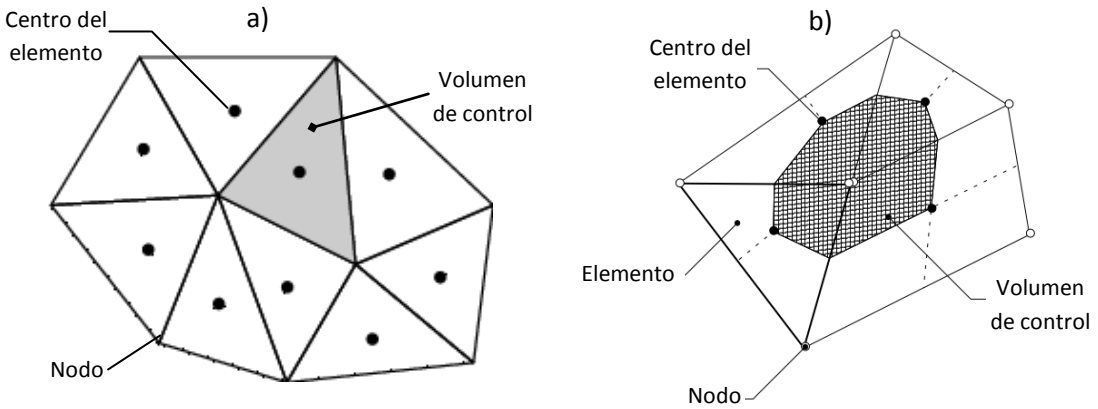

Figura 3.4 Volúmenes de control según el método de volúmenes finitos: a) centrado en las celdas delimitadas por nodos (Fluent), b) centrado en los vértices o nodos de la malla (CFX)

En el caso de los reactores planos (pseudo-bidimensionales) el dominio computacional simula, por simetría, la mitad del lecho experimental real y ha sido discretizado por una malla tetraédrica (desestructurada) de más de 25000 nodos de cálculo, con tamaños de malla entre 0,2 y 1 mm. En el caso de los reactores con geometría de revolución (3D), el tamaño de malla varía entre 1 y 2,5 mm para un dominio de más de 10^5 nodos. En todos los casos, el paso temporal aplicado ha sido de entre 10^{-4} y $2 \cdot 10^{-4}$ segundos, para evitar errores de cálculo y facilitar la convergencia.

En cuanto a las condiciones de contorno, se han aplicado condiciones de flujo de entrada con dirección normal a las superficies de los dos distribuidores de gas. A la salida de gases se le ha aplicado una condición abierta u '*opening*' para la libre entrada y salida de gas, evitando así problemas numéricos derivados de gradientes negativos de presión transitorios, y la presión de referencia en esa región se ha fijado en 0 Pa (relativa a la atmosférica). Además, se ha definido una condición 'no-slip' para el sólido en las paredes del reactor. Esto quiere decir que la velocidad de las partículas en contacto con la pared es nula. Por el contrario, una condición de '*free-slip*' o libre circulación ha sido definida para la interacción entre el gas y la pared.

En el caso concreto de las simulaciones fluidodinámicas de RLFDZ-CS con membranas extractivas, la condición de contorno aplicada a las paredes del dominio que actúan como membranas es tipo "flujo de entrada" con dirección normal a dichas paredes y sentido negativo. En la presente tesis se ha estudiado el comportamiento fluidodinámico de dos configuraciones diferentes de RLFDZ-CS+MB, según se detalla en la Figura 3.4: con membrana tubular inmersa en el lecho (3.5 (a)) y con membrana de pared (3.5 (b)).

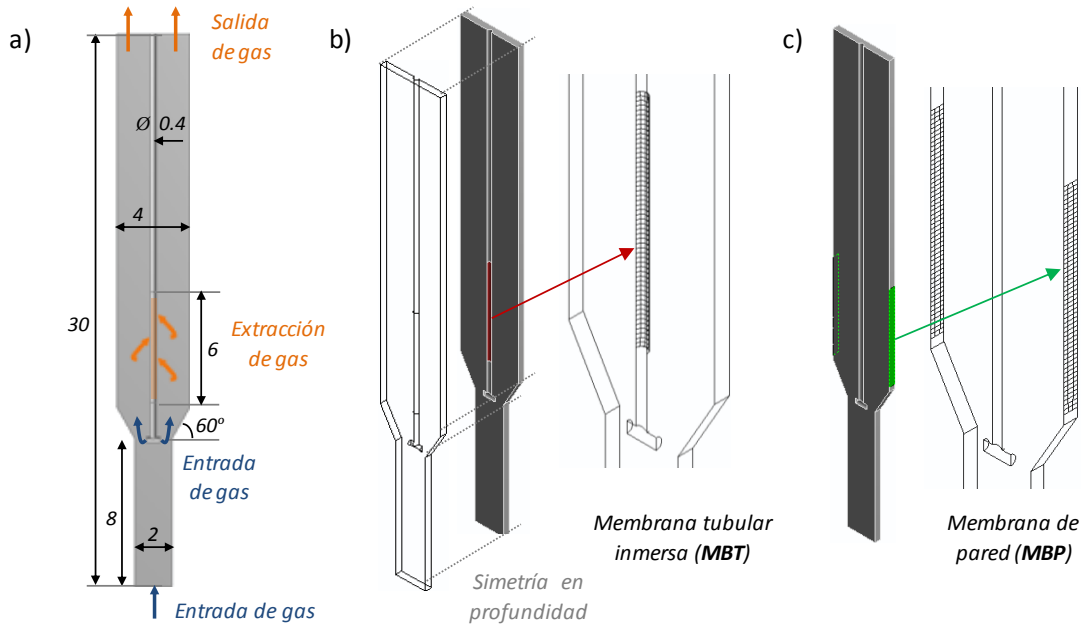

Figure 3.5 a) Dimensiones del reactor de membrana simulado, b) Reactor de membrana tubular (RLFDZ-CS+MBT), c) Reactor de membrana de pared (RLFDZ-CS+MBP)

El listado de parámetros utilizados a lo largo de las simulaciones fluidodinámicas, común a todas las geometrías y configuraciones de reactor, así como a los distintos códigos CFD empleados (CFX y Fluent), se detalla en la Tabla 3.1.

Todas las simulaciones parten de un lecho en reposo, sin alimentación inferior de gas, con un empaquetamiento máximo e igual al medido en un lecho fijo experimental para el tipo de partículas simuladas. Operando de este modo, es posible determinar la expansión del lecho y la fracción volumétrica ocupada por las burbujas en éste una vez fluidizado.

Tabla 3.1. Listado de los parámetros del modelo TFM utilizado en las simulaciones CFD

Parámetro del modelo	Valor
Altura del reactor (cm)	30 (*'1x'*) – 50 (*'2x'*)
Densidad de partícula, ρ_s (kg/m^3)	2500
Diámetro de partícula, d_p (μm)	200
Partículas por unidad celda, $d_p/celda$(-)	≤ 12
Fracción volumétrica de sólidos, ε_{s0} (-)	0,25
Empaquetamiento máximo, $\varepsilon_{s,m}$ (-)	0,65
Coeficiente de restitución, e (-)	0,90 – 0,95
Temperatura del gas (ºC)	25

Al igual que en las mediciones experimentales, en las simulaciones se ha estudiado el efecto de los tres parámetros fundamentales (velocidad de gas, posición del distribuidor y ángulo de cambio de sección) en el comportamiento fluidodinámico del lecho. Adicionalmente, en el caso del RLFDZ-CS+MB se ha estudiado el efecto de la ubicación de la membrana acoplada al reactor y del caudal permeado en la distribución de sólidos en el lecho. Por último, se ha estudiado la adaptabilidad de los regímenes de burbujeo 2D a RLFDZ-CS con geometría de revolución. El listado de todos los aspectos analizados y condiciones en las simulaciones llevadas a cabo, se detalla en la Tabla 3.2.

Tabla 3.2 Simulaciones fluidodinámicas llevadas a cabo en reactores tipo RLFDZ-CS

Descripción del efecto a estudiar	Escala	u_{gas}/u_{mf} (-)	Config.	α (º)	z_{dis}-z_{cs} (cm)	Vol. gas permeado
Régimen fluidodinámico	1x	1,5 – 3,0	pseudo-2D	45º – 85º	0 – 2	0%
Ángulo de defluidización	1x	1,5 – 3,5	pseudo-2D	0º	0	0%
Escalado	2x	1,5 – 3,0	pseudo-2D	80º	0 – 2	0%
Escalado sobre defluidización	2x	1,5 – 3,5	pseudo-2D	0º	0	0%
Extracción con membr. tubular	1x	1,5 – 2,5	pseudo-2D	60º	0	20% – 50%
Extracción con membr. de pared	1x	1,5 – 2,5	pseudo-2D	60º	0	20% – 50%
Geometría de revolución	2x	2,5	3D	80º	0	0%

3.3.1 Detección de burbujas 3D mediante 'formas-α'

La detección de burbujas simuladas se ha realizado a partir de los mapas de porosidad estableciendo una fracción volumétrica umbral de sólidos, ε_s = 0,15, por debajo de la cual una región pasa a considerarse fase burbuja. Dicho valor umbral ha sido propuesto por varios autores (44, 102, 112-115) como un valor razonable y realista para establecer el contorno de

las burbujas de gas en simulaciones fluidodinámicas realizadas con la aproximación Euleriana de dos fases fluidas.

En el caso de lechos pseudo-2D, el contorno de burbuja viene dado por la unión de puntos que cumplen la condición ε_s = 0,15 y que se encuentran proyectados sobre un plano vertical a una profundidad de lecho dada, tal y como se muestra en la Figura 3.6 (a). Para el reactor con simetría de revolución (3D), la binarización del lecho en función de la porosidad umbral genera superficies irregulares con ε_s = 0,15 a lo largo del dominio según la Figura 3.6 (b).

Como se ha expuesto en la Sección 2.2, las propiedades de las burbujas 2D son fácilmente medibles a través del paquete de procesado de imágenes digitales (*Image Processing Toolbox*) de Matlab®. Sin embargo, la medición del volumen ocupado por las burbujas 3D así como la ubicación de su centro de masas no es trivial. Los programas comerciales de procesado CFD facilitan la visualización de los resultados fluidodinámicos, por ejemplo mostrando los contornos superficiales de burbujas 3D (Figura 3.7 (a)), pero no son capaces de discriminar subdominios de computación (burbujas aisladas) y determinar sus propiedades de manera individualizada.

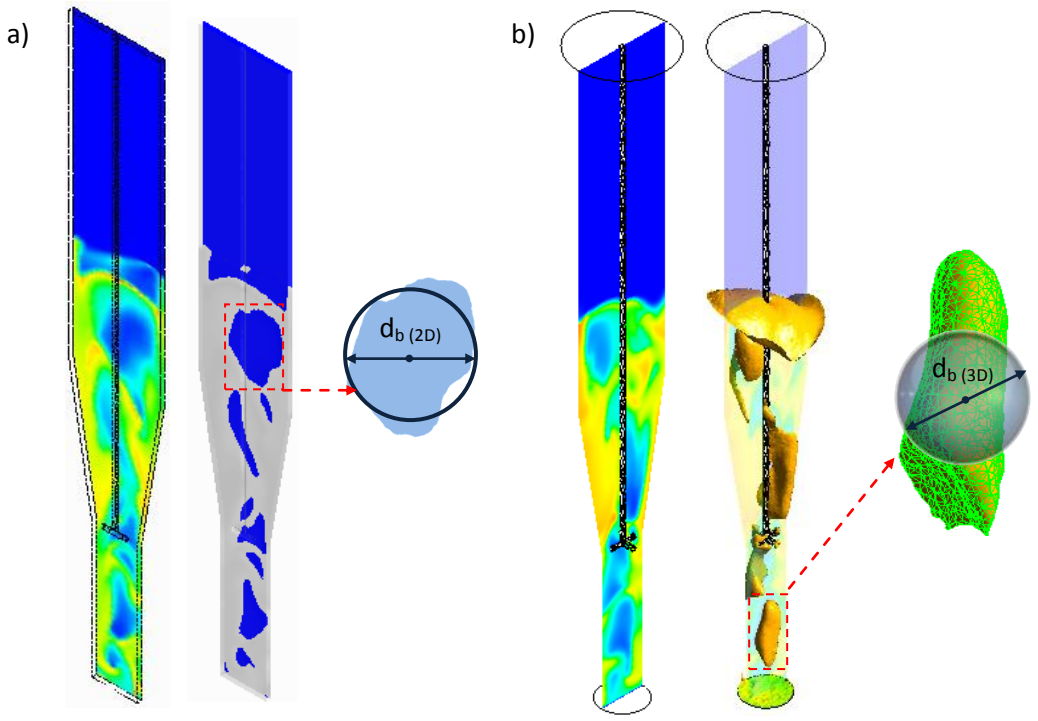

Figura 3.6 Diámetro de burbuja equivalente en: a) RLFDZ-CS pseudo-2D, b) RLFDZ-CS 3D

Para hacer frente a esta limitación, diversos autores (116, 117) han recurrido a técnicas tomográficas para estimar el volumen encerrado por burbujas tridimensionales a partir de simulaciones con el modelo de dos fluidos. La resolución de dichas técnicas depende de la cantidad de imágenes analizadas a lo largo de la profundidad del objeto a medir o caracterizar. La tomografía de alta resolución es computacionalmente muy costosa (un estudio estadísticamente robusto de las propiedades de burbuja requiere el análisis de muchos estados transitorios de burbujeo), mientras que la de baja resolución puede dar lugar a imprecisiones en la medición de volúmenes por interpolación de datos entre planos de profundidad significativamente alejados entre sí.

En esta tesis, se propone la utilización de las llamadas "formas-alpha" (118) para estimar el volumen real ocupado por las burbujas 3D simuladas. Este método supone la reconstrucción topológica del volumen encerrado en las regiones del dominio en las que $\varepsilon_s \leq 0{,}15$ conectando todos los nodos mediante tetraedros según una triangulación de Delaunay y la posterior eliminación de aquellos tetraedros cuyo tamaño sea superior al nivel de detalle geométrico descrito por α_{3D}, generando así subdominios o volúmenes independientes que se corresponden con cada una de las burbujas.

El uso de una malla fija con distancia máxima entre nodos de 2,5 mm para las simulaciones CFD llevadas a cabo facilita la elección del valor de α_{3D} para discriminar burbujas individuales. Si la distancia espacial entre dos nodos del dominio $\varepsilon_s \leq 0{,}15$ es superior a α_{3D} = 0,25 cm dichos nodos no pueden estar conectados y, por tanto, representan el contorno de diferentes burbujas. Si el nivel de detalle es bajo (ej. α_{3D} = 0,50 cm) puede que burbujas muy cercanas entre sí se identifiquen como una sola entidad, mientras que si el nivel de detalle es mayor que el tamaño de malla (α_{3D} < 0,25 cm) puede que se eliminen conexiones internas de burbuja subestimando su verdadero volumen y generando falsos subdominios. La Figura 3.7 ilustra el efecto del valor de α_{3D} en la identificación de burbujas individuales en un fotograma de burbujeo.

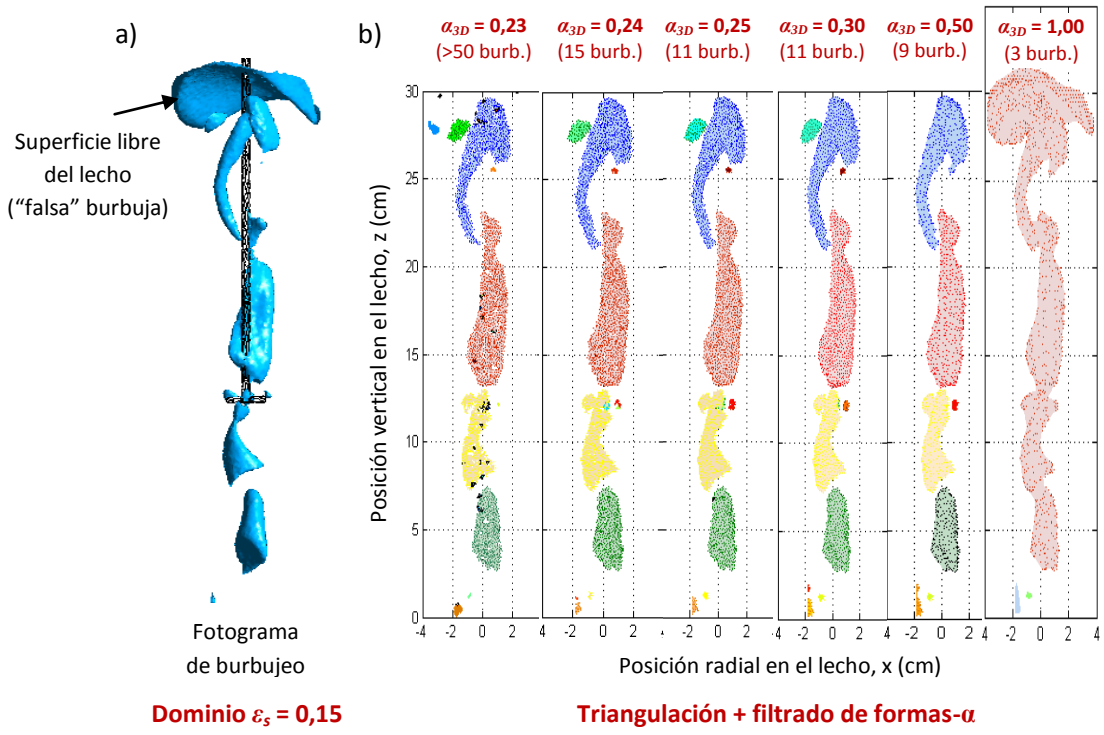

Figure 3.7 a) Contornos de burbuja detectados con fracción volumétrica de sólidos ε_s = 0,15, b) Efecto del valor de α en la discretización de las burbujas

El volumen y centro de masas de las burbujas 3D identificadas por el método de las "formas-alpha" se puede hallar a partir de las ecuaciones 40 y 41, respectivamente. En la ecuación 40, $v_{b,i}$ es el volumen de la burbuja *i* calculado como la suma de los volúmenes de los *T* tetraedros que la conforman, siendo *A*, *B*, *C* y *D* los nodos del tetraedro *t* con coordenadas espaciales (*x*, *y*,

z). En la ecuación 41, $b_{CoM,i}$ es el centro de masas de la burbuja *i* y *N* es el número de nodos que la conforman, siendo $(n_x, n_y, n_z)_n$ las coordenadas espaciales del nodo *n*.

Según la ecuación 42, el diámetro equivalente de burbuja 3D ($d_{b\ (3D)}$) se define como el diámetro de una esfera que ocuparía el mismo volumen que la burbuja. Por su parte, el diámetro equivalente promedio de burbuja 3D a una determinada altura del lecho, $\overline{d_{b(3D)}}(z)$, se calcula según se ha descrito previamente en la Sección 2.2 (ecuación 3), promediando las burbujas en función de su tamaño.

Para calcular la velocidad de burbuja 3D se determina la variación de la coordenada axial del centro de masas de la burbuja entre fotogramas simulados, de acuerdo con el algoritmo del "vecino más próximo" bajo las restricciones descritas en la Sección 2.2.

$$v_{b,i} = \sum_{t=1}^{T}\left(\frac{1}{6}\begin{vmatrix} A_x & B_x & C_x \\ A_y & B_y & C_y \\ A_z & B_z & C_z \end{vmatrix}\right)_t = \sum_{t=1}^{T}\left(\frac{1}{6}\,\overline{AD}\cdot(\overline{BD}\times\overline{CD})\right)_t \tag{E.40}$$

$$b_{CoM,i}(x,y,z) = \frac{1}{N}\left(\sum_{n=1}^{N}(n_x)_n\,,\sum_{n=1}^{N}(n_y)_n\,,\sum_{n=1}^{N}(n_z)_n\right) \tag{E.41}$$

$$d_{b(3D),i} = 2\left(\frac{3}{4\pi}v_{b,i}\right)^{1/3} \tag{E.42}$$

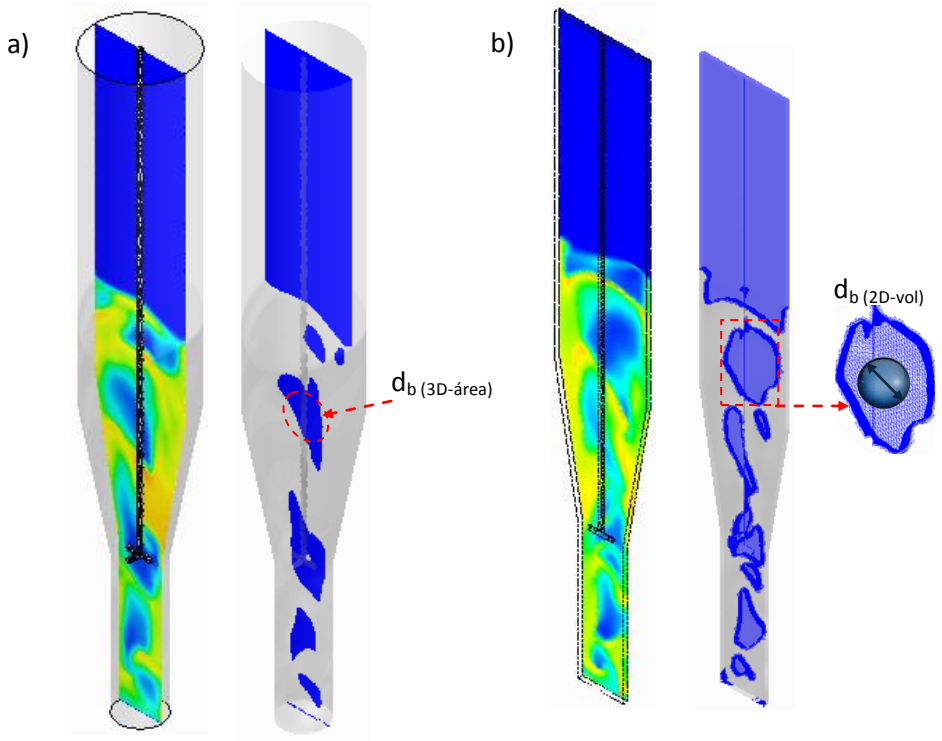

Figure 3.8 Diámetro de burbuja equivalente para RLFDZ-CS con configuración: a) 3D basado en el área proyectada a través de un plano central, b) pseudo-2D basado en el volumen encerrado

De manera análoga, sería posible definir un diámetro de burbuja equivalente para el RLFDZ-CS pseudo-2D en función del volumen de gas encerrado en las burbujas pseudo-bidimensionales. En tal caso, d_b sería el diámetro de la esfera equivalente que contiene el mismo volumen que el del área de burbuja 2D (A_b) proyectada a lo largo de la profundidad del lecho (L_{bed}), según la ecuación 43. Respecto al lecho con geometría de revolución, sería igualmente posible describir el diámetro equivalente en función del área de burbuja (A_b) proyectada a través de cualquiera de los infinitos planos que pasan por el eje central del reactor (ecuación 44).

$$d_{b(2D-vol),i} = 2\left(\frac{3}{4\pi}A_{b,i}L_{bed}\right)^{1/3} \tag{E.43}$$

$$d_{b(3D-área),i} = 2\left(\frac{A_{b,i}}{\pi}\right)^{1/2} \tag{E.44}$$

Así pues, en este trabajo se consideran cuatro formulaciones para el diámetro de burbuja equivalente en función de la configuración de reactor (pseudo-2D ó 3D) y de la magnitud equivalente considerada (área proyectada de un círculo o volumen encerrado en una esfera): $d_{b(2D)}$, $d_{b(3D)}$ (Figuras 3.6 (a) y (b)), $d_{b(2D\text{-}vol)}$, y $d_{b(3D\text{-}área)}$ (Figuras 3.8 (a) y (b)).

4 RESULTADOS Y DISCUSIÓN

4. RESULTADOS Y DISCUSIÓN

4.1 Velocidad de mínima fluidización en reactores pseudo-2D

En la presente sección se van a presentar los resultados más relevantes relativos al efecto de la geometría y la altura del lecho en la determinación de la velocidad de mínima fluidización para reactores de lecho fluidizado pseudo-bidimensionales. Los resultados mostrados están referidos, en esencia, a los descritos en el Artículo VI del compendio.

4.1.1 Efecto de la geometría y la altura del lecho

La velocidad de mínima fluidización (u_{mf}) es una propiedad intrínseca a un grupo de partículas, dependiente de sus propiedades físicas (distribución de tamaños, densidad, relación de aspecto,...) e independiente, en general, de la altura o diámetro del lecho. Sin embargo, algunos autores (119, 120) han probado que las paredes del reactor tienen efecto sobre el lecho modificando su u_{mf} aparente, especialmente en configuraciones pseudo-bidimensionales. En el presente trabajo, dado que se plantea hacer estudios en sistemas 2D, se ha estudiado el efecto de la altura y anchura del lecho en la variación de la velocidad de mínima fluidización aparente. Para tal fin, se han utilizado dos lechos pseudo-bidimensionales de profundidad fija (0,8 cm) y anchura 4 y 8 cm, respectivamente, además de un lecho cilíndrico de 2,6 cm de diámetro. A su vez, en cada configuración de reactor se han llevado a cabo mediciones con entre tres y cuatro alturas de lecho distintas en el rango 5 – 25 cm. Los resultados experimentales resumidos en la Tabla 4.1 sugieren que la configuración de reactor efectivamente afecta a la estimación de u_{mf}. En particular, el reactor que ofrece una menor sección de paso por perímetro de pared (S_{lecho}/L_{lecho}) da lugar a una notable variación de u_{mf} con la altura de lecho. De hecho, bajas relaciones S_{lecho}/L_{lecho} favorecen el *efecto pared* sobre la fluidización de las partículas, ya que su interacción dificulta el movimiento de las partículas en las inmediaciones de la pared dando lugar a valores de u_{mf} aparentemente mayores a los propios del lecho en cuestión. El efecto de la altura del lecho sobre u_{mf} resulta crítico en los casos en los que se utilizan lechos estrechos. Por ejemplo, el valor de u_{mf} se incrementa en un 37% al triplicar la altura de un lecho pseudo-2D estrecho, mientras que para una configuración cilíndrica un incremento de altura similar únicamente supone una variación en torno al 5% en u_{mf}.

Tabla 4.1 Velocidad de mínima fluidización en función de la configuración de reactor

Configuración Lecho Fluidizado	S_{lecho}/L_{lecho} (cm)	$H_{lecho\ fijo}$ (cm)	$w_{catalizador}$ (g)	u_{mf} (cm/s)
2D (w_{lecho} = 4,0 cm)	0,33	6,2	31,1	11,1
		11,6	58,7	12,1
		18,7	93,7	15,2
		26,8	135,3	15,6
2D (w_{lecho} = 8,0 cm)	0,36	5,3	53,6	11,9
		9,4	95,6	12,8
		16,5	167,1	13,4
3D ($Ø_{lecho}$ = 2,6 cm)	0,65	5,9	57,7	10,9
		9,0	87,6	11,0
		14,2	138,7	11,4

No obstante, considerando que u_{mf} es única y una propiedad intrínseca del grupo de partículas en cuestión, la u_{mf} de los sólidos utilizados irá siempre referida a la medida realizada en lechos cilíndricos, configuración para la cual el efecto pared se reduce respecto al de reactores 2D. A pesar de que la posterior experimentación fluidodinámica se lleva a cabo en lechos pseudo-bidimensionales, los valores de u_{mf} obtenidos por el método descrito han sido los utilizados para calcular las velocidades relativas de gas y, por tanto, para el modelado fluidodinámico a partir de correlaciones hidrodinámicas (JHM), mezcla axial (CCBM) y fluidodinámica computacional (TFM).

4.2 Mezcla axial de sólidos

El estudio de la mezcla axial de sólidos y del fenómeno de defluidización en un RLFDZ-CS (recogido en los Artículos I y II del compendio) se ha llevado a cabo analizando el efecto de la velocidad del gas, geometría del reactor y posición axial del distribuidor inmerso en el grado de mezcla. Se ha implementado y validado un modelo de retromezcla (CCBM) para predecir macroscópicamente la evolución temporal del grado de mezcla axial entre las dos zonas del lecho.

4.2.1 Efecto de la velocidad del gas

Para estudiar el efecto de la velocidad del gas alimentado en la mezcla axial de sólidos se han determinado los perfiles axiales de concentración de trazador a velocidades relativas de gas comprendidas entre 1,5 y 3,0 veces la de mínima fluidización a través de ambas zonas del lecho. Experimentalmente, se ha comprobado que cuanto mayor es la velocidad de gas alimentado más rápida es la mezcla axial de sólidos y por tanto más rápidamente se homogeneiza la concentración de trazador a lo largo del lecho. Esta tendencia se ilustra en la Figura 4.1, donde se muestran perfiles axiales de concentración de trazador a diferentes u_r manteniendo constantes el resto de parámetros del sistema. El método experimental utilizado permite medir el tiempo que tarda en alcanzarse la mezcla completa bajo ciertas condiciones de operación e incluso cuantificar el grado de mezcla puntual a lo largo del tiempo. Para ello, basta con calcular el *Índice de Mezcla* (*IM*) resultante de los perfiles de concentración de acuerdo con la expresión presentada en la ecuación 1 de esta Memoria.

La Figura 4.2 muestra la evolución temporal del *IM* experimental en función de la velocidad relativa de gas (u_r = 1,5 – 3,0). Independientemente de las condiciones de operación, se observa una acusada mezcla inicial de trazadores. Esto es debido a la súbita transición entre lecho fijo y fluidizado cuando el primer pulso de gas asciende por el lecho. Tras el rápido incremento inicial del grado de mezcla, se observa como a bajos caudales de gas el sistema no es capaz de alcanzar la mezcla completa entre las partículas inicialmente segregadas. Sin embargo, a regímenes de fluidización mayores la mezcla completa se alcanza en cuestión de 20 segundos. La sustancial variabilidad de los perfiles de mezcla en un pequeño rango de velocidades relativas indica lo sensible que es el fenómeno de la mezcla axial a u_r. Por tanto, es necesario un estricto control del caudal alimentado para garantizar una circulación axial de sólidos apropiada de cara a la integración de procesos en el RLFDZ-CS. Se observa que para velocidades de gas $u_r \geq 2{,}0$ es posible alcanzar la mezcla completa en este sistema. Por tanto, extrapolando estos resultados a partículas Geldart B cualesquiera, se recomienda usar un exceso de gas u_{gas}–u_{mf} > 10 cm/s para favorecer la mezcla.

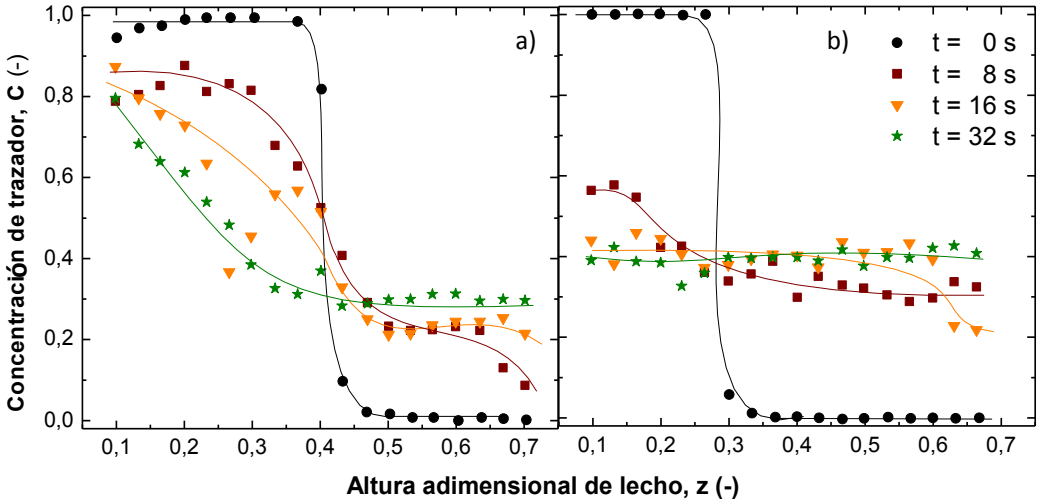

Figura 4.1 Perfiles experimentales de concentración de trazador para RLFDZ-CS (α = 45º, z_{dis} = z_{cs} = 8 cm) a velocidades relativas de gas: a) $u_{r,inf}$ = $u_{r,sup}$ = 1,5, b) $u_{r,inf}$ = $u_{r,sup}$ = 3,0.

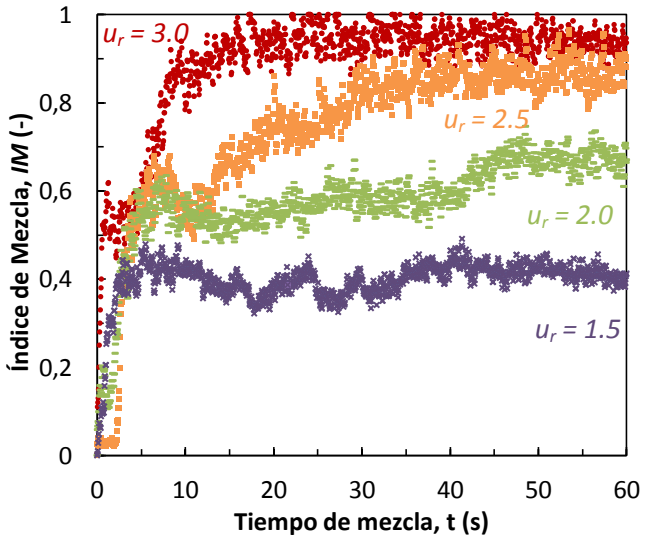

Figura 4.2 Índice de mezcla para RLFDZ-CS (α = 60º) a velocidades de gas, u_r = [1,5 – 3,0]

4.2.2 Efecto de la geometría del reactor. Defluidización

Analizando el efecto del ángulo de cambio de sección, α = 0º – 85º, en el grado de mezcla (manteniendo constantes los flujos de gas a introducir por ambas entradas del lecho) se observó que si el ángulo de cambio de sección entre las dos zonas del lecho era muy brusco (α < 45º) el trazador nunca llegaba a alcanzar las regiones laterales inmediatamente por encima del cambio de sección. Aquellas regiones del lecho en las que no se aprecia movimiento de sólidos a lo largo del tiempo se denominan zonas "muertas" o defluidizadas y están originadas por velocidades de gas puntualmente inferiores a la de mínima fluidización o por la formación de canales preferenciales en la circulación de gas que dificultan el contacto gas-sólido en determinadas zonas del lecho.

El uso de trazadores fosforescentes y las técnicas experimentales de análisis PIV/DIA permitieron detectar y cuantificar la extensión de las regiones defluidizadas en reactores RLFDZ-CS en función del exceso de gas en el lecho a partir de un RLFDZ-CS (α = 0º). El rango de valores de u_{gas}–u_{mf} experimentados comprendió de 5 a 30 cm/s. En el caso de los trazadores ópticos, se excitaron inicialmente las partículas de la parte superior del lecho (Figura 4.3 (a)) y se midió el tamaño y geometría de las regiones de sólido inmóvil transcurrido cierto tiempo de fluidización por diferencia de intensidad de luz emitida en las imágenes recogidas (Figura 4.3 (b)). En el caso del método PIV/DIA, se obtuvieron los mapas promedio de circulación de sólidos y de porosidad del lecho y se establecieron una velocidad mínima ($u_s \leq$ 0,5 cm/s) y una fracción volumétrica de sólidos máxima ($\varepsilon_s \geq$ 0,62) para delimitar el contorno de las regiones defluidizadas correspondientes a varios tipos de sólidos y excesos de gas (Figura 4.3 (c)).

Al ángulo de talud que formó el contorno de las zonas muertas con la horizontal a ambos lados de la zona de cambio de sección se le denominó "*ángulo de defluidización*", *β*. Dicho ángulo es característico de cada tipo de partículas y varía con el caudal de gas alimentado. Experimentalmente se encontró que cuanto mayor es la turbulencia del flujo de gas, menor es el tamaño de la región defluidizada y, por tanto, menor es *β*.

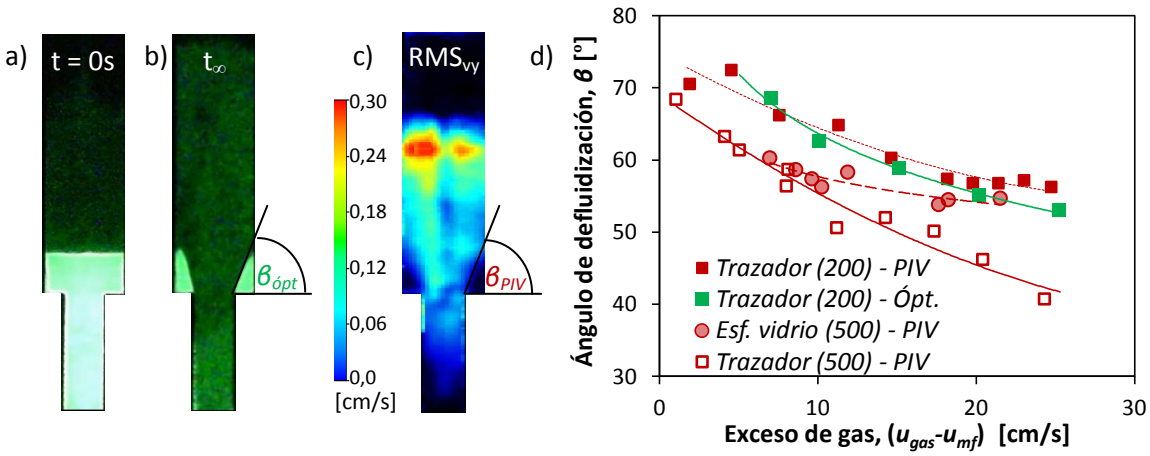

Figura 4.3 Defluidización del RLFDZ-CS a partir de trazadores ópticos: a) Iluminación inicial, b) Iluminación residual (t = 55 s), c) Defluidización del RLFDZ-CS a partir mapas de variabilidad PIV, d) Efecto del exceso de gas en el ángulo de defluidización (*β*) en un RLFDZ-CS (α = 0º)

Este estudio se llevó a cabo en una configuración de reactor en la que la posición axial del distribuidor de gas inmerso coincide con la altura del lecho a la que comienza el cambio de sección, $z_{dis} = z_{cs}$. En estas condiciones, se observó que el ángulo de defluidización varía en el rango $45^o - 75^o$ independientemente del tipo de partícula y exceso de gas experimentado, según se muestra en la Figura 4.3 (d).

Al modificar la altura relativa del distribuidor respecto a la posición del cambio de sección, el régimen fluidodinámico de la zona cónica se vió afectado, variando el grado de defluidización en consecuencia. Se observó que al localizar el distribuidor de gas secundario dos centímetros por encima del comienzo del cambio de sección, incluso en geometrías con ángulo de transición suave ($\alpha = 60^o - 80^o$), las regiones defluidizadas incrementaron su tamaño y empeoró el comportamiento fluidodinámico del lecho debido a la aparición de *slugs* o burbujas que ocupan toda la superficie transversal del lecho produciendo un cortocircuito en la recirculación axial de sólidos. Este fenómeno se relaciona con la defluidización incipiente de la región cónica que queda por debajo de la segunda alimentación de gas. El sólido queda apelmazado en dicha región generando cierta pérdida de carga al paso de gas a su través y favoreciendo la acumulación de gas en forma de grandes burbujas en la zona inferior del lecho, lo que da lugar al régimen de *slugging* y al cortocircuito en la mezcla axial de sólidos.

A la vista de estos resultados, se estableció que la posición axial más adecuada para el distribuidor de gas inmerso es la altura a la cuál comienza el cambio de sección ($z_{dis} = z_{cs}$). Esta ubicación permite minimizar la formación de regiones defluidizadas y facilitar la mezcla axial de sólidos entre las dos zonas del RLFDZ-CS.

4.2.3 Validación del Modelo de Retromezcla a Contracorriente (CCBM)

En este trabajo se ha propuesto utilizar el modelo de Retromezcla a Contracorriente, CCBM, estimando los parámetros del modelo (f_1, k_w y u_1) a partir de las correlaciones hidrodinámicas descritas en la Sección 3.2 de esta Memoria. La Figura 4.4 muestra un ejemplo de la capacidad del modelo para predecir tanto los perfiles axiales de concentración de trazador a lo largo del tiempo (Figura 4.4 (a)) como la evolución transitoria del grado de mezcla axial entre las dos zonas del lecho (Figura 4.4 (b)). Como se puede observar, el modelo de mezcla es capaz de estimar de manera precisa el tiempo experimental de fluidización hasta mezcla axial completa.

Como regla general, cuanto mayor es la velocidad del gas, mayor es la velocidad ascensional de los sólidos, mayor la fracción de sólidos en la fase ascendente y más rápida la tasa de intercambio estela-emulsión. De acuerdo con las correlaciones hidrodinámicas, la velocidad de la estela es entre 0,4 y 0,7 veces la velocidad del exceso de gas, ($u_{gas} - u_{mf}$). El coeficiente de transferencia de materia interfacial es del mismo orden que la velocidad ascensional de partículas y la fracción volumétrica de sólidos en la estela, creciente con la velocidad del gas, es del orden del 8% – 10% en el rango de condiciones de operación estudiadas.

Los coeficientes de regresión (r^2) en la predicción de la evolución del índice de mezcla experimental alcanzan valores entre 0,6 y 0,75 en todo el rango de condiciones de operación estudiadas. Estos valores suponen regresiones razonablemente buenas teniendo en cuenta la simplicidad del modelo, el hecho de que el ajuste se realiza sobre casi 5000 puntos

experimentales y la propia variabilidad del índice de mezcla experimental para un tiempo determinado, como se observa en la figura 4.4.b.

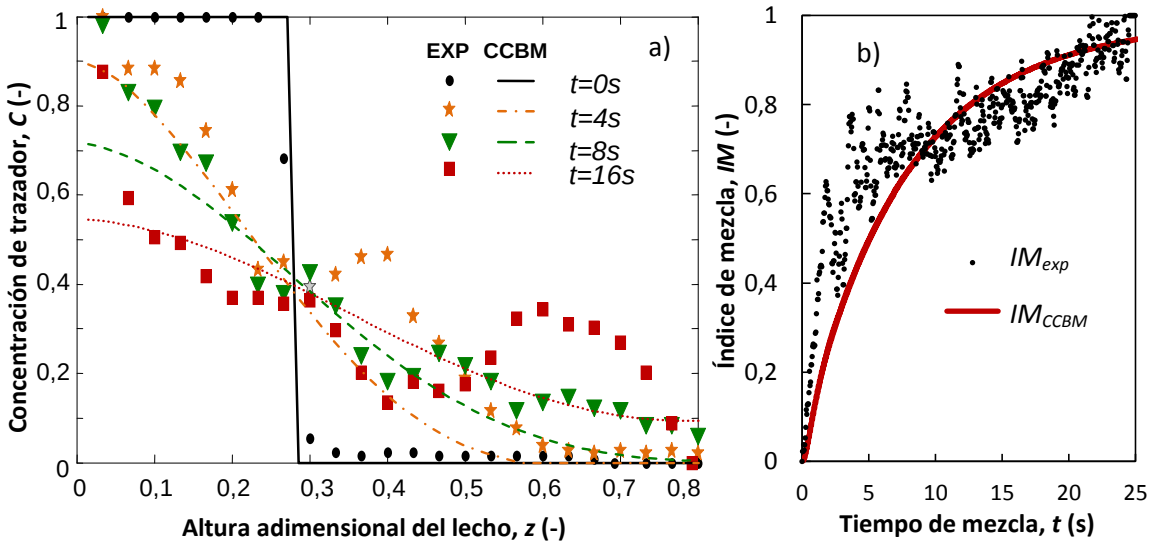

Figura 4.4 Mezcla axial de sólidos para RLFDZ-CS (α = 85º) a $u_{r,inf} = u_{r,sup}$ = 2,5. a) Perfil axial de concentraciones de trazador, b) Evolución temporal del Índice de mezcla experimental

4.3 Regímenes de burbujeo

El grado de mezcla axial en un lecho fluidizado gas-sólido está íntimamente relacionado con el régimen de burbujeo en tanto que, en su ascenso, las burbujas de gas son las responsables del arrastre de sólido hacia la superficie libre del lecho. A continuación, se detalla el efecto de diferentes variables de operación en las propiedades de burbuja, tanto experimentales como simuladas (a partir del modelo computacional de dos fluidos) en reactores RLFDZ-CS. Los resultado de este estudio están referidos, esencialmente, a los Artículos III y IV del compendio.

4.3.1 Reproducibilidad y significancia de las propiedades de burbuja en RLFDZ-CS

Los regímenes de burbujeo dan lugar a una elevada variabilidad de las características de burbuja debido a la cierta aleatoriedad en su formación y crecimiento durante la fluidización. Por ello, es necesario realizar inicialmente un análisis estadístico de la variabilidad de las propiedades de burbuja a fin de obtener resultados reproducibles y representativos. Algunas de las propiedades de burbuja analizadas en este estudio son: la distribución de tamaños o *Probability Size Distribution* (*PSD*), el perfil axial de tamaños ($d_b(z)$), el perfil axial de velocidades ($u_b(z)$), la frecuencia de aparición (n_b/cm^{2}s), la distribución radial (PD_r), la distribución de relaciones de aspecto o *Aspect ratios* (*AR*), la fracción del gas alimentado que asciende en forma de burbujas o *bubbles hold-up* (b_h), etc.

La Figura 4.5 muestra un estudio de reproducibilidad y dispersión estadística en la caracterización del perfil axial de tamaños de burbuja para un RLFDZ-CS. En concreto, la Figura 4.5 (a) ilustra el efecto del tiempo de muestreo en la obtención de un perfil de tamaños de burbuja reproducible mientras que la Figura 4.5 (b) muestra un ejemplo de la dispersión de datos relativos al perfil axial de tamaños de burbuja para distintas velocidades de gas de

fluidización. Como se aprecia la Figura 4.5 (a), sería necesario tomar datos de en torno a 40 segundos de fluidización (1000 fotogramas a 25 fps y, aproximadamente, 5000 datos de burbuja) para obtener un perfil axial de tamaños de burbuja susceptible de ser considerado libre de error estadístico. Respecto a la variabilidad de los datos en función del caudal de gas alimentado, las características de burbuja son tanto más variables cuanto más turbulento es el régimen fluidodinámico. El uso de intervalos de confianza para la media poblacional permite establecer si las diferencias encontradas al comparar los resultados obtenidos en dos regímenes de fluidización distintos son significativas, o no, en términos estadísticos. En el caso de la Figura 4.5 (b), se podría afirmar que los perfiles axiales de tamaño de burbuja obtenidos con velocidades relativas de gas 1,5 y 3,0, respectivamente, difieren significativamente y, por tanto, el caudal de gas afecta significativamente al régimen de burbujeo en un RLFDZ-CS.

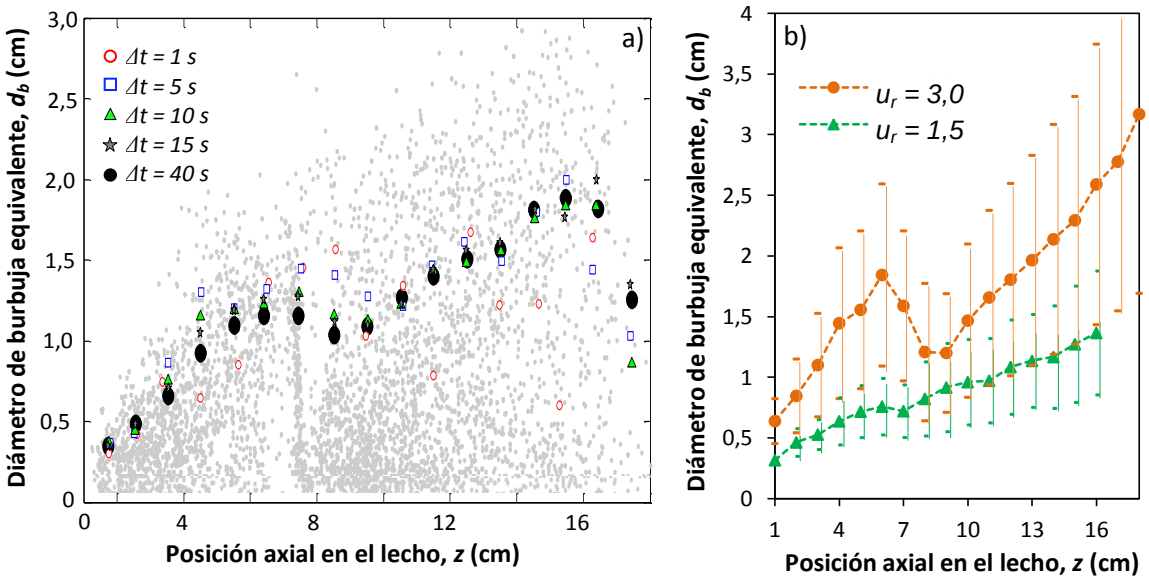

Figura 4.5 a) Efecto del tiempo de muestreo en la reproducibilidad del perfil $d_b(z)$ para RLFDZ-CS (α = 45º) a velocidad relativa, u_r = 2,0; b) Dispersión estadística de $d_b(z)$ en función del régimen de burbujeo

4.3.2 Efecto de las condiciones de operación en el perfil axial de tamaños de burbuja

Se ha analizado el efecto de cuatro variables del sistema en la evolución del diámetro de burbuja equivalente con la altura del lecho: tipo de partícula fluidizada, geometría del reactor, velocidad de gas y posición axial del distribuidor secundario.

Respecto al efecto del tipo de partícula, se ha encontrado que si los sólidos evaluados corresponden a un mismo grupo en la clasificación de Geldart (54) el perfil de tamaños de burbuja no difiere significativamente al operar con un mismo exceso de gas sobre el de mínima fluidización. Por tanto, dado que el RLFDZ-CS está pensado para trabajar con sólidos tipo Geldart B, basta con analizar el comportamiento hidrodinámico del lecho para un único tipo de partículas y extrapolar los resultados de burbujeo obtenidos a otros sólidos fluidizables con un mismo exceso de gas.

Asimismo, se ha comprobado que los perfiles axiales de tamaño de burbuja conducen en todos los casos a una característica disminución puntual del diámetro de burbuja en un punto

intermedio del lecho, no contemplada en ninguna correlación hidrodinámica existente en literatura (96, 121-128) (ver Figura 4.6). Dicha disminución del tamaño de burbuja se ha achacado a dos posibles causas complementarias. Por un lado, el incremento de la sección transversal en la zona cónica hace que, para un mismo caudal de gas atravesando el lecho, el exceso de gas sobre el de mínima fluidización disminuya al aumentar la sección de paso. Esto conllevaría una reducción progresiva del tamaño de burbuja que asciende desde la parte inferior del lecho a través de la zona cónica. Por otro lado, la formación de burbujas de gas de pequeño tamaño en de los orificios del distribuidor de gas secundario contribuiría a disminuir el tamaño promedio de burbuja en la zona cónica. Ambas tendencias, ilustradas en la Figura 4.6, redundan en la justificación del característico perfil axial de tamaños de burbuja obtenido en reactores RLFDZ-CS.

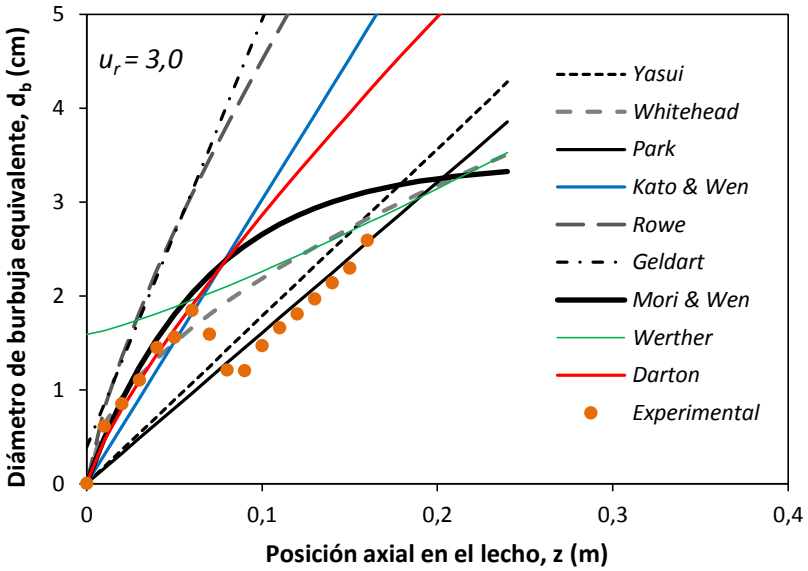

Figura 4.6 Comparativa entre el perfil axial de tamaño de burbuja experimental en RLFDZ-CS y las predicciones de distintas correlaciones fluidodinámicas

Como se aprecia en la Figura 4.7, el ángulo de cambio de sección entre las dos zonas del lecho influye tanto en la tasa inicial de crecimiento de las burbujas provenientes del segundo distribuidor como en el grado de disminución del tamaño de burbuja para aquellas burbujas provenientes de la zona inferior del lecho. Naturalmente, esto tiene que ver con el diferente incremento axial de la sección de paso propio de cada α. Si el cambio de sección es gradual, la disminución del tamaño de burbuja será también gradual, en consecuencia, y el tamaño de las burbujas provenientes del segundo distribuidor aumentará por contar con un mayor exceso de gas sobre u_{mf} en la región cónica. Por el contrario, si el cambio de sección es brusco, la caída del tamaño de burbuja será más brusca y el crecimiento inicial de las burbujas incipientes del segundo distribuidor será menor.

Llama la atención que el comportamiento de las burbujas bajo ángulos de cambio de sección comprendidos entre 0º y 45º es casi idéntico. Esta similitud sugiere que el área de paso no viene dada necesariamente por el ángulo de inclinación del reactor (α) sino por el área efectiva de circulación de gas que excluye las zonas muertas o regiones defluidizadas (β), de acuerdo con lo expuesto en Sección 4.2.2 de esta Memoria. Así, siempre que las condiciones de

operación hagan que el ángulo de defluidización sea mayor que el de cambio de sección, el perfil axial de tamaño de burbuja esperado en la zona cónica será idéntico para cualquier geometría de reactor tal que $\alpha \leq \beta$.

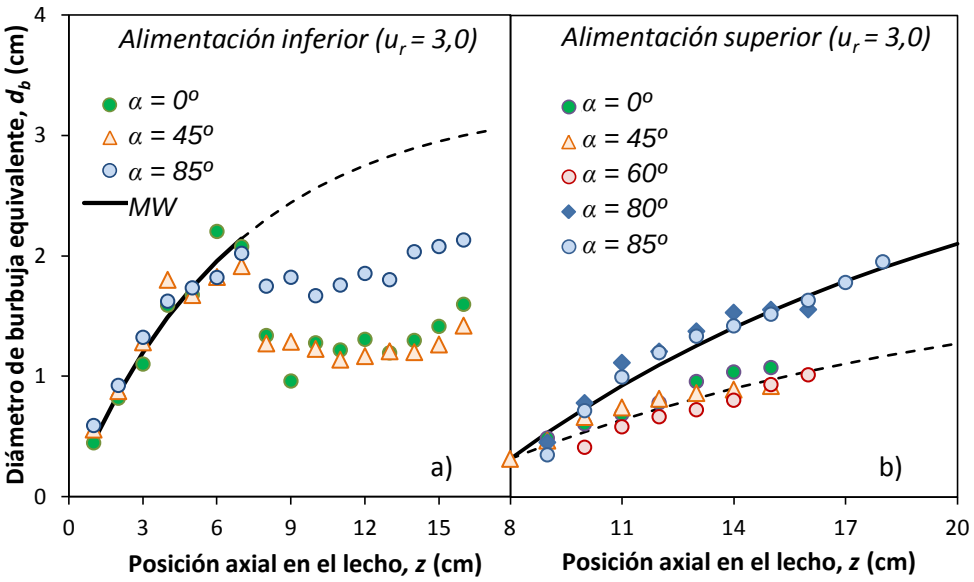

Figura 4.7 Evolución axial del diámetro de burbuja equivalente con: a) alimentación única de gas por la zona inferior del lecho, b) alimentación única por la zona superior del lecho

4.3.3 Validación del modelo JHM para predecir tamaño y velocidad de burbujas

Se ha expuesto anteriormente que ninguna de las correlaciones clásicas para modelar la evolución axial del tamaño de burbuja es capaz de predecir la disminución del tamaño de burbuja en un punto intermedio del lecho en reactores RLFDZ-CS. Por ese motivo, se ha tratado de modelar el perfil $d_{b,RLFDZ\text{-}CS}(z)$ según el modelo matemático denominado *Julián-Herguido-Menéndez* (JHM) descrito en la Sección 3.1.

Experimentalmente, se ha demostrado que la aplicación del balance de materia a la fase gas en la zona cónica del lecho permite predecir satisfactoriamente la reducción del tamaño de burbuja en dicha región y que la correlación clásica de Mori y Wen es adecuada para predecir la evolución del tamaño de burbuja en las zonas de sección constante del RLFDZ-CS. A modo de ejemplo, la Figura 4.8 muestra las predicciones del modelo para $d_b(z)$ utilizando partículas fosforescentes en RLFDZ-CS con tres geometrías diferentes (α = 0º, 45º, 60º) y una velocidad de gas en ambas zonas del lecho, u_r = 2,5. El modelo JHM es igualmente capaz de predecir razonablemente el perfil axial de diámetros de burbuja para geometrías de reactor con cambios de sección más graduales en el rango de velocidades de gas experimentadas (u_r = 1,5 – 3,0).

Además, el modelo mejora sustancialmente su capacidad predictiva teniendo en consideración el efecto de la defluidización (Figura 4.3 (d)) en la reducción de la sección efectiva de paso del gas.

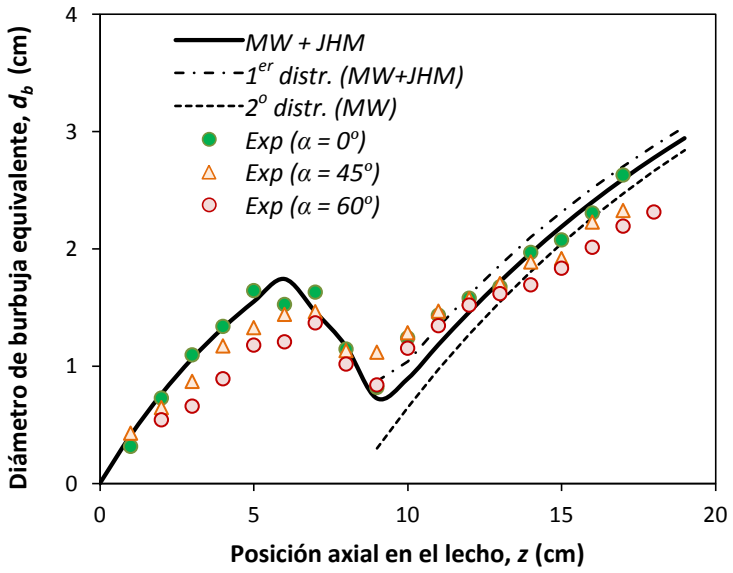

Figura 4.8 Comparativa entre el perfil axial de tamaños de burbuja experimental para RLFDZ-CS (α) y la predicción del modelo JHM (u_r = 2,5, d_p = 0,2 mm)

La Figura 4.9 ilustra ejemplos en los que el uso de α o β, en función de las condiciones de operación, permite mejorar la predicción de los perfiles de tamaño de burbuja experimentales.

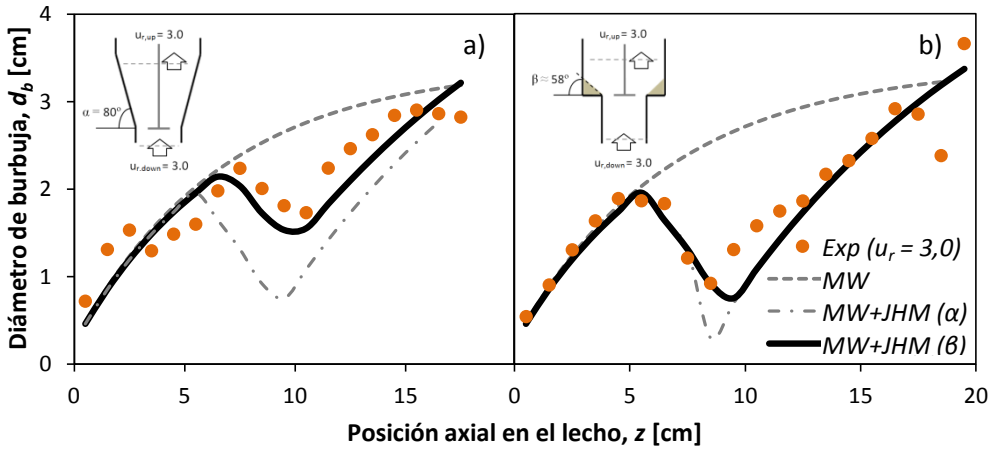

Figura 4.9 Predicción del modelo JHM para el perfil $d_b(z)$ experimental en RLFDZ-CS con velocidad relativa de gas, u_r = 3,0, y cambio de sección: a) suave (α = 80º), b) brusco (α = 0º)

Por otro lado, de acuerdo con la correlación de Davidson y Harrison (DH) (19), el diámetro de burbuja equivalente es proporcional a la velocidad ascensional de las burbujas, u_b. Teniendo esto en cuenta y considerando el modelo JHM para predecir la evolución axial del tamaño de burbuja es posible estimar la variación de $u_b(z)$ en un reactor RLFDZ-CS. Experimentalmente, se ha encontrado que la capacidad predictiva del modelo DH+JHM es máxima utilizando un valor para el parámetro K de la correlación de Davidson y Harrison, K = 0,4 (Figura 4.10). Este valor coincide con el que los autores definen como óptimo para lechos pseudo-bidimensionales, como el usado en este estudio. El uso del modelo puede extender al rango de condiciones experimentales utilizadas en este trabajo; α = 0º – 85º y u_r = 1,5 – 3,0.

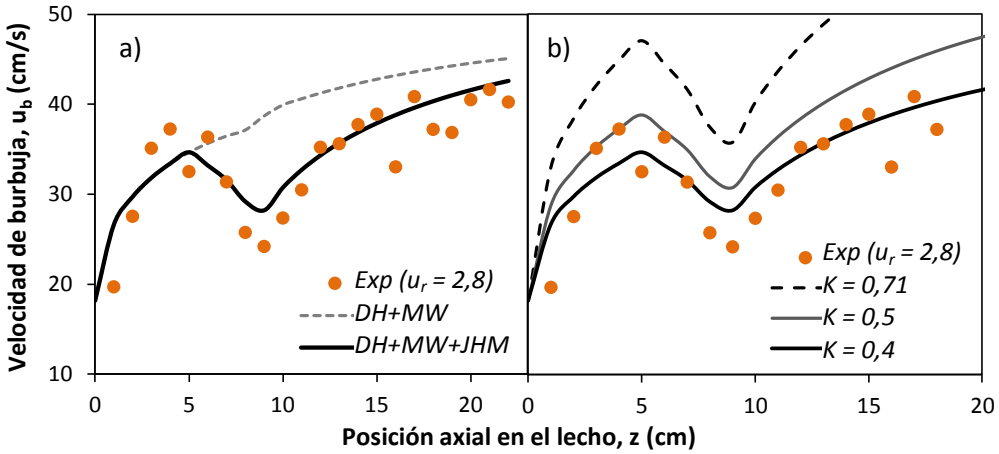

Figura 4.10 a) Predicción de $u_b(z)$ en RLFDZ-CS a partir de correlaciones hidrodinámicas teniendo o sin tener en cuenta el modelo JHM, b) Influencia del parámetro *K* de la correlación de Davidson y Harrison (DH) en la predicción de $u_b(z)$ para un RLFDZ-CS

4.3.4 Validación del modelo computacional TFM

Para validar la capacidad del modelo computacional TFM para simular el régimen de burbujeo en un RLFDZ-CS es necesario comparar de manera exhaustiva las características de burbujas experimentales y simuladas, no siendo suficiente el comprobar que los perfiles axiales de tamaño (Figura 4.11) y velocidad de burbuja sean predichos razonablemente por el simulador.

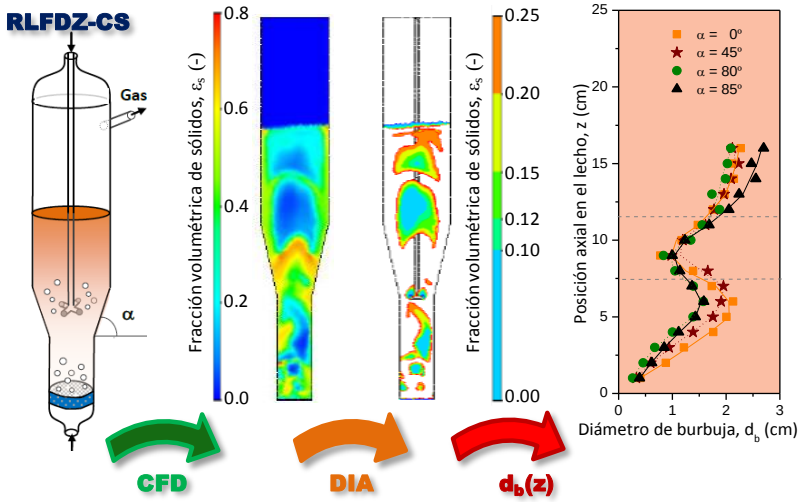

Figura 4.11 Obtención de perfiles $d_b(z)$ a partir de simulaciones fluidodinámicas en RLFDZ-CS pseudo-2D

En este trabajo se ha analizado la capacidad del modelo para simular la distribución experimental del tamaño, morfología, dispersión radial o frecuencia de aparición de burbujas, así como la fluctuación en la altura de la superficie libre, expansión del lecho o la variación temporal de la fracción volumétrica del gas alimentado que asciende en forma de burbujas.

El estudio se ha realizado simulando la respuesta fluidodinámica detallada de un RLFDZ-CS en Ansys CFX con α = 80º y con el distribuidor de gas secundario situado a la misma altura que la base de la región cónica del lecho, $z_{dis} = z_{cs}$, de acuerdo con las condiciones fluidodinámicas óptimas establecidas en la Sección 4.2.2, a partir de la Figura 4.3. De este modo, se ha

analizado la variación de las características de burbujas experimentales y simuladas con la velocidad de gas.

En primer lugar, se han comparado los perfiles axiales de tamaños de burbuja experimentales y simulados en el rango de velocidades de gas, u_r = 1,5 – 3,0 (Figura 4.12 (a)). Como se puede observar, las simulaciones son capaces de predecir razonablemente el aumento del diámetro equivalente de burbuja con la velocidad de gas y la disminución de su tamaño promedio en la zona cónica afectada por la alimentación adicional de gas. La caída de d_b en esta región es tanto más grande cuanto mayor es la velocidad del gas. No obstante, el mínimo valor de d_b detectado en la zona cónica parece no estar relacionado con la velocidad del gas, sino con el tamaño inicial de burbuja proveniente del distribuidor inmerso, prácticamente coincidente en todos los casos.

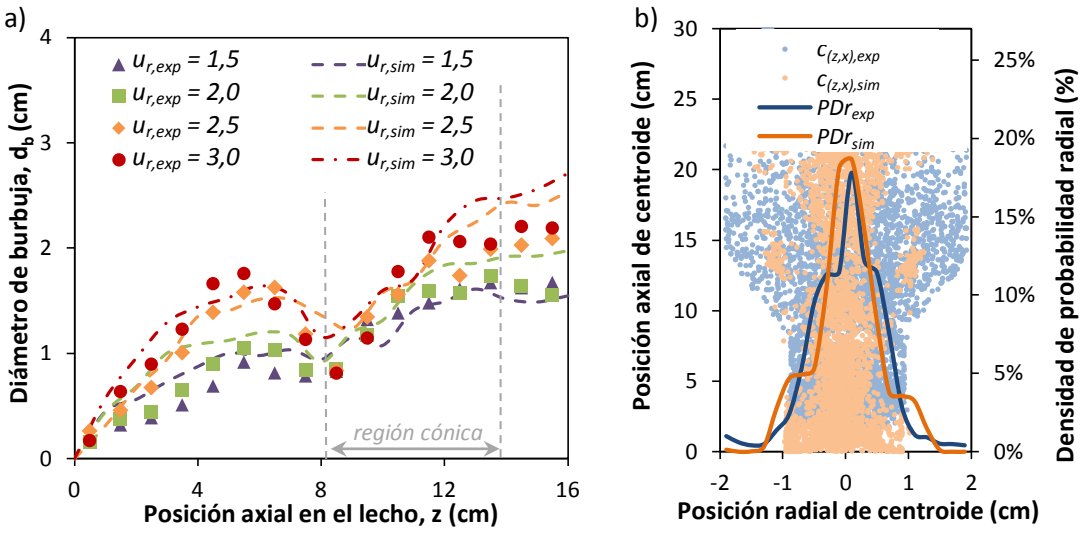

Figura 4.12 a) Efecto de la velocidad de gas en los perfiles $d_b(z)$ experimentales y simulados para un RLFDZ-CS (α = 80º), b) Distribución radial de probabilidad de aparición de burbujas en el lecho

En apariencia, el modelo fluidodinámico es capaz de simular los tamaños de burbuja a lo largo del lecho. Sin embargo, la Figura 4.12 (a) no da ninguna información acerca de la frecuencia de aparición de burbujas ni de su distribución espacial a lo largo del lecho. Para tal fin, se han comparado los mapas experimentales y simulados de dispersión radial de burbujas y de densidad espacial de burbujas en el lecho (número de burbujas por unidad de tiempo y de área). En la Figura 4.12 (b) se muestra la distribución de probabilidades para la posición radial del centroide de burbujas en el lecho para RLFDZ-CS (α = 80º) a u_r = 2,5. Se observa que las burbujas ascienden mayoritariamente por el centro del lecho y de manera marginal por los laterales, de acuerdo con lo observado frecuentemente en lecho fluidizados de pequeño tamaño. Respecto a la distribución axial de la densidad de burbujas (Figura 4.13 (a)), la frecuencia de burbujeo está ligeramente sobreestimada por las simulaciones. Sin embargo, el modelo fluidodinámico reproduce la tendencia experimental por la cual en la zona inferior del lecho hay una notable densidad de burbujas que decrece con la altura (por coalescencia de burbujas adyacentes) hasta alcanzar un mínimo al inicio de la región cónica. A partir de ese punto, la densidad de burbujas repunta por la adición de burbujas desde el distribuidor secundario y cae, de nuevo, en la zona alta del lecho por coalescencia. La forma que adopta la

distribución axial de densidad de burbujas en este estudio es característica del RLFDZ-CS y está influenciada por la singular configuración del lecho.

Otro parámetro que permite evaluar la capacidad del modelo para simular el régimen de burbujeo es la medición de la fracción volumétrica promedio ocupada por las burbujas respecto al volumen total del lecho o *bubble hold-up*, b_h. El parámetro b_h, comprendido entre 0% y 100%, fluctúa con el tiempo como resultado de la formación, coalescencia, ruptura y erupción de burbujas a través de la superficie libre del lecho. Las frecuencias de oscilación y las amplitudes de b_h experimentales y simuladas, son comparables. El valor promedio de b_h varía de manera proporcional con la velocidad relativa del gas alimentado de tal forma que $b_{h,ur=1,5} \sim$ 11%, mientras que $b_{h,ur=2,5} \sim$ 20% y $b_{h,ur=3.0} \sim$ 25%.

Adicionalmente, la comparativa entre las distribuciones simulada y experimental de tamaños de burbujas (Figura 4.13 (b)) muestra un máximo de probabilidad común en torno a un diámetro de burbuja equivalente en el rango d_b = 0,2 – 0,4 cm, correspondiente al tamaño inicial de las burbujas formadas junto a los dos distribuidores de gas. La probabilidad de encontrar grandes burbujas de gas disminuye gradualmente con el tamaño de burbuja, con una tasa de decaimiento muy similar en ambos casos.

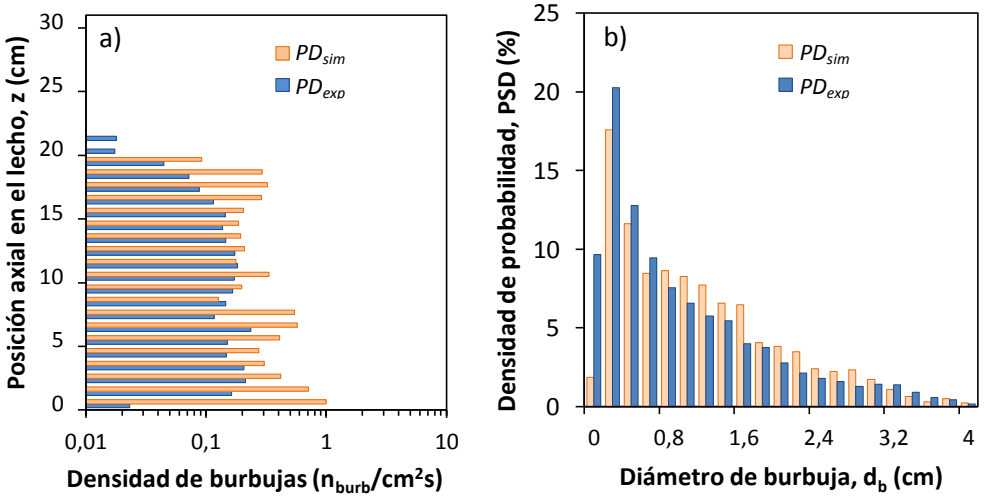

Figura 4.13 a) Frecuencia de aparición de burbujas a lo largo del lecho, b) Densidad de probabilidad para el tamaño de burbuja. Condiciones de operación: RLFDZ-CS (α = 80º) a u_r = 2,5

La geometría característica de las burbujas fue igualmente analizada para estudiar si el modelo fluidodinámico es capaz de simular burbujas morfológicamente similares a las experimentales. Los resultados muestran que la distribución de relaciones de aspecto (cociente entre la altura y la anchura, *AR*) de las burbujas es prácticamente coincidente entre experimentos y simulaciones con un máximo claramente definido en torno a *AR* = 1 (Figura 4.14 (a)). Esto implica el predominio de burbujas de geometría esférica respecto a burbujas 'planas' (*AR* < 1) o 'afiladas' (*AR* > 1). Experimentalmente, se ha encontrado que cuanto mayor es el caudal de gas más se desplaza la curva de probabilidad hacia valores de relación de aspecto altos.

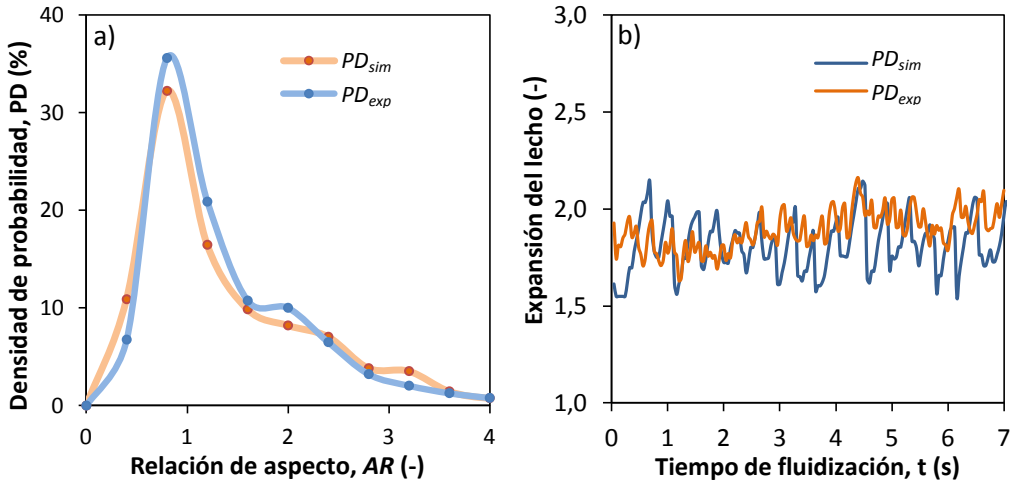

Figura 4.14 a) Distribución de probabilidades de la relación de aspecto de las burbujas, b) Evolución transitoria de la expansión del lecho. Condiciones de operación: RLFDZ-CS (α = 80º) a u_r = 2,5

Por último, se comparó la expansión del lecho experimental con la del simulado, a fin de estudiar la capacidad del modelo fluidodinámico para simular la porosidad del lecho real, tanto en estado aflojado como en distintos regímenes de fluidización. La expansión del lecho se define en este estudio como el incremento relativo del volumen del lecho al pasar de estado aflojado a fluidizado. En el caso del RLFDZ-CS no sería correcto utilizar la diferencia de alturas de lecho entre los dos estados, debido a la particular geometría del reactor. Aunque la posición axial de la superficie libre del lecho fluctúa con el tiempo, es posible medir la altura media del lecho en estado fluidizado, así como la frecuencia y amplitud de la fluctuación. La Figura 4.14 (b) muestra como la fluctuación de la expansión experimental tiene mayor amplitud que la simulada. Teniendo en cuenta que el modelo simula la variación de la fracción volumétrica de burbujas en el lecho con gran exactitud, las discrepancias encontradas en las medidas de expansión del lecho podrían atribuirse a una deficiente predicción de la fracción volumétrica de sólidos a lo largo de la fase emulsión.

4.4 Velocimetría de partículas (PIV). Perfiles de flujo másico

Una vez estudiadas en detalle las propiedades de burbuja y validados los modelos fluidodinámicos JHM y TFM bajo distintos los regímenes de burbujeo, se va a profundizar en el movimiento local de sólidos en el lecho. Si bien el estudio de mezcla axial de trazadores ópticos detalla la evolución temporal del grado de mezcla global entre las dos zonas del RLFDZ-CS, la velocimetría de partículas (PIV) ofrece un análisis mucho más detallado de la tasa de intercambio axial y del flujo másico local de sólidos a lo largo de todo el lecho. El estudio experimental de la circulación de sólidos en un RLFDZ-CS mediante PIV, llevado a cabo en las instalaciones del Grupo de Reactores Multifásicos (SMR) de la Universidad Tecnológica de Eindhoven (Países Bajos), se recoge en los Artículos II y V del compendiio.

4.4.1 Circulación de sólidos en RLFDZ-CS

El análisis PIV da como resultado mapas vectoriales transitorios, con información detallada acerca de la velocidad instantánea de partículas sólidas en las diferentes regiones en las que se divide la imagen del lecho. Entre la información que es posible recabar a partir de un

resultado PIV se encuentra la determinación de las trayectorias de circulación de sólidos, su movimiento en presencia de elementos internos al lecho, la detección de burbujas junto con sus estelas y nubes de sólidos en movimiento, la lluvia de partículas (*particle raining*) en el interior de dichas burbujas, la formación de regiones libres de sólido o *gas pockets* bajo la influencia de elementos internos o la detección de regiones defluidizadas (Figura 4.15 (a)).

El análisis de los mapas de velocidad obtenidos a distintos tiempos de grabación, junto con sus correspondientes mapas de porosidad (Sección 2.3.2), permiten determinar mapas promediados de circulación de sólidos y flujos másicos en la dirección axial del lecho para estudiar la mezcla de sólidos entre las distintas zonas del RLFDZ-CS.

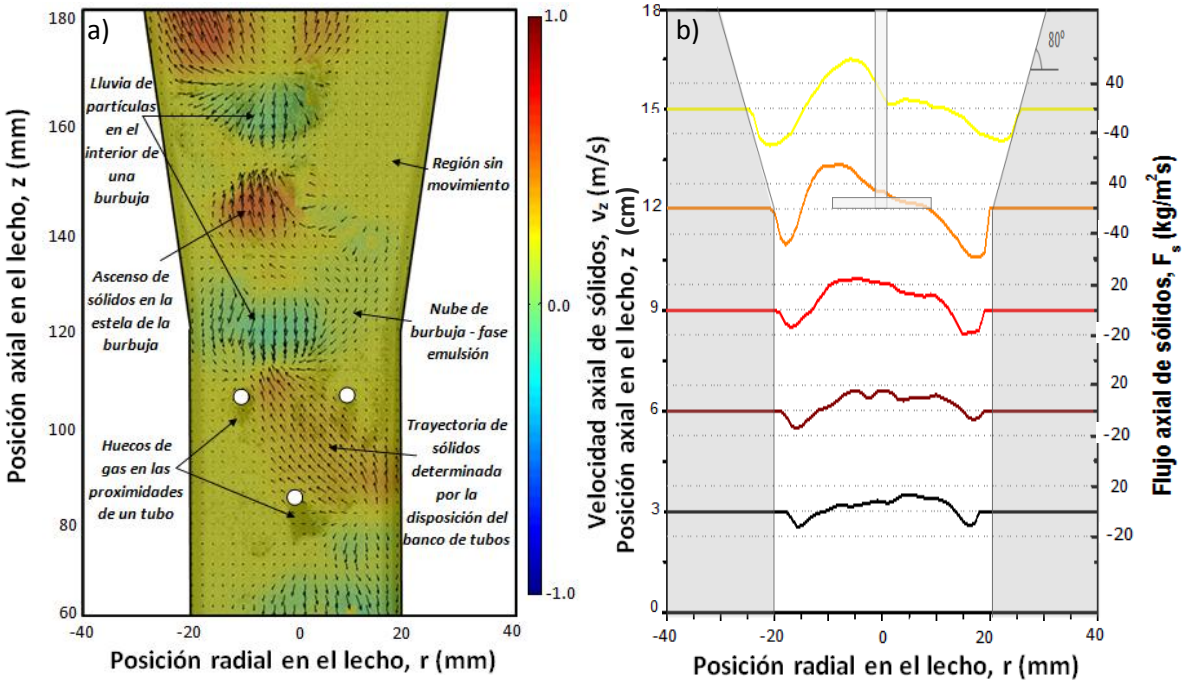

Figura 4.15 a) Interpretación de mapas transitorios de circulación de sólidos, b) Perfiles radiales de flujo axial de sólidos promedio a diferentes alturas de lecho en RLFDZ-CS

A modo de ejemplo, la Figura 4.15 (b) muestra la distribución radial de flujos másicos (F_s) promedio en la dirección axial a diferentes alturas en el lecho para un RLFDZ-CS (α = 80º) a u_r = 3,0. Como se puede observar, los sólidos ascienden preferencialmente por la parte central del lecho y caen junto a las paredes laterales. Los perfiles de flujo másico promedio son suaves en la zona inferior del lecho y localmente más acusados en la zona de aporte de gas secundario, donde el caudal de gas se duplica manteniéndose la estrecha sección de paso. La morfología del distribuidor inmerso juega un importante papel en la circulación de sólidos a lo largo de la zona cónica del lecho. El uso de un distribuidor con forma de 'T' y dos orificios de salida supone una canalización del flujo de gas (y, por tanto, del flujo de sólido) a ambos lados del distribuidor. La aparición de dos máximos relativos de flujo ascendente a una altura de lecho z = 15 cm en la Figura 4.15 (b) ilustra este fenómeno.

Cabe destacar que la distribución radial de F_s en la dirección axial no da información acerca de la variación axial del flujo ascensional promedio de sólidos en la fase estela ($F_{s,a}$) ni del flujo descendente promedio de la fase emulsión ($F_{s,d}$). Para ello es necesario analizar flujos positivos

(ascendentes) y negativos (descendentes) por separado y determinar los perfiles axiales $F_{s,a}(z)$ y $F_{s,d}(z)$. A modo de ejemplo, la Figura 4.16.a muestra la variación axial de los flujos promedio de sólidos en las fases estela y emulsión para un RLFDZ-CS (α = 80º) a u_r = 3,0, a partir de resultados PIV y de simulaciones fluidodinámicas llevadas a cabo en Ansys Fluent. Como se puede observar, el perfil axial del flujo de sólidos en un RLFDZ-CS guarda relación con el régimen de burbujeo descrito en la Sección 4.3 (Figura 4.16 (b)). La comparativa entre los resultados experimentales, referidos al movimiento de partículas en la pared frontal del reactor, y los flujos de sólido simulados a 1 mm de profundidad ilustra la capacidad del modelo para predecir el perfil axial de F_s promedio ascendentes y descendentes. La condición *'no slip'* aplicada al modelo fluidodinámico, por la cual la velocidad de la fase sólida en la pared es cero, hace que el efecto pared experimental esté igualmente presente en las simulaciones. No obstante, las simulaciones sobreestiman el flujo axial junto a la base del reactor y subestiman el flujo ascensional en la zona superior del lecho. Ambas discrepancias pueden achacarse a la incertidumbre en el modo en el que el gas accede al lecho experimental a través de los distribuidores. Mientras la velocidad del gas alimentado es homogénea a través de toda la sección de paso de los distribuidores simulados, experimentalmente el gas accede al lecho por aquella región del distribuidor que minimice la pérdida de carga a su paso. En la entrada inferior del RLFDZ-CS experimental, el elevado empaquetamiento del lecho junto a las paredes laterales conduce el gas hacia la zona central, dando lugar a un menor movimiento axial de sólidos (F_s) en la región próxima al distribuidor.

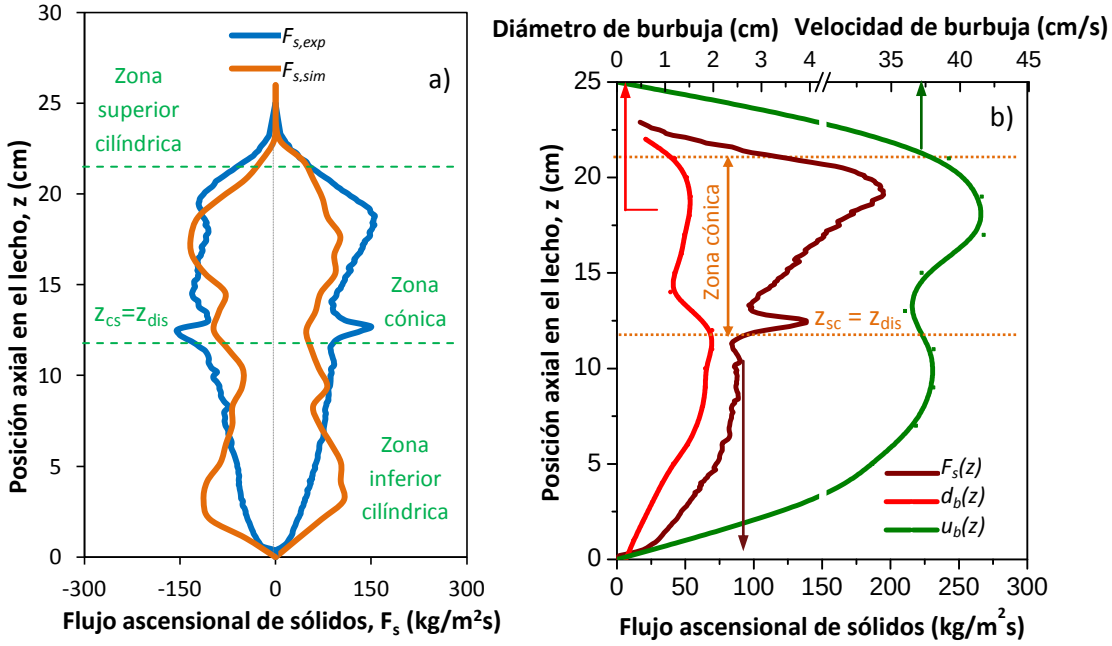

Figura 4.16 a) Perfil axial de flujos másicos experimentales (PIV/DIA) y simulados (TFM) a 1 mm de profundidad, b) Comparativa entre los perfiles experimentales de tamaño y velocidad de burbuja y el de flujo de sólidos. Condiciones de operación: RLFDZ-CS (α =80º) a u_r = 3,0

En el caso del distribuidor inmerso, el taponamiento experimental de uno de los orificios podría generar una alimentación asimétrica puntual de gas con una velocidad de inyección efectiva mayor que la asignada al distribuidor simulado. Esto explicaría que los flujos

ascensionales experimentales sean mayores que los simulados en las proximidades del distribuidor secundario.

El análisis de los flujos de sólido ascendentes y descendentes por separado permite establecer una comparativa entre las mediciones de mezcla axial de trazadores ópticos y los resultados obtenidos mediante el método PIV/DIA. En la Tabla 4.2 se detallan los valores promedio de F_s calculados experimentalmente (PIV/DIA) y estimados según las correlaciones hidrodinámicas utilizadas en la implementación del modelo de retromezcla a contracorriente (CCBM), en función de la velocidad relativa de gas y para diferentes tamaños de reactor.

Tabla 4.2 Comparativa entre flujos másicos promedio obtenidos a partir de resultados PIV y de correlaciones hidrodinámicas de acuerdo con el modelo CCBM

Escala de lecho	u_r (-)	Parámetros del modelo CCBM				Resultados PIV
		f_1 (-)	k_w (s^{-1})	u_1 (cm/s)	$F_{s,CCBM}$ (kg/m^2s)	$F_{s,PIV}$ (kg/m^2s)
2x	1,5	0,02	7,1	4,7	37,6	-
	2,0	0,04	7,6	7,0	56,0	40,0 ± 20,9
	2,5	0,06	8,2	9,0	72,0	60,4 ± 23,1
	3,0	0,06	9,0	10,9	87,2	95,2 ± 36,9
1x	1,5	0,02	7,9	4,2	33,6	16,3 ± 11,3
	2,0	0,04	9,2	6,3	50,4	37,7 ± 20,6
	2,5	0,05	10,8	8,2	65,6	58,6 ± 34,1
	3,0	0,07	11,9	10,0	80,0	84,2 ± 44,9

De acuerdo con trabajos previos (129), la determinación del F_s promedio para las fases ascendente y descendente permite estimar el tiempo teórico de circulación de sólidos (t_c) en lechos fluidizados. En concreto, t_c se define como el tiempo medio requerido para que una partícula alcance la superficie libre del lecho y regrese a su posición de origen (130). El tiempo teórico de circulación se calcula en función de la altura media del lecho fluidizado (h_{fb}), la mínima altura a la cual las burbujas promueven el movimiento de sólidos (h_{min}) y la velocidad promedio ascendente ($\overline{v_a}$) y descendente ($\overline{v_d}$) de los sólidos, según la ecuación 45.

$$\bar{t_c} = \int_{h_{min}}^{h_{fb}} \frac{dz}{\overline{v_a}(z)} + \int_{h_{min}}^{h_{fb}} \frac{dz}{\overline{v_d}(z)} \qquad \text{(E.45)}$$

En esta expresión, tanto la altura mínima como la altura de la superficie libre dependen de la velocidad del gas de fluidización, de tal forma que un aumento de u_r supone una disminución de h_{min} y un incremento de h_{fb}. Los valores promedio de velocidad se han determinado a partir de la distribución axial de F_s, de la densidad de lecho (ρ_{bulk}) y de la distribución axial de porosidades de lecho (ε_s). Se ha observado que el tiempo de circulación aumenta dramáticamente conforme se reduce la velocidad de gas hasta valores próximos a la velocidad de mínima fluidización, a la cual deja de haber mezcla axial de sólidos. A modo de ejemplo, se ha determinado que para un RLFDZ-CS (α = 80º) el tiempo promedio de circulación a u_r = 3,0 es de seis minutos mientras que para u_r = 2,0 éste se incrementa hasta más de once minutos.

4.4.2 Relación entre el régimen de burbujeo y el flujo de sólidos en RLFDZ-CS

Como se ha adelantado anteriormente, la forma del perfil axial de tamaño y velocidad de burbuja promedio en el RLFDZ-CS se asemeja a la de la variación axial del flujo de sólidos. En la Figura 4.16 (b) se comparan los perfiles $d_b(z)$ y $u_b(z)$ frente a $F_s(z)$ para un experimento realizado con una velocidad relativa de gas, u_{gas}/u_{mf} = 3,0, a fin de relacionar el régimen de burbujeo con el movimiento de sólidos en el lecho. Experimentalmente, se observa que las burbujas de mayor tamaño son más rápidas que las pequeñas, en concordancia con las correlaciones hidrodinámicas clásicas (19). Asumiendo una fracción volumétrica de sólidos constante en la estela (87), independientemente del tamaño y velocidad de la burbuja, el flujo ascensional de sólidos debería seguir un perfil axial similar al de $d_b(z)$ y $u_b(z)$, como se demuestra experimentalmente.

Junto a la base del reactor, las burbujas incipientes de pequeño tamaño apenas arrastran sólidos en su estela y la movilidad del lecho en la región más próxima al punto de inyección de gas es muy limitada. Conforme se incrementa el tamaño de las burbujas con la altura y su velocidad, el flujo axial de sólidos a contracorriente aumenta. Al alcanzar la región cónica, la disminución promedio del tamaño de las burbujas no se traduce en una disminución del flujo de sólidos sino que éste aumenta puntualmente. Esto se debe a que el gas proveniente del distribuidor inmerso, a pesar de formar pequeñas burbujas, es propulsado a gran velocidad a través de los orificios de distribución arrastrando consigo los sólidos bajo su área de influencia. Tras la aceleración puntual, la evolución del flujo axial de sólidos vuelve a estar ligada al régimen de burbujeo, variando en función del tamaño y velocidad de burbuja a lo largo de la zona superior del lecho.

4.4.3 Mapas de variabilidad RMS: detección de canales preferenciales, regiones defluidizadas y presencia de slugs

Junto con los mapas de flujo másico de sólidos, el análisis PIV permite obtener mapas de variabilidad de la velocidad en cada punto del lecho a lo largo del tiempo, expresada en función de su media cuadrática (o *Root Mean Square*, RMS). A partir de los mapas RMS es posible detectar regiones del lecho defluidizadas (aquellas en las que la variabilidad de las medidas tiende a cero), caminos preferenciales de circulación de sólido o incluso regímenes de *slugging*.

Los canales preferenciales son producto de la tendencia del gas a ascender a través del lecho por el camino que le ofrece una menor pérdida de carga. Experimentalmente, se ha comprobado que el acanalamiento o *channeling* en la circulación ascensional de sólidos es significativo en la zona superior del RLFDZ-CS trabajando a bajas velocidades de gas (u_r < 1,5). En estas condiciones, el bajo exceso de gas y el grado de empaquetamiento del lecho generan regiones parcialmente defluidizadas, reduciendo la superficie efectiva del paso de gas. En la Figura 4.17 (a) se muestra el fenómeno de *channeling* a partir de un mapa RMS. La gran variabilidad observada en la velocidad de una estrecha zona del lecho contrasta con la pequeña o nula variabilidad de velocidades a ambos lados de esta región, indicando la presencia de un canal preferencial de circulación de sólidos.

La detección de zonas con frecuente formación de *slugs* es posible gracias al efecto de la lluvia de partículas (*particle raining*) en los mapas de velocidad. La lluvia de partículas afecta especialmente al interior de burbujas de gran tamaño y tiene como resultado la detección de elevadas velocidades de caída de partículas en el interior de las mismas. Como la técnica PIV no distingue entre zonas densamente cargadas y zonas libres de sólido, los mapas RMS que muestran una elevada variabilidad de velocidades a lo largo de la sección transversal, especialmente en la zona estrecha del lecho, son indicativos de un régimen de *slugging* (Figura 4.17 (b)). Este fenómeno suele aparecer de manera general en reactores estrechos y altos y, en lo que respecta al RLFDZ-CS, aparece al utilizar bajas velocidades de gas en la zona superior del lecho combinadas con elevadas velocidades en la zona inferior. En tal caso, las burbujas de gas formadas en la parte baja del lecho alcanzan la región cónica parcialmente defluidizada, quedando el gas atrapado entre ambas zonas de lecho y produciendo un cortocircuito en la circulación axial de sólidos.

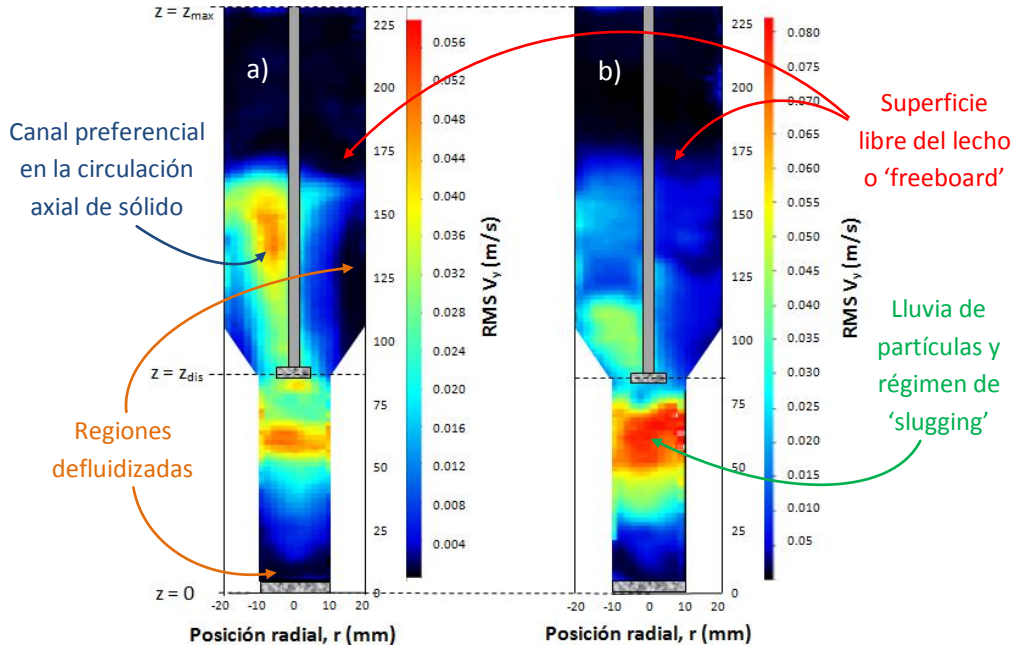

Figura 4.17 Mapas de desviación promedio para la velocidad axial de sólidos (*RMS* V_y) en un reactor RLFDZ-CS (α = 45°) con: a) $u_{r,inf}$ = 1.8 y $u_{r,sup}$ = 1,5, b) $u_{r,inf}$ = 2,5 y $u_{r,sup}$ = 1,3

4.5 Efecto del uso de elementos internos en el lecho

A fin de minimizar los problemas fluidodinámicos asociados a la formación periódica de burbujas de gran tamaño que a menudo cortocircuitan la mezcla axial de sólidos en la zona inferior del RLFDZ-CS, se decidió implementar un banco de tubos a modo de elementos internos para romper las burbujas de gas y mejorar el contacto gas-sólido en dicha región del lecho. En concreto, se utilizaron seis configuraciones diferentes, de acuerdo con el esquema de la Figura 2.8, para optimizar la disposición del banco de tubos con el objetivo de reducir el tamaño promedio de burbuja. A continuación, se presentan los resultados más relevantes relativos al efecto del uso de distintas configuraciones de elementos internos en el comportamiento fluidodinámico de un RLFDZ-CS, tanto en lo que respecta a las propiedades de burbuja como a la circulación de sólidos. Dichos resultados pertenecen, en esencia, al Artículo V del compendio.

4.5.1 Reducción del tamaño promedio de burbuja

La Figura 4.18 muestra el efecto de tres de esas configuraciones de tubos (*3i*, *5i* y *8i*) en la reducción del tamaño de burbuja con respecto al obtenido utilizando la configuración de reactor sin *internals* a altas velocidades de gas, u_r = 3,0. Los resultados experimentales sugieren que las diferentes filas de tubos asumen distintos roles en la reducción del diámetro de burbuja promedio. Por ejemplo, el tubo central de la segunda fila del banco en la configuración *3i* no conduce sustancialmente a la ruptura de burbujas. De hecho, el diámetro equivalente promedio en ese punto del lecho es del orden de 1,7 cm, inferior a la distancia entre el tubo y las paredes laterales y a la distancia vertical entre filas de tubos consecutivas. Así, las burbujas tenderán a rodear el tubo por ambos lados sin reducir su tamaño. En esa misma configuración, la fila superior consta de dos tubos. Como la fase emulsión tiende a caer junto a las paredes laterales del lecho, se fuerza a las burbujas a pasar por el hueco central entre dichos tubos, provocando la reducción del tamaño promedio de burbuja.

Utilizando una configuración de cinco tubos al tresbolillo (*5i*), la disminución del diámetro de burbuja promedio resulta más efectiva. Los dos tubos de la fila inferior reducen el tamaño de burbuja ya que la distancia entre ellos es inferior al tamaño de la burbuja que penetra a su través. Las burbujas alcanzan el tubo central de la segunda fila rodeándolo sin aumentar su tamaño y acceden a los dos tubos de la fila superior, donde tiene lugar el mismo efecto que el comentado para la configuración *3i*.

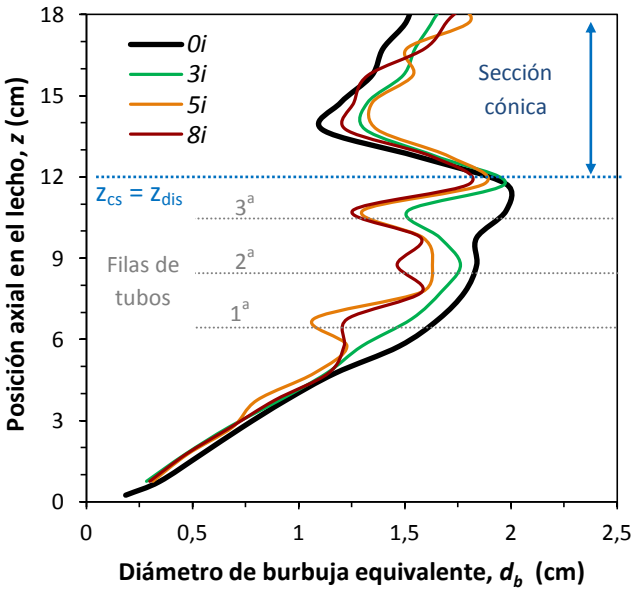

Figura 4.18 Efecto de la configuración del banco de tubos en la reducción del tamaño de burbuja en la dirección axial

Por último, la configuración híbrida (ni alineada ni al tresbolillo) de ocho tubos conduce a la mayor reducción del tamaño de burbuja de entre las investigadas. Su primera fila, común con la de la configuración *5i*, fuerza a las burbujas a pasar por el hueco central entre tubos contrayendo su tamaño. Al llegar a la segunda fila de *internals* con tres tubos alineados, se produce la ruptura de burbujas, reduciendo drásticamente su tamaño promedio.

Sin embargo, en esta configuración la fila superior de tubos no ejerce gran influencia en la disminución del tamaño de burbuja, por lo que el rendimiento global de la reducción del diámetro equivalente al paso de las tres filas de tubos es similar al obtenido con la configuración 5i.

Se concluye, pues, que la configuración de cinco tubos al tresbolillo es suficientemente efectiva para disminuir el tamaño de burbuja. El uso de un mayor número de tubos no solo no ha demostrado ser más eficaz en la reducción del tamaño promedio de burbuja sino que, además, penaliza el comportamiento fluidodinámico del lecho incrementando el tiempo teórico de circulación, como se expondrá más adelante.

4.5.2 Circulación de sólidos

La Figura 4.19 (a) muestra la distribución radial de los flujos de sólido obtenidos bajo las mismas condiciones de operación, es decir, utilizando una velocidad relativa de gas, u_r = 3,0, para las configuraciones *5i* y *8i* respecto a la de referencia (sin tubos, *0i*). Los resultados mostrados están referidos a las posiciones axiales de lecho, z = 6,5, 8,5 y 10,5 cm, en las cuales se encuentran ubicadas las diferentes filas de tubos.

En primera instancia, la circulación axial en la configuración sin banco de tubos parece menor que en los otros casos debido sus achatados perfiles radiales de flujo másico. Sin embargo, esto no es necesariamente cierto y únicamente implica que la circulación de sólidos está menos dirigida que en las configuraciones con banco de tubos: los tubos actúan como canalizadores de flujo. de tal manera que la fase ascendente circula preferencialmente por el centro del lecho y la fase descendente lo hace junto a las paredes laterales.

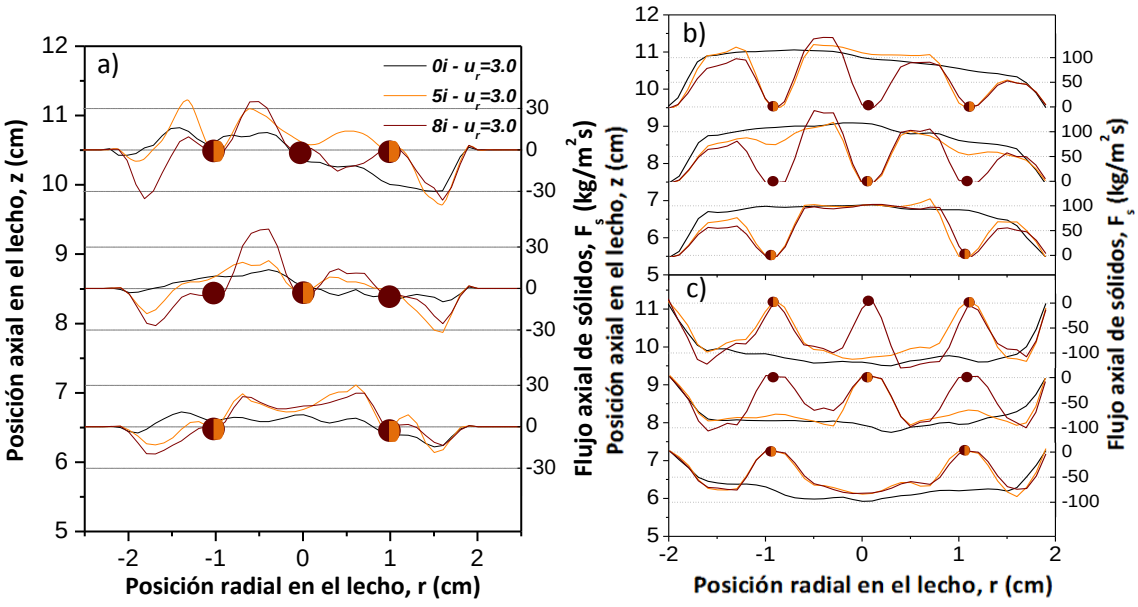

Figura 4.19 a) Distribución radial de flujos másicos en la dirección axial para tres configuraciones del banco de tubos (*0i*, *5i*, *8i*), b) Flujos ascendentes, c) Flujos descendentes

Así pues, el diagrama de la Figura 4.19 (a) no facilita información sobre la mezcla axial, sino sobre los patrones de circulación de sólidos. Para evaluar el efecto del banco de tubos en la mezcla axial y, por tanto, en el tiempo de circulación teórico, es necesario analizar los flujos

ascendentes y descendentes por separado, tal y como se ha descrito en la Sección 4.4.1. Como se puede apreciar en la Figura 4.19 (b), el perfil radial de F_s para las fases estela y emulsión es cuantitativamente similar y de signo opuesto. Independientemente de la presencia o ausencia del banco de tubos, los perfiles radiales muestran características de flujo turbulento (flujo homogéneo en el centro del lecho y elevado gradiente de flujo junto a las paredes laterales). Se observa que a mayor número de tubos, menor es el flujo axial de sólidos a través del banco. Por tanto, menor es la tasa de mezcla axial. Además, se constata que los perfiles radiales de flujo másico en la primera fila de tubos de las configuraciones *5i* y *8i* coinciden, lo que sugiere que la disposición de los tubos en las filas superiores no afecta al comportamiento fluidodinámico del sólido a través de la fila inferior de tubos. Operando de la manera descrita en la Sección 4.4.1 se ha podido determinar la variación axial de F_s ascendentes y descendentes para las distintas configuraciones de tubos, así como su t_c. Los resultados mostrados en la Figura 4.20 y en la Tabla 4.3 sugieren que los perfiles axiales de F_s son similares entre las distintas configuraciones y únicamente se diferencian en la región afectada por la existencia del banco de tubos. A este respecto, se ha calculado que el flujo másico a través de una configuración *8i* es un 30% menor que en el caso sin tubos.

Tabla 4.3 Efecto de la velocidad de gas y el número de tubos en el tiempo de circulación promedio

u_r (-)	Número de tubos	h_{min} (cm)	h_{fb} (cm)	$t_{c,asc}$ (s)	$t_{c,desc}$ (s)	t_c (min)
2,0	0	0,9	20,4	358,4	319,9	11,3
2,5	0	0,6	22,1	223,0	215,9	7,3
3,0	0	0,5	22,9	172,5	187,6	6,0
3,0	5	0,5	22,9	195,4	211,3	6,7
3,0	8	0,5	22,9	199,2	211,7	6,8

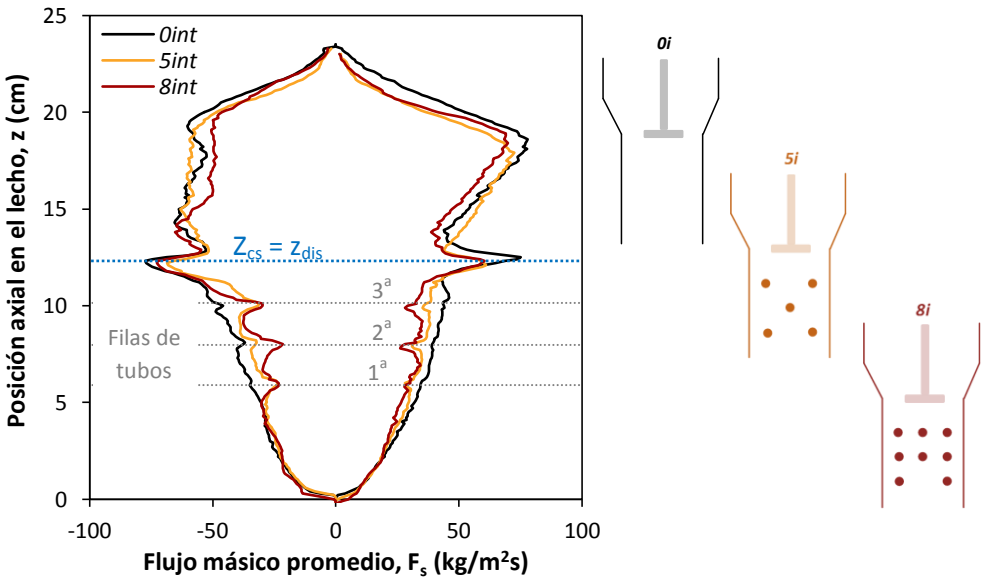

Figura 4.20 Perfil axial de flujos másicos ascendente y descendente en RLFDZ-CS (α = 80º) a u_r = 3,0 para tres configuraciones de tubos

4.6 Efecto del cambio de escala

Hasta este punto, los resultados relativos al movimiento de sólidos y propiedades de burbuja se han referido exclusivamente a RLFDZ-CS de pequeñas dimensiones o '*1x*', análogos a los utilizados a escala de laboratorio en investigaciones paralelas dentro del grupo CREG (12, 14, 131). A continuación, se va a estudiar el efecto del cambio de escala en el comportamiento fluidodinámico de un RLFDZ-CS analizando, tanto de manera experimental como a partir de simulaciones, dicho efecto en las propiedades de burbuja, en la mezcla axial de sólidos y en la capacidad predictiva del modelo JHM. Los resultados mostrados en esta sección están referidos al Artículo VI del compendio.

4.6.1 Mezcla axial de sólidos

La Figura 4.21 presenta una comparativa entre los resultados de mezcla axial a partir trazadores ópticos llevados a cabo en reactores RLFDZ-CS pseudo-2D de distinto tamaño, a igualdad de velocidades relativas de gas y de relación entre secciones del lecho inicialmente iluminadas y no iluminadas. En concreto, se muestran los perfiles transitorios de grado de mezcla axial, *IM*, experimental y modelado (según el modelo CCBM) para diferentes u_{gas}/u_{mf} y escalas de reactor, obtenidos tal y como se describe en las Secciones 2.1 y 3.2.

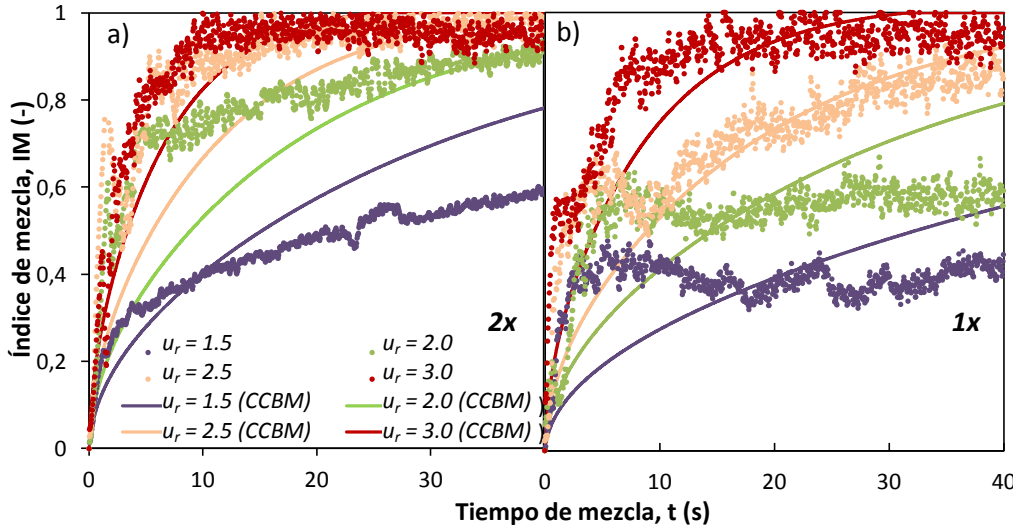

Figura 4.21 Evolución del grado de mezcla experimental y modelado en función de la velocidad de gas y la configuración de reactor: a) RLFDZ-CS (α = 80º) escalado, *'2x'*, b) RLFDZ-CS (α = 80º) original, *'1x'*

Las curvas de mezcla experimentales sugieren que la mezcla axial es más rápida a mayor tamaño de reactor bajo las mismas condiciones de gas alimentado. Este resultado podría relacionarse con lo descrito en la Sección 4.1 acerca de la velocidad de mínima fluidización aparente (u_{mf}^*) medida en lechos estrechos por efecto de las paredes laterales sobre el movimiento de sólidos en sus proximidades. Según esto, la menor relación S_{lecho}/L_{lecho} en el reactor a pequeña escala puede suponer un menor exceso de gas aparente, $u_{gas} - u_{mf}^*$, lo que implicaría una menor tasa de mezcla axial. Otra posible explicación sería la variación del tamaño de burbuja entre escalas. Asumiendo que u_{mf}^* fuera idéntica para ambas escalas de reactor, y por tanto también lo fuera el exceso de gas, las burbujas de gas generadas en reactores a mayor escala llegarían a ser más grandes debido a la mayor altura del lecho y al

fenómeno de coalescencia. Así, cuanto más alto y ancho sea el lecho, mayor es la probabilidad de encontrar grandes burbujas y, siendo que estas dan lugar al movimiento axial de sólidos, ello explicaría la tendencia experimental observada respecto a la variación temporal del índice de mezcla entre escalas.

A partir de los perfiles axiales de flujo de sólidos ascendentes y descendentes obtenidos mediante PIV/DIA ha sido posible estudiar el efecto del cambio de escala en el comportamiento fluidodinámico del RLFDZ-CS: se han cuantificado los flujos másicos axiales promedio relativos a cada velocidad de gas y se han comparado las curvas $F_s(u_r)$ obtenidas para las diferentes escalas de reactor.

La Figura 4.22 ilustra el efecto del escalado en el perfil $F_s(u_r)$ experimental. Se observa que, independientemente del tamaño del lecho, la variación de tasa de circulación de sólidos no es lineal con el caudal de gas. El incremento del flujo de sólidos con u_r es tanto mayor cuanto más turbulento es el régimen de fluidización. Asimismo, se ilustra la elevada variabilidad de los flujos de sólido con la posición axial y se cuantifica la tendencia apuntada por los mapas de mezcla axial: que el incremento del tamaño del lecho repercute en mayores flujos másicos a igualdad de velocidades de gas alimentado.

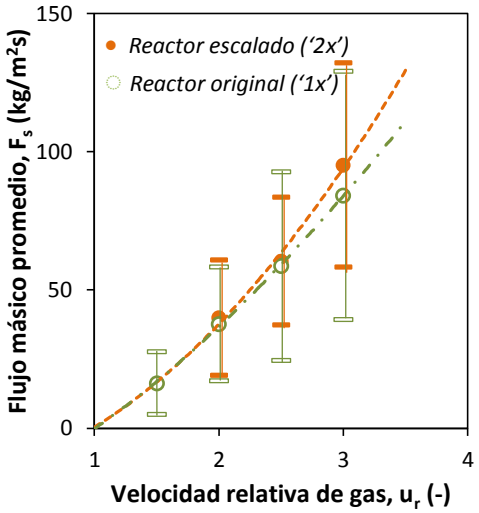

Figura 4.22 a) Efecto del cambio de escala en el perfil $F_s(u_r)$ para un RLFDZ-CS

4.6.2 Propiedades de burbuja

La Figura 4.23 detalla la evolución de los perfiles axiales de tamaño de burbuja experimentales (DIA), simulados (TFM) mediante Ansys CFX y modelados (JHM), obtenidos para ambas escalas de reactor a diferentes velocidades de gas en el rango u_r = 1,5 – 3,0. Se comprueba que a altas velocidades de gas, u_r = 3,0, el tamaño de las burbujas en la configuración '*1x*' (pequeña escala) crece tanto como permite la anchura del lecho o sección de paso (w_{1x} = 2 cm), lo que conduce a la frecuente aparición de *slugs,* reduciendo la mezcla axial de sólidos. Por el contrario, para un mismo régimen de burbujeo en la configuración '*2x*' (reactor escalado) las burbujas no llegan a representar ni la mitad de la anchura del lecho (w_{2x} = 4 cm), por lo que su crecimiento no está limitado. Dado que la altura del lecho es el doble de grande, las burbujas pueden seguir creciendo por coalescencia. La diferencia en el tamaño de

burbuja promedio entre los lechos a distinta escala bajo una misma velocidad de gas confirma lo expuesto anteriormente acerca del incremento de la tasa de mezcla axial al aumentar la escala del reactor. En lo que respecta a la capacidad predictiva del simulador y el modelo JHM, ambos modelos son capaces de predecir cualitativamente la evolución axial del tamaño de burbuja experimental de manera satisfactoria en el rango de velocidades de gas experimentadas.

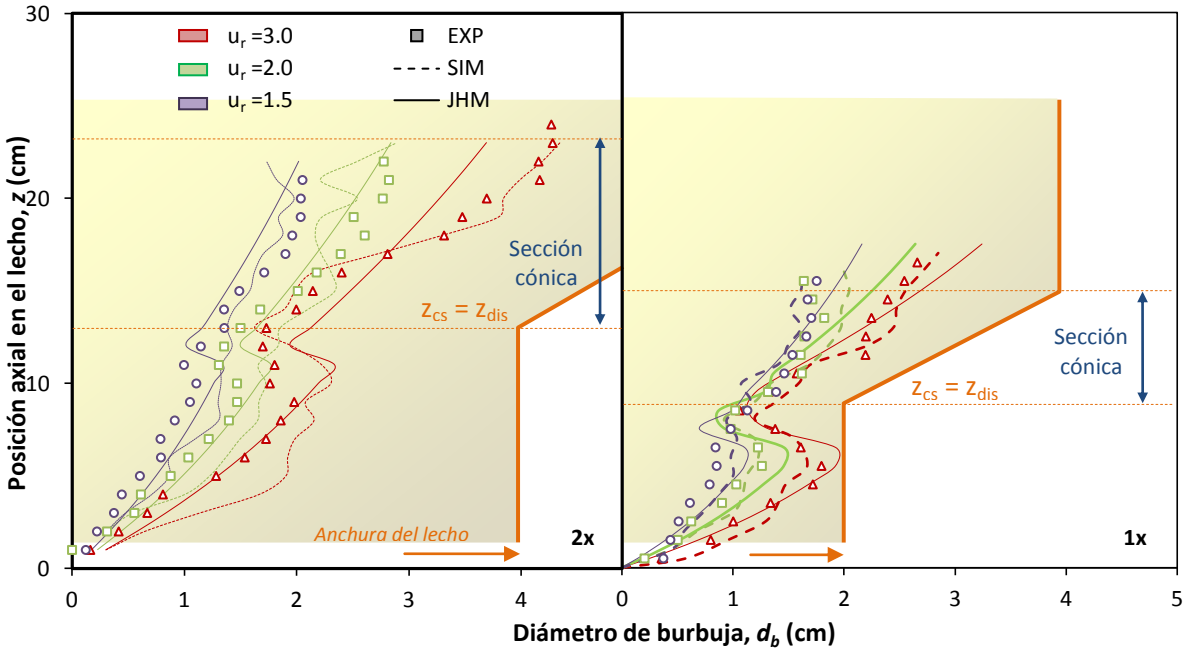

Figura 4.23 Distribución axial de tamaños de burbuja experimental (EXP), simulada (SIM) y modelada (JHM) en función de la velocidad del gas: a) RLFDZ-CS (α = 80º) escalado, b) RLFDZ-CS (α = 80º) original

Atendiendo a la distribución de tamaños de burbuja, se ha encontrado que la probabilidad de aparición de grandes burbujas (d_b > 3 cm) en el reactor escalado es sustancialmente mayor que para la configuración '*1x*' mientras que, por el contrario, la probabilidad de encontrar burbujas pequeñas (0 < d_b < 2 cm) es hasta ocho puntos mayor en el reactor a pequeña escala, en función de la velocidad de gas utilizada (Figura 4.24).

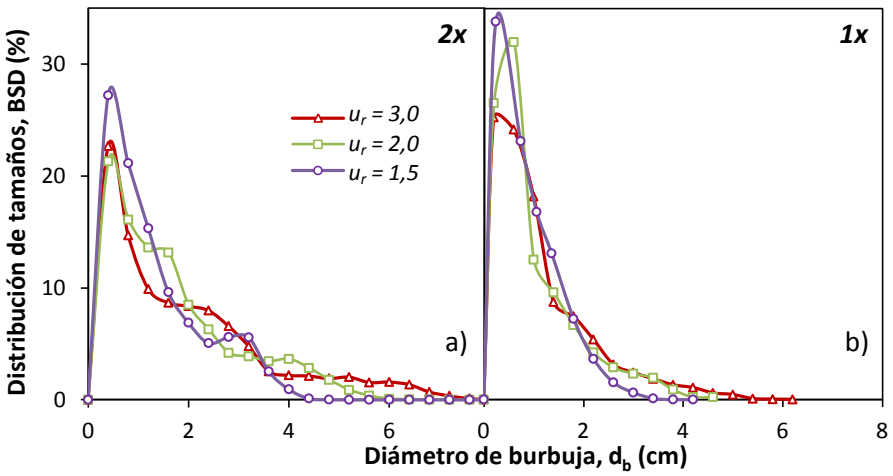

Figura 4.24 Distribución de probabilidades del tamaño de burbuja experimental en función de la velocidad del gas y del tamaño del reactor: a) RLFDZ-CS (α = 80º) escalado, b) RLFDZ-CS (α = 80º) original

La relación de aspecto de las burbujas también se ve ligeramente afectada por el cambio de escala. Los resultados experimentales sugieren que las burbujas son eminentemente esféricas con una ligera tendencia hacia relaciones de aspecto mayores que 1, lo que indica que las burbujas "verticales" o rápidas predominan sobre las "achatadas" o lentas. Sin embargo, las curvas de relaciones de aspecto para la configuración '*1x*' tienden a valores de AR más altos que las del reactor escalado. Una posible explicación a esta discrepancia pasa por el hecho de que la sección estrecha del reactor '*1x*' limita el crecimiento horizontal de las burbujas y las fuerza a adoptar formas más alargadas en dirección vertical. En cuanto al efecto de la velocidad de gas en la distribución de relaciones de aspecto, se observa que cuanto mayor es el flujo de gas, más alargadas en dirección vertical son las burbujas desplazándose las curvas hacia la zona de valores mayores de AR.

Por otro lado, se ha analizado si la fracción volumétrica del lecho ocupada por burbujas (b_h) varía con la escala del reactor para un determinado régimen de burbujeo. En la Tabla 4.4 se detallan los valores promedio y las desviaciones típicas de b_h experimentales y simuladas para distintas velocidades de gas y escalas de reactor. La capacidad predictiva del modelo computacional para estimar el volumen promedio de lecho ocupado por burbujas y su fluctuación a lo largo del tiempo es satisfactoria, especialmente trabajando a elevadas velocidades de gas dentro del intervalo experimentado. Además, aunque se ha mostrado que la configuración '*2x'* da lugar a tamaños de burbuja mayores, el volumen ocupado por el lecho también es mayor en el reactor escalado. Como resultado, la fracción volumétrica de burbujas en el lecho prácticamente coincide a ambas escalas.

Tabla 4.4 Efecto de escala en el volumen de lecho ocupado por burbujas y en la altura de la superficie libre para un RLFDZ-CS (α = 80º) operado a distintos regímenes de burbujeo

Tamaño del lecho (escala)	Velocidad relativa, u_r (-)	Fracción de burbujas, b_h (%)		Altura de superficie libre, h_{fb}(cm)	
		Experimental	Simulación	Experimental	Simulación
2x	1,5	11,1 ± 3,8	7,8 ± 3,1	29,5 ± 0,7	27,9 ± 0,7
	2,0	17,6 ± 5,6	11,8 ± 4,9	31,4 ± 0,8	30,2 ± 0,9
	2,5	22,8 ± 7,6	20,0 ± 5,2	33,1 ± 1,6	32,0 ± 0,9
	3,0	24,3 ± 7,8	22,0 ± 7,4	34,3 ± 2,1	33,8 ± 1,1
1x	1,5	13,8 ± 5,7	7,8 ± 3,9	16,3 ± 0,4	18,2 ± 0,4
	2,0	17,6 ± 5,6	12,7 ± 5,3	19,6 ± 0,9	19,8 ± 0,6
	2,5	20,8 ± 7,8	20,1 ± 5,5	21,0 ± 1,3	21,2 ± 0,6
	3,0	26,1 ± 9,9	23,1 ± 7,5	21,9 ± 1,7	22,1 ± 0,7

En lo que respecta al movimiento de burbujas, se han analizado tanto el perfil $u_b(d_b^{0.5})$ como el $u_b(z)$, es decir, la dependencia de la velocidad de burbuja con su tamaño y con la posición axial en el lecho, para el rango usual de velocidades de gas y las dos configuraciones de reactor. Se ha comprobado que las velocidades de burbuja promedio simuladas en función de su tamaño y la posición se corresponden satisfactoriamente con las experimentales. Además, la correlación clásica de Davidson y Harrison es capaz de predecir cualitativamente la velocidad de las burbujas en un RLFDZ-CS para los tamaños de lecho utilizadas, sugiriendo que el efecto de escala en los perfiles $u_b(z)$ y $u_b(d_b^{0.5})$ es despreciable utilizando el mismo tipo de partícula y velocidad de gas entre escalas.

4.6.3 Ángulo de defluidización

Los ensayos de defluidización llevados a cabo en reactores RLFDZ-CS (α = 0º) de distintos tamaños revelan que, incluso en el peor de los escenarios de fluidización (u_r ~ 1,1) dentro del rango de operación estudiado, las regiones defluidizadas a ambos lados del cambio de sección no alcanzarían ángulos de talud mayores de 80º.

No obstante, se ha demostrado que el escalado del reactor conlleva un sustancial incremento de β para todos los regímenes de burbujeo experimentados, independientemente de la forma de alimentar el gas al lecho (bien dividiendo el caudal entre los dos distribuidores o alimentando el caudal total únicamente por el distribuidor inferior). Una posible explicación es la variación de la distancia relativa entre el punto de alimentación de gas inmerso y la pared lateral de la zona superior del lecho, duplicada en el caso del reactor escalado. La lejanía del punto de inyección a las paredes laterales limita la propagación radial de las burbujas, favoreciendo la defluidización de la zona de cambio de sección. La Figura 4.25 ilustra este fenómeno.

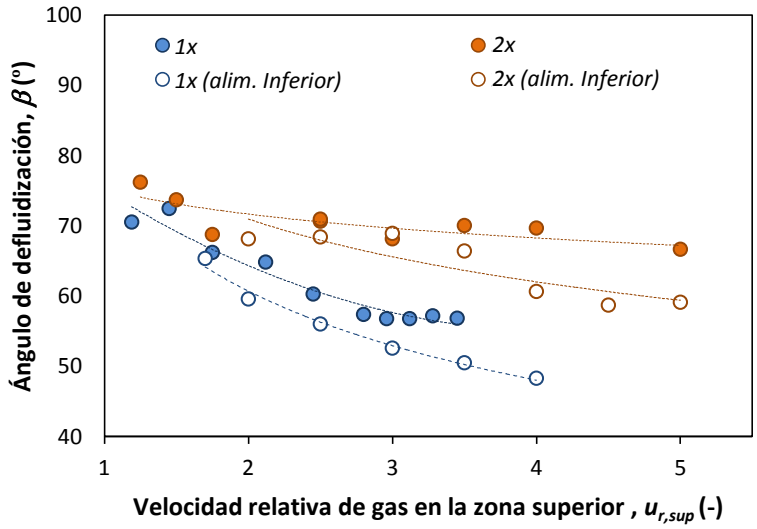

Figura 4.25 Efecto del cambio de escala y de la alimentación de gas en el ángulo de defluidización experimental

Además, se ha comprobado que la alimentación de gas localizada en la zona inferior del reactor da lugar a menores valores de β respecto a si el caudal total de gas se introduce por ambos distribuidores de manera fraccionada, a pesar de utilizar velocidades de gas similares en la zona superior del lecho ($u_{r,sup}$). Esto es debido a que el comportamiento fluidodinámico difiere entre ambos casos. Al alimentar desde los dos distribuidores, las burbujas provenientes del distribuidor inmerso ascienden junto a la varilla distribuidora por el centro del lecho sin favorecer la circulación de sólidos junto a la pared. En caso de alimentar únicamente desde el distribuidor inferior, el régimen de burbujeo es más turbulento alcanzándose burbujas de mayor tamaño en la zona estrecha del lecho y favoreciendo la mezcla de sólidos una vez superado el ensanchamiento.

4.7 Efecto de la configuración de membrana y extracción de gas en un RLFDZ-CS+MB

Un diseño del reactor propuesto incluye la integración de membranas para la permeación selectiva de uno o varios productos de reacción, a fin de generar un dispositivo multifuncional capaz de llevar a cabo de manera simultánea los procesos de reacción, regeneración catalítica y separación molecular. Por ello, se antoja imprescindible evaluar el efecto de la extracción de gas a través de membranas y, más aún, de la localización óptima de dichas membranas en el lecho sobre el comportamiento fluidodinámico del RLFDZ-CS+MB. A continuación se detallan los resultados de las simulaciones más relevantes a este respecto, los cuales se encuentran recogidos en el Artículo VII del compendio.

4.7.1 Régimen de burbujeo

La Figura 4.26 ilustra el efecto conjunto de la ubicación de la membrana en el reactor (con la membrana en la pared, RLFDZ-CS+MBP o con la membrana en el centro RLFDZ-CS+MBT), el grado de extracción (fracción permeada respecto al gas total alimentado) y la velocidad del gas de fluidización (u_r) en el perfil axial de tamaños de burbuja simulado con Ansys CFX.

En la Figura 4.26 (a) se muestra que la extracción de una fracción del gas alimentado a través de una membrana ubicada a una altura intermedia del lecho supone una disminución del tamaño de burbuja promedio en su región de influencia. Se observa además que, para un grado de extracción dado, la disminución de $d_b(z)$ es mayor en el caso de la configuración MBP. Esta tendencia se constata independientemente de la velocidad de gas alimentado y del grado de extracción (Figuras 4.26 (b) y (c)).

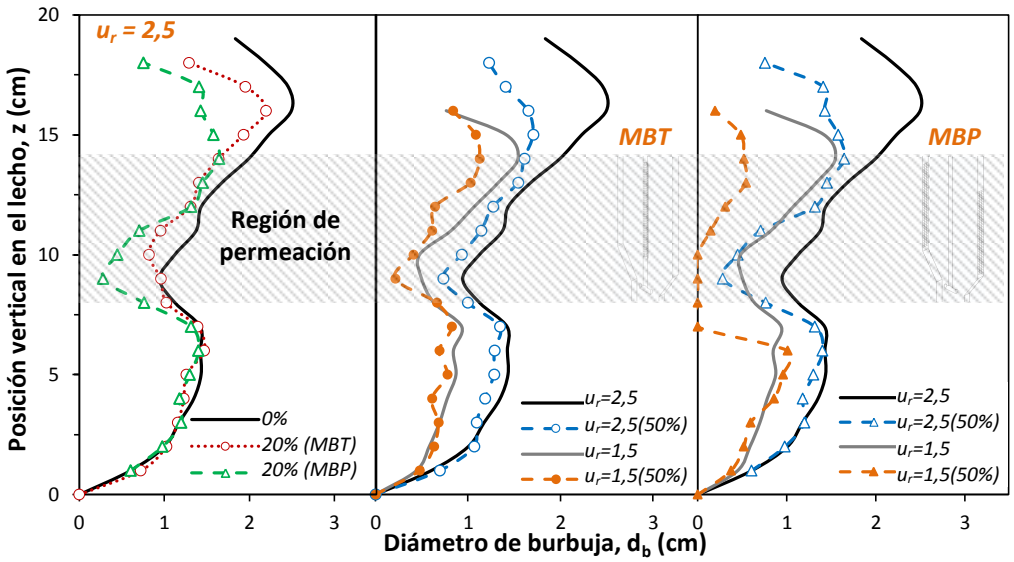

Figura 4.26 Perfil axial de tamaños de burbuja promedio en función de la configuración de membrana, la velocidad relativa del gas alimentado y el grado de extracción. a) Configuraciones: "tubular" (MBT) y "de pared" (MBP) con extracción e = 20%, b) MBT con e = 50% a velocidades de gas: u_r = 1,5 – 2,5, c) MBP con e = 50% a velocidades de gas: u_r = 1,5 – 2,5

En el caso extremo en el que se mantiene la zona superior del lecho en condiciones de defluidización incipiente (u_r = 1,5 con 50% de extracción), la configuración MBT mantiene

cierto régimen de burbujeo mientras que para MBP no se detectan burbujas en la zona de influencia de la membrana.

La discrepancia encontrada entre los perfiles $d_b(z)$ correspondientes a MBP y MBT motivó el estudio de la distribución de sólidos en el lecho y su movimiento en función de la ubicación de la membrana, para tratar de explicar el comportamiento de las burbujas.

4.7.2 Fluidodinámica del lecho

Para los reactores de membrana con configuraciones MBT y MBP se han determinado mapas de porosidad y velocidad promedio (tiempo de simulación: 8 segundos) para la fase densa en Ansys Fluent, a fin de estudiar la distribución espacial de sólidos en el lecho, su movimiento y la variabilidad temporal RMS de ambas propiedades en función de la configuración de membrana, el grado de extracción de gas y el régimen de fluidización.

La Figura 4.27 muestra los mapas promedio de distribución de sólidos en función del grado de extracción (0%, 20% y 50%) para un régimen de fluidización u_r = 1,5 en las configuraciones de reactor MBT y MBP, respectivamente. La extracción de gas genera un gradiente radial de porosidad entre las paredes laterales y la zona central del lecho mucho más acusado en la configuración MBP que en la MBT, a igualdad de caudales de gas permeado. El elevado empaquetamiento del lecho junto a las paredes del RLFDZ-CS+MBP al llevar a cabo la extracción lateral de gas repercute en una menor expansión del lecho. Esto, unido a la aparente circulación preferencial del flujo de gas por la zona central del lecho en la configuración MBP (especialmente observable en el caso con extracción del 50% del gas alimentado), sugiere que la mezcla de sólidos se encuentra más favorecida en el reactor de membrana tubular interna.

La comparativa de los mapas de porosidad entre las configuraciones MBP y MBT a un régimen de fluidización más turbulento, u_r = 2,5, arroja resultados cualitativamente similares. Se ha observado que independientemente del caudal de fluidización empleado, la configuración MBP genera un gradiente radial de concentración de sólidos mayor en la zona de influencia de la membrana. En relación con las aplicaciones del reactor de membrana a diseñar, la configuración MBP podría dar lugar a peores tasas de contacto gas-sólido y de transferencia de calor entre las distintas zonas del lecho que la configuración con membrana tubular interna. El elevado empaquetamiento detectado en la zona superior del RLFDZ-CS+MBP al extraer diferentes fracciones de gas a través de las membranas laterales explica el menor tamaño de las burbujas de gas observadas en esta región del lecho (Figura 4.26) respecto a sus homólogas en la configuración MBT.

A partir de los mapas promedio simulados de porosidad, velocidad axial de sólidos y variabilidad de propiedades (Figura 4.28 (a)-(d)), se han identificado las regiones de lecho defluidizadas o “muertas” (Figura 4.28 (e)). La Tabla 4.5 detalla la variación del ángulo de defluidización en función de la configuración de reactor de membrana, el grado de extracción y el régimen de fluidización. En las simulaciones, las regiones defluidizadas se han determinado en función de los valores promedio de fracción volumétrica de sólidos, velocidad axial y su variabilidad según los siguientes límites: $\varepsilon_s \geq 0.62$, $v_z \leq 0.5$ cm/s, RMS(ε_s) ≤ 0.05 and RMS(v_z) ≤ 0.03 cm/s.

Si bien se ha descrito anteriormente que un ángulo de cambio de sección α = 80º sería suficiente para evitar la aparición de regiones defluidizadas en el RLFDZ-CS bajo cualquier condición de operación, la extracción de gas a través de la zona superior del lecho modifica el comportamiento fluidodinámico de éste favoreciendo la generación de zonas "muertas" en la región cónica, especialmente si la extracción se realiza a través de las paredes laterales del reactor.

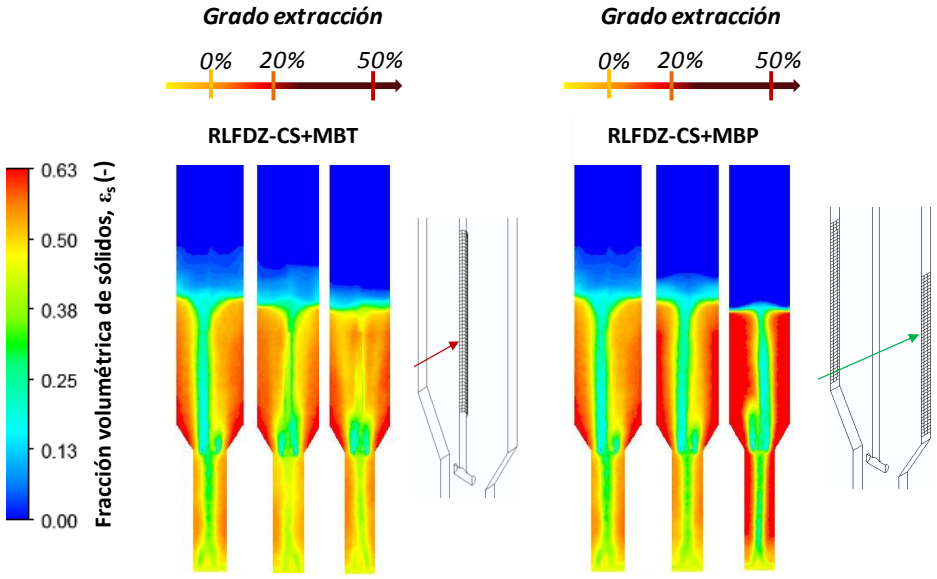

Figura 4.27 Distribución espacial de sólidos en el lecho en función del grado de permeación de gas para las distintas configuraciones de reactor de membrana operados a u_r = 1,5. a) RLFDZ-CS+MBT, b) RLFDZ-CS+MBP

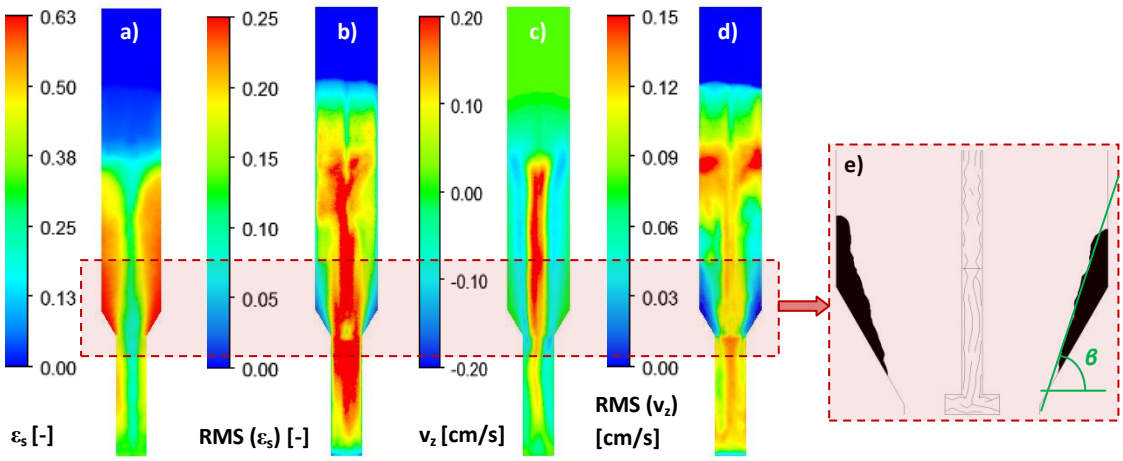

Figura 4.28 Distribución espacial de: a) porosidad del lecho, b) variabilidad de la porosidad, c) velocidad axial de sólidos, d) variabilidad de la velocidad axial de sólidos, e) regiones "muertas" o defluidizadas del lecho. Condiciones de operación: RLFDZ-CS+MBT (u_r = 2,5, 20% de extracción)

Según se muestra en la Tabla 4.5, en condiciones extremas (configuración MBP con u_r = 1,5 y 50% de extracción) la inclinación de la región defluidizada llegaría a superar ligeramente los 80º establecidos como ángulo de diseño óptimo para el reactor. No obstante, dichas condiciones de operación no son de aplicación práctica ya que, por un lado, la baja velocidad

relativa del gas de fluidización dificultaría la mezcla axial de sólidos entre las dos zonas del lecho (lo cual es clave para poder integrar reacción y regeneración catalítica en el lecho) y, por otro, los flujos de permeación de las membranas de interés para este tipo de reactor (por ejemplo, aleaciones paladio-plata para separación de hidrógeno) no suele ser tan elevada ya que en ellas prima la selectividad frente a la permeabilidad.

Tabla 4.5 Ángulo de defluidización, β, para distintas configuraciones de reactor de membrana

Reactor de membrana tubular interna (RLFDZ-CS+MBT)		
Ext. ↓ u_r →	*1,5*	*2,5*
0%	74,1 ± 0,4	69,7 ± 0,1
20%	74,4 ± 0,3	73,2 ± 1,2
50%	76,9 ± 0,3	73,6 ± 1,1
Reactor de membrana de pared (RLFDZ-CS+MBP)		
Ext. ↓ u_r →	*1,5*	*2,5*
0%	74,1 ± 0,4	69,7 ± 0,1
20%	81,7 ± 1,0	79,0 ± 2,5
50%	82,6 ± 0,1	81,5 ± 0,4

4.8 Burbujeo 2D vs. 3D

El estudio fluidodinámico previo está referido a lechos pseudo-bidimensionales bajo la hipótesis de que el comportamiento de dichos lechos es representativo de un plano axial de un reactor real 3D (con geometría de revolución) trazado a través de su eje central. Para validar dicha hipótesis, se han llevado a cabo simulaciones fluidodinámicas en Ansys CFX para lechos 3D análogos a los utilizados en condiciones reactivas a escala de laboratorio. El propósito de este estudio es relacionar los regímenes de burbujeo pseudo-2D de las secciones previas con los regímenes reales en sistemas con geometría de revolución. Los resultados mostrados a continuación se engloban en el Artículo VIII del compendio.

4.8.1 "Diámetro de burbuja equivalente" para sistemas pseudo-2D y 3D

En la Sección 3.3.1 se ha puesto de manifiesto que el diámetro de burbuja equivalente, d_b, puede estimarse atendiendo esencialmente a dos criterios: a partir del volumen de gas que ocupa la burbuja o a partir del área proyectada por la burbuja a través de un plano bidimensional, independientemente de llevar a cabo la medición en un lecho fluidizado pseudo-2D o con geometría de revolución.

La comparativa entre perfiles axiales de tamaño de burbuja para reactores pseudo-2D y 3D utilizando la formulación superficial de d_b para el lecho plano (la usada a lo largo de la Memoria de la tesis) y la formulación volumétrica para el lecho tridimensional, sugiere que las burbujas medidas en el lecho pseudo-2D son sustancialmente "mayores" que las del tridimensional bajo un mismo régimen de fluidización (Figura 4.29). Esto puede dar lugar a una interpretación equívoca de la validez de las mediciones en lechos pseudo-2D para predecir el comportamiento fluidodinámico de un lecho real.

Desde el punto de vista del lecho pseudo-2D que pretende simular una rodaja vertical de un lecho cilíndrico, el diámetro de burbuja equivalente del reactor plano $d_{b(2D)}$ debería ser

comparado con el de la burbuja proyectada en el plano central de la configuración 3D, $d_{b(3D\text{-}área)}$.

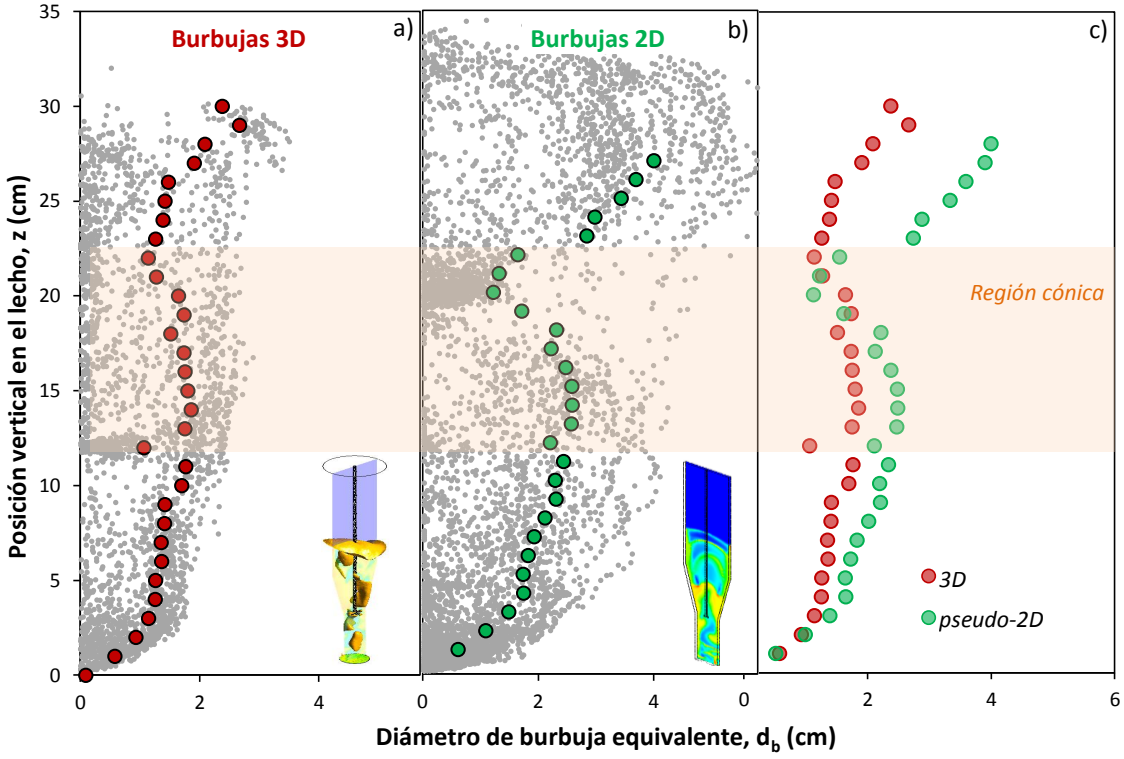

Figura 4.29 Evolución del perfil $d_b(z)$ para un RLFDZ-CS operado a u_r = 2,5. a) $d_{b(3D)}$, b) $d_{b(2D)}$, c) Comparativa entre valores promedio de $d_{b(3D)}$ y $d_{b(2D)}$

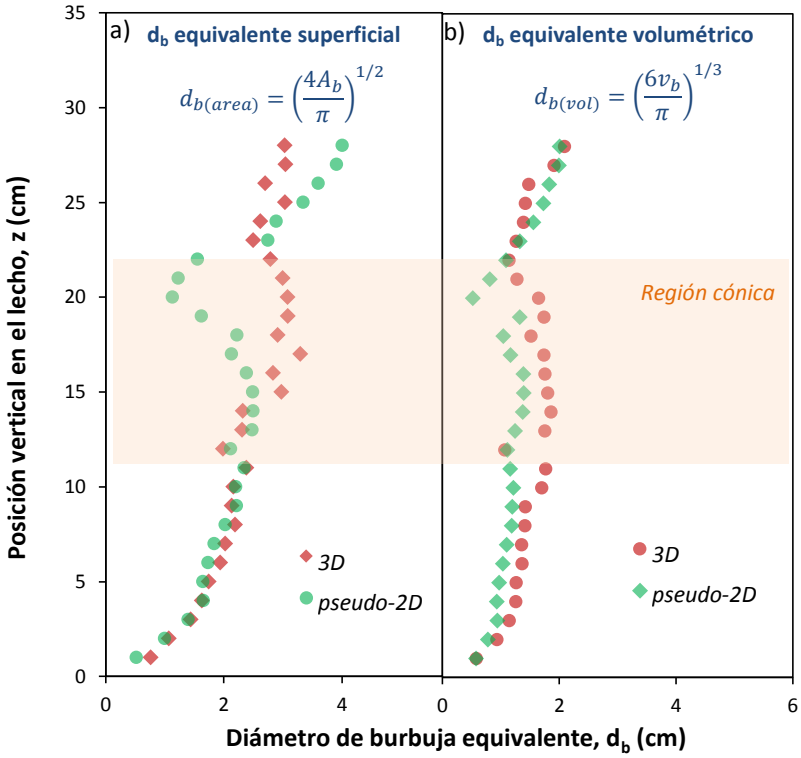

Figura 4.30. Evolución del perfil $d_b(z)$ para un RLFDZ-CS operado a u_r = 2,5. a) $d_{b(3D\text{-}área)}$ frente a $d_{b(2D)}$, b) $d_{b(3D)}$ frente a $d_{b(2D\text{-}vol)}$

Desde el punto de vista del volumen de gas efectivo transportado por las burbujas, la formulación volumétrica del diámetro de burbuja ($d_{b(3D)}$ y $d_{b(2D\text{-}vol)}$) es la que evalúa de manera más representativa el comportamiento hidrodinámico del lecho entre las distintas configuraciones de reactor.

La Figura 4.30 muestra una comparativa entre perfiles $d_b(z)$ obtenidos para RFLFDZ-CS pseudo-2D y 3D atendiendo a las formulaciones superficial (4.30 (a)) y volumétrica (4.30 (b)) del diámetro de burbuja equivalente. En la Figura 4.30 (a) se observa una sustancial disminución del tamaño promedio de burbuja en la sección inclinada del lecho pseudo-2D no correspondida por su homóloga en el lecho 3D. Sin embargo, la Figura 4.30 (b) confirma que la evolución axial del tamaño de burbuja (entendido como cantidad de gas transportada) es similar en ambas configuraciones de reactor, reproduciéndose las tendencias de crecimiento y disminución de $d_{b(3D)}$ a lo largo del lecho 2D. Esto valida la hipótesis de que el comportamiento hidrodinámico de un lecho fluidizado pseudo-2D es representativo de éste en un lecho cilíndrico.

4.8.2 Comparativa fluidodinámica entre RLFDZ-CS 2D y 3D

Se ha evaluado el efecto de la configuración de reactor en propiedades de burbuja tales como: distribución de tamaños, relación de aspecto o dispersión radial, observándose una elevada correspondencia entre las tendencias de burbujeo en ambos lechos. Adicionalmente, se ha determinado la fluctuación transitoria del volumen ocupado por las burbujas y de la altura promedio de la superficie libre del lecho (z_{fb}) en las configuraciones plana y cilíndrica. Como se observa en la Figura 4.31, tanto la frecuencia como la amplitud de las fluctuaciones del volumen hueco y de la altura del lecho tridimensional se describen satisfactoriamente por el reactor pseudo-2D.

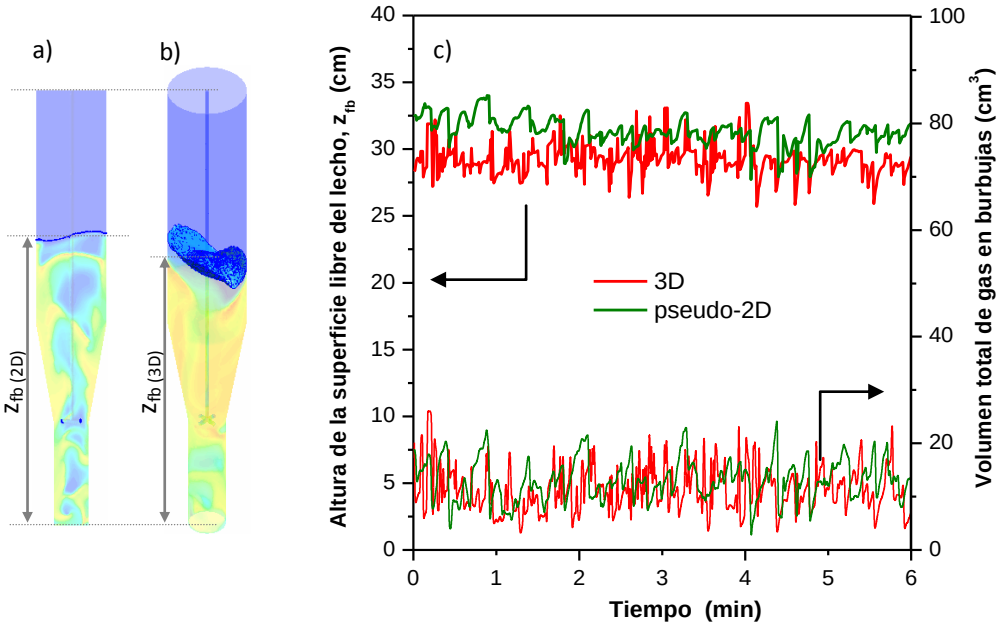

Figura 4.31 Detección de la superficie libre del lecho para un RLFDZ-CS: a) pseudo-2D, b) 3D. c) Evolución transitoria de la altura de la superficie libre del lecho y del volumen ocupado por burbujas

En lo que respecta a la velocidad promedio de las burbujas de gas en ambas configuraciones, la Figura 4.32 muestra que el lecho 3D da lugar a burbujas más rápidas, tal y como predice la clásica correlación de Davidson y Harrison (19) (ecuación 25) que relaciona la velocidad de burbujas (u_{br}) con su tamaño para reactores planos y cilíndricos.

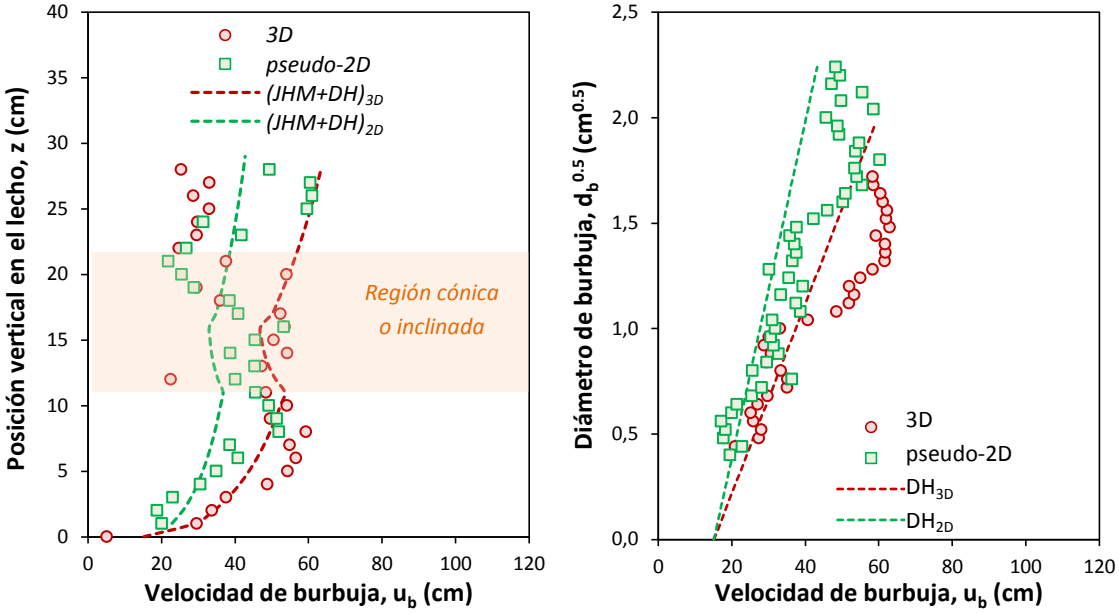

Figura 4.32 a) Evolución axial de la velocidad promedio de burbujas, b) Correlación entre velocidad y tamaño de burbujas. Simulaciones en lechos 2D y 3D frente a predicciones de los modelos JHM y DH

A su vez, la Figura 4.32 (a) ilustra como la correlación JHM desarrollada en la presente tesis es capaz de predecir cualitativamente la evolución axial de la velocidad promedio de burbuja en ambas configuraciones de RLFDZ-CS para las condiciones catalogadas como óptimas (α = 80º, u_r = 2,5 y $z_{dis} = z_{cs}$).

4.9 Aplicación: deshidrogenación catalítica de propano en RLFDZ-CS+MB

Tras caracterizar el comportamiento fluidodinámico de las fases presentes en el RLFDZ-CS+MB en base a diversas variables de operación (u_{gas}, d_p, z_{dis}-z_{cs}, α, ...) y configuraciones de reactor (MBT, MBP, elementos internos, geometría de revolución, escalado, ...), se va a aplicar el diseño óptimo del reactor en condiciones reactivas para evaluar su comportamiento multifuncional en un proceso real, como es la producción de propileno a partir de la deshidrogenación catalítica de propano. Los resultados presentados a continuación se encuentran detallados en los Artículos IX, X y XI del compendio.

En primer lugar se mostrará el efecto estabilizador del RLFDZ-CS frente al RLF convencional en la obtención de una productividad a propileno estable con el tiempo. Se determinará la fracción óptima de oxidante en la composición para llevar a cabo la regeneración catalítica in situ, así como la temperatura óptima de reacción. Posteriormente se analizará el comportamiento del sistema multifuncional RLFDZ-CS+MB para terminar con una reseña sobre el efecto de la composición de los gases de reacción en el comportamiento de las membranas.

4.9.1 RLF convencional vs. RLFDZ-CS para deshidrogenación de propano

Una vez sintetizado y caracterizado el catalizador consistente en Pt-Sn/$MgAl_2O_4$ mesoporoso (d_p = 75 – 150 µm, S_{BET} = 123 m^2/g, V_p = 0,26 cm^3/g) así como estabilizado en ciclos consecutivos de reducción, reacción y regeneración a la temperatura usual de trabajo, se ha estudiado el comportamiento de la deshidrogenación catalítica de propano en reactores de lecho fluidizado convencional (RLF) y lecho fluidizado de dos zonas con cambio de sección (RLFDZ-CS) a fin de comparar la evolución temporal del rendimiento de la reacción hacia la producción de propileno. La Figura 4.33 (a) muestra el efecto de la temperatura en la conversión catalítica de propano y selectividad a propileno a lo largo del tiempo en un RLF mientras que la Figura 4.33 (b) detalla la evolución de la conversión y selectividad para el mismo rango de temperaturas en un sistema RLFDZ-CS.

Como se puede observar en la Figura 4.33 (a), el reactor de lecho fluidizado convencional es incapaz de alcanzar un rendimiento a propileno (estimado como el producto de conversión por selectividad) constante a lo largo del tiempo debido a la desactivación transitoria del catalizador en presencia de hidrocarburos ligeros. La formación de depósitos carbonosos sobre la superficie activa del catalizador supone la caída progresiva de conversión de propano a lo largo del tiempo. Esta caída es tanto más acusada cuanto mayor es la temperatura de operación, ya que ésta favorece la deposición de coque. Asimismo, se observa como la selectividad a propileno decae con la temperatura debido, por un lado, a la mayor tendencia a la formación de coque y por otro al favorecimiento de reacciones competitivas como el craqueo catalítico de propano, dando lugar a subproductos de reacción como metano y etileno. La conversión inicial de reactivo sobre el catalizador libre de coque viene limitada por el equilibrio termodinámico y es tanto mayor cuanto mayor es la temperatura.

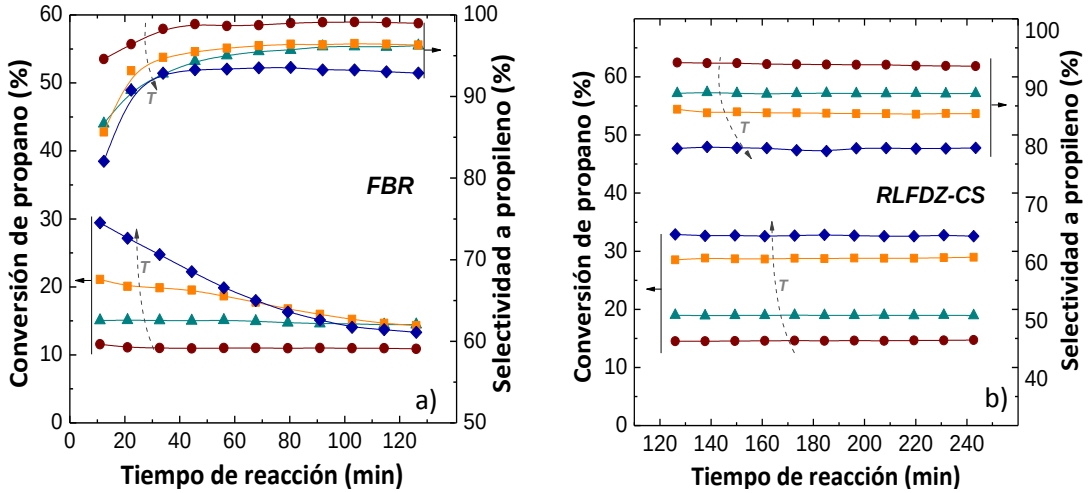

Figura 4.33 Evolución temporal de la conversión de propano y selectividad a propileno en función de la temperatura de operación (○ 500ºC; Δ 525ºC; □ 550ºC; ◊ 575ºC) y del tipo de reactor utilizado: a) RLF, b) RLFDZ-CS. Condiciones de operación: $u_{r,inf}$ = 1,75, $u_{r,sup}$ = 2,5, w_{cat}/F_{C3H8} = 21,1 (g·min/mmol), $x_{F,C3H8}$ = 50%, $x_{F,O2\ (RLFDZ-CS)}$ = óptimo para cada temperatura

Por el contrario, la Figura 4.33 (b) sugiere que es posible encontrar unas condiciones de operación (velocidad y composición de los gases de fluidización) tales que el sistema sea capaz

de operar en continuo sin desactivación catalítica aparente manteniendo constantes la conversión y selectividad del proceso independientemente de la temperatura de trabajo. En concreto, es necesario ajustar la fracción de agente oxidante en la zona de regeneración para quemar el coque depositado sobre el catalizador, teniendo en cuenta que un defecto de oxígeno puede conllevar la lenta desactivación del sistema y un exceso provocaría que el excedente de oxígeno alcanzase la zona de reacción produciendo la combustión del propano, reduciendo así el rendimiento global del sistema. Dado que la cinética de coquización del catalizador depende sensiblemente de la temperatura de operación (Figura 4.34 (a)), el porcentaje óptimo de oxígeno empleado para cada experimento de los presentados en la Figura 4.33 (b) ha sido calculado en base a los resultados que se muestran en la Figura 4.34 (b), ilustrando la fracción de oxidante en la alimentación que compensa la desactivación catalítica por deposición de coque. Como se puede apreciar, conforme aumenta la temperatura, la necesidad de agente oxidante para contrarrestar la desactivación del catalizador crece de manera exponencial ya que, como ilustra la Figura 4.34 (a), la disminución de la conversión de propano (o, análogamente, el rendimiento a propileno) está íntimamente relacionada con la cantidad de coque depositado sobre la superficie del catalizador.

De acuerdo con la gráfica comparativa mostrada en la Figura 4.33, el RLFDZ-CS permite alcanzar un régimen estacionario relativo a la conversión de propano, estabilizando la producción de propileno a lo largo del tiempo de reacción. Sin embargo, el sistema reduce la selectividad a propileno debido a que el balance de carbono asocia en este caso el CO_2 producto del proceso al coque quemado por el agente oxidante, que proviene necesariamente del propano alimentado al no haber más fuentes de entrada de carbono al sistema.

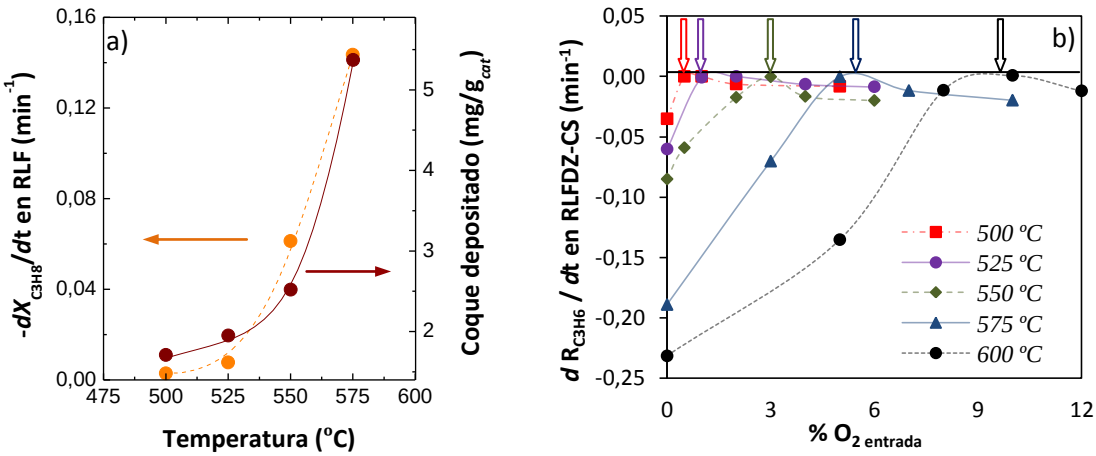

Figura 4.34 a) Variación de la tasa de desactivación y deposición de coque con la temperatura en un RLF, b) Variación del rendimiento a propileno en función de la temperatura y del porcentaje de oxidante en la corriente de entrada al RLFDZ-CS

4.9.2 RLFDZ-CS+MB para deshidrogenación de propano

A pesar de la gran estabilidad exhibida por el RLFDZ-CS para llevar a cabo el proceso de deshidrogenación de propano, la conversión de C_3H_8 sigue estando limitada por el equilibrio

termodinámico. Para desplazar el equilibrio de reacción hacia la formación de propileno se ha propuesto el uso de diferentes membranas permeoselectivas a hidrógeno basadas en capas densas compuestas bien de Pd o de aleaciones Pd-Ag, cuyas propiedades se detallan en la Tabla 2.2 de la Memoria. La Figura 4.35 muestra el efecto del tipo de membrana en el flujo de permeación de H_2 en función de la temperatura de operación y la fuerza impulsora utilizada.

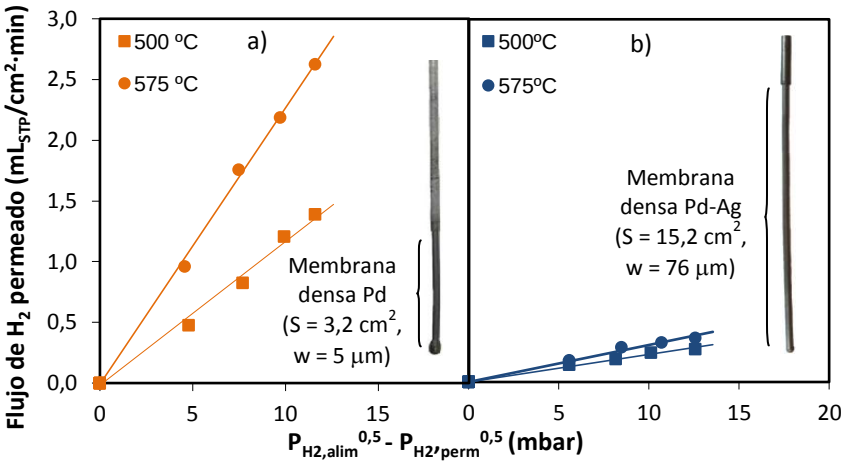

Figura 4.35 Efecto del tipo de membrana, temperatura de operación y fuerza impulsora en la evolución transitoria del rendimiento a propileno. a) Membrana no-comercial, b) Membrana comercial REB®

Las membranas suministradas por el Imperial College de Londres proporcionan tasas de permeación mucho mayores. Sin embargo, su área de permeación es sensiblemente menor que la de REB® Research & Consulting por lo que el caudal de H_2 efectivo a través de ambas membranas es del mismo orden. Esto, unido a la baja resistencia mecánica de la membrana no-comercial y las dificultades operativas que supone el acoplamiento de una carcasa protectora en el interior del lecho, motiva la elección de la membrana comercial para el desarrollo de la experimentación cuyos resultados se muestran a continuación.

La Figura 4.36 ilustra el efecto de la retirada selectiva de hidrógeno a través de una membrana híbrida de Pd-Ag en el rendimiento del proceso a propileno en un RLFDZ-CS + MB en comparación con los resultados obtenidos para las configuraciones RLF y RLFDZ-CS. La comparativa se ha llevado a cabo para las cuatro temperaturas de operación analizadas en este trabajo.

Se ha observado que el reactor multifuncional RLFDZ-CS+MB no solo es capaz de mantener la estabilidad del sistema respecto a la producción de propileno sino que, además, por efecto de la retirada de hidrógeno a través de las membranas permeoselectivas, el equilibrio de reacción se desplaza hacia la formación de propileno aumentando el rendimiento del proceso. Si bien es conocido que la presencia de hidrógeno inhibe parcialmente la formación de coque (ej. (132-134), la retirada selectiva de H_2 no representa un problema para el funcionamiento del RLFDZ-CS+MB debido a su capacidad para regenerar el catalizador in-situ ajustando la fracción de oxidante a introducir. El desplazamiento del equilibrio se ha traducido en el incremento del rendimiento a propileno detallado a continuación, en función de la temperatura de trabajo: $\Delta R_{C3H6\,(500ºC)}$ = 2,54 %, $\Delta R_{C3H6\,(525ºC)}$ = 1,97 %, $\Delta R_{C3H6\,(550ºC)}$ = 1,88 % y $\Delta R_{C3H6\,(575ºC)}$ = 1,83 %.

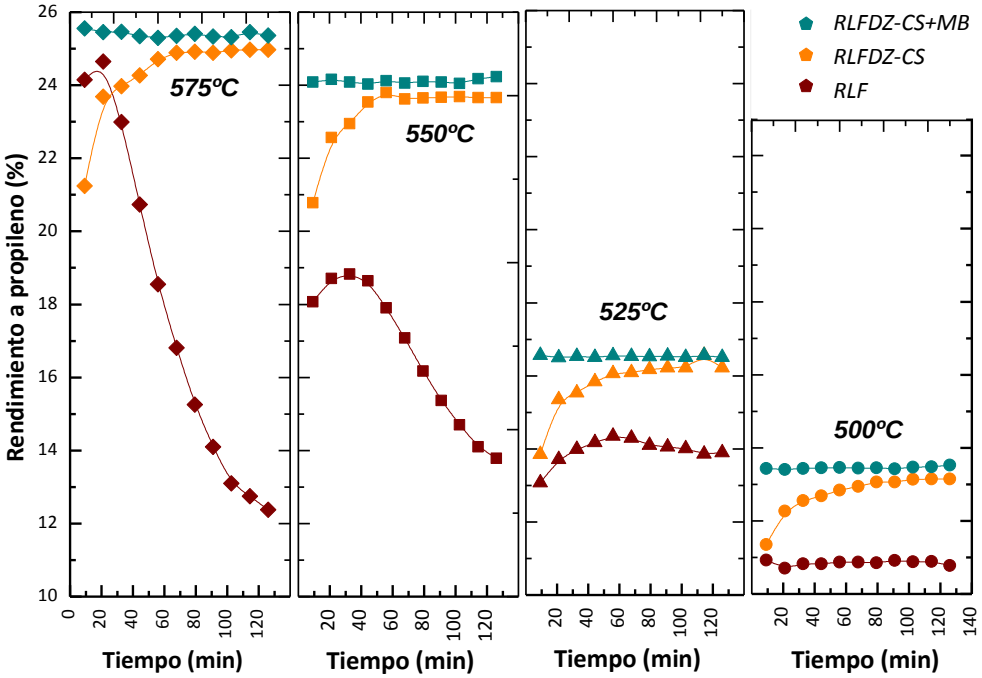

Figura 4.36 Efecto del tipo de reactor y temperatura de operación en la evolución transitoria del rendimiento a propileno

4.9.3 Efecto de la relación peso-caudal en el rendimiento a propileno

Los resultados previos están referidos a una relación peso de catalizador / caudal de propano, w_{cat} / F_{C3H8}, constante tal que el peso de catalizador se ha mantenido en 70 gramos a lo largo de la serie experimental, la velocidad relativa de gas no se ha variado a lo largo del estudio y la fracción de propano alimentada sobre el total de gas introducido en el lecho se ha fijado en 50%. A continuación, se detalla el efecto de la dilución de propano o análogamente la variación de la relación peso-caudal en el comportamiento de la reacción en presencia y ausencia de membranas permeoselectivas.

La Figura 4.37 muestra la evolución temporal del rendimiento a propileno en función del tipo de reactor y de la relación w_{cat} / F_{C3H8} para una temperatura de operación de 550ºC, la cual se ha establecido como óptima para el proceso ya que aúna elevada reactividad y moderada tasa de coquización.

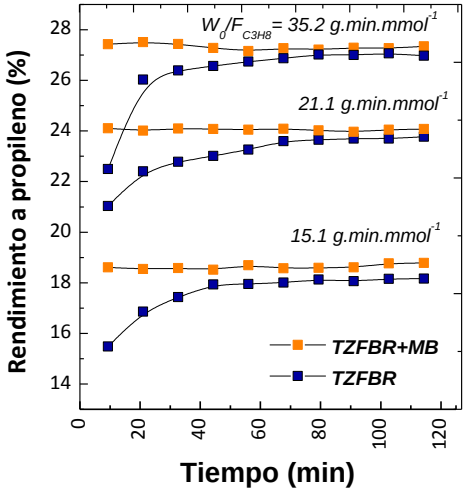

Figura 4.37 Efecto de la relación entre el peso de catalizador y el caudal de propano alimentado en el rendimiento de la deshidrogenación de propano a propileno en RLF, RLFDZ-CS y RLFDZ-CS + MB

Cuanto mayor es la relación peso-caudal, mayor es el tiempo de contacto entre el agente reactivo y el catalizador, lo que conduce a mayores conversiones de propano. Además, al disminuir la concentración de propano aumenta la conversión de equilibrio. Sin embargo, la variación del tiempo de residencia no se traduce en diferencias de selectividad sustanciales entre la reacción principal de deshidrogenación, el craqueo catalítico y la formación de depósitos carbonosos. Como resultado, el rendimiento a propileno incrementa con el parámetro w_{cat} / F_{C3H8}, siendo mayor en todos los casos al utilizar la configuración de reactor RLFDZ-CS +MB con retirada selectiva de hidrógeno. La variación relativa del rendimiento del proceso respecto al obtenido en la configuración sin membranas se detalla a continuación para cada relación peso-caudal: $\Delta R_{15,1\ (g\cdot min/mmol)}$ = 2,69 %, $\Delta R_{21,1}$ = 1,85 % y $\Delta R_{35,2}$ = 1,12 %. Esto implica que cuanto menor es w_{cat} / F_{C3H8}, menor es el rendimiento a propileno pero mayor es el incremento de productividad al utilizar membranas permeoselectivas. Al estar el sistema menos diluido en gas inerte (Ar), la presión parcial del hidrógeno formado en el lecho es mayor, generando un mayor gradiente de P_{H2} a ambos lados de la membrana y favoreciendo la permeación de éste.

4.9.4 Comparativa con resultados bibliográficos

Los resultados obtenidos en los sistemas reactivos multifuncionales RLFDZ-CS y RLFDZ-CS+MB han sido comparados con resultados existentes en literatura para la deshidrogenación catalítica de propano en diferentes configuraciones de reactor (47, 51, 53, 135-138). Ya que los resultados descritos en la literatura están obtenidos en diferentes condiciones de operación, las conversiones de propano detalladas en dichos trabajos se han normalizado respecto a las conversiones de equilibrio para las temperaturas de reacción en cada caso. La Figura 4.38 muestra la comparación entre los resultados obtenidos en RLFDZ-CS (círculos blancos) y RLFDZ-CS+MB (círculos rojos) y los reportados en literatura en función de la conversión de propano normalizada y la selectividad estacionaria a propileno.

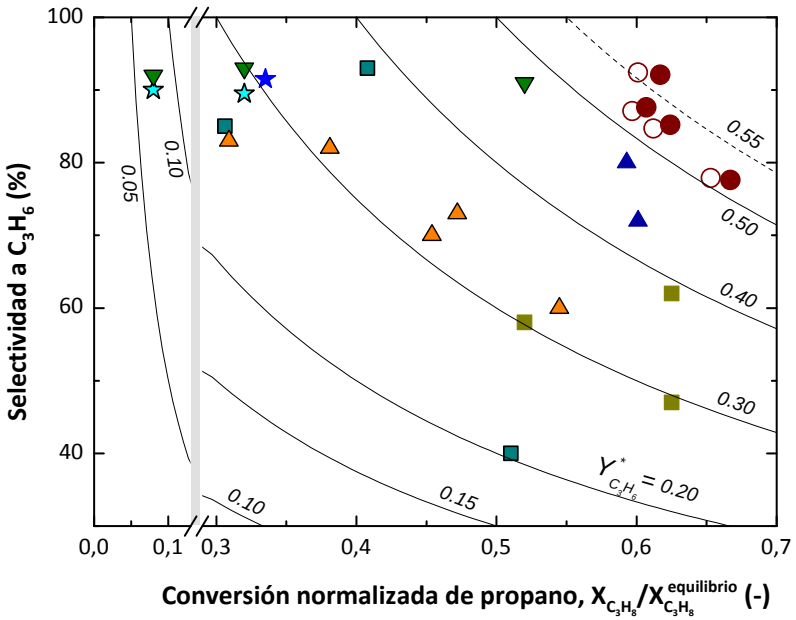

Figura 4.38 Selectividad a propileno vs. conversión normalizada de propano para ○ RLFDZ-CS y ● RLFDZ-CS+MB, ★ Jablonsky y cols., ☆ Assabumrungrat y cols., ▼ Salmones y cols., ■ Schäfer y cols., ■ Nawaz y cols., ▲ Chen y cols., ▲ Wang y cols. Las curvas representan líneas de iso-rendimiento a propileno normalizado (Y^*_{C3H6}) respecto a la conversión de propano en equilibrio termodinámico

Como se puede observar, los rendimientos a propileno (normalizados respecto a la conversión de equilibrio) alcanzados en el presente trabajo superan con creces a los obtenidos en otros sistemas reactivos. Además, cabe destacar que la mayoría de los resultados extraídos de trabajos previos se corresponde con datos puntuales de conversión y selectividad a un tiempo de reacción dado, ya que en ninguno de los sistemas reportados se lleva a cabo la regeneración catalítica in situ.

4.9.5 Efecto de la presencia de C_3H_8 y C_3H_6 en la permeabilidad de las membranas

Si bien es cierto que la introducción de membranas permeoselectivas en el RLFDZ-CS es capaz de desplazar ligeramente la reacción de deshidrogenación hacia la producción de propileno (Figura 4.36), se comprobó experimentalmente que los flujos de permeación de hidrógeno en régimen de reacción son sustancialmente menores que los obtenidos en ensayos de permeación (Figura 4.39 (a)), utilizando mezclas Ar/H_2 con membranas densas de Pd-Ag. Por tanto, el incremento del rendimiento a propileno por retirada de H_2 fue menor que el esperado y este hecho motivó el estudio del efecto de la presencia de mezclas propano/propileno en la permeabilidad de la membrana, abordado en el Artículo XI del compendio.

Se analizó la evolución temporal del flujo de permeación de hidrógeno a través de la membrana en presencia y ausencia de hidrocarburos ligeros en la alimentación y se comprobó que, por un lado, la coalimentación de propileno disminuye la permeabilidad transitoria de la membrana y, por otro lado, que la superficie de la membrana densa actúa como un catalizador en la hidrogenación de propileno. Los resultados del ensayo se muestran en la Figura 4.39 (b).

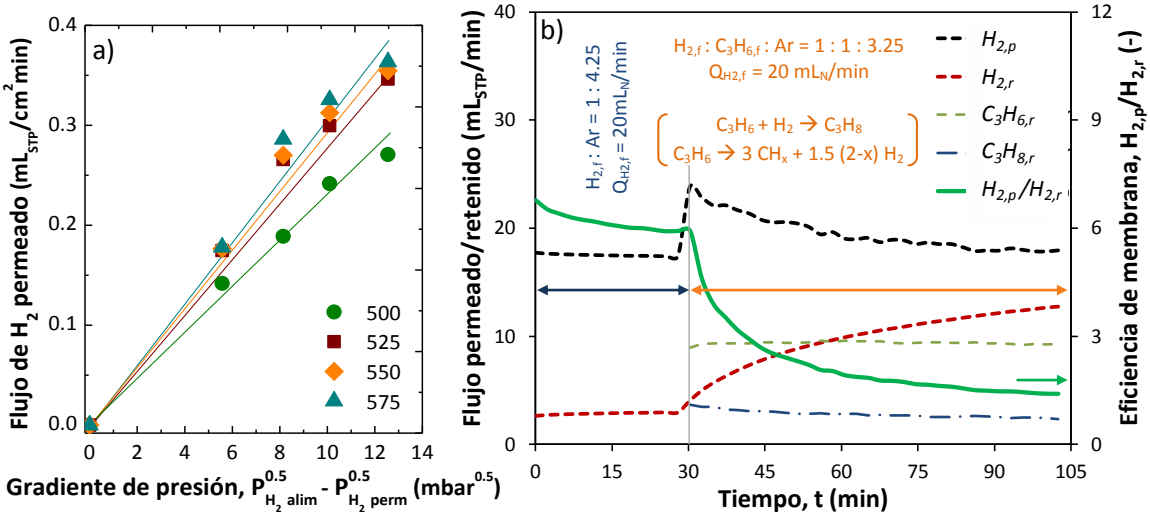

Figura 4.39 a) Ensayos de permeación para las membranas Pd-Ag con mezclas H_2/Ar a diferentes temperaturas, b) Evolución transitoria de la eficiencia de la membrana al coalimentar H_2/C_3H_6/Ar

En concreto, se alimentó en primer lugar una mezcla al 19% de hidrógeno en argón a 550ºC y se observó la evolución de los flujos permeado y retenido de H_2 a lo largo del tiempo, definiendo el parámetro *eficacia de membrana* (E_m) como el cociente entre el flujo permeado y el retenido. Al cabo de media hora de operación, se modificó la alimentación introduciendo un 19% de propileno al sistema (C_3H_6 : H_2 : Ar = 1 : 1 : 3.25). La alimentación del hidrocarburo

supuso un cambio drástico en la permeabilidad, reduciéndose bruscamente la eficiencia de la membrana en la permeación de hidrógeno a su través. En la Figura 4.39 (b) se observa como al introducir propileno aumenta inicialmente el flujo de hidrógeno permeado. Esto sugiere que, en presencia de C_3H_6, la capa densa de Pd-Ag se comporta como catalizador de la hidrogenación de propileno dando lugar a propano que abandona el sistema en la corriente retenida y que, además, el propileno se descompone en contacto con la superficie de la membrana dando lugar a depósitos de coque y liberando hidrógeno. El efecto conjunto de la hidrogenación de propileno y coquización de la membrana es la producción de hidrógeno y la disminución de la superficie permeable de la membrana a lo largo del tiempo por ensuciamiento. Como resultado, la señal de hidrógeno permeado disminuye a lo largo del tiempo (aumentando la del retenido) y, al mismo tiempo, disminuye la señal inicial de propano retenido aumentando la de propileno, ya que la deposición de coque inhibe la hidrogenación de C_3H_6. De modo cuantitativo, la eficiencia de la membrana disminuye a la tercera parte al cabo de una hora en presencia de hidrocarburos ligeros, lo que explica la discrepancia encontrada entre los flujos de permeación medidos en ensayos con mezclas H_2/Ar y la permeación experimental encontrada en el sistema RLFDZ-CS+MB.

Realizando un balance de carbono a partir de los resultados mostrados en la Figura 4.39 (b), es posible determinar la evolución temporal de la conversión de propileno en contacto con la superficie de la membrana, la selectividad a propano o a coque y la cantidad de residuos carbonosos acumulados sobre la capa densa de Pd-Ag. La Figura 4.40 (a) detalla la evolución de estas variables en función del tiempo.

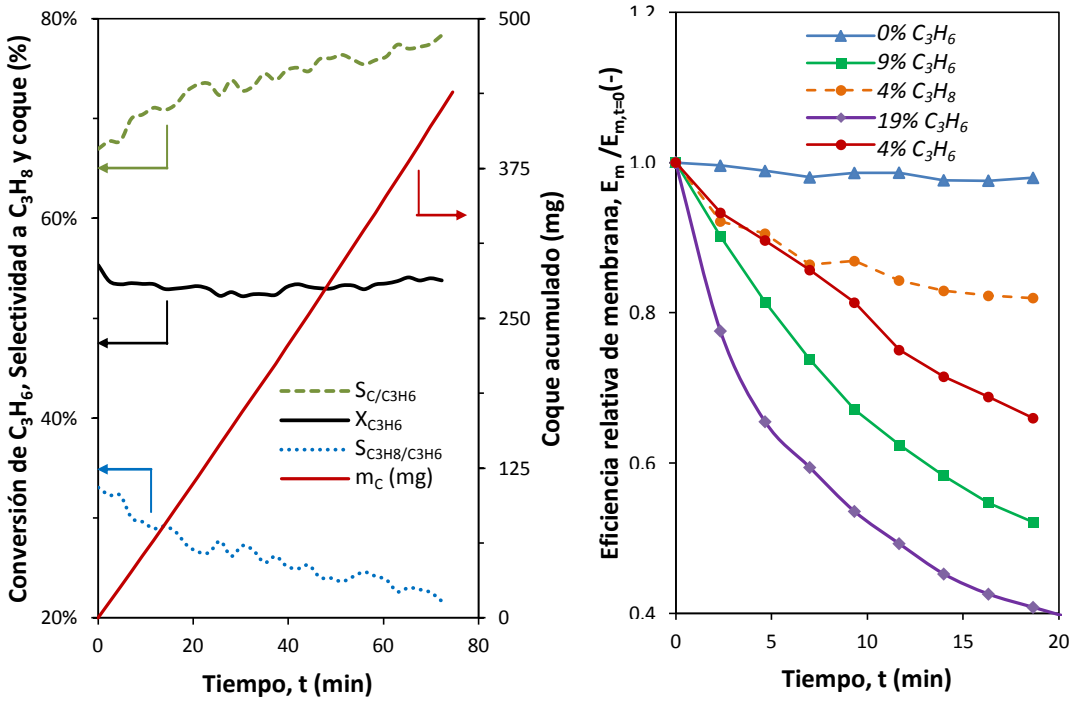

Figura 4.40 a) Evolución temporal de conversión de propileno, selectividad a propano y a coque y acumulación de residuos carbonosos sobre la pared de la membrana para las condiciones experimentales de la Figura 4.39, b) Efecto del tipo de hidrocarburo (C_3H_6 ó C_3H_8) y su contenido en la alimentación en la evolución transitoria de la eficiencia de la membrana

Como se puede apreciar, más de la mitad del propileno alimentado se convierte, bien hidrogenándose o descomponiéndose en forma de coque. La coquización es mayoritaria y representa entre 70% y 80% del C_3H_6 convertido.

La hidrogenación de propileno disminuye con el tiempo debido al ensuciamiento de la membrana por deposición de coque, lo que aumenta la selectividad a éste. La tasa de deposición de coque es prácticamente lineal con el tiempo hasta el cubrimiento total de la superficie activa de la membrana, acumulándose más de 350 mg en una hora en las condiciones de operación descritas en la Figura 4.39 (b).

Para evaluar el efecto de la composición de la alimentación en la permeabilidad de las membranas, se ha llevado a cabo una serie experimental con distintas fracciones de propano y propileno en la corriente de entrada, realizando un seguimiento temporal de la eficiencia relativa de la membrana, referida a la E_m inicial para una mezcla H_2/Ar al 19% en hidrógeno. La Figura 4.40 (b) muestra que para una alimentación libre de hidrocarburos la eficiencia se mantiene prácticamente constante a lo largo del tiempo con una ligera disminución, frecuentemente asociada a fenómenos de polarización por concentración, que genera una cierta resistencia a la permeación. En los demás casos, en los que se han alimentado fracciones crecientes de C_3H_6 y C_3H_8 se observa que cuanto mayor es la concentración inicial de hidrocarburo en la corriente alimentada, más brusca es la disminución de eficacia de la membrana. La relación entre la fracción de hidrocarburo alimentada y la pérdida de permeabilidad aparente no es lineal y se observa que incluso para concentraciones muy bajas de propileno, la disminución de la eficiencia de la membrana es ya muy notable. Además, se observa que el efecto del propileno sobre la coquización y pérdida de eficiencia es sustancialmente mayor que el del propano. Al tratarse de un hidrocarburo insaturado, el propileno es más reactivo que el propano. Esto explicaría su mayor tendencia a la descomposición en presencia de la membrana densa metálica.

Sabiendo que la relación de hidrógeno y propileno en los productos de reacción de la deshidrogenación catalítica de propano en RLFDZ-CS + MB es aproximadamente 1:1, la disminución teórica de la eficiencia de la membrana seguiría la tendencia del ensayo al 19% C_3H_6 de entre los presentados en la Figura 4.40 (b), dando explicación a los bajos flujos de permeación encontrados en reacción. No obstante, los depósitos carbonosos encontrados sobre la superficie de la membrana en los ensayos en ausencia de catalizador no han sido observados en régimen de fluidización debido al arrastre de sólidos por fricción entre el lecho fluidizado y la membrana. Por tanto, es de esperar que llevando a cabo la reacción catalítica en RLFDZ-CS + MB la eficiencia de la membrana no disminuya tan bruscamente como en los ensayos sin lecho. Por otro lado, se ha encontrado experimentalmente que la disminución de E_m es tanto mayor cuanto más alta es la temperatura de operación. Esto explicaría que a mayor temperatura, menor es el incremento del rendimiento a propileno haciendo uso de membranas permeoselectivas en el RLFDZ-CS + MB, como se ha discutido en la sección 4.9.2.

5 CONCLUSIONES

5. CONCLUSIONES

El comportamiento fluidodinámico del reactor de lecho fluidizado de dos zonas con cambio de sección y membrana permeoselectiva (RLFDZ-CS+MB) ha sido analizado a fin de estudiar la mezcla axial de sólidos en su interior, la cual determina la integración de procesos en este novedoso reactor multifuncional, incluyendo: reacción catalítica, regeneración del catalizador y separación selectiva de productos de reacción.

Los resultados del estudio fluidodinámico han sido aplicados a la implementación experimental de la deshidrogenación catalítica de propano en RLFDZ-CS+MB a escala de laboratorio. El reactor propuesto resulta idóneo para mitigar las limitaciones del proceso en cuestión: desactivación catalítica por deposición de coque, alta endotermicidad y conversión limitada por el equilibrio termodinámico.

Las conclusiones generales extraídas del estudio fluidodinámico se presentan a continuación:

1.a) La variabilidad observada en las propiedades de burbuja y en la circulación de sólidos, propia de los lechos fluidizados, ha requerido de un estudio estadístico y probabilístico para evaluar el efecto de las diferentes variables de operación en el régimen fluidodinámico del RLFDZ-CS+MB.

1.b) La técnica experimental de análisis de imágenes digitales (DIA) ha permitido estudiar en detalle el fenómeno de burbujeo y la mezcla axial de sólidos en configuraciones de RLFDZ-CS pseudo-bidimensionales. Asimismo, la velocimetría de partículas experimental (PIV) ha hecho posible medir la circulación de sólidos en el lecho y cuantificar su mezcla axial en función de las condiciones de operación.

1.c) Se ha desarrollado un modelo matemático (JHM) capaz de predecir la evolución de las propiedades de burbuja, esencialmente su tamaño y velocidad, en función de la posición axial en el lecho y de la geometría de reactor. El modelo JHM se apoya en correlaciones hidrodinámicas clásicas y no introduce nuevos parámetros empíricos, ya que su formulación está basada en el balance de materia a la fase gas para un lecho fluidizado no convencional con sección de paso variable y con múltiples entradas de gas.

1.d) Se ha usado un código comercial de fluidodinámica computacional (CFD) basado en el modelo de dos fluidos (TFM) para simular el comportamiento fluidodinámico del RLFDZ-CS. La herramienta de simulación constituye un elemento esencial para la predicción del comportamiento del reactor en el proceso de escalado, así como para reducir la futura carga experimental. Los resultados derivados del estudio experimental han sido utilizados para validar el modelo TFM en cuanto a la predicción de las propiedades de burbuja y el movimiento de sólidos en un RLFDZ-CS.

1.e) Se han identificado las limitaciones fluidodinámicas del reactor y se ha establecido una ventana de operación para reducir o mitigar el efecto adverso de la deficiente mezcla axial de sólidos que puede tener lugar bajo determinadas condiciones en un RLFDZ-CS+MB. Experimentalmente se ha encontrado lo siguiente:

1.e.1) Se aconseja trabajar con velocidades de gas similares en ambas zonas del lecho para favorecer el intercambio de sólidos entre las distintas regiones del RLFDZ y un exceso de gas no inferior a 10 $cm^3_{STP}/cm^2 \cdot s$ (en sólidos tipo B) para no generar canales preferenciales, zonas muertas, *slugging* u otros fenómenos que pudieran reducir la eficacia del reactor. Dado que la alimentación de gas es fraccionada, se requiere que el RLFDZ conste de dos zonas con diferente sección (RLFDZ-CS).

1.e.2) El cambio de sección entre las distintas zonas del lecho debe ser gradual para evitar fenómenos de defluidización, que afectarían negativamente al funcionamiento del reactor. Idealmente, el uso de una región de transición con una inclinación de 80^o respecto a la posición horizontal garantizaría que no se formasen zonas muertas en el lecho, incluso en las condiciones de operación más desfavorables entre las estudiadas.

1.e.3) Es preciso que la relación de aspecto entre la altura de la zona inferior del lecho (z_{cs}) y su anchura ($w_{lecho,inf}$) no sea muy elevada para evitar fenómenos de *slugging* o formación de burbujas de gran tamaño que ocupen la sección transversal del lecho produciendo un cortocircuito en la mezcla axial de sólidos. En este estudio, se ha comprobado que relaciones $(z_{cs}/w_{lecho,inf}) \leq 3$ disminuyen en gran medida la probabilidad de formación de *slugs* para sólidos tipo B en RLFDZ-CS.

1.e.4) Se ha propuesto el uso de un banco de tubos en la zona inferior del lecho para provocar la ruptura de burbujas, reducir la formación de *slugs* y mejorar el contacto gas-sólido en dicha región. La configuración óptima de 5 tubos al tresbolillo ha dado lugar a reducciones del tamaño de burbuja promedio del 30% sin producir un aumento dramático en el tiempo de circulación promedio de las partículas en el lecho.

1.e.5) Se ha comprobado que la localización axial óptima de la entrada adicional de gas es el comienzo del ensanchamiento del lecho, independientemente de la inclinación de la región de transición, a fin de favorecer la mezcla axial de sólidos entre zonas y evitar fenómenos de defluidización.

1.f) Se ha determinando que la tasa de crecimiento de las burbujas con la altura sigue la tendencia descrita por la correlación clásica de Mori y Wen en las regiones de sección constante en el lecho, observándose una característica disminución del tamaño de burbuja en

la zona cónica del RLFDZ-CS relacionada con el incremento de la sección de paso y la adición de nuevas burbujas desde el distribuidor de gas inmerso en el lecho.

1.g) La velocidad promedio de burbuja varía con el tamaño de la misma, de acuerdo con la correlación de Davidson y Harrison, y de modo general crece con la altura excepto en la región cónica del lecho, por lo anteriormente expuesto.

1.h) Las tendencias experimentales de tamaño y velocidad de burbuja han sido razonablemente bien predichas por las simulaciones CFD llevadas a cabo. Asimismo, el modelo computacional de dos fluidos (TFM) ha sido capaz de predecir otros parámetros estadísticos de burbujeo como la distribución de tamaños de burbuja, su relación de aspecto promedio, la fracción volumétrica de burbujas en el lecho, la frecuencia de aparición o la distribución radial de burbujas a lo largo del reactor.

1.i) El uso de partículas fosforescentes, a modo de trazadores ópticos, ha permitido hacer un seguimiento de la evolución temporal del grado de mezcla axial entre sólidos inicialmente segregados. Los resultados experimentales han sido utilizados para validar el modelo clásico de retromezcla a contracorriente (CCBM), debidamente modificado para tener en consideración la especial geometría del RLFDZ-CS y la entrada adicional de gas. Para partículas tipo B, se ha demostrado que excesos de gas inferiores a 5 $cm^3_{STP}/cm^2 \cdot s$ dificultan la mezcla axial incrementando exponencialmente el tiempo hasta mezcla completa. Sin embargo, para excesos de gas superiores a 10 $cm^3_{STP}/cm^2 \cdot s$ la mezcla total se alcanza en cuestión de segundos.

1.j) El análisis PIV ha permitido estimar el tiempo de circulación promedio de las partículas en el lecho a partir del perfil axial de flujo ascensional de sólidos. Se ha demostrado experimentalmente que dicho perfil está íntimamente relacionado con el del tamaño y velocidad de burbuja, siendo tanto mayor cuanto más grandes y rápidas son las burbujas de gas.

1.k) Se ha demostrado la validez de los modelos matemáticos de tamaño de burbuja (JHM), mezcla axial (CCBM) y flujos multifásico (CFD) para predecir las propiedades fluidodinámicas del RLFDZ-CS a diferentes escalas de reactor. El cambio esperado en las propiedades experimentales de burbuja y circulación de sólidos ha sido asumido por los modelos de flujo utilizados.

1.l) La discretización del dominio computacional en base a "formas-α" ha permitido caracterizar las burbujas 3D resultantes de simulaciones CFD en lechos con geometría de revolución. La formulación volumétrica del diámetro de burbuja equivalente es la más representativa para comparar los perfiles $d_b(z)$ entre lechos planos y cilíndricos. La configuración pseudo-2D predice de manera satisfactoria el comportamiento fluidodinámico del lecho 3D.

1.m) El uso de membranas extractivas en la zona superior del lecho modifica el comportamiento fluidodinámico del RLFDZ-CS. La configuración RLFDZ-CS+MBT, acoplando una membrana tubular interna al lecho, minimiza el impacto sobre la mezcla axial de sólidos,

el régimen de burbujeo y el tiempo de contacto gas-sólido respecto a la configuración con membrana de pared (RLFDZ-CS+MBP).

Respecto a la aplicación del reactor multifuncional RLFDZ-CS+MB en la deshidrogenación catalítica de propano, las conclusiones más relevantes se detallan a continuación:

2.a) La deshidrogenación de propano es una reacción gas-sólido catalítica limitada esencialmente por: su elevada endotermicidad, su equilibrio termodinámico, la existencia de reacciones secundarias y la tendencia a la deposición de coque sobre la superficie activa del catalizador. El uso de un catalizador basado en Pt-Sn/$MgAl_2O_4$ en un sistema RLFDZ-CS+MB, permite hacer frente a las limitaciones gracias a que:

2.a.1) El catalizador cuenta, como soporte, con una espinela con elevada superficie específica y baja acidez, lo que limita la deposición de residuos carbonosos. El platino es muy activo catalíticamente y el estaño mejora la relación deshidrogenación/craqueo y disminuye la capacidad de hidrogenólisis del Pt.

2.a.2) El uso de un RLFDZ ha permitido llevar a cabo la regeneración catalítica in situ por combustión de los depósitos carbonosos en presencia de un agente oxidante. Además, la oxidación del coque genera parte del calor necesario para llevar a cabo la deshidrogenación reduciendo el coste energético del proceso. El uso de dos zonas de lecho con diferente sección (RLFDZ-CS) ha permitido adaptar los caudales de entrada de reactivo y oxidante para trabajar en condiciones de fluidización semejantes en ambas zonas del lecho.

2.a.3) La retirada de H_2 del lecho a partir de membranas permeoselectivas basadas en Pd o aleaciones Pd-Ag permiten desplazar el equilibrio termodinámico de la deshidrogenación catalítica hacia la formación de propileno en el sistema RLFDZ-CS+MB.

2.b) A pesar de que la conversión catalítica de propano es tanto mayor cuanto mayor es la temperatura de reacción, las altas temperaturas favorecen también la deposición de coque y el craqueo térmico. Por tanto, ha sido necesario alcanzar un compromiso entre actividad y selectividad en el proceso. La temperatura óptima de trabajo para el RLFDZ-CS+MB con Pt-Sn/$MgAl_2O_4$ se ha estimado en 550^{o}C.

2.c) Gracias a la generación de zonas oxidante y reductora en el RLFDZ-CS, ha sido posible alcanzar regímenes estacionarios de conversión de propano sin desactivación catalítica neta o aparente, independientemente de la temperatura de operación, únicamente modificando la fracción volumétrica de agente oxidante alimentado al sistema. En el rango de temperaturas utilizado, T = 500^{o}C – 575^{o}C, el porcentaje de O_2 requerido para la regeneración del catalizador ha variado entre 2% y 10%, creciendo exponencialmente con la temperatura.

2.d) El uso de velocidades relativas de gas en el rango de las sugeridas en el estudio fluidodinámico (u_r = 1.75 – 2.5) ha proporcionado un tiempo de contacto gas-sólido adecuado para alcanzar conversiones de propano próximas al equilibrio termodinámico. Además, el uso de una sección inclinada de 60^o en el reactor, la ubicación de la alimentación de propano al comienzo del cambio de sección y la disposición de las membranas en el interior del lecho han permitido una buena mezcla axial de sólidos entre las dos zonas del reactor (sin formación de

regiones defluidizadas o canales preferenciales), consiguiéndose un régimen estacionario de reacción sin desactivación catalítica.

2.e) La utilización de membranas densas de Pd-Ag en la zona de reacción del RLFDZ-CS supone la retirada de hidrógeno de los productos de reacción y la intensificación de la producción de propileno por desplazamiento del equilibrio termodinámico, obteniéndose los mejores resultados (S_{C3H6} = 92%, Y_{C3H6}^{*} = 58%) entre los reportados en literatura. No obstante, las tasas de permeación inherentes a las membranas densas son bajas y la mejora del rendimiento a propileno es discreta en el sistema RLFDZ-CS+MB respecto a la obtenida en el sistema RLFDZ-CS.

2.f) La presencia de hidrocarburos ligeros en la zona de permeación ha demostrado tener un significativo efecto en la disminución de la permeabilidad de la membrana densa por ensuciamiento con depósitos carbonosos. La superficie de Pd-Ag es activa a la deshidrogenación y a la descomposición de hidrocarburos, reduciendo el flujo de permeación de hidrógeno respecto al hallado en los ensayos realizados en atmósfera libre de hidrocarburos. No obstante, se ha demostrado que la coquización de las membranas densas es reversible, al igual que para el catalizador, por lo que se propone como trabajo de futuro un aumento de la superficie de permeación en el RLFDZ-CS+MB (por ejemplo, utilizando la pared lateral del reactor como membrana permeoselectiva, en lugar de membranas tubulares metálicas o de fibra hueca) a fin de mejorar los rendimientos a propileno presentados en este trabajo. En ese caso, deberá tenerse en cuenta la mayor tendencia a la formación de zonas defluidizadas en el lecho que esta configuración conlleva, tal y como se ha encontrado en su análisis fluidodinámico.

6 REFERENCIAS

6. REFERENCIAS

1. A. I. Stankiewicz, J. A. Moulijn, Process intensification: Transforming Chem. Eng.. *Chem. Eng. Prog.* **96**, 22-34 (2000).

2. J. Herguido, M. Menéndez, J. Santamaría, On the use of fluidized bed catalytic reactors where reduction and oxidation zones are present simultaneously. *Catal. Today.* **100**, 181-189 (2005).

3. A. L. Waddams, Chem.s from petroleum. *4th Edition, Gulf Publishing Company, Houston, 1978* (1980).

4. G. F. Froment, Coke formation in catalytic processes: Kinetics and catalyst deactivation. *Catal. Deact.,* **111**, 53-68 (1997).

5. C. H. Bartholomew, Mechanisms of catalyst deactivation. *Applied Catal. A-General,* **212**, 17-60 (2001).

6. M. P. Gimeno, Z. T. Wu, J. Soler, J. Herguido, K. Li, M. Menéndez, Combination of a Two-Zone Fluidized Bed Reactor with a Pd hollow fibre membrane for catalytic alkane dehydrogenation. *Chem. Eng. J.* **155**, 298-303 (2009).

7. J. A. Medrano, I. Julián, F. R. García-García, K. Li, J. Herguido, M. Menéndez, Two-Zone Fluidized Bed Reactor (TZFBR) with palladium membrane for catalytic propane dehydrogenation: experimental performance assessment. *Ind. Eng. Chem. Res.* **52**, 3723-3731, (2013).

8. J. A. Medrano, I. Julián, J. Herguido, M. Menéndez, Pd-Ag membrane coupled to a Two-Zone Fluidized Bed Reactor (TZFBR) for propane dehydrogenation on a Pt-Sn/$MgAl_2O_4$ catalyst. *Membranes.* **3**, 69-86 (2013).

9. J. Gascón, C. Téllez, J. Herguido, M. Menéndez, A two-zone fluidized bed reactor for catalytic propane dehydrogenation. *Chem. Eng. J.* **106**, 91-96 (2005).

10. C. Callejas, J. Soler, J. Herguido, M. Menéndez, J. Santamaría, Catalytic dehydrogenation of n-butane in a fluidized bed reactor with separate coking and regeneration zones, *Stud. Surf. Sci. Catal.* **130**, 2717-2722 (2000).

11. M. P. Lobera, C. Tellez, J. Herguido, M. Menendez, Pt-Sn/$MgAl_2O_4$ as n-butane dehydrogenation catalyst in a Two-Zone Fluidized-Bed Reactor. *Ind Eng Chem Res.* **48**, 6573-6578,(2009).

12. M. P. Lobera, C. Tellez, J. Herguido, M. Menendez, Propane dehydrogenation over Pt-Sn-K/γ-Al_2O_3 catalyst in a Two-Zone Fluidized Bed Reactor. *Ind Eng Chem Res.* **47**, 9314-9320 (2008).

13. M. L. Pacheco, J. Soler, A. Dejoz, J. M. L. Nieto, J. Herguido, M. Menéndez, J. Santamaría, MoO_3/MgO as a catalyst in the oxidative dehydrogenation of n-butane in a two-zone fluidized bed reactor. *Catal. Today.* **61**, 101-107 (2000).

14. M. P. Gimeno, J. Soler, J. Herguido, M. Menendez, Counteracting catalyst deactivation in methane aromatization with a Two Zone Fluidized Bed Reactor. *Ind. Eng. Chem. Res.* **49**, 996-1000 (2010).

15. R. Ramos, J. Herguido, M. Menéndez, J. Santamaría, Oxidation of hydrocarbons in an in-situ redox fluidized bed reactor. *J. Catal.* **163**, 218-221 (1996).

16. J. Herguido, D. Lafarga, M. Menéndez, J. Santamaría, C. Guimón, Characterization of porous ceramic membranes for their use in catalytic reactors for methane oxidative coupling. *Catal. Today.* **25**, 263-269 (1995).

17. T. B. Anderson, R. Jackson, A fluid mechanical description of fluidized beds. *Ind. Eng. Chem. Fund.* **6**, 527-539 (1967).

18. D. Kunii, O. Levenspiel, Bubbling bed model - Model for flow of gas through a fluidized bed. *Ind. Eng. Chem. Fund.* **7**, 446-452 (1968).

19. J. F. Davidson, D. Harrison, The behaviour of a continuously bubbling fluidised bed. *Chem. Eng. Sci.* **21**, 731-738 (1966).

20. J. J. van Deemter, Mixing and contacting in gas-solid fluidized beds. *Chem. Eng. Sci.* **13**, 143-154 (1961).

21. P. N. Rowe, B. A. Partridge, E. Lyall, Cloud formation around bubbles in gas fluidized beds. *Chem. Eng. Sci.* **19**, 973-985 (1964).

22. T. M. Gernon, M. A. Gilbertson, Segregation of particles in a tapered fluidized bed. *Powder Technol.* **231**, 88-101 (2012).

23. D. C. Sau, S. Mohanty, K. C. Biswal, Experimental studies and empirical models for the prediction of bed expansion in gas–solid tapered fluidized beds. *Chem. Eng. Proc. Proc. Intensif.* **49**, 418-424 (2010).

24. T. M. Gernon, M. A. Gilbertson, R. S. J. Sparks, M. Field, Gas-fluidisation in an experimental tapered bed: Insights into processes in diverging volcanic conduits. *J. Volcanol. Geotherm. Res.* **174**, 49-56 (2008).

25. M. H. Khani, Models for prediction of hydrodynamic characteristics of gas–solid tapered and mini-tapered fluidized beds. *Powder Technol.* **205**, 224-230 (2011).

26. D. C. Sau, K. C. Biswal, Computational fluid dynamics and experimental study of the hydrodynamics of a gas–solid tapered fluidized bed. *Appl. Math. Model.* **35**, 2265-2278 (2011).

27. B. Chalermsinsuwan, P. Kuchonthara, P. Piumsomboon, CFD modeling of tapered circulating fluidized bed reactor risers: Hydrodynamic descriptions and chemical reaction responses. *Chem. Eng. Process.* **49**, 1144-1160 (2010).

28. W. Duangkhamchan, F. Ronsse, F. Depypere, K. Dewettinck, J. G. Pieters, Comparison and evaluation of interphase momentum exchange models for simulation of the solids volume fraction in tapered fluidised beds. *Chem. Eng. Sci.* **65**, 3100-3112 (2010).

29. G. Agarwal, B. Lattimer, S. Ekkad, U. Vandsburger, Influence of multiple gas inlet jets on fluidized bed hydrodynamics using Particle Image Velocimetry and Digital Image Analysis. *Powder Technol.* **214**, 122-134 (2011).

30. T. Li, K. Pougatch, M. Salcudean, D. Grecov, Numerical simulation of single and multiple gas jets in bubbling fluidized beds. *Chem. Eng. Sci.* **64**, 4884-4898 (2009).

31. P. Pei, K. Zhang, B. Yu, J. Gao, G. Wu, D. Wen, Dynamic characteristics of binary mixtures in a two-jet fluidized bed. *Chem. Eng. Sci.* **66**, 1702-1714 (2011).

32. P. Pei, K. Zhang, J. Ren, D. Wen, G. Wu, CFD simulation of a gas–solid fluidized bed with two vertical jets. *Particuology.* **8**, 425-432 (2010).

33. J. F. de Jong, M. v. S. Annaland, J. A. M. Kuipers, Experimental study on the effects of gas permeation through flat membranes on the hydrodynamics in membrane-assisted fluidized beds. *Chem. Eng. Sci.* **66**, 2398-2408 (2011).

34. T. Li, A. Mahecha-Botero, J. R. Grace, Computational Fluid Dynamic Investigation of Change of Volumetric Flow in Fluidized-Bed Reactors. *Ind. Eng. Chem. Res.* **49**, 6780-6789 (2010).

35. T. Y. N. Dang, F. Gallucci, M. van Sint Annaland, Micro-structured fluidized bed membrane reactors: Solids circulation and densified zones distribution. *Chem. Eng. J.* **239**, 42-52 (2014).

36. T. Y. N. Dang, F. Gallucci, M. van Sint Annaland, Gas back-mixing study in a membrane-assisted micro-structured fluidized bed. *Chem. Eng. Sci.* **108**, 194-202 (2014).

37. T. W. Asegehegn, M. Schreiber, H. J. Krautz, Investigation of bubble behavior in fluidized beds with and without immersed horizontal tubes using a digital image analysis technique. *Powder Technol.* **210**, 248-260 (2011).

38. M. Schreiber, T. W. Asegehegn, H. J. Krautz, Numerical and Experimental Investigation of Bubbling Gas-Solid Fluidized Beds with Dense Immersed Tube Bundles. *Ind. Eng. Chem. Res.* **50**, 7653-7666 (2011).

39. S. Maurer, T. J. Schildhauer, J. Ruud van Ommen, S. M. A. Biollaz, A. Wokaun, Scale-up of fluidized beds with vertical internals: Studying the sectoral approach by means of optical probes. *Chem. Eng. J.* **252**, 131-140 (2014).

40. T. Dyakowski, A. J. Jaworski, Application of non-invasive techniques for imaging fluidized beds - A review, *Handbook of Powder Technol.* **10** 807-823 (2001).

41. M. Liu, Y. Zhang, H. Bi, J. R. Grace, Y. Zhu, Non-intrusive determination of bubble size in a gas–solid fluidized bed: An evaluation. *Chem. Eng. Sci.* **65**, 3485-3493 (2010).

42. L. Shen, F. Johnsson, B. Leckner, Digital image analysis of hydrodynamics two-dimensional bubbling fluidized beds. *Chem. Eng. Sci.* **59**, 2607-2617 (2004).

43. A. Busciglio, G. Vella, G. Micale, L. Rizzuti, Analysis of the bubbling behaviour of 2D gas solid fluidized beds. Part I: Digital image analysis technique. *Chem. Eng. J.* **140**, 398-413 (2008).

44. A. Busciglio, G. Vella, G. Micale, L. Rizzuti, Analysis of the bubbling behaviour of 2D gas solid fluidized beds. Part II: Comparison between experiments and numerical simulations via Digital Image Analysis Technique. *Chem. Eng. J.* **148**, 145-163 (2009).

45. ICIS, Propylene production and manufacturing process. *Http://www.Icis.com/v2/Chem.s/9076456/propylene/process.Html*.(2010).

46. SRI consulting, Propylene. *www.Sriconsulting.com/CEH/Public/Reports/436.0000/*.(2011).

47. J. Wang, F. Zhang, W. Hua, Y. Yue, Z. Gao, Dehydrogenation of propane over MWW-type zeolites supported gallium oxide. *Catal. Comm.* **18**, 63-67 (2012).

48. M. A. Botavina, C. Evangelisti, Y. A. Agafonov, N. A. Gaidai, N. Panziera, A. L. Lapidus, G. Martra, CrOx/SiO_2 catalysts prepared by metal vapour synthesis: Physical–Chem. characterisation and functional testing in oxidative dehydrogenation of propane. *Chem. Eng. J.* **166**, 1132-1138 (2011).

49. M. Fattahi, F. Khorasheh, S. Sahebdelfar, F. T. Zangeneh, K. Ganji, M. Saeedizad, The effect of oxygenate additives on the performance of Pt–Sn/γ - Al2O3 catalyst in the propane dehydrogenation process. *Sci. Iranica.* **18**, 1377-1383 (2011).

50. M. P. Lobera, C. Téllez, J. Herguido, Y. Schuurman, M. Menéndez, TAP studies of Pt–Sn–K/γ-Al_2O_3 catalyst for propane dehydrogenation. *Chem. Eng. J.* **171**, 1317-1323 (2011).

51. S. Assabumrungrat, W. Jhoraleecharnchai, P. Praserthdam, S. Goto, Kinetics for dehydrogenation of propane on Pt-Sn-K/gamma-Al2O3 catalyst. *J. Chem. Eng. Japan.* **33** 529-532 (2000).

52. M. D. Putra, S. M. Al-Zahrani, A. E. Abasaeed, Oxidative dehydrogenation of propane to propylene over Al_2O_3-supported Sr–V–Mo catalysts. *Catal. Communications.* **14**, 107-110 (2011).

53. Z. Nawaz, X. Tang, Q. Zhang, D. Wang, W. Fei, SAPO-34 supported Pt–Sn-based novel catalyst for propane dehydrogenation to propylene. *Catal. Comm.* **10**, 1925-1930 (2009).

54. D. Geldart, Effect of Particle-Size and Size Distribution on Behavior of Gas-Fluidized Beds. *Powder Technol.* **6**, 201-205 (1972).

55. G. Grasa, J. C. Abanades, A calibration procedure to obtain solid concentrations from digital images of bulk powders. *Powder Technol.* **114**, 125-128 (2001).

56. E. A. Patrick, F. P. Fischer III, A generalized k-nearest neighbor rule. *Inf. Control.* **16**, 128-152 (1970).

57. J. Westerveel, Fundamentals of digital particle image velocimetry data. *Meas. Sci. Technol.* **8**, 1373-1379 (1997).

58. J. A. Laverman, I. Roghair, M. v. S. Annaland, H. Kuipers, Investigation into the hydrodynamics of gas-solid fluidized beds using particle image velocimetry coupled with digital image analysis. *Can. J. Chem. Eng.* **86**, 523-535 (2008).

59. J. Link, C. Zeilstra, N. Deen, H. Kuipers, Validation of a Discrete Particle Model in a 2D Spout-Fluid Bed using non-intrusive optical measuring techniques. *Can. J. of Chem. Eng.* **82**, 30-36 (2004).

60. M. S. van Buijtenen, M. S. Burner, N. G. Deen, S. Heinrich, S. Antonyuk, J. A. M. Kuipers, An experimental study of the effect of collision properties on spout fluidized bed dynamics. *Powder Technol.* **206**, 139-148 (2011).

61. J. F. de Jong, M. van Sint Annaland, J. A. M. Kuipers, Experimental study on the hydrodynamic effects of gas permeation through horizontal membrane tubes in fluidized beds. *Powder Technol.* **241**, 74-84 (2013).

62. P. K. Agarwal, A. S. Hull, K. S. Lim, Digital Image Analysis techniques for the study of bubbling fluidized beds, *Non-Invasive monitoring of multiphase flows*, J. Chaouki, F. Larachi, M. P. Duduković, Eds. (Elsevier Science B.V., Amsterdam, 1997), 407-454 (1997).

63. M. J. V. Goldschmidt, J. M. Link, S. Mellema, J. A. M. Kuipers, Digital image analysis measurements of bed expansion and segregation dynamics in dense gas-fluidised beds. *Powder Technol.* **138**, 135-159 (2003).

64. J. F. de Jong, S. Odu, M. van Buijtenen, N. Deen, M. van Sint Annaland, J. A. M. Kuipers, Development and validation of a novel Digital Image Analysis method for fluidized bed Particle Image Velocimetry. *Powder Technol.* **230**, 193-202 (2012).

65. T. M. Knowlton, S. B. R. Karri, A. Issangya, Scale-up of fluidized-bed hydrodynamics. *Powder Technol.* **150**, 72-77 (2005).

66. L. R. Glicksman, M. R. Hyre, P. A. Farrell, Dynamic similarity in fluidization. *Int. J. Multiphase Flow.* **20**, 331-386 (1994).

67. L. R. Glicksman, Scaling relationships for fluidized beds. *Chem. Eng. Sci.* **39**, 1373-1379 (1984).

68. F. P. Di Maio, A. Di Renzo, Verification of scaling criteria for bubbling fluidized beds by DEM–CFD simulation. *Powder Technol.* **248**, 161-171 (2013).

69. T. M. Knowlton, in Fluidized Bed Technologies for Near-Zero Emission Combustion and Gasification, F. Scala, Ed. (Woodhead Publishing, , 2013), 481-523 (2013).

70. O. Levenspiel, Difficulties in trying to model and scale-up the bubbling fluidized bed (BFB) reactor. *Ind. Eng. Chem. Res.* **47**, 273-277 (2008).

71. I. Julián, F. Gallucci, M. van Sint Annaland, J. Herguido, M. Menéndez, Coupled PIV/DIA for fluid dynamics studies on a Two-Section Two-Zone Fluidized Bed Reactor. *Chem. Eng. J* **207-208**, 122-132 (2012).

72. S. Lechner, M. Merzsch, H. J. Krautz, Heat-transfer from horizontal tube bundles into fluidized beds with Geldart A lignite particles. *Powder Technol.* **253**, 14-21 (2014).

73. N. Masoumifard, N. Mostoufi, A. Hamidi, R. Sotudeh-Gharebagh, Investigation of heat transfer between a horizontal tube and gas–solid fluidized bed. *Int. J. Heat Fluid Flow.* **29**, 1504-1511 (2008).

74. S. W. Kim, J. Y. Ahn, S. D. Kim, D. Hyun Lee, Heat transfer and bubble characteristics in a fluidized bed with immersed horizontal tube bundle. *Int. J. Heat Mass Transfer.* **46**, 399-409 (2003).

75. D. Moslemian, M. M. Chen, B. T. Chao, Heat transfer to horizontal tubes in a fluidized bed: The role of superficial gas and local particle velocities. *Exp. Therm. Fluid Sci.* **4**, 76-89 (1991).

76. V. A. Borodulya, V. L. Ganzha, A. I. Zheltov, S. N. Upadhyay, S. C. Saxena, Heat transfer between gas-solid fluidized beds and horizontal tube bundles. *Letters Heat Mass Transfer.* **7**, 83-95 (1980).

77. P. A. Olowson, Influence of pressure and fluidization velocity on the hydrodynamics of a fluidized bed containing horizontal tubes. *Chem. Eng. Sci.* **49**, 2437-2446 (1994).

78. S. E. Olsson, J. Wiman, A. E. Almstedt, Hydrodynamics of a pressurized fluidized bed with horizontal tubes: Influence of pressure, fluidization velocity and tube-bank geometry. *Chem. Eng. Sci.* **50**, 581-592 (1995).

79. A. S. Hull, Z. Chen, J. W. Fritz, P. K. Agarwal, Influence of horizontal tube banks on the behavior of bubbling fluidized beds: 1. Bubble hydrodynamics. *Powder Technol.* **103**, 230-242 (1999).

80. O. Sitnai, Solids mixing in a fluidized-bed with horizontal tubes. *Ind. Eng. Chem. Proc. Des. Dev.* **20**, 533-538 (1981).

81. A. Hull, Z. Chen, P. Agarwal, Influence of horizontal tube banks on the behavior of bubbling fluidized beds 2. Mixing of solids. *Powder Technol.* **111**, 192-199 (2000).

82. H. Armendáriz, A. Guzmán, J. A. Toledo, M. E. Llanos, A. Vázquez, G. Aguilar-Ríos, Isopentane dehydrogenation on Pt-Sn catalysts supported on Al-Mg-O mixed oxides: effect of Al/Mg atomic ratio. *Applied Catal. A: General.* **211**, 69-80 (2001).

83. J. E. Gwyn, J. H. Moser, W. A. Parker, A three-phase model for gas-fluidized beds. *Chem. Eng. Prog. Symp. Ser.* **66**, 19-27 (1970).

84. K. Lim, J. Zhu, J. Grace, Hydrodynamics of gas-solid fluidization. *Int. J. Multiphase Flow.* **21**, 141-193 (1995).

85. J. C. Abanades, G. S. Grasa, Modeling the axial and lateral mixing of solids in fluidized beds. *Ind. Eng. Chem. Res.* **40**, 5656-5665 (2001).

86. G. Grasa, J. C. Abanades, The use of two different models to describe the axial mixing of solids in fluidised beds. *Chem. Eng. Sci.* **57**, 2791-2798 (2002).

87. P. N. Rowe, B. A. Partridge, An X-Ray Study of Bubbles in Fluidised Beds. *Trans. Inst. Chem. Eng.* **43**, 157-175 (1965).

88. B. Kozanoglu, E. K. Levy, Wake fractions of small bubbles in gas fluidized beds. *Powder Technol.* **68**, 285-286 (1991).

89. E. A. Basesme, E. K. Levy, Solids exchange between the bubble wake and the emulsion phase in a two-dimensional gas-fluidized bed. *Powder Technol.* **72**, 45-50 (1992).

90. S. Sane, H. Haynes, P. Agarwal, An experimental and modelling investigation of gas mixing in bubbling fluidized beds. *Chem. Eng. Sci.* **51**, 1133-1147 (1996).

91. T. Chiba, H. Kobayashi, Gas exchange between the bubble and emulsion phases in gas-solid fluidized beds. *Chem. Eng. Sci.* **25**, 1375-1385 (1970).

92. K. S. Lim, V. S. Gururajan, P. K. Agarwal, Mixing of homogeneous solids in bubbling fluidized beds: Theoretical modelling and experimental investigation using digital image analysis. *Chem. Eng. Sci.* **48**, 2251-2265 (1993).

93. G. Song, K. Tsuchiya, L. S. Fan, Image processing technique for measurement of solids holdup in near wake behind a single bubble in a liquid—solid fluidized bed. *Chem. Eng. Sci.* **46**, 2933-2941 (1991).

94. S. Karimipour, T. Pugsley, A critical evaluation of literature correlations for predicting bubble size and velocity in gas–solid fluidized beds. *Powder Technol.* **205**, 1-14 (2011).

95. A. Farshi, H. Javaherizadeh, M. A. Hamzavi-Abedi, Investigation of the effect of bubble diameter on the performance of gas-solid fluidized bed reactor and two-phase modelling of gas fluidized bed reactor in melamine production. *Petroleum Coal.* **50**, 11-22 (2008).

96. S. Mori, C. Y. Wen, Estimation of bubble diameter in gaseous fluidized-beds. *AIChE J.* **21**, 109-115 (1975).

97. M. Horio, A. Nonaka, A generalized bubble diameter correlation for gas-solid fluidized-beds. *AIChE J.* **33**, 1865-1872 (1987).

98. P. Agarwal, Effect of bed diameter on bubble-growth and incipient slugging in gas-fluidized beds. *Chem. Eng. Res. Des.* **65**, 345-354 (1987).

99. N. Herzog, M. Schreiber, C. Egbers, H. J. Krautz, A comparative study of different CFD-codes for numerical simulation of gas-solid fluidized bed hydrodynamics. *Comput. Chem. Eng.* **39**, 41-46 (2012).

100. A. Busciglio, G. Vella, G. Micale, L. Rizzuti, Experimental analysis of bubble size distributions in 2D gas fluidized beds. *Chem. Eng. Sci.* **65**, 4782-4791 (2010).

101. V. V. Ranade, Computational flow modelling for Chem. Reactor Eng.. *Academic Press, London.*(2002).

102. D. J. Patil, M. van Sint Annaland, J. A. M. Kuipers, Critical comparison of hydrodynamic models for gas–solid fluidized beds—Part II: freely bubbling gas–solid fluidized beds. *Chem. Eng. Sci.* **60**, 73-84 (2005).

103. E. Stenmark, On multiphase flow models in Ansys CFD software. *Master Thesis, Chalmers University of Technology* (2013).

104. W. Jeong, J. Seong, Comparison of effects on technical variances of computational fluid dynamics (CFD) software based on finite element and finite volume methods. *Int. J. Mech. Sci.* **78**, 19-26 (2014).

105. G. H. Lee, Y. S. Bang, S. W. Woo, D. H. Kim, M. K. Kang, Comparative study of commercial CFD software performance for prediction of reactor internal flow. *Trans. KSME. B* **37**, 1175-1183 (2013).

106. C. K. K. Lun, S. B. Savage, D. J. Jeffrey, N. Chepurniy, Kinetic Theories for Granular Flow - Inelastic Particles in Couette-Flow and Slightly Inelastic Particles in a General Flowfield. *J. Fluid Mech.* **140**, 223-256 (1984).

107. F. Taghipour, N. Ellis, C. Wong, Experimental and computational study of gas-solid fluidized bed hydrodynamics. *Chem. Eng. Sci.* **60**, 6857-6867 (2005).

108. C. K. K. Lun, S. B. Savage, The Effects of an Impact Velocity Dependent Coefficient of Restitution on Stresses Developed by Sheared Antigranulocytes-Materials. *Acta Mech.* **63**, 15-44 (1986).

109. ANSYS CFX-Solver User's guide. *ANSYS Ltd.*(2009) http://orange.engr.ucdavis.edu/Documentation12.1/121/CFX/xmgr.pdf.

110. D. Gidaspow, R. Bezburuah, J. Ding, Hydrodynamics of circulating fluidized beds, Kinetic Theory approach. *Fluidization VII, Proceedings of the 7th Engineering Foundation Conference on Fluidization*, 75-82 (1992).

111. D. G. Schaeffer, Instability in the evolution equations describing incompressible granular flow. *J. Diff. Eq.* **66**, 19-50 (1987).

112. T. W. Asegehegn, M. Schreiber, H. J. Krautz, Numerical simulation and experimental validation of bubble behavior in 2D gas-solid fluidized beds with immersed horizontal tubes. *Chem. Eng. Sci.* **66**, 5410-5427 (2011).

113. R. P. Utikar, V. V. Ranade, Singlejet fluidized beds: Experiments and CFD simulations with glass and polypropylene particles RID A-5627-2009. *Chem. Eng. Sci.* **62**, 167-183 (2007).

114. J. A. M. Kuipers, K. J. Vanduin, F. P. H. Vanbeckum, W. P. M. Vanswaaij, A numerical-model of gas-fluidized beds. *Chem. Eng. Sci.* **47**, 1913-1924 (1992).

115. J. A. M. Kuipers, K. J. Vanduin, F. P. H. Vanbeckum, W. P. M. Vanswaaij, Computer-Simulation of the Hydrodynamics of a 2-Dimensional Gas-Fluidized Bed. *Comp. Chem. Eng.* **17**, 839-858 (1993).

116. C. Sobrino, A. Acosta-Iborra, M. A. Izquierdo-Barrientos, M. de Vega, Three-dimensional two-fluid modeling of a cylindrical fluidized bed and validation of the Maximum Entropy method to determine bubble properties. *Chem. Eng. J.* **262**, 628-639 (2015).

117. V. Verma, N. G. Deen, J. T. Padding, J. A. M. Kuipers, Two-fluid modeling of three-dimensional cylindrical gas–solid fluidized beds using the kinetic theory of granular flow. *Chem. Eng. Sci.* **102**, 227-245 (2013).

118. H. Edelsbrunner, E. P. Mucke, 3-Dimensional Alpha-Shapes. *Acm Transactions on Graphics.* **13**, 43-72 (1994).

119. S. Sánchez-Delgado, J. A. Almendros-Ibáñez, N. García-Hernando, D. Santana, On the minimum fluidization velocity in 2D fluidized beds. *Powder Technol.* **207**, 145-153 (2011).

120. G. Ramos Caicedo, M. García Ruiz, J. J. Prieto Marqués, J. Guardiola Soler, Minimum fluidization velocities for gas–solid 2D beds. *Chem. Eng. Proc.: Proc. Intensif.* **41**, 761-764 (2002).

121. G. Yasui, L. N. Johanson, Characteristics of gas pockets in fluidized beds. *AIChE J.* **4**, 445-452 (1958).

122. A. B. Whitehead, A. D. Young, Fluidization performance in large scale equipment, part I: *Proc. Int. Symp. on Fluidization, Eindhoven (Netherlands).*(1967).

123. W. H. Park, W. K. Kang, C. E. Capes, G. L. Osberg, The properties of bubbles in fluidized beds of conducting particles as measured by an electroresistivity probe. *Chem. Eng. Sci.* **24**, 851-865 (1969).

124. K. Kato, C. Y. Wen, Bubble Assemblage Model for Fluidized Bed Catalytic Reactors. *Chem. Eng. Sci.* **24**, 1351-1369 (1969).

125. P. N. Rowe, Prediction of Bubble-Size in a Gas-Fluidized Bed. *Chem. Eng. Sci.* **31**, 285-288 (1976).

126. D. Geldart, Size and frequency of bubbles in 2-Dimensional and 3-Dimensional gas-fluidised beds. *Powder Technol.* **4**, 41-55 (1970).

127. J. Werther, Modeling and scale-Up of industrial fluidized-bed reactors. *Chem. Eng. Sci.* **35**, 372-379 (1980).

128. R. C. Darton, R. D. Lanauze, J. F. Davidson, D. Harrison, Bubble-growth due to coalescence in fluidized-beds. *Trans. Inst. Chem. Eng.* **55**, 274-280 (1977).

129. S. Sánchez-Delgado, C. Marugán-Cruz, A. Soria-Verdugo, D. Santana, Estimation and experimental validation of the circulation time in a 2D gas–solid fluidized beds. *Powder Technol.* **235**, 669-676 (2013).

130. P. N. Rowe, Estimation of solids circulation rate in a bubbling fluidised bed. *Chem. Eng. Sci.* **28**, 979-980 (1973).

131. L. Pérez-Moreno, J. Soler, J. Herguido, M. Menéndez, Stable hydrogen production by methane steam reforming in a two-zone fluidized-bed reactor: Effect of the operating variables. *Int. J. Hydrogen Energ.* **38**, 7830-7838 (2013).

132. D. S. Thakur, M. G. Thomas, Catalyst deactivation in heavy petroleum and synthetic crude processing: a review. *Applied Catal.* **15**, 197-225 (1985).

133. C. H. Bartholomew, Catalyst Deactivation. *Chem. Eng.* **91**, 96-112 (1984).

134. G. F. Froment, Kinetic Modeling of Hydrocarbon Conversion Processes Subject to Catalyst Deactivation by Coke Formation. *Abstracts of Papers Am. Chem. Soc.* **210**, 33-PETR (1995).

135. E. L. Jablonski, A. A. Castro, O. A. Scelza, S. R. de Miguel, Effect of Ga addition to Pt/Al2O_3 on the activity, selectivity and deactivation in the propane dehydrogenation. *Applied Catal. A: General.* **183**, 189-198 (1999).

136. J. Salmones, J. Wang, J. A. Galicia, G. Aguilar-Rios, H_2 reduction behaviors and catalytic performance of bimetallic tin-modified platinum catalysts for propane dehydrogenation. *J. Molec. Catal. A: Chem.* **184**, 203-213 (2002).

137. R. Schäfer, M. Noack, P. Kölsch, M. Stöhr, J. Caro, Comparison of different catalysts in the membrane-supported dehydrogenation of propane. *Catal. Today.* **82**, 15-23 (2003).

138. M. Chen, J. Xu, Y. Cao, H.-Y. He, K.-N. Fan, J.-H. Zhuang, Dehydrogenation of propane over In_2O_3–Al_2O_3 mixed oxide in the presence of carbon dioxide. *J. Catal.* **272**, 101-108 (2010).

APÉNDICE

APÉNDICE

Esta tesis doctoral se presenta en la modalidad de compendio de publicaciones. En primer lugar, se indica el tipo de contribución en cada uno de los trabajos publicados o pendientes de publicación. Posteriormente, se detalla el factor de impacto de las revistas (obtenidos del Journal of Citation Reports, JCR), tanto en el año de publicación como en el último disponible, así como su clasificación en las correspondientes áreas temáticas indicando el cuartil en el que se encuentran englobadas. Los datos relativos a factores de impacto y áreas temáticas se muestran tabulados en la Tabla A.1.

Informe de contribución, factores de impacto y área temática de las revistas

I. *I. Julián, J. Herguido, M. Menéndez, Particle Mixing in a Two-Section Two-Zone Fluidized Bed Reactor. Experimental Technique and Counter-Current Back-Mixing Model Validation, Ind. Eng. Chem. Res. 52 (2013) 13587 – 13596.*

Mi contribución en este trabajo ha consistido en la implementación del modelo de mezcla de sólidos (CCBM) en Matlab, el montaje de la instalación experimental, su puesta a punto, la grabación experimental de vídeos de mezcla, el tratamiento digital de las imágenes resultantes y la redacción del artículo.

II. *I. Julián, F. Gallucci, M. v. Sint Annaland, J. Herguido, M. Menéndez, Coupled PIV/DIA for fluid dynamic studies on a Two-Section Two-Zone Fluidized Bed Reactor, Chem. Eng. J. 207 – 208 (2012) 122 – 132.*

En este trabajo, realizado en colaboración con el Grupo de Reactores Multifásicos (SMR) de la Universidad Tecnológica de Eindhoven (Países Bajos), mi contribución ha consistido en el desarrollo de fase experimental, la optimización de los parámetros de post-procesado de imágenes mediante las técnicas *Particle Image Velocimetry* y *Digital Image Analysis* y la redacción del artículo.

III. *I. Julián, J. Herguido, M. Menéndez, A non-parametric bubble size correlation for a Two-Section Two-Zone Fluidized Bed Reactor (TS-TZFBR), Powder Technol. 256 (2014) 146-157.*

Mi contribución a este artículo incluye el montaje y puesta a punto de la instalación experimental, el diseño de experimentos, la experimentación, el desarrollo del modelo matemático *JHM* (Julián – Herguido – Menéndez) para predecir la variación del tamaño de burbuja en reactores TS-TZFBR y la redacción del documento.

IV. *I. Julián, J. Herguido, M. Menéndez, CFD model prediction of a Two-Section Two-Zone Fluidized Bed Reactor (TS-TZFBR) hydrodynamics, Chem. Eng. J. 248 (2014) 352-362.*

En este trabajo llevé a cabo tanto las simulaciones fluidodinámicas en Ansys CFX como la experimentación en lechos pseudo-2D para validar la herramienta de simulación. Asimismo, me encargué de la redacción del artículo final.

V. *I. Julián, F. Gallucci, M. v. Sint Annaland, J. Herguido, M. Menéndez, Hydrodynamic study of a Two-Section Two-Zone Fluidized Bed Reactor with an immersed tube bank via PIV/DIA, Chem. Eng. Sci. (2015).*

En esta nueva colaboración con el grupo SMR de los Países Bajos, mi contribución abarca desde el diseño de las configuraciones de tubos (*'internals'*), pasando por la experimentación e implementación de los algoritmos de tratamiento de imágenes, hasta la redacción del artículo.

VI. *I. Julián, J. Herguido, M. Menéndez, Experimental and simulated solids mixing and bubbling behaviour in a scaled Two-Section Two-Zone Fluidized Bed Reactor, Chem. Eng. Sci. (2015). Enviado.*

En este trabajo hice uso de resultados publicados previamente en un reactor a pequeña escala y utilicé los mismos métodos experimentales y herramientas de simulación para caracterizar el comportamiento fluidodinámico de un reactor a mayor escala. Me ocupé, igualmente, de la redacción del artículo.

VII. I. Julián, J. Herguido, M. Menéndez, *Gas permeation effect on the Two-Section Two-Zone Fluidized Bed Membrane Reactor (TS-TZFBMR) fluid dynamics: a CFD simulation study, Chem. Eng. J. (2015). Enviado.*

Mi contribución en este trabajo abarca desde el diseño de los reactores hasta la escritura del artículo científico, incluyendo la configuración y puesta a punto del modelo de simulación, la realización de experimentos y el análisis de resultados.

VIII. *I. Julián, D. González, J. Herguido, M. Menéndez, On the use of α–shapes for the measurement of 3D bubbles in fluidized beds from Two-Fluid Model simulations, Powder Technol. (2015). Enviado.*

En este trabajo realicé el modelado de reactor tridimensional, su mallado y simulación además de procesar los resultados simulados. Asimismo, redacté el artículo científico.

IX. *J.A. Medrano, I. Julián, J. Herguido, M. Menéndez, Pd-Ag membrane coupled to a Two-Zone Fluidized Bed Reactor (TZFBR) for propane dehydrogenation on a Pt-Sn/$MgAl_2O_4$ catalyst, Membranes 3 (2013) 69 – 86.*

Mi contribución a este trabajo incluye el diseño de experimentos, la supervisión de la experimentación y la revisión la redacción del artículo.

X. *J.A. Medrano, I. Julián, F. García, K. Li, J. Herguido, M. Menéndez, Two-Zone Fluidized Bed Reactor (TZFBR) with palladium membrane for catalytic propane dehydrogenation: experimental performance assessment, Ind. Eng. Chem. Res. 52 (2013) 3723 – 3731.*

En este trabajo llevé a cabo el diseño de experimentos, supervisé la labor experimental del primer autor y redacté la Memoria del artículo.

XI. *H. Montesinos, I. Julián, J. Herguido, M. Menéndez, Effect of the presence of light hydrocarbon mixtures on the hydrogen permeation through Pd-Ag alloyed membranes, Int. J. Hydrogen. Energ. 40 (2015) 3462-3471.*

Análogamente, mi contribución en este trabajo incluye la supervisión de la experimentación llevada a cabo por el primer autor y la redacción del artículo. Asimismo, colaboré en el diseño de experimentos y en la experimentación en planta.

Tabla A.1 Factores de impacto y áreas temáticas de las revistas

Artículo	Revista	Factor de impacto (año publ.)	Factor de impacto (JCR 2013)	Posición de la revista dentro de su área temática (número de cuartil)
I.	*Industrial & Engineering Chemistry Research*	2,235	2,235	Engineering, Chemical: 36/133 (Q2)
II.	*Chemical Engineering Journal*	3,473	4,058	Engineering, Chemical: 8/133 (Q1) Engineering, Environmental: 7/44 (Q1)
III.	*Powder Technology*	2,269	2,269	Engineering, Chemical: 34/133 (Q2)
IV.	*Chemical Engineering Journal*	4,058	4,058	Engineering, Chemical: 8/133 (Q1) Engineering, Environmental: 7/44 (Q1)
V.	*Chemical Engineering Science*	2,613	2,613	Engineering, Chemical: 24/133 (Q1)
VI.	*Chemical Engineering Science*	-	2,613	Engineering, Chemical: 24/133 (Q1)
VII.	*Chemical Engineering Journal*	-	4,058	Engineering, Chemical: 8/133 (Q1) Engineering, Environmental: 7/44 (Q1)
VIII.	*Powder Technology*	-	2,269	Engineering, Chemical: 34/133 (Q2)
IX.	*Membranes*	-	-	-
X.	*Industrial & Engineering Chemistry Research*	2,235	2,235	Engineering, Chemical: 36/133 (Q2)
XI.	*International Journal of Hydrogen Energy*	2,930	2,930	Chemistry, Physical: **47/136 (Q2)** Electrochemistry: **7/27 (Q2)** Energy and Fuels: **28/82 (Q2)**

ANEXOS

Anexo A.1: Obtención de perfiles de concentración de trazador

```
function [M,Im]=solmixing(nombreexp,tl)

%Esta función representa el perfil axial de concentraciones de
trazador experimentales para los distintos tiempos de mezcla indicados
por el vector de fotogramas "tl" (introducido como parámetro de
entrada). Además, representa la evolución temporal del índice de
mezcla experimental. El parámetro "nombreexp" representa el nombre de
la carpeta contenedora de los fotogramas de mezcla en cuestión.
La matriz M contiene la concentración de trazador para cada altura del
lecho (columnas) y tiempo de mezcla (filas). La discretización
espacial es: Δz = 1 (cm). La temporal es: Δt = 1/fps (s), siendo fps
la frecuencia (fotogramas por segundo) de la grabación.

EJEMPLO:
[Czt,IM] = solmixing('2x_a80_ur30_z0',[1,8,14,26,51,101,401,1000]);

2x -> video con reactor a escala
a80 -> Geometría de RLFDZ con ángulo de cambio de sección: α = 80°
ur30 -> velocidad relativa de gas u_r = 3.0 a lo largo del lecho
z0 -> distancia relativa entre z_dis y z_cs igual a 0.

Si fps = 25 el vector de tiempos indica que la concentración axial de
trazador se representará a los siguientes tiempos de mezcla: [0, 0.3,
0.6, 1, 2, 4, 16 y 40] (s).

La matriz Czt tendrá tantas columnas como centímetros de reactor y
tantas filas como fotogramas transitorios de mezcla.

El vector IM contendrá tantos valores como fotogramas de mezcla
analizados.

%=========================================================================%
%                          COMIENZO DE LA FUNCIÓN:                        %
%=========================================================================%

close all % Cierra todas las figuras abierta.

% Añade al directorio de trabajo la ruta a la carpeta contenedora de
los videos de mezcla y almacena en "fpat" la ruta a la carpeta
contenedora
addpath(genpath('G:\Videos escalado\Videoimagenes'));
fpat = 'G:\Videos escalado\Videoimagenes\';

% "alfa", "ur" y "zdis" almacenan los datos del ángulo de cambio de
sección, la velocidad relativa de gas y la altura relativa de la
alimentación 2aria a partir del nombre del archivo.
alfa = str2num(nombreexp(5:6));
ur   = str2num(nombreexp(10:11))/10;

      if nombreexp(1) == '1' % escala "1x"
            % dimensiones reales del lecho en cm
            hcs_cm=8; wbed_cm=2; wbedup_cm=4;

            elseif nombreexp(1)=='2'% "2x"
            hcs_cm=12; wbed_cm=4; wbedup_cm=8;
      end

zdis = str2num(nombreexp(14))+hcs_cm;
```

```
%=========================================================================%
%                CONDICIONES INICIALES (modificables)                     %
%=========================================================================%

vfot   = 1:1000; % vector de fotogramas a analizar
n      = numel(vfot); % número de fotogramas a analizar

% Coordenadas del lecho en la imagen (¡Comprobar para cada video!)
x0        = 607;              % Límite superior izquierdo del lecho
y0        = 1;                % Límite superior izquierdo del lecho
wx        = 922-x0;           % Anchura del lecho (pixels)
hy        = 1715;             % Altura del lecho (pixels)
hcs_pix   = 1248;             % Altura del cambio de sección (pixels)
xini      = 689-x0;           % Límite izquierdo de sección inferior
xfin      = 845-x0;           % Límite derecho de sección inferior
hmax_cm   = round(19.025);    % Altura del lecho fijo inicial
expans    = 1.164;            % Expansión volumétrica del lecho
angrot    = 270;              % Ángulo rotación imagen
fps       = 25;               % Frecuencia de grabación


%=========================================================================%
%                          DEFINICIÓN DE VARIABLES                        %
%=========================================================================%

coordcrop = [x0 y0 wx hy];    % Coordenadas de recorte de imagen
wbed_pix  = xfin-xini;        % Anchura inferior del lecho (pixels)
pix2cm    = ((hy-hcs_pix)/hcs_cm+wbed_pix/wbed_cm)/2; % Resolución
nrod      = ceil(hy/pix2cm);  % Número de "rodajas" axiales de lecho

% Vector de anchuras de lecho en función de la altura
peso_geom = [wbedup_cm*ones(1,nrod-hcs_cm-
numel(1:ceil(2*tan(alfa*pi()/180)))),wbed_cm+2*(ceil(2*tan(alfa*pi()/1
80)):-1:1)/ceil(tan(alfa*pi()/180)), wbed_cm*ones(1,hcs_cm)]';
pesos=repmat(peso_geom',n,1);

M         = zeros(n,nrod);    % Inicialización de la matriz C(t,z)
Media     = zeros(1,nrod);    % Inic. del vector de concent. medias
Areatracer= zeros(1,n);       % Inic. del vector de áreas bajo curva

%=========================================================================%
%           LECTURA Y ANÁLISIS DEL 1er FOTOGRAMA DE MEZCLA                %
%=========================================================================%

I     = imread(strcat(nombreexp,' (1).jpg'));   % Lectura 1er fotograma
Irc   = imcrop(imrotate(I,angrot),coordcrop);   % Giro + recorte imagen

% Algoritmo para eliminar la luminosidad externa al reactor:
Ircg  = rgb2gray(Irc);
pol1  = roipoly(Ircg,[1,xini,xini,1],[hcs_pix-tan(alfa*pi()/180)*2*
pix2cm , hcs_pix,hy,hy]);
pol1c = uint8(ones(size(pol1))-pol1);
pol2  = roipoly(Ircg,[wx,xfin,xfin,wx],[hcs_pix-tan(alfa*pi()/180)*2*
pix2cm,hcs_pix,hy,hy]);
pol2c = uint8(ones(size(pol2))-pol2);
I4    = Ircg.*pol1c;
I5    = I4.*pol2c;
```

```
% Captura de la intensidad inicial promedio (en escala de grises) en
las zonas iluminada y no iluminada del lecho:

% -> Zona "de reacción" o zona superior del lecho
I6reac= imcrop(I5,[1 hy-hmax_cm*pix2cm wx hcs_pix-hy+hmax_cm*pix2cm]);
[counts1 ind1]    = imhist(I6reac);
ci1               = [counts1 ind1];
P0                = find(ci1==max(ci1(4:50,1)));      % Lum. mínima

% -> Zona "de regeneración" o zona inferior del lecho
I6reg             = imcrop(I5,[1 hcs_pix wx hy-hcs_pix]);
[counts2 ind2]    = imhist(I6reg);
ci2               = [counts2 ind2];
Pmax              = find(ci2==max(ci2(50:255,1)));    % Lum. máxima

%=========================================================================%
%        ALGORITMO DE CÁLCULO DE CONCENTRACIONES DE TRAZADOR              %
%=========================================================================%

b=1; % contador
thr   = P0; % umbral inferior de intensidad (t=0s, zona superior)

while b<=n % Desde 1 hasta el número total de fotogramas a analizar

    % Lectura y adecuación de imagen para análisis
    I       = imread(strcat(nombreexp,' (',num2str(b),').jpg'));
    Irc     = imcrop(imrotate(I,angrot),coordcrop);
    Ircg    = rgb2gray(Irc);
    I4      = Ircg.*pol1c;
    I5      = I4.*pol2c;

    for i=1:nrod % Desde 1 hasta el número máximo de rodajas de lecho

      % Captura de la rodaja
      I6    = imcrop(I5,[1 ceil((hy/nrod)*(i-1)) wx ceil((hy/nrod))]);

      % Detección de burbujas (bajas intensidades no computables)
      if i>(hy/pix2cm-hcs_cm) % Zona inferior del lecho
              thraux    = findlocalminima(I6,4,5,0);
              if numel(thraux)==1 % No hay burbujas, fase densa homog.
                  thr   = thraux;
              elseif thraux(2)<30 % Coexisten fase densa y burbujas
                  thr   = thraux(2);
              else
      % Hay más de un valle pero el 2° valle aparece más allá de lo
      atribuible a luminosidad de burbuja => fase densa poco iluminada
                  thr   = thraux(1);
              end
      elseif i>(hy/pix2cm-hmax_cm*expans) && i<=(hy/pix2cm-hcs_cm) %ZS
              thraux    = findlocalminima(I6,4,5,0);
              if numel(thraux)==1 && thraux<30
                  thr   = thraux;
              elseif thraux(1)>=30
                  thr   = P0;
              else
                  thr   = thraux(1);
              end
      end
```

```
        % Cálculo del histograma correspondiente a cada rodaja. "counts"
        devuelve el numero de pixeles con una determinada intensidad
        [counts ind]      = imhist(I6);

        % Intensidad promedio en la rodaja "i"
        Media(i)
        =(mean(counts(thr:255).*ind((thr:255))))/mean(counts(thr:255);
        % Si no hay intensidades superiores a la umbral (thr) en dicha
        rodaja, se le asigna como intensidad promedio la del sólido no
        iluminado.
        Media(isnan(Media))     = P0;

    end % correspondiente al "for"

    % Cálculo del vector de concentraciones unitarias, truncamiento de
    las concentraciones entre [0-1] y almacenamiento en la matriz M
    concunit                = (Media-P0)/(Pmax-P0);
    concunit(concunit<0)    = 0;
    concunit(concunit>1)    = 1;
    M(b,:)                  = concunit;

    % Área bajo la curva de concentraciones unitarias a tiempo "b"
    Areatracer(b)=sum(concunit(nrod-floor(hmax_cm*expans):nrod));


b=b+1; % Contador

end % correspondiente al "while"

% Normalización de concentraciones corrigiendo el área bajo la curva
C(z) para tener el cuenta el decaimiento de la intensidad de emisión
de los trazadores con el tiempo
Areamax         = Areatracer(1);
Area1           = repmat(Areatracer',1,nrod);
Mcor1           = M.*(Areamax./Area1);
Mcor1(Mcor1>1)  = 1;
M               = Mcor1;

%=========================================================================%
%                    CÁLCULO DEL ÍNDICE DE MEZCLA                         %
%=========================================================================%

Cinf        = 1*(sum(peso_geom(nrod-hcs_cm:nrod))*Areatracer(1)/((hy-
hcs_pix)/pix2cm)/sum(peso_geom(nrod-round(hmax_cm):nrod)));

Im          = (((sum((M(:,nrod-round(hmax_cm*expans)-1:1:nrod-hcs_cm-
1).*pesos(:,nrod-round(hmax_cm*expans)-1:1:nrod-hcs_cm-1)+M(:,nrod-
round(hmax_cm*expans):1:nrod-hcs_cm).*pesos(:,nrod-
round(hmax_cm*expans):1:nrod-hcs_cm)),2))/2)./sum(pesos(1,nrod-
round(hmax_cm*expans):1:nrod-hcs_cm)))/Cinf;

%=========================================================================%
%                 REPRESENTACIÓN GRÁFICA DE RESULTADOS                    %
%=========================================================================%

% Variables para representación: altura adimensional del lecho (z1) y
vector de "rodajas" a representar (a)

z1          = (hmax_cm+expans-1:-(1/expans):1)./(hmax_cm);
a           = nrod-round(hmax_cm*expans):nrod-1;
```

```
% Figura 1: C(z,t) para los tiempos de mezcla indicados por "tl"
figure(1),
hold on
title('Tracer Concentration Profiles');
xlabel('Dimensionless vertical position, z [cm]');
ylabel('Tracer Concentration, C [-]');

plot(z1,M(tl(1),a),'k*')
plot(z1,M(tl(2),a),'b.')
plot(z1,M(tl(3),a),'g+')
plot(z1,M(tl(4),a),'yx')
plot(z1,M(tl(5),a),'ro')
plot(z1,M(tl(6),a),'c-.')
plot(z1,M(tl(7),a),'m-')
plot(z1,M(tl(8),a),'b:')

t1    = round((tl(1)-1)/fps);
t2    = round((tl(2)-1)/fps);
t3    = round((tl(3)-1)/fps);
t4    = round((tl(4)-1)/fps);
t5    = round((tl(5)-1)/fps);
t6    = round((tl(6)-1)/fps);
t7    = round((tl(7)-1)/fps);
t8    = round((tl(8)-1)/fps);

legend(sprintf('t=%ds',t1),sprintf('t=%ds',t2),sprintf('t=%ds',t3),spr
intf('t=%ds',t4),sprintf('t=%ds',t5),sprintf('t=%ds',t6),sprintf('t=%d
s',t7),sprintf('t=%ds',t8));

axis([0 1.0 0 1.0]);
hold off

% Figura 2: IM(t)
t=(0:n-1)./fps;
figure(2),
title('Mixing Index');
xlabel('Mixing time, t [s]');
ylabel('Mixing Index, MI [-]');
axis([0 40 0 1.0]);
hold on
plot(t,Im(1:n)','k*');

% Almacenamiento de las figuras C(z,t) e IM(t) y de las matrices M e
IM en sendas hojas excel
nombre1=strcat(nombreexp,'TracerConcProf');
saveas(figure(1),[fpat,filesep,nombre1],'fig');

nombre2=strcat(nombreexp,'MixingIndex');
saveas(figure(2),[fpat,filesep,nombre2],'fig');

xlswrite(strcat(nombresinavi,'.xlsx'),M,'Hoja1');
xlswrite(strcat(nombresinavi,'.xlsx'),Im','Hoja2');

end % Fin de la función
```

Anexo A.2: Determinación de propiedades de burbuja

```
function  hidrodinamica_exp ( videoexp )

%Esta función realiza un estudio estadístico de las propiedades de
burbuja experimentales previa identificación de éstas en videos de
fluidización llevados a cabo en lechos pseudo-2D. Las propiedades
relativas al tamaño y velocidad de burbuja, así como su relación de
aspecto, distribución de tamaños y frecuencias de aparición, evolución
transitoria de la altura de la superficie libre del lecho y fracción
del gas en burbujas se representan gráficamente y se almacenan en una
hoja de cálculo para posterior tratamiento de datos.

EJEMPLO: hidrodinámica_exp('2x_a60_ur25')

close all % Cierre de figures abiertas

%=========================================================================%
%           RUTA A LOS ARCHIVOS DE VIDEO EXPERIMENTALES                   %
%=========================================================================%

addpath(genpath('D:\SoftI3A\TESIS\Videos escalado\Videoimagenes'));
name='Eu-Dy/SrAl_2O_4 (d_p=0.10-0.32mm)';

%=========================================================================%
%              CONDICIONES INICIALES (pueden ser modificadas)             %
%=========================================================================%

nfexp             = 999;      % Número de fotogramas a analizar
fpsexp            = 30;       % Frecuencia de adquisición (fps)
dens_lecho        = 1.5;      % Densidad del lecho experimental(g/cm^3)
g                 = 981;      % Gravedad (cm/s^2)
peso_lecho        = 155.3;    % Peso de catalizador introducido (g)
prof_lechoexp     = 0.8;      % Profundidad del lecho (cm)
vol_lechofijo     = peso_lecho/dens_lecho; %volumen de lecho fijo
wreac_exp         = 8;        % Anchura de la "zona de reacción" (cm)
wreg_exp          = 4;        % Anchura de la "zona de regenerac." (cm)
hreg_exp          = 12;       % Altura de la "zona de regenerac." (cm)
umf_fosfo         = 10.1;     % Vel. mínima fluidización (cm/s)

alfa_exp          = str2num(videoexp(5:6)); % Ángulo de cambio de secc.
urd_exp           = str2num(videoexp(10:11))/10; % Velocidad rel. "up"
uru_exp           = str2num(videoexp(10:11))/10; % Velocidad rel."down"

% Coordenadas del lecho en la imagen (¡Comprobar para cada video!)
    coordexp      = [1,133,1800,446-133];
    polig1_x      = [890,1321,coordexp(3),coordexp(3)];
    polig1_y      = [coordexp(4),225,225,coordexp(4)];
    polig2_x      = polig1_x;
    polig2_y      = [1,65,65,1];

pix2cm_exp        = coordexp(4)/wr_exp;     % Resolución de la imagen
hr_exp            = coordexp(3)/pix2cm_exp; % Altura del reactor (cm)
% Altura de la zona de transición (región troncocónica) (cm):
hrt_exp           = tan(alfa_exp*pi/180)*(wreac_exp-wreg_exp)/2;
```

```
%=========================================================================%
%                      INICIALIZACIÓN DE VARIABLES                        %
%=========================================================================%

xaux              = []; % Posición horizonal del centroid de burbuja
dbaux             = []; % Diámetro equivalente de burbuja
zaux              = []; % Posición vertical del centroide de burbuja
aspectratioaux    = []; % Relación de aspecto de las burbujas
ztaux             = zeros(1,2); % Gráfico z(t)
ubz               = zeros(1,2); % Gráfico u_b(z)
ubdb              = zeros(1,2); % Gráfico u_b(d_b^0.5)
dbz               = zeros(1,2); % Gráfico d_b(z)
zfreeboard_exp    = zeros(1,nfexp); % Evolución altura sup. libre (cm)
sbed_exp          = zeros(1,nfexp); % Evol. superficie frontal lecho
holdup            = zeros(1,nfexp); % Evol. Fracción de gas en burbujas

%=========================================================================%
%               INICIO DEL BUCLE DE CÁLCULO EXPERIMENTAL                  %
%=========================================================================%

for i_exp         = 1:nfexp

%=========================================================================%
%                    ALGORITMO DE TRATAMIENTO DE IMAGEN                   %
%=========================================================================%

% 1) TRANSFORMACIÓN DE LAS IMÁGENES ORIGINALES:
- Lectura de imágenes "i" (I) e "i+1" (I2) a efectos de medir la u_b
entre fotogramas consecutivos
- Recorte de imagen hasta los límites del reactor
- Conversión de intensidades de color a escala de grises
- Rotación, ya que la imagen original muestra el lecho en posición
horizontal para ganar resolución
- Eliminación de las intensidades de pixel externas al lecho:
I     =
rgb2gray(imcrop(imread(strcat(videoexp,'(',num2str(i_exp),').jpg')),co
ordexp));

I2    =
rgb2gray(imcrop(imread(strcat(videoexp,'(',num2str(i_exp+1),').jpg')),
coordexp));

bwaux       = uint8(roipoly(I,polig1_x,polig1_y));
bwaux2      = uint8(roipoly(I,polig2_x,polig2_y));
bwaux_      = uint8(roipoly(I2,polig1_x,polig1_y));
bwaux2_     = uint8(roipoly(I2,polig2_x,polig2_y));
I           = I.*(1-bwaux)
I           = I.*(1-bwaux2);
I2          = I2.*(1-bwaux_);
I2          = I2.*(1-bwaux2_);
I           = imrotate(I,270);
I2          = imrotate(I2,270);

% 2) DETECCIÓN DE "OBJETOS" -> BURBUJAS EN CADA IMAGEN:
- Definición del límite inferior de tamaño de burbuja experimental
- Detección de gradientes de intensidad verticales y horizontales
- Aplicación de filtro para la homogeneización local de intensidades y
mejora del contraste entre regiones con altos y bajos gradientes
- Transformación de imagen a binaria en base a una intensidad umbral
- Rellenado de las regiones con altos gradientes
```

```
- Filtrado de objetos que forman líneas rectas (contornos del reactor)
- Detección de contornos de burbuja. Identificación de burbujas

burbmin     = 8;
threxp      = 0.5;

[FX,FY]     = gradient(double(I));
I           = ordfilt2((uint8(FX+FY).*I),30,true(6));
Ibw         = im2bw(I,threxp);
Ibwf        = imfill(Ibw,'holes');
Ib_sp       = bwareaopen(Ibwf,burbmin);
squaremoval = strel('disk',3);
Imaux       = imopen(Ib_sp,squaremoval);
Iedge       = edge(Imaux,'canny');

% Mismas operaciones para la imagen I2:
[FX2,FY2]   = gradient(double(I2));
I2          = ordfilt2((uint8(FX2+FY2).*I2),30,true(6));
Ibw2        = im2bw(I2,threxp);
Ibwf2       = imfill(Ibw2,'holes');
Ib_sp2      = bwareaopen(Ibwf2,burbmin);
Imaux2      = imopen(Ib_sp2,squaremoval);
Iedge2      = edge(Imaux2,'canny');

% 3) DETERMINACIÓN DE LAS PROPIEDADES DE BURBUJA EN CADA IMAGEN:
- Búsqueda de objetos -> "connected components" en la imagen binaria
- Detección del objeto superior -> "freeboard"
- Determinación de la altura promedio del lecho en la imagen
- Eliminación del objeto-freeboard del cómputo de burbujas
- Conteo de burbujas reales y almacenamiento de sus propiedades
- Determinación de la superficie frontal ocupada por el lecho
(sbed_exp), diámetro de burbuja (d_b), fracción de gas en burbujas
(holdup), posición horizontal (x) y vertical (z) del centroide de
burbuja y relación de aspecto (aspectratio)
cc          = bwconncomp(Imaux,4);
burbdata    = regionprops(cc,'Extrema');
freeb       = burbdata(1).Extrema;
zfreeboard_exp(i_exp)         = hr_exp-mean(freeb(4:7,2))/pix2cm_exp;
Imaux(cc.PixelIdxList{1})     = 0;
cc2         = bwconncomp(Imaux2,4);
Imaux2(cc2.PixelIdxList{1})   = 0;

cc          = bwconncomp(Imaux,4);
burbdata    = regionprops(cc,'all');
nburb       = cc.NumObjects;
N           = [];
cc2         = bwconncomp(Imaux2,4);
burbdata2   = regionprops(cc2,'all');
nburb2      = cc2.NumObjects;
N2          = [];

if nburb>0
      for nb = 1:nburb
            N_1   = [burbdata(nb).Centroid burbdata(nb).Area
            burbdata(nb).BoundingBox(4)./burbdata(nb).BoundingBox(3)];
            N     = cat(1,N,N_1);
      end % del for

sbed_exp(i_exp)   =
hreg_exp*wreg_exp+((wreg_exp+wreac_exp)/2*tan(alfa_exp*pi()/180)*(wrea
```

```
c_exp-wreg_exp)/2)+(zfreeboard_exp(i_exp)-hreg_exp-
tan(alfa_exp*pi()/180)*(wreac_exp-wreg_exp)/2)*wreg_exp;

db                = (sqrt(((N(:,3))/(pix2cm_exp^2))/pi()))*2;
holdup(i_exp)     = sum((db./2).^2*pi())/(sbed_exp(i_exp))*100;
z                 = hr_exp-(N(:,2))/pix2cm_exp;
x                 = (N(:,1)-1)/pix2cm_exp-wr_exp/2;
aspectratio       = N(:,4);
zt                = [z ones(size(z)).*i_exp/fpsexp];

end % del if

if nburb2>0
      for nb2=1:nburb2
            N2_1  = [burbdata2(nb2).Centroid burbdata2(nb2).Area
      burbdata2(nb2).BoundingBox(4)./burbdata2(nb2).BoundingBox(3)];
            N2    = cat(1,N2,N2_1);
      end

db2               = (sqrt(((N2(:,3))/(pix2cm_exp^2))/pi()))*2;
z2                = hr_exp-(N2(:,2))/pix2cm_exp;.
x2                = (N2(:,1))/pix2cm_exp-wr_exp/2;
aspectratio2      = N2(:,4);

end

% Vectores auxiliares de almacenamiento de datos de burbuja
dbaux             = cat(1,dbaux,db);
zaux              = cat(1,zaux,z);
xaux              = cat(1,xaux,x);
aspectratioaux    = cat(1,aspectratioaux,aspectratio);
ztaux             = cat(1,ztaux,zt);

%=========================================================================%
%      COMPARATIVA ENTRE AMBOS FOTOGRAMAS. DETERMINACIÓN DE u_b          %
%=========================================================================%

% IDENTIFICACIÓN DE BURBUJAS UNÍVOCAS ENTRE FOTOGRAMAS MEDIANTE EL
ALGORITMO DEL VECINO MÁS PRÓXIMO ("k-nearest-neighbour"):
- El algoritmo busca las mínimas "distancias" (relativas a tamaño de
burbuja, posición del centroide y relación de aspecto) entre
poblaciones de burbujas de dos imágenes consecutivas
- Se eliminan múltiples correspondencias (derivadas de fenómenos de
coalescencia y ruptura de burbujas) para simplificar el análisis
- Se correlacionan las posiciones verticales del centroide y se
determina u_b como el cociente entre la distancia vertical recorrida y
el tiempo transcurrido entre fotogramas
- Se descartan velocidades de burbuja negativas o superiores a 1m/s
- Se reordenan las propiedades de burbuja recogidas y se almacenan en
la matriz "M" [db,z,x,aspect-ratio]

Naux1             = [db,z,x,aspectratio];
Naux2             = [db2,z2,x2,aspectratio2];

    if nburb>0 && nburb2>0
      Idx         = knnsearch(Naux1,Naux2,'Distance','seuclidean');
      [fila,pos]  = unique(Idx);
      rep         = histc(Idx,fila);
      repet       = Idx(rep>1);
      veces       = numel(repet);
```

```
      mat         = [fila,pos];

      for vez=1:veces
        mat(mat(:,1)==repet(vez,:),:)     = [];
      end

      fila        = mat(:,2);
      pos         = mat(:,1);
      ub_exp      = (Naux2(fila,2)-Naux1(pos,2)).*fpsexp;
      z_exp       = (Naux2(fila,2)+Naux1(pos,2))./2;
      db_exp      = (Naux2(fila,1)+Naux1(pos,1))./2;
      raizdb_exp  = sqrt(db_exp);
      ubdb1       = [ub_exp raizdb_exp];
      fi_exp      = (ub_exp-(((urd_exp+uru_exp)/2-1)*umf_fosfo))./
      raizdb_exp/g^0.5;
      ubdb1fi     = cat(2,ubdb1,fi_exp);
      ubdb1fi(ubdb1fi(:,3)>2,:)     = [];
      ubdb1fi(ubdb1fi(:,3)<-0.5,:)  = [];
      ubdb1                         = ubdb1fi(:,1:2);
      ubz1                          = [ub_exp z_exp];
      dbz1                          = [db_exp z_exp];
      dbz                           = cat(1,dbz,dbz1);
      ubdb1(find(ubdb1(:,1)<1),:)   = [];
      ubdb1(find(ubdb1(:,1)>100),:) = [];
      ubdb                          = cat(1,ubdb,ubdb1);
      ubz1(find(ubz1(:,1)<1),:)     = [];
      ubz1(find(ubz1(:,1)>100),:)   = [];
      ubz                           = cat(1,ubz,ubz1);
    end

dbaux             = cat(1,dbaux,db);
zaux              = cat(1,zaux,z);
xaux              = cat(1,xaux,x);
aspectratioaux    = cat(1,aspectratioaux,aspectratio);
ztaux             = cat(1,ztaux,zt);
end

M                 = [dbaux,zaux,xaux,aspectratioaux];

%=====================================================================%
%  FIN DEL BUCLE DE CÁLCULO. SE DISPONE DE LOS SIGUIENTES VALORES:    %
%  ub (VEL. BURBUJA EXP.) CON SUS CORRESPONDIENTES ub(z) Y ub(db^0.5)  %
%      db (DIÁM. BURBUJA EXP. PARA TODAS LAS BURBUJAS DEL VÍDEO)      %
%     CON SUCORRESPONDIENTE db(z, x, aspectratio), ADEMÁS DE z(t)     %
%=====================================================================%

%=====================================================================%
%        REORGANIZACIÓN DE DATOS DE PROPIEDADES DE BURBUJA:           %
%=====================================================================%
%=====================================================================%
%        Probability distribution (PD) para la "aspect ratio"         %
%=====================================================================%

PDardef     = zeros(1,numel(0.05:0.05:10));
for arpd    = 0.05:0.05:10
    PDar    = aspectratioaux;
    PDar(find(PDar<(arpd-0.05)))    = [];
    PDar(find(PDar>(arpd)))         = [];
    PDardef(int32(arpd/0.05))  = numel(PDar)/numel(aspectratioaux)*100;
end
```

```
%=========================================================================%
%    Obtención del db promedio para cada incremento de z en db(z)     %
%=========================================================================%

Mdb         = zeros(1,numel(ceil(mean(zfreeboard_exp))));
for I       = 1:ceil(zfreeboard_exp)
    Naux    = M;
    Naux(find(Naux(:,2)<(i-1)),:)   = [];
    Naux(find(Naux(:,2)>(i)),:)     = [];
    Mdb(i)  = sum(Naux(:,1).^2)/sum(Naux(:,1));
end

%=========================================================================%
%  Obtención del ub prom. para cada incremento de db en ub(db^0.5)    %
%=========================================================================%

Mub         = [];
for j       = 0:0.04:8
    Naux2   = ubdb;
    Naux2(find(Naux2(:,2)<(j-0.04)),:)    = [];
    Naux2(find(Naux2(:,2)>(j)),:)         = [];
    Mub     = cat(1,Mub,mean(Naux2(:,1)));
end

%=========================================================================%
%     Obtención del ub prom. para cada incremento de z en ub(z)       %
%=========================================================================%

Mubz        = [];
for k       = 1:ceil(mean(zfreeboard_exp))
    Naux3   = ubz;
    Naux3(find(Naux3(:,2)<(k-1)),:) = [];
    Naux3(find(Naux3(:,2)>(k)),:)   = [];
    Mubz    = cat(1,Mubz,mean(Naux3(:,1)));
end

%=========================================================================%
%     Probability density para db respecto a la posición vertical     %
%=========================================================================%

M25                                 = [dbaux zaux];
M25(M25(:,2)>0.25*(max(zaux)),:)    = [];
M50                                 = [dbaux zaux];
M50(M50(:,2)>0.5*(max(zaux)),:)     = [];
M50(M50(:,2)<0.25*(max(zaux)),:)    = [];
M75                                 = [dbaux zaux];
M75(M75(:,2)>0.75*(max(zaux)),:)    = [];
M75(M75(:,2)<0.5*(max(zaux)),:)     = [];
PDdb25                              = zeros(1,numel(0.08:0.08:8));
PDdb50                              = zeros(1,numel(0.08:0.08:8));
PDdb75                              = zeros(1,numel(0.08:0.08:8));
PDdb                                = zeros(1,numel(0.08:0.08:8));
for dbdiam  = 0.04:0.08:8
      PD25                                      = M25;
      PD25(find(PD25(:,1)<(dbdiam-0.08)),:)     = [];
      PD25(find(PD25(:,1)>(dbdiam)),:)          = [];
      PDdb25(round(dbdiam/0.08))=numel(PD25(:,1))/numel(M25(:,1))*100;
      PD50                                      = M50;
      PD50(find(PD50(:,1)<(dbdiam-0.08)),:)     = [];
```

```
        PD50(find(PD50(:,1)>(dbdiam)),:)          = [];
        PDdb50(round(dbdiam/0.08))=numel(PD50(:,1))/numel(M50(:,1))*100;
        PD75                                      = M75;
        PD75(find(PD75(:,1)<(dbdiam-0.08)),:)     = [];
        PD75(find(PD75(:,1)>(dbdiam)),:)          = [];
        PDdb75(round(dbdiam/0.08))=numel(PD75(:,1))/numel(M75(:,1))*100;
        PD                                        = [dbaux zaux];
        PD(find(PD(:,1)<(dbdiam-0.08)),:)         = [];
        PD(find(PD(:,1)>(dbdiam)),:)              = [];
        PDdb(round(dbdiam/0.08))= numel(PD(:,1))/numel(dbaux)*100;
end

%=========================================================================%
% Densidad de burbujas (n°burbujas/cm2s) en función de z en el lecho %
%=========================================================================%

Densb       = zeros(1,numel(ceil((mean(zfreeboard_exp)))));

for k       = 1:ceil(mean(zfreeboard_exp))
    s       = [dbaux zaux];
    s(find(s(:,2)<(k-1)),:)   = [];
    s(find(s(:,2)>(k)),:)     = [];
    densb(k)= numel(s(:,1))/(nfexp/fpsexp*mean(sbed_exp));
end

%=========================================================================%
%       FIN DE: REORGANIZACIÓN DE DATOS DE PROPIEDADES DE BURBUJA    %
%             COMIENZA LA GENERACIÓN DE FIGURAS DE RESULTADOS        %
%=========================================================================%

%=========================================================================%
%        FIGURA 1: Nube de puntos db(z) con db promediado en z       %
%=========================================================================%

figure(1),
hold on
xlabel('Reactor vertical position, z(cm)');
ylabel('Equivalent bubble Diameter, d_b(cm)');
axis([0 40 0 8]);
nombref1    = 'u_{r,up}:'; nombref2='u_{r,down}:';
nombref3    = 'sc_{angle}:';
d           = {nombref1 ' ' uru_exp '(-)   ' nombref2 ' ' urd_exp '(-)
' nombref3 ' ' alfa_exp '(°)'};
title(d);
legend(char(name),'Location','NorthEast');
plot(zaux,dbaux,'k.');
plot(1:ceil((zfreeboard_exp)),Mdb,'ko');

%==============MODELO MATEMÁTICO PROPUESTO PARA db(z)================%

db_mm       = zeros(1,numel(1:ceil(mean(zfreeboard_exp))));
zdown       = 1:hreg_exp-1;
db_mm(1:numel(zdown))   = 0.65*(pi()/4*wreg_exp^2*umf_fosfo*(urd_exp-
1))^0.4*(1-exp(-0.3*zdown/wreg_exp));
dbm_orif    = 0.65*(pi()/4*wreac_exp^2*umf_fosfo*(uru_exp-1))^0.4;
dborif0     = 0.32;
betafosfo   = 0.02*((urd_exp-1)*umf_fosfo)^2-1.26*(urd_exp-1)*umf_fosfo
+75.02;
beta        = betafosfo;
```

```
if alfa_exp       <= beta
    ztrans        =
hreg_exp:ceil(hreg_exp+tan(beta*pi()/180)*(wreac_exp-wreg_exp)/2);
    dborif_mm     =
zeros(1,numel(hreg_exp:ceil((mean(zfreeboard_exp)))));
    dborif_mm(1:numel(ztrans))      =
dbm_orif-(dbm_orif-dborif0)*exp(-0.3*(ztrans-hreg_exp)/wreac_exp);
    raiz          = 1-(ztrans-hreg_exp+1)/(urd_exp-1)/tan(alfa_exp);
    raiz(raiz<0)  = 0;
    db1e_mm       = db_mm(numel(zdown))*sqrt(raiz);
else
    ztrans        =
hreg_exp:ceil(hreg_exp+tan(alfa_exp*pi()/180)*(wreac_exp-wreg_exp)/2);
    dborif_mm     =
zeros(1,numel(hreg_exp:ceil((mean(zfreeboard_exp)))));
    dborif_mm(1:numel(ztrans))      =
dbm_orif-(dbm_orif-dborif0)*exp(-0.3*(ztrans-hreg_exp)/wreac_exp);
    raiz          = 1-(ztrans-hreg_exp+1)/(urd_exp-1)/tan(beta);
    raiz(raiz<0)  = 0;
    db1e_mm       = db_mm(numel(zdown))*sqrt(raiz);
end
db_mm(hreg_exp:hreg_exp+(numel(ztrans)-1))      =
(dborif_mm(1:numel(ztrans)).^2+db1e_mm.^2)./(dborif_mm(1:numel(ztrans)
)+db1e_mm);
zreg        = hreg_exp+numel(ztrans):ceil((mean(zfreeboard_exp)));
dbm_orif1   = 0.65*(pi()/4*wreac_exp^2*umf_fosfo*(urd_exp-1))^0.4;
d1_mm       = dbm_orif1-(dbm_orif1-max(db1e_mm))*exp(-0.3*(zreg-
hreg_exp-numel(ztrans))/wreac_exp);
dborif_mm(numel(ztrans)+1:numel(dborif_mm))     =
dbm_orif-(dbm_orif-dborif0)*exp(-0.3*(zreg-hreg_exp)/wreac_exp);
db_mm(numel(ztrans)+hreg_exp:ceil((mean(zfreeboard_exp)))) =
(dborif_mm(numel(ztrans)+1:numel(dborif_mm)).^2+d1_mm.^2)./(dborif_mm(
numel(ztrans)+1:numel(dborif_mm))+d1_mm);

%==========FIN DE MODELO MATEMÁTICO PROPUESTO PARA db(z)=============%

plot(1:ceil(mean(zfreeboard_exp)),db_mm,'g-');
hold off

%=====================================================================%
%      FIGURA 2: Coordenadas de centroide z(x) para sim y exp         %
%=====================================================================%

figure(2),
hold on
xlabel('Horizontal bubble centroiod position, x(cm)');
ylabel('Vertical bubble centroid position, z(cm)');
plot(xaux,zaux,'k.');
axis([-4 4 0 40]);
hold off

%=====================================================================%
%     FIGURA 3: Densidad de probabilidad (%) para db, sim y exp       %
%=====================================================================%

figure(3)
dbdiam=0.08:0.08:8;
hold on
xlabel('Equivalent bubble diameter, d_b(cm)');
ylabel('Probability density (%)');
```

```
plot(dbdiam,PDdb,'k.');
axis([0 8 0 10]);
hold off

%=========================================================================%
%   FIGURA 4: Densidad de probabilidad (%) para db(z), sim y exp          %
%=========================================================================%

figure(4)
hold on
xlabel('Equivalent bubble diameter, d_b(cm)');
ylabel('Probability density (%)');
plot(dbdiam,PDdb25,'k.');
plot(dbdiam,PDdb50,'k*');
plot(dbdiam,PDdb75,'k^');
axis([0 8 0 10]);
hold off

%=========================================================================%
%  FIGURA 5: Densidad de burbujas (n°/cm2s) para db(z), sim y exp         %
%=========================================================================%

figure(5)
hold on
xlabel('Reactor vertical position (cm)');
ylabel('Bubble density (n°/cm2s)');
plot(1:ceil((mean(zfreeboard_exp))),densb,'k.');
axis([0 40 0 1]);
hold off

%=========================================================================%
% FIGURA 6: Altura del lecho en función del tiempo de fluidización       %
%=========================================================================%

figure(6)
hold on
xlabel('Fluidization time (s)');
ylabel('Freeboard location (cm)');
plot((1:nfexp)/fpsexp,zfreeboard_exp(1:nfexp),'k-');
plot((1:nfexp)/fpsexp,ones(size(1:nfexp))*mean(zfreeboard_exp),'k.');
axis([0 40 0 40]);
hold off

%=========================================================================%
%  FIGURA 7: %gas en burbujas en función del tiempo de fluidización       %
%=========================================================================%

figure(7)
hold on
xlabel('Fluidization time (s)');
ylabel('Bubbles hold up (%)');
plot((1:1:nfexp)/fpsexp,holdup,'k.');
plot((1:1:nfexp)/fpsexp,ones(size(1:nfexp))*mean(holdup),'k-');
axis([0 40 0 60]);
hold off
```

```
%=========================================================================%
% FIGURA 8: Densidad de probabilidad (%) de la forma de las burbujas %
%=========================================================================%

figure(8)
hold on
xlabel('Bubble aspect ratio (-)');
ylabel('Probability density (%)');
plot(0.05:0.05:10,PDardef,'k.');
axis([0 10 0 20]);
hold off

%=========================================================================%
%FIGURA 9:Posición axial del centroide vs tiempo de fluidización,z(t)%
%=========================================================================%

figure(9)
hold on
xlabel('Fluidization time (s)');
ylabel('Distance from 1st distributor (cm)');
plot(ztaux(:,2),ztaux(:,1),'k.');
axis([0 40 0 40]);
hold off

%=========================================================================%
%FIGURA 10: Velocidad de burbuja, ub(db^0.5), para sim, exp y modelo %
%=========================================================================%

figure(10),
hold on
diamb2      = 0:0.04:8;
ubDH        = umf_fosfo*((uru_exp+urd_exp)/2-1)+0.4.*(g.*diamb2).^0.5;
plot(ubdb(:,2),ubdb(:,1),'k.');
axis([0 3 0 80]);
xlabel('Square root of Bubble diameter, d_b^{0.5}(cm)');
ylabel('Bubble velocity, u_b(cm/s)');
nombref1    = 'u_{r,up}:'; nombref2='u_{r,down}:';
nombref3    = 'sc_{angle}:';
d           = {nombref1 ' ' uru_exp '(-)  ' nombref2 ' ' urd_exp '(-)
' nombref3 ' ' alfa_exp '(°)'};
title(d);
plot(0:0.04:8,Mub','ko');
plot(diamb2,ubDH,'k--');
hold off

%=========================================================================%
%FIGURA 11: ub(z), para sim, exp y modelo matemático db(z) propuesto %
%=========================================================================%

figure(11),
hold on
plot(ubz(:,2),ubz(:,1),'k.');
axis([0 40 0 80]);
xlabel('Reactor vertical position (cm)');
ylabel('Bubble velocity (cm/s)');
nombref1    = 'u_{r,up}:';
nombref2    = 'u_{r,down}:';
nombref3    = 'sc_{angle}:';
d           = {nombref1 ' ' uru_exp '(-)  ' nombref2 ' ' urd_exp '(-)
' nombref3 ' ' alfa_exp '(°)'};
```

```
title(d);
plot(1:ceil((mean(zfreeboard_exp))),Mubz,'ko');
ub_mm=umf_fosfo*((uru_exp+urd_exp)/2-1)+0.4.*(db_mm*981).^0.5;
plot(1:ceil((mean(zfreeboard_exp))),ub_mm,'g-');
hold off

%=========================================================================%
%                    FIGURA 12: Expansión del lecho                       %
%=========================================================================%

vol_fluidizado    = zeros(1,nfexp);
for j1 = 1:nfexp
      if (zfreeboard_exp(j1)-hbd_exp)>hrt_exp
      vol_fluidizado(j1)      =
      prof_lechoexp*(wbd_exp*hbd_exp+hrt_exp*(wbd_exp+wbu_exp)/2+wbu_e
      xp*(zfreeboard_exp(j1)-hbd_exp-hrt_exp));
      else
      vol_fluidizado(j1)      =
      prof_lechoexp*(wbd_exp*hbd_exp+(zfreeboard_exp(j1)-hbd_exp)
      *(wbd_exp+(zfreeboard_exp(j1)-hbd_exp)/tan(alfa_exp*pi/180)));
      end
end

figure(12)
hold on
xlabel('Fluidization time (s)');
ylabel('Bed expansion (cm)');
plot((1:nfexp)/fpsexp,vol_fluidizado(1:nfexp)./vol_lechofijo,'k-');
axis([0 40 0 3]);
hold off

%=========================================================================%
%  Generación del fichero con todas las variables recogidas en excel %
%=========================================================================%

nf=30000; %número de filas de datos

dbaux       = cat(1,dbaux,zeros(nf-numel(dbaux),1));
zaux        = cat(1,zaux,zeros(nf-numel(zaux),1));
Mdb         = cat(1,Mdb',zeros(nf-numel(Mdb),1));
db_mm       = cat(1,db_mm',zeros(nf-numel(db_mm),1));
rango       = 1:ceil((mean(zfreeboard_exp)));
rango       = cat(1,rango',zeros(nf-numel(rango),1));
rango2      = 0:0.04:8;
rango2      = cat(1,rango2',zeros(nf-numel(rango2),1));
zaux        = cat(1,zaux,zeros(nf-numel(zaux),1));
xaux        = cat(1,xaux,zeros(nf-numel(xaux),1));
PDdb        = cat(1,PDdb',zeros(nf-numel(PDdb),1));
dbdiam      = cat(1,dbdiam',zeros(nf-numel(dbdiam),1));
PDdb25      = cat(1,PDdb25',zeros(nf-numel(PDdb25),1));
PDdb50      = cat(1,PDdb50',zeros(nf-numel(PDdb50),1));
PDdb75      = cat(1,PDdb75',zeros(nf-numel(PDdb75),1));
densb       = cat(1,densb',zeros(nf-numel(densb),1));
zfreeboard_exp    = cat(1,zfreeboard_exp(1:nfexp)',zeros(nf-
numel(zfreeboard_exp(1:nfexp)),1));
rango3      = (1:nfexp)/fpsexp;
rango3      = cat(1,rango3',zeros(nf-numel(rango3),1));
holdup      = cat(1,holdup',zeros(nf-numel(holdup),1));
rango5      = ones(size(1:nfexp))*mean(holdup);
rango5      = cat(1,rango5',zeros(nf-numel(rango5),1));
```

```
PDardef     = cat(1,PDardef',zeros(nf-numel(PDardef),1));
rango7      = 0.05:0.05:10;
rango7      = cat(1,rango7',zeros(nf-numel(rango7),1));
ztaux       = cat(1,ztaux(:,1:2),zeros(nf-numel(ztaux(:,1)),2));
nombrehoja  = strcat('ang',num2str(alfa_exp),' urd',num2str(urd_exp),'
uru',num2str(uru_exp));

matrizdatos = [dbaux zaux Mdb db_mm rango2 zaux xaux PDdb dbdiam PDdb25
PDdb50 PDdb75 densb rango zfreeboard_exp rango3 holdup rango3 rango5
rango3 PDardef rango7 ztaux(:,1) ztaux(:,2)];

xlswrite(strcat('D:\SoftI3A\TESIS\TESIS_Nacho\Gráficas_Análisis_hidro
dinámico\',nombrehoja,'.xlsx'),matrizdatos,nombrehoja,'A4:X30005');

end % Fin de la función
```

Anexo A.3: Tratamiento de imágenes (DIA) para la determinación de las propiedades fluidodinámicas del lecho a partir mapas PIV

```
function
PIVDIA_background_imp3_faster(nombrearchivoIm,nombrearchivoPIV)

% Obtención de mapas 2D promedio de flujo másico axial a partir de
datos provenientes del análisis PIV (llevado a cabo en DaVis) y este
DIA de Matlab para calcular la porosidad local en cada región del
lecho y fotograma. Datos de entrada: nombre de la carpeta contenedora
de los fotogramas de fluidización (nombrearchivoIm) y los mapas PIV
(nombrearchivoPIV)

close all; % Cierre de figures abiertas
warning('off', 'Images:initSize:adjustingMag'); % Desact. advertencias

%=========================================================================
%     Generación de rutas a los ficheros de entrada y salida          %
%=========================================================================%

path_inVF    = strcat('F:\VideosFiltrados2\',nombrearchivoIm,'\out_(');
path_inBG    =
strcat('F:\VideosFiltrados2\',nombrearchivoIm,'\background_lim06_prc95
_contour0.tif');
path_inPIV   = strcat('F:\VideosFiltrados2\',nombrearchivoPIV,'\PIV(');
path_outVF   = strcat('F:\VideosFiltrados2\',nombrearchivoIm,'\');
name_inVF    = strcat(path_inVF,'00',int2str(1),').tif');

%=========================================================================%
%Definición de las variables de entrada (¡modificarlas si necesario!)%
%=========================================================================%

Mp_real      = 0.0451;   % Masa real del lecho [kg]
rho          = 2650;     % Densidad de particula [kg/m^3]
rho_fixbed   = 1590;     % Densidad del lecho [kg/m3]
width        = 0.04;     % Anchura del lecho [m]
zcs          = 0.12;     % Altura del cambio de sección[m]
ang          = 80;       % Ángulo de cambio de sección[°]
eps_max_mf   = 0.54;     % Máxima fracción de sólidos en régimen fluidi.
hmin         = 24;       % Posición de la base del reactor [pixels]
s_max        = 200;      % Número de imágenes a procesar
% Coordenadas de los vértices del reactor (cambio de sección):
xc1          = 35;
xc2          = 299;
yc           = 273;
% Eliminación de la intensidad externa al lecho ("polígonos negros")
X            = [1 xc1 xc1 1];
x_1          = [size(X,2) xc2 xc2 size(X,2)];
y            = [1 yc size(X,1)-1 size(X,1)-1];
y_1          = [1 yc size(X,1)-1 size(X,1)-1];
bwaux        = roipoly(zeros(size(X)),x,y);
bwaux_1      = roipoly(bwaux,x_1,y_1);
bwaux        = bwaux+bwaux_1;
bwaux        = double(bwaux);

Vfixbed      = Mp_real/rho_fixbed; % Volumen de lecho fijo[m^3]
eps_fixbed   = rho_fixbed/rho; %Fracción volumétrica de sólidos [-]
material     = ('Phosphorescent particles');
Im_size      = imread(name_inVF,'tif'); % Lectura de la 1a imagen
```

```
[Zpx,Xpx]   = size(Im_size); % Tamaño de la 1a imagen
height      = (Zpx-hmin)/((293-37)/(width)); % Altura del reactor[pix]
eps3Dmax    = eps_max_mf; % Máxima fracción volumétrica de sólidos 3D

%=========================================================================%
%     Variables de ajuste para el análisis relacionadas con PIV           %
%=========================================================================%

overlap     = 0.5;   % Solapamiento de "interrogation areas" [%]
xinta       = 8;     % "Interrogation area" en dirección x [pixels]
yinta       = 8;     % "Interrogation area" en dirección y [pixels]
XMAXpx      = Xpx;
ZMAXpx      = Zpx;
XMAXinta    = (XMAXpx-(xinta*overlap*0.5)+1); % Posición x de la
última "interrogation area"
ZMAXinta    = (ZMAXpx-(yinta*overlap*0.5)+1);
NX          = ceil(XMAXpx/(xinta*overlap)); % Número de "inter. areas"
NZ          = ceil(ZMAXpx/(yinta*overlap));

%=========================================================================%
%   Inicialización de variables para mejorar velocidad de cálculo        %
%=========================================================================%

volfract2D_exp          = zeros(NZ,NX);
volfract2D_exp_tot      = zeros(NZ,NX,s_max);
volfract3D_exp          = zeros(NZ,NX,s_max);
zvel_norm_tot           = zeros(NZ,NX,s_max);
zflux_tot               = zeros(NZ,NX,s_max);
X_data                  = zeros(NX,1);
Z_data                  = zeros(NZ,1);


%=========================================================================%
%  Lee imagen "background" para corregir la iluminación del lecho         %
%=========================================================================%

Xbg=imread(path_inBG,'tif');

%=========================================================================%
%             ALGORITMO DE TRATAMIENTO DE IMAGEN (PIV/DIA)                %
%=========================================================================%


%=================Inicio del bucle de cálculo=============================%

for s=1:s_max
        name_inPIV= strcat(path_inPIV,int2str(s),').dat');
      if s<6
        name_inVF = strcat(path_inVF,'00',int2str(2*s-1),').tif');
      elseif (s>5) && (s<51)
        name_inVF = strcat(path_inVF,'0',int2str(2*s-1),').tif');
      else
        name_inVF = strcat(path_inVF,int2str(2*s-1),').tif');
      end

X     = imread(name_inVF,'tif'); % Lee la imagen .tif del lecho
X     = double(X).*(1-bwaux);    % Elimina la luminosidad externa
X     = double(X)./double(Xbg);  % Corrige intensidad con "background"
X(X>3)      = 0; % Si la intensidad local es 3*background, hacerla 0
X(X<0)      = 0; % Si la intensidad local es negativa, hacerla 0
X           = X./max(max(X)); % Normaliza intensidades respecto máxima
```

```
[A,B]       = size(X);
i           = 1:1:A;
k           = 1:1:B;
X2_norm     = double(X(A+1-i,k));   % Reorganiza matriz de abajo-arriba

%=========================================================================%
% Lectura de los mapas PIV generados por DaVis (1 mapa -> 2 imágenes)%
%=========================================================================%

p           = importdata(name_inPIV);
vfield      = p.data;               % Campo de velocidades
sizeY       = sum(vfield(:,1)==max(vfield(:,1)));
sizeX       = sum(vfield(:,2)==max(vfield(:,2)));
velY        = reshape(vfield(:,4),sizeX,sizeY);
zvel_norm   = rot90(velY);          % Reorganiza matriz de velocidades
zvel_norm_tot(:,:,s)                = zvel_norm;
zvel_norm_tot(isnan(zvel_norm_tot)) = 0;

%=========================================================================%
% Algoritmo de análisis de "interrogation areas" para poder comparar %
%                   mapas de porosidad con mapas PIV                    &
%=========================================================================%

Zstart = (0.5*yinta*overlap)+1;
Xstart = (0.5*xinta*overlap)+1;

for cc=Zstart:yinta*overlap:ZMAXinta
    for bb=Xstart:xinta*overlap:XMAXinta
        if bb == Xstart && cc == Zstart
        a1 = X2_norm(1:cc+yinta*overlap-3,1:bb+xinta*overlap-2);
        elseif bb == XMAXinta && cc == ZMAXinta
        a1 = X2_norm(cc-yinta*overlap:ZMAXpx,bb-xinta*overlap:XMAXpx);
        elseif bb == XMAXinta && cc == Zstart
        a1 = X2_norm(1:cc+yinta*overlap-3,bb-xinta*overlap:XMAXpx);
        elseif bb == Xstart && cc == ZMAXinta
        a1 = X2_norm(cc-yinta*overlap:ZMAXpx,1:bb+xinta*overlap-2);
        elseif cc == Zstart
         a1 = X2_norm(1:cc+yinta*overlap-3,bb-xinta*overlap:bb+xinta*
overlap-2);
        elseif bb == Xstart
        a1 = X2_norm(cc-yinta*overlap:cc+yinta*overlap-3,1:bb+xinta*
overlap-2);
        elseif cc == ZMAXinta
        a1 = X2_norm(cc-yinta*overlap:ZMAXpx,bb-xinta*overlap:bb+xinta
*overlap-2);
        elseif bb == XMAXinta
        a1 = X2_norm(cc-yinta*overlap:cc+yinta*overlap-3,bb-xinta*
overlap:XMAXpx);
        else
        a1 = X2_norm(cc-yinta*overlap:cc+yinta*overlap-3,bb-xinta*
overlap:bb+xinta*overlap-2);
        end

        if ((bb == Xstart && cc == Zstart) || (bb == XMAXinta && cc ==
ZMAXinta) || (bb == XMAXinta && cc == Zstart) || (bb == Xstart && cc
== ZMAXinta))
        a2 = (sum(sum(a1)))/(xinta*((1.5*overlap).^2)*yinta);
```

```
        elseif ((cc == Zstart) || (bb == Xstart) || (cc == ZMAXinta)
|| (bb == XMAXinta))
        a2 = (sum(sum(a1)))/(xinta*1.5*overlap*yinta-1);
        else
        a2 = (sum(sum(a1)))/(xinta*yinta-1);
        end

      z_pos = ((cc-1)+0.5*yinta*overlap)/(yinta*overlap);
      x_pos = ((bb-1)+xinta*0.5*overlap)/(xinta*overlap);

      % "volfract2D_exp" almacena el mapa de intensidades en cada
      "interrogation area" del lecho:
      volfract2D_exp(z_pos,x_pos) = a2;

            if s == s_max
            X_data(x_pos) = bb-1;
            Z_data(z_pos) = cc-1;
            end
     end % del for bb
end % del for cc

% Se analiza el histograma de intensidades de lecho resultante. Casos:

a) Se detecta un único pico en la zona de alta luminosidad: los
píxeles sobre-iluminados (intensidad > I_umbral) se corrigen a la
intensidad umbral (sobreiluminación->I_umbral).

b) Se detecta un pico en la zona de baja luminosidad: se corresponde
con la intensidad del "freeboard" libre de sólido (I_min). Se corrigen
las intensidades haciendo 0 la del freeboard (I_min->0).

c) Se detectan al menos 2 picos: el superior se corresponde con
I_umbral y el inferior con I_min. Se corrige el mapa de intensidades
de modo que I_min->0 y sobreiluminación->I_umbral.

[peaks]=findlocalminima_IJB(volfract2D_exp(volfract2D_exp>0)./max(max(
volfract2D_exp)));

if (numel(peaks)<2 && peaks(1)>100)
volfract2D_exp(volfract2D_exp>peaks(numel(peaks))/255*max(max(volfract
2D_exp))) = peaks(numel(peaks))/255*max(max(volfract2D_exp));
elseif (numel(peaks)<2 && peaks(1)<100)
volfract2D_exp = volfract2D_exp-peaks(1)/255*max(max(volfract2D_exp));
else
volfract2D_exp = volfract2D_exp-peaks(1)/255*max(max(volfract2D_exp));
volfract2D_exp(volfract2D_exp>peaks(numel(peaks))/255*max(max(volfract
2D_exp))) = peaks(numel(peaks))/255*max(max(volfract2D_exp));
end

% Se normalizan las intensidades respecto a la máxima y se almacenan
en la  matriz 3D "volfract2D_exp_tot"
volfract2D_exp=volfract2D_exp./max(max(volfract2D_exp));
volfract2D_exp_tot(:,:,s) = volfract2D_exp;
end % del for s

%====================Fin del bucle de cálculo=======================%

volfract2D_exp_tot(isnan(volfract2D_exp_tot))=0;
```

```
%=========================================================================%
%       Cálculo de los parámetros A y B en la correlación 2D-3D           %
%        para determinar la porosidad volumétrica del lecho               &
%=========================================================================%

% Algoritmo de optimización multivariable "fminsearch" para minimizar
el error en la función "myfunAB(X)" (diferencia entre la masa real del
lecho y la estimada a partir del mapa de porosidades 3D, dadas A y B.
El parámetro de entrada de la función, X, es un vector tal que: X =
[A,B]. La función "myfunAB(X)" se describe a continuación:

=======================FUNCIÓN myfunAB(X)============================
 function f=myfunAB(X)
 for j=1:s_max
 volfract3D_exp(:,:,j) =
 volfract2D_exp_tot(:,:,j)./(1-volfract2D_exp_tot(:,:,j)/X(1))*X(2);
 eps3d                                = volfract3D_exp(:,:,j);
 eps3d(eps3d>eps3Dmax | eps3d<0)      = eps3Dmax;
 eps3Dmax(isnan(eps3Dmax))            = 0;
 Vols(j)                              = numel(eps3d(eps3d>0.01));
 volfract3D_exp(:,:,j)                = eps3d;
 end
 avg_volfract3D_exp=mean(mean(volfract3D_exp(volfract3D_exp>0.02),3));
 Vol         = mean(Vols)/pix2cm^2*0.8;
 htubo       =
 (-4+(16+4*(Vol-38.4)/tan(80*pi()/180))^0.5)/(2/tan(80*pi()/180));
 Voltubo     = (htubo+2)*pi()*0.2^2;
 Vol         = Vol-Voltubo;
 Mp          = avg_volfract3D_exp*Vol*(rho_fixbed/1000);
 f           = (abs(Mp_real*1000 - Mp)/(Mp_real*1000));
 end
=======================FUNCIÓN myfunAB(X)============================

% Los parámetros de entrada para el algoritmo de optimización
multivariable "fminsearch" son el número máximo de evaluaciones de la
función, la tolerancia máxima para "f" y para "X", así como unos
valores iniciales para A y B (en este caso A0=1.1, B0=0.02):

options      = optimset('MaxFunEvals',100,'TolFun',1e-2,'TolX',1e-3);
a            = fminsearch(@(X) myfunAB(X),[1.1;0.02], options)

% Los valores óptimos para A y B son, respectivamente: A=a(1) y B=a(2)

for s=1:s_max
volfract3D_exp(:,:,s)   =
volfract2D_exp_tot(:,:,s)./(1-volfract2D_exp_tot(:,:,s)/a(1))*a(2);
volfract3D_exp(isnan(volfract3D_exp))     = 0;
eps3d                                     = volfract3D_exp(:,:,s);
eps3d(eps3d>eps3Dmax | eps3d<0)           = eps3Dmax;
volfract3D_exp(:,:,s)                     = eps3d;
zflux_tot(:,:,s) =
zvel_norm_tot(:,:,s).*volfract3D_exp(:,:,s)*rho_fixbed;
end

%=========================================================================%
% Combinación de DIA y PIV para determinar los flujos másicos axiales%
%=========================================================================%

zvel_norm_tot2    = mean(zvel_norm_tot,3);
zflux_tot2        = mean(zflux_tot,3);
poszflux          = zflux_tot;
```

```
negzflux                = zflux_tot;
poszflux(poszflux<0)    = 0;
negzflux(negzflux>0)    = 0;
poszfluxaux             = poszflux;
negzfluxaux             = negzflux;
poszfluxaux(poszfluxaux>0)    = 1;
negzfluxaux(negzfluxaux<0)    = 1;

PosFlux     = sum(poszflux,3)./sum(poszfluxaux,3);
NegFlux     = sum(negzflux,3)./sum(negzfluxaux,3);
s           = sum(volfract3D_exp,3)/numel(volfract3D_exp(1,1,:));

filename1   =
strcat(path_outVF,'PIVDIAresults_16x16_bg_lim06prc95cont0.mat');

save(filename1,'zflux_tot','zvel_norm_tot','volfract2D_exp','zvel_norm
_tot2','zflux_tot2','s','PosFlux','NegFlux');

%=========================================================================%
%              REPRESENTACIÓN GRÁFICA DE RESULTADOS                       %
%=========================================================================%

%=========================================================================%
%      Figura 1: Mapa de intensidades, porosidad 3D, velocidad            %
%                superficial y flujo másico transitorios                  %
%=========================================================================%

q=figure(1);
set(q,'name','Transient PIV/DIA','color',[1 1 1])

hold on;
subplot(2,2,1);
pcolor(((1:1:NX)*((height-zcs)/tan(ang*pi()/180)*2+width)/NX-(height-
zcs)/tan(ang*pi()/180))*100,((1:1:NZ)-1)*height/NZ*100,
volfract2D_exp_tot(:,:,s_max));
colormap(jet);
shading flat;
colorbar('eastoutside');
caxis([0 1.2]);
xlabel('x [px]','fontweight', 'b');
ylabel ('z [px]','fontweight', 'b');
axis image;
tit1 = title('Intensity [-]');
get(tit1, 'Position');

hold on
subplot(2,2,2);
pcolor(((1:1:NX)*((height-zcs)/tan(ang*pi()/180)*2+width)/NX-(height-
zcs)/tan(ang*pi()/180))*100,((1:1:NZ)-1)*height/NZ*100,
volfract3D_exp(:,:,s_max));
colormap(jet);
shading flat;
colorbar('eastoutside');
caxis([0 0.6]);
axis image;
xlabel('x [cm]','fontweight', 'b');
ylabel ('z [cm]','fontweight', 'b');
tit2 = title('<\epsilon_{p,3D}^{exp}> [-]');
get(tit2, 'Position');
```

```
hold on;
subplot(2,2,3);
zvel_norm_tot(zvel_norm_tot==0)=nan;
pcolor(((1:1:NX)*((height-zcs)/tan(ang*pi()/180)*2+width)/NX-(height-
zcs)/tan(ang*pi()/180))*100,((1:1:NZ)-1)*height/NZ*100,
zvel_norm_tot(:,:,s_max));
caxis([-1 1])
axis image
shading flat;
colormap(jet);
map=colormap;
map(find(map==1,1)+1,:)=[1,1,1];
colormap(map)
colorbar('eastoutside');
tit1 = title('SpF velocity [m/s]');
get(tit1, 'Position');
xlabel('x [cm]','fontweight', 'b');
ylabel ('z [cm]','fontweight', 'b');

hold on
subplot(2,2,4);
pcolor(((1:1:NX)*((height-zcs)/tan(ang*pi()/180)*2+width)/NX-(height-
zcs)/tan(ang*pi()/180))*100,((1:1:NZ)-1)*height/NZ*100,
zflux_tot(:,:,s_max));
colormap(jet);
colorbar('eastoutside');
caxis([-200 200])
axis image
shading flat;
tit3 = title('<Mass Flow _{p,z}> [kg/m^{2}·s]');
get(tit3, 'Position');
xlabel('x [cm]','fontweight', 'b');
ylabel ('z [cm]','fontweight', 'b');
hold off;

%=========================================================================%
%                  Figura 2: porosidad 3D, velocidad                      %
%                 superficial y flujo másico promedios                    %
%=========================================================================%

q1=figure(2);
set(q1,'name','Average PIV/DIA','color',[1 1 1])
hold on;

subplot(1,3,1);
zvel_norm_tot2(zvel_norm_tot2==0)=nan;
pcolor(((1:1:NX)*((height-zcs)/tan(ang*pi()/180)*2+width)/NX-(height-
zcs)/tan(ang*pi()/180))*100,((1:1:NZ)-
1)*height/NZ*100,zvel_norm_tot2);
caxis([-0.5 0.5])
axis image
shading flat;
colormap(jet);
map=colormap;
map(find(map==1,1)+1,:)=[1,1,1];
colormap(map)
colorbar('eastoutside');
tit1 = title('SpF velocity [m/s]');
get(tit1, 'Position');
xlabel('x [cm]','fontweight', 'b');
ylabel ('z [cm]','fontweight', 'b');
```

```
hold on
subplot(1,3,2);
s(s==0)=nan;
pcolor(((1:1:NX)*((height-zcs)/tan(ang*pi()/180)*2+width)/NX-(height-
zcs)/tan(ang*pi()/180))*100,((1:1:NZ)-1)*height/NZ*100,s);
colormap(jet);
shading flat;
colorbar('eastoutside');
caxis([0 0.6]);
axis image;
xlabel('x [cm]','fontweight', 'b');
ylabel ('z [cm]','fontweight', 'b');
tit2 = title('<\epsilon_{p,3D}^{exp}> [-]');
get(tit2, 'Position');

hold on
subplot(1,3,3);
zflux_tot2(zflux_tot2==0)=nan;
pcolor(((1:1:NX)*((height-zcs)/tan(ang*pi()/180)*2+width)/NX-(height-
zcs)/tan(ang*pi()/180))*100,((1:1:NZ)-1)*height/NZ*100,zflux_tot2);
colormap(jet);
colorbar('eastoutside');
caxis([-50 50])
axis image
shading flat;
tit3 = title('<Mass Flow _{p,z}> [kg/m^{2}·s]');
get(tit3, 'Position');
xlabel('x [cm]','fontweight', 'b');
ylabel ('z [cm]','fontweight', 'b');
hold off;

%=========================================================================%
%      Figura 3: flujo másico promedio positivo, negativo y neto      %
%=========================================================================%

q2=figure(3);
set(q1,'name','Average MassFlows','color',[1 1 1])
hold on;

subplot(1,3,1);
pcolor(((1:1:NX)*((height-zcs)/tan(ang*pi()/180)*2+width)/NX-(height-
zcs)/tan(ang*pi()/180))*100,((1:1:NZ)-1)*height/NZ*100,PosFlux);
caxis([0 150])
axis image
shading flat;
colormap(jet);
map=colormap;
map(find(map==1,1)+1,:)=[1,1,1];
colormap(map)
colorbar('eastoutside');
tit1 = title('<PosFlux> [kg/m^{2}·s]');
get(tit1, 'Position');
xlabel('x [cm]','fontweight', 'b');
ylabel ('z [cm]','fontweight', 'b');

hold on
subplot(1,3,2);
pcolor(((1:1:NX)*((height-zcs)/tan(ang*pi()/180)*2+width)/NX-(height-
zcs)/tan(ang*pi()/180))*100,((1:1:NZ)-1)*height/NZ*100,NegFlux);
colormap(jet);
shading flat;
```

```
colorbar('eastoutside');
caxis([-150 0]);
axis image;
xlabel('x [cm]','fontweight', 'b');
ylabel ('z [cm]','fontweight', 'b');
tit2 = title('<NegFlux> [kg/m^{2}·s]');
get(tit2, 'Position');

hold on
subplot(1,3,3);
zflux_tot2(zflux_tot2==0)=nan;
pcolor(((1:1:NX)*((height-zcs)/tan(ang*pi()/180)*2+width)/NX-(height-
zcs)/tan(ang*pi()/180))*100,((1:1:NZ)-1)*height/NZ*100,zflux_tot2);
colormap(jet);
colorbar('eastoutside');
caxis([-50 50])
axis image
shading flat;
tit3 = title('<Mass Flow _{p,z}> [kg/m^{2}·s]');
get(tit3, 'Position');
xlabel('x [cm]','fontweight', 'b');
ylabel ('z [cm]','fontweight', 'b');
hold off;

%=========================================================================%
%          Almacenamiento de las figuras como imágenes .jpg               %
%=========================================================================%

saveas(q,strcat(path_outVF,'TransientPIVDIA.jpg'),'jpg');
saveas(q,strcat(path_outVF,'TransientPIVDIA.fig'),'fig');
saveas(q1,strcat(path_outVF,'AveragePIVDIA.jpg'),'jpg');
saveas(q1,strcat(path_outVF,'AveragePIVDIA.fig'),'fig');
saveas(q2,strcat(path_outVF,'MassFlows.jpg'),'jpg');
saveas(q2,strcat(path_outVF,'MassFlows.fig'),'fig');

end   % fin de la función
```

Anexo A.4: Implementación del Modelo de Retromezcla a Contractorriente (CCBM) con desacoplamiento de variables espacio-tiempo

```
function [IM] = CCBMsinparametros(escala,ur,angulo,delta,zsolfluid)

%Esta funcion determina el valor teórico de las funciones C(z,t) e
IM(t) sin parámetros ajustables: los valores de u1, f1 y kw del modelo
CCBM se estiman a partir de correlaciones hidrodinámicas.

%Notación:
 -> "escala" del lecho -> '1x' ó '2x';
 -> "ur" = velocidad relativa del gas de entrada;
 -> "angulo" de cambio de sección en el rango [0°-85°];
 -> "delta": fracción de burbujas en el lecho;
 -> "zsolfluid": posición axial promedio del freeboard.

%CONSTANTES:
    g       = 981; % Gravedad (cm/s^2)
    umf     = 10.1; % Velocidad de mínima fluidización (cm/s)

%PARÁMETROS DEL MODELO:
-> Se estima que la estela supone un 20% de la burbuja
independientemente del tamaño de ésta

    fw      = 0.20;     % Fracción de burbuja ocupada por la estela
    dt      = 0.01;     % Paso temporal (s)
    tmezcla = 40;       % Tiempo de mezcla a modelar (s)
    nfilas  = round(tmezcla/dt); % Número de filas de la matriz C(z,t)

En cada fila se representarán consecutivamente los valores de
concentración de sólido, transcurrido un tiempo dt.

%ECUACIONES:
    ugas    = umf*ur;   % Velocidad del gas de entrada (cm/s)
    umb     = 1.15*umf; % Velocidad de mínimo burbujeo (cm/s)

%PARÁMETROS DE ESCALA:
    if strcmp(escala,'1x')
        zdis      = 8; % Altura distribuidor (cm) = zcs
        ancho     = 2; % Anchura del lecho en la zona inferior (cm)
        angbeta   = 3.9343*ur^2-26.921*ur+102.6; % Ángulo defluidizac.
    elseif strcmp(escala,'2x')
        zdis      = 12;
        ancho     = 4;
        angbeta   = 0.4394*ur^2-4.4448*ur+78.863;
    end

%GEOMETRÍA:
    Ailum0        = zdis*ancho; %área iluminada inicialmente

% Área total del lecho fluidizado (cm^2):
      Atotalt     =
Ailum0+(ancho+2*ancho)/2*(ancho/2)*tan(angulo*pi()/180)+(zsolfluid-
zdis-ancho/2*tan(angulo*pi()/180))*2*ancho;
% Altura del lecho empaquetado inicial (cm)
      Zsolidofijo =
((1-delta)*Atotalt-Ailum0-(ancho+2*ancho)/2*(ancho/2)
*tan(angulo*pi()/180))/2/ancho+zdis+ancho/2*tan(angulo*pi()/180);
```

```
% DETERMINACIÓN DE u1 (cm3/cm2s):
  a) Diámetro de burbuja según JHM:
    db            = zeros(1,ceil(zsolfluid));
    db_o          = zeros(1,ceil(zsolfluid));
    db_e          = zeros(1,ceil(zsolfluid));
    ugasz         = zeros(1,ceil(zsolfluid));
    anchuras      = zeros(1,ceil(zsolfluid));
    for z         = 1:ceil(zsolfluid)
     if z         <= zdis
      db(z)       =
                  0.65*(pi()/4*ancho^2*umf*(ur-1))^0.4*(1-exp(-
                  0.3*z/ancho));
      ugasz(z)    = ugas;
      anchuras(z) = ancho;
     else
      db_o(z)     =
                  0.65*(pi()/4*(2*ancho)^2*umf*(ur-1))^0.4*(1-exp(-
                  0.3*(z-zdis)/(2*ancho)));
      if (1-(z-zdis)/(ur-1)/tan(angbeta*pi()/180))    > 0
       db_e(z)  =
                db(zdis)*(1-(z-zdis)/(ur-1)/tan(angbeta*pi()/180))^0.5;
      else
       db_e(z)  = 0;
      end
       db(z)    = (db_e(z)+db_o(z))/2;

       if z < (zdis+ancho/2*tan(angulo*pi()/180))
        ugasz(z)  = (2-(z-zdis)/(ancho/2*tan(angulo*pi()/180)))*ugas;
        anchuras(z)=ancho*(1+(z-zdis)/(ancho/2*tan(angulo*pi()/180)));
       else ugasz(z)= ugas;
        anchuras(z) = 2*ancho;
       end
      end
    end

 b) Veloc. ascens. de partículas, u1(cm/s) -> Modelo Kunii Levenspiel,
considerando que la velocidad ascensional de los sólidos es del orden
del 30% respecto a la velocidad de las burbujas (estudios paralelos):

    umf     = umf.*ones(1,ceil(zsolfluid));
    umb     = umb.*ones(1,ceil(zsolfluid));
    u1      = 0.3*((ugas-umb)+0.4*(g*db).^0.5);

% DETERMINACIÓN DE kw (transferencia de sólido debida a la diferencia
de concentración entre las fases ascendente y descendente, [1/s]) ->
Modelo de Lim et al. 1993:
    if ur   <= 3.0
        kw  = (7.5.*(ugasz-umb))./(umb.*db);
    else
        kw  = 15./db;
    end

% DETERMINACIÓN DE f1 (fracción de sólido que asciende en la estela
respecto al total del sólido que circula, [-]) -> del Balance de
Materia a la fase sólida
    f1      = (delta*fw)/((delta*fw)+1-delta);

% VALORES PROMEDIO:
    u1      = mean(u1(u1>0));
    kw      = mean(kw(kw>0));
```

```
% PARÁMETRO ADICIONAL:
Parámetro que se repite en la formulación del método cinemático del
modelo CCBM (desacoplamiento de variables espacio-tiempo).
    beta    = -kw/(1-f1);

% Definición del número de rodajas (columnas) de las matrices C_1
(concentración de sólido en la estela, entendida en valor unitario:
C_1=0 para sólido no iluminado y C_1=1 para sólido iluminado) y C_2
(concentración del sólido en la emulsión, también unitario).

% Ambas matrices contienen el mismo número de rodajas con un espeso
exactamente la mitad del desplazamiento 'dz' que se da entre sólido
que asciende con la estela y el que cae con la emulsión.
ncol_c1     = round(2*(1-f1)*zsolidofijo/(dt*u1)/(2-f1));
ncoldis_c1  = round(2*(1-f1)*zdis/(dt*u1)/(2-f1));

% Definición de las matrices C_1 y C_2 a tiempo 0 (sólamente la zona
inferior a zdis está iluminada, esto es, con valor de concentración
C_1 = C_2 = 1).
C_1                     = zeros(nfilas,ncol_c1);
C_1(1,1:ncoldis_c1)     = 1;
C_2                     = zeros(nfilas,ncol_c1);
C_2(1,1:ncoldis_c1)     = 1;

% Matriz de concentraciones asociada a cada rodaja (promediando las
concentraciones de estela, C_1, y emulsión, C_2, con la fracción
volumétrica que ocupan).
C(1,:)                  = C_1(1,:).*f1+C_2(1,:).*(1-f1);

%=========================================================================%
%              BUCLE para resolver el modelo CCBM                         %
%     a partir del desacoplamiento de variables espacio-tiempo            %
%=========================================================================%

for t=2:nfilas

% Variación de la concentración con el tiempo en cada rodaja
C_1(t,:)    =

C_1(t-1,:).*(exp(beta*dt)+f1*(1-exp(beta*dt)))+C_2(t-1,:).*(1-f1)*(1-
exp(beta*dt));

C_2(t,:)    =

C_1(t-1,:).*(1-f1)*(1-exp(beta*dt))+C_2(t-1,:).*(1-(1-f1)*(1-
exp(beta*dt)));

C_1(t,2:ncol_c1)        = C_1(t,1:ncol_c1-1);
C_2(t,1:ncol_c1-1)      = C_2(t,2:ncol_c1);

% En las rodajas superior e inferior del lecho, la fase estela pasa a
ser emulsión y viceversa.
C_1(t,1)                = C_2(t,1);
C_2(t,ncol_c1)          = C_1(t,ncol_c1);
C(t,:)                  = (C_1(t,:).*f1+C_2(t,:).*(1-f1));

end

%======================FIN DEL BUCLE DE CÁLCULO=====================%
```

```
%Definición del ÍNDICE DE MEZCLA. Mediante IMaux añadimos el índice de
mezcla inicial = 0.
IM                      =

sum((C(:,ncoldis_c1+1:ncol_c1-1)+C(:,ncoldis_c1+2:ncol_c1)),2)./
sum((C(:,1:ncol_c1-1)+C(:,2:ncol_c1)),2)./(1-ncoldis_c1/ncol_c1)
+0.01*ur;

IM(IM>1)                = 1;
IMaux                   = zeros(1,numel(IM)+1);
IMaux(1,2:numel(IM)+1)  = IM;
IM                      = IMaux;

%Se definen los vectores con los datos a representar y la leyenda de
la gráfica C(z,t).
hreac       =(1:ncol_c1)/ncol_c1;
fps         = 25;
dos         = round(50/fps);
tresc       = round(100/fps);
tresc1      = round(150/fps);
tresc2      = round(200/fps);
setec       = round(700/fps);
z1          = numel(C(1,:));

%=========================================================================%
%                            FIGURA 1: C(z,t)                             %
%=========================================================================%

figure(1),
hold on
plot(hreac,C(2,1:z1),'c-',hreac,C(200,1:z1),'g-',hreac,C(400,1:z1),'m-
',hreac,C(600,1:z1),'y-',hreac,C(800,1:z1),'r-',hreac,C(2800,1:z1),'k-
');
legend(sprintf('t=%ds',0),sprintf('t=%ds',dos),sprintf('t=%ds',tresc),
sprintf('t=%ds',tresc1),sprintf('t=%ds',tresc2),sprintf('t=%ds',setec)
);
axis([0 1 0 1]);
title('Tracer Concentration Profiles');
xlabel('Dimensionless reactor height, z [-]');
ylabel('Tracer concentration, C [-]');
hold off

%=========================================================================%
%                            FIGURA 2: IM(t)                              %
%=========================================================================%
figure(2),
plot((0:nfilas)*dt,IM,'k-');
hold on
title('Mixing Index');
xlabel('Mixing time, t [s]');
ylabel('Mixing Index, MI [-]');
axis([0 40 0 1]);

end   % Fin de la función
```

COMPENDIO

Artículo I

I. Julián, J. Herguido, M. Menéndez,
Particle Mixing in a Two-Section Two-Zone Fluidized Bed Reactor. Experimental Technique and Counter-Current Back-Mixing Model Validation,
Ind. Eng. Chem. Res. 52 (2013) 13587 – 13596.

I&EC research
Industrial & Engineering Chemistry Research

Article

pubs.acs.org/IECR

Particle Mixing in a Two-Section Two-Zone Fluidized Bed Reactor. Experimental Technique and Counter-Current Back-Mixing Model Validation

Ignacio Julián, Javier Herguido, and Miguel Menéndez*

Catalysis, Molecular Separations and Reactor Engineering Group (CREG), Aragon Institute of Engineering Research (I3A), Universidad de Zaragoza, Mariano Esquillor s/n, 50018 Zaragoza, Spain

ABSTRACT: Effective particle circulation between the two zones is a prerequisite for ensuring the simultaneous reaction and catalyst regeneration inside a two-zone fluidized bed reactor (TZFBR). An appropriate degree of particle mixing provides a steady state catalytic operation, whereas poor solid circulation between the bed zones leads to unhampered catalyst deactivation. To achieve effective control of the fluid dynamic regime within the two bed regions, a new design has been proposed with a different cross sectional area in each zone. The transition angle (α) between these zones represents the most characteristic feature of the so-called two-section TZFBR (TS-TZFBR). In the present study, the influence of operational variables (α, gas velocities, gas distributor location) on the particle circulation has been determined. Phosphorescent particles have been used as optical tracers to measure the solid axial mixing between the zones in a cold pseudo-2D TS-TZFBR facility. Additionally, a modified counter-current back-mixing model (CCBM) without adjustable parameters has been developed to explain and predict the solid mixing rate for different TS-TZFBR geometries. The experimental mixing results show a reasonably good agreement with the suggested mixing model predictions in a wide range of operational conditions: $u_{gas}-u_{mf}$ = [5−20] $cm^3/(cm^2\ s)$, α = [0°−85°].

1. INTRODUCTION

The two zone fluidized bed reactor (TZFBR) has been proposed as an attractive solution to perform gas−solid catalytic reactions where the catalyst suffers from a rapid loss of activity due to coke deposition over its surface.[1] Catalyst coking is a common phenomenon when treating gas hydrocarbons at high temperatures.[2] To overcome this process limitation, the TZFBR is able to provide catalytic reaction and catalyst regeneration in a single fluidized bed reactor thanks to its singular configuration[2] (Figure 1a). The use of two separated gaseous feed points with reactive and regenerative gas feeds generates two different atmospheres or reaction zones inside the TZFBR. An immersed gas distributor feeds the reactive hydrocarbon from a certain catalytic bed height, whereas an oxidizing agent flows up from the bottom part of the bed.[2] In a steady state operation, catalytic particles become partially deactivated above the immersed distributor and are simultaneously regenerated under it. Therefore, the catalyst circulation between these two zones in a fluidized bed regime results in the desired process integration.

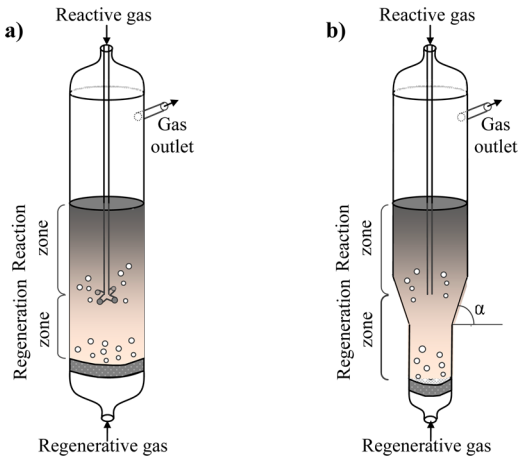

Figure 1. (a) Scheme of a 3D TZFBR, (b) pseudo-2D TS-TZFBR facility.

The TZFBR performance has been successfully tested in several dehydrogenation reactions (e.g., propane and butane dehydrogenation) as well as in ethanol reforming, using different catalysts.[3−7] Experimental results have proved that the TZFBR is an effective system to overcome deactivation problems, leading to increased steady state conversions in all these processes.

Recently, a new TZFBR configuration has been proposed. It incorporates two zones with different cross sectional area in order to achieve effective control of the fluid dynamic regime within the two bed regions (Figure 1b). The proposed design allows the use of low oxidant-to-reactive stream ratios when required.[8] The transition angle (α) between the zones in the so-called two-section TZFBR (TS-TZFBR) has to be carefully selected in order to avoid defluidization problems and a short-circuit in the solid recirculation.[9] A suitable TS-TZFBR design is thus essential to achieve a good reactor performance.

In this reactor concept, the solid axial mixing represents a fluid dynamic key factor, and the mixing rates between bed

Received: April 26, 2013
Revised: July 30, 2013
Accepted: August 29, 2013
Published: August 29, 2013

   dx.doi.org/10.1021/ie401334x | *Ind. Eng. Chem. Res.* 2013, 52, 13587−13596

zones need to be carefully controlled. The mixing of particles in a fluidized bed is usually difficult to control and can easily lead to reactor malfunction when mixing is too poor or too intense. Therefore, a detailed modeling of the mixing process within the TS-TZFBR needs to be carried out.

The fluid dynamic study of the dense phase in a fluidized bed reactor involves great challenges. Many efforts have been made in recent decades to develop reliable experimental techniques to measure particle motion and solids axial mixing.[10−16] A recent review[17] evaluates the available measurement techniques in fluidized beds. The most common method is the use of tracer solids, since they allow particle tracking along the bed. Tracers can be discriminated from other bed particles by any singular property such as magnetism, color, radioactivity, fluorescence, or conductance.[17,18]

The use of optical tracers (e.g., phosphorescent particles) coupled with the nonintrusive digital image analysis (DIA) technique for fluidized beds introduced by Agarwal and co-workers[19] allows, in this work, the continuous measurement of tracer concentration along the mixing time and bed position. Although DIA can just be applied to pseudo-2D bed facilities where only the facial mixing is taken into account, this technique allows the study of the axial solids mixing in fluidized beds and provides an experimental tool to validate classical mixing models, i.e. the three-phase *counter-current back-mixing* (CCBM) model.

The main aims of this work are (a) to find an operational window that ensures a good fluid dynamic behavior inside the TS-TZFBR and (b) to develop a predictive mixing model for the TS-TZFBR. For this purpose, experimental mixing measurements have been conducted in cold pseudo-2D TS-TZFBR to evaluate the effect of some operational variables on the solids axial mixing. These variables are tapered section angle (α), immersed distributor vertical position (z_{dis}), and relative gas velocity ($u_r = u_{gas}/u_{mf}$) entering both the reactive and the regenerative bed zones.

Besides, a modified CCBM model has been developed to predict the solids axial mixing on a TS-TZFBR. The modified model takes into account the TS-TZFBR geometry and the dual gas distribution. Both model and experimental features are described in the following sections.

2. EXPERIMENTAL SETUP

Experimental studies have been carried out in *Perspex* pseudo-2D TS-TZFBR (300 mm height × 40 mm width × 8 mm depth) with different transition angles, α, between the bed zones. The tested transition angles were 0°, 45°, 60°, 80°, and 85° with respect to the horizontal axis. The bottom gas distributor was a porous glass plate (pore size: 40−70 μm), whereas the immersed distributor was a T-shaped orifice distributor (2 mm diameter). Geldart B phosphorescent particles were used as fluidized particles, and compressed air was used as fluidizing gas. The phosphorescent solids provided by Materiales Inteligentes S.L. were $SrAl_2O_4$-based particles, doped with rare earth elements (Eu and Dy). Their main properties are: d_p = 100−320 μm, ρ_{bulk} = 3.6 g/cm^3 and u_{mf} = 10.1 cm^3/(cm^2 s). Both phosphorescent particle size and density are similar to those of the $MgAl_2O_4$-based catalytic particles employed in reactive conditions on the TS-TZFBR (see for example, refs 20 and 21).

These phosphorescent particles have been used as optical tracers to measure the axial mixing between particles from the reaction and regeneration zones in a TS-TZFBR. Such kind of particles has already been used elsewhere[22] to study the particle mixing in a conventional fluidized bed reactor due to their optical properties. Compared to colored tracers, phosphorescent particles do not need to be segregated after each mixing experiment by means of particle size or density. Thus, segregation effects can be here neglected. These particles have adequate resistance to attrition and nonhazardous properties.[23] Their luminance intensity decays exponentially with time (Figure 2). Nevertheless, they kept an intense afterglow along the experimental recording time that allowed the tracer mixing measurement.

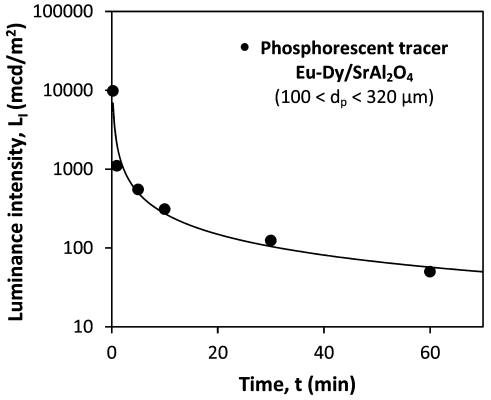

Figure 2. Transient emissivity decay for Eu−Dy/$SrAl_2O_4$ particles.

The cold pseudo-2D TS-TZFBR facility was placed in a black box to avoid the phosphorescent particles becoming excited due to external lighting. Images were recorded in darkness with a high-definition low luminance-level camcorder (recording frequency: 25 Hz). A scheme of the experimental setup is shown in Figure 3.

The experimental TS-TZFBR mixing behavior was analyzed under the effect of three operational variables: fluidization relative gas velocity, location of the immersed gas distributor and reactor geometry (transition angle, α = [0° − 85°]).

The relative gas velocities in both "reaction" and "regeneration" zones have been evaluated ranging from $u_r = u_{gas}/u_{mf}$ = 1.5 to 3.5. These u_r values were previously proved as suitable conditions to provide sufficient axial mixing of solids (in order to ensure continuous catalyst regeneration in the reactor) and a relatively high gas−solid contact time for the tested Geldart B particles in a TS-TZFBR.[9]

The T-shaped gas distributor was located at different bed vertical positions (z_{dis}) above the lower point of the tapered section (z_{sc}). The distributor was usually located at the beginning of the section enlargement ($z_{dis} = z_{sc}$ = 8 cm). Two additional distributor positions, z_{dis} = 9 cm and z_{dis} = 10 cm, were also evaluated. The variable z^* represents the relative distance between the immersed distributor position and the lower point of the tapered section, $z^* = z_{dis} - z_{sc}$, and is used to indicate the secondary gas feed location.

Finally, the singular α = 0° geometry was tested at different gas velocities to validate the experimental results relating to the existence of defluidized zones as reported by Julián et al.[9] These defluidization results, that is, defluidization angles (β) over the transition section, were obtained from particle image velocimetry (PIV) measurements.

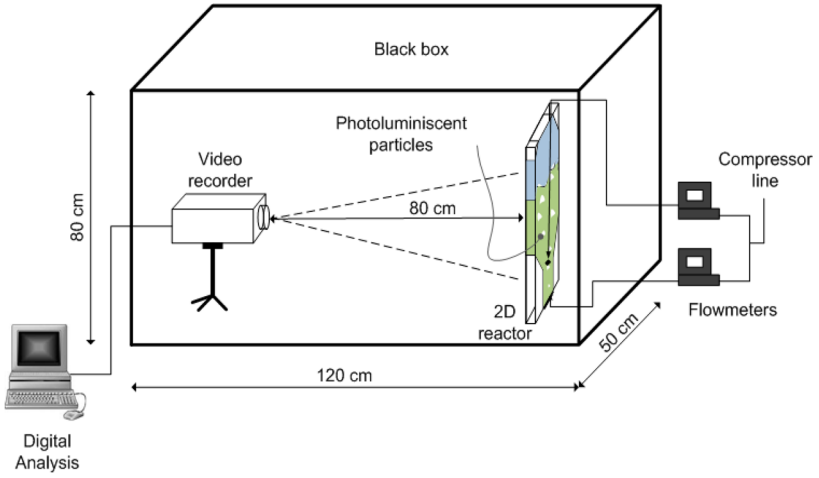

Figure 3. Scheme of the experimental setup.

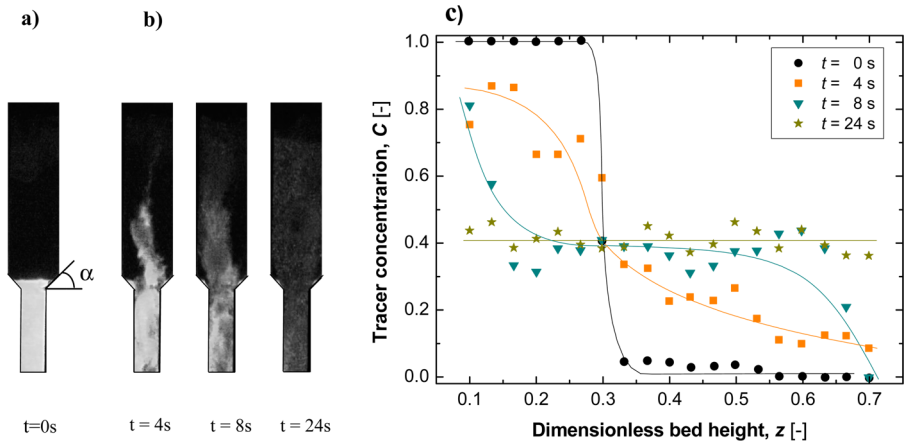

Figure 4. (a) Initial conditions, (b) tracer mixing images, (c) tracer concentration profile. Lines are for visual help.

3. ANALYSIS PROCEDURE

Several algorithms were home-developed (Matlab 2010a) to carry out the CCBM model implementation as well as the digital image analysis (DIA) of the recorded frames. The following sections describe the analysis procedure in both cases.

3.1. Mixing Experiments and DIA. Phosphorescent particles become optically active once excited. This property allows the use of such particles throughout the whole bed. A region of interest is initially excited to subsequently follow particle mixing from this region to the rest of the bed.

According to this method, mixing experiments start as a fixed bed, where only particles from the bottom front face of the bed ("regeneration zone") are excited (Figure 4a). The mean illumination values of the different regions in which the bed frame is divided are used to measure the mixing rate between illuminated and dark particles inside the reactor when fluidized (Figure 4b). In the pseudo-2D reactor, only the facial particle motion is considered; that is, the particle displacement in the bed depth direction is not taken into account.

In this study, a DIA algorithm was developed to read the recorded mixing frames and show tracer concentration profiles as a function of time and bed position (Figure 4c). This postprocessing analysis was performed with the aid of the Image Processing Toolbox (Matlab 2010a).

To determine the tracer concentration in each cross section of a mixing frame, the bed was divided into 1 cm height slices (Figure 5b). For every slice, a grayscale histogram was obtained (Figure 5c). The mean value of each histogram was related to the tracer concentration at such a bed height. This tracer concentration was then normalized (eq 1) according to the maximum and the minimum illumination values, that is, regeneration and reaction zones at t = 0 s (Figure 5a).

$$\bar{C}_{z,t} = \frac{\bar{I}_{z,t} - \bar{I}_{\min}}{\bar{I}_{\max} - \bar{I}_{\min}} \quad (1)$$

In addition, the experimental concentrations, $\bar{C}_{z,t}$, were corrected to take into account the tracer emissivity decay along the recording time. For this purpose, the area under the tracer concentration curve (Figure 4c) was forced to be the same for every mixing time. This postprocessing analysis is similar to the method used by Abanades and Grasa (2001).[22]

Once the tracer concentration profiles were obtained, the so-called "mixing index" (MI) plot could be determined. This MI measures the mixing degree between particles that initially come from the upper (nonilluminated) and lower (illuminated) zones as a function of the fluidization time. The MI varies between 0 (fully segregated particles) and 1 (full mixing). Equation 2 shows a mathematical definition of the MI, where z_{max} represents the maximum bed height, z_{ilum} is the initially illuminated height, $C(z,t)$ is the tracer concentration as a function of bed height and mixing time, and C_∞ represents the full mixing tracer concentration.[24]

dx.doi.org/10.1021/ie401334x | Ind. Eng. Chem. Res. 2013, 52, 13587−13596

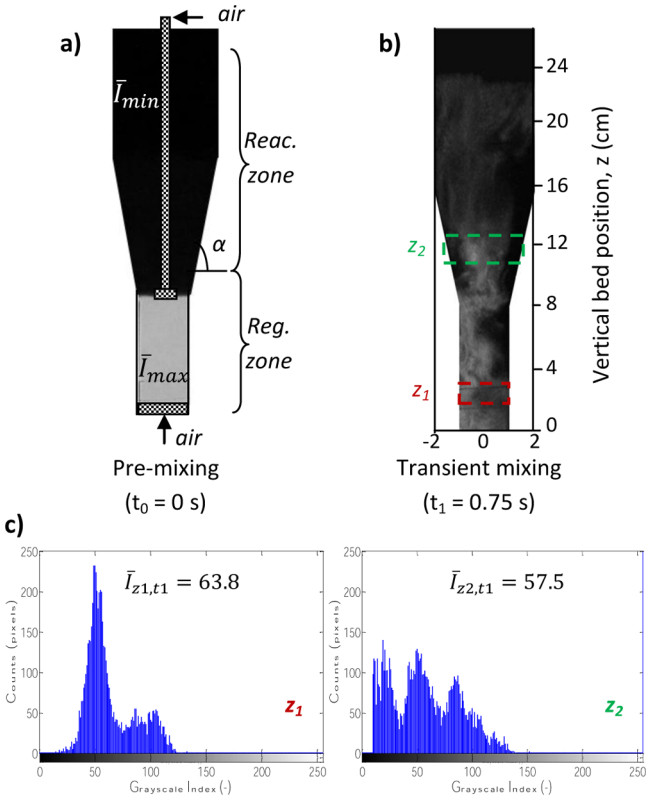

Figure 5. (a) Initial conditions, (b) transient mixing frame, (c) histograms to determine average local light intensities, $\bar{I}$, at heights z_1 and z_2.

$$\mathrm{MI} = \frac{\int_{z_{\mathrm{ilum}}}^{z_{\max}} C(z,\,t)\,\mathrm{d}z}{(z_{\max} - z_{\mathrm{ilum}})C_{\infty}} \tag{2}$$

3.2. Counter-Current Back-Mixing Model (CCBM). The solid transport inside a TS-TZFBR has been modeled with a modified version of the classical CCBM model. The CCBM model was originally proposed by van Deemter (1961) and further generalized by Gwyn et al. (1970).[18] This model depicts the bed as a system with three different phases: an upward flow of gas (bubbles), an upward flow of particulate solid (wake), and a downward dense flow of particles in the emulsion phase. Additionally, the model considers a solid exchange between the wake and emulsion phases.[18] The CCBM model is outlined in Figure 6.

Mass balances for both wake and emulsion phases have been represented by a system of hyperbolic partial differential equations.[24] Equations 3 and 4 represent the temporal evolution of the tracer concentration in the wake (C_1) and the emulsion phase (C_2), as a function of the vertical position of the bed. These equations define a phase of volume fraction f_1 moving upward at velocity u_1, which exchanges solid at a volumetric rate of k_w with a dense phase falling downward at velocity $u_1 f_1/(1 - f_1)$.[22,25]

$$\frac{\partial C_2}{\partial t} = -u_1\frac{f_1}{1-f_1}\frac{\partial C_2}{\partial z} + k_w\frac{f_1}{1-f_1}(C_2 - C_1) \tag{3}$$

$$\frac{\partial C_1}{\partial t} = u_1\frac{\partial C_1}{\partial z} + k_w(C_1 - C_2) \tag{4}$$

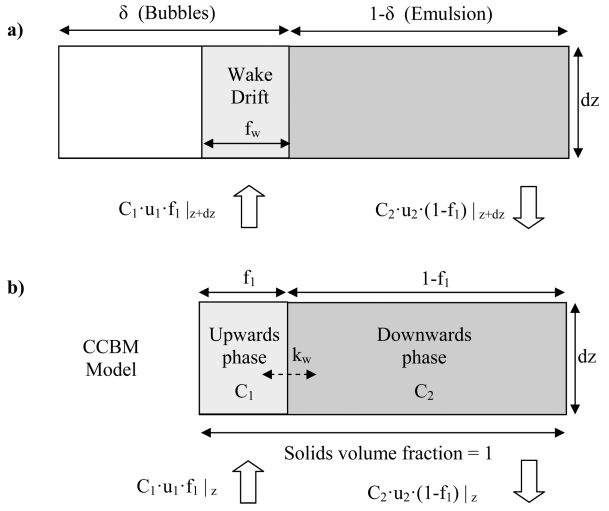

Figure 6. Counter-current backmixing (CCBM) model: (a) three-phase model, (b) solid phase model.

An in-house developed Matlab2010a algorithm provides the model prediction of the solid axial mixing inside a TS-TZFBR. As a first approximation, the bed was considered as a straight column with a single bottom gas inlet and similar solid circulation behavior as that of a TS-TZFBR. The solid back-mixing was related to the three parameters discussed above: particles upward velocity (u_1), upward solid fraction (f_1), and wake-emulsion exchange coefficient (k_w). A kinematic method as described by Grasa and Abanades[25] was used to solve the partial hyperbolic differential equations system set out in eqs 3 and 4. This method consists in uncoupling time (t) and position (z) variables. Therefore, wake and emulsion phases are divided into small compartments which move in instantaneous jumps after spending some time (Δt) exchanging solids with the adjacent phases. The distance they jump (Δz) is the product of the phase velocity (u_1, u_2) and the time spent exchanging solids. This results in eqs 5 to 7.

$$C_2(t+\Delta t) = C_1(t)(1-f_1)(1-e^{-k_w/(1-f_1)\Delta t}) + C_2(t)(1-(1-f_1)(1-e^{-k_w/(1-f_1)\Delta t})) \tag{5}$$

$$C_1(t+\Delta t) = C_1(t)(e^{-k_w/(1-f_1)\Delta t} + f_1(1-e^{-k_w/(1-f_1)\Delta t})) + C_2(t)(1-f_1)(1-e^{-k_w/(1-f_1)\Delta t}) \tag{6}$$

$$\Delta z = \overline{u}_1 \Delta t \tag{7}$$

The tracer concentration can be obtained as the average concentration value in every reactor slice, i (eq 8).

$$C_i = C_{1,i}f_1 + C_{2,i}(1-f_1) \tag{8}$$

The estimation of the model parameters u_1, f_1, and k_w can be carried out by two methods: by fitting experimental, $C_{exp}(z,t)$, and modeled, $C_{CCBM}(z,\,t,\,u_1,\,f_1,\,k_w)$, tracer concentration profiles or by using hydrodynamic correlations. In the first case, a Nelder-Mead multivariable optimization algorithm finds the most suitable [u_1, f_1, k_w] combination to fit the experimental data. The data fitting is quite accurate but it normally leads to nonsensical parameter values. The second method is more versatile, since the three model parameters are related to hydrodynamic properties and, therefore, experimental mixing

dx.doi.org/10.1021/ie401334x | Ind. Eng. Chem. Res. 2013, 52, 13587−13596

data are not necessary to obtain the modeled tracer concentration profile. The use of classical bubbling bed correlations, where inputs are already known from the TS-TZFBR operational conditions, leads to a simple but accurate prediction of the solid axial mixing without fitting model parameters.

Although the phase velocity remains constant, the TS-TZFBR configuration is taken into account in the model since $\overline{u_1}$ represents the phase upward velocity averaged along the whole bed, that is, the mean value of the $u_1(z)$ distribution. According to Kunni and Levenspiel (KL), $u_1(z)$ depends on the bubble velocity, $u_b(z)$, and the bubble fraction in the bed, δ. Similarly, the bubble velocity distribution can be expressed as a function of $u_{gas}(z)$ and $d_b(z)$, according to the Davidson and Harrison (DH) correlation.[26] Equation 9 shows the coupled correlation to obtain $u_1(z)$ from the $d_b(z)$, $u_{gas}(z)$ and δ values.

$$u_1(z) = (1-\delta)u_b(z) = (1-\delta)[(u_{gas}(z) - u_{mf}) + 0.4(g d_b(z))^{0.5}] \quad (9)$$

The bubble size (d_b) as function of the bed height has been modeled with the classical Mori–Wen (MW) correlation.[27] Among the reported d_b correlations,[28] the MW equation fits the TS-TZFBR experimental d_b values reasonably well.[9] On the other hand, the bubble fraction (δ) can be directly estimated from the average bed expansion, while the experimental gas velocity distribution, $u_{gas}(z)$, is an input variable related to the TS-TZFBR geometry. Therefore, both the influence of the section change and the additional gas feed at z_{dis} are considered in this modified CCBM model.

In addition, a mass balance of the three-phase system represented in Figure 6a leads to a useful expression to calculate the upward solid fraction (f_1) as a function of the bubble wake fraction, f_w, and the experimental bed expansion, δ (eq 10). Several authors[29−32] assume that the wake fraction in a bubble does not depend on the bubble size and that it represents approximately 20% of the bubble's volume. Thus, a constant f_w = 0.2 has been considered.

$$f_1 = \frac{\delta f_w}{\delta f_w + 1 - \delta} \quad (10)$$

Lastly, the wake-emulsion exchange coefficient (k_w) has been reported to be proportional to the relative gas velocity ($u_r = u_{gas}/u_{mf}$) and inversely proportional to the bubble diameter.[33−35] In this work, the correlation of Lim et al.[35] has been used (eqs 11a and 11b).

$$k_w = \frac{15}{d_b} \quad \text{for } u_r > 3 \quad (11a)$$

$$k_w = \frac{7.5(u_r - 1)}{d_b} \quad \text{for } u_r \le 3 \quad (11b)$$

4. RESULTS AND DISCUSSION

The following subsections illustrate the effect of the different operational variables on the axial mixing of the solids as well as the quality of the modified CCBM model predictions.

4.1. Effect of Gas Velocity on the Solids Mixing. A series of experiments were performed to quantify the effect of the relative gas velocity on the mixing time. Various relative gas velocities ranging from 1.5 to 3.0 were tested in both the regenerative ($u_{r,down}$) and the reactive ($u_{r,up}$) reactor zones. Figure 7 shows the tracer concentration profile for a α = 45° geometry at two different u_r values, 1.5 (Figure 7a) and 3.0 (Figure 7b), and four fluidization times, t = [0−32] s.

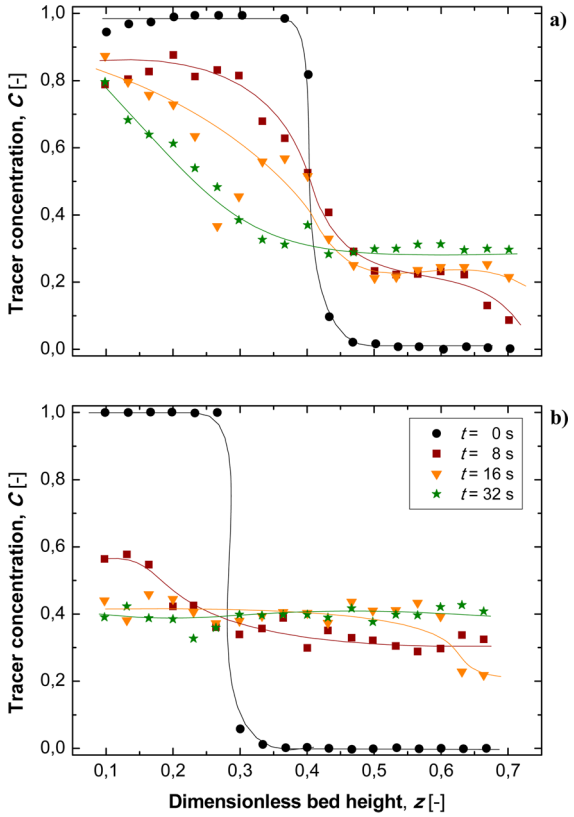

Figure 7. Tracer concentration profiles: (a) $u_{r,up} = u_{r,down} = 1.5$; (b) $u_{r,up} = u_{r,down} = 3.0$.

Figure 7 shows that a higher gas velocity leads to a faster solid mixing, that is, a faster tracer concentration homogenization. This can be observed by comparing Figure 7 panels a and b concentration profiles at the same mixing time, for example, t = 32 s. Since a horizontal data plot represents a completely homogeneous axial tracer concentration, a u_r = 3.0 regime provides an almost full mixing at a fluidization time of 16 s. In the case of u_r = 1.5, complete mixing was not reached after 32 s.

A better way to compare the mixing rates among experiments performed at different operational conditions is the use of the mixing index (MI),[22,25] defined in section 3.1. Figure 8 shows the temporal evolution of MI for four different relative velocities in a pseudo-2D TS-TZFBR with a transition angle α = 60°.

All the tests presented in Figure 8 show a sharp initial particle mixing, which is related to the rapid transition between the fixed and fluidized bed regime when the gas starts to flow through the bed. After the first mixing pulse, it can be observed how a low relative gas velocity (u_r = 1.5) seems not to be able to achieve the full mixing between particles from the reaction and regeneration zones. However, at high gas velocities (u_r = 3.0) the complete mixing was achieved in almost 20s. As expected, a higher gas excess over the minimum fluidization (u_{gas}-u_{mf}) leads to a faster solid mixing and, thus, a better reactor performance can be expected in terms of process integration.

dx.doi.org/10.1021/ie401334x | Ind. Eng. Chem. Res. 2013, 52, 13587−13596

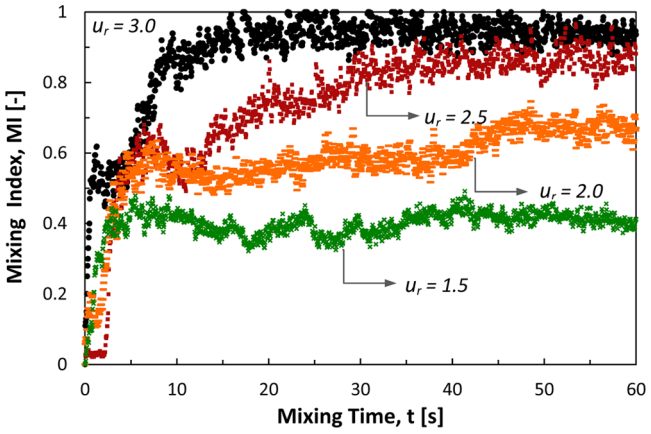

Figure 8. Mixing index in $\alpha = 60°$ TS-TZFBR at relative gas velocities, $u_r = [1.5–3.0]$.

For the phosphorescent particles used, Figure 8 suggests that there is a boundary u_r value from which a full mixing can be achieved. Under this value, the particle mixing can only be partially reached. In this case, the boundary gas velocity can be estimated as $u_r = 2.0$. If the relative gas velocity (or the gas excess) is very low, the fluidization leads to the formation of small bubbles. Therefore, only a few particles can be dragged up in the bubble wake ($f_w \approx 0.2$) and, as a result, a poor solid circulation takes place. As a conclusion, it is advisable to use a gas excess $u_{gas} - u_{mf} > 10$ cm/s in order to favor mixing when working with similar B-type solids.

4.2. Effect of Reactor Geometry on the Solids Mixing. A series of experiments were conducted to study the effect of different reactor geometries on the mixing of the particles. Various transition section angles (α) were tested using the same u_r for both reactor zones. As an example, Figure 9 shows

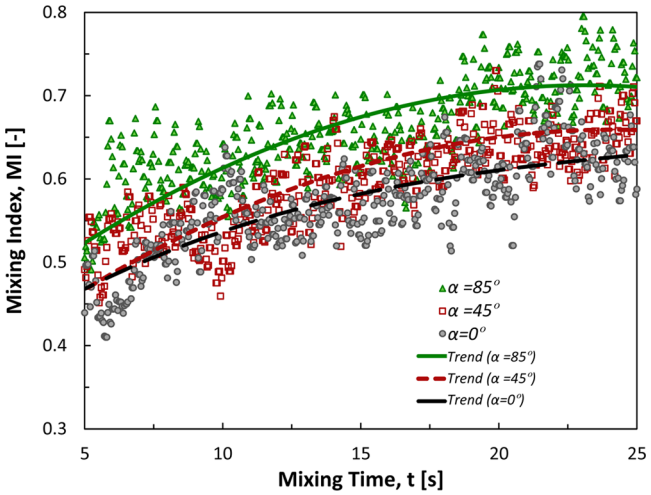

Figure 9. Mixing index at $u_r = 2.5$ for different bed geometries ($\alpha = 0°$, 45°, 85°).

the experimental mixing results obtained for $\alpha = 0°$, 45°, 85°, TS-TZFBR geometries for fluidized particles at $u_r = 2.5$. As discussed in section 4.1, the selected u_r value guarantees a complete mixing regime and can thus be used to carry out a proper comparison among the mixing responses of different reactor configurations.

The experimental results suggest that the influence of the transition angle, α, is not as critical as the relative gas velocity variation in terms of solid mixing. There is, however, a slight MI deviation among the three different mixing trend lines shown in Figure 9. The sharpest transition angle configuration ($\alpha = 0°$) leads to the poorest particle mixing. However, the smoothest transition ($\alpha = 85°$) leads to an almost 10% higher mixing rate. This effect may be related to two causes. First, a smoother transition angle results in a higher local velocity above the upper feed point. This increases the upward velocity of the particles and favors the solid mixing. Second, low α values lead to defluidized regions within the transition section. These "death" regions do not interact with tracer particles coming up from the regeneration section and thus lead to a global MI reduction. The defluidization phenomenon will be discussed in section 4.3.

4.3. Defluidization in TS-TZFBR. Effect of Gas Velocity. The use of phosphorescent particles allows the detection of defluidized regions inside a TS-TZFBR. The "inactive" bed zones may appear on both reactor sides in the lower part of the upper section, when using a sharp transition TS-TZFBR configuration. Here the effect of the gas excess ($u_{gas} - u_{mf}$) on the defluidization angle, β, is described. A series of experiments were conducted varying $u_{gas} - u_{mf}$ in a range of 5–30 $cm^3/(cm^2\ s)$ for a $\alpha = 0°$ geometry. Particles from the upper bed section were also excited with light in this case. Thus, "death" zones appear as segregated tracer regions after a mixing experiment. Figure 10 panels a and b show raw images of a TS-TZFBR in a defluidization experiment ($u_r = 2.0$). Figure 10a shows the initial frame of the experiment, $t = 0$ s (fixed bed), and Figure 10b shows two clearly identified "death" regions after a mixing time, $t = 55$ s.

Figure 10c shows the effect of the gas excess on β. Higher $u_{gas} - u_{mf}$ values, that is, bigger bubbles, lead to a more turbulent solid circulation and thus to a reduction in the defluidized region. The defluidization study provides useful information for choosing and designing the most suitable TS-TZFBR geometry for certain fluidization conditions. The generation of defluidized regions could represent a serious problem in a large scale operation. Therefore, the transition angle, α, plays a key role in a TS-TZFBR and must be carefully selected to avoid defluidization effects in such a scale-up operation. As an example, it has been previously established[9] that a proper optical tracer circulation can be achieved at $u_r \geq 2.5$ ($u_{gas} - u_{mf} \geq 15$ cm/s). In such conditions, the experimental defluidization angle reaches $\beta \approx 60°$ for this kind of particle. Therefore, a smooth TS-TZFBR geometry (e.g, a conservative value such as $\alpha \approx 80°$) should be recommended in order to avoid unmixed particles.

4.4. Effect of Secondary Gas Inlet Position. The axial location of the upper gas entry with respect to the tapered section position determines the fluid dynamic performance of the TS-TZFBR. Several experiments were conducted to evaluate the effect of the immersed gas distributor position on the solid mixing. It has been observed that the distributor position strongly affects the solid circulation. When the immersed distributor was located 2 cm above the beginning of the tapered section ($z^* = z_{dis} - z_{sc} = 2$ cm), two main problems were observed. Figure 11 illustrates these two findings for different transition angles, $\alpha = [60°, 80°]$. First, the defluidized regions increased (Figure 11 panels a and b). Second, a short-circuit in the solid recirculation ($u_r < 2.0$) related to the formation of bubble "slugs" appeared (Figure 11

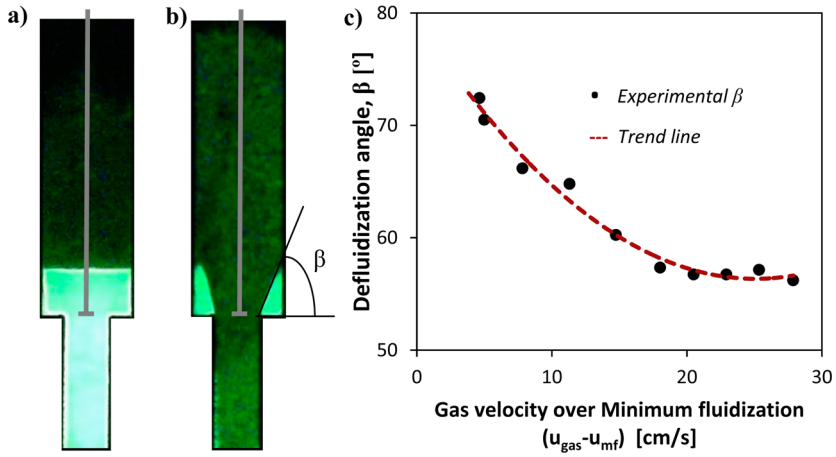

Figure 10. Defluidization angle experiments (z^* = 0 cm): (a) mixing time, t = 0 s; (b) mixing time, t = 55 s; (c) effect of $u_{gas} - u_{mf}$ on the defluidization angle in α = 0° geometry. Trendline is for visual help.

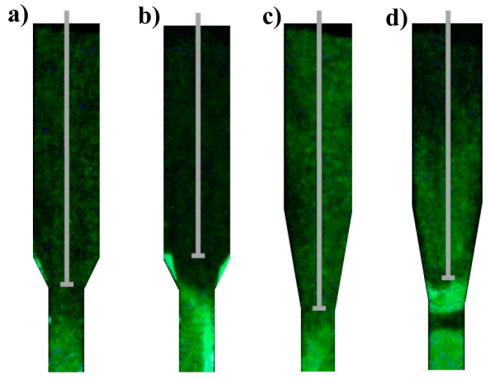

Figure 11. Effect of the immersed distributor location on the solid circulation: u_r = 2.0, (a,b) α = 60°, (c,d) α = 80°, (a,c) z^* = 0 cm, (b,d) z^* = 2 cm.

panels c and d). This second effect has already been reported[36] for a similar system but in which an additional gas feed was not used.

In the case of Figure 11b, an incipient defluidization appears under the distributor. This leads to poor mixing between illuminated and dark particles. Besides, defluidized regions start to be formed on both sides of the transition section. In the case of Figure 11d, a short-circuit in the solid recirculation can clearly be seen. The gas slug that occupies the whole bed section impedes the particle exchange between the upper and lower bed sections. Therefore, the optimal distributor location was found to be the beginning of the bed section enlargement (z^* = 0 cm). This location provides a good solid circulation and reduces defluidization and short-circuiting problems.

4.5. CCBM Model Validation. The experimental series provided useful information about the effect of several process variables on the solid circulation. However, the performance and postprocessing of mixing experiments is very time-consuming. Therefore, the implementation of a particle axial mixing model, for example, the modified CCBM model, could become a powerful tool to easily predict the TS-TZFBR mixing behavior and reduce the experimental effort.

To validate the proposed axial mixing model, the multiparametric CCBM (u_1, f_1, k_w) was first tested. The purpose was to find the most suitable combination of the three parameters involved (u_1, f_1, and k_w) to fit the experimental mixing results. Figure 12a shows a comparison between the experimental

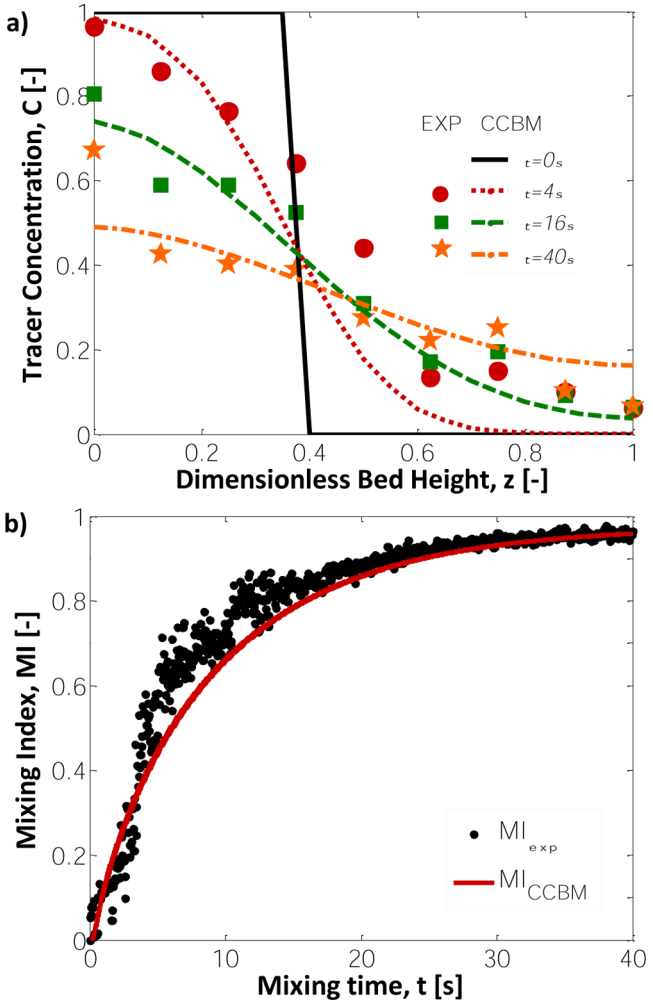

Figure 12. Comparison between experimental results and CCBM model for α = 45°, u_r = 2.5, and z^* = 0 cm: (a) tracer concentration profiles; (b) solid mixing index.

tracer concentration profile at certain operational conditions ($u_{r,down} = u_{r,up}$ = 2.5, α = 45° and z^* = 0) and the CCBM three-parameter model fitting. Figure 12b shows the fitting quality of the experimental and modeled mixing index.

dx.doi.org/10.1021/ie401334x | Ind. Eng. Chem. Res. 2013, 52, 13587−13596

Both panels a and b of Figure 12 show relatively good agreement in terms of model fitting (regression coefficient, r^2 = 0.85). The CCBM circulation model seems to be able to reproduce the experimental tracer concentration profiles. The high agreement between model predictions and experiments for the conditions presented in Figure 12 was achieved for almost all the tested experimental conditions. However, the model solution frequently led to nonrepresentative values for the three considered parameters. Depending on the selected initial values to start up the algorithm, $[u_{1,0}, f_{1,0}, k_{w,0}]$, several fitting solutions with similar regression coefficients could be found. For instance, in the experimental conditions of Figure 12, two different parameter combinations led to similar fittings: $[u_1, f_1, k_w]_1$ = [6.43 cm/s, 0.14, 2.47 s^{-1}] and $[u_1, f_1, k_w]_2$ = [2.62 cm/s, 0.33, 0.67 s^{-1}]. This suggests that the three model parameters are related to each other, as discussed by Grasa and Abanades.[25] Although both solutions result in reasonable values for the upward solid fraction, f_1, the particle upward velocity, $\overline{u}_1$, in the second solution was substantially lower than the experimental average bubble velocity ($\overline{u}_b$ = 20.7 cm/s) in the tested conditions. Moreover, the k_w exchange rate in this case remains far from the range reported in the literature.[25] Therefore, to avoid uncertain and unrealistic solutions, the most accurate way to estimate these three CCBM model parameters is the use of the widely accepted hydrodynamic correlations presented in section 3.2.

Figure 13 shows a comparison between the experimental results and the CCBM model prediction using hydrodynamic correlations to estimate u_1, f_1, and k_w. The model fitting is still reasonably good (r^2 = 0.72), but the parameter values are now in agreement with those expected for the tested experimental conditions: $[u_1, f_1, k_w]$ = [7.49 cm/s, 0.07, 8.03 s^{-1}]. Moreover, the model could predict the "complete mixing time" (CM_t) precisely. For instance, in the case of Figure 13b the experimental CM_t is around 25 s, whereas the model prediction indicates a mixing index MI = 96% at that time.

The estimated values of each model parameter vary with the applied relative gas velocity and TS-TZFBR geometry, as can be observed in Figure 14. As a general trend, a higher u_r leads to higher upward velocities, faster solid exchange between the wake and emulsion phases and a bigger upflow of solid fractions. The u_1 values are among 0.4−0.7 times the gas excess velocity. The phase exchange coefficient is of the same order as the particle upward velocity and the solid fraction within the wake phase is around 8−10% in all cases. The regression coefficients range approximately between 0.6 and 0.75 for all the experimental tests in terms of MI fitting. This represents reasonably good regressions, taking into account both the simplicity of the model and the fact that the fitted data cloud consisted of almost 5000 experimental MI values.

The great advantage of this nonparametric CCBM model is the ability to predict the experimental axial mixing of particles using only hydrodynamic correlations from the literature and the operational conditions (TS-TZFBR configuration and solid properties).

5. CONCLUSIONS

The fluid dynamics properties of the dense phase have been studied for a pseudo-2D TS-TZFBR configuration. The use of phosphorescent particles as optical tracers allowed the study of the solid axial mixing, which represents a key factor in the TS-TZFBR performance.

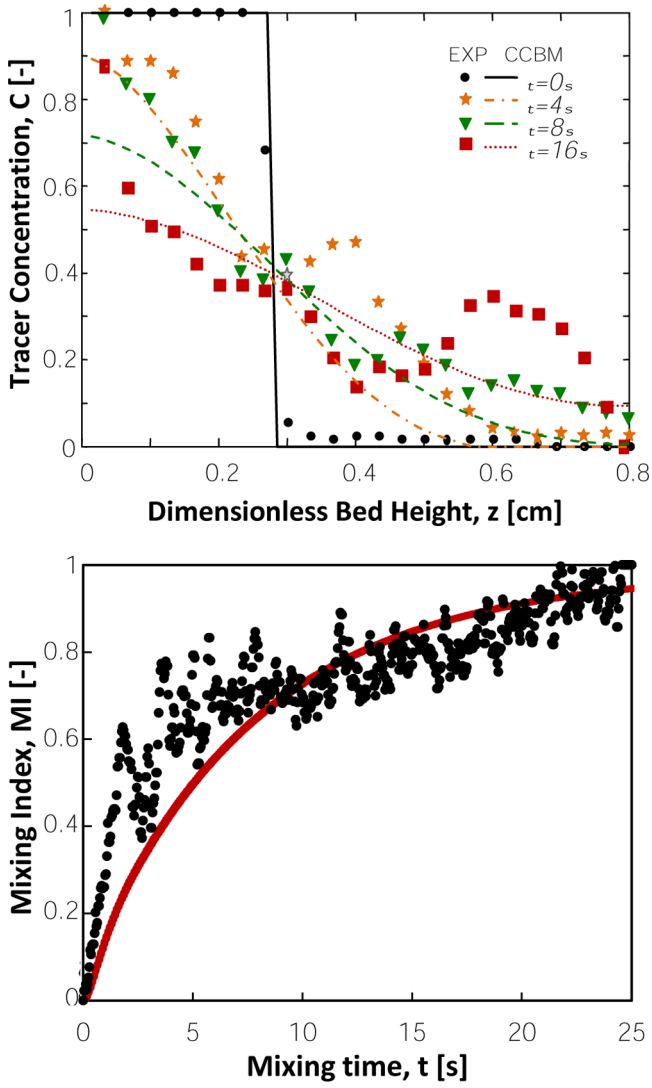

Figure 13. Comparison between experimental results and CCBM model without adjustable parameters for α = 85°, u_r = 2.5, and z^* = 0 cm: (a) tracer concentration profiles; (b) solid mixing index.

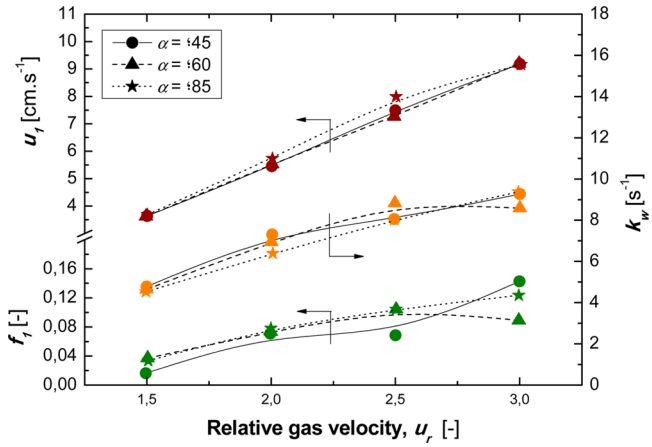

Figure 14. Estimated CCBM model parameters (u_1, f_1, k_w) from hydrodynamic correlations as a function of the relative gas velocity and the TS-TZFBR geometry: z^* = 0 cm.

The solid mixing rate was strongly dependent on the relative gas velocity in both the regenerative and reactive bed zones.

dx.doi.org/10.1021/ie401334x | Ind. Eng. Chem. Res. 2013, 52, 13587−13596

The axial mixing degree was followed quantitatively by means of the so-called "mixing index".

In certain fluidization conditions, a sharp transition section between the reactor zones may generate defluidized regions above the section change. The application of a α = 80° TS-TZFBR configuration will usually prevent "death" bed zones.

The optimal location of the immersed gas distributor is close to the beginning of the section change. When located far from the section enlargement, some fluidization problems may be found.

Despite its simplicity, the CCBM was found to be a suitable model to predict the solid axial mixing in a nonconventional fluidized bed. The use of empirical bubbling bed correlations coupled with the CCBM model led to a reasonably good prediction of the experimental TS-TZFBR mixing behavior.

AUTHOR INFORMATION

Corresponding Author

*Tel.: +34 976761152. E-mail: qtmiguel@unizar.es.

Notes

The authors declare no competing financial interest.

ACKNOWLEDGMENTS

Financial support from the *Spanish Ministerio de Economía y Competitividad* (MINECO), through Project CTQ2010-15568, is gratefully acknowledged. Financial aid for the maintenance of the consolidated research group CREG has been provided by the *Fondo Social Europeo* (FSE) through the *Gobierno de Aragón*, Aragón, Spain.

NOTATION

α = transition section angle, [deg]
β = defluidization angle, [deg]
δ = bed bubble fraction, i.e. gas hold-up, [−]
ρ_{bulk} = bed density, [g/cm^3]
C_1 = tracer concentration in the upward phase, [−]
C_2 = tracer concentration in the downward phase, [−]
C_∞ = tracer concentration in a full mixed bed, [−]
$\overline{C}_{z,t}$ = normalized transient tracer concentration at a bed height z [−]
CCBM = counter-current back-mixing model
CM_t = complete mixing time, [s]
d_b = equivalent bubble diameter, [cm]
$d_{b,MW}$ = bubble diameter estimated by 'Mori and Wen' correlation, [cm]
d_p = particle diameter, [μm]
DH = 'Davidson and Harrison' correlation for $u_b(d_b)$
f_1 = upward solid fraction, [−]
f_w = bubble wake fraction, [−]
$\overline{I}_{max}$ = maximum image signal (grayscale index) for initial tracers emissivity, [−]
$\overline{I}_{min}$ = minimum image signal (grayscale index) for nonexcited tracers, [−]
$\overline{I}_{z,t}$ = average image signal (grayscale index) at certain height (z) and time (t), [−]
KL = 'Kunii and Levenspiel' correlation for $u_1(u_b)$
k_w = mass exchange coefficient between wake and emulsion particles, [s^{-1}]
L_I = luminance intensity, [mcd/m^2]
MI = mixing index, [−]
MW = 'Mori and Wen' correlation for $d_b(z)$
r^2 = regression coefficient between experimental MI and model prediction, [−]
t = fluidization time, [s]
TS-TZFBR = two-section two-zone fluidized bed reactor
TZFBR = straight two-zone fluidized bed reactor
u_1 = wake upward velocity, [cm/s]
$\overline{u_1}$ = average wake upward velocity, [cm/s]
u_b = bubble velocity, [cm/s]
u_{gas} = fluidization gas velocity, [cm/s]
u_{mf} = minimum fluidization velocity, [cm^3/cm^{2}s]
u_r = relative gas velocity, [−]
$u_{r,down}$ = relative gas velocity at the 'regenerative' bed zone, [−]
$u_{r,up}$ = relative gas velocity at the 'reactive' bed zone, [−]
z = vertical bed position, [cm]
z* = distance between immersed distributor and section change location, [cm]
z_{dis} = vertical location of the immersed gas distributor from the bottom, [cm]
z_{ilum} = nondimensional height of the initially illuminated bed front face, [-]
z_{max} = nondimensional maximum bed height, [−]
z_{sc} = vertical location of the TS-TZFBR section change, [cm]

REFERENCES

(1) Menéndez, M.; Herguido, J.; Tellez, C.; Soler, J.; Gimeno, M. P. Two zone fluidized bed reactor. Spanish Patent Application P200801857, 2008.

(2) Herguido, J.; Menéndez, M.; Santamaría, J. On the use of fluidized bed catalytic reactors where reduction and oxidation zones are present simultaneously. *Catal. Today* **2005**, *100*, 181−189.

(3) Gimeno, M. P.; Wu, Z. T.; Soler, J.; Herguido, J.; Li, K.; Menéndez, M. Combination of a Two-Zone Fluidized Bed Reactor with a Pd hollow fibre membrane for catalytic alkane dehydrogenation. *Chem. Eng. J.* **2009**, *155*, 298−303.

(4) Soler, J.; Téllez, C.; Herguido, J.; Menéndez, M.; Santamaría, J. Modelling of a two-zone fluidised bed reactor for the oxidative dehydrogenation of *n*-butane. *Powder Technol.* **2001**, *120*, 88−96.

(5) Gascón, J.; Téllez, C.; Herguido, J.; Menéndez, M. A two-zone fluidized bed reactor for catalytic propane dehydrogenation. *Chem. Eng. J.* **2005**, *106*, 91−96.

(6) Lobera, M. P.; Tellez, C.; Herguido, J.; Menéndez, M. Propane dehydrogenation over Pt-Sn-K/γ-Al_2O_3 catalyst in a two-zone fluidized bed reactor. *Ind. Eng. Chem. Res.* **2008**, *47*, 9314−9320.

(7) Pérez-Moreno, L.; Soler, J.; Herguido, J.; Menéndez, M. Stable steam reforming of ethanol in a two zone fluidized bed reactor. *Ind. Eng. Chem. Res.* **2012**, *51*, 8840−8848.

(8) Gimeno, M. P.; Soler, J.; Herguido, J.; Menéndez, M. Counteracting catalyst deactivation in methane aromatization with a two zone fluidized bed reactor. *Ind. Eng. Chem. Res.* **2010**, *49*, 996−1000.

(9) Julián, I.; Gallucci, F.; van Sint Annaland, M.; Herguido, J.; Menéndez, M. Coupled PIV/DIA for fluid dynamics studies on a two-section two-zone fluidized bed reactor. *Chem. Eng. J.* **2012**, *207*, 122−132.

(10) Norouzi, H. R.; Mostoufi, N.; Mansourpour, Z.; Sotudeh-Gharebagh, R.; Chaouki, J. Characterization of solids mixing patterns in bubbling fluidized beds. *Chem. Eng. Res. Des.* **2011**, *89*, 817−826.

(11) Laverman, J. A.; Fan, X.; Ingram, A.; van Sint Annaland, M.; Parker, D. J.; Seville, J. P. K.; Kuipers, J. A. M. Experimental study on the influence of bed material on the scaling of solids circulation patterns in 3D bubbling gas-solid fluidized beds of glass and polyethylene using positron emission particle tracking. *Powder Technol.* **2012**, *224*, 297−305.

(12) Mostoufi, N.; Chaouki, J. On the axial movement of solids in gas-solid fluidized beds. *Chem. Eng. Res. Des.* **2000**, *78*, 911−920.

(13) Mostoufi, N.; Chaouki, J. Local solid mixing in gas-solid fluidized beds. *Powder Technol.* **2001**, *114*, 23−31.
(14) Cody, G. D.; Goldfarb, D. J.; Storch, G. V.; Norris, A. N. Particle granular temperature in gas fluidized beds. *Powder Technol.* **1996**, *87*, 211−232.
(15) Godfroy, L.; Larachi, F.; Kennedy, G.; Grandjean, B.; Chaouki, J. On-line flow visualization in multiphase reactors using neural networks. *Appl. Radiat. Isotopes* **1997**, *48*, 225−235.
(16) Bellgardt, D.; Werther, J. A novel method for the investigation of particle mixing in gas-solid systems. *Powder Technol.* **1986**, *48*, 173−180.
(17) Werther, J. Measurement techniques in fluidized beds. *Powder Technol.* **1999**, *102*, 15−36.
(18) Lim, K. S.; Zhu, J. X.; Grace, J. R. Hydrodynamics of gas-solid fluidization. *Int. J. Multiphase Flow* **1995**, *21*, 141−193.
(19) Agarwal, P. K., Hull, A. S., Lim, K. S., Eds. Digital Image Analysis techniques for the study of bubbling fluidized beds. *Non-invasive Monitoring of Multiphase Flows*; Elsevier Science: Amsterdam, 1996; Chapter 12, pp 407−454.
(20) Lobera, M. P.; Téllez, C.; Herguido, J.; Menéndez, M. Pt-Sn/$MgAl_2O_4$ as *n*-butane dehydrogenation catalyst in a two-zone fluidized-bed reactor. *Ind. Eng. Chem. Res.* **2009**, *48*, 6573−6578.
(21) Medrano, J. A.; Julián, I.; García-García, F. R.; Li, K.; Herguido, J.; Menéndez, M. Two-zone fluidized bed reactor (TZFBR) with palladium membrane for catalytic propane dehydrogenation: experimental performance assessment. *Ind. Eng. Chem. Res.* **2013**, *52*, 3723−3731.
(22) Abanades, J. C.; Grasa, G. S. Modeling the axial and lateral mixing of solids in fluidized beds. *Ind. Eng. Chem. Res.* **2001**, *40*, 5656−5665.
(23) Grasa, G.; Abanades, J. C.; Oakey, J. Investigation of the solid flow between two fluidized beds connected by an orifice. *Chem. Eng. Sci.* **2004**, *59*, 5869−5872.
(24) Gwyn, J. E.; Moser, J. H.; Parker, W. A. A three-phase model for gas-fluidized beds. *Chem. Eng. Prog. Symp. Ser.* **1970**, *66*, 19−27.
(25) Grasa, G.; Abanades, J. C. The use of two different models to describe the axial mixing of solids in fluidized beds. *Chem. Eng. Sci.* **2002**, *57*, 2791−2798.
(26) Davidson, J. F.; Harrison, D. The behaviour of a continuously bubbling fluidized bed. *Chem. Eng. Sci.* **1966**, *21*, 731−738.
(27) Mori, S.; Wen, C. Y. Estimation of bubble diameter in gaseous fluidized beds. *AIChE J.* **1975**, *21*, 109−115.
(28) Karimipour, S.; Pugsley, T. A critical evaluation of literature correlations for predicting bubble size and velocity in gas−solid fluidized beds. *Powder Technol.* **2011**, *205*, 1−14.
(29) Rowe, P. N.; Partridge, B. A. An X-ray study of bubbles in fluidized beds. *Trans. Inst. Chem. Eng.* **1965**, *43*, 157−175.
(30) Kozanoglu, B.; Levy, E. K. Wake fractions of small bubbles in gas fluidized beds. *Powder Technol.* **1991**, *68*, 285−286.
(31) Basesme, E. A.; Levy, E. K. Solids exchange between the bubble wake and the emulsion phase in a two-dimensional gas-fluidized bed. *Powder Technol.* **1992**, *72*, 45−50.
(32) Sane, S. U.; Haynes, H. W.; Agarwal, P. K. An experimental and modeling investigation of gas mixing in bubbling fluidized beds. *Chem. Eng. Sci.* **1996**, *51*, 1133−1147.
(33) Hull, A. S.; Chen, Z.; Agarwal, P. K. Influence of horizontal tube banks on the behavior of bubbling fluidized beds: 2. Mixing of solids. *Powder Technol.* **2000**, *111*, 192−199.
(34) Chiba, T.; Kobayashi, H. Gas exchange between the bubble and emulsion phases in fluidized beds. *Chem. Eng. Sci.* **1970**, *25*, 1375−1385.
(35) Lim, K. S.; Gururajan, V. S.; Agarwal, P. K. Mixing of homogeneous solids in bubbling fluidized beds: Theoretical modeling and experimental investigation using digital image analysis. *Chem. Eng. Sci.* **1993**, *48*, 2251−2265.
(36) Corella, J.; Bilbao, R. Fluid dynamic study of a new type of solid gas contactor. The fluidized fixed or fluidized-bed. *Ind. Eng. Chem. Proc. Des. Dev.* **1982**, *21*, 545−550.

Artículo II

I. Julián, F. Gallucci, M. v. Sint Annaland, J. Herguido, M. Menéndez,
Coupled PIV/DIA for fluid dynamic studies on a Two-Section Two-Zone Fluidized Bed Reactor,
Chem. Eng. J. 207 – 208 (2012) 122 – 132.

Chemical Engineering Journal 207–208 (2012) 122–132

Contents lists available at SciVerse ScienceDirect

Chemical Engineering Journal

journal homepage: www.elsevier.com/locate/cej

Coupled PIV/DIA for fluid dynamics studies on a Two-Section Two-Zone Fluidized Bed Reactor

I. Julián [a,*], F. Gallucci [b], M. van Sint Annaland [b], J. Herguido [a], M. Menéndez [a]

[a] Catalysis, Molecular Separations and Reactor Engineering Group (CREG), Aragon Institute of Engineering Research (I3A), Universidad de Zaragoza, 50018 Zaragoza, Spain
[b] Multiphase Reactors Group, Department of Chemical Engineering and Chemistry, Eindhoven University of Technology, P.O. Box 513, 5612 AZ Eindhoven, The Netherlands

HIGHLIGHTS

- Digital Image Analysis and Particle Image Velocimetry have been applied to 2D fluidized beds.
- The bed has two sections and two gas feed points.
- Four different solids have been employed.
- Several gas velocities and transition zone angle studied.
- Bubble diameter and velocity profiles and solid velocity profiles have been obtained.

ARTICLE INFO

Article history:
Available online 19 June 2012

Keywords:
Fluidization
Bubble analysis
Particle Image Velocimetry
Defluidization zone detection

ABSTRACT

The Two-Zone Fluidized Bed Reactor (TZFBR) is an effective solution to integrate reactions and catalyst regeneration in a single fluidized bed reactor. In the present study an experimental investigation on the fluid dynamics of a Two Section TZFBR is presented. Bubble and particle fluidization properties have been analyzed for this new reactor concept using a combination of two non-invasive techniques, viz. Digital Image Analysis (DIA) coupled with Particle Image Velocimetry (PIV) in a pseudo-2D TS-TZFBR. Results show how the reactor geometry affects the average equivalent bubble diameter and bubble velocity profiles, as well as the particle circulation patterns (between the two zones). It has been found that channeling and local defluidization phenomena are strongly influenced by the particle diameter, which therefore plays a key role in the design of an optimal geometry of a TS-TZFBR.

1. Introduction

The Two-Zone Fluidized Bed Reactor (TZFBR) provides a high level of process integration, allowing chemical reaction and, in situ, continuous catalyst regeneration inside a single fluidized bed (Fig. 1a). This novel reactor concept is based on the generation of two different atmospheres inside a single vessel, due to a separated gas inlet for each of the two gaseous reactants. A reactive gas is fed into the reactor at an intermediate point of the catalyst bed, while an oxidizing agent flows up from the bottom of the reactor [1]. The desired reaction (e.g. catalytic dehydrogenation) is carried out within the upper reactor zone, leading to catalyst deactivation via coke deposition over the catalyst surface. At the same time, a diluted oxygen feed from the bottom regenerates the partially deactivated catalyst by burning the coke generated in the upper zone, which covers the catalytic active sites. The circulation of solids between both zones, caused by the action of gas bubbles, provides a steady state operation. The TZFBR operation has been successfully tested for several dehydrogenation reactions (e.g., propane and butane dehydrogenation), as well as in ethanol reforming, employing different catalysts [2–6]. The use of TZFBR is especially effective to overcome deactivation problems due to coke formation on the catalyst surface, which represents a characteristic phenomenon in this type of reactions.

In order to maintain similar fluidization behavior in both reactor zones, a new TZFBR design has been proposed. It incorporates two sections with different cross-sectional area to allow small flow rates in the regeneration zone when required [7]. The reactor geometry, e.g. the transition angle α between the two zones (Fig. 1b) in this Two Section-Two Zone Fluidized Bed Reactor (TS-TZFBR), has a significant effect on the performance of this reactor.

To achieve proper process integration, both reaction and catalyst regeneration must take place continuously and at the same time. Therefore, particle circulation between bed zones determines the process efficiency. For this reason, in order to design and optimize this novel TS-TZFBR, a better understanding of the fluidization phenomena occurring inside the reactor is required.

* Corresponding author. Tel.: +34 976 765486; fax: +34 976 761879.
E-mail address: ijulian@unizar.es (I. Julián).

1385-8947/$ - see front matter © 2012 Elsevier B.V. All rights reserved.
http://dx.doi.org/10.1016/j.cej.2012.06.015

Nomenclature

α	physical transition angle between reactor zones (°)
β	defluidization angle over the section change (°)
δ	bubble fraction inside a fluidized bed (–)
ρ_s	solid density (g/cm^3)
A_i	bubble area (pixels)
d_b	bubble diameter (cm)
$d_{b,eq}$	equivalent bubble diameter (cm)
di	differential reactor radial coordinate (cm)
h_{dist}	orifice distributor height with respect to the bottom plate distributor (cm)
m_{up}	average particle upward mass (bubble wake) (kg)
m_{down}	average particle downward mass (emulsion) (kg)
m_i	particle mass related to the reactor radial position i (kg/s)
rr	resolution ratio (cm^2/pixels)
u_b	bubble velocity (cm/s)
u_{gas}	gas velocity (cm/s)
u_{mf}	minimum fluidization velocity (cm/s)
$u_{r,up}$	relative gas velocity (u_{gas}/u_{mf}) in the upper constant section bed zone (–)
$u_{r,down}$	relative gas velocity (u_{gas}/u_{mf}) in the lower bed zone (–)
u_s	upward particle velocity (cm/s)
v_i	axial particle average velocity related to reactor radial position i (cm/s)
thr	threshold value for bubble detection (–)
z	axial reactor coordinate (cm)

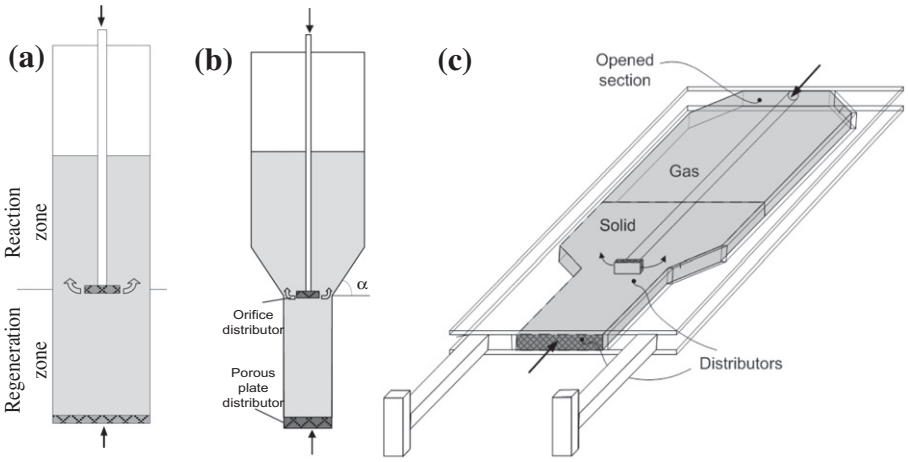

Fig. 1. (a) Scheme of a 3D-TZFBR, (b) scheme of a 3D-TS-TZFBR, (c) 2D TS-TZFB facility.

In particular, detailed information on the solids fluxes between the two bed zones is required to optimize the reactor geometry and operation. The exchange of particles between the two zones is strongly related to the bubble properties and induced solids circulation patterns.

In the past, numerous studies on bubbling fluidized beds have been performed and several analysis techniques have been developed to describe bubble formation, evolution and properties [8–13]. A number of researchers have also studied the influence of these factors on particle circulation, both with invasive and non-invasive techniques, as can be observed in some recent reviews [14,15]. However, the differences in feed configuration and reactor geometry of the TS-TZFBR as compared to conventional fluidized beds make direct application of the experimental results from these studies unsuitable for the TS-TZFBR.

In this work, an experimental investigation into the fluidization characteristics of a TS-TZFBR is presented. For that purpose, a combination of two optical non-invasive techniques has been used to study the fluid dynamics of a cold pseudo-2D TS-TZFBR facility. The applied techniques are Particle Image Velocimetry (PIV) and Digital Image Analysis (DIA). The use of an Ultrafast High Resolution Camera to perform PIV provides particle tracking (high resolution) and particle motion detection (high velocity) [16–18]. Moreover, an in-house developed image post-processing algorithm (DIA) allowed bubble detection and the possibility to perform a statistical hydrodynamic analysis. The coupled PIV–DIA represents a powerful tool to carry out a detailed fluid dynamic study [16].

The main advantages of the optical techniques are their simple implementation and the large amount of valuable data that can be obtained from the recorded images. Moreover, PIV/DIA allows collecting a simultaneous unique combination of solid velocity pattern and bubble size (distribution) data. On the other hand, the visual techniques are restricted to the study of two dimensional fluidized beds because they need visual access to the bed [8]. It implies that this technique may not be fully representative of what happens in an axial cut of a three dimensional TS-TZFBR. Thus, some quantitative differences between 2D and 3D fluidization characteristics may exist, e.g. different bubble size and bubble velocity [19,20]. However, the TS-TZFBR main fluidization characteristics can be qualitatively obtained by the coupled PIV/DIA technique. The reactor performance limitations can be checked by analyzing some key factors such as gas velocity or reactor geometry.

The reported results are referring to experimental observations through the reactor front wall. In order to minimize the wall effect on the fluid dynamics analysis, the reactor geometry has been carefully chosen according to literature recommendations [21]. The bed depth is significantly shorter than its height and width. Thus, a pseudo 2D analysis can be performed and the velocity profiles along the bed depth can be neglected in comparison to those related to reactor height or width.

Table 1
List of solid particles.

	d_p (μm)	ρ_{bulk} (g/cm^3)	ε_{packed} (−)	u_{mf} (cm/s)
Glass beads	500 ± 50	1.5	0.40	20.5
γ-Alumina	130 ± 30	0.8	0.47	1.2
Phosphorescent particles A	200 ± 100	1.5	0.58	10.1
Phosphorescent particles B	500 ± 50	1.3	0.64	48.5

Further image post-treatment (DIA) was performed to carry out a statistical analysis of bubble size and bubble growth rate for different operating conditions. Therefore, an experimental investigation into the fluid dynamics of a pseudo-2D TS-TZFBR is presented. Both bubble and particle properties have been analyzed for this new reactor concept.

The aim of this study is to apply this analysis technique in order to understand and quantify the fluidization characteristics of a TS-TZFBR.

2. Experimental set-up

Experiments have been carried out in a Perspex pseudo-2D TS-TZFBR with the following dimensions (height × width × depth): 300 mm × 40 mm × 8 mm. Compressed air was used as fluidization gas. Four Geldart B particle types of different particle diameter and/or density (γ-alumina, glass beads and optical tracers) were used to test five different reactor geometries. Those geometries differ in their transition angles, α, ranging from 0° to 85°, with respect to the horizontal. The lower gas distributor consisted of a porous glass plate, while the upper gas distributor was T-shaped with two orifices (2 mm diameter), symmetrically set with respect to the bed center (Fig. 1). Table 1 shows the main fluidization characteristics of the solid particles used in this work: bulk density, packed porosity, average diameter and minimum fluidization velocity. The materials and size distributions were selected to study the influence of particle diameter, solid densities and morphologies (particle sphericity, e.g. packing fraction) on the fluidization characteristics, i.e. particle circulation and bubbling behavior. As Table 1 shows, the use of particles of different size and density leads to significantly different minimum fluidization velocities, calculated in air at 298 K [22]. All the particles tested were commercial solids. Phosphorescent particles, used as optical tracers in further studies, consisted of commercial solids based on strontium aluminate (Eu–Dy/$SrAl_2O_4$, ρ_s = 3.6 g/cm^3).

The image acquisition set-up consisted of two LED lamps and a high speed–high resolution camera (*LaVision Imager Pro*) connected to a software package (*DaVis 7.0*) for image post-processing and PIV analysis (Fig. 2). The recording frequency was fixed at 500 fps in order to obtain short delayed subsequent frames (2 ms). Also, a sufficiently long video sequence was recorded to quantify representative solid circulation and bubbling results. The recording time was fixed at 40 s (20,000 frames/video). The frame resolution was adjusted to 28 pixel/cm so that each single particle could be detected with a resolution of at least 4 pixels. This value represents a lower bound to carry out a proper PIV analysis. The interrogation area for PIV analysis was fixed to 16 × 16 pixels and a cross-correlation was used to obtain the PIV results.

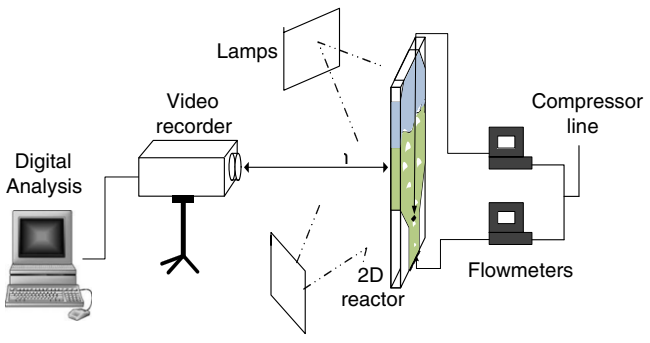

Fig. 2. Image acquisition set-up.

In case of glass beads studies, some particle–wall sticking problems were found when fluidizing with dry air. This effect has been widely reported [24–27]. Several authors [28–30] found that powder flowability can be enhanced by increasing gas humidity in fluidized beds, due to the reduction of electrostatic and cohesive forces. In this work, two water bottles were placed prior to the reactor inlet in order to humidify the feed air and overcome the sticking effect. To keep the relative humidity constant in all test runs, the water content and the gas jet position inside the bottle were carefully measured. Experiments were performed at the same temperature. Besides, in order to avoid light reflections, the glass tube of the upper air distributor was covered with a black tape.

For each particle type, the experiments consisted of evaluating the influence of three different system variables on the TS-TZFBR fluidization characteristics: the relative gas velocity at each of the two reactor feed points ($u_r = u_{gas}/u_{mf}$) and the transition angle between the reactor zones (α). The relative gas velocity in both the reaction ($u_{r,up}$) and regeneration ($u_{r,down}$) zones was tested ranging from values close to minimum fluidization velocity (u_r = 1.1) to almost four times u_{mf}. This velocity range was selected to meet two operational purposes. First, the bed has to be completely fluidized, allowing catalyst particle mixing between the bed zones. Second, large residence times favor higher chemical conversions, so moderate gas velocities are required. Moreover, higher $u_{r,up}$ values are avoided in order to maintain a gas flow without significant backmixing in the emulsion phase. That is, maintaining the independence of the atmospheres of each zone in this reactor configuration. For studying defluidization phenomena related to the transition angle between the catalytic bed zones, five reactor geometries were tested. The studied transition angles, α, were 0°, 45°, 60°, 80°, 85° with respect to the horizontal.

3. Analysis procedure

Several DIA functions have been developed with the aid of the Image Processing Toolbox® (Matlab R2010a® to carry out image post-processing. Specifically, two different algorithms have been implemented to perform a hydrodynamics analysis and a 'particle raining' filter.

3.1. Hydrodynamics analysis algorithm

This algorithm consists of a function to detect bubbles and calculate their growing rate and velocity as a function of the vertical position in the bed.

3.1.1. Bubble detection

Bubbles are firstly detected via a black and white thresholding in the recorded images. For each bubble, the centroid coordinates

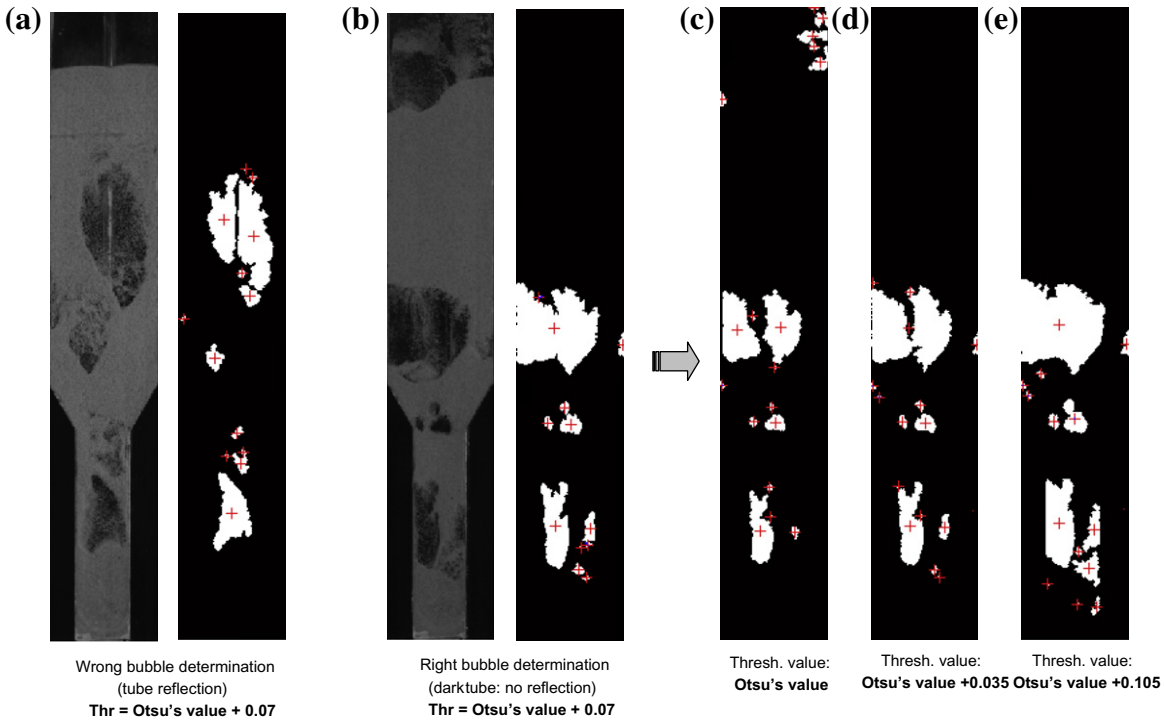

Fig. 3. Threshold selection for bubble detection. (a) Raw vs. thresholded image. Effect of light reflection. (b) Raw vs. thresholded image. Proper bubble detection: thr = Otsu's + 0.07. (c) Thresholded image, thr = Otsu's. (d) Thresholded image, thr = Otsu's + 0.035. (e) Thresholded image, thr = Otsu's + 0.105.

and the bubble area (in pixels) are saved. The key point in bubble detection is the selection of an accurate threshold value. This value depends on the bed illumination and the image contrast between the dense phase and the bubbles [8]. Matlab R2010a® has its own tool to apply a 'proper' threshold value based on Otsu's method. However, such value seemed to underestimate the bubble size according to our observations. After a careful observation of the recorded images, a threshold thr = [Otsu's value + 0.07] has been selected. This value seems to provide good bubble edge detection (Fig. 3). Initially, the light reflection produced by the immersed gas distributor lead to a wrong bubble edge determination in the upper part of the bed (Fig. 3a). This effect could be removed by covering the distributor tube with a black tape, as previously described (Fig. 3b–e).

3.1.2. Bubble size analysis

By analyzing all recorded frames in a video sequence, a statistical analysis of the average bubble size can be carried out as a function of the vertical position in the bed. For this purpose, the obtained bubble area (pixels) is transformed to an equivalent

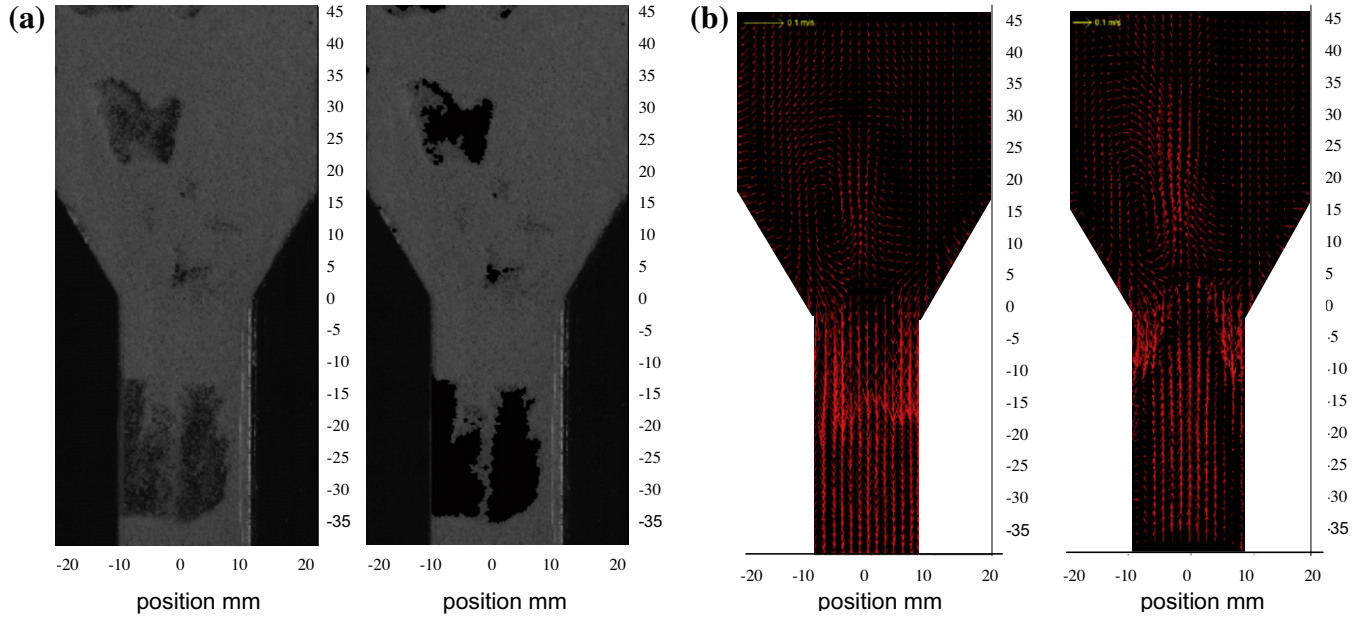

Fig. 4. Effect of 'particle raining' filter on PIV results. (a) Raw image vs. filtered image. (b) PIV results: particle average velocity vector plot from raw data vs. from filtered images.

bubble diameter ($d_{b,eq}$). The $d_{b,eq}$ represents the diameter of a circle (sphere in a 3D analysis), which area corresponds to the experimental bubble area. Eq. (1) shows how $d_{b,eq}$ was calculated from area measurements. The 'resolution ratio' (rr) represents the ratio cm^2/pixels of the recorded images. From now on, the bubble diameter (d_b) will be considered to be the $d_{b,eq}$. After tracking all the bubbles with their axial coordinate and size, a wide distribution of bubble diameters along the reactor height is obtained.

$$(d_{b,eq})_i = \sqrt{\frac{4A_i}{\pi} rr^2} \quad (1)$$

To compare results from different runs, the average bubble diameter has been calculated for each reactor slice i (length = 1 cm). In this study, it has been considered that bigger bubbles are 'more representative' of the gas flow than smaller ones. Thus, the average bubble diameter has been calculated as a weighted mean of the different bubble diameters in every slice. The weight factor is the bubble diameter itself, as Eq. (2) indicates.

$$\overline{d_{b,i}} = \left.\frac{\sum_{j=1}^{N} d_{b,j}^2}{\sum_{j=1}^{N} d_{b,j}}\right|_i \quad (2)$$

3.1.3. Bubble velocity analysis

Once bubbles have been detected, the bubble motion has been measured by comparing pairs of subsequent frames. Each frame is associated to a matrix that contains X–Y centroid coordinates and area of every detected bubble. A K-Nearest-Neighbor algorithm ('knnsearch' in Matlab2010a®) has been used to track bubbles between consecutive frames. The bubble velocity is thus, obtained from the bubble centroid displacement and the time delay between the considered frames. The recording frequency, 500 fps, was selected so that bubble movement could be easily followed. Moreover, coalescence phenomena were removed from the u_b analysis. The coalescence generally implies a large change in the centroid coordinates of a bubble, leading to uncommonly high bubble velocities. This effect could be masked by establishing maximum centroid displacement and size reduction criteria, as discussed by Busciglio et al. [8] and Asgehegn et al. [23].

3.2. 'Particle raining' filter

The 'particle raining' effect occurs inside bubbles and strongly affects PIV results [16]. For this reason, this particle rain has been removed from pictures using an in-house developed DIA algorithm: a modified version of the median filter ('medfilt2') available in the Image Processing Toolbox® of Matlab2010®. This filter turns to black all regions (and surroundings) with a luminance level lower than a threshold value specified by the user. Thus, low particle concentration regions are turned to black masking those raining particles. Fig. 4 shows the difference between PIV results from raw and filtered images. Filtering of the 'particle raining' is a technique to account in a binary fashion for the solids hold-up and obtain the number averaged particle velocity, representative for the particle fluxes. The PIV related to filtered images shows the expected solids circulation pattern: particles flow upwards in the center of the bed as bubble wake and fall down close to the reactor wall as emulsion phase. This methodology has already been used in the literature [16] to obtain the time averaged particle flux profiles.

4. Results and discussion

4.1. Defluidization angle, β, in a TS-TZFBR

An evaluation of defluidization phenomena was carried out for glass beads and optical tracer particles applying PIV. Experiments were performed in a $\alpha = 0°$ pseudo-2D TS-TZFBR. After carrying out image post processing, the particle tracking algorithm obtains an average scalar map of particle velocity in the reactor. This map shows particle axial velocities in each region along the bed. Besides, an rms map is also obtained (Fig. 5a). The rms map shows the standard deviation of particle velocity within a bed region. The black regions indicate no 'velocity errors', i.e. regions where there is no particle movement or where there is a very homogeneous particle displacement (the same velocity and flow direction). Since the probability of having a region with that last behavior is extremely small, the black regions in the scalar map are related to defluidized sections, i.e. denser zones with hardly any particle movement. The slope of this defluidized section, β, will be named the defluidization angle (Fig. 5a).

Results show that the increase of gas velocity favors particle circulation inside the bed and reduces the slope of the defluidized region over the section change (Fig. 5b). Moreover, when comparing different particle sizes from the same material, it can be observed that bigger particles lead to a more pronounced defluidization reduction at the same u_r. This trend is related to bubbling phenomena. Since u_{mf} is much higher for phosphorescent

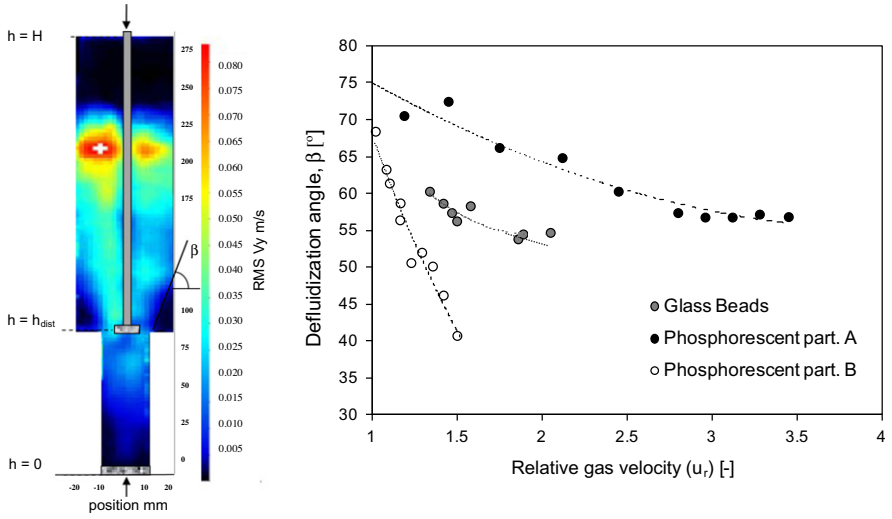

Fig. 5. (a) Average values of PIV related to bed position (phosphorescent part. A, $\alpha = 0°$, $u_{r,down} = u_{r,up} = 1.8$). (b) Analysis of defluidization after section change for different particles and gas velocities.

particles B than for particles A, the same u_r values result in a greater gas excess in case of bigger particles. Thus, larger bubbles are formed in case of phosphorescent particles B. These larger bubbles allow banked particles over the section change to move more easily. For this reason, a smaller defluidization angle, β is measured for phosphorescent particles B. In contrast, the fluidization behavior of small particles leads to smaller bubbles that flow upwards dragging up a smaller amount of particles in their wake.

By comparing experiments with particles of the same size, at the same u_r but different density materials (glass beads and phosphorescent particles B), it can be observed that the defluidization phenomena are affected differently. Spherical glass beads have a lower u_{mf}, thus, smaller bubbles are formed. However, the comparison between experiments with the same u_{gas}–u_{mf} but different particle type shows a similar defluidization angle. For example, in case of u_{gas}–u_{mf} = 10 cm/s (i.e. $u_{r,PPB} \approx 1.2$, $u_{r,GB} \approx 1.5$), the defluidization angles are: $\beta_{PPB} \approx 53°$ and $\beta_{GB} \approx 56°$. This indicates that the particle type does not affect β as much as the gas excess over minimum fluidization.

4.2. Channeling phenomena and slugging regime in TS-TZFBR

The channeling phenomena can also be analyzed using PIV results. Ascending gas finds preferential paths to minimize the pressure drop while circulating through the fluidized bed. PIV shows that, under specific operational conditions related to low relative gas velocity and the presence of cohesive particles and particle–wall interactions, channeling may occur. For the particles tested in this work, channeling appears to be significant at relative gas velocities ($u_{r,up}$) under 1.5, when bubbles are not large enough to drag particles up and produce pronounced solids circulation. Fig. 6a shows channeling in a fluidization regime for phosphorescent particles A under an upper velocity, $u_{r,up}$ = 1.5, obtained from a PIV axial velocity errors map. Fig. 6c ($u_{r,up}$ = 3.3) shows a good symmetry of the particle axial flow.

Slugging regimes can also occur in a TS-TZFBR, reducing dramatically the mixing rates between solids of the two reactor zones. The most critical slugging section is the upper part of the regeneration zone, just below the upper gas distributor and section change. Slugs commonly appear when there are high relative gas velocities in the regeneration zone (high $u_{r,down}$) and low $u_{r,up}$. In this scenario, big bubbles ascending from the bottom occupy the whole narrow reactor section. The reason is that the relative gas velocity after section change ($u_{r,up}$) is not enough to avoid defluidization at this point. As a result, bubbles coalesce at the critical section change leading to short-circuit in solids recirculation and thus deterioration of TS-TZFBR performance. Fig. 6b shows the effect of an inconvenient fluidization regime leading to slugs between reactor zones. This figure denotes high axial velocity standard deviation values under the section change point. This is both due to particle raining inside the slugs, and low particle movement over the second gas distributor.

Besides, experimental results show a higher slug formation in case of Fig. 6b although its gas velocity is lower than that of Fig. 6c. The bed breaking phenomenon takes place under the section change at low upper gas velocities. This phenomenon has been also reported for two-section fluidized beds (a similar system to a TS-TZFBR without a secondary gas entry) [31]. In the case of Fig. 4c, higher gas flows overcome the pressure drop above the upper distributor and it enables particles to mix between the reactor zones. This prevents the system from slugs formation.

4.3. Circulation patterns between reactor zones

The PIV analysis also gives information about circulation patterns inside the TS-TZFBR, via vector field velocity maps. Vector orientation and length provide an idea of particle velocity and

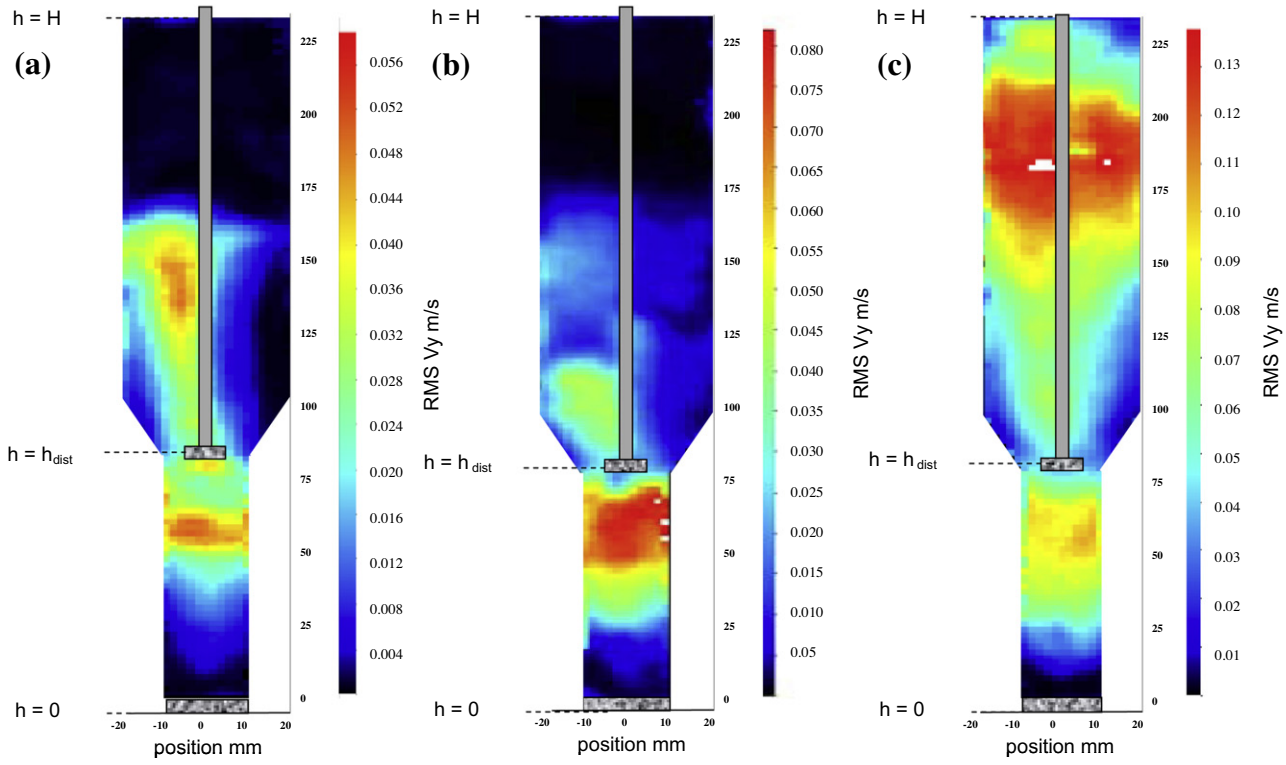

Fig. 6. Particle scalar field velocities. Errors map (RMS) for phosphorescent particles A, α = 45° (a) $u_{r,down}$ = 1.8, $u_{r,up}$ = 1.5, (b) $u_{r,down}$ = 2.5, $u_{r,up}$ = 1.3, (c) $u_{r,down}$ = 3.7, $u_{r,up}$ = 3.3.

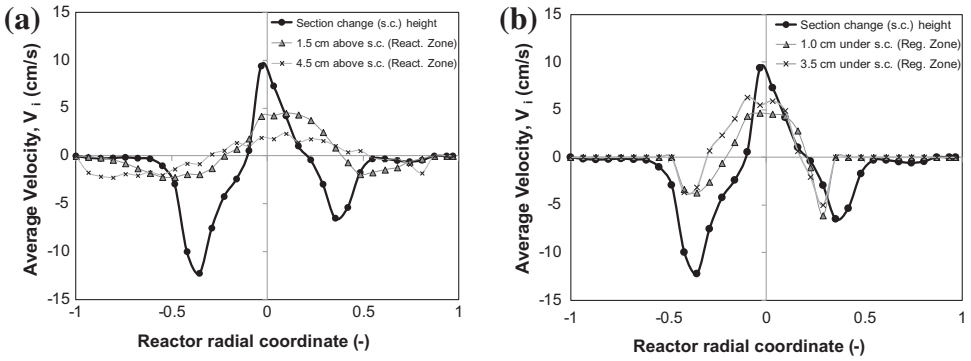

Fig. 7. Particle axial velocity profile at three heights with respect to section change height (phosphorescent particles A, $\alpha = 0°$, $u_{r,down} = u_{r,up} = 2.8$, $h = 0$ cm = $h_{section\ change}$). (a) Above the section change height ($h > h_{section\ change}$). (b) Below the section change height ($h < h_{section\ change}$).

direction in each bed interrogation area. Thus, such vector field can be used as an estimation of the exchange rate of solids between the two bed zones. In the reacting mode, catalytic reaction and catalyst regeneration processes occur continuously, so the mixing rate between "regenerated" and "deactivated" catalyst particles through the critical section must be studied. The mixing rate in this region, where the section changes and the reagent gas inlets, represents the key factor of the TS-TZFBR.

Several sets of pictures were recorded, zooming in on this critical section of the bed. The reactor geometry and relative gas flow rates were varied. The aim was to obtain axial velocities at different radial locations to understand how particles are transferred from one reactor zone to the other.

4.3.1. Radial profiles of particle axial velocities

The performed experiments zooming in on the critical section reveal a well defined circulation path. In the transition region, particles mainly flow up from the regeneration zone as bubble wakes centered in the bed and fall down from the reaction zone near the walls (Fig. 7).

Moreover, the axial velocity profile at different radial locations show that particles below and above the transition section follow similar trends, but with lower maximum velocities. This is related to the fact that, in the transition zone, additional gas is fed and thus particles move faster at that point. Far above the section change height, the average velocity values tend to zero. The reason is that, there are no preferential paths for ascending or descending particles.

In a bubbling fluidization regime without particles elutriation, the mass balance must be always accomplished for each reactor cross section. That means that the net particle flow rate through the transition section must be zero. Eq. (3) defines the mass balance for this system in a reactor cross section at a certain height, z. In this equation i represents the reactor radius coordinate, m_i the ascending/descending particle mass and v_i its average velocity.

$$\int_{i=-1}^{i=1} m_i \bar{v}_i di = 0 \tag{3}$$

To determine the ratio of ascending/descending particles through a reactor cross section (m_{up}/m_{down}), a numerical method can be applied. For each cross section, z, the numerical solution of Eq. (3) implies a finite increment integration of the continuous lines from Fig. 7a (regeneration zone) and Fig. 7b (reaction zone). The emulsion void fraction was assumed to be constant and equal to the wake void fraction in every interrogation section, since the use of phosphorescent solids does not allow the calculation of

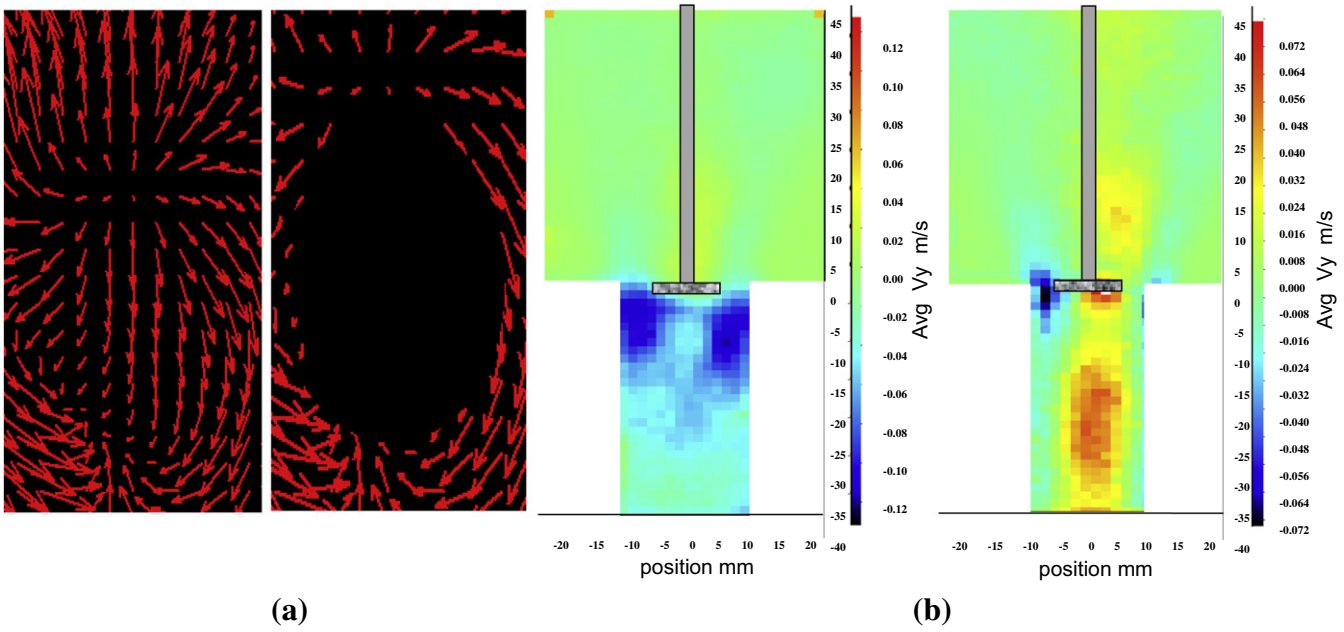

Fig. 8. Effect of bubble particle raining in PIV results (phosphorescent particles A, $\alpha = 0°$, $u_{r,down} = u_{r,up} = 2.8$): (a) particle velocity vector plot inside a single bubble without and with 'particle raining' filtering, (b) average axial velocity profile without and with 'particle raining' filtering.

the local void fraction with the methods described in literature [18,32,33]. These methods are based on the differences in light intensity between front and rear particles in a fluidized bed. In case of PPA and PPB solids, the particles from the front and the rear part of the bed cannot be distinguished from each other in terms of light intensity, since all of them become light-emitting particles once excited. Besides, a filter was used to remove the velocities of the particles raining down inside the bubble, thus assuming zero particles inside the bubble. This assumption has been already reported [16] when performing PIV analysis.

Concretely, for the operation conditions of Fig. 7, the ratio of ascending/descending particles through the transition cross section ('section change height') is, approximately, $m_{up}/m_{down} = 1.4$. This value means that the number of particles with an upward velocity, at this point, is bigger than the number of those descending within the emulsion phase. The big bubbles formed at these operation conditions together with a narrow reactor bed width explain the obtained result.

4.3.2. Particle raining effect

The 'particle raining' implies a region of low solid concentration with a very high downward velocity that influences the average solid circulation pattern. In the case of Fig. 8, particle raining effects under the section change lead to a false interpretation of the fluid dynamic regime inside the bed. Due to the high particle downward velocity inside the bubbles (Fig. 8a without filtering), average velocity values would show that all particles are descending through the whole cross sectional area (Fig. 8b without filtering). Obviously, this cannot happen since mass balance in every reactor cross section must be accomplished, i.e. net flux must be null. By filtering the recorded images (Fig. 8a with filtering), the average velocity regions map differs significantly from the previous one. This new map shows upward particles located at the center of the bed (hot-colored regions) and descending particles (cold-colored regions) close to the walls (Fig. 8b with filtering). It can also be observed that the maximum upward velocity is reached close to the second gas distributor. At this point, the narrow section still applies, but there are two gas flow contributions.

After applying this kind of filter, it was possible to determine vector and scalar velocity fields for several operation conditions. These results provide useful information about the solids circulation patterns, mixing rates and defluidization angle variations related to gas velocities. As an example, Fig. 9 shows the effect of gas velocities on the vector and scalar velocity maps.

The vector velocity map of Fig. 9a, that represents a $u_r = 2.1$ regime, shows a quite ordered particle circulation pattern inside the reactor. However, higher gas velocities as $u_r = 2.8$ (Fig. 9c) lead to a more turbulent fluidization with irregular particle paths and lower defluidization angles over the section change. Using a normalized velocity color bar, it can be observed how particle velocity increases through the transition cross section when applying higher gas velocities. Higher particle velocities imply shorter mixing times between reactor zones and a better control of the TS-TZFBR performance.

4.4. DIA: bubble properties related to particle type and relative gas velocities in a TS-TZFBR

In the above sections, particle velocity profiles have been characterized with the aid of PIV software. However, a TS-TZFBR is a complex multiphase reactor where gas phase (bubbling regime) plays a key role, as in every fluidized bed reactor. Therefore, both gas and particle fluid dynamics influence each other and must be studied together. For this purpose, several *Matlab*® routines have been home-developed in order to understand and analyze bubbling phenomena inside a TS-TZFBR.

Although several correlations have been reported to describe both bubble size and bubble velocity evolution inside bubbling columns [34], the integration of a tapered section and an immersed jet in the novel TS-TZFBR may affect the bubbling behavior. This fact motivates the study of the TS-TZFBR hydrodynamics.

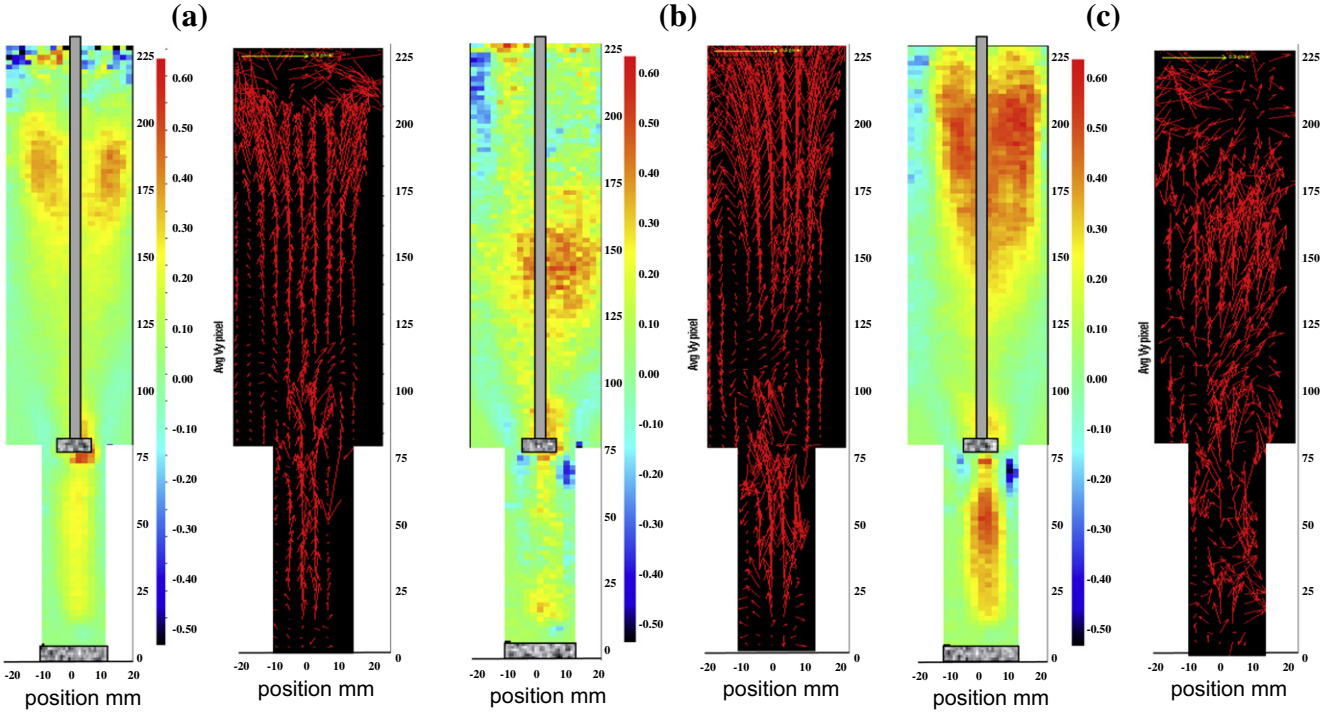

Fig. 9. Vector and scalar PIV results for several gas velocities. Phosphorescent particles A, $\alpha = 0°$. (a) $u_{r,down} = u_{r,up} = 2.1$. (b) $u_{r,down} = u_{r,up} = 2.5$. (c) $u_{r,down} = u_{r,up} = 2.8$.

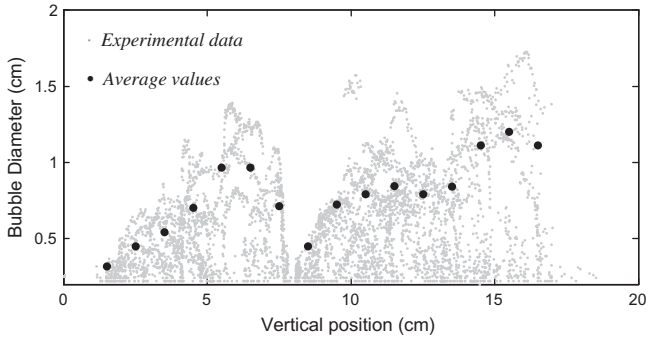

Fig. 10. Bubble diameter vs. reactor vertical position: experimental data (gray) and average values (black) for glass beads, $u_{r,down} = u_{r,up} = 1.5$, $\alpha = 0°$, $h_{dist} = 8$ cm, $h_{section\ change} = 8$ cm.

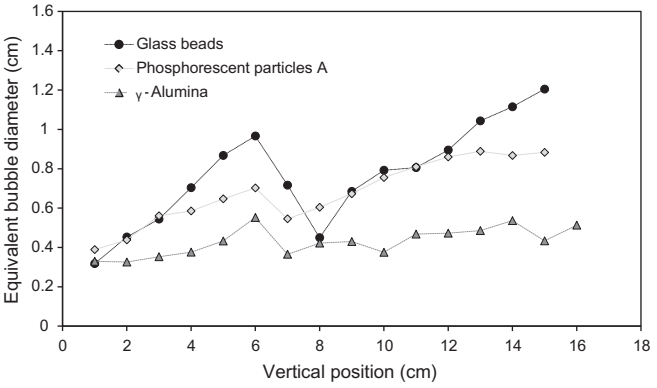

Fig. 11. Bubble diameter vs. reactor vertical position for phosphorescent particles A (same conditions as Fig. 8).

Among the general findings [13–18], it is well known that the average bubble diameter increases continuously with bed height within straight columns. Moreover, the increase of gas velocity over u_{mf} leads to bigger bubbles. Also, particles with higher u_{mf} produce bigger bubbles when working at the same u_r. The reason is that the flow rate excess over the minimum fluidization (u_{gas}–u_{mf}) is larger [22].

4.4.1. Influence of particle type and gas flow on bubble size and bubble growing rate along reactor height

The present study evaluates bubble diameter (d_b) evolution as a function of reactor height (z) and particle type for this novel TS-TZFBR. In this section, results and further discussion will be referred to average $\overline{d_b}(z)$ values. Those data represent a mean value for every 1 cm height slice from a dispersed $d_b(z)$ distribution. To illustrate the data scattering, Fig. 10 shows the measured and average $d_b(z)$ in a 40 s fluidization time for glass beads under a relative gas velocity $u_{r,down} = u_{r,up} = 1.5$ in a $\alpha = 0°$ reactor geometry. The $d_b(z)$ results show a significant bubble size reduction after the section change for all tested solids. The bubble shrinkage phenomenon takes place when a sharp gas velocity reduction occurs due to a section enlargement. In the case of a TS-TZFBR, the average bubble diameter reduction is enhanced by the formation of incipient small bubbles coming from the upper orifice distributor. Thus, both the transition angle between the zones, α, and the distributor orifice size affect the minimum bubble diameter over the section change. Fig. 11 shows experimental results for three different particle types at the same relative gas velocity in both reactor zones ($u_{r,down} = u_{r,up} = 1.5$). For a single particle type, the bubble diameter growth rate is similar in both regeneration and reaction zones.

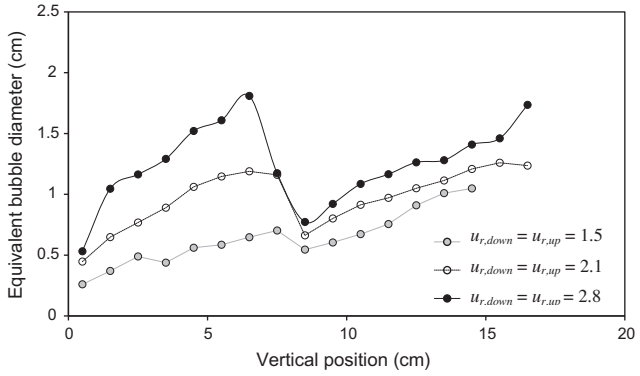

Fig. 12. Bubble diameter vs. reactor vertical position for different gas velocities (phosphorescent particles A, $\alpha = 0°$, $h_{section\ change} = 8$ cm, $h_{dist} = 8$ cm).

Moreover, it can be observed how the bubble size depends on the particle size, i.e. on u_{mf}. Larger solids (glass beads) lead to larger bubble diameters and faster growth rates than smaller particles (γ-alumina). The reason is the larger flow rate excess over the minimum fluidization in case of glass beads. Also, the sharp bubble diameter reduction in the transition section becomes more significant in the case of bigger particles and higher relative gas velocities. This is related to the incipient bubble size from the second distributor. The initial size of this bubble seems to depend mainly on the orifice size. The almost constant d_b values found in Figs. 11 and 12 for different operating conditions just over the distributor height ($h \approx 8$ cm) illustrate this finding. The average bubble diameter at this bed position is around 0.5 cm. This value seems not to be strongly modified, when varying particle type or gas velocity in the regeneration zone. This is in agreement with the prior observation.

To investigate how the gas velocity affects the bubble diameter as a function of the vertical position, three different fluidization experiments were carried out with relative gas velocities ranging from 1.5 to 2.8 for phosphorescent particles A with the same properties as those presented in Fig. 10. As expected, higher u_r led to bigger bubbles and even to faster growth rates (Fig. 12). Moreover, a bubble diameter of approximately 0.5 cm was determined in all cases above the section change just over the second distributor. This trend confirms the prior hypothesis.

A qualitative comparison between the bubble size results from Figs. 10–12 and those obtained by other authors in straight bubbling columns [9,10,35] shows a big difference in terms of d_b evolution. In straight columns, bubble growth is well described by the

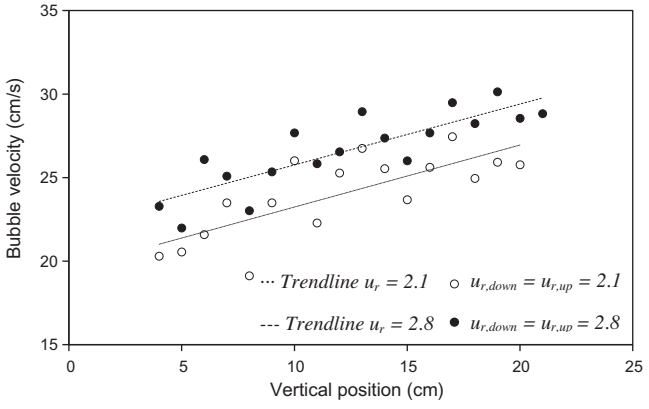

Fig. 13. Bubble velocity vs. reactor vertical position for different gas velocities (phosphorescent particles A, $\alpha = 0°$, $h_{dist} = 8$ cm).

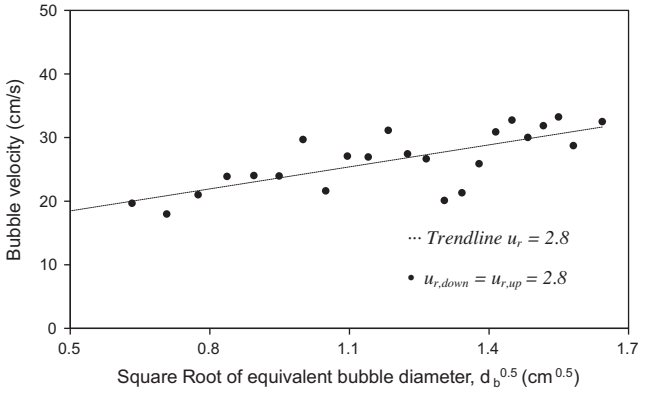

Fig. 14. Bubble velocity vs. bubble diameter (phosphorescent particles A, $\alpha = 0°$, $u_{r,down} = u_{r,up} = 2.8$).

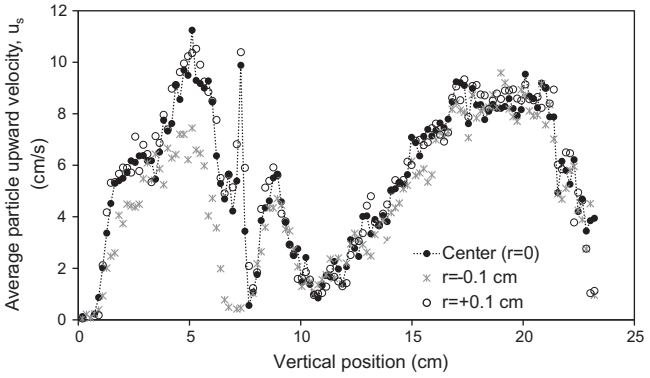

Fig. 15. Particle upwind velocity vs. reactor vertical position (phosphorescent particles A, $u_{r,down} = 2.8$, $u_{r,up} = 2.8$).

classical Wen and Mori or Darton correlations. Considering a TS-TZFBR, a similar bubble size evolution can also be observed in both the regeneration and the reaction zones separately. However, the secondary gas addition and the section change lead to sharp bubble shrinkage in an intermediate point of the bed, as already discussed. Thus, the classical correlations cannot predict the bubble size evolution beyond the transition section.

4.4.2. Bubble velocity related to gas flow, bubble diameter and reactor height

Fig. 13 shows experimental average bubble velocity values (u_b) as function of the vertical position at two different gas velocities. The experiments were carried out in a $\alpha = 0°$ transition angle geometry with phosphorescent particles A. The results indicate that reactor height slightly influences the bubble velocity profiles, since u_b varies from the bottom to the top ranging from 20 cm/s to 30 cm/s. Moreover, the higher the inlet gas velocity, the higher the bubble velocity, as expected.

The bubble velocity variation with reactor height may be linked to the bubble diameter variation along the bed, as indicated by the velocity decrease over h_{dist}. Fig. 14, where bubble velocity u_b is related to the square root of the average bubble diameter, $d_b^{0.5}$, validates this hypothesis. The linear trend in the $u_b(d_b^{0.5})$ plot agrees with the correlation suggested by Kunii and Levenspiel Eq. (4) to describe the u_b evolution as a function of d_b. In Eq. (4), $k = 0.71$ for 3D fluidized bed reactors, whereas $k = 0.4$ for 2D beds. The calculated trend line in Fig. 14 leads to a u_b growing rate: $k = 0.36$. It agrees with Kunii and Levenspiel predictions for 2D beds and further validates the developed DIA for bubble velocity measurement.

$$u_b = (u_{gas} - u_{mf}) + k(gd_b)^{0.5} \tag{4}$$

Similar experiments were performed with glass beads and alumina particles. Results suggested that bubble velocity mainly depends on the gas excess over the minimum fluidization and not so much on the particle type (not shown here). This is in agreement with the fact that all the tested particles showed Geldart B type behavior.

4.5. Particle upward velocity related to bubble properties. Coupled PIV + DIA

As discussed above, the final aim of this study is to relate dense phase fluid dynamics and gas phase hydrodynamics for the novel TS-TZFBR. Both particle circulation and bubble properties have been analyzed separately using PIV and DIA, respectively. From the PIV results (scalar average velocity maps), it is possible to bring out axial velocity profiles for different radial positions. As an example, Fig. 15 shows the particle upward velocity profile, denoted as $u_s(z)$, for three different radial positions: at the center of the reactor and at 0.1 cm far from the center (left and right hand side). The experimental $u_s(z)$ profile has a similar curvature as the $d_b(z)$ profiles discussed above, so both variables appear to be related with each other. This is what classical correlations suggest. According to the Kunii-Levenspiel correlation Eq. (5), the particle velocity can be described as a function of the relative gas velocity and the square root of the bubble diameter.

$$u_s = (1 - \delta)\left((u_{gas} - u_{mf}) + 0.4(gd_b)^{0.5}\right) \tag{5}$$

In the system studied in this work, a bulk comparison of u_s and d_b cannot be carried out because the reactor characteristics differ from the straight one-feed column used to obtain Eq. (5) correlation. Such an equation does not fit with experimental data in a TS-TZFBR, because in this reactor 'fast-moving' small bubbles and 'slow-moving' larger bubbles coexist in the single vessel and at the same height. The small bubbles come from the upper gas distributor and the big ones come from the regeneration zone. The last ones rise loosing velocity due to the section enlargement. For this reason, a 'bulk' analysis would lead to a wrong interpretation. However, a qualitative comparison of $u_s(z)$ and $d_b(z)$ profiles (Figs. 11, 12 and 15) show a high agreement between the axial variations of both variables.

It can also be observed that u_s values have low radial dependence in the interval [−0.1 cm,+0.1 cm] with the exception of the transition section. In this section, the particle upward velocity varies substantially in the radial direction due to a well defined circulation pattern. This leads to a sharp axial velocity profile in the radial direction, as discussed in Section 4.3 (Fig. 9). As can be observed in Fig. 15, the coupled section enlargement and gas feed addition at h_{dist} lead to a particle velocity reduction after the h_{dist} feed point. This was caused by the small bubble sizes, since a smaller amount of particles are pushed up within the bubble wake. Bubble size reduction over the h_{dist} distributor would, however, have a positive effect in case a catalytic reaction takes place. In that case, the gas–solid contact would be favored by small bubbles and it would lead to larger gas conversion. Besides, a bubbling regime far from slug formation within the critical section would favor solids transfer between the reactor zones.

Lastly, it is worth noticing that the average particle upward velocity values (Fig. 15) are in a good agreement with the average bubble velocities (Fig. 13) obtained under the same experimental conditions. According to several authors [36,37], the experimental relation between solids and gas velocity could be calculated as: $u_s = K \cdot u_b$, being K a value between 0.4 and 0.6. In this work, the solid upward velocity in the bed center is around 8 cm/s (in the upper

section) while the gas velocity (Fig. 13) is around 22 cm/s. Thus, the ratio u_s/u_b is close to the range proposed in the above references.

5. Conclusions

The fluid dynamics performance of a TS-TZFBR has been studied to identify operational limitations. The particle exchange rate between the reactor zones provides information about the degree of solid mixing inside the two-zone bed, which is crucial for the reactor performance.

In order to operate with similar relative gas velocities in the reaction and regeneration zones, a suitable transition angle between the zones is essential. Such a transition angle depends on the particle type and gas velocity above the section change, which strongly influences the bubbling regime. To avoid the presence of a defluidization area in any fluidization condition, a transition angle over $\alpha = 80^\circ$ is required (conservative value). However, a transition angle $\alpha = 60^\circ$ seems to be sufficient to avoid defluidization at $u_{r,up} > 1.5$ and $d_p = 0.5$ mm or bigger.

For lab scale narrow reactor sections, high $u_{r,down}$ coupled with low $u_{r,up}$ lead to a slugging regime. This effect produces short-circuit in the solid recirculation between reactor zones. Slugging could be avoided by working at similar $u_{r,down}$ and $u_{r,up}$ (proved at $u_{r,down} < 3.5$ for $d_p = 200$ μm).

The PIV analysis allowed the study of channeling phenomena. This appeared to be important at low relative gas velocities ($u_{r,up} < 1.5$) over the section change. Thus, a gas velocity operational window $1.5 < u_r < 3.5$ allows both particle circulation and significant gas–solid contact times. The PIV analysis also provided useful information about the solids circulation pattern in the transition section. A particle velocity profile (u_s) with respect to reactor height showed that u_s heavily depends on the radial position in the section change boundaries.

From DIA post-processing, the TS-TZFBR hydrodynamics was studied. The bubble diameter profile as a function of the vertical position showed a significant bubble size reduction within the transition section in all the experiments. This was related to: (a) the addition of small new bubbles emerging from the second gas distributor, and (b) bottom gas redistribution from ascending bubbles to the emulsion phase to maintain a fluidized regime over the section enlargement. As a result, the mass transfer is favored and the contact between the oxidizing atmosphere and the reactant gas is limited.Summarizing the above conclusions, PIV and DIA have shown the effects of operating variables on the particle movement and on the bubble flow characteristics in a TZFBR, providing valuable information to be taken into account in the design of such reactors.

Acknowledgement

Financial support from FECYT, Spain (Project CTQ2010-15568) is gratefully acknowledged.

References

[1] J. Herguido, M. Menéndez, J. Santamaría, On the use of fluidized bed catalytic reactors where reduction and oxidation zones are present simultaneously, Catal. Today 100 (2005) 181–189.
[2] M. Menéndez, J. Herguido, C. Téllez, J. Soler, M.P. Gimeno, Two Zone Fluidized Bed Reactor, Spanish Patent Application P200801857, 2008.
[3] M.P. Gimeno, Z.T. Wu, J. Soler, J. Herguido, K. Li, M. Menéndez, Combination of a two-zone fluidized bed reactor with a Pd hollow fibre membrane for catalytic alkane dehydrogenation, Chem. Eng. J. 155 (2009) 298–303.
[4] J. Soler, C. Téllez, J. Herguido, M. Menéndez, J. Santamaría, Modelling of a two-zone fluidised bed reactor for the oxidative dehydrogenation of *n*-butane, Powder Technol. 120 (2001) 8–96.
[5] J. Gascón, C. Téllez, J. Herguido, M. Menéndez, A two-zone fluidized bed reactor for catalytic propane dehydrogenation, Chem. Eng. J. 106 (2005) 91–96.
[6] M.P. Lobera, C. Tellez, J. Herguido, M. Menéndez, Propane dehydrogenation over Pt–Sn–K/γ-Al_2O_3 catalyst in a two-zone fluidized bed reactor, Ind. Eng. Chem. Res. 47 (2008) 9314–9320.
[7] M.P. Gimeno, J. Soler, J. Herguido, M. Menéndez, Counteracting catalyst deactivation in methane aromatization with a two zone fluidized bed reactor, Ind. Eng. Chem. Res. 49 (2010) 996–1000.
[8] A. Busciglio, G. Vella, G. Micale, L. Rizzuti, Analysis of the bubbling behaviour of 2D gas solid fluidized beds Part I. Digital image analysis technique, Chem. Eng. J. 140 (2008) 398–413.
[9] A. Busciglio, G. Vella, G. Micale, L. Rizzuti, Experimental analysis of bubble size distributions in 2D gas fluidized beds, Chem. Eng. Sci. 65 (2010) 4782–4791.
[10] L. Shen, F. Johnsson, B. Leckner, Digital image analysis of hydrodynamics two-dimensional bubbling fluidized beds, Chem. Eng. Sci. 59 (2004) 2607–2617.
[11] G.R. Caicedo, J.J.P. Marqués, M.G. Rúiz, J.G. Soler, A study on the behaviour of bubbles of a 2D gas–solid fluidized bed using digital image analysis, Chem. Eng. Process: Process Intensif. 42 (2003) 9–14.
[12] J.A. Almendros-Ibanez, D. Pallares, F. Johnsson, D. Santana, Voidage distribution around bubbles in a fluidized bed: influence on throughflow, Powder Technol. 197 (2010) 73–82.
[13] J. Soler, J. Marques, M. Ruiz, G. Caicedo, Calibration of the method to measure bubble properties in 2D fluidized beds, Chem. Eng. Commun. 190 (2003) 285–298.
[14] J.R. van Ommen, R.F. Mudde, Measuring the gas–solids distribution in fluidized beds – a review, Int. J. Chem. React. Eng. 6 (2008) R3.
[15] T. Dyakowski, A.J. Jaworski, Application of non-invasive techniques for imaging fluidized beds – a review, Handbook Powder Technol. 10 (2001) 807–823.
[16] J.A. Laverman, I. Roghair, Mv. Sint Annaland, J.A.M. Kuipers, Investigation into the hydrodynamics of gas–solid fluidized beds using particle image velocimetry coupled with digital image analysis, Can. J. Chem. Eng. 86 (2008) 523–535.
[17] J.F. de Jong, Mv. Sint Annaland, J.A.M. Kuipers, Experimental study on the effects of gas permeation through flat membranes on the hydrodynamics in membrane-assisted fluidized beds, Chem. Eng. Sci. 66 (2011) 2398–2408.
[18] G. Agarwal, B. Lattimer, S. Ekkad, U. Vandsburger, Influence of multiple gas inlet jets on fluidized bed hydrodynamics using particle image velocimetry and digital image analysis, Powder Technol. 214 (2011) 122–134.
[19] J. Villa Briongos, J. Guardiola, New methodology for scaling hydrodynamic data from a 2D fluidized bed, Chem. Eng. Sci 60 (2005) 5151–5163.
[20] N. Xie, F. Battaglia, S. Pannala, Effect of using two vs. three-dimensional computational modeling of fluidized beds. Part I: Hydrodynamics, Powder Technol. 182 (2008) 1–13.
[21] J.R. Grace, T. Li, Complementarity of CFD, experimentation and reactor models for solving challenging fluidization problems, Particuology 8 (2010) 498–500.
[22] D. Geldart, Effect of particle-size and size distribution on behavior of gas-fluidized beds, Powder Technol. 6 (1972) 201–215.
[23] T.W. Asegehegn, M. Schreiber, H.J. Krautz, Investigation of bubble behavior in fluidized beds with and without immersed horizontal tubes using a digital image analysis technique, Powder Technol. 210 (2011) 248–260.
[24] J. Ciborowski, A. Wlodarski, On electrostatic effects in fluidized beds, Chem. Eng. Sci. 17 (1962) 23–32.
[25] L. Yao, H.T. Bi, A.H. Park, Characterization of electrostatic charges in freely bubbling fluidized beds with dielectric particles, J. Electrostat. 56 (2002) 183–197.
[26] A. Sowinski, A. Mayne, P. Mehrani, Effect of fluidizing particle size on electrostatic charge generation and reactor wall fouling in gas–solid fluidized beds, Chem. Eng. Sci 71 (2012) 552–563.
[27] W.O. Moughrabiah, J.R. Grace, X.T. Bi, Electrostatics in gas–solid fluidized beds for different particle properties, Chem. Eng. Sci. 75 (2012) 198–208.
[28] G. Landi, D. Barletta, M. Poletto, Modelling and experiments on the effect of air humidity on the flow properties of glass powders, Powder Technol. 207 (2011) 437–443.
[29] J. Guardiola, V. Rojo, G. Ramos, Influence of particle size, fluidization velocity and relative humidity on fluidized electrostatics, J. Electrostat. 27 (1996) 1–20.
[30] A.H. Park, H. Bi, J.R. Grace, Reduction of electrostatic charges in gas–solid fluidized beds, Chem. Eng. Sci. 57 (2002) 153–162.
[31] J. Corella, R. Bilbao, Fluid dynamic study of a new type of solid–gas contactor: the fluidized/fixed or fluidized bed, Ind. Eng. Chem. Process Des. Dev. 21 (1982) 545–550.
[32] R. Boerefijn, M. Ghadiri, High speed video image analysis of flow of fine particles in fluidized bed jets, Adv. Powder Technol. 9 (1998) 229–243.
[33] M.J.V. Goldschmidt, J.M. Link, S. Mellema, J.A.M. Kuipers, Digital image analysis measurements of bed expansion and segregation dynamics in dense gas-fluidised beds, Powder Technol. 138 (2003) 135–159.
[34] S. Karimipour, T. Pugsley, A critical evaluation of literature correlations for predicting bubble size and velocity in gas–solid fluidized beds, Powder Technol. 205 (2011) 1–14.
[35] K.S. Lim, P.K. Agarwal, B.K. O'neill, Measurement and modelling of bubble parameters in a 2-dimensional gas-fluidized bed using image analysis, Powder Technol. 60 (1990) 159–171.
[36] M. Stein, Y.L. Ding, J.P.K. Seville, D.J. Parker, Solids motion in bubbling gas fluidized beds, Chem. Eng. Sci. 55 (2000) 5291–5300.
[37] G. Grasa, J.C. Abanades, The use of two different models to describe the axial mixing of solids in fluidized beds, Chem. Eng. Sci. 57 (2002) 2791–2798.

Artículo III

I. Julián, J. Herguido, M. Menéndez,
A non-parametric bubble size correlation for a Two-Section Two-Zone Fluidized Bed Reactor,
Powder Technol. 256 (2014) 146-157

Powder Technology 256 (2014) 146–157

Contents lists available at ScienceDirect

Powder Technology

journal homepage: www.elsevier.com/locate/powtec

A non-parametric bubble size correlation for a Two-Section Two-Zone Fluidized Bed Reactor (TS-TZFBR)

I. Julián, J. Herguido, M. Menéndez *

Catalysis, Molecular Separations and Reactor Engineering Group (CREG), Aragon Institute of Engineering Research (I3A), Universidad de Zaragoza, 50018 Zaragoza, Spain

ARTICLE INFO

Article history:
Received 29 April 2013
Received in revised form 18 September 2013
Accepted 1 February 2014
Available online 8 February 2014

Keywords:
Bubble size correlation
Bubble measuring technique
Tapered fluidized bed
Redox reactor

ABSTRACT

The Two-Zone Fluidized Bed Reactor (TZFBR) provides a high level of process integration, allowing heterogeneous catalytic reaction and simultaneous catalyst regeneration in two different zones of a single fluidized bed. This work considers a new reactor design that incorporates a different cross-sectional area in each zone to allow low flow rates in the regeneration zone. The reactor geometry, e.g. the transition angle α between the two zones in this Two-Section Two-Zone Fluidized Bed Reactor (TS-TZFBR), has a strong effect on the bubbling behavior. The present study focuses on obtaining a bubble size (d_b) correlation able to predict the experimental hydrodynamic behavior inside this novel TS-TZFBR. Experimental studies have been conducted on acrylic glass pseudo-2D TS-TZFBRs using several particle types and reactor geometries (α). Experimental results validate classical d_b correlations within the straight region of the reactor. A novel non-parametric bubble size correlation has been developed to predict the bubbling behavior within the tapered bed section, where an additional gas feed is also applied. This non-parametric model agrees with experimental results along the whole TS-TZFBR bed height for a wide range of operational conditions: u_{gas}/u_{mf} = 1.5–3.5, $u_{gas} - u_{mf}$ = 5–25 cm/s, α = 0°–85°, u_{mf} = 1.2–20.5 cm/s.

1. Introduction

Catalysts often suffer from deactivation due to carbon deposition, i.e. coke, over the active surface. The coverage of the catalytic sites and, thus, the catalyst deactivation may occur after a few seconds (e.g. Fluid Catalytic Cracking process), or minutes (e.g. alkane dehydrogenation), hours or even days. For those gas–solid catalytic processes in which a relatively fast deactivation takes place, the Two-Zone Fluidized Bed Reactor (TZFBR) has been proposed as an effective solution to integrate a catalytic chemical reaction and catalyst regeneration in a single fluidized bed reactor. The generation of two different atmospheres inside a TZFBR, via two separated gas inlets, allows a continuous catalytic operation without net catalyst deactivation. The heterogeneous catalytic reaction takes place within the upper bed zone, where a reactant gas flow is fed, whereas the catalyst regeneration by coke combustion occurs in the lower section with a second reactive gas feed [1]. An oxidizing gas feed enters the TZFBR bed at the bottom to bring about this coke burning. To obtain a satisfactory reactor performance, the mixing rate of the solids and the reaction and regeneration kinetics must be of the same order. Thus, particle circulation between the two bed zones determines the performance of a TZFBR and provides the process integration [1].

A modified TZFBR has recently been developed [2–4] for processes in which a low oxidant-to-reactive stream ratio is required. The new proposal consists of using a smaller section in the lower zone to allow low oxidant flow rates in the regeneration zone while maintaining a relative gas velocity ($u_r = u_{gas}/u_{mf}$) similar to that in the reaction zone [2]. This results in the so called Two-Section Two Zone Fluidized Bed Reactor, TS-TZFBR (Fig. 1), in which fluid dynamic characteristics need to be studied.

It is well known that the solid circulation inside a fluidized bed is promoted by the gas bubble dynamics [5]. In certain operation conditions, the bubbling regime provides a continuous mixing of the solids between reactor zones that could lead to a desirable fluid dynamic performance of a TS-TZFBR. Therefore, the purpose of a hydrodynamic analysis is to find the most suitable conditions to be applied in a specific fluidized bed regime.

The estimation of bubble properties provides useful information for predicting the mixing of the solids and the gas–solid contact in each cross section of the reactor. Many authors have studied bubble fluid dynamics inside bubble columns and gas–solid fluidized bed reactors. Several correlations have been published for predicting the bubble size and velocity evolution along the vertical axis of fluidized beds with constant cross section and with gas fed from the bottom. Some of the existing correlations have been compared and evaluated in a recent review [6]. A few authors have provided correlations for predicting some hydrodynamic characteristics inside a gas–solid tapered bed [7–10] as a function of the cross-sectional transition angle, α, but no one has presented a correlation for understanding and predicting the bubble behavior when there is a section change and an additional gas feed in a single vessel. Therefore, this work aims to quantify and further

Corresponding author.
E-mail address: qtmiguel@unizar.es (M. Menéndez).

0032-5910/$ – see front matter © 2014 Elsevier B.V. All rights reserved.
http://dx.doi.org/10.1016/j.powtec.2014.02.004

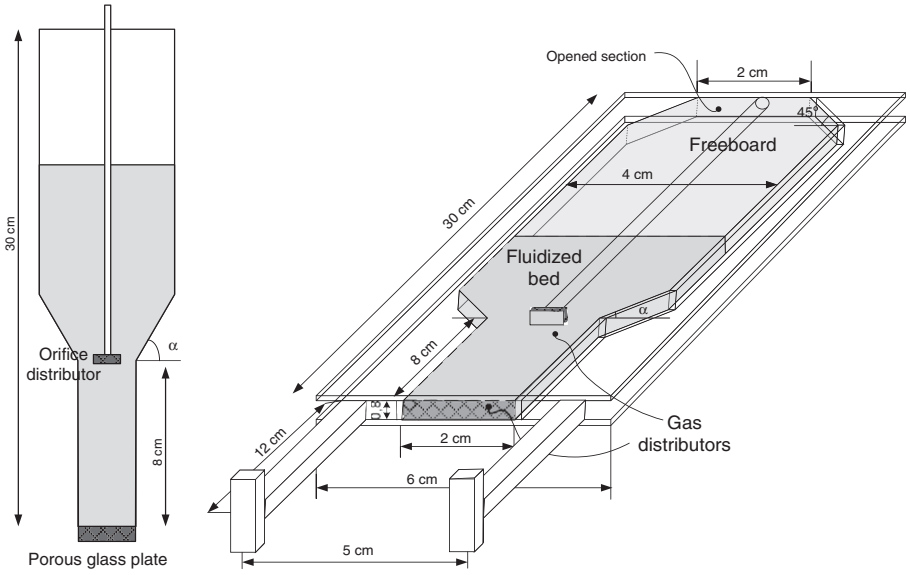

Fig. 1. a) Front view of a TS-TZFBR, b) pseudo-2D TS-TZFBR view.

predict the effect of both system variables on the bubble size behavior, which strongly determines the particle fluid dynamics of a TS-TZFBR.

The main purpose of the study is thus to develop a mathematical model that enables the prediction of the average bubble size along the vertical position in a TS-TZFBR. The model will be based on classical correlations and will take into account the special reactor configuration for a proper estimation of the bubble size in every region of the bed. The novel correlation will be validated with the results of an experimental analysis under several fluidization regimes.

Of the various available non-invasive techniques for measuring the bubbling regime in a fluidized bed [11,12], a Digital Image Analysis (DIA) technique has been selected. Its major advantages are the simplicity of its implementation and the large amount of useful information that can be extracted from recorded pseudo-2D fluidization frames [13,14].

In this work, an experimental study has been carried out to analyze the bubbling behavior under the influence of different operational conditions: various particle types, different gas flow rates in the reaction and regeneration zones, or different reactor geometries (TS-TZFBR transition angle, α). The determined equivalent bubble diameter values (d_b) have been related to the TS-TZFBR vertical position (z). Thus, $d_b(z)$ profiles have been obtained for each operational condition. The experimental bubble growing trends have been compared with some classical hydrodynamic correlations (e.g. the Mori and Wen $d_b(z)$ correlation [15]). The experimental data and this classical correlation have shown a high agreement in the separate reaction and regeneration straight zones, but the correlation was unable to predict the characteristic bubble shrinkage [2] that takes place within the transition section in a TS-TZFBR.

To overcome the fitting limitations in the transition section, this work will provide a new non-parametric correlation for predicting the bubble size reduction as a function of the transition section angle, α, the relative gas velocity and the particle type.

This expression will be combined with the widely used Davidson and Harrison equation to predict the average bubble velocity in upward direction (u_b) profile [16], and the prediction will be compared with experimental u_b data.

2. Experimental procedure

2.1. Experimental set up

Experiments have been carried out in acrylic glass pseudo-2D TS-TZFBRs with the following dimensions: 300 mm × 40 mm × 8 mm (height × width × depth). The wide section (reaction zone) is 40 mm wide, whereas the narrow section (regeneration zone) is 20 mm wide. The front reactor wall is transparent, whereas the rear wall is translucent in order to avoid non-homogeneous illumination along the reactor bed. The illumination system consists of three fluorescent lamps located behind the rear wall of the reactor.

Five TS-TZFBR reactors with different transition angles, α, have been tested, α ranging from 0° to 85° with respect to the horizontal position. For each reactor geometry, four different particle types were fluidized. The reactor had two gas distributors: the lower one at the bottom was a porous glass plate (3 μm pore diameter) and the upper distributor was a T-shaped tube with two orifice distributors (3 mm orifice diameter), symmetrically located with respect to the radial centre of the reactor (Fig. 1).

The selected particles were taken from three different materials: FCC catalyst, inert beads commonly used in cold fluidization experiments and optical tracers (phosphorescent particles, for further studies on the mixing of the solids). Table 1 shows the main properties of each tested particle type. The total mass of particles within the bed in each case was 50 g. Compressed air was used as fluidization gas.

The video recording system consisted of a standard high-resolution low luminance camcorder, which is able to record full HD (1920 × 1080 pixels) frames. The Digital Image Analysis tool was a home-developed Matlab 2010a® algorithm. The entire set up was located inside a black box in order to avoid wall light reflections from the room illumination. Fig. 2 shows a scheme of the experimental set up.

The recording time was fixed at 40 s in all the recorded videos in order to ensure stabilized bubble size distribution results with respect to the vertical position of the reactor. In this period more than 50 single bubbles would be averaged out for each axial position slice (1 cm height) in a single video. Thus, the selected recording time was sufficient for performing a significant bubble size statistical analysis.

Table 1
Properties of the fluidized particles.

Particle type	d_p (μm)	ρ_{bed} (g/cm^3)	$\varepsilon_{bed.}$ (−)	u_{mf} (cm/s)
Glass beads	480 ± 60	1.5	0.40	20.5
γ-Al_2O_3	135 ± 30	0.8	0.47	1.2
$SrAl_2O_4$-A	195 ± 50	1.5	0.58	10.1
$SrAl_2O_4$-B	680 ± 100	1.3	0.64	48.5

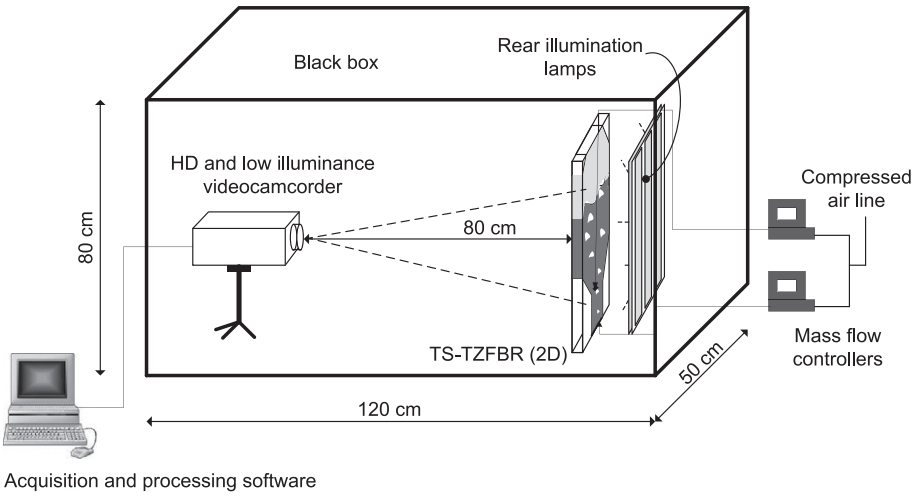

Fig. 2. Experimental set up for the hydrodynamic study in a pseudo-2D TS-TZFBR.

2.2. DIA for experimental video data

The characteristic bubbling regime inside a TS-TZFBR has been determined by measuring the average bubble size and the evolution of the bubble velocity in the upward direction along the vertical axis of the reactor. The bubbles were detected and quantified with a home-developed Digital Image Analysis (DIA) algorithm. This algorithm involves the transformation of the video frame to a binary image (black and white) for bubble tracking. The key point of DIA in bubbling fluidized beds is to measure the bubble size correctly [13]. For this purpose, it is necessary to define the bubble boundaries accurately. This operation may not be simple, since the bubble cloud porosity differs slightly from the dense phase porosity. Therefore, the selected luminance threshold value (I_{thr}) to distinguish between both bed phases determines the whole experimental analysis. A proper threshold selection may be quite a time-consuming process. As an example, Figs. 3 and 4 show a bubble tracking result for different I_{thr} tested values. In the case of Fig. 3, the overestimation of the bubble size under the reactor transition section is caused by an inhomogeneous axial bed illumination. In Fig. 4, a correct bubble tracking has been carried out for a threshold value between $I_{thr} = 0.25$ and $I_{thr} = 0.30$. As a general trend, the most suitable I_{thr} for this kind of image does not exactly correspond to Otsu's threshold prediction [17], which is used by default in Matlab 2010a®. Thus, a visual determination of I_{thr} for each video sequence was employed. The use of rear bed illumination makes I_{thr} dependent on the fluidization regime. The higher gas flow rate leads to the bigger gas bubbles and, thus, to the brighter recorded images. The I_{thr} values used in this work slightly overestimate Otsu's predictions, ranging from Otsu's threshold + 0.04 (at low u_{gas}) to Otsu's + 0.07 (at high u_{gas}).

In order to determine the bubble size, an equivalent bubble diameter (d_b) was calculated. This d_b is defined in a 3D configuration as the diameter of a sphere that would occupy the same volume as a bubble under the assumption of rotational symmetry. Similarly, the equivalent diameter represents the diameter of a circular bubble that occupies the same area as a bubble in a pseudo-2D bed [13]. A single bubble velocity in the upward direction (u_b) can then be calculated by measuring the bubble centroid displacement between short delayed subsequent frames. The bubble tracking between frames was done by using a k-nearest-neighbor algorithm [13,18] from the Matlab 2010® libraries.

Eq. (1) describes the relation between the bubble cross section i (A_i, in pixels) and its equivalent bubble diameter, $d_{b,I}$, as a function of an

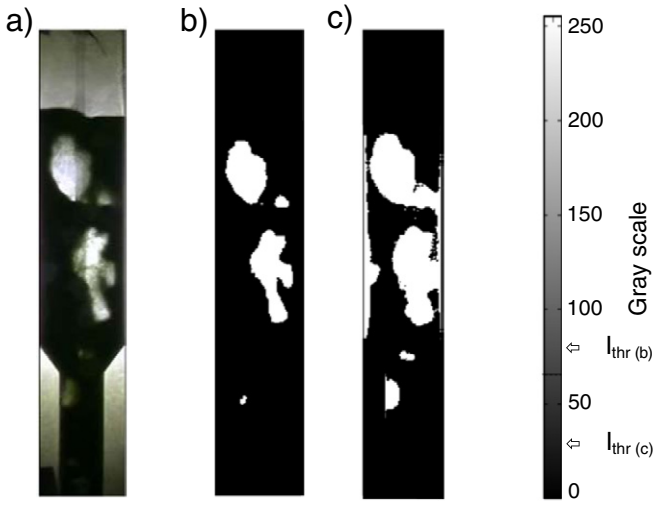

Fig. 3. Inaccurate bubble detection due to an inhomogeneous bed illumination. a) Raw image, b) $I_{thr} = 0.3$, underestimation of regeneration-zone bubbles, c) $I_{thr} = 0.1$, overestimation of reaction-zone bubbles and front face dirt detection.

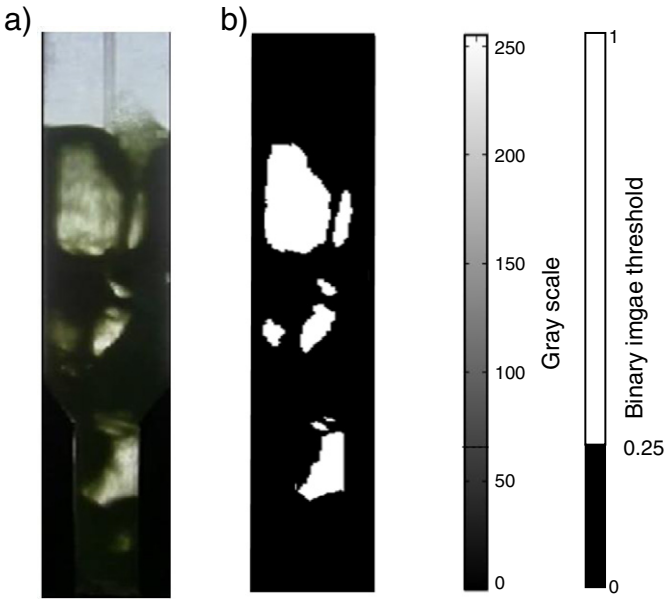

Fig. 4. Accurate bubble detection. a) Raw image, b) $I_{thr} = 0.25$.

image resolution factor (rf), which is used to transform size data from pixels to bubble areas: $A_i \times rf^2$, in cm^2.

The way of weighting the bubble size data determines subsequent $d_b(z)$ correlation studies, since all existing correlations in the literature refer to an equivalent bubble diameter that belongs to a certain d_b distribution. From a fluid dynamic point of view, the larger bubbles have an influence on the mixing of the solids inside a fluidized bed [2] greater than the smaller bubbles. In addition, small spurious bubbles are less representative of the bubbling gas flow than big bubbles. For these reasons, the average equivalent bubble diameter has been calculated in all cases as shown in Eq. (2). This equation weights bubble diameters proportionally to their size.

$$d_{b,i} = \sqrt{\frac{4A_i}{\pi} rf^2} \tag{1}$$

$$\bar{d}_b(z) = \frac{\sum_{i=1}^{n} d_{b,i}(z) \cdot d_{b,i}(z)}{\sum_{i=1}^{n} d_{b,i}(z)}. \tag{2}$$

Therefore, the experimental equivalent bubble diameter values correspond to a weighted mean value of a bubble size distribution along the axial position. A statistically consistent DIA method must consider certain number of bubble size data to get reliable results (related to the recording time) and must have good reproducibility. Bubble size measurements in fluidized beds usually imply great data dispersion. For this reason, the study of the standard data deviation together with the mean bubble size values is a must to get an idea on the variability of the bubble size data. The analysis of the average bubble size reproducibility along the recording time and the evaluation of the bubble data dispersion as a function of the operational conditions will be presented in Section 3.1.

2.3. Mathematical model to predict $d_b(z)$ in a TS-TZFBR

A critical evaluation of the literature has been carried out [6,19] to find a suitable correlation able to predict the experimental bubbling trends in a TS-TZFBR, considering the bed dimensions and the range of solid properties shown in Table 2. Although a number of empirical models to predict the evolution of $d_b(z)$ in conventional fluidized bed reactors have been described, few authors take into account the wall effect in the formulation of the bubble size correlation. For narrow vessels, the wall effect implies an asymptotic growth of the bubble size, limited by the bed width. These authors are, essentially, Mori and Wen [15], Horio and Nonaka [20] and Agarwal [21]. The two last authors suggest quite complicated correlations based on a number of empirical parameters, whereas Mori and Wen (MW) developed a more simple correlation based on a hypothetical maximum bubble diameter, d_{bm}. This d_{bm} is calculated as a function of gas velocity and the column diameter. The MW correlation can be applied in a wide range of operation conditions, as shown in Table 2. However, this model can only predict the bubbling behavior in straight fluidized beds. For this reason, an adaption of the MW correlation needs to be carried out to get a model that enables the prediction of the bubble characteristics within a TS-TZFBR, where a combined effect of a tapered region and an immersed gas inlet applies.

Previous studies [2] showed that both the section enlargement and the additional feed lead to an average bubble size reduction. On the one hand, bubbles coming from the narrow bed section exchange gas with the dense phase in order to maintain a minimum fluidization regime within the emulsion phase along the section enlargement. On the other hand, small incipient bubbles flow up from the secondary gas distributor located in the transition region and decrease the average bubble size within this zone. The different gas flows to be considered in the critical transition bed region have been schematized in Fig. 5.

Table 2
Comparison between the application range of the Mori–Wen correlation [15] and experimental conditions in the tested TS-TZFBR.

Operational variable	Mori–Wen correlation	Experimental TS-TZFBR
d_p (μm)	60–450	100–500
u_{mf} (cm/s)	0.5–20	1.2–20.5
$u_{gas} - u_{mf}$ (cm/s)	≤48	1–25
$D_{reactor}$ (cm)	≤130	2–4

In order to analyze the bubble size shrinkage due to the gas exchange between bubbles and the dense phase, a mass balance for the gas phase has been suggested. The control volume is comprised between two axial bed positions with different cross-sectional areas (S_0 and S_e). For a certain reactor section, S, the relative gas velocity can be expressed as: $u_{r,s} = Q_{gas,s}/Q_{mf,s}$. Considering that the whole gas excess over the minimum fluidization flows up as a gas bubble (Eq. (3)) and establishing that the gas flow remains constant between the sections S_0 and S_e, Eq. (4) shows the minimum fluidization flow in section S_0 as a function of the gas flow in bubbles ($Q_{b,0}$) and the relative gas velocity ($u_{r,0}$). The minimum fluidization velocity does not depend on the bed width ($u_{mf,0} = u_{mf,e}$), so the minimum fluidization flow at section 'e' can be related to the one at section '0' by Eq. (5). Substituting $Q_{mf,0}$ and $Q_{mf,e}$ in Eq. (3), a relation between the gas flow in bubbles for two different sections, $Q_{b,e}$ and $Q_{b,0}$, is obtained (Eq. (6)). The quotient $Q_{b,e}/Q_{b,0}$ can be expressed as a function of the equivalent bubble diameter: $(d_{b,e}/d_{b,0})^2$, assuming that the change in the bubble velocity within the tapered section is small against the change in bubble size, i.e. $d^2_{b,e}/d^2_{b,0} \gg u_{b,e}/u_{b,0}$ or analogously $u_{b,e} \approx u_{b,0}$. It is assumed that, in that region, bubbles exchange gas with the emulsion phase to meet minimum fluidization conditions in the tapered dense phase, thus, shrinking bubble size with a low affection to its velocity. Taking into account the changing section angle, α, and a constant bed depth in a pseudo-2D reactor configuration, w_{bed}, Eq. (7) shows the bubble size reduction along the vertical position (z) through the transition section due to the gas exchange between the bubbles and the dense phase.

When using TS-TZFBRs with sharp transition section angles and low gas velocities, a defluidization effect takes place affecting the particle region just over the section enlargement. The generation of defluidized or 'death' zones was observed by Julián et al. [2]. In such conditions, a banked region of particles is generated on both sides of the bed section enlargement. The 'death' region shape forms a so-called 'defluidization angle', β, with respect to the horizontal position. β varies with particle type and gas velocity (Fig. 8) and affects the bubble properties within the transition section. When working with reactor geometries and operational conditions that lead to $\beta > \alpha$, α must be substituted by β in Eq. (7). Otherwise, when working with soft transition section angles $\beta \le \alpha$, Eq. (7) remains as shown.

$$Q_{gas} = Q_{mf,0} + Q_{b,0} = Q_{mf,e} + Q_{b,e} \tag{3}$$

$$Q_{mf,0} = \frac{Q_{b,0}}{u_{r,0} - 1} \tag{4}$$

$$Q_{mf,e} = \frac{S_e}{S_0} Q_{mf,0} \tag{5}$$

$$Q_{b,e} = Q_{b,0} + \frac{Q_{b,0}}{u_{r,0} - 1} - \left(\frac{Q_{b,0}}{u_{r,0} - 1}\right)\frac{S_e}{S_0} = Q_{b,0}\left(1 + \frac{1}{u_{r,0} - 1}\left(1 - \frac{S_e}{S_0}\right)\right) \tag{6}$$

$$d_{b,e} = d_{b,0}\sqrt{1 + \frac{1}{u_{r,0} - 1}\left(1 - \frac{S_e}{S_0}\right)} = d_{b,0}\sqrt{1 - 2 \cdot \frac{z_e - z_0}{\left(u_{r,0} - 1\right) L_0 \tan\alpha}}. \tag{7}$$

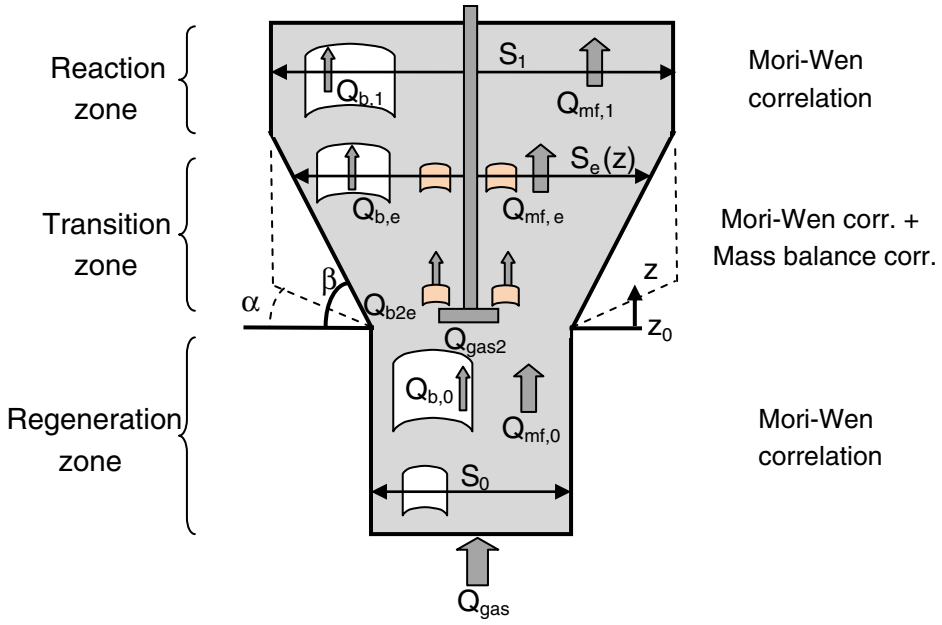

Fig. 5. Gas flow scheme within the transition section.

The height interval where Eq. (7) applies ranges from z_0 (beginning of the section change) to $z_{e,1}$, being $z_{e,1} = z_0 + \tan\alpha \cdot (L_{e,1} - L_0)/2$. In the case $\beta < \alpha$, $z_{e,1}$ will still be the maximum height of the hypothetical defluidized region that would correspond to the gas flow and the tested particle type, according to the results obtained by Julián et al. [2] and presented in Fig. 6.

The small incipient bubbles flowing up from the secondary gas distributor are supposed to be independent from the regeneration flow. This means that the bubble size profile for these bubbles could be well predicted by the MW correlation. As a result, two bubble size trends will be considered in the transition section: a shrinking one related to bubbles coming from the bottom region of the bed (regeneration zone) and a growing one related to the small bubbles from the secondary gas distributor. The average d_b within the critical section will be calculated with Eq. (2), by assuming that the bubbling frequency is similar for both bubble flows. Eqs. (8) to (16) describe the complete model to predict the evolution of the average equivalent bubble diameter along the vertical position of the reactor for a pseudo-2D TS-TZFBR.

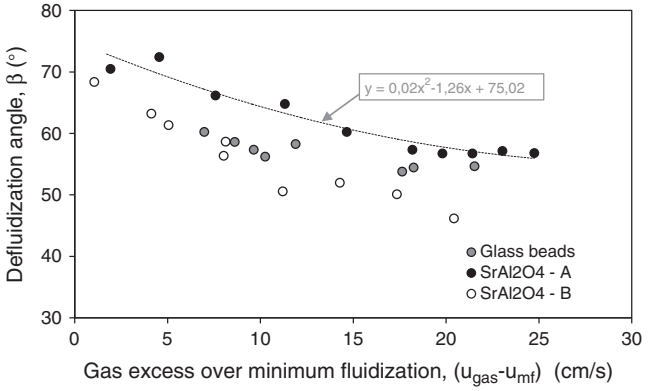

Fig. 6. Defluidization angle, β, as a function of particle type and gas velocity. Trendline shows the fit to an empirical curve for $SrAl_2O_4$-A particles.

– *Regeneration zone*:

$$z<z_0 : d_b(z) = 0.65(\pi/4 D_{bottom}{}^2\, u_{mf}\,(u_{r,0}-1))^{0.4} (1-\exp(-0.3z/D_{bottom})). \quad (8)$$

– *Transition region*:

• Bubbles coming from the regeneration zone (primary distributor):

$$z_{e,1}>z>z_0 : \quad d_{b,e}(z) = d_{b,0}\sqrt{1+\frac{1}{u_{r,0}-1}\left(1-\frac{S_e}{S_0}\right)} = d_{b,0}\sqrt{1-\frac{z-z_0}{\left(u_{r,0}-1\right)\tan\beta}}. \quad (9)$$

• Incipient bubbles from the secondary gas distributor:

$$z_{e,1}>z>z_0 : \quad d_{b,orif}(z) = d_{b,m} - \left(d_{b,m} - d_{b,orif}(z_0)\right)\exp(-0.3z/D_{top}) \quad (10)$$

being:

$$d_{b,m} = 0.65\left(\pi/4 D_{up}{}^2\, u_{mf}\,\left(u_{r,1}-1\right)\right)^{0.4}. \quad (11)$$

• Average bubble in the transition zone:

$$z_{e,1}>z>z_0 : \quad d_b(z) = \frac{d_{b,e}(z)^2 + d_{b,orif}(z)^2}{d_{b,e}(z) + d_{b,orif}(z)}. \quad (12)$$

– *Reaction zone*:

• Bubbles from the primary distributor:

$$z>z_{e,1} : \quad d_{b,1}(z) = d_{b,m1} - \left(d_{b,m1} - d_{b,1}\left(z_{e,1}\right)\right)\exp(-0.3z/D_{top}) \quad (13)$$

being:

$$d_{b,m1} = 0.65\left(\pi/4 {D_{top}}^2 u_{mf}\left(u_{r,0}-1\right)\right)^{0.4}. \quad (14)$$

- Bubbles coming from the secondary gas distributor:

$$z>z_{e,1}: \quad d_{b,orif}(z) = d_{b,m}-\left(d_{b,m}-d_{b,orif}\left(z_{e,1}\right)\right)\exp\left(-0.3z/D_{top}\right) \quad (15)$$

- Average bubble in the reaction zone:

$$z>z_{e,1}: \quad d_b(z) = \frac{d_{b,1}(z)^2 + d_{b,orif}(z)^2}{d_{b,1}(z) + d_{b,orif}(z)}. \quad (16)$$

2.4. Prediction of $u_b(z)$ in a TS-TZFBR

In addition to the classical bubble size correlations, some authors have obtained mathematical models to predict the average bubble velocity in the upward direction as a function of the bubble size and axial position in a fluidized bed. Among the most widely accepted correlations, the Davidson–Harrison equation (DH) gives the upward velocity of gas bubbles as a function of the gas excess over the minimum fluidization and the bubble size (Eq. (17)) [16].

$$u_b = \left(u_{gas}-u_{mf}\right) + K\sqrt{g\ d_b}. \quad (17)$$

The empirical parameter, K, has been determined to be 0.4 for pseudo-2D beds and 0.71 for bubble columns (3D beds). In the case of a TS-TZFBR, the axial variation of the bubble velocity can be related to the bubble size given by Eqs. (8) to (16). The gas excess, $u_{gas} - u_{mf}$, can also be calculated for every bed region considering the inlet gas flow through each gas distributor and the tested reactor geometry (α). Combining Eqs. (7) to (17) by a mass balance for the gas phase in the transition section, the Davidson–Harrison + Mori–Wen + Julián–Herguido–Menéndez model (DH + MW + JHM) is able to predict the average bubble velocity profile along the vertical position of the bed for every reactor region.

3. Results and discussion

In this section, the effects of different operation variables on the bed fluid dynamics is experimentally described and discussed. Moreover, the ability of the proposed hydrodynamic model to predict the TS-TZFBR bubbling properties (axial size and velocity profiles) is studied.

3.1. Experimental bubbling reproducibility and bubble data dispersion in TS-TZFBR

The bubbling regime in fluidized beds can be studied by means of the bubble size (d_b) or bubble velocity (u_b) evolution along the vertical axis. Usually, a mean d_b or u_b value is described for every axial cross-section in the bed to determine the average $d_b(z)$ or $u_b(z)$ trend. The bubbling behavior in a turbulent fluidization regime generally leads to a wide range of bubble sizes and velocities in upward direction. The bubble size data dispersion depends on the experimentally applied relative gas velocity. Fig. 7 shows an example of different bubble size data dispersions for the same reactor geometry but different gas flow rates. The dispersion interval of the bubble diameter distribution has been calculated according to the sample standard deviation (for each axial position slice, Δz). Fig. 7 suggests that higher gas velocities (turbulent regime) lead to bigger bubbles with a more dispersed bubble size distribution, whereas a lower gas flow rate leads to narrower data dispersion and smaller bubbles. For this reason, the amount of bubble data to be considered in order to reduce the statistical error has to be defined as a function of the variability in the bubble properties.

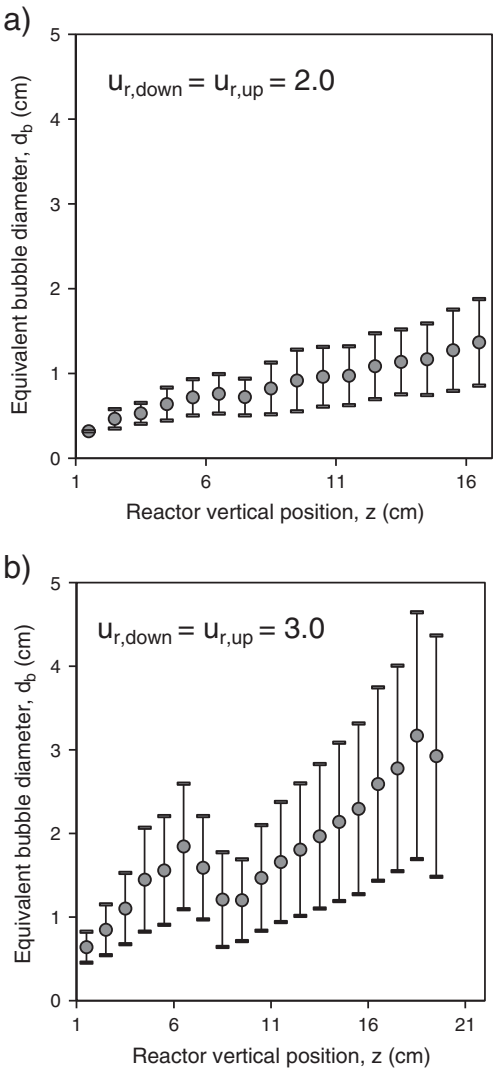

Fig. 7. Bubble size dispersion vs. reactor height for two fluidization regimes ($u_{r,i}$). $SrAl_2O_4$-A particles, $\alpha = 45°$, $z_{dis} = 8$ cm.

In Fig. 8, the average $d_b(z)$ profile is presented for different video recording times. The use of a large data series, i.e. large video sequences (Δt), results in a proper average $d_b(z)$ profile determination. A recording time of 40 s (almost 1000 frames and approximately 5000 bubble size data) seems to be enough to obtain a bubble size profile along the vertical axis without significant statistical error. In these conditions, the mean $d_b(z)$ profile was well reproduced when repeating experiments under the same operational conditions.

3.2. Bubble size profile in a TS-TZFBR. Predictive capabilities of classical correlations

The comparison between experimental bubble size profiles obtained in TS-TZFBR against several classical $d_b(z)$ correlations [15,22–29] (Fig. 9) illustrates how none of the existing models enables the prediction of the bubble size shrinkage within the tapered bed region of the TS-TZFBR. Nevertheless, it can be observed how the classical MW correlation fits very well within the straight column region (lower bed zone), but it over-predicts the bubble size above the transition angle zone. The over-prediction of the bubble size above the tapered region together with the impossibility to predict a bubble size decay in an intermediate point of the bed make all existing correlations

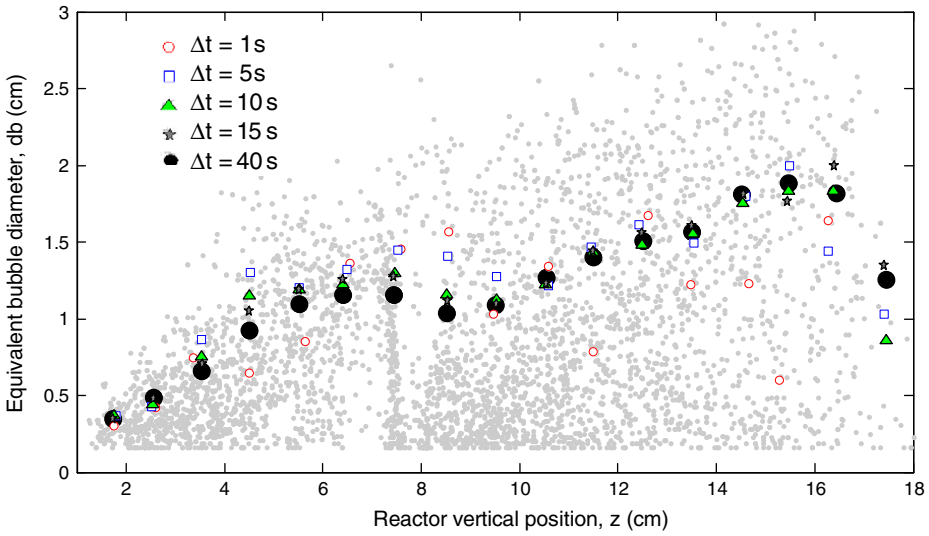

Fig. 8. Effect of the recording time on the axial $d_b(z)$ profile. $SrAl_2O_4$-A particles, $\alpha = 45°$, $z_{dis} = z_{cs} = 8$ cm, $u_{r,bottom} = u_{r,top} = 2.0$.

unable to model the bubbling behavior in a TS-TZFBR. Therefore, the use of the so called 'JHM model' is required to model the bubble size evolution within this reactor configuration.

3.3. Effect of particle type on the bubble size in a TS-TZFBR

Three different kinds of particles were tested to evaluate the effect of the particle type on the axial $d_b(z)$ profile. Experiments were performed using the same reactor geometries. Firstly, the same relative velocity was used for all the tested particles (Fig. 10a). Then, a similar gas excess was applied to all of them (Fig. 10b). In the first case, bigger particles led to bigger bubbles and higher bubble growth rates. This effect is related to the fact that the bigger particles have a higher u_{mf} and, thus, a higher gas excess when working at the same u_r with respect to smaller particles. However, if the same gas excess is used for all particle types (Fig. 10b) a similar axial d_b profile is obtained in all cases. This means that the effect of the particle type on the bubble size evolution is negligible compared to the effect of the fluidization gas velocity. This has been found to be applicable if all tested particles belong to the same Geldart particle type (in this case B-group) [30]. This also means that the hydrodynamic results obtained for a single particle type could be extrapolated to all kinds of particles in the same group by simply using the same gas excess over the minimum fluidization conditions, as may be expected from Eq. (8) (MW correlation).

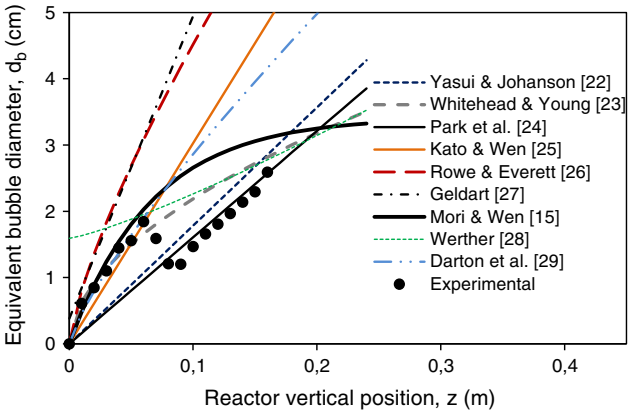

Fig. 9. Comparison between experimental $d_b(z)$ results and classical hydrodynamic correlation predictions [6]. Experimental conditions: $SrAl_2O_4$-A particles, $\alpha = 0°$, $z_{dis} = 8$ cm, $u_{r,bottom} = u_{r,top} = 3.0$.

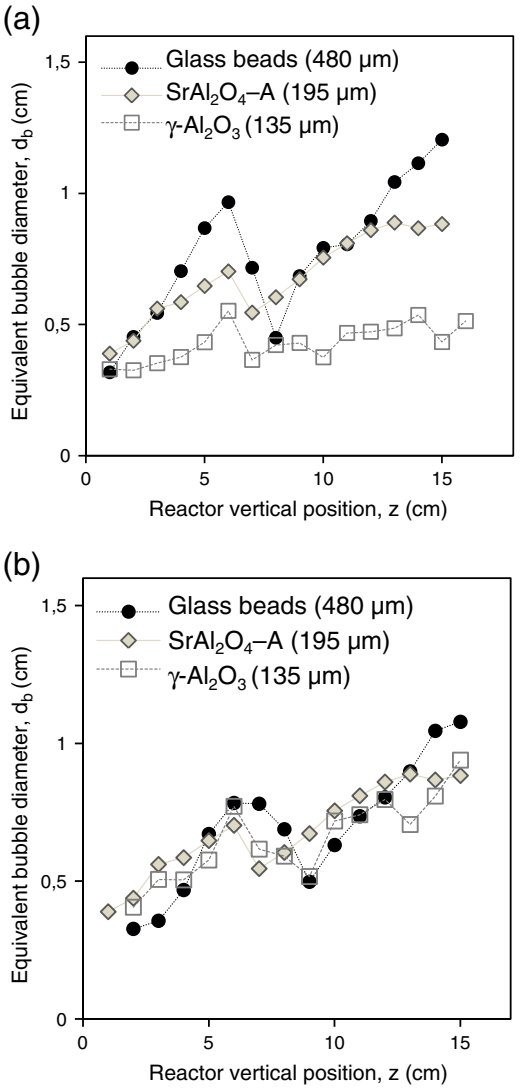

Fig. 10. Bubble size profile for three different B-group particles, $\alpha = 0°$, $z_{dis} = z_{cs} = 8$ cm, $u_{r,bottom} = u_{r,top}$. a) Same relative gas velocity: $u_r = 1.5$. b) Same gas excess: $u_{gas} - u_{mf} = 4$ cm.s^{-1}.

Another important effect to be considered is the equivalent bubble diameter shrinkage, which takes place within the transition section. The average bubble shrinkage appears to be sharper at higher gas excess over the minimum fluidization gas flow.

3.4. Effect of the transition angle (α) on the bubble shrinkage along the vertical reactor axis for a single bottom reactor inlet. Defluidization angle (β) analysis

An experimental series has been carried out in a single bottom gas inlet 'Two Section Fluidized Bed Reactor (TS-FBR)' to understand and quantify the gas transfer phenomenon between the bubbles and the dense phase within the transition section (to maintain the minimum fluidization condition). The same relative gas flows were fed into three different reactor geometries to test the influence of the transition angle on the decrease in the bubble size (Fig. 11a). The experimental results show how gradual transition angles ($\alpha = 85°$) lead to a smoother bubble size reduction, whereas geometries ranging from 0° to 45° show very similar results leading to sharp bubble shrinkage. This similarity suggests that the hydrodynamic behavior within sharp transition bed geometries could be affected by the so-called 'defluidization angle', β, instead of α. In these cases, 'death zones' of banked particles (defluidized regions) can be formed on both sides of the transition section and therefore the bubbling behavior may not be affected by the reactor geometry. Otherwise, the reactor geometry influences the equivalent bubble diameter shrinkage within the transition section only when $\alpha > \beta$.

As shown in Fig. 11a, the classical correlation for narrow straight bubble columns, i.e. the MW correlation [15], predicts an exponential bubble-growing trend that fits quite well with the experimental data within the lower zone. However, the tapered section cannot be modeled with such a correlation, since the bubble shrinkage effect is not negligible. This means a new correlation needs to be implemented for the upper zone.

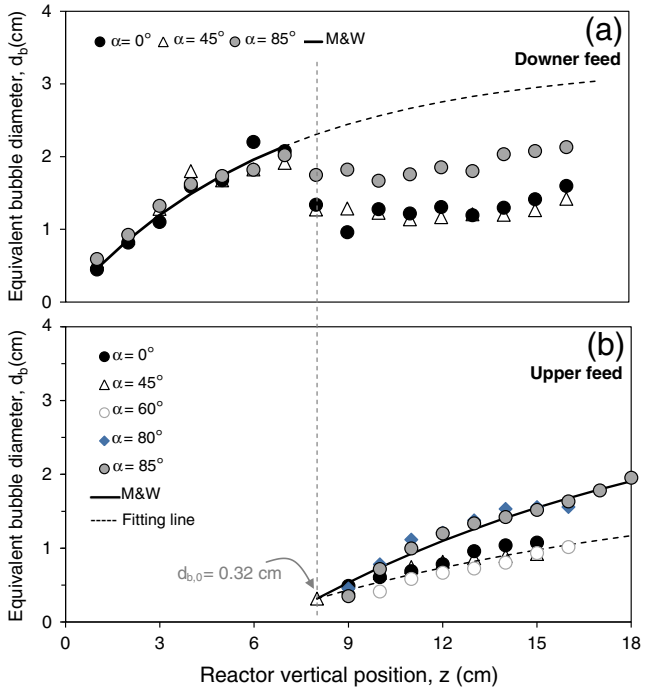

Fig. 11. Equivalent bubble diameter profiles for different transition angles $\alpha = 0°–85°$. Comparison with Mori–Wen correlation [15] for d_b (z). $SrAl_2O_4$-A particles, $z_{dis} = z_{cs} = 8$ cm. a) Lower feed: $u_{r,bottom} = 3.0$, $u_{r,top} = 0$. b) Upper feed: $u_{r,bottom} = 0$, $u_{r,top} = 3.0$.

3.5. Effect of the transition angle (α) on the bubble growth rate within the upper reactor section. Single upper inlet

In this section the bottom gas feed is set to zero and only an upper gas feed applies. The experimental series determines how the tapered section angle affects the bubble growth rate from the two-orifice T-shaped distributor, which is located at the bottom end of the tapered section. Again, the results show a different bubbling regime for reactor geometries with α ranging from 0° to 60° with respect to those at $\alpha = [80°–85°]$ (Fig. 11b). This trend may be related to the formation of banked regions with a certain defluidization angle (β), taking into account the same consideration as in Section 3.3. In this case, β should be very close to 60° according to the experimental results shown in Fig. 6.

However, both the Mori–Wen model and the fitting trend from Fig. 11b suggest a similar initial bubble size ($d_{b,0}$) related to the diameter of the orifice gas distributor, i.e. orifice cross sectional area (A_t), the number of orifices (n) and the applied differential velocity ($u_{gas} - u_{mf}$). When comparing this experimental $d_{b,0}$ value with those predicted by classical Miwa (Eq. (18)) [31] and Chiba (Eq. (19)) [32] correlations for orifice distributors, both result in a good agreement. The Miwa and Chiba predictions differ from each other by almost 30%. This deviation gives an idea of how difficult it is to accurately estimate the initial bubble diameter for a certain orifice distributor. Nevertheless, such deviations result in a small absolute error for the estimation of $d_{b,0}$, since low gas velocities and small orifice distributor diameters have been tested here.

$$d_{b,0} = 0.347\left(\frac{A_t\left(u_{gas}-u_{mf}\right)}{n}\right)^{0.4} \rightarrow\rightarrow \left|d_{b,0}\right|_{ur=3.0,\ n=2,\ At=0.07} = 0.30\ \text{cm} \quad (18)$$

$$d_{b,0} = 0.431\left(\frac{A_t\left(u_{gas}-u_{mf}\right)}{n}\right)^{0.4} \rightarrow\rightarrow \left|d_{b,0}\right|_{ur=3.0,\ n=2,\ At=0.07} = 0.38\ \text{cm} \quad (19)$$

The MW correlation is able to predict the bubble size evolution within the reaction zone for gradual transition section angles ($\alpha > 60°$). For sharp section changes ($\alpha \leq 60°$), this equation over-predicts the experimental results due to the fact that the cross-sectional area in such cases is larger and thus the gas excess over u_{mf} is lower, leading to smaller bubbles.

3.6. Bubbling regime in a TS-TZFBR. Experimental $d_b(z)$ profiles and model predictions

Hitherto, the effect of the particle type and reactor geometry on the TS-TZFBR hydrodynamic performance has been determined. Also, the bubble size evolution along the vertical axis has been studied for bubbles from the primary and secondary gas distributors, separately. Now the predictions of the proposed mathematical model will be tested for the axial $d_b(z)$ evolution along the three regions in the TS-TZFBR. The MW correlation was used to predict both the size of the bubbles from the primary distributor in the regeneration zone and the size of those coming up from the secondary distributor along the reaction zone. The bubble shrinkage in the transition zone was described from a mass balance for the gas phase in that region (Eqs. (13)–(16)).

Fig. 12a shows the model prediction of $d_b(z)$ for $SrAl_2O_4$-A particles tested with three different sharp transition section geometries (0°, 45° and 60°) and the same relative gas velocity in both reaction and regeneration zones: $u_r = 2.5$. The model provides a reasonably good agreement with the experimental values obtained for the same flow conditions and different reactor geometries. Similar trends can be found when predicting the hydrodynamic behavior in a TS-TZFBR with a gradual section change and for different relative gas velocities (Fig. 12b).

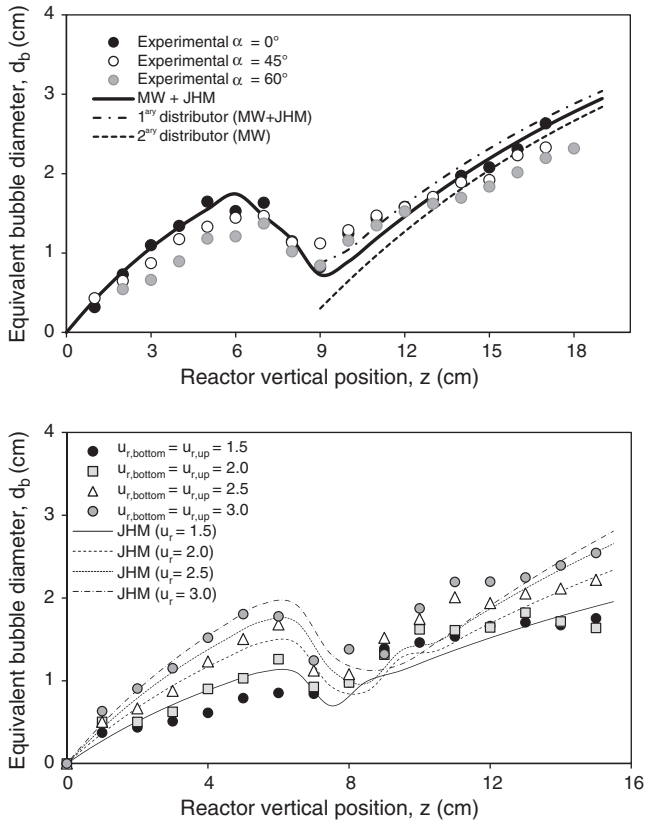

Fig. 12. Experimental bubble size evolution and MW + JHM model predictions: a) at three different TS-TZFBR sharp geometries ($\alpha = 0°$, 45° and 60°) and $u_{r,bottom} = u_{r,top} = 2.5$. b) at a soft geometry ($\alpha = 85°$) and four different gas flow rates. $SrAl_2O_4$-A particles, $z_{dis} = z_{cs} = 8$ cm.

The consideration of 'defluidization' effects in the mass balance improves the model predictions. Fig. 13a and b illustrate different examples where the use of α or β is required in order to better explain and predict the experimental trends. In the case of Fig. 13a, the use of a high relative gas velocity coupled with a gradual section change determines that the transition section angle, α, must be used [MW + JHM(α)] to predict the bubble shrinkage within the transition region. Fig. 13b shows experimental results obtained in a sharp transition geometry ($\alpha = 0°$) at the same u_r. As a consequence, a certain 'death zone' appears over the section change and its slope needs to be considered. For this reason, the use of β in the model [MW + JHM(β)] leads to a better prediction of the bubble size reduction. This defluidization angle was calculated from the correlation shown in Fig. 6, as a function of u_r for $SrAl_2O_4$-A particles (57.7°).

3.7. Bubbling regime in a TS-TZFBR. Experimental $u_b(z)$ profiles and model predictions

The use of a combined MW correlation and the model suggested in this work (JHM) allows a reasonably good prediction of the bubble size evolution along the whole axial bed position in a TS-TZFBR for the operational conditions tested. Moreover, the equivalent bubble diameter has been found to be proportional to the bubble velocity in the upward direction in a TS-TZFBR (Fig. 14), as the classical DH [16] correlation (Eq. (17)) for conventional fluidized beds suggests. Then, Eq. (17) can predict the axial evolution of the bubble velocity in the upward direction, $u_b(z)$, in a TS-TZFBR. The comparison between experimental average u_b values and the model prediction shows quite a good agreement when using a parameter value K = 0.4 in the DH equation (Fig. 15a). This value was found by Davidson and Harrison to be the most suitable one to predict u_b within pseudo-2D fluidized beds [5,16]. A parametric study of K (Fig. 15b) to predict the bubbling behavior in a TS-TZFBR also gives K = 0.4 for the best fit.

Once the K value is defined in accordance with the suggestion of Davidson and Harrison for pseudo-2D reactors, the complete model (DH + MW + JHM) provides a reasonably good prediction of the bubble properties d_b and u_b along the bed height without adjustable parameters. This means that the experimental data fitting can be carried out simply by considering physical parameters of the TS-TZFBR such as gas flows through the different bed zones, transition section angle, defluidization angle, particle type (minimum fluidization velocity), axial position of the secondary gas distributor and bed diameter.

4. Conclusions

Hydrodynamic behavior determines the axial particle circulation between the two considered bed zones and, therefore, the performance of a TS-TZFBR in terms of allowing continuous catalyst regeneration in a single fluidized bed. The experimental imaging technique based on fluidization video recording provides a substantial amount of useful data for studying the bubbling phenomenon in a TS-TZFBR pseudo-2D. The experimental data has been analyzed and classified in order to carry out a statistical analysis of the axial variation of bubble properties, such as size and velocity in the upward direction. The effect of several operational variables on the hydrodynamic behavior has been determined. A full predictive model without adjustable parameters has been developed to predict the evolution of bubble properties d_b and u_b along the reactor vertical axis. The so called MW + JHM model suggested in this work is able to predict the experimental $d_b(z)$ evolution in a range of relative velocities, $u_r = [1.5–3.0]$ considering the tested $SrAl_2O_4$-A particles in a TS-TZFBR, e.g. a gas excess range: $u_{gas} - u_{mf} = [5–20]$ cm/s. At the highest value of gas excess the 'slugging' phenomenon that modifies the hydrodynamic behavior appears to be important within the narrow bed section (i.e., the regeneration section). At the lowest value, incipient defluidization and 'channeling' effects also influence the bubble size, leading to a poor $d_b(z)$ profile prediction.

Notation

α	transition section angle in a TS-TZFBR, [°]
β	defluidization angle in a TS-TZFBR, [°]
ε_{bed}	fixed bed porosity, [−]
ρ_{bed}	fixed bed density, [g/cm^3]
ρ_s	particle density, [g/cm^3]
A_i	bubble cross section, [pixels]
A_t	orifice cross section, [cm^2]
CFD	Computational Fluid Dynamics
d_b	equivalent bubble diameter, [cm]
$d_{b,m}$	hypothetical maximum bubble diameter in the Mori–Wen correlation, [cm]
$d_{b,max}$	maximum bubble diameter within the regeneration zone, [cm]
$d_{b,orif}$	initial bubble diameter of bubbles coming up from the distributor orifice, [cm]
$d_{b,0}$	bubble diameter at the bottom of the section enlargement, [cm]
$d_{b,e}$	bubble diameter at an intermediate point of the section enlargement, [cm]
d_{orif}	diameter of the distributor orifice, [cm]
d_p	average particle diameter, [μm]
D_{bottom}	reactor diameter in the bottom section, [cm]
D_{top}	reactor diameter in the upper straight section, [cm]

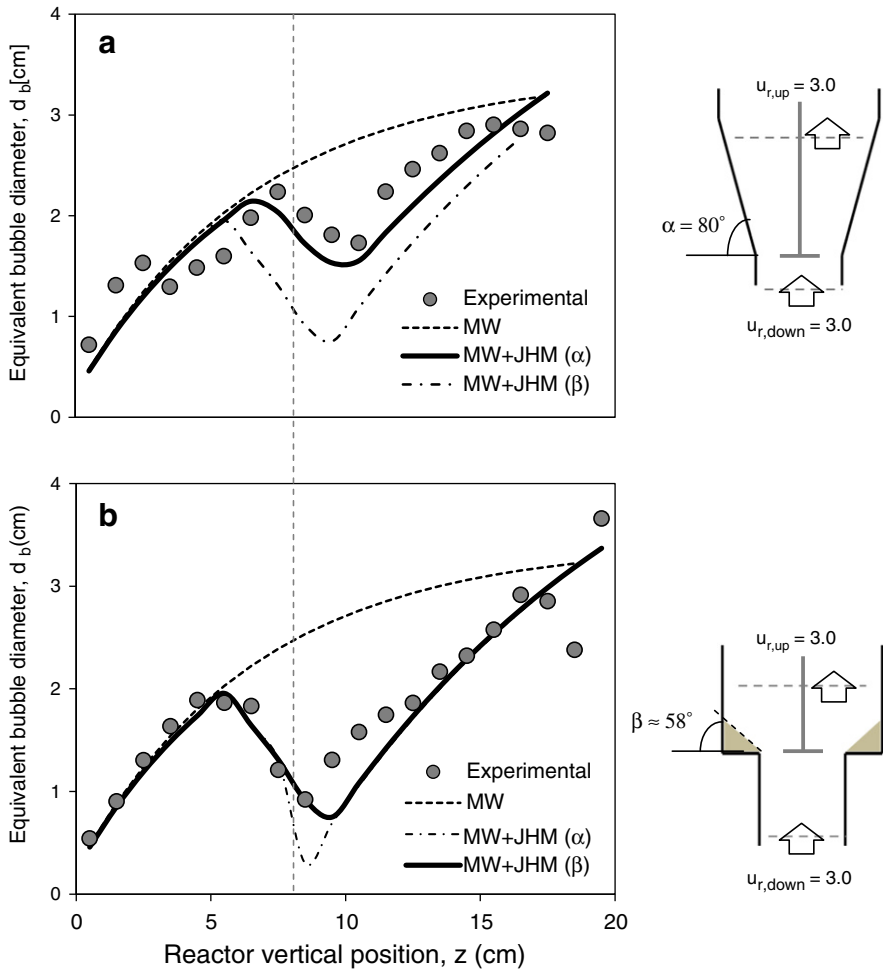

Fig. 13. Experimental $d_b(z)$ prediction using: a) the transition section angle, α, for gradual geometries and high gas velocities, b) the defluidization angle, β, for sharp transition geometries. $z_{dis} = z_{cs} = 8$ cm.

DH Davidson–Harrison hydrodynamic correlation to predict $u_b(d_b)$

DH + MW + JHM Davidson–Harrison + Mori–Wen + Julián–Herguido–Menéndez model to predict $u_{b,TS\text{-}TZFBR}(z)$

DIA Digital Image Analysis

g gravitational constant, [cm/s^2]

I_{thr} normalized intensity threshold value (range 0–1), [−]

K constant factor in the Davidson–Harrison hydrodynamic correlation, [−]

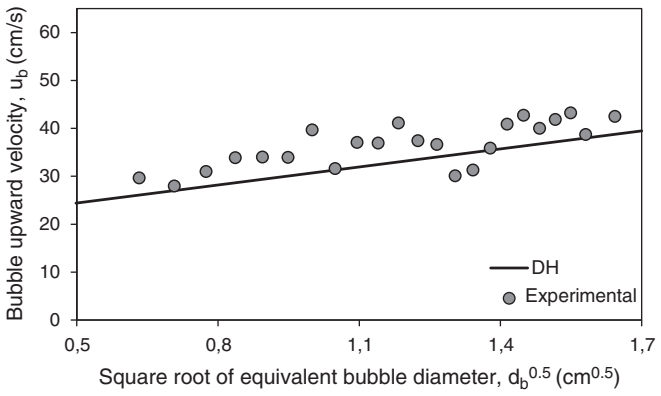

Fig. 14. Proportionality between bubble size and upward velocity in a TS-TZFBR.

L_0 bed width at '0' axial location, [cm]

$L_{e,1}$ bed width at the top axial location of the effective tapered region ('e,1'), [cm]

MW Mori–Wen hydrodynamic correlation to predict $d_b(z)$

MW + JHM Mori–Wen + Julián–Herguido–Menéndez hydrodynamic correlation to predict $d_{b,TS\text{-}TZFBR}(z)$

n number of orifices, [−]

$Q_{b,0}$ bubble gas flow within the lower zone, [cm^3/s]

$Q_{b,1}$ bubble gas flow within the upper zone, [cm^3/s]

$Q_{b,e}$ bubble gas flow coming from the lower zone within the tapered region, [cm^3/s]

$Q_{b,2e}$ bubble gas flow from the immersed distributor within the tapered region,[cm^3/s]

Q_{gas} gas flow from the primary gas distributor, [cm^3/s]

$Q_{gas,2}$ gas flow from the immersed gas distributor, [cm^3/s]

$Q_{mf,0}$ minimum fluidization gas flow in the regeneration zone, [cm^3/s]

$Q_{mf,e}$ minimum fluidization gas flow in a region with cross-sectional area: S_e, [cm^3/s]

$Q_{mf,1}$ minimum fluidization gas flow in the reaction zone, [cm^3/s]

TZFBR Two-Zone Fluidized Bed Reactor

TS-TZFBR Two-Section Two-Zone Fluidized Bed Reactor

rf image resolution factor, [cm/pixels]

S cross-sectional area in a TS-TZFBR, [cm^2]

S_e equivalent cross-sectional area in a TS-TZFBR (defluidized region limited), [cm^2]

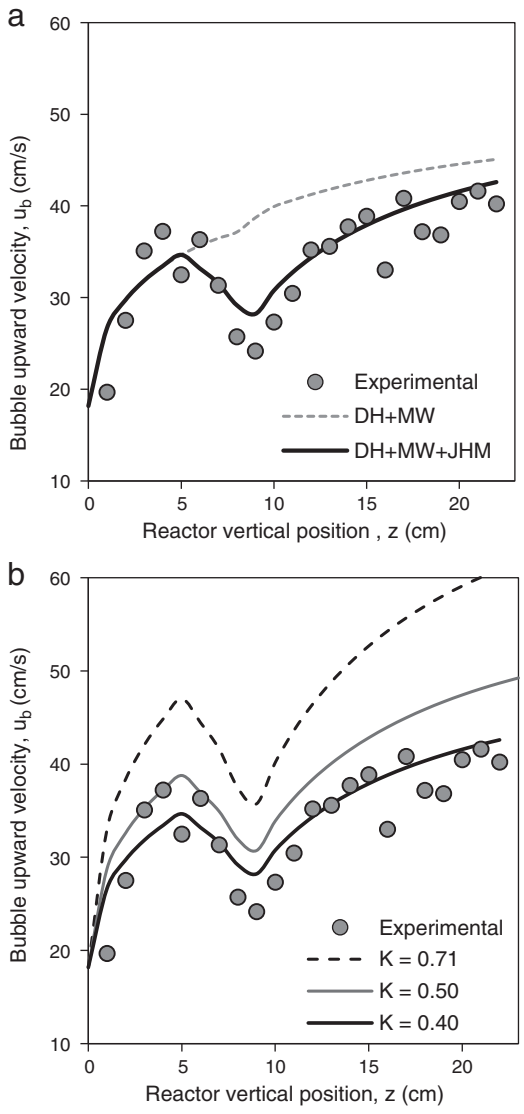

Fig. 15. a) Comparison between the DH + MW and the DH + MW + JHM model prediction for the experimental $u_b(z)$ profile. b) Parametric study of K in the DH + MW + JHM model for the prediction of $u_b(z)$. $SrAl_2O_4$-A particles, $\alpha = 0°$, $z_{dis} = z_{cs} = 8$ cm, $u_{r,bottom} = u_{r,top} = 2.8$.

S_0	cross-sectional area in the regenerative region in a TS-TZFBR, [cm^2]
S_1	cross-sectional area in the reactive region in a TS-TZFBR, [cm^2]
u_b	bubble velocity in the upward direction, [cm/s]
$u_{b,exp}$	experimental bubble velocity in the upward direction, [cm/s]
u_{gas}	inlet gas velocity, [cm/s]
$u_{mf,i}$	minimum fluidization velocity for a particle type i, [cm/s]
u_r	relative gas velocity, [−]
$u_{r,bottom}$	relative gas velocity within the regenerative section, [−]
$u_{r,top}$	relative gas velocity within the reactive region, [−]
w_{frame}	frame width, [pixels]
W_{bed}	bed weight, [g]
w_{bed}	bed depth, [cm]
z	reactor vertical position coordinate, [cm]
z_0	bottom end location of the section change and 2^{ary} gas distributor location, [cm]
z_{cs}	bottom end location of the section change, [cm]
z_{dis}	vertical position of the secondary gas distributor feed point, [cm]
$z_{e,1}$	top axial location of the effective tapered region ('e,1'), [cm]

Acknowledgment

Financial support from the *Spanish Ministerio de Economía y Competitividad* (MINECO) through Project CTQ2010-15568 is gratefully acknowledged. Financial aid for the maintenance of the consolidated research group CREG has been provided by the *Fondo Social Europeo* (FSE) through the *Gobierno de Aragón* (Aragón, Spain).

References

[1] J. Herguido, M. Menéndez, J. Santamaría, On the use of fluidized bed catalytic reactors where reduction and oxidation zones are present simultaneously, Catal. Today 100 (2005) 181–189.
[2] I. Julián, F. Gallucci, M. van Sint Annaland, J. Herguido, M. Menéndez, Coupled PIV/DIA for fluid dynamics studies on a Two-Section Two-Zone Fluidized Bed Reactor, Chem. Eng. J. 207–208 (2012) 122–132.
[3] M.P. Gimeno, J. Soler, J. Herguido, M. Menéndez, Counteracting catalyst deactivation in methane aromatization with a Two Zone Fluidized Bed Reactor, Ind. Eng. Chem. Res. 49 (2010) 996–1000.
[4] M.P. Gimeno, J. Soler, Z.T. Wu, J. Herguido, K. Li, M. Menéndez, Combination of a Two-Zone Fluidized Bed Reactor with a Pd hollow fiber membrane for catalytic alkane dehydrogenation, Chem. Eng. J. 155 (2009) 298–303.
[5] D. Kunii, O. Levenspiel, Fluidization Engineering, Butterworth-Heinemann, 1991.
[6] S. Karimipour, T. Pugsley, A critical evaluation of literature correlations for predicting bubble size and velocity in gas–solid fluidized beds, Powder Technol. 205 (2011) 1–14.
[7] M.H. Khani, Models for prediction of hydrodynamic characteristics of gas–solid tapered and mini-tapered fluidized beds, Powder Technol. 205 (2011) 224–230.
[8] D.C. Sau, K.C. Biswal, Computational Fluid Dynamics and experimental study of the hydrodynamics of a gas–solid tapered fluidized bed, Appl. Math. Model. 35 (2011) 2265–2278.
[9] D.C. Sau, S. Mohanty, K.C. Biswal, Experimental studies and empirical models for the prediction of bed expansion in gas–solid tapered fluidized beds, Chem. Eng. Process. 49 (2010) 418–424.
[10] D.C. Sau, S. Mohanty, K.C. Biswal, Correlations for critical fluidization velocity and maximum bed pressure drop for heterogeneous binary mixture of irregular particles in gas–solid tapered fluidized beds, Chem. Eng. Process. 47 (2008) 2386–2390.
[11] T. Dyakowski, A.J. Jaworski, Application of non-invasive techniques for imaging fluidized beds — a review, Handbook of Powder Technology, Elsevier Science B.V., 2001. 807–823.
[12] M. Liu, Y. Zhang, H. Bi, J.R. Grace, Y. Zhu, Non-intrusive determination of bubble size in a gas–solid fluidized bed: an evaluation, Chem. Eng. J. 65 (2010) 3485–3493.
[13] A. Busciglio, G. Vella, G. Micale, L. Rizzuti, Analysis of the bubbling behaviour of 2D gas solid fluidized beds Part I. Digital Image Analysis technique, Chem. Eng. J. 140 (2008) 398–413.
[14] L.H. Shen, F. Johnsson, B. Leckner, Digital Image Analysis of hydrodynamics two-dimensional bubbling fluidized beds, Chem. Eng. Sci. 59 (2004) 2607–2617.
[15] S. Mori, C.Y. Wen, Estimation of bubble diameter in gaseous fluidized-beds, AIChE J 21 (1975) 109–115.
[16] J.F. Davidson, D. Harrison, The behaviour of a continuously bubbling fluidised bed, Chem. Eng. Sci. 21 (1966) 731–738.
[17] T. Kurita, N. Otsu, N. Abdelmalek, Maximum-likelihood thresholding based on Population Mixture-models, Pattern Recogn. 25 (1992) 1231–1240.
[18] T.W. Asegehegn, M. Schreiber, H.J. Krautz, Investigation of bubble behavior in fluidized beds with and without immersed horizontal tubes using a Digital Image Analysis technique, Powder Technol. 210 (2011) 248–260.
[19] A. Farshi, H. Javaherizadeh, M.A. Hamzavi-Abedi, Investigation of the effect of bubble diameter on the performance of gas–solid fluidized bed reactor and two-phase modelling of gas fluidized bed reactor in melamine production, Pet. Coal 50 (2008) 11–22.
[20] M. Horio, A. Nonaka, A generalized bubble diameter correlation for gas–solid fluidized-beds, AIChE J 33 (1987) 1865–1872.
[21] P.K. Agarwal, Effect of bed diameter on bubble-growth and incipient slugging in gas-fluidized beds, Chem. Eng. Res. Des. 65 (1987) 345–354.
[22] G. Yasui, L.N. Johanson, Characteristics of gas pockets in fluidized beds, AIChE J 4 (1958) 445.
[23] A.B. Whitehead, A.D. Young, Fluidization performance in large scale equipment, part I, Proc. Int. Symp. on Fluidization, Eindhoven (Netherlands), 1967.
[24] W.H. Park, W.K. Kang, C.E. Copes, G.L. Osberg, The properties of bubble in fluidized beds of conducting particles as measured by an electroresistivity probe, Chem. Eng. Sci. 24 (1969) 851.
[25] K. Kato, C.Y. Wen, Bubble assemblage model for fluidized bed catalytic reactors, Chem. Eng. Sci. 24 (1969) 1351–1369.
[26] P.N. Rowe, Prediction of bubble size in a gas fluidized bed, Chem. Eng. Sci. 31 (1976) 285–288.

[27] D. Geldart, The size and frequency of bubbles in two and three dimensional gas fluidized beds, Powder Technol. 4 (1971) 41.
[28] J. Werther, Mathematical modeling of fluidized bed reactors, Int. J. Chem. Eng. 20 (1980) 529–541.
[29] R.C. Darton, R.D. Lanauze, J.F. Davidson, D. Harrison, Bubble growth due to coalescence in fluidized beds, Trans. Inst. Chem. Eng. 55 (1977) 274.
[30] D. Geldart, The effect of particle size and size distribution on the behaviour of gas-fluidised beds, Powder Technol. 6 (1972) 201–215.
[31] K. Miwa, S. Mori, T. Kato, I. Muchi, Behavior of bubbles in a gaseous fluidized-bed, Int. Chem. Eng. 12 (1972) 187–194.
[32] T. Chiba, K. Terashima, H. Kobayashi, Behaviour of bubbles in gas–solids fluidized beds: initial formation of bubbles, Chem. Eng. Sci. 27 (1972) 965–972.

Artículo IV

I. Julián, J. Herguido, M. Menéndez,
CFD model prediction of a Two-Section Two-Zone Fluidized Bed Reactor hydrodynamics,
Chem. Eng. J. 248 (2014) 352-362

Chemical Engineering Journal 248 (2014) 352–362

Contents lists available at ScienceDirect

Chemical Engineering Journal

journal homepage: www.elsevier.com/locate/cej

CFD model prediction of the Two-Section Two-Zone Fluidized Bed Reactor (TS-TZFBR) hydrodynamics

I. Julián, J. Herguido, M. Menéndez *

Catalysis, Molecular Separations and Reactor Engineering Group (CREG), Department of Chemical and Environmental Engineering (IQTMA), Aragon Institute of Engineering Research (I3A), Universidad de Zaragoza, 50018 Zaragoza, Spain

HIGHLIGHTS

- Gas and solid hydrodynamics in a two-zone fluidized bed reactor.
- A two-fluids model was employed to predict the hydrodynamics.
- Good agreement in bubble size and velocity with previous experimental results.
- Prediction of defluidized zones in some operating conditions.
- Good prediction for gas hydrodynamics but not for solid flow in this reactor.

GRAPHICAL ABSTRACT

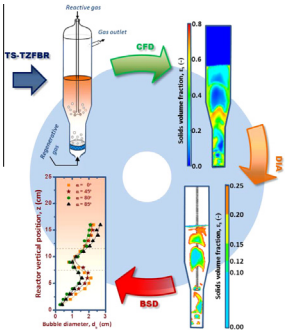

ARTICLE INFO

Article history:
Received 20 December 2013
Received in revised form 26 February 2014
Accepted 9 March 2014
Available online 21 March 2014

Keywords:
CFD
Fluidized bed
Bubble hydrodynamics
Two-zone fluidized bed reactor

ABSTRACT

Computational simulations and experiments have been carried out to study the bed hydrodynamics in a Two-Section Two-Zone Fluidized Bed Reactor (TS-TZFBR). An Eulerian–Eulerian two-fluid approach has been used to simulate the reactor bubbling behavior, while cold fluidization measurements have been made in pseudo-2D TS-TZFBR facilities. The characteristic bubble shrinkage within the transition bed section as well as the eventual formation of defluidized bed regions have been well predicted by the CFD model. The effect of TS-TZFBR geometry, i.e. the transition section angle (α), superficial gas velocity in the bed and immersed gas distributor location, on the experimental hydrodynamic behavior has been compared to that in computational simulations, resulting in a reasonably good agreement. Bubble related properties have been analyzed for both simulations and experimental measurements. The experimental results validate the standard Eulerian–Eulerian model for simulating the TS-TZFBR bubble hydrodynamics in a wide range of operational conditions: u_{gas}–u_{mf} = [5–20] cm/s, α = [0°–85°].

1. Introduction

The Two-Zone Fluidized Bed Reactor (TZFBR) is a multifunctional reactor configuration designed to overcome the problem of catalyst deactivation that occurs in some catalytic processes (Fig. 1a). In a TZFBR, a desired gas–solid catalytic reaction and catalyst regeneration take place simultaneously within a single fluidized bed. This is achieved by the use of two separated gas feeds with different compositions and by taking advantage of the particle axial mixing, a well-known characteristic of fluidized beds. As described elsewhere [1], the regenerative gas, i.e. an oxidizer agent, flows up from the bottom of the fluidized bed, burning the coke that partially covers the catalytic surface. At the same time, the reactive gas, usually a hydrocarbon, which is fed at an intermediate point of the bed, reacts within the upper bed region where the catalyst is deactivated. The solid circulation between the bed zones

* Corresponding author. Tel.: +34 976 761152; fax: +34 976 762043.
E-mail address: qtmiguel@unizar.es (M. Menéndez).

http://dx.doi.org/10.1016/j.cej.2014.03.028
1385-8947/

Nomenclature

b_d	bubble population density ($n_{bub.}$/cm^2 s)
B_e	bed expansion (–)
b_h	bubbles holdup (%)
C_D	drag coefficient (–)
CFD	Computational Fluid Dynamics
d_b	equivalent bubble diameter (cm)
d_p	particle diameter (m)
DIA	Digital Image Analysis
e	restitution coefficient (–)
g	acceleration due to gravity (m/s^2)
g_0	radial distribution function (–)
$\bar{\bar{I}}$	stress tensor (–)
K_{gs}	interphase momentum exchange coefficient (kg/m^3 s)
KTGF	Kinetic Theory of Granular Flow
P	pressure (Pa)
PIV	Particle Image Velocimetry
Re	Reynolds number (–)
TS-TZFBR	Two-Section Two Zone Fluidized Bed Reactor
TZFBR	Two-Zone Fluidized Bed Reactor
u_{gas}	gas velocity (cm/s)
u_{mf}	minimum fluidization velocity (cm^3/cm^2 s)
$u_{r,bottom}$	relative velocity (u_{gas}/u_{mf}) within the lower bed section (–)
$u_{r,top}$	relative velocity (u_{gas}/u_{mf}) within the upper bed section (–)
$\vec{v}$	local velocity (m/s)
z_{dis}	immersed distributor axial location (cm)
z_{sc}	TS-TZFBR section change axial location (cm)

Greek symbols

α	tapered section angle (°)
β	defluidization angle (°)
ε	volume fraction (–)
θ	granular temperature (m^2/s^2)
λ	bulk viscosity (kg/(m s))
μ	shear viscosity (kg/(m s))
μ_{col}	collisional shear viscosity (kg/(m s))
ρ	density (kg/m^3)
$\bar{\bar{\tau}}$	stress–strain tensor (kg/(m s^2))
φ	bubble aspect ratio (–)
ω	probability density of bubble size (%)

Subscripts

i	phase i, either fluid or solid
g	fluid phase (gas)
s	solid phase
m	maximum
0	initial

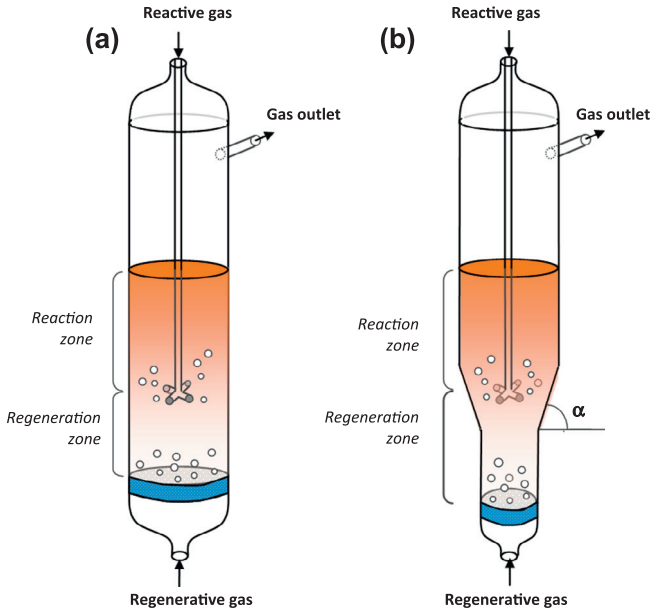

Fig. 1. (a) Scheme of a 3D TZFBR, (b) scheme of a 3D TS-TZFBR.

with different atmospheres (reactive and regenerative) provides the process integration.

A recent modification to the TZFBR configuration provides different cross-sectional areas in each bed zone in order to achieve better fluid dynamic control. This allows low regenerative-to-reactive flow rates when required (Fig. 1b) [2,3]. The so-called Two-Section TZFBR (TS-TZFBR) includes a tapered bed region that connects the upper and lower reactor zones. The transition section angle between bed zones, α, is a critical factor for achieving a proper solid circulation and, therefore, its effect on the TS-TZFBR fluid dynamic behavior has recently been studied [2].

The TS-TZFBR has proved to be effective in counteracting catalyst deactivation due to coke deposition in several dehydrogenation reactions [3–5] and ethanol reforming [6] at lab scale. At this scale, the fluid dynamic limitations of the TS-TZFBR are well-known and a suitable operational window has been proposed in previous studies [2] to achieve a satisfactory reactor performance. However, a scaling-up process is required in order to make this system feasible for large scale operation.

Computational Fluid Dynamics (CFD) is a useful tool for reducing the number of scale-up steps in multiphase flows such as gas–solid flow systems (e.g. [7–9]). Many efforts have been made to develop realistic models to predict fluid-particle interactions accurately [9–17]. In addition, the large increase in computational resources during recent decades makes the solution of this kind of complex multiphase fluid dynamics problem feasible. Among the available simulation models, the Eulerian–Eulerian model is widely preferred for the simulation of macroscopic hydrodynamics in dense fluidized beds because it provides a reasonable compromise between accuracy and computational cost [16,18–20]. According to this Eulerian model [21], both particulate and gas phases are considered as continuum interpenetrating media and the kinetic theory approach is employed for the solid phase formulation. The Kinetic Theory of Granular Flow (KTGF) considers instantaneous binary particle–particle interactions similar to those between molecules in gas phase. Mass, momentum and energy balances can thus be described for each phase separately. Additionally, an inter-phase momentum transfer correlation needs to be addressed, as a closure equation, to solve the problem [21,22]. Several authors have recently used the Eulerian approach to describe the tapered bed dynamics [23,24] as well as the hydrodynamic behavior of fluidized beds with multiple jets [25]. In this work, the Eulerian–Eulerian model, i.e. the Two-Fluid Model (TFM), is first applied to simulate the TS-TZFBR bed dynamics where both a tapered section and multiple gas inlets are present in a single fluidized bed.

Given that CFD models involve several assumptions, they must be experimentally validated. Some of the challenges regarding CFD

model validation for gas–solid fluidized beds have been reviewed by Grace and Taghipour [26]. In the present study, CFD hydrodynamic results from different TS-TZFBR configurations are validated with experimental cold pseudo-2D measurements via Digital Image Analysis (DIA). The comparison between simulations and experimental results for a number of bubble characteristics, e.g. bubble size, velocity distribution, aspect ratio, bubbling density, etc., illustrates the accuracy of the TFM predictions for a TS-TZFBR reactor configuration.

2. Experimental set-up

The experiments were conducted in Perspex® pseudo-2D TS-TZFBR facilities. Four reactor geometries with tapered section angles, α, ranging from 0° to 85° were tested. The lower straight bed region was 8 cm in height for every configuration whereas the bed depth was 0.8 cm. The reactor height was 30 cm and the width was 2 cm in the lower zone and 4 cm in the upper straight zone.

Rear bed illumination was used for the discrimination of bubbles from the dense phase in the recorded video sequences, as described in Julián et al. [2]. Strontium aluminate based particles (d_p = 197 ± 55 μm, ρ_{bulk} = 1.5 g/cm^3, provided by Materiales Inteligentes, Spain) were used as bed particles. The entire set-up was located inside a black box to avoid external light reflections on the front reactor wall. A commercial high definition and low luminance-level camcorder was used to perform the experimental recordings.

Three different reactor variables were analyzed to study their effect on the bubble hydrodynamics: the transition section angle (α), the superficial gas velocity within each reactor zone (u_{gas}) and the position of the immersed gas distributor (z_{dis}). Gas velocities were tested in the range 1.5–3.0 u_{mf} for the considered particles. Experiments were conducted with four different transition section angle geometries: α = [0°, 45°, 80°, 85°]. Moreover, three different immersed distributor heights were tested: z_{dis} = 0, 2 and 3.5 cm above the section change height (z_{sc}), as shown in Table 1. As a result, a large number of combinations were tested to gain insight into the hydrodynamic behavior of the novel TS-TZFBR system.

Table 1
Experimental series to study the effect of operational variables on TS-TZFBR hydrodynamics.

	α (°)	u_r (–)	$z_{dis} - z_{sc}$ (cm)
Series #1	[0°, 45°, 80°, 85°]	2.5	0
Series #2	80°	[1.5, 2.0, 3.0]	0
Series #3	80°	2.5	[2.0, 3.5]

Video sequences were post-processed with an in-house developed DIA algorithm (Matlab 2010a®) to carry out the statistical hydrodynamic analysis.

3. Computational model

CFD simulations were performed using commercial Ansys CFX 12.1 software. Among the available standard model options to simulate multiphase flows, the Eulerian–Eulerian approach was selected. The Lagrangian Particle Tracking formulation was discarded due to the high computational demand of considering the individual motion of several thousands of polydispersed bed particles, as reported by some authors [19,27]. The Eulerian model considers both solid and gas phase as interpenetrating continua, where the volume of a phase cannot be occupied by others. Therefore, the concept of phase volume fraction is introduced. The model equations consider mass and momentum conservation for each phase, i (gas or solid).

$$\frac{\partial}{\partial t}(\varepsilon_i\rho_i) + \nabla\cdot(\varepsilon_i\rho_i\vec{v}_i) = 0 \tag{1}$$

$$\frac{\partial}{\partial t}(\varepsilon_g\rho_g\vec{v}_g) + \nabla\cdot(\varepsilon_g\rho_g\vec{v}_g\vec{v}_g) = -\varepsilon_g\nabla P + \varepsilon_g\nabla\cdot\bar{\bar{\tau}}_g + \varepsilon_g\rho_g\vec{g} + K_{gs}(\vec{v}_g - \vec{v}_s) \tag{2}$$

$$\frac{\partial}{\partial t}(\varepsilon_s\rho_s\vec{v}_s) + \nabla\cdot(\varepsilon_s\rho_s\vec{v}_s\vec{v}_s) = -\varepsilon_s\nabla P - \nabla P_s + \varepsilon_s\nabla\cdot\bar{\bar{\tau}}_s + \varepsilon_s\rho_s\vec{g} + K_{gs}(\vec{v}_s - \vec{v}_g) \tag{3}$$

The left hand side of the momentum conservation equation represents the temporal and spatial transport terms. The right hand side represents the various interacting forces: buoyancy, pressure drop, viscous stress, gravity and interphase drag force. K_{gs} is the interphase momentum exchange coefficient whereas $\bar{\bar{\tau}}_i$ is the i phase stress–strain tensor. Lift forces, external body forces, virtual mass forces or wall lubrication forces are considered not to be significant against drag forces. Therefore, these are not included in the model formulation.

Some closure equations must be added for describing the interaction between phases. The solid–fluid interphase momentum exchange coefficient is here determined with the Gidaspow drag function. This function considers the Wen-Yu expression for dilute systems ($\varepsilon_g > 0.8$) and the Ergun packed-bed pressure drop based equation for dense regions ($\varepsilon_g \leqslant 0.8$). In order to avoid numerical difficulties, CFX modifies the original Gidaspow model by linearly interpolating between the Wen-Yu and Ergun correlations over the range $0.7 < \varepsilon_g \leqslant 0.8$.

$$\varepsilon_g \leqslant 0.8 \rightarrow K_{gs} = 150\frac{\varepsilon_s(1-\varepsilon_g)\mu_g}{\varepsilon_g d_p^2} + 1.75\frac{\varepsilon_s\rho_g|\vec{v}_s - \vec{v}_g|}{d_p} \tag{4}$$

$$\varepsilon_g > 0.8 \rightarrow K_{gs} = \frac{3}{4}C_D\frac{\varepsilon_s\rho_g|\vec{v}_s - \vec{v}_g|}{d_p}\varepsilon_g^{-1.65} \tag{5}$$

where C_D is here estimated using the Schiller–Naumann drag coefficient model:

$$C_D = \begin{cases} \frac{24}{\varepsilon_g Re_s}[1 + 0.15(\varepsilon_g Re_s)^{0.687}] & Re_s \leqslant 1000 \\ 0.44 & Re_s > 1000 \end{cases} \tag{6}$$

being:

$$Re_s = \frac{d_p\rho_g|\vec{v}_s - \vec{v}_g|}{\mu_g} \tag{7}$$

The interphase stress–strain tensor for the phase i (either gas or solid) is assumed to follow the Newtonian strain-rate relation defined as:

$$\bar{\bar{\tau}}_i = \varepsilon_i\mu_i(\nabla\vec{v}_i + \nabla\vec{v}_i^T) + \varepsilon_i\left(\lambda_i - \frac{2}{3}\mu_i\right)\nabla\cdot\vec{v}_i\bar{\bar{I}} \tag{8}$$

where λ_i and μ_i represent the i-phase bulk and shear viscosity, $\bar{\bar{I}}$ the unit tensor. The solids bulk viscosity refers to the resistance to compression or expansion of the granular particles whereas the gas bulk viscosity is a measure of the difference between the thermodynamic and mechanical pressure. The gas bulk viscosity has been here neglected, according to Stoke's assumption for Newtonian fluids [28]. The solids bulk viscosity has been modeled using the correlation of Lun et al. [29].

$$\lambda_s = \frac{4}{3}\varepsilon_s^2\rho_s d_p g_0(1+e)\left(\frac{\theta}{\pi}\right)^{1/2} \tag{9}$$

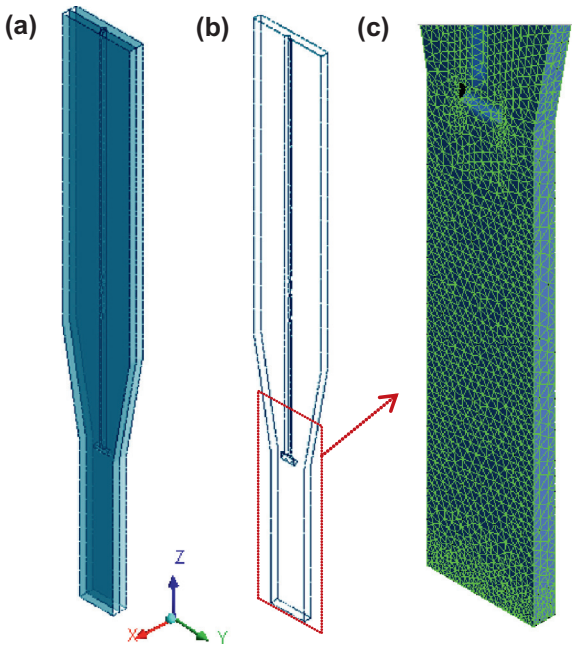

Fig. 2. (a) Simulated TS-TZFBR symmetry with respect to XY plane, (b) computational domain, (c) adaptive mesh grid.

where g_0 represents the radial distribution function described by Lun and Savage [30], θ the granular temperature and e the restitution coefficient of inelastic particle–particle collisions. The restitution coefficient has been set to 0.95 for all simulations and the granular temperature has been determined algebraically under the assumption of local equilibrium in a transport equation model, i.e. energy production equals energy dissipation. A detailed description of the algebraic equilibrium model implemented in Ansys CFX 12.1 can be found in the CFX-Solver Theory user's guide [31].

The solids shear viscosity is here estimated from the collisional contribution, as shown in Eq. (10). Kinetic contributions are omitted from Ansys CFX 12.1.

$$\mu_s = \mu_{s,col} = \frac{4}{5}\varepsilon_s^2 \rho_s d_p g_0 (1+e)\left(\frac{\theta}{\pi}\right) \quad (10)$$

Lastly, the solids pressure has been modeled according to the kinetic theory model of gases, being adapted to consider the inelastic collisions between particles and the maximum solid packing, $\varepsilon_{s,m}$, which has been set to 0.65 in this work. If bed packing (ε_s) becomes larger than $\varepsilon_{s,m}$, the maximum solids packing is used in Eq. (11) instead.

$$P_s = \varepsilon_s \rho_s \theta (1 + 2\varepsilon_s g_0 (1+e)) \quad (11)$$

The set of governing equations was solved using the finite element approach for the different TS-TZFBR reactor geometries described in Section 2. The computational domain mimicked half of the symmetric experimental pseudo-2D facility (Fig. 2a and b) and was discretized by more than 25 000 nodes and 113,000 tetrahedra, with adaptive mesh size between 0.2 and 1 mm (Fig. 2c). This represents a grid size of the same order as the particle size. CFD simulations were solved using adaptive time steps ($\Delta t = [10^{-4} - 2 \times 10^{-4}]$ s). The bulk mass flow rate was selected as the boundary condition for the reactor gas inlets to avoid dense phase outflow. A no-slip boundary was applied to the reactor walls. The reactor outlet was defined with an opening boundary to avoid numerical problems from gas flow entrainments related to pressure gradients. The flow direction was defined as normal to the reactor outlet and the relative pressure in that region was set to 0 Pa. The selected numerical method to solve the set of ODE was a robust first order Backward Euler. Numerical discretization was done with an upwind scheme with convergence criteria based on a RMS residual target of 10^{-3}. Coarser grids coupled with longer time steps resulted in low CPU time consumption but substantially reduced accuracy in terms of bubble properties and defluidized region prediction. Finer grids and shorter time steps increased the CPU time dramatically without showing significant change in the prediction of the bubble hydrodynamic behavior.

As in the experimental measurements, three TS-TZFBR parameters were tested to study their effect on the reactor hydrodynamics: the immersed gas distributor position, the relative gas velocity for the selected bed particles and the tapered angle between the straight zones of the reactor. In order to obtain fully comparable data, the simulations mimicked conditions of the experimental series. CFD simulation parameters are listed in Table 2.

Table 2
List of model parameters used in the CFD simulation.

Model parameter	Value
Reactor height (cm)	30
Particle density, ρ_s (kg/m^3)	2500
Particle diameter, d_p (μm)	200
Particles per cell unit, d_p/*cell* (–)	⩽5
Initial solids volume fraction, ε_{s0} (–)	0.25
Maximum packing fraction, $\varepsilon_{s,m}$ (–)	0.65
Restitution coefficient, e (–)	0.95
Gas temperature (°C)	25

All tested simulations began with a bed sedimentation stage. A certain volume fraction for the dense phase in the whole computational domain was defined. The dense phase settled due to gravity in the absence of fluidization gas. A packed bed was then obtained. After some seconds, the gas started to flow through the distributors leading to a fluidized bed regime. Operating in this way, bed expansion and bubble holdup could be determined.

4. Results

This section illustrates the accuracy of the simulation model to predict the bubble characteristics on a TS-TZFBR and the effect of the different reactor parameters on the reactor hydrodynamics.

In a first step, experimental bubble growing trends will be compared to simulation macro hydrodynamics. Secondly, a more detailed comparison between experimental and simulated bubble characteristics will be carried out to validate the simulation tool. In particular, simulated bubble size distribution, aspect ratio,

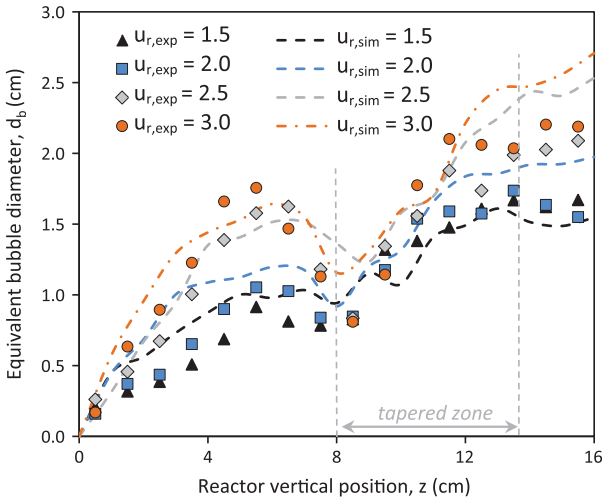

Fig. 3. Comparison between experimental and CFD simulated bubble size profiles as a function of the relative gas velocity. Further TS-TZFBR experimental parameters: $\alpha = 80°$, $z_{dis} = z_{sc} = 8$ cm.

holdup, bubble radial distribution and bed expansion profiles will be evaluated and compared to experimental results at this step. Finally, the effect of the transition section geometry, the relative gas velocity and the immersed distributor location on the experimental bubbling behavior in a pseudo-2D TS-TZFBR will be presented.

4.1. Comparison between $d_b(z)$ experimental trends and simulation results

As discussed in previous works [2], a conservative tapered section angle $\alpha = 80°$ avoids the emergence of defluidized regions for $u_{gas} - u_{mf} > 5$ cm/s, which represented the minimum gas excess to achieve full solid axial mixing in the same reactor configuration as that used in this work. Besides, Julián et al. [32] found that the most suitable location for the immersed gas distributor to avoid an eventual slugging regime in the narrower bed region is the beginning of the TS-TZFBR tapered section. Therefore, this validation study focuses mainly on the most suitable reactor configuration, i.e. $\alpha = 80°$ and $z_{dis} - z_{sc} = 0$ cm.

Since the computational domain mimics the experimental setup, experimental bubble growing rates can be directly compared to the simulation results. For this purpose, a proper definition of bubble boundaries for both experimental recordings and simulations is a must. In case of experimental videos, bubbles were tracked after binarizing raw images by applying a threshold pixel intensity value based on Otsu's method [33], according to the procedure described by Julián et al. [34]. Analogously for CFD simulations, computational regions in which solids volume fraction became lower than 0.15 were considered as bubbles. This threshold value is suggested by several authors [20,35–39].

Fig. 3 shows how the CFD model predicts the bubble size profile for the reactor configuration described above and different gas velocity conditions, ranging from $u_r = 1.5$ to 3.0.

As can be observed, the higher the gas velocity, the bigger the gas bubbles and the sharper the bubble shrinkage within the transition section. The smallest bubble size within the critical transition region (at $z = 9$ cm height, in this case), similar for all experiments, seems not to be related to the gas velocity but to other factors. These factors could be the initial bubble size from the immersed gas distributor orifices or the transition section angle.

The simulated bubble diameter slightly overestimates the experimental bubble size measurements for every tested condition. However, both the growing rate and the characteristic bubble shrinkage within the transition section are fully reproduced in every case. A number of factors could explain the observed over-prediction: the uncertainty when determining experimental bubble boundaries from recorded video frames, the monodispersed definition of the solid particles in the CFD model, the bubble discrimination by means of simulated volumetric fractions, the morphology of gas distributors, etc. As an example, Fig. 4 shows the effect of the volumetric fraction cut-off on the average simulated bubble diameter profile. Nevertheless, taking into account the wide hydrodynamic data dispersion that normally takes place in fluidized bed measurements; the model prediction of the equivalent bubble diameter profile is reasonably good for a wide range of TS-TZFBR gas velocities.

The sole comparison between the experimental and bubble size profiles does not provide complete information about the ability of the CFD model to predict the hydrodynamic behavior in a TS-TZFBR. Some other bubble characteristics such as bubble size probability density, aspect ratio or holdup need to be compared in order to validate the simulation tool. The following section presents a critical comparison between the experimental and simulated results concerning additional bubble characteristics for the reference case conditions: $\alpha = 80°$, $u_r = 2.5$ and $z_{dis} - z_{sc} = 0$ cm.

4.2. CFD validation for predicting the hydrodynamic behavior inside a TS-TZFBR

A home-developed DIA tool has been used to post-process recorded frames and transient volume fraction maps. A critical comparison has been made between the experimental and simulated bubble characteristics.

Fig. 5 shows experimental and simulated bubble size raw data with superimposed average equivalent bubble diameters and the JHM ('*Julián–Herguido–Menéndez*') bubble size model prediction for TS-TZFBR$|_{\alpha=80°,\ ur=2.5,\ zdis-zsc=0}$ [34]. The JHM model accounts for the effect that the change in bed section causes in the bubble size by considering that some gas lefts the bubbles in order to keep the gas velocity in the emulsion phase at the minimum fluidization velocity. It also accounts for new bubbles generated in the immersed feed. The bubble data cloud from both CFD simulation and experimental analysis leads to similar average bubble diameter profiles, $d_b(z)$, in agreement with the JHM prediction. Nevertheless, some differences between the experimental and simulated $d_b(z)$ raw data can be found regarding the very bottom section of the bed as well as the transition section. The bubble size overestimation in the first centimeters above the bottom gas distributor can be explained by the size of the computational grid in the inlet gas region. The 0.2 mm mesh size used in the simulation leads to

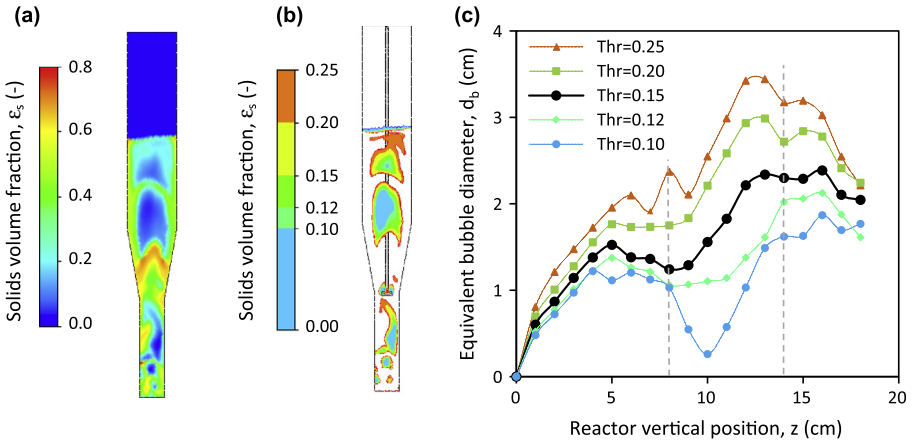

Fig. 4. Effect of the threshold porosity on the simulated bubble size profile along the vertical TS-TZFBR position. (a) Transient solids volume fraction snapshot, (b) bubble contours for different threshold values, (c) average bubble size profiles considering different threshold porosities. Simulation conditions: $\alpha = 80°$, $u_{r,bottom} = u_{r,top} = 2.5$, $z_{dis} = z_{sc} = 8$ cm.

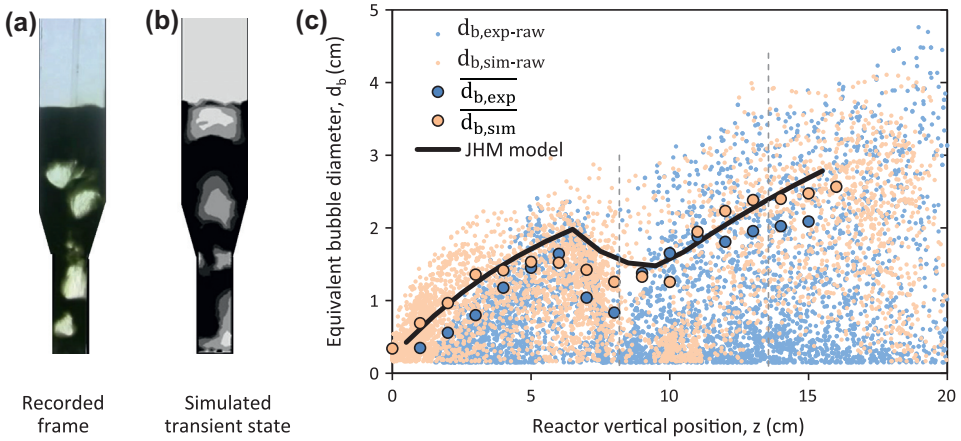

Fig. 5. Bubble size distribution along the TS-TZFBR bed height for the simulation, experiment and JHM prediction. Operational conditions: $\alpha = 80°$, $u_{r,bottom} = u_{r,top} = 2.5$, $z_{dis} - z_{sc} = 0$ cm.

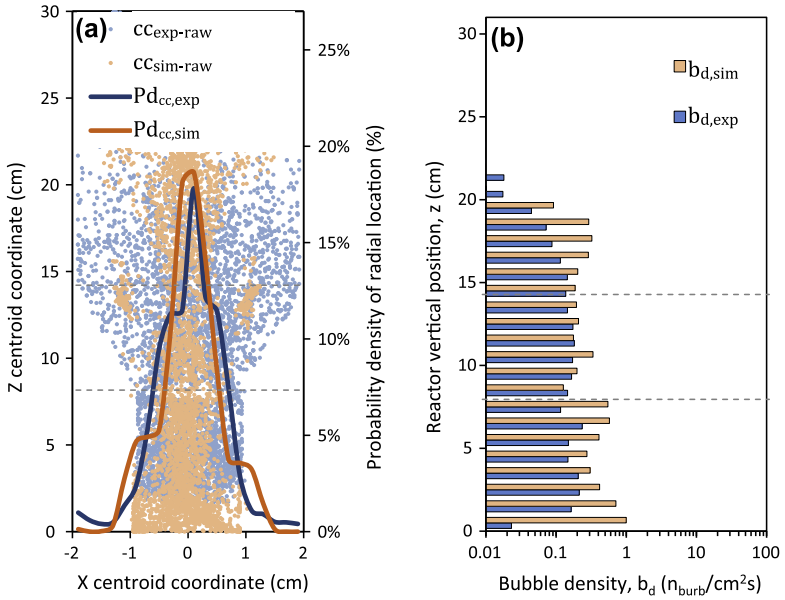

Fig. 6. (a) Bubble centroid position. (b) Bubble density along the TS-TZFBR bed height for simulation and experimental measurements. Operational conditions: $\alpha = 80°$, $u_{r,bottom} = u_{r,top} = 2.5$, $z_{dis} - z_{sc} = 0$ cm.

an insufficient number of facial nodes to simulate the gas flow through a 3 μm pore-size porous glass plate distributor. Therefore, the initial simulated equivalent bubble diameter becomes greater than the experimentally measured one and this determines the bubble size profile along the vertical position throughout the lower bed zone. Regarding the transition section, bubble size differences can be related again to the overestimation of the initial size of bubbles coming from the T-shaped immersed gas distributor.

Bubble centroid distribution and bubble density plots (Fig. 6a and b) give an idea of the bubble radial dispersion and bubbling frequency. The probability plot of the radial centroid location (Fig. 6a) shows that, experimental and simulated bubbles flow up mainly through the bed center. According to the centroid distribution plot this trend is more significant in the case of simulated bubbles. Thus, CFD results suggest classical solid circulation patterns: gas bubbles would drag up a wake of particles through the bed center whereas solids from the bed top would fall down within the emulsion phase close to the reactor walls. In contrast, the experimental centroid distribution map suggests a more chaotic bubble circulation without preferential paths. Nevertheless, the radial probability distributions of experimental and simulated bubbles are in reasonably good agreement.

The bubble density plot represents the local population of bubbles per time and area unit ($n_{bubbles}$/cm^2 s). According to Fig. 6b, the CFD simulations predict a greater frequency of bubble formation compared to the experimental measurements. This trend is especially perceptible in the region close to the bottom gas distributor. In this bed section, bubbles are hardly observed experimentally whereas they appear frequently in the simulations. This effect could be related to the differences between the real porous plate distributor and the modeled computational grid for the bottom gas inlet, as previously discussed. However, the experimental and simulated bubble frequencies along the vertical bed position are comparable and result in the same order density values around 0.2 bubbles/cm^2 s. Several reported bubble density studies for straight fluidized bed columns illustrate that the density decreases with the vertical position in the bed due to bubble coalescence e.g. [36,40]. However, Fig. 6b shows that the bubble density picks up (both in simulations and experimentally) at an intermediate point of the bed. This may be related to the TS-TZFBR singularity: the

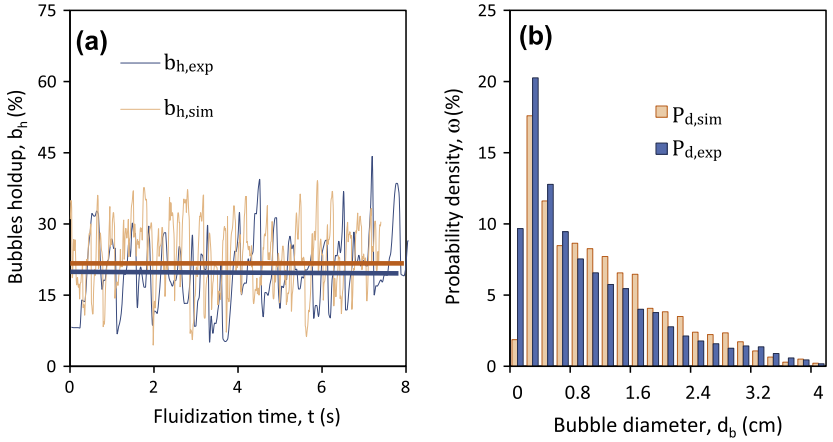

Fig. 7. (a) Bubbles holdup for simulation and experimental measurements. (b) Bubble size probability density. Operational conditions: $\alpha = 80°$, $u_{r,bottom} = u_{r,top} = 2.5$, $z_{dis} - z_{sc} = 0$ cm.

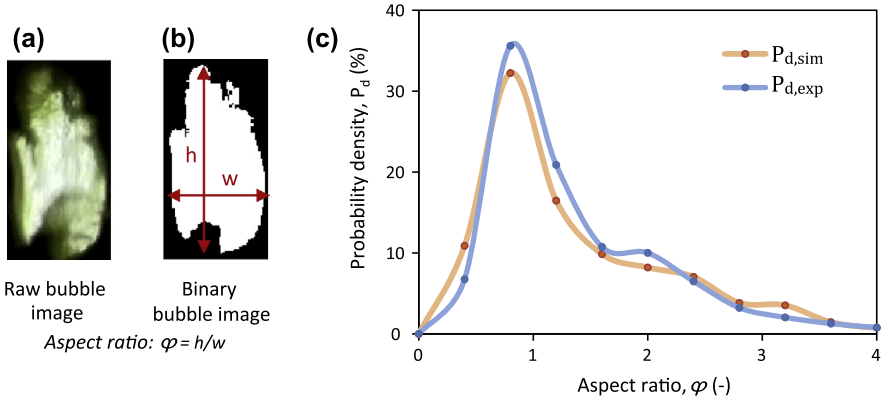

Fig. 8. (a) Raw bubble image. (b) Binary bubble image and aspect ratio definition, (c) probability density for the bubble aspect ratio in a TS-TZFBR. Simulation and experimental measurement. Operational conditions: $\alpha = 80°$, $u_{r,bottom} = u_{r,top} = 2.5$, $z_{dis} - z_{sc} = 0$ cm.

addition of small new bubbles through the immersed distributor located at the beginning of the section change increases the bubble density within that region.

The bubbling holdup is another parameter that helps to describe the hydrodynamic behavior in a fluidized bed. This holdup represents the rate between the gas volume in bubbles and the total volume of the bed. Its value can be determined for each fluidization time step by calculating the instantaneous gas volume in bubbles and the average freeboard height from the lower distributor to the free bed surface. The bubble holdup fluctuates with the fluidization hydrodynamics, i.e. bubble formation and eruption, as can be observed in Fig. 7.a. Experimental and simulated oscillation frequencies and amplitudes are comparable. The average holdup in both cases was around 22%.

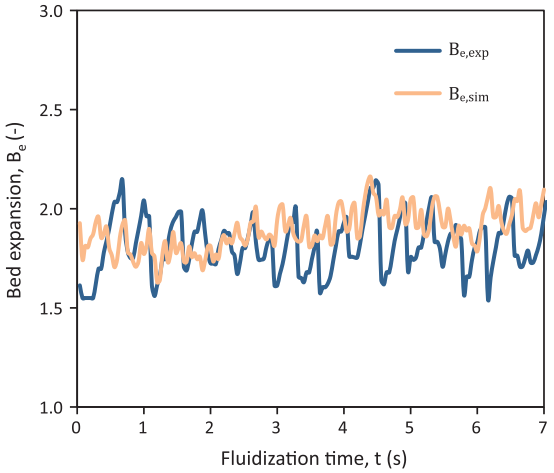

Fig. 9. Bed expansion along the fluidization time for experiments and CFD simulations in a TS-TZFBR. Operational conditions: $\alpha = 80°$, $u_{r,bottom} = u_{r,top} = 2.5$, $z_{dis} - z_{sc} = 0$ cm.

The probability density plot (Fig. 7b) shows the distribution of bubble sizes within the whole bed over the fluidization time. As expected, small bubbles appear more frequently than bigger ones. Fig. 7b shows how similar the computational and experimental probability densities are for the bubble size. Only the probability of having very small bubbles differs significantly between the simulations and recorded videos. This may be related to the experimental bubble size filter applied in the DIA post-processing in order not to consider small spurious bubbles when describing the average bubble size profile.

The bubble aspect ratio (φ) represents an estimation of the characteristic bubble shape. The aspect ratio is normally influenced by the bubble velocity and describes how the bubble geometry differs from the spherical form ($\varphi = 1$). In this study, φ is defined as the ratio between the maximum vertical and horizontal bubble extension (Fig. 8a and b). Fig. 8c shows the experimental and simulated cumulative bubble aspect ratio distributions for the reference case. As can be observed, the average experimental bubble

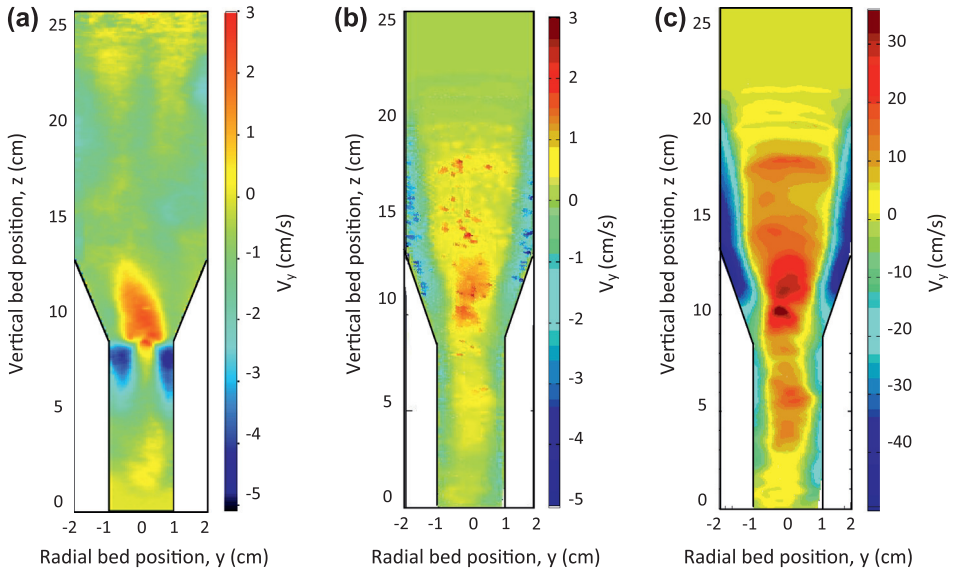

Fig. 10. Average particles axial velocity distribution along the TS-TZFBR bed height and width for: (a) PIV measurement (extracted from Julián et al. [2]). (b) CFD simulation at 0.05 cm depth from the front wall. (c) CFD simulation at 2 mm depth from the front wall. Operational conditions: $\alpha = 80°$, $u_{r,bottom} = u_{r,top} = 2.5$, $z_{dis} - z_{sc} = 0$ cm.

shape tends to the spherical form with a slight skewness towards φ values lower than 1. This aspect ratio distribution could be explained by the eventual appearance of slugs within the lower narrow bed section, where bubble widths are close to the bed diameter. Analogously, simulated bubbles tend to the spherical shape with a similar skewness and a slightly wider distribution curve. That is, the slugging effect seems to be well reproduced by simulations.

Finally, the simulated and the experimental bed expansion are compared in Fig. 9. The bed expansion is here defined as the relative bed volume increase, instead of the conventional bed height increase, due to the special TS-TZFBR configuration with its characteristic section change. Although the freeboard location changes with a similar frequency in both cases, the experimental bed expansion fluctuates with larger amplitude. Taking into account that the simulated bubble holdup (Fig. 9) remains similar to the experimental one, the bed expansion discrepancy could be attributed to a poor prediction of the dense phase packing fraction along the bed.

In fact, although hydrodynamic predictions have been proved to be quite accurate, several authors suggest that experimental solid flows can only be qualitatively described by commercial CFD packages for particulate fluidized beds [41,42]. Regarding this assertion, the resulting CFD map of average superficial solid axial velocity has been compared to experimental Particle Image Velocimetry (PIV) results obtained by Julián et al. [2] in an identical TS-TZFBR configuration (Fig. 10). To consider the experimental wall effect on the simulated axial velocity of the particles, two velocity maps at different distances from the front no-slip pseudo-2D reactor wall (0.05 cm and 0.2 cm depth) have been obtained. Obviously, in a 3D reactor this wall effect would be negligible but in order to compare simulated an experimental particle velocities, the simulation data must be taken near the wall. The simulation velocity results corresponding to a distance of 0.05 cm from the reactor front wall (Fig. 10b) agree reasonably well with the experimental PIV results (Fig. 10a). In both cases same order axial particle velocities and similar circulation patterns through the TS-TZFBR transition region are obtained. The solids velocity reaches its highest value just above the immersed gas distributor, which enhances the solid axial mixing through the transition bed section. In some cases, significant differences were observed between the modeled (Fig. 10b) and experimental (Fig. 10a) particle velocity at certain bed regions. Nevertheless, these differences could have only a small effect on the solid flux if there is a large mean porosity in these regions. For instance, the CFD model is not able to predict high downward velocity of particles inside bubbles whereas some particle raining was observed in the experiments. This may explain some disagreement between experimental and simulated particle velocity results.

The average superficial velocity map obtained at the bed depth center, i.e. 2 mm depth (Fig. 10c), showed that the particle axial velocity was there one order of magnitude faster than close to the walls. The substantial over-prediction of the experimental average superficial velocity values at certain bed depth suggests that only CFD "facial" solid velocity values can be compared to experimental results obtained by pseudo-2D imaging techniques, since experimental measurements are likewise affected by these wall effects.

By contrast, the effect of the front and rear reactor walls on the void fraction along the bed depth could be neglected, as can be observed in Fig. 11a. This figure shows transient solids volume fraction maps at three different bed depths. Their similarity suggests that the volume occupied by a bubble in a pseudo-2D facility can be well predicted by the depth projection of the simulated facial bubble surface. Though, according to some authors [43,44] this could not be the case in PIV measurements, in which the facial void fraction may be affected by particle raining inside bubbles. Therefore, the 3D bed porosity may differ from that obtained from 2D images.

Fig. 11b illustrates how the no-slip condition on the front wall of the simulated TS-TZFBR affects the transient superficial solids velocity in the axial direction, as previously discussed.

4.2.1. CFD model prediction of defluidized bed regions inside a TS-TZFBR

The ability of the CFD model to predict the formation of defluidized bed regions within the tapered section of the TS-TZFBR has been evaluated. Fluid dynamic simulations have been carried out in a sharp transition-section TS-TZFBR ($\alpha = 0°$) with different gas velocities. Following a previous work [45], the defluidization angle, β, has here been determined for the CFD simulations as the tangent to the banked bed region curve, measured at two thirds of the total height of the defluidized area (Fig. 12a). The average β is obtained as the mean value between the defluidization slope

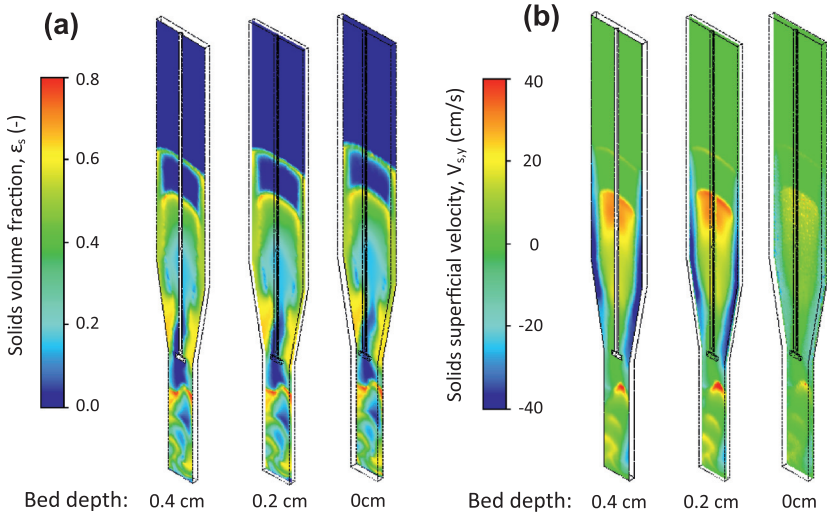

Fig. 11. (a) Transient solids volume fraction at three different bed depths (x = 0.4, 0.2 and 0 cm), (b) wall effect on the simulated vertical solids superficial velocity. Simulation conditions: $\alpha = 80°$, $u_{r,bottom} = u_{r,up} = 2.5$, $z_{dis} = z_{sc} = 8$ cm.

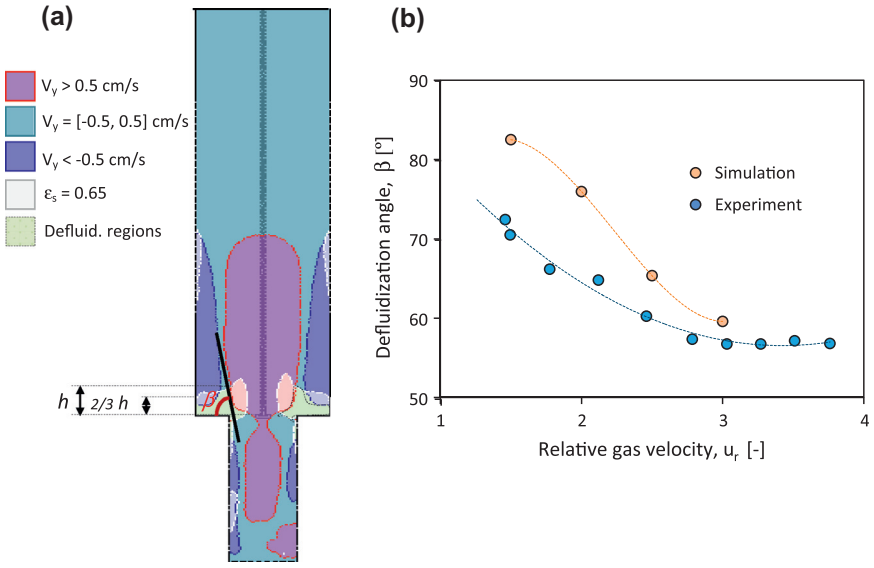

Fig. 12. (a) Determination of β from simulated time averaged bed volume fraction map in a sharp transition section TS-TZFBR ($u_{r,bottom} = u_{r,top} = 1.5$, $z_{dis} - z_{sc} = 0$ cm). (b) Comparison between experimental and simulated defluidization angles for different gas flow rates. Experimental data have been extracted from Julián et al. [2].

measurements on both sides of the section enlargement. The following conditions have to be simultaneously accomplished in order to consider a region as defluidized in CFD simulations: the average solid volume fraction must remain equal to or greater than 0.65 (imposed maximum packed bed fraction) and the average particle axial velocity in the bed depth center cannot be higher than a certain threshold value, $u_{bed} = 0 \pm 0.5$ cm/s.

Experimental PIV defluidization results from Julián et al. [2] and the CFD simulated β values obtained in this work for phosphorescent particles (d_p = 200 μm) are compared in Fig. 12b. As can be observed, the simulation over-predicts the experimental defluidization angles. Besides, the CFD morphology of the banked regions slightly differs from that of the experimental observations. The simulations predict flat densely packed or defluidized areas whereas the experiments reveal almost triangular shapes of these areas, i.e. well defined angles between the fluidized core and the marginal regions on both sides of the TS-TZFBR over the section change. The same trends have been found for every tested gas flow.

Summing up the results, we conclude that the Two-Fluid Model is able to predict the hydrodynamic behavior within a TS-TZFBR qualitatively. However, we accept that there are shortcomings both in the computational domain (unrealistic definition of inlet boundaries for gas distribution) and in the model (continuum fluid phase approach for granular matter). The use of an Eulerian–Lagrangian model in future works, i.e. Discrete Particle Model (DPM), could increase the accuracy of the bed dynamics prediction since it provides a more reliable and detailed representation of the fluidized bed. Nevertheless, some authors suggest that DPM predictions are still unsatisfactory in terms of quantitative comparisons with experimental results [39]. Therefore, further work is still necessary to improve existing fluid dynamic models.

4.3. Effect of operational variables on the performance of the TS-TZFBR

The average equivalent bubble diameter profile along the reactor vertical position, $d_b(z)$, is one of the most significant

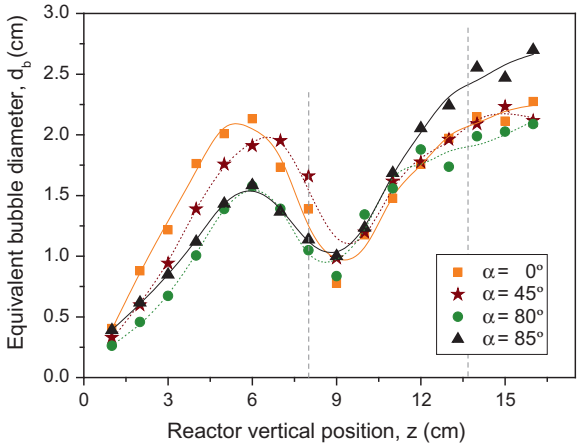

Fig. 13. Bubble size profile as a function of the transition section angle. TS-TZFBR experimental parameters: $z_{dis} = z_{sc} = 8$ cm, $u_{r,bottom} = u_{r,top} = 2.5$.

hydrodynamic variables in a fluidized bed reactor. The effect of the fluidization gas velocity on the bubble growth within a TS-TZFBR has been previously discussed and illustrated in Fig. 3. In this section, the influence of parameters that determine the reactor configuration, i.e. α and z_{dis}, on the bubble growth will be evaluated. Experimental series are detailed in Table 1.

In the first series the transition section angle was varied while maintaining constant both the relative gas velocity in the reactive ($u_{r,top}$) and regenerative ($u_{r,bottom}$) reactor zones and the immersed distributor axial position. The results show how the tapered angle strongly influences the bubble size far from the transition region (Fig. 13). On the one hand, the smoothest section change ($\alpha = 85°$) leads to the biggest bubble size within the reactive region. This is related to the fact that the gas excess over the minimum fluidization, in the case of smooth transitions, is higher within the transition section (i.e. the same gas flows through narrower bed sections). The higher gas excess promotes this bubble growth. On the other hand, sharper transition angles ($\alpha = 0°$) lead to markedly increased bubble size under the section change. This non-trivial effect has already been reported elsewhere [2] and has been related to a slugging regime. Slugs are gas bubbles that occupy the whole bed section and decrease the axial solid recirculation. Slugs may appear when using high gas flows within narrow columns or when having partial defluidized regions over a fluidized bed section. In the latter scenario, bubbles coalesce along the lower bed zone before reaching the tapered section. If the transition between zones is sharp, the gas bubbles strongly reduce their velocity through this region. As a consequence, incipient dense defluidized zones may appear over the section change. Therefore, the pressure drop increases locally and faster bubbles coming from the bottom gas distributor coalesce under the tapered section. This leads to the substantially bigger bubbles observed for $\alpha = [0°–45°]$ geometries in the lower bed zone (Fig. 13). Since slugs complicate the solid axial mixing, a soft transition angle between reactor zones is advisable in order to achieve a satisfactory TS-TZFBR performance without slugging or defluidization phenomena.

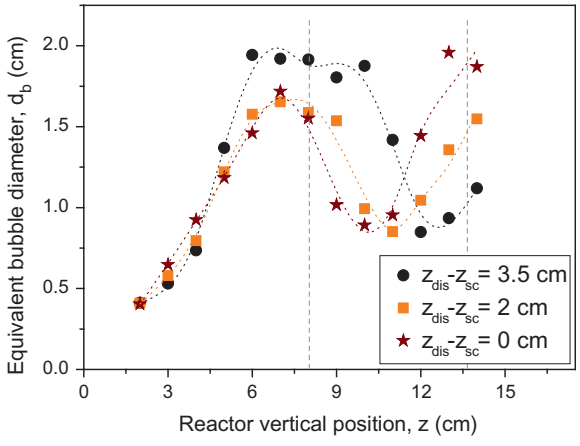

Fig. 14. Bubble size profile as a function of the immersed distributor axial location ($z_{dis} - z_{sc}$). Further TS-TZFBR experimental parameters: $z_{sc} = 8$ cm, $\alpha = 80°$, $u_{r,bottom} = u_{r,top} = 2.5$.

Concerning the effect of the immersed distributor axial location, Fig. 14 shows how a slugging regime seems to appear when the distributor is located 3.5 cm above the section change: bubbles do not grow within the initial zone of the transition region and their size is similar to the column diameter in the narrow section. The sharp average bubble size shrinkage over the immersed distributor axial position ($z_{dis} = 11.5$ cm) can be explained by the addition of new and small bubbles from the distributor and by the transfer of gas from the bubble phase to the emulsion phase, due to the section enlargement. Regarding the TS-TZFBR chemical operation, small bubbles are of interest within the regeneration zone since they provide a better gas–solid contact and reduce the chance of gas-phase oxygen arriving in the reaction zone. Thus, according to Fig. 14, the most suitable reactor configuration is the one that locates the immersed gas distributor close to the beginning of the tapered section ($z_{dis} - z_{sc} = 0$ cm).

Both the effect of the tapered section angle and the immersed distributor axial location agree with results obtained in previous works [2,32].

5. Conclusions

A multifluid Eulerian–Eulerian model using Ansys-CFX software with Gidaspow drag functions was able to predict time-averaged bed hydrodynamics for the special fluidized bed configuration presented in this work. A critical comparison between CFD model predictions and TS-TZFBR experimental measurements shows good agreement in terms of bubble characteristics for a fluid dynamic optimized TS-TZFBR reactor configuration. The bubble size evolution was reasonably well predicted in a wide range of fluidization regimes. However, simulated particle dynamics and average volume fraction do not provide accurate results in comparison to experimental measurements. As a conclusion, further CFD model improvement is required in order to fully predict TS-TZFBR bed properties and continue with the scaling process.

Acknowledgements

Financial support from spanish MINECO (Project CTQ2010-15568) is gratefully acknowledged. Financial aid for the maintenance of the consolidated research group CREG has been provided by the Fondo Social Europeo (FSE) through the Gobierno de Aragón (Aragón, Spain).

References

[1] J. Herguido, M. Menéndez, J. Santamaría, On the use of fluidized bed catalytic reactors where reduction and oxidation zones are present simultaneously, Catal. Today 100 (2005) 181–189.
[2] I. Julián, F. Gallucci, M. van Sint Annaland, J. Herguido, M. Menéndez, Coupled PIV/DIA for fluid dynamics studies on a two-section two-zone fluidized bed reactor, Chem. Eng. J. 207–208 (2012) 122–132.
[3] J.A. Medrano, I. Julián, F. García, K. Li, J. Herguido, M. Menéndez, Two-zone fluidized bed reactor (TZFBR) with palladium membrane for catalytic propane dehydrogenation: experimental performance assessment, Ind. Eng. Chem. Res. 52 (2013) 3723–3731.

[4] M.P. Gimeno, Z.T. Wu, J. Soler, J. Herguido, K. Li, M. Menéndez, Combination of a two-zone fluidized bed reactor with a Pd hollow fibre membrane for catalytic alkane dehydrogenation, Chem. Eng. J. 155 (2009) 298–303.
[5] M.P. Lobera, C. Tellez, J. Herguido, M. Menéndez, Pt–Sn/$MgAl_2O_4$ as *n*-butane dehydrogenation catalyst in a two-zone fluidized-bed reactor, Ind. Eng. Chem. Res. 48 (2009) 6573–6578.
[6] L. Perez-Moreno, J. Soler, J. Herguido, M. Menéndez, Stable steam reforming of ethanol in a two-zone fluidized-bed reactor, Ind. Eng. Chem. Res. 51 (2012) 8840–8848.
[7] J.A.M Kuipers, W.P.M. van Swaaij, Computational fluid dynamics applied to chemical reaction engineering, Advances in Chemical Engineering, vol. 24, Academic Press, 1998, pp. 227–328.
[8] M.A van der Hoef, M. Ye, M. van Sint Annaland, A.T. Andrews, S. Sundaresan, J.A.M. Kuipers, Multiscale modeling of gas-fluidized beds, Advances in Chemical Engineering, vol. 31, Academic Press, 2006, pp. 65–149.
[9] J.R. Grace, T. Li, Complementarity of CFD, experimentation and reactor models for solving challenging fluidization problems, Particuology 8 (2010) 498–500.
[10] M. van Sint Annaland, G.A. Bokkers, M.J.V. Goldschmidt, O.O. Olaofe, M.A. van der Hoef, J.A.M. Kuipers, Development of a multi-fluid model for poly-disperse dense gas–solid fluidised beds, Part II: Segregation in binary particle mixtures, Chem. Eng. Sci. 64 (2009) 4237–4246.
[11] M. Goldschmidt, R. Beetstra, J.A.M. Kuipers, Hydrodynamic modelling of dense gas-fluidised beds: Comparison and validation of 3D discrete particle and continuum models, Powder Technol. 142 (2004) 23–47.
[12] J. Li, J.A.M. Kuipers, Gas-particle interactions in dense gas-fluidized beds, Chem. Eng. Sci. 58 (2003) 711–718.
[13] N. Mahinpey, F. Vejahati, N. Ellis, CFD simulation of gas–solid bubbling fluidized bed: an extensive assessment of drag models, Comput. Meth. Multiphase Flow IV 56 (2007) 51–60.
[14] D. Gidaspow, J.W. Jung, R.K. Singh, Hydrodynamics of fluidization using kinetic theory: an emerging paradigm, flour-daniel lecture, Powder Technol. 148 (2004) 123–141.
[15] H.A. Jakobsen, H. Lindborg, C.A. Dorao, Modeling of bubble column reactors: progress and limitations, Ind. Eng. Chem. Res. 44 (2005) 5107–5151.
[16] N. Herzog, M. Schreiber, C. Egbers, H.J. Krautz, A comparative study of different CFD-codes for numerical simulation of gas–solid fluidized bed hydrodynamics, Comput. Chem. Eng. 39 (2012) 41–46.
[17] W. Duangkhamchan, F. Ronsse, F. Depypere, K. Dewettinck, J.G. Pieters, Comparison and evaluation of interphase momentum exchange models for simulation of the solids volume fraction in tapered fluidised beds, Chem. Eng. Sci. 65 (2010) 3100–3112.
[18] A. Busciglio, G. Vella, G. Micale, L. Rizzuti, Experimental analysis of bubble size distributions in 2D gas fluidized beds, Chem. Eng. Sci. 65 (2010) 4782–4791.
[19] V.V. Ranade, Computational Flow Modelling for Chemical Reactor Engineering, Academic Press, London, 2002.
[20] D.J. Patil, M. van Sint Annaland, J.A.M. Kuipers, Critical comparison of hydrodynamic models for gas–solid fluidized beds—Part II: Freely bubbling gas–solid fluidized beds, Chem. Eng. Sci. 60 (2005) 73–84.
[21] D. Gidaspow, Multiphase Flow and Fluidization: Continuum and Kinetic Theory Descriptions, Academic Press, San Diego, 1994.
[22] P. Pei, K. Zhang, D. Wen, Comparative analysis of CFD models for jetting fluidized beds: the effect of inter-phase drag force, Powder Technol. 221 (2012) 114–122.
[23] D.C. Sau, K.C. Biswal, Computational fluid dynamics and experimental study of the hydrodynamics of a gas–solid tapered fluidized bed, Appl. Math. Model. 35 (2011) 2265–2278.
[24] W. Duangkhamchan, F. Ronsse, K. Dewettinck, J.G. Pieters, CFD study of solids concentration in a fluidised-bed coater with variation of atomisation air pressure, Powder Technol. 212 (2011) 103–114.
[25] P. Pei, K. Zhang, J. Ren, D. Wen, G. Wu, CFD simulation of a gas–solid fluidized bed with two vertical jets, Particuology 8 (2010) 425–432.
[26] J.R. Grace, F. Taghipour, Verification and validation of CFD models and dynamic similarity for fluidized beds, Powder Technol. 139 (2004) 99–110.
[27] C.C. Pain, S. Mansoorzadeh, C.R.E. de Oliveira, A study of bubbling and slugging fluidised beds using the two-fluid granular temperature model, Int. J. Multiphase Flow 27 (2001) 527–551.
[28] F. Taghipour, N. Ellis, C. Wong, Experimental and computational study of gas–solid fluidized bed hydrodynamics, Chem. Eng. Sci. 60 (2005) 6857–6867.
[29] C.K.K. Lun, S.B. Savage, D.J. Jeffrey, D.J. Chepurniy, Kinetic theories for granular flow: inelastic particles in couette flow and slightly inelastic particles in a general flow field, J. Fluid Mech. 140 (1984) 223–256.
[30] C.K.K. Lun, S.B. Savage, The effects of an impact velocity dependent coefficient of restitution on stresses developed by sheared granular materials, Acta Mech. 63 (1986) 15–44.
[31] ANSYS CFX-Solver User's guide. ANSYS Ltd. 2009.
[32] I. Julián, J. Herguido, M. Menéndez, Particle mixing in a two-section two-zone fluidized bed reactor (TS-TZFBR). Experimental technique and CCBM model validation, Ind. Eng. Chem. Res. 52 (2013) 13587–13596.
[33] N. Otsu, A threshold selection method from gray-level histograms, IEEE Trans. Syst. Man Cyber. 9 (1979) 62–66.
[34] I. Julián, J. Herguido, M. Menéndez, A non-parametric bubble size correlation for a two-section two-zone fluidized bed reactor (TS-TZFBR), Powder Technol. 256 (2014) 146–157.
[35] T.W. Asegehegn, M. Schreiber, H.J. Krautz, Numerical simulation and experimental validation of bubble behaviour in gas–solid fluidized bed with immersed horizontal tubes, Chem. Eng. Sci. 66 (2011) 5410–5427.
[36] A. Busciglio, G. Vella, G. Micale, L. Rizzuti, Analysis of the bubbling behaviour of 2D gas solid fluidized beds: Part II. Comparison between experiments and numerical simulations via digital image analysis technique, Chem. Eng. J. 148 (2009) 145–163.
[37] R.P. Utikar, V.V. Ranade, Single jet fluidized beds: experiments and CFD simulations with glass and polypropylene particles, Chem. Eng. Sci. 62 (2007) 167–183.
[38] J.A.M. Kuipers, K.J. van Duin, F.P.H. van Beckum, W.P.M. van Swaaij, A numerical model of gas-fluidized beds, Chem. Eng. Sci. 47 (1992) 1913–1924.
[39] J.A.M. Kuipers, K.J. van Duin, F.P.H. van Beckum, W.P.M. van Swaaij, Computer simulation of the hydrodynamics of a two-dimensional gas-fluidized bed, Comput. Chem. Eng. 17 (1993) 839–858.
[40] J.F. de Jong, M. van Sint Annaland, J.A.M. Kuipers, Experimental study on the hydrodynamic effects of gas permeation through horizontal membrane tubes in fluidized beds, Powder Technol. 241 (2013) 74–84.
[41] J.F. de Jong, T.Y.N. Dang, M. van Sint Annaland, J.A.M. Kuipers, Comparison of a discrete particle model and a two-fluid model to experiments of a fluidized bed with flat membranes, Powder Technol. 230 (2012) 93–105.
[42] M.S. van Buijtenen, W. van Dijk, N.G. Deen, J.A.M. Kuipers, T. Leadbeater, D.J. Parker, Numerical and experimental study on multiple-spout fluidized beds, Chem. Eng. Sci. 66 (2011) 2368–2376.
[43] J.F. de Jong, S.O. Odu, M.S. van Buijtenen, M. van Sint Annaland, J.A.M. Kuipers, Development and validation of a novel digital image analysis method for fluidized bed particle image velocimetry, Powder Technol. 230 (2012) 193–202.
[44] S. Cloete, A. Zaabout, S.T. Johansen, M. van Sint Annaland, F. Gallucci, S. Amini, The generality of the standard 2D TFM approach in predicting bubbling fluidized bed hydrodynamics, Powder Technol. 235 (2013) 735–746.
[45] T.M. Gernon, M.A. Gilbertson, Segregation of particles in a tapered fluidized bed, Powder Technol. 231 (2012) 88–101.

Artículo V

I. Julián, F. Gallucci, M. v. Sint Annaland, J. Herguido, M. Menéndez,
Hydrodynamic study of a TS-TZFBR with an immersed tube bank via PIV/DIA,
Chem. Eng. Sci. 134 (2015) 238-250

Chemical Engineering Science 134 (2015) 238–250

Contents lists available at ScienceDirect

Chemical Engineering Science

journal homepage: www.elsevier.com/locate/ces

Hydrodynamic study of a Two-Section Two-Zone Fluidized Bed Reactor with an immersed tube bank via PIV/DIA

I. Julián [a], F. Gallucci [b], M. van Sint Annaland [b], J. Herguido [a,*], M. Menéndez [a]

[a] Catalysis, Molecular Separations and Reactor Engineering Group (CREG), Aragon Institute of Engineering Research (I3A), Universidad de Zaragoza, 50018 Zaragoza, Spain

[b] Chemical Process Intensification, Department of Chemical Engineering and Chemistry, Eindhoven University of Technology, P.O. Box 513, 5612 AZ, Eindhoven, The Netherlands

HIGHLIGHTS

- Coupled PIV/DIA allows the hydrodynamic study of a pseudo-2D TS-TZFBR with internals.
- DIA has been optimized to accomplish global bed mass balances.
- The effect of diverse tube bank alignments on the reactor dynamics has been determined.
- High agreement between experimental trends for solids and bubble dynamics.
- Bubble size decreases by 30% while only slightly affecting the solids circulation time.

GRAPHICAL ABSTRACT

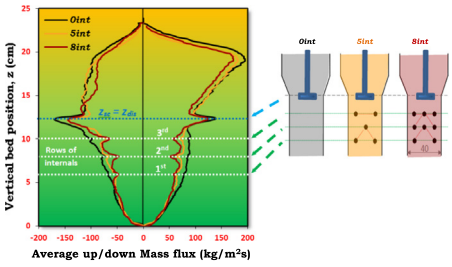

ARTICLE INFO

Article history:
Received 23 January 2015
Received in revised form
6 May 2015
Accepted 10 May 2015
Available online 15 May 2015

Keywords:
Two-zone Fluidized Bed Reactor
Immersed tube bank
Particle Image Velocimetry (PIV)
Digital Image Analysis (DIA)
Fludized bed
Hydrodynamic

ABSTRACT

The hydrodynamic behaviour of a pseudo-2D Two-Section Two-Zone Fluidized Bed Reactor (TS-TZFBR) with an immersed tube bundle in its lower zone has been studied using non-invasive Particle Image Velocimetry (PIV) and Digital Image Analysis (DIA). Coupled porosity distribution maps from DIA post-processing and solids velocity vector fields from PIV analysis allowed the reconstruction of the transient and time-averaged solid fluxes along the bed. Six different tube bank configurations at several different superficial gas velocities have been tested to evaluate the hydrodynamic behaviour within the lower zone of the TS-TZFBR. The solids axial mixing along the vertical bed position has been quantified for this novel reactor configuration. Besides, the effect of the internals on the gas-solid mass transfer has been estimated by means of bubble size. A five-staggered tube bundle configuration was able to diminish the average bubble size by 30% within the lower bed zone at usual TS-TZFBR gas flow rates, $u_{gas}/u_{mf}=3.0$, without increasing the solids circulation time dramatically.

1. Introduction

The Two-Zone Fluidized Bed Reactor (TZFBR) allows performing heterogeneous gas-solid catalytic reactions with in situ catalyst regeneration (Herguido et al., 2005). The reactor design has two separated gas inlets to the fluidized bed: an immersed gas inlet for the gaseous reactant and a gas distributor at the bottom of the bed for the oxidizing agent. Heterogeneous catalytic reactions take place in the upper region of the TZFBR whereas catalyst regeneration takes place below the reactant injection point. This process integration is possible owing to the continuous catalyst axial circulation through the bed typical of fluidization processes. This

* Corresponding author.
E-mail address: j.hergui@unizar.es (J. Herguido).

http://dx.doi.org/10.1016/j.ces.2015.05.009
0009-2509/

reactor concept becomes especially interesting for the conversion of gaseous hydrocarbons, where the catalyst suffers from deactivation by carbon (coke) deposition on its active surface. Under certain process conditions, the continuous coke burning within the lower bed zone in the presence of an oxidizer, i.e. diluted oxygen, may result in a long term steady state reactant conversion without net catalytic deactivation. The performance of this reactor has been successfully tested for alkane dehydrogenation (Medrano et al., 2013a, 2013b) as well as for ethanol reforming (Pérez-Moreno et al., 2012) and methane aromatization (Gimeno et al., 2010). The achievement of a steady state operation in a TZFBR depends on several process variables such as operating temperature, catalyst performance or reaction-to-regeneration kinetics, but also on the bed hydrodynamics and the gas-solid mass transfer rates. Indeed, a proper axial solids circulation between the lower and the upper bed zones would enhance the process integration. Analogously, control of the fluidization regime within the bed would help to decrease mass transfer limitations.

Recently, novel TZFBR configurations that incorporate two zones with different cross sectional areas, i.e. Two-Section TZFBR (TS-TZFBR), have been proposed (Julián et al., 2013, 2014a, 2012). These improved reactor configurations allow the use of low regenerative-to-reactive gas flow rates if required. Their main feature is the use of a tapered transition region between the two bed zones. Julián et al. (2013), (2012) studied the formation of defluidized bed regions above the section change under certain fluidization conditions, both experimentally and by Computational Fluid Dynamics (CFD) simulations (Julián et al., 2014b). It was suggested to adopt a conservative tapered section angle (α) limit to avoid defluidization effects: $\alpha \geq 80^{\circ}$, with respect to the horizontal position. Moreover, the most suitable axial location of the immersed gas distributor to attain a proper solids circulation pattern has been identified and suggested. However, as a result of using narrow bed sections in the lower zone of the TS-TZFBR, new fluid dynamic issues arose. Under certain fluidization gas flow conditions, slugging regimes tend to appear leading to short-circuit in the solids recirculation within the lower bed region (Julián et al., 2013). Furthermore, these regimes decrease the gas-solid mass transfer rates and may lead to high concentrations of oxidizing agent in the reactive zone, if the contact between the oxygen and the deactivated catalyst surface becomes poor.

The novel reactor configuration that is proposed in this work consists of a TS-TZFBR ($\alpha = 80^{\circ}$) with a tube bundle in its lower zone to allow bubble breakage and improve gas-solid contact while also possibly feeding the oxidizing agent through the tubes. It is widely accepted that the use of tube banks normally decreases axial solids mixing (e.g. (Hull et al., 2000; Sitnai, 1981)). However, if the tube bundle is attached to a column in which slugging regimes normally take place the circulation time could be significantly decreased.

The purpose of this work is, thus, to evaluate the effect of different configurations of internals, as well as some other operational variables (gas velocity and immersed distributor location) on the fluid dynamic behaviour of a TS-TZFBR scaled-up with respect to that used by Julián et al. (2012). The determination of the axial solids mixing and bubble properties has been carried out using a combination of non-invasive Particle Image Velocimetry (PIV) and Digital Image Analysis (DIA) in pseudo-2D reactors. Although the quantitative extrapolation of the phenomena observed in the 2D beds to real 3D fluidized beds is in general not trivial, the obtained results should help to gain a better understanding on the effect of immersed tube banks on these fluid dynamic behaviors; as well as to validate numerical models with which 3D beds can be investigated.

2. Experimental set-up

The experimental set up consists of a Perspex® pseudo-2D Two-Section Two-Zone Fluidized Bed Reactor, an ultra-fast high-resolution camera, a software for image post-processing, two led lamps and two mass flow controllers for gas supply. A detailed scheme of the experimental set up is presented in Fig. 1.

The dimensions of the reactor used in this work are $65 \times 8 \times 0.8$ cm (height × max. width × depth). The maximum width corresponds to the upper bed zone width. The straight lower zone is 4 cm wide and 12 cm high. The tapered region between bed zones has an angle, α, of 80° with respect to the horizontal position and connects the two straight bed zones. This tapered section angle has been defined elsewhere (Julián et al., 2012, 2013, 2014b) to be suitable to avoid defluidized bed regions in a TS-TZFBR. The reactor had an immersed T-shaped orifice gas distributor ($d_{orif} = 3$ mm). The external diameter of the distributor was 4 mm and it could be shifted along the vertical bed position. The bottom inlet consists of a glass porous plate with a small pore size, d_{pore}, of 40–100 μm to obtain uniform gas distribution. Fluidization gas was pressurized air and bed particles were non-spherical $SrAl_2O_4$ based phosphorescent solids (Geldart-type B), used as optical tracers in previous studies (Julián et al., 2013). Their size distribution, d_p, was in the range 200–320 μm with a bulk density, ρ_b, of 1.43 g/cm^3 and a fixed bed porosity, ε_{packed}, of 0.58. The minimum fluidization velocity of these particles, $u_{mf} = 10.1$ cm/s, was determined by measuring the bed pressure drop at decreasing gas velocities in a straight vessel.

Compressed air was fed through two mass flow controllers (Brooks® 20 NL/min). Air was first humidified to minimize electrostatic effects between the walls and the solids. A black sheet

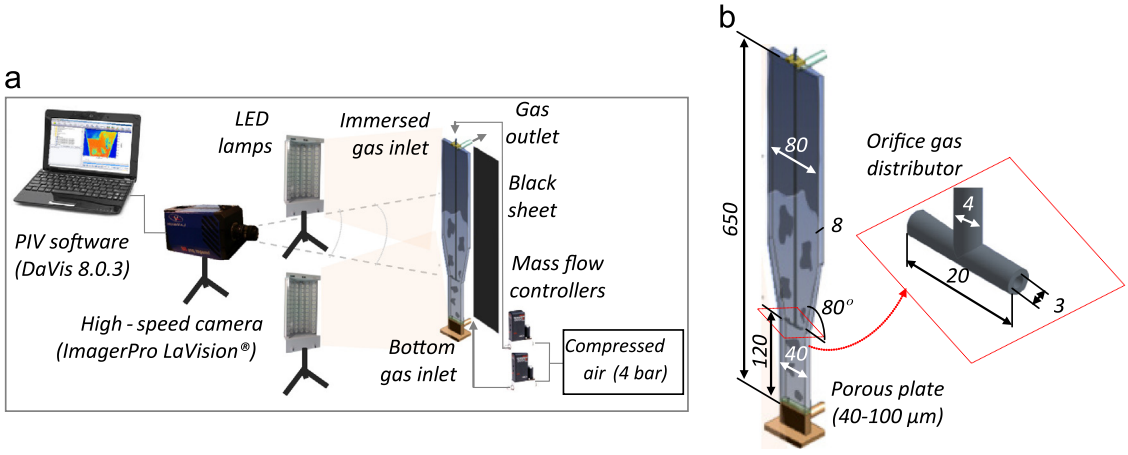

Fig. 1. (a) Experimental set-up, (b) Reactor scheme and dimensions (all lengths in mm).

was placed behind the rear reactor wall to increase the image contrast between the dense and dilute phases, i.e. emulsion and gas bubbles, within the fluidized bed.

Fluidization recordings were performed with a LaVision® Imager Pro high speed camera and analyzed in DaVis 8.0.3, a commercial software for image processing. The recording frequency was adjusted to 750 Hz to avoid image blurriness related to the fast solids movement and a time delay, Δt, of 0.3 ms between two consecutive frames was selected for PIV processing. For each 12 s video, a total amount of 9000 double-frame images were recorded. Some of them were discarded to get, finally, 900 images (1800 frames) at 1/75 s rate. For each experimental condition, three different recordings were performed. Therefore, experimental results shown in this study have been averaged out from 2700 pairs of frames and 36 s of fluidization. Previous studies on similar reactors with the same particles and gas flow rates indicate that both this recording time and the number of images are suitable to get representative results in terms of solids mixing and bubble properties (Julián et al., 2012, 2014b). The image resolution has been adjusted to 90 pixels per cm or, analogously, between 2 and 3 pixels per particle depending on the particle size, as some authors recommend (de Jong et al., 2012; Westerveel, 2000) to get proper PIV analysis performance.

Two dimmable led lamps have been used to get homogeneous illumination on the front reactor wall. The intensity has been adjusted together with the shutter speed of the camera to avoid overexposure or low illumination of the bed. A homogeneous and proper light intensity for the raw images is a must, since bed porosity results depend directly on the image intensity map. Although some image filters can be applied in the DIA post-processing to improve image contrast or homogenize light intensity, illumination settings have been kept constant throughout the experimental series.

Essentially, the effect of three operational parameters on the TS-TZFBR hydrodynamics has been tested: the fluidization regime, the relative axial location of the immersed orifice gas distributor (z_{dis}) with respect to the bottom end of the tapered bed section (z_{sc}) and the presence of internal elements, i.e. tube bundle (horizontal cylinders, $d_{tube}=4$ mm) in the lower bed zone. Three different relative gas velocities, u_{gas}/u_{mf}, have been tested ranging from 2 to 3 times u_{mf}. Besides, two axial distributor locations, $z_{dis}-z_{cs}=[0–1.5]$ cm, and six different configurations of the tube bank have been evaluated. The number of internal elements located within the narrow bed section of the TS-TZFBR varied among the experiments between 3 and 8. The tube bundle configurations were either staggered or hybrid (staggered+in-line), as illustrated in Fig. 2. A total of 36 experimental conditions have been performed to study the coupled effect of these operational variables. Nevertheless, experimental results shown throughout this paper will only be referred to 3, 5 and 8-tube configurations in order not to crowd graphs and figures. The other tube bundle arrangements tested do not lead to significant differences in solids motion and bubbling behaviour in comparison to results from the three shown configurations.

3. Particle Image Velocimetry

Particle Image Velocimetry (PIV) is a widely used experimental technique for the measurement of solids motion in pseudo 2D fluidized beds. PIV/DIA has been selected for this experimental study due to its simplicity, its non-intrusiveness and the detailed whole-field information on both gas and emulsion phase with high spatial and temporal resolution that this technique can give (Laverman et al. 2008; Westerveel, 1997). Further available experimental techniques for fluid dynamic studies on fluidized beds are:

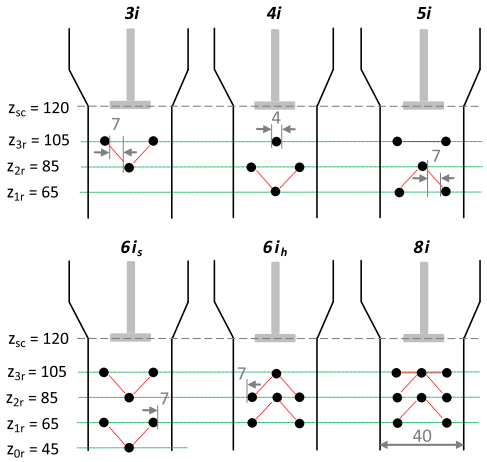

Fig. 2. Tube bank arrangements (lengths in mm).

Electrical Capacitance Tomography, X-ray Tomography, Magnetic Resonance Imaging or Positron Emission Particle Tracking (van Ommen and Mudde, 2008). Although PIV was originally developed to visualize fluid flow patterns using disperse tracer particles, several authors (de Jong et al., 2012; Laverman et al., 2008; Link et al., 2004; van Buijtenen et al., 2011; Westerveel, 1997) successfully extended the technique to dense gas-solids systems. The non-intrusiveness becomes here essential, since the tested TS-TZFBR configurations are small and in case immersed probes were necessary they could dramatically change the fluid dynamics of the bed. The main disadvantage of the technique is the requirement of visual access. That means, only pseudo-2D reactor configurations can be effectively studied.

The way to determine the experimental solids velocity field is to compare two consecutive instantaneous images separated by a short time delay, Δt, and apply a cross-correlation analysis to the interrogation areas in which every image is divided. Fig. 3a shows an example of raw image divided by interrogation areas (32×32 px) from which the PIV analysis is carried out. The most likely volume-average displacement of the particles in the selected interrogation area divided by the time delay between frames gives the solids spatial velocity in each region of the bed.

The PIV post-processing of the recorded pairs of images was carried out using the commercial software package DaVis (LaVision). A multi-pass algorithm was employed using, initially, 32×32 px interrogation areas (with 50% overlap) and, afterwards, two steps of 16×16 px (50% overlap) to reconstruct the corresponding vector images. Interrogation areas need to be small enough to represent regions with nearly uniform motion but not too small to miss particles displacement between consecutive frames if it exceeds the length of the interrogation area. The use of a multi-pass algorithm allows the reduction of image noise and increases the spatial resolution with respect to the standard cross-correlation algorithm. After applying PIV, the solids velocity field is obtained for every pair of images (Fig. 3b). However, resulting velocity vectors cannot be directly transposed into solids flux profiles since the PIV software does not discriminate between dense and dilute phases. Therefore, a method to account for the solids fraction in every interrogation zone is required to determine the local solids fluxes. The information about the bed porosity distribution can be extracted from the Digital Image Analysis post-processing. The DIA method used in this work will be described in detail in Section 4. The solids flux provides the physically most important information on the solids motion in gas-solid fluidized beds. Therefore, the coupled use of PIV and DIA becomes essential to reconstruct both the solids velocity and porosity and get detailed information on the solids fluxes throughout the TS-TZFBR.

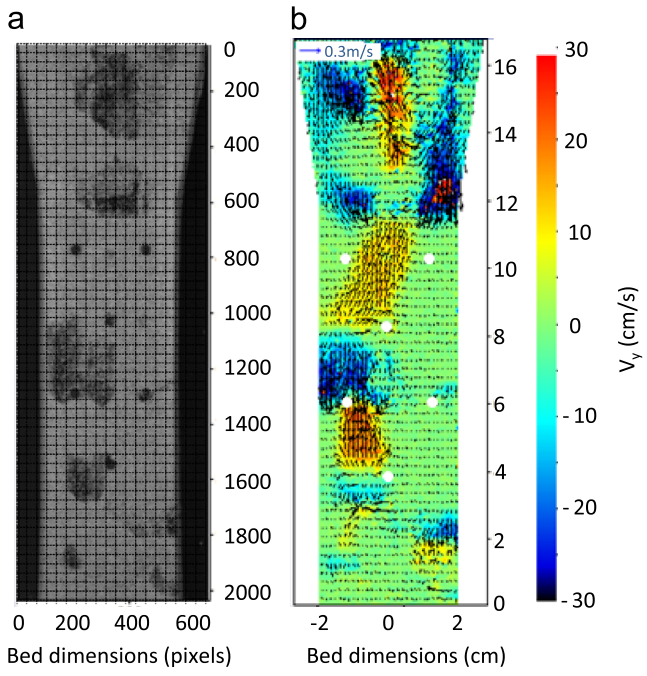

Fig. 3. (a) Cropped raw image (6-staggered internals configuration, $6i_s$) with interrogation areas 32×32 px, (b) Transient PIV velocity vectors map.

To determine the solids flux profiles from the solids velocity profiles, a reliable correlation between the 2D and 3D solids fraction (or porosity) is required.

4. Digital Image Analysis technique

Digital Image Analysis (DIA) is a technique that allows the extraction of useful information from 2D digital images. Applied to fluidized beds, DIA represents the use of algorithms to find out relevant aspects of the bed such as porosity distribution and gas bubble statistics by means of local pixel intensity. DIA was first applied in bubbling fluidized beds by Agarwal et al. (1997) to detect bubbles. Goldschmidt et al. (2004) used this technique to detect particles and Link et al. (2004) successfully applied DIA to study spout fluidized beds. The conventional DIA algorithm applied to bubbly fluidized beds discriminates between the bubble and solids phases on the basis of the pixel intensity, employing a prescribed threshold value. The algorithm corrects the velocity vector maps generated by PIV filtering out high negative velocity vectors that frequently occur within big gas bubbles as a result of particle raining. Therefore, the conventional DIA binarizes the solids fraction into bubbles, i.e. regions free of solids, and emulsion, having this last phase a constant porosity which is usually referred to the minimum fluidization porosity (Hernández-Jiménez et al., 2011; Laverman et al., 2008). Using pixel intensities of the acquired images as a measurement of the local solids fraction may introduce an error, because the pixel intensity does not contain any depth information of the solids hold-up, since this is not visible from the frontal projection (de Jong et al., 2012). Moreover, the conventional DIA algorithm does not account for local variations in the solids fractions. These shortcomings led to the development of a new DIA algorithm with improved accuracy and wider applicability.

To improve accuracy and overcome conventional DIA limitations, van Buijtenen et al. (2011) and de Jong et al. (2012) developed a correlation (Eq. (1)) between the image 2D bed intensity and the solids 3D volume fraction based on reconstructed artificial images from Discrete Particle Modeling (DPM) simulations. When using a "linear" intensity decay along the bed depth to generate the DPM artificial images, these authors found that the "true" 3D solids fraction from simulations displayed a linear profile with a small slope for low image intensities (or analogously "2D solid fractions"). Besides, the 3D solids fraction for high intensities showed a steep asymptotic increase until the maximum 3D packing fraction, i.e. minimum fluidization porosity. Two fitting parameters (A and B) were used to take into account the effect of the bed depth to particle size ratio, $\Delta z/d_p$.

$$\varepsilon_{s,3D} = \frac{\varepsilon_{s,2D}}{1-\frac{\varepsilon_{s,2D}}{B}}A, \quad for\ \varepsilon_{s,3D} < \varepsilon_{s,3D\ max}$$

$$\varepsilon_{s,3D} = \varepsilon_{s,3D\ max}, \qquad for\ \varepsilon_{s,3D} \geq \varepsilon_{s,3D\ max} \tag{1}$$

Artificial images from DPM obtained by these authors were expected to mimic experimental light intensity variation of the acquired images.

In the present work, however, the map of pixel intensities rarely became completely homogeneous in experimental video recordings due to inhomogeneous illumination issues. Therefore, the 2D to 3D volume fraction correlation (Eq. (1)) could not be directly applied to the recorded raw images. The map of intensities of experimental fluidization images (Fig. 4a) needed certain improvements before the correlation could be used. The first step was to subtract a "background" intensity map (Fig. 4b) to the raw images in order to minimize inhomogeneous illumination effects along the bed (Fig. 4c). The "background" image was here determined as the local averaged bed intensity along the recording time once outliers, i.e. overexposed pixels, and gas bubbles were filtered out from the raw images. In practice, local intensities under 80% of the maximum image intensity were not considered in the calculation of the local average bed intensity. Secondly, a median filter was applied in order to smooth the local variation of intensities within the emulsion phase due to image noise (Fig. 4d). Next, corrected image intensities were normalized to 1 dividing by the maximum corrected intensity of the emulsion phase (Fig. 4e). This step allowed the comparison between our experimental values and the normalized intensities obtained from DPM artificial images by de Jong et al. (2012). The histogram of the normalized images was, then, used to get the 3D volume fraction based on the correlation developed by de Jong et al., 2012, Eq. (1) (Fig. 4f). Fitting parameters A and B have been selected in this work minimizing errors in the total bed mass. Their value differ slightly from these obtained by de Jong et al. These authors considered spherical particles with mono-modal distribution and, thus, with a constant bed depth-to-particle size ratio ($\Delta z/d_p$). This $\Delta z/d_p$ mainly influences the $\varepsilon_{2D}-\varepsilon_{3D}$ curve shape. The correlation curve obtained in this work suggests that the experimental light intensity transition between low and high bed porosities is more gradual than in artificial images from DPM simulations. This will be discussed in detail below. Once the ε_{2D}-ε_{3D} correlation was applied, the transient volumetric bed porosity maps (Fig. 4g) were determined. Although it seems that the majority of the emulsion phase has the same porosity, the improvement compared with the binary approach suggested by some authors (Hernández-Jiménez et al., 2011; Laverman et al., 2008) lays in the high precision for the determination of bubble wake and cloud porosities. Solids motion in bubble surroundings is normally high. Therefore, this DIA improvement may have a critical impact on the proper determination of time-averaged solid fluxes, since 3D porosity data are then coupled with transient PIV results to quantify axial mass fluxes within the bed.

As already discussed, experimental histograms do not fit completely with reconstructed artificial images from DPM within the emulsion phase. In artificial images, a quite narrow range of intensities represents a wide interval of volumetric solid fractions

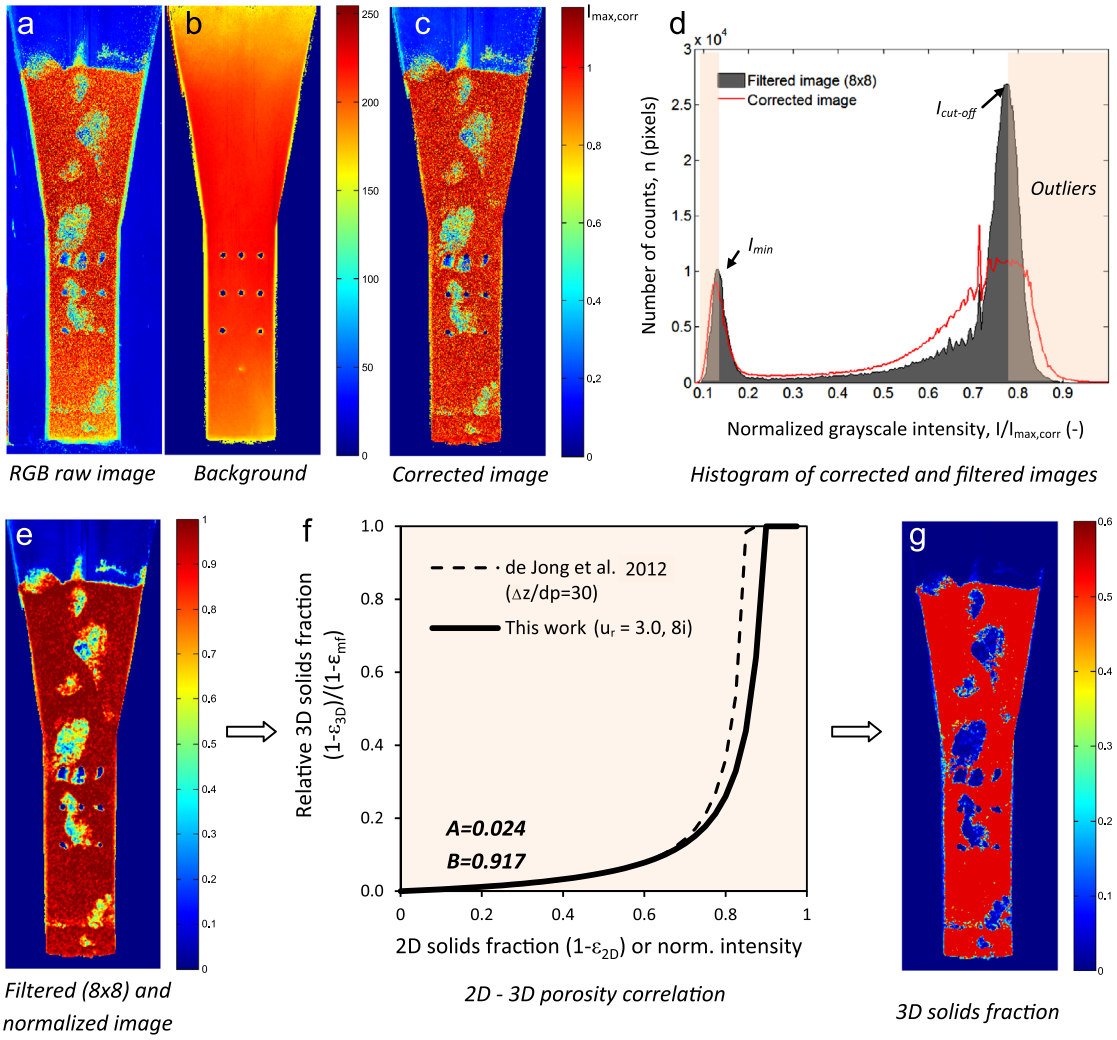

Fig. 4. DIA method applied to a single frame of an 8-internals configuration (8*i*) at $u_{gas}/u_{mf}=3.0$: (a) Raw image, (b) Image background, (c) Background subtraction, (d) Image histogram before and after applying a median filter (8×8 px), (e) Normalized image in the range intensity $0-1$, (f) 2D–3D correlation for the local solids fraction, (g) 3D porosity map.

(see 2D–3D curve in Fig. 4f). However, experimental histograms suggest that the porosity of the emulsion phase corresponds to a wide range of pixel intensities (Fig. 4d). Therefore, some assumptions need to be made.

As can be observed in the histogram of Fig. 4d, the distribution of intensities within the emulsion phase for a filtered image (corresponding to a grayscale value between 0.8 and 1, in this case) is still wide. Due to the asymptotic shape of the 2D-to-3D correlation at high image intensities, the cut-off intensity value must be selected carefully in order not to underestimate the solids fraction of the low-intensity regions of the emulsion phase. A number of criteria could be applied to get the most suitable cut-off value regarding either the maximum pixel intensity, the average pixel intensity within the emulsion phase (range 0.8–1) or the minimum intensity in the range of the emulsion phase (the whole emulsion may have uniform maximum porosity). In this work, the second criterion has been applied. With this criterion, the most representative intensity within the emulsion phase, i.e. intensity mode, is selected as cut-off intensity, $I_{cut\text{-}off}$ (Fig. 4d). Bed intensities over $I_{cut\text{-}off}$ are then assigned to $I_{cut\text{-}off}$ and intensities under it are normalized against $I_{cut\text{-}off}$.

The determination of the fitting parameters A and B in the 2D–3D porosity correlation (Eq. (1)) was carried out by minimizing errors in the total bed mass for every fluidization experiment. The optimal values of *A* and *B* for each experimental condition differ from each other and need to be determined individually. Therefore, a multivariable root-seeking algorithm has been applied to minimize the target function, which is here defined as the bed mass relative error, i.e. $E_m=(m_{real}-m_{calc})/m_{real}$. The real bed mass ($m_{real}$) is well known and m_{calc} represents the estimated bed mass from DIA 3D porosity maps. As an example, Fig. 5a shows the evolution of the errors in the bed mass estimation for different pairs of tested parameter values *A* and *B* (from Eq. (1)) for a 0-internals configuration at $u_{gas}/u_{mf}=3.0$. In this case, it can be observed that parameter values in the range $A=[0–0.1]$ and $B=[0.8–1.0]$ may lead to a suitable estimation of bed mass and, thus, bed porosity. Within the 'valley' of different pairs of values of A–B that lead to low errors in the estimation of the real bed mass (Fig. 5a), it has been found that the optimal window of values that minimize errors in this test was: $A=[0.02–0.03]$ and $B=[0.94–0.96]$ (Fig. 5b). In particular, the optimal values of *A* and *B* for some tests performed at $u_r=3.0$ in different reactor configurations are: $[A, B]_{0i}=[0.023, 0.948]$, $[A, B]_{3i}=[0.023, 0.942]$, $[A, B]_{5i}=[0.023, 0.935]$ or $[A, B]_{8i}=[0.024, 0.917]$. These values are in agreement with those obtained by de Jong et al. (2012), based on DPM simulations.

With such optimal parameter values, the bed mass constraint (estimation error $\leq 0.5\%$) was accomplished for every test. Regarding

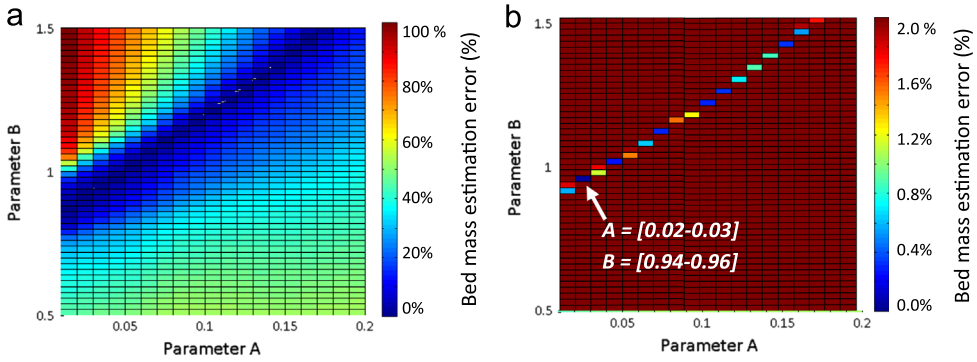

Fig. 5. (a) Effect of parameters *A* and *B* on the minimization of the error in the estimation of the real bed mass. (b) Optimal window of *A* and *B* for the estimation of the real bed mass (zooming the error scale). Experimental conditions: 0*i* configuration at $u_r=3.0$, with $\alpha=80^\circ$.

the mass flux conservation it was found that the global unbalance of axial solids fluxes, i.e. sum of positive and negative local mass fluxes along the bed height, was very low (<5 kg/m^2 s in the worst scenario).

In order to check the solids mass flux conservation as a function of *A* and *B*, an additional target function was tested. The alternative function was defined as the product of the bed mass estimation error by the global axial mass flux unbalance. For both target functions same optimal A and B values were found, illustrating that the own minimization of the bed mass estimation error enhances mass flux conservation. Therefore, the use of the suggested 'E_m-method' to estimate the correlation parameters *A* and *B* allows a proper determination of the 3D solids hold up and local axial mass fluxes. Nevertheless, the use of this method is restricted to recordings in which the entire bed is captured. Otherwise, further assumptions need to be made.

Concerning the different sources of errors that may affect the proper PIV/DIA analysis, non-uniform illumination issues have been solved by subtracting a background image to the raw frames, as already discussed. In addition, the bed discretization into 16×16 interrogation windows (1.8×1.8 mm bed regions at a resolution of 90 pixels/cm) allowed enough spatial resolution for the proper determination of the porosity gradient within bubble clouds. Lastly, cross-correlation errors from PIV analysis were minimized applying a multi-pass algorithm with window size reduction, interrogation areas overlapping and removal of eventual outliers. Therefore, velocity vector maps should not represent a relevant source of errors to be considered in the bed mass and mass conservation balances.

5. Results and discussion

This section illustrates the main experimental findings on the TS-TZFBR hydrodynamics from coupled PIV–DIA analysis in terms of solids circulation patterns, quantitative axial solids mass fluxes, particle mixing between bed zones, bubbling regimes at different gas velocities and effect of different tube bank configurations on the particle and bubble dynamics.

5.1. Interpretation of transient PIV results

Axial solids velocity vector maps provide useful information about particles motion around gas bubbles. Indeed, bubble wake contours and even clouds of single bubbles may be estimated from transient PIV velocity maps. As Fig. 6 illustrates, bubbles usually appear as regions with high solids velocity in the downward direction as a result of particle raining. Immediately under bubbles, solids upward velocity regions are found. These regions are normally well enclosed and represent bubble wakes. Therefore, PIV

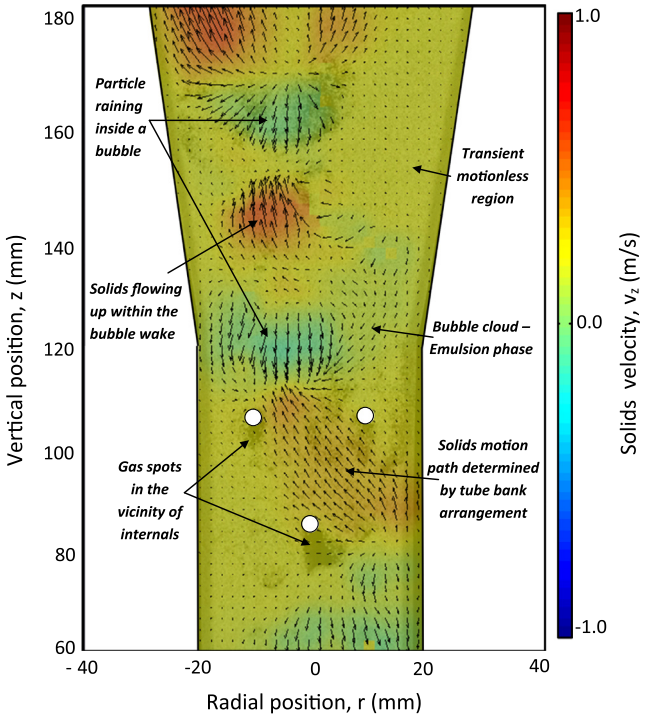

Fig. 6. Interpretation of transient PIV analysis results.

results would allow estimating bubble wake fractions as a function of bubble size and fluidization regime if required. Moreover, transient solids velocity maps illustrate solids circulation paths in the presence of internal elements, as shown in Fig. 6. Analogously, it can be observed that bed regions which are far enough from a gas bubble show velocities close to zero. This is in agreement with the fact that only the presence of gas bubbles promotes solids motion in a fluidized bed. Bubble clouds can also be distinguished in Fig. 6 as the regions with low solids downward velocity in the bubble surroundings. Particles in the bottom-end of bubble clouds flow towards bubble wakes. Lastly, the transient raw image of Fig. 6 illustrates the effect of internal elements on the formation of 'gas pockets' under the tubes. It has been observed experimentally that the fluidization gas gets partially trapped under the internals, whereas the dense phase moves axially on both sides of the tube. As a result, particle-free regions grow at the bottom side of the tubes. From a fluid dynamic point of view, these regions should not be strictly considered as gas bubbles but as particle-free gaps or 'gas pockets'. Therefore, these low porosity regions which would be detected as gas bubbles by the DIA algorithm were filtered out from bubble size distribution results presented in Section 5.5. A more detailed investigation of the occurrence of gas pockets and their

effect on heat and mass transfer rates will be presented in a future work.

5.2. Solids circulation patterns in a TS-TZFBR

Solids circulation provides particles mixing between the two bed zones in a TS-TZFBR and allows integration of reaction and catalyst regeneration. In Fig. 7, the time-averaged radial distribution of axial solids fluxes at different vertical bed positions is presented. The radial distribution gives an idea on how solids circulate along the bed. Particles preferentially flow upwards through the bed center and downwards close to the lateral walls. Average solids flux profiles are smoother in case of the lower reactor zone whereas they become sharper above the secondary gas injection. Just above this injection point, gas flow is twice higher while the cross-section remains almost constant. This is the reason why the positive and negative solids fluxes become locally higher at this stage. The morphology of the immersed distributor plays also a role in the particles circulation within the tapered bed region. The use of a T-shaped distributor with two orifices results in gas channeling over both sides of the distributor. The bimodal upwards circulation peak can be clearly observed in the radial distribution of solid fluxes at $z=15$ cm. Only if the immersed distributor is strictly well aligned in the bed center and gas nozzles are strictly of same size, uniform lateral solids flux profiles can be achieved within the upper bed region. Otherwise, slightly asymmetric lateral profiles would be obtained, as it is illustrated in Fig. 7. At every bed cross-section, positive fluxes prevail at the bed center occupying around 2/3 of the total projected area. On the contrary, negative fluxes are more frequent in the surroundings of the reactor walls. The reactor tube bank configuration presented in Fig. 7 consists of 3 staggered internals located at the positions described in Fig. 2. The upper aligned internals seem to act as draft tubes since they drive upwards flows through the inner region between them and downwards flow outer. The lower internal may play the role of breaking gas bubbles and redirecting solid fluxes through its surroundings. This internal may slightly decrease the solids axial mixing.

5.3. Solids flux profiles along the bed height

As previously discussed, solids fluxes provide the physically most important information on the solids motion in gas-solid fluidized beds. Fig. 8 shows the average radial distribution of axial solids fluxes for 3 different reactor configurations at the different vertical bed positions at which the tube bank are located. The reference case, i.e. TS-TZFBR without internals, is compared to two different configurations with 5 staggered and 8 hybrid (staggered and in-line) internals. The same gas velocity ($u_{gas}/u_{mf}=3.0$) has been used in every experiment.

A first comparison between the radial distributions of solids fluxes for the three cases suggests that the axial circulation in the case without internals is substantially lower than in the other configurations, since the axial profile of fluxes becomes smoother in this case. This assertion is not necessarily true; it only means that the circulation patterns are clearer in the case in which internals are used, since they act as draft tubes providing preferential solids circulation paths in the upward and downward direction, respectively. Therefore, the solids flux diagram presented in Fig. 8 does not give detailed information on the axial mixing rate but on the circulation patterns.

In order to evaluate solids axial mixing, the average solids mass flux in the upward (Fig. 9a) and downward directions (Fig. 9b) have been analyzed separately. Figs. 9a and b illustrate the average positive (towards the bed top) and negative (towards the bottom) solids fluxes, respectively, for the three experiments presented in Fig. 8. The calculation of positive and negative mass fluxes has been carried out considering the average positive and negative value of the transient solids mass flux in each bed interrogation area. If there is no particles movement in a certain interrogation area at a certain fluidization time, i.e. mass flux=0, this value is

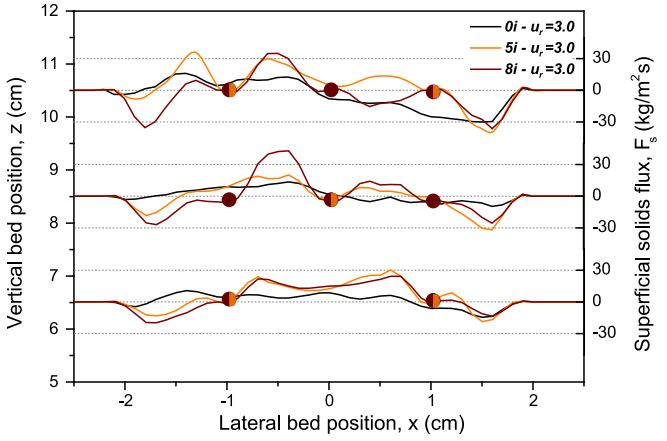

Fig. 8. Average axial solid fluxes at $u_{gas}/u_{mf}=3.0$ for three different configurations of internals at tube array vertical locations ($z_{int}=6.5$, 8.5 and 10.5 cm).

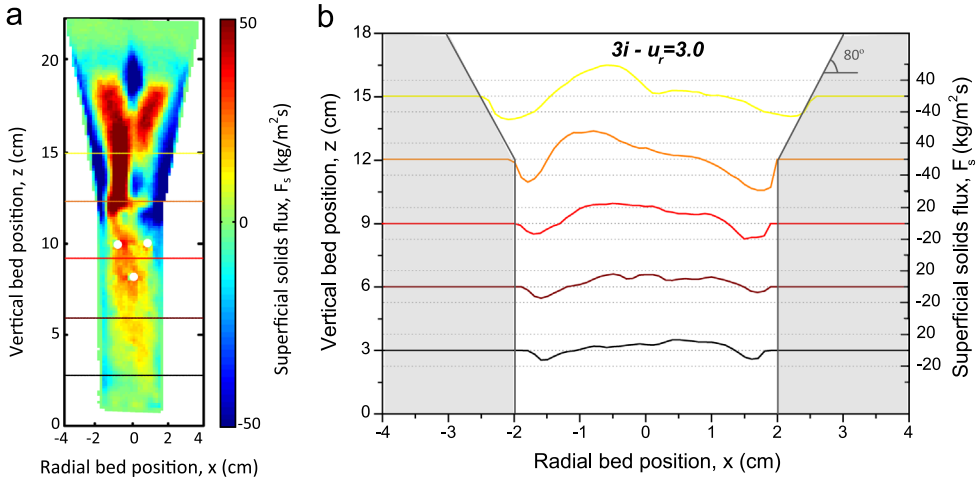

Fig. 7. Average axial solids flux map (a) and corresponding average axial solids fluxes at different vertical bed positions (b) for a reactor configuration with 3 staggered internals, 3*i*, at $u_{gas}/u_{mf}=3.0$.

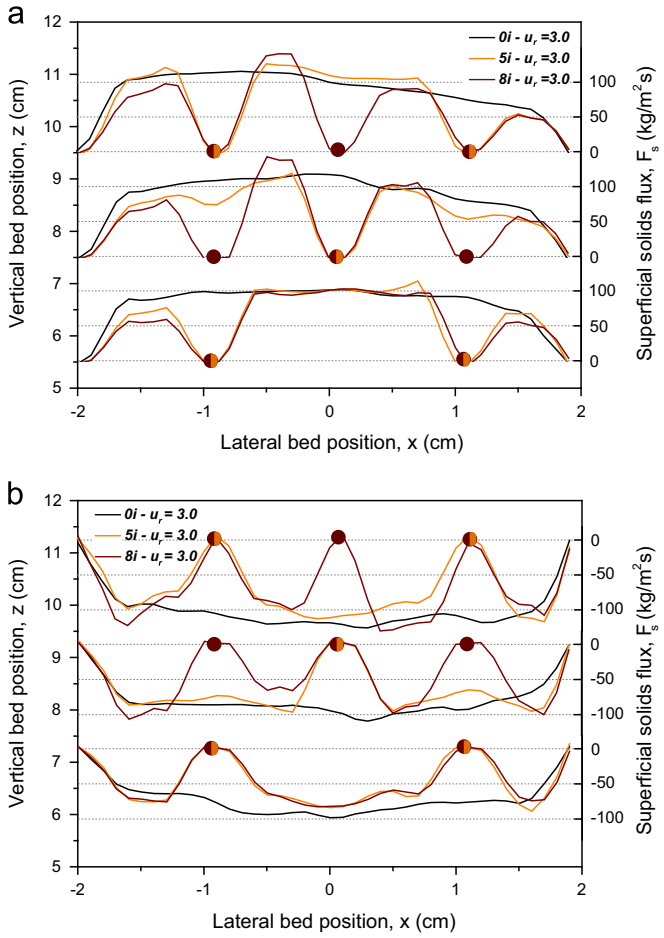

Fig. 9. Positive (a) and negative (b) radial distribution of the average solids superficial mass flux for 3 vertical bed positions and 3 different reactor configurations (0, 5 and 8 internals) at $u_{gas}/u_{mf}=3.0$.

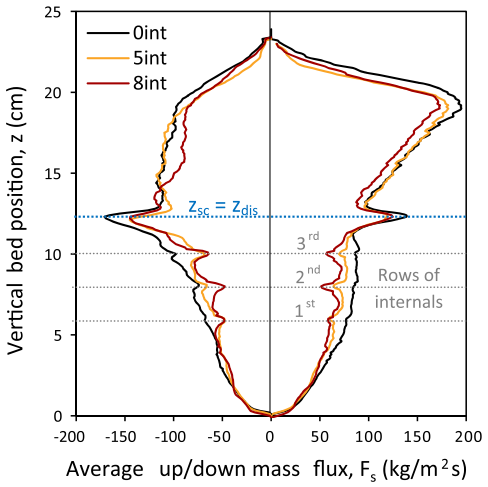

Fig. 10. Positive and negative average solids flux along the vertical bed position for 0, 5 and 8 internals configurations (0*i*, 5*i* and 8*i*) at $u_{gas}/u_{mf}=3.0$.

not considered when averaging out either positive or negative mass fluxes.

As can be observed in both Figs. 9a and b, the radial profile of average solids flux in the upward (+) and downward (−) direction is quantitatively similar either in experiments without or with internals. In the experiment without tube bank (0*i* – $u_r=3.0$), it can be seen that both the positive and negative average mass fluxes follow a turbulent flow profile along the radial position, i.e. almost constant solids flux within the bed center with a sharp mass flux gradient close to the reactor walls where no net particles movement is detected. In case internals are used, positive and negative radial profiles are affected by the location of the internals. Local positive (upward) and negative (downward) fluxes in interrogation areas far from the region of influence of an internal differ in less than 3% with respect to those obtained for the base case without internals. However, particles movement in the surroundings of an internal is strongly decreased, as can be observed for both positive and negative mass fluxes in experiments with 5 and 8 internals (5*i* and 8*i*, respectively).

Regarding the effect of different configurations on the +/− mass fluxes, results show that the highest number of internals (8*i*) leads to the lowest solids hold-up and, thus, to a lower axial mixing with respect to the 0*i* case. Besides, it can be observed that 5*i* and 8*i* configurations mimic their first row of internals ($z=6.5$ cm) and their mass flux profile at that height becomes similar regardless the different configurations of the second and third rows at $z=8.5$ and 10.5 cm, respectively. It suggests that, in this case, the arrangement of the upper tubes does not affect the solids motion through the lowest row of the tube bank.

Fig. 10 represents the axial profile of the average radial solids flux in the upward and downward direction for the 0*i*, 5*i* and 8*i* configurations. The general trend for a 0*i* configuration shows that both the positive and negative average solids mass fluxes increase from the very bottom of the bed along the vertical position within the lower straight section. Mass flux peaks observed at $z=12$ cm above the porous plate are related to the immersed secondary gas inlet. The secondary gas feed leads to high local gas velocities, i.e. fast solids transport, in this region of the bed where the reactor width is still narrow (bottom-end of the tapered bed section). Furthermore, the average solids mass flux increases substantially along the tapered region and finally drops around the freeboard.

The axial profiles of mass flux for different configurations of internals follow a similar trend. However, a local solids flux decrease is found at the bed height at which the tube bank is located. For instance, the axial mass flux in the upper region of the lower bed zone (immediately under the secondary gas injection) is around 30% lower in case of 8*i* than without internals at $u_r=3.0$. Therefore, the use of internals may have an important role on the solids axial mixing or, analogously, on the TS-TZFBR reactor performance.

For every experiment, the accomplishment of global (whole bed) and local mass balances was checked. Of course, the direct summation of axial positive and negative average mass fluxes for an experiment is not representative of its mass balance, since the frequency of positive and negative transient mass flux occurrence is not taken into account. For instance, considering the 0*i* case of Fig. 10, the rate of solids flowing in the upward direction against those flowing down within the lower bed zone is around 0.9 whereas upward-to-downward ratios within the tapered section are between 0.6 and 0.8. Actually, it has been found that the upward-to-downward ratio increases with the gas flow rate in the tapered region over the immersed gas distributor location and decreases with u_{gas}/u_{mf} in the lower bed zone. Moreover, the upward-to-downward solids flux frequency varies locally in the presence of internal elements. If the positive and negative axial mass flux profiles as these presented in Fig. 10 are multiplied by the frequency of positive and negative events, i.e. mass fluxes, along the fluidization time then the so-called 'cross-sectional mass flux profiles' (F_c) in the upward and downward directions can be obtained. Physically, F_c would represent the average positive and negative mass fluxes if these are referred to the entire bed cross-section at each vertical position. The symmetry between positive

and negative cross-sectional mass flux profiles indicates the qualitative mass balance accomplishment along the vertical bed position and, thus, gives an idea on the validity of the method to obtain porosity maps from bed intensities and the 2D–3D correlation described in Eq. (1). In this regard, Fig. 11a shows the vertical profiles of positive and negative F_c for the experiments of Fig. 10 and Fig. 11b illustrates the time average errors in the F_c solids flux accomplishment at every vertical bed position. It can be observed that local errors are low in comparison to the average positive and negative mass fluxes. Besides, the global mass balance to the whole bed is accomplished for all tests. This illustrates the validity of the method used to obtain the map of porosities through the minimization of the error in the estimation of the real bed mass.

5.4. Particle mixing between lower and upper bed zones. Solids circulation time

According to previous works (Sánchez-Delgado et al., 2013), the solids circulation time within a fluidized bed can be measured from PIV/DIA experiments once the average axial solids mass flux has been determined. The theoretical circulation time of a group of particles is described elsewhere (Rowe, 1973) as the mean time required by the particles to reach the freeboard and return to their original position. The mean circulation time, $\overline{t_c}$, can be expressed as shown in Eq. (2), being h_{fb} the average fluidized bed height (or, analogously, the height at which the freeboard starts), h_{min} the minimum height at which bubbles promote solids axial movement, and $\overline{v_u}$ and $\overline{v_d}$ the mean solids velocity in the upward (u) and downward (d) direction.

$$\overline{t_c} = \int_{h_{min}}^{h_{fb}} \frac{dz}{\overline{v_u}(z)} + \int_{h_{min}}^{h_{fb}} \frac{dz}{\overline{v_d}(z)} \quad (2)$$

Both the minimum height, at which solids movement is promoted, and the average fluidized bed height depend on the gas velocity. High gas velocities increase h_{fb} due to an enhanced bed expansion and decrease h_{min} due to an increased gas excess over the minimum fluidization with a subsequent bubble size and solids drag enhancement. The mean solids velocity in the upward and downward direction has been determined taking into account the axial solids mass flow profiles, the bulk density of the bed (ρ_b) and its average porosity ($\varepsilon_s(z)$) from the DIA post-processing. The effect of gas velocity and internals configuration on the circulation time is presented in Table 1. As already discussed h_{min} and h_{fb} are not affected by the presence of internals in the lower bed zone but by the inlet gas velocity. The circulation time slightly increases with the number of internals and increases dramatically at gas flow rates close to the minimum fluidization velocity conditions. The rough estimation of the circulation time may be helpful to improve the TS-TZFBR reactor design.

5.5. Bubble properties

Solids motion is promoted by gas bubbles, which drag upward certain amount of solids on their wakes. It is well known that the wake fraction of a bubble remains almost constant for a wide range of fluidized particle sizes (Rowe and Partridge, 1965). Therefore, the study of the average bubble size evolution along the vertical bed position may help to understand and validate experimental PIV results on axial solids fluxes. DIA post-processing allowed the study of bubble hydrodynamics as presented in the following sub-sections. Firstly, the bubble size distribution (BSD) along the bed vertical position for a 0*i* TS-TZFBR configuration will be discussed and further compared to that obtained in similar reactor configurations at smaller scale, using the same gas velocities and bed particles. Next, the effect of the tube bundle configuration on the bubble size along the lower TS-TZFBR bed zone will be analyzed. Finally, the effect of the relative gas velocity on the bubble growth will be presented.

Table 1
Effect of gas velocity and configuration of internals on the solids circulation time.

u_r (−)	*No. internals*	h_{min} (cm)	h_{fb} (cm)	$t_{c,u}$ (s)	$t_{c,d}$ (s)	t_c (min)
2.0	0	0.9	20.4	358.4	319.9	11.3
2.5	0	0.6	22.1	223.0	215.9	7.3
3.0	0	0.5	22.9	172.5	187.6	6.0
3.0	5	0.5	22.9	195.4	211.3	6.7
3.0	8	0.5	22.9	199.2	211.7	6.8

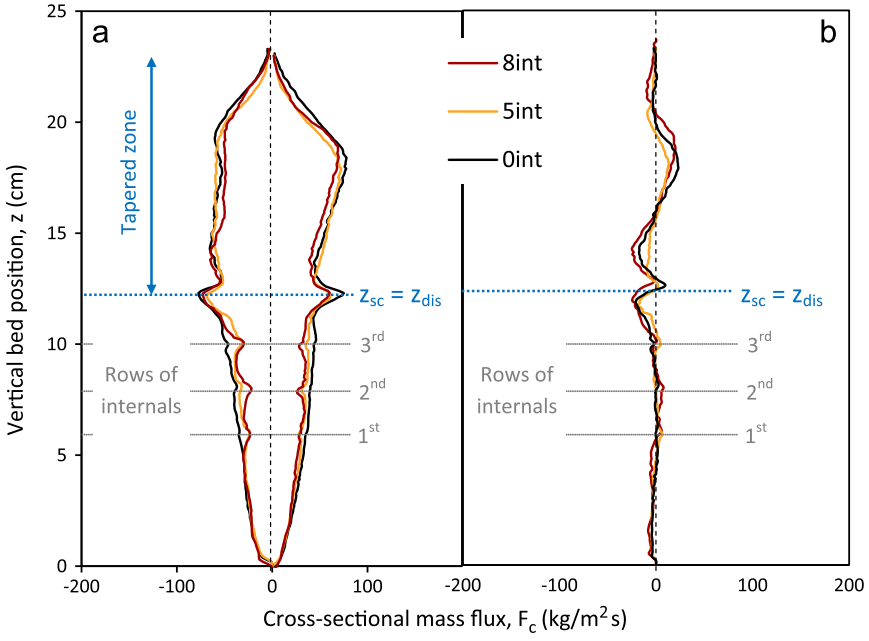

Fig. 11. (a) Positive and negative cross-sectional average solids flux (F_c) along the vertical bed position for 0, 5 and 8 internals configurations (0*i*, 5*i* and 8*i*) at u_{gas}/u_{mf}=3.0. (b) Average errors in the F_c solids flux accomplishment along the vertical bed position for 0*i*, 5*i* and 8*i* configurations at u_{gas}/u_{mf}=3.0.

5.5.1. Bubble size distribution in TS-TZFBR

Fig. 12 illustrates typical bubble size profiles along the vertical bed location for different TS-TZFBR sizes without tube bundle. Experimental DIA results obtained for the reactor configuration described in Section 2 are compared to bubble size profiles from TS-TZFBR reactors used by Julián et al. (2012) in previous experimental works. The reactors used in these studies were twice smaller in terms of height and width but preserved the same depth, particle size and density. The section change height of the reactors used in previous studies was $z_{sc,1x}=8$ cm (in this work: $z_{sc,2x}=12$ cm). In both cases, an almost linear bubble growing trend has been found along the narrow zone of the bed whereas a sharp bubble size decrease was found within the tapered bed section, where an additional gas injection takes place. The equivalent bubble diameter increases, analogously, along the wide reactor section towards the bed freeboard in both configurations. The TS-TZFBR scaling seems to affect significantly neither the bubble growing trends nor the bubble size shrinkage in the surroundings of the bed section enlargement. In a previous study (Julián et al., 2014a), we described a model to predict the average axial bubble size profile in TS-TZFBR reactors based on the Mori–Wen correlation, incorporating some equations to take into account the coupled effect of section enlargement and additional gas feed on the bubble size. The so called JHM model was able to fit experimental measurements at small bed scale ('1*x*'). However, same JHM model formulation has been applied to model DIA results in a twice bigger ('2*x*') TS-TZFBR leading to a poor estimation of both the maximal bubble size under the bed section change (up to 19% deviation) and its evolution through the tapered region. Nevertheless, the model results are still satisfactory in terms of qualitative prediction of growing trends and bubble shrinking effects in the same range of operational conditions.

5.5.2. Effect of tube bundle configuration on BSD

Fig. 13a shows the effect of different configurations of internals (3*i*, 5*i* and 8*i*) on the bubble size reduction within the upper region of the narrow reactor zone fluidized at $3\cdot u_{mf}$ gas velocity. Error bars have been added to the case without internals to illustrate that the bubble shrinkage in the presence of internals is, at least for the 5*i* and 8*i* configurations, representative. These refer to the standard deviation of the average $d_b(z)$ among the three recordings performed at each experimental condition. Error bars for the bubble size profiles obtained with different tube bundle configurations are of the same order but have been removed from the figure for clarity. Experimental results suggest that the different rows of internals play different roles on the average shrinkage of the bubble diameter, i.e. bubble breaking, with respect to the 0*i* configuration case. The BSD obtained for the 3*i* configuration illustrates that the single-centered internal of the second row does not lead to substantial bubble breaking. The average bubble diameter at this vertical position is around 1.7 cm, which is lower than both the distance between the internal and the bed side walls and the distance between the rows. Therefore, bubbles tend to round the tube on both sides without decreasing their size. The third row of the 3*i* configuration consists of two staggered internals. Since the emulsion phase tends to flow downwards close to the reactor walls, bubbles are forced to flow through the narrow gap between these tubes, thus, leading to bubble shrinkage and breaking effects.

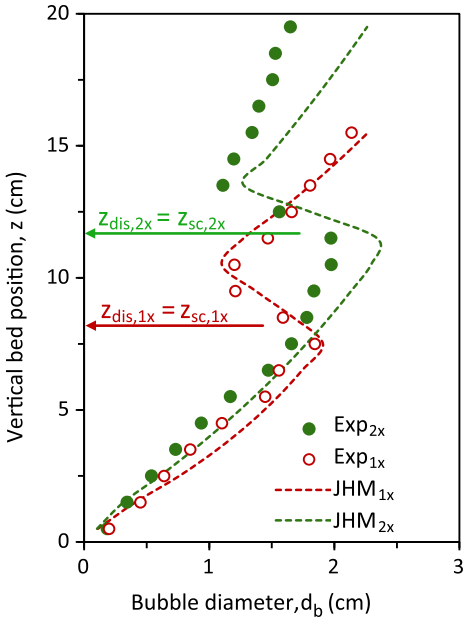

Fig. 12. Comparison between experimental and modeled bubble size profiles obtained at different reactor scales (1*x*, 2*x*) at $u_{gas}/u_{mf}=3.0$, with $\alpha=80^{\circ}$.

The staggered 5*i* configuration leads to an effective bubble size reduction. The two tubes located at the first row height have a clear shrinking effect. Small bubbles coming up from that first row round easily the single tube located at the bed center without increasing their size. The two staggered tubes on the third row lead, then, to bubble diameter reduction as in the 3*i* configuration case. Bubbles are, at this height, big enough to be affected by internals.

The hybrid 8*i* configuration leads to the highest bubble size reduction, as expected. Its first row of internals forces bubbles to shrink passing through the gap between tubes. The next row consists of 3 internals through which bubbles break. Resulting bubbles tend to break again in the presence of the 3 internals of the third row, thus, leading to a sharp reduction of the average bubble diameter with respect to experiments without internals. Nevertheless, the final bubble size reduction obtained with 8*i* and 5*i* configurations is very similar. This suggests that the 5*i* staggered configuration is effective enough for bubble breaking. An increase in the number of internals would not enhance bubble size reduction. Moreover, it would lead to an almost 2% circulation time increase, as described in Section 5.4.

Regarding the faster bubble growing trend above the immersed distributor for the configurations with internals compared to that without tubes, this effect may be related to the average bubble size just under the distributor. It has been experimentally observed that 'slugs', i.e. bubbles that tend to occupy the whole bed section ($d_b > D_{bed}/2$), reduce their size drastically when reaching the tapered region. Therefore, the average bubble size at that height is mainly related to the bubble diameter of gas bubbles coming from the immersed distributor. On the other hand, the shrinkage of the medium size bubbles ($d_b < D_{bed}/2$) due to bed section enlargement is not as sharp. As a consequence, the use of a tube bank to break 'slugs' in the vicinity of the section enlargement may result in an increased average bubble size upwards.

5.5.3. Effect of fluidization regime on BSD

Fig. 13b shows the effect of the relative gas velocity (u_r) on the average bubble diameter within the lower bed zone for the TS-TZFBR configuration without internals. As can be observed, the lowest gas velocities tested, $2\cdot u_{mf}$, lead to quite small bubble sizes. Under these fluidization conditions, the effect of the tube bank on the bubble size reduction is marginal. It has been experimentally observed that such small bubbles flow up rounding internals without breaking. It is remarkable that, in this fluidization regime, no shrinking effect in the bubble size is observed through the transition region, i.e. tapered bed section with additional gas

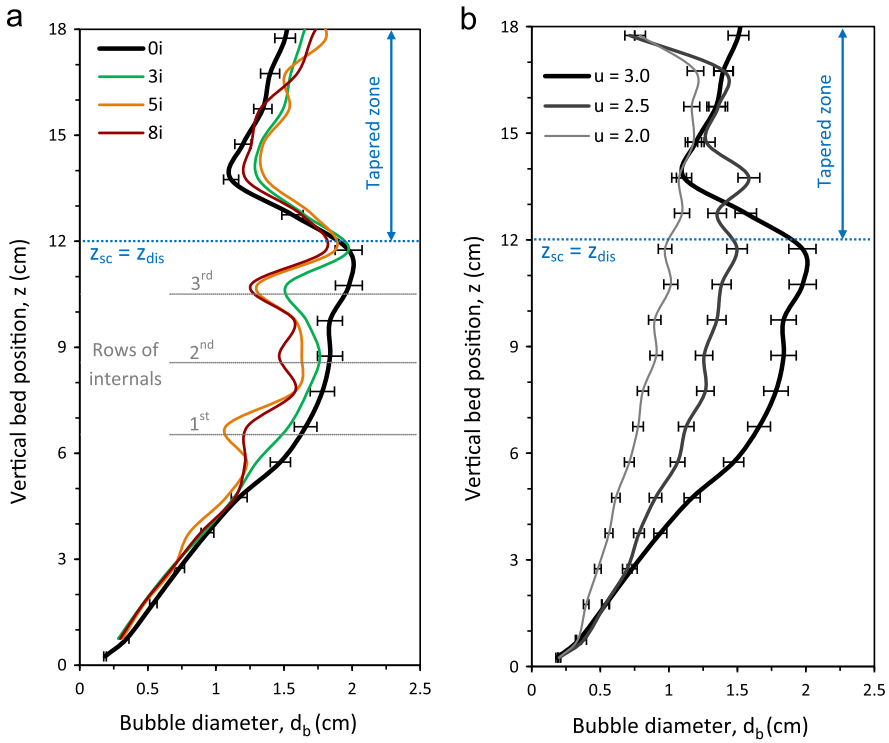

Fig. 13. Average bubble size profile along the vertical bed position for 4 different reactor configurations (a) at $u_{gas}/u_{mf}=3.0$ and for 3 different gas velocities (b) in the configuration without internals, 0*i*. Error bars ($CI_{95\%}$) are included in the 0*i* configuration.

supply. This suggests that the biggest bubbles coming from the lower bed zone are almost of the same size as these new bubbles coming from the secondary gas distributor. An increase from $u_r=2.0$ to 3.0 in the gas flow rate makes gas bubbles to be around two times bigger along the whole narrow bed section. The relation between bubble size and relative gas velocity (u_{gas}/u_{mf}) or, analogously, gas excess over the minimum fluidization (u_{gas} – u_{mf}) in fluidized beds has been extensively reported in literature, leading to a number of well-known correlations that are listed and evaluated in a recent review (Karimipour and Pugsley, 2011).

5.6. Bubble hydrodynamics as promoter of solids motion

In this section, axial average bubble size (d_b) and bubble velocity (u_b) profiles obtained from DIA are compared to experimental PIV/DIA solids flux profiles. Fig. 14 shows the evolution of d_b and u_b along the vertical bed position, together with axial profile of the solids flux in the upward direction for a 0*i* configuration at $u_r=3.0$. It can be observed that average bubble size and velocity are intimately related to each other: bigger bubbles are faster than smaller ones, leading to similar size growth and velocity profiles in agreement with classical hydrodynamic correlations (Davidson and Harrison, 1966). It is well known that solids motion in the upward direction is promoted by ascending gas bubbles that transport certain amount of particles in their wake. Assuming an almost constant volumetric fraction of solids in the bubble wake (Rowe and Partridge, 1965), regardless of the bubble size and velocity, the experimental axial solids upward flow would follow a similar trend as the $d_b(z)$ and $u_b(z)$ profiles. Indeed, taking into account that wake and emulsion porosities are similar, the evolution of solids mass flux along the bed height agrees with that of the bubbles. The only region in which DIA bubbling results do not match the experimental solids flux profile is the surrounding area of the immersed gas distributor. We accept that local solids velocity enhancement takes place as an effect of the secondary gas injection. However, we have not observed a similar change in

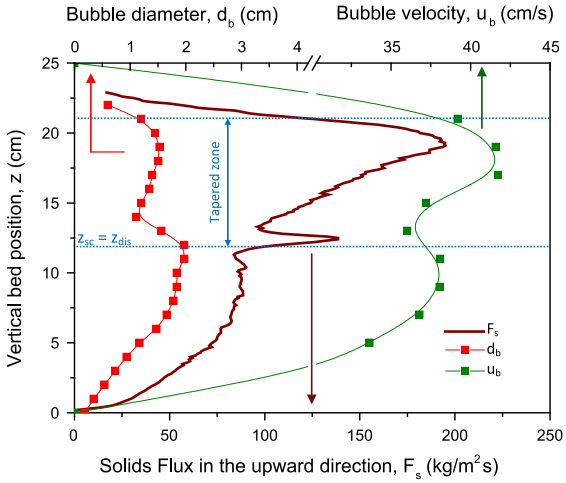

Fig. 14. Comparison between bubble size, bubble velocity and solids mass flux profiles along the vertical bed position for a 0*i* TS-TZFBR configuration at $u_r=3.0$ and $z_{dis} - z_{cs}=0$ cm.

bubble velocity in that region. This may be related either to the cut-off maximal bubble velocity imposed in the DIA algorithm to track bubble centroids between subsequent frames or to the fact that solids may have been sprayed up by the gas jet as a local pseudo-spouted regime without gas bubble formation within that region.

6. Conclusions

Coupled PIV/DIA techniques allowed the hydrodynamic study of a pseudo-2D Two-Section Two-Zone Fluidized Bed Reactor using internals in its lower zone. The correlation developed by de Jong et al. (2012) to determine the local bed voidage from

image intensity was improved in this work to reduce inaccuracies in the estimation of the emulsion phase porosity. A new DIA algorithm for image processing has been developed and the intensity-to-porosity correlation parameters have been optimized to accomplish global bed mass and local solids flux balances.

The effect of different tube bank configurations on the reactor dynamics has been determined for a range of fluidization conditions. A staggered configuration of 5 internals was able to reduce the average bubble size around 30% within the upper region of the lower reactor zone, avoiding slugging regimes at usual TS-TZFBR fluidization flow rates. The use of internals slightly increased the solids circulation time. Nevertheless, the axial solids mixing did not change substantially within the tube bank region. The radial profiles showed that internals play a role in the solids circulation patterns, acting as draft tubes that re-direct the particle flow towards the center of the bed.

A DIA procedure was developed to quantify solid fluxes in upward and downward directions, respectively. This allowed the determination of average wake and emulsion solids fluxes along the bed. The axial profile of the upwards solids fluxes was compared to DIA bubbling size and velocity results. The high agreement between experimental trends for solids and bubble dynamics suggests that the PIV/DIA procedure was well implemented.

The scaled reactor dimensions used in this work, with respect to the TS-TZFBR geometries used in previous studies, provided satisfactory results in terms of repeatability of experimental bubble and solids hydrodynamic trends.

Nomenclature

Acronyms

BSD	Bubble size distribution, (-)
DIA	Digital Image Analysis Technique
PIV	Particle Image Velocimetry Technique
TS-TZFBR	Two-Section Two-Zone Fluidized Bed Reactor
TZFBR	Two-Zone Fluidized Bed Reactor

Greek symbols

α	Tapered section angle with respect to horizontal position, (°)
ε_{packed}	Packed bed solids volume fraction, (−)
$\varepsilon_{s,2D}$	Superficial solids volume fraction, (−)
$\varepsilon_{s,3D}$	Solids volume fraction, (−)
$\varepsilon_{s,3D\ max}$	Maximum solids volume fraction, i.e. packed bed solids volume fraction, (−)
ρ_b	Bulk solids density, (g/cm^3)

Symbols

A	Fitting parameter in the $\varepsilon_{s,2D} - \varepsilon_{s,3D}$ correlation, (-)
B	Fitting parameter in the $\varepsilon_{s,2D} - \varepsilon_{s,3D}$ correlation, (-)
D_{bed}	Bed diameter, (cm)
d_b	Equivalent bubble diameter, (cm)
d_{orif}	Diameter of the immersed gas distributor orifices, (cm)
d_{pore}	Pore size of the porous glass plate distributor, (μm)
d_p	Particle diameter, (μm)
d_{tube}	Diameter of internal tubes, (cm)
Δz	Bed depth, (cm)
Δt	Time delay between subsequent fluidization frames, (ms)
E_f	Absolute error in the mass conservation equation, (kg/m^{2}s)
E_f	Relative error in the bed mass determination, (−)
E_T	Coupled bed mass and mass conservation error in PIV/DIA results, (a.u.)
F_c	Cross-sectional solids mass flux, (kg/m^{2}s)
F_s	Solids mass flux, (kg/m^{2}s)
F_{up}	Solids mass flux in the upward direction, (kg/m^{2}s)
F_{down}	Solids mass flux in the downward direction, (kg/m^{2}s)
h_{fb}	Average bed height or height above which the freeboard starts, (cm)
h_{min}	Minimum bed height at which bubbles promote solids motion, (cm)
$I_{cut\text{-}off}$	Pixel intensity mode within the emulsion phase in fluidization frames, (−)
m_{real}	Real bed mass, (g)
m_{calc}	Calculated bed mass via DIA porosity maps, (g)
u_b	Bubble velocity, (cm/s)
u_{gas}	Gas velocity, (cm^3/cm^{2}s)
u_{mf}	Minimum fluidization velocity, (cm/s)
u_r	Relative gas velocity, u_{gas}/u_{mf} (-)
$\overline{t_c}$	Particles axial circulation time, (min)
$\overline{v_d}$	Average particles velocity in the downward direction, (cm/min)
$\overline{v_u}$	Average particles velocity in the upward direction, (cm/min)
z	Vertical bed axis, (cm)
z_{dis}	Bed height at which the immersed distributor is located, (cm)
z_{sc}	Bed height at which the section change is located, (cm)
$z_{sc,1x}$	Section change location used in previous studies [6–9], (cm)
$z_{sc,2x}$	Section change location in the present reactor configuration, (cm)

Acknowledgments

Financial support from MINECO, Spain (Projects CTQ2010-15568 and ENE2013-44350-R) is gratefully acknowledged. Financial aid for the maintenance of the consolidated research group CREG has been provided by the Fondo Social Europeo (FSE) through the Gobierno de Aragón (Aragón, Spain).

References

Agarwal, P.K., Hull, A.S., Lim, K.S., 1997. Digital Image Analysis Techniques for the Study of Bubbling Fluidized Beds. In: Chaouki, J., Larachi, F., Dudukovic, M.P. (Eds.), Non-Invasive monitoring of multiphase flows. Elsevier Science B.V., Amsterdam (The Netherlands), pp. 407–454.

Davidson, J.F., Harrison, D., 1966. The behaviour of a continuously bubbling fluidised bed. Chem. Eng. Sci. 21, 731–738.

de Jong, J.F., Odu, S.O., van Buijtenen, M.S., Deen, N.G., van Sint Annaland, M., Kuipers, J.A.M., 2012. Development and validation of a novel digital image analysis method for fluidized bed Particle Image Velocimetry. Powder Technol. 230, 193–202.

Goldschmidt, M., Beetstra, R., Kuipers, J.A.M., 2004. Hydrodynamic modelling of dense gas-fluidised beds: comparison and validation of 3D discrete particle and continuum models. Powder Technol. 142, 23–47.

Herguido, J., Menéndez, M., Santamaría, J., 2005. On the use of fluidized bed catalytic reactors where reduction and oxidation zones are present simultaneously. Catal. Today 100, 181–189.

Hernández-Jiménez, F., Sánchez-Delgado, S., Gómez-García, A., Acosta-Iborra, A., 2011. Comparison between Two-Fluid Model simulations and Particle Image Analysis & Velocimetry (PIV) results for a two-dimensional gas–solid fluidized bed. Chem. Eng. Sci. 66, 3753–3772.

Hull, A., Chen, Z., Agarwal, P., 2000. Influence of horizontal tube banks on the behavior of bubbling fluidized beds. 2. Mixing of solids. Powder Technol. 111, 192–199.

Julián, I., Gallucci, F., van Sint Annaland, M., Herguido, J., Menéndez, M., 2012. Coupled PIV/DIA for fluid dynamics studies on a Two-Section Two-Zone Fluidized Bed Reactor. Chem. Eng. J. 207–208, 122–132.

Julián, I., Herguido, J., Menéndez, M., 2013. Particle mixing in a Two-Section Two-Zone Fluidized Bed Reactor. Experimental technique and Counter-Current Back-Mixing model validation. Ind. Eng. Chem. Res. 52, 13587–13596.

Julián, I., Herguido, J., Menéndez, M., 2014a. A non-parametric bubble size correlation for a Two-Section Two-Zone Fluidized Bed Reactor (TS-TZFBR). Powder Technol. 256, 146–157.
Julián, I., Herguido, J., Menéndez, M., 2014b. CFD model prediction of the Two-Section Two-Zone Fluidized Bed Reactor (TS-TZFBR) hydrodynamics. Chem. Eng. J. 248, 352–362.
Karimipour, S., Pugsley, T., 2011. A critical evaluation of literature correlations for predicting bubble size and velocity in gas–solid fluidized beds. Powder Technol. 205, 1–14.
Laverman, J.A., Roghair, I., van Sint Annaland, M., Kuipers, J.A.M., 2008. Investigation into the hydrodynamics of gas-solid fluidized beds using Particle Image Velocimetry coupled with Digital Image Analysis. Can. J. Chem. Eng. 86, 523–535.
Link, J., Zeilstra, C., Deen, N., Kuipers, J.A.M., 2004. Validation of a discrete particle model in a 2D spout-fluid bed using non-intrusive optical measuring techniques. Can. J. Chem. Eng. 82 (1), 30–36.
Medrano, J.A., Julián, I., García, F., Li, K., Herguido, J., Menéndez, M., 2013a. Two-Zone Fluidized Bed Reactor (TZFBR) with palladium membrane for catalytic propane dehydrogenation: experimental performance assessment. Ind. Eng. Chem. Res. 52, 3723–3731.
Medrano, J.A., Julián, I., Herguido, J., Menéndez, M., 2013b. Pd–Ag membrane coupled to a Two-zone Fluidized Bed Reactor (TZFBR) for propane dehydrogenation on a Pt–Sn/$MgAl_2O_4$ catalyst. Membranes 3, 69–86.
Pérez-Moreno, L., Soler, J., Herguido, J., Menéndez, M., 2012. Stable steam reforming of ethanol in a Two-Zone Fluidized-Bed Reactor. Ind. Eng. Chem. Res. 51, 8840–8848.
Gimeno, M.P., Soler, J., Herguido, J., Menéndez, M., 2010. Counteracting catalyst deactivation in methane aromatization with a two zone Fluidized Bed Reactor. Ind. Eng. Chem. Res. 49, 996–1000.
Rowe, P.N., 1973. Estimation of solids circulation rate in a bubbling fluidised bed. Chem. Eng. Sci. 28, 979–980.
Rowe, P.N., Partridge, B., 1965. An X-ray study of bubbles in fluidised beds. Trans. Inst. Chem. Eng. Chem. Eng. 43, T157.
Sánchez-Delgado, S., Marugán-Cruz, C., Soria-Verdugo, A., Santana, D., 2013. Estimation and experimental validation of the circulation time in a 2D gas–solid fluidized beds. Powder Technol. 235, 669–676.
Sitnai, O., 1981. Solids mixing in a fluidized-bed with horizontal tubes. Ind. Eng. Chem. Process Des. Dev. 20, 533–538.
van Buijtenen, M.S., Börner, M., Deen, N., Heinrich, S., Antonyuk, S., Kuipers, J.A.M., 2011. An experimental study of the effect of collision properties on spout fluidized bed dynamics. Powder Technol. 206, 139–148.
van Ommen, J.R., Mudde, R.F., 2008. Measuring the gas-solids distribution in fluidized beds - a review. Int. J. Chem. React. Eng. 6, R3.
Westerveel, J., 1997. Fundamentals of digital Particle Image Velocimetry data. Measurement Sci. Technol. 8, 1379–1392.
Westerveel, J., 2000. Theoretical analysis of the measurement precision in Particle Image Velocimetry. Exp. Fluids 29, S3–S12.

Artículo VI

I. Julián, J. Herguido, M. Menéndez,
Experimental and simulated solids mixing and bubbling behaviour in a scaled TS-TZFBR,
Chem. Eng. Sci. (2015)

Experimental and simulated solids mixing and bubbling behavior in a scaled Two-Section Two-Zone Fluidized Bed Reactor

I. Julián*, J. Herguido, M. Menéndez
*Catalysis, Molecular Separations and Reactor Engineering Group (CREG), Aragon Institute of Engineering Research (I3A), Universidad de Zaragoza, Mariano Esquillor s/n, 50018 Zaragoza, Spain; tel. +34 876555168, e-mail: ijulian@unizar.es

Abstract

Digital Image Analysis techniques, a phenomenological Counter-Current Back-Mixing model (*CCBM*) and Two-Fluid Model (*TFM*) simulations were employed to evaluate the effect of scale on the Two-Section Two-Zone Fluidized Bed Reactors (TS-TZFBR) fluid dynamics, i.e. bubble characteristics, axial mixing of solids and defluidization phenomena. The reactor scaling did not affect the quality of the *TFM* bubble size predictions. A bubble size correlation previously proposed by the authors for *TS-TZFBR* units was able to predict the experimental axial bubble size evolution at the different reactor scales and gas velocities (u_{gas}/u_{mf} = 1.5 – 3.0) with a relative error under 17%. The *TFM* simulated axial solid mass fluxes were same order as these obtained by Particle Image Velocimetry for every reactor size. However, the classical *CCBM* model was unable to predict the effect of scale on the solids axial mixing in a *TS-TZFBR*. The inclination angle of the defluidized bed regions found within the TS-TZFBR tapered zone, θ, increased by $(u_{gas}/u_{mf})^{0.25}$ when duplicating the reactor size. Nevertheless, it did not exceed the prescribed upper limit of $\theta = 80^{o}$ for any of the conditions tested.

1. Introduction

Process intensification in chemical engineering aims to optimize safety, profits and capital or energy costs by reducing the chemical plant size (Stankiewicz and Moulijn, 2000). In this context, the Two-Zone Fluidized Bed Reactor (*TZFBR*) represents a potential tool for process intensification in the field of heterogeneous catalysis since its design provides two simultaneous catalytic processes in one single apparatus. The *TZFBR* technology has been proven to be effective at lab-scale for carrying out gas-solid catalytic reactions where the catalyst suffers from fast deactivation due to coke deposition and those catalytic oxidations where the catalyst can be used as oxygen carrier (Herguido et al., 2005).

The *TZFBR* reactor design has two separated gas inlets to the fluidized bed: an immersed gas inlet for the gaseous hydrocarbon reactant and a gas distributor at the bottom of the bed for the oxidizing agent. Heterogeneous catalytic reactions take place in the upper region of the *TZFBR* whereas catalyst regeneration takes place below the reactant injection point (Figure 1.a). This process integration is possible owing to the catalyst axial mixing, which is typical of fluidized beds. Under certain process conditions, the continuous coke burning within the lower bed zone in the presence of an oxidizer, i.e. diluted oxygen, may result in a long term steady state reactant conversion without net catalytic deactivation. The performance of the *TZFBR* has been successfully tested for light alkane dehydrogenations, ethanol steam reforming or methane aromatization (Medrano et al., 2013; Pérez-Moreno et al., 2012; Gimeno et al.,

2010). The required residence time for particles in the two bed zones depends on the process variables such catalyst type, reactor temperature, hydrocarbon conversion or coke burning kinetics and needs to be optimized for each process individually. In any case, the characteristic catalyst deactivation that takes place in the above mentioned processes becomes important after several minutes on stream (Froment, 2008; Lobera et al., 2008; Pérez-Moreno et al., 2013). Therefore, the solids residence time needs to be adapted accordingly, modifying either the gas velocity or the relative height of each bed zone.

Regarding energy consumption and the heat transfer potentials of fluidized beds, the heat generated by the catalyst oxidation in the lower *TZFBR* zone is used to perform the endothermic hydrocarbon conversion in the upper zone, thus, decreasing heat consumption in the reactor unit towards an autothermal regime. In contrast, a downstream separation unit may be required to remove the CO_x contents of the exhaust gas as a result of the in-situ coke burning.

Two critical issues affect the satisfactory *TZFBR* performance: the oxygen flow must be consumed in the lower bed zone before reaching the upper region and the hydrocarbon back-mixing, which is related to the mixing of solids, must be avoided. The first issue implies the need to optimize and carefully select the most suitable oxygen flow for each reaction condition. The second requires the control of the fluid dynamic regime in each bed region separately. On this regard, novel *TZFBR* configurations that incorporate two zones with different cross sectional areas, i.e. Two-Section *TZFBR* (*TS-TZFBR*), were proposed in a previous work (Julián et al., 2012). These improved reactor configurations allow the use of low regenerative-to-reactive gas flow ratios if required. Their main feature is the use of a tapered transition region between the two bed zones (Figure 1.b).

A comprehensive effort has been made to understand and characterize the lab scale *TS-TZFBR* bed hydrodynamics. Our previous works focused mainly on the study and prediction of the bubble size distribution along the vertical position of the bed (Julián et al., 2014a), on the experimental particle mixing between bed zones and the detection of defluidized regions (Julián et al., 2013), on the validation of a *CFD* tool to simulate the experimental hydrodynamic behavior (Julián et al., 2014b) and on the use of advanced imaging techniques (Particle Image Velocimetry, *PIV,* and Digital Image Analysis*, DIA*) to study the dense phase motion in detail within *pseudo-2D TS-TZFBR* configurations (Figure 1.a) without and with a horizontal tube bank (Julián et al., 2015) . Although the quantitative extrapolation of the phenomena observed in the 2D beds to real 3D fluidized beds is in general not trivial, the obtained results help to gain a better understanding and to validate numerical models, with which 3D beds can be investigated.

The motivation to develop a novel bubble size correlation for a *TS-TZFBR* arose from the lack of correlations in the existing literature that take into account both bed section enlargement and additional gas feed, simultaneously. Experimental findings from cold pseudo-2D measurements, which resulted in the so called *JHM* model (Julián et al., 2014a), were then used to validate Two-Fluid Model (*TFM*) simulations for different *TS-TZFBR* configurations (Julián et al., 2014b).

Analogously, the motivation to perform solids mixing studies was to find an operational window for some *TS-TZFBR* variables (superficial gas velocity, tapered section angle and immersed distributor location) that would allow a certain axial mixing rate between bed zones. Experimental mixing tests were performed using phosphorescent particles as optical tracers. The degree of axial mixing of solids was determined by means of transient tracer concentration profiles. Experimental results were compared to the axial mixing predictions of the two-phase Counter Current Back Mixing model (*CCBM*). Model parameters, viz. wake velocity (u_1), wake-emulsion mass transfer coefficient (K_w) and wake fraction (f_1), were estimated from classical hydrodynamic correlations (Julián et al., 2013).

Lastly, *PIV*/*DIA* studies allowed the motion of solids to be measured inside a *pseudo-2D TS-TZFBR* (Julián et al., 2012; Julián et al., 2015). Applying image processing algorithms to the high-resolution shortly delayed subsequent frames, detailed average solids velocity and mass flux bed maps were obtained.

The present work aims to evaluate the effect of scale on the experimental and simulated *TS-TZFBR* bed hydrodynamics, taking advantage of the previously developed bubble size correlation (Julián et al., 2014a), axial mixing model (Julián et al., 2013) and *CFD* code (Julián et al., 2014b). In particular, the predictability of the experimental axial mixing of solids by the *CCBM* model is tested at scaled *TS-TZFBR* configurations. Moreover, experimental flux of solids and bubble characteristics from *PIV*/*DIA* are coupled with the *CCBM* model formulation in order to predict the experimental axial mixing inside a *TS-TZFBR*, directly from *PIV*/*DIA* results. Besides, the ability of the recently developed 'Julián-Herguido-Menéndez' (*JHM*) correlation to predict the average bubble size evolution along the vertical bed position in a scaled *TS-TZFBR* is evaluated and discussed. The hydrodynamic *CFD* results at the two different reactor scales are compared and the effect of scale on the simulated multiphase flow dynamics is also discussed. To summarize, this study deals with the validation of the hydrodynamic modeling tools at a greater reactor scale.

At this stage, it is important to distinguish between 'scaling' and the 'scale-up' process. As described by Knowlton et al. (Knowlton et al., 2005), fluidized bed scaling consists of applying a set of dimensionless parameters and geometric similarity (derived from the dimensionless form of the governing hydrodynamic equations of the multiphase flow) to modify the scale of the system. The different combinations of dimensionless parameters that are effectively independent are included in the so-called Glicksman's full set: Reynolds number, Froude number, gas-to-particle density ratio and all other length ratios (particle size-to-bed diameter, bed diameter-to-bed height, sphericity and particle size distribution) (Glicksman et al., 1984, 1994) . According to the scaling approach, the physical values do not need to be the same between scales, but the dimensionless numbers have to be equal in both small and large scale. In practice, the maintenance of every dimensionless group as constant among different systems is extremely complicated. Di Maio and Di Renzo (Di Maio and Di Renzo, 2013) summarize some subsets of dimensionless groups adopted by several authors for their scaling attempts. Nevertheless, scaling laws do not ensure the mimicking of hydrodynamic conditions across different scales. According to Levenspiel (Levenspiel, 2008), design and scale-up in bubbling fluidized beds are fraught with uncertainty. Besides, as Knowlton et al. (Knowlton et

al., 2005) assert the use of scaling laws is generally unacceptable for the scale-up of a new process. For instance, if the scaling process requires the modification of particle size or density and this involves a change in the particle Geldart type, the fluidization behavior may change dramatically and the information obtained from the testing would not be directly applicable to the process.

For this reason the experimental and simulated pseudo-2D scaled reactors used in this work are twice the size (in terms of height and width) as those used in previous works. Here "pseudo-2D" refers to the fact that the displacement of solids in the depth direction is neglected in comparison to that in the axial and radial directions. However, they have the same bed properties, viz. particle size and density, in order not to modify the particle Geldart type and thus the *TS-TZFBR* hydrodynamic behavior across the different scales.

2. Experimental set-up

2.1 Solids mixing

Solids mixing experiments were carried out in Perspex® *pseudo-2D TS-TZFBR* facilities (Figure 2.a) using phosphor particles as optical tracers and compressed air as fluidization gas. The reactor dimensions were 60 x 8 x 0.8 cm (height x width x depth), i.e. scaled *TS-TZFBR* height and width with respect to the reactor used in previous tests (30 x 4 x 0.8 cm) (Julián et al., 2013). The lower straight bed zone was 12 cm height. In the main reactor configuration, the *TS-TZFBR* tapered section had an inclination (α) of 80^o with respect to the horizontal position. Additionally, a *TS-TZFBR* (α = 0^o) configuration was used to determine the so-named defluidization angle (β) over a sharp bed section change at different operational conditions. An immersed T-shaped secondary gas distributor was used to feed additional gas through the tapered bed section. The bottom inlet consisted of a 40-100 μm porous plate whereas the inner diameter of the immersed distributor orifices was 3 mm. The phosphor particles were Eu-Dy/$SrAl_2O_4$ based solids provided by Materiales Inteligentes S.L. (d_p = 214 ± 100 μm, ρ_{bulk} = 1.5 g/cm^3, u_{mf} = 11.0 cm/s). The size distribution of the optical tracers is shown in Table 1. The *pseudo-2D TS-TZFBR* was placed inside a black box to increase image contrast in order to follow the solids mixing between activated and non-illuminated phosphor particles by Digital Image Analysis, *DIA* (Figure 2.b). Tested relative inlet gas velocities ranged from 1.5 to 3.0 u_{gas}/u_{mf}. Although the relative axial location of the immersed distributor (z_{dis}) with respect to the bottom-end of the tapered bed region (z_{sc}) may be adapted, experimental and simulated results given in this work refer to the configuration in which the distributor was located at the beginning of the section enlargement, z_{dis} = z_{sc} = 12 cm. This distributor location was proven to be the most suitable one for avoiding defluidization within the tapered region and slugging downwards (Julián et al., 2013, 2014a).

The choice of a twice bigger pseudo-2D reactor allowed preserving a suitable image resolution for solids mixing measurements while studying the effect of scale on the *TS-TZFBR* hydrodynamics.

Every mixing experiment started from a fixed bed loaded with non-excited tracer particles. Initially, the tracer particles located at the front face of the lower bed zone were excited by an external UV-VIS light source during several minutes. Once excited, the phosphorescent particles became light-emitting and the experiment started by feeding compressed air through the gas distributors (Figure 3). From that moment on, the axial mixing between light-emitting and non-excited tracers took place. A home-developed image processing algorithm (Matlab® 2010a) determined the concentration of light-emitting solids within each horizontal slice in which the bed frame is divided. Tracer concentration was related with pixel intensity. For each bed region, a bimodal intensity grayscale histogram was obtained. The two peaks corresponded to the intensities of the non-illuminated and excited tracers, respectively. The mean pixel intensity of each histogram was then used to estimate the local light-emitting tracer concentration (from now on 'tracer concentration', C_t). The transient light intensity decay was taken into account. For this purpose, a dimensionless tracer concentration was defined as the raw average pixel intensity at a certain time t divided by the initial maximal intensity within the lower reactor zone ($C_t(z) = I_t(z)/I_{t=0,max}$). To eliminate intensity decay during the time on stream, the tracer concentration profile along the vertical bed position was forced to have the same area under the $C(z)$ curve for every mixing time, i.e. the overall tracer concentration remained constant throughout the fluidization time. In the pseudo 2D reactor only the facial particle motion is considered, i.e. the particle displacement in the bed depth direction is neglected. For further details, readers are referred to a previous work (Julián et al., 2013).

Once the transient tracer concentration profiles were obtained, the so called 'Mixing Index' (*MI*) was calculated as the degree of mixing between particles that initially come from the upper (non-illuminated) and lower (illuminated) zones as a function of time. The mathematical definition of *MI* is given by in Equation 1, where z_{max} represents the maximum bed height, z_{ilum} is the initially illuminated height, $C(z,t)$ is the tracer concentration as a function of bed height and mixing time and C_∞ represents the full mixing tracer concentration (Grasa and Abanades, 2002a). The *MI* varies between 0 (fully segregated particles) and 1 (full mixing).

2.2 Bubbling

Similar reactor configuration, bed particles and image recording conditions as those described in Section 2.1 were used in this experimental series. Besides, the system was again located inside a black box to avoid external light reflection on the front bed wall. However, led lamps were also placed behind the rear transparent bed wall to illuminate the bed from behind. This configuration allowed the detection of gas bubbles as regions where light crossed the entire bed and reached the camera lens. The dense phase was defined as the bed region through which the light reached the camera with intensity under a prescribed threshold value. A 'maximum light intensity gradient' algorithm (Matlab® 2010a) was used to detect gas bubble contours. As an example, Figure 4.a shows experimental transient fluidization snapshots performed on a scaled *pseudo-2D TS-TZFBR*.

$$MI = \frac{\int_{z_{ilum}}^{z_{max}} C(z,t) \cdot dz}{(z_{max} - z_{ilum}) C_\infty} \quad (1)$$

The equivalent bubble diameter, d_b, is here estimated as the diameter of a round bubble i ($d_{b,i}$) that occupies the same area (A_i) as that enclosed within the experimental bubble contours. In Equation 2, *rf* is the image resolution factor which is used to transform size data from pixels to cm^2.

$$d_{b,i} = \sqrt{\frac{4\,A_i}{\pi} rf^2} \tag{2}$$

The way of weighting bubble size data determines the subsequent statistical analysis on the bubble properties. The time-average equivalent bubble diameter at certain bed position was here calculated using Equation 3. This equation, that weights bubble diameters proportionally to their size, has been already used elsewhere (Julián et al., 2014a) for *pseudo-2D TS-TZFBR* configurations.

$$\overline{d_{b,J}}(z) = \frac{\sum_{i=1}^{n} d_{b,i}(z) \cdot d_{b,i}(z)}{\sum_{i=1}^{n} d_{b,i}(z)} \tag{3}$$

The single bubble upward velocity (u_b) has been calculated by measuring the bubble centroid displacement between short delayed subsequent frames. The bubble tracking between frames was done by using a k-nearest-neighbour algorithm (Asegehegn et al., 2011; Busciglio et al., 2008) from the Matlab 2010® libraries.

We have carried out a comprehensive study of bubble hydrodynamics that includes the analysis of the following bubble properties: equivalent bubble diameter profile along the vertical bed position, $d_b(z)$, bubble size probability distribution (*BSD*), bubble aspect ratio (*AR*), bubbling frequency ($n_b/cm^2 \cdot s$), bubble velocity profile as a function of either the vertical bed position ($u_b(z)$), or the bubble size ($u_b(d_b^{0.5})$), bubble hold-up (b_h) and transient bed height evolution (z_{fb}).

3. Two-Fluid Model *CFD* simulations

The Eulerian-Eulerian approach or Two-Fluid Model (*TFM*) has been used to simulate the hydrodynamic behavior of a *TS-TZFBR* in the commercial software, Ansys CFX 14.5. The Eulerian model considers both solid and gas phase as interpenetrating continua, where the volume of a phase cannot be occupied by others. Therefore, the concept of phase volume fraction is introduced. The model equations (Eq. 4 to 6) consider mass and momentum conservation for each phase, *i* (gas or solid).

$$\frac{\partial}{\partial t}(\varepsilon_i \rho_i) + \nabla \cdot (\varepsilon_i \rho_i \vec{v}_i) = 0 \tag{4}$$

$$\frac{\partial}{\partial t}\left(\varepsilon_g \rho_g \vec{v}_g\right) + \nabla \cdot \left(\varepsilon_g \rho_g \vec{v}_g \vec{v}_g\right) = -\varepsilon_g \nabla P + \varepsilon_g \nabla \cdot \bar{\bar{\tau}}_g + \varepsilon_g \rho_g \bar{g} + K_{gs}(\vec{v}_g - \vec{v}_s) \tag{5}$$

$$\frac{\partial}{\partial t}(\varepsilon_s \rho_s \vec{v}_s) + \nabla \cdot (\varepsilon_s \rho_s \vec{v}_s \vec{v}_s) = -\varepsilon_s \nabla P - \nabla P_s + \varepsilon_s \nabla \cdot \bar{\bar{\tau}}_s + \varepsilon_s \rho_s \bar{g} + K_{gs}(\vec{v}_s - \vec{v}_g) \tag{6}$$

The left hand side of the momentum conservation equation represents the temporal and spatial transport terms. The right hand side represents the considered interacting forces: buoyancy, pressure drop, viscous stress, gravity and interphase drag force, K_{gs} being the interphase momentum exchange coefficient and $\bar{\bar{\tau}}_i$ the *i* phase stress-strain tensor. Lift forces, external body forces, virtual mass forces or wall lubrication forces have been not included in the model, since they have been assumed to be negligible against drag forces.

Some closure equations have been added to describe interphase interactions. The Gidaspow drag function has been used to determine the solid-fluid momentum exchange coefficient. In order to avoid numerical difficulties, CFX modifies the original Gidaspow model by linearly interpolating between the Wen Yu and Ergun correlations over the range $0.7 < \varepsilon_g \leq 0.8$. The Schiller-Naumann model has been used to estimate the drag coefficient. The interphase stress-strain tensor for both phases is assumed to follow the Newtonian strain-rate relation, depending on bulk and shear viscosities. The gas bulk viscosity has been neglected according to Stoke's assumption for Newtonian fluids (Taghipour et al., 2005) and the bulk viscosity of solids has been modeled using the correlation of Lun et al. (Lun et al., 1984). For simplicity, a monodisperse 200 μm particle size has been used to simulate the fluid dynamic behaviour of the optical tracers in a pseudo-2D TS-TZFBR. The restitution coefficient of inelastic particle-particle collisions has been set to 0.90 for all simulations, following the recommendations of some authors (Hernández-Jiménez et al., 2011, 2015) for similar particle properties. The granular temperature has been determined algebraically under the assumption of local equilibrium in a transport equation model. This assumption is often used in dense, slow moving fluidized beds where the local generation and dissipation of granular temperature far outweigh the transport by convection and diffusion (Cloete et al., 2013). A detailed description of the algebraic equilibrium model implemented in Ansys CFX 14.5 can be found in the CFX-Solver Theory user's guide (ANSYS CFX-solver user's guide.2009). The radial distribution function, g_0, (which measures the average distance between particles) was modeled according to the description of Lun and Savage (Lun and Savage, 1986).The shear viscosity of solids is here estimated from the collisional contribution (kinetic contributions are omitted from Ansys CFX 14.5). Lastly, the solid pressure has been modeled according to the kinetic theory model of gases, being adapted to consider the inelastic collisions between particles and the maximum solid packing, which has been set to 0.65 throughout the study.

The set of governing equations described in Table 2 was solved using an element-based finite volume method. In this method, the discretization of the spatial domain using a mesh is followed by the construction of finite volumes to solve mass and momentum conservation equations. The computational domain mimicked half of the depth-wise symmetric experimental scaled pseudo-2D facility (including the void volume occupied by the immersed T-shaped gas distributor) and was discretized by more than 44000 nodes and 193000 tetrahedra. On this regard, mesh independence studies have been conducted to find suitable conditions in terms of computational cost, numerical stability and reproducibility of hydrodynamic results. The unstructured mesh size ranged from 0.5 to 1.25 mm (2 to 5 times the fluidized particle size). Adaptive time steps, $\Delta t = [10^{-4} - 2{\cdot}10^{-4}]$ s, were used to solve the *TFM* simulations. As in our previous work (Julián et al., 2014b), the bulk mass flow rate was selected as the boundary condition for the reactor gas inlets to avoid dense phase outflow. A

fluid-dependant boundary was applied to the reactor walls. The used no-slip condition for the gas phase is widely accepted and generally proposed. However, the proper selection of the particle-wall boundary condition is not so straightforward for Euler-Euler models and different formulations can be found in the open literature: no-slip (Ahuja and Patwardhan, 2008), partial-slip (Cloete et al., 2013; Hernández-Jiménez et al., 2013; Verma et al., 2014) and free-slip (Bahramian et al., 2013; Li and Benyahia, 2013). Although it seems that the partial-slip is the most realistic approach, the selection of an appropriated specularity coefficient is not trivial. Since the detailed analysis of the wall-particle friction is out of the scope of this work, a free-slip boundary condition was applied for the dense phase as a first approach. The reactor outlet was defined with an opening boundary to avoid numerical problems from gas flow entrainments related to pressure gradients. The flow direction was defined as normal to the reactor outlet and the relative pressure in that region was set to 0 Pa. The numerical discretization of the model equations followed a first-order upwind scheme for the phase volumetric fractions and second-order upwind scheme for pressure and velocity fields. The gradients were discretized by least squares and the discretization of the transient terms followed a robust first-order backward Euler for improved numerical stability. The pressure and velocity fields of the momentum equation were solved iteratively via a SIMPLE (*Semi Implicit Method for Pressure Linked Equations*) scheme. The convergence criterion was based on 10^{-3} residual error in the mass and momentum equations. The simulation parameters are listed in Table 3. The initial simulation conditions depict the scaled pseudo-2D TS-TZFBR as a 19 cm high fixed bed with a constant volume fraction, $\varepsilon_{s,0} = 0.5$.

4. Counter-current Back-mixing model (*CCBM*)

The solid transport inside a *TS-TZFBR* has been modelled with the classical *CCBM* model, which depicts the bed as a system with three different phases: gas (bubbles), an upward particulate flow (wake) and a downward dense flow (emulsion) (Lim et al., 1995).

Mass balances over wake and emulsion were represented by a system of hyperbolic partial differential equations (Gwyn et al., 1970). Equations 7 and 8 represent the temporal evolution of the tracer concentration in the wake (C_1) and the emulsion phase (C_2), as a function of the bed vertical position (z). The wake flows up at a velocity u_1 with a volume fraction f_1. Wake and emulsion exchange solid at a volumetric rate of K_w. The velocity of the emulsion (u_2) in the downward direction is related to that of the wake by the expression: $u_2 = u_1 f_1/(1-f_1)$ (Abanades and Grasa, 2002; Grasa and Abanades, 2002a).

$$\frac{\partial C_2}{\partial t} = -u_1 \frac{f_1}{1-f_1}\frac{\partial C_2}{\partial z} + K_w \frac{f_1}{1-f_1}(C_2 - C_1) \tag{7}$$

$$\frac{\partial C_1}{\partial t} = u_1 \frac{\partial C_1}{\partial z} + K_w (C_1 - C_2) \tag{8}$$

A kinematic method (Equations 9 to 11) as described by Grasa and Abanades (Grasa and Abanades, 2002a) has been used to solve the partial hyperbolic differential equations system, by uncoupling time (t) and position (z) variables.

$$C_1(t+\Delta t) = C_1(t)\left(e^{\frac{-k_w}{(1-f_1)}\Delta t} + f_1\left(1 - e^{\frac{-k_w}{(1-f_1)}\Delta t}\right)\right) + C_2(t)\,(1-f_1)\left(1 - e^{\frac{-k_w}{(1-f_1)}\Delta t}\right) \quad (9)$$

$$C_2(t+\Delta t) = C_1(t)\,(1-f_1)\left(1 - e^{\frac{-k_w}{(1-f_1)}\Delta t}\right) + C_2(t)\left(1 - (1-f_1)\left(1 - e^{\frac{-k_w}{(1-f_1)}\Delta t}\right)\right) \quad (10)$$

$$\Delta z = \overline{u_1}\,\Delta t \quad (11)$$

The tracer concentration can be obtained as the average concentration value in every reactor slice, *i* (Equation 12).

$$C_i = C_{1,i}\,f_1 + C_{2,i}\,(1-f_1) \quad (12)$$

The estimation of the model parameters u_1, f_1 and K_w has been carried out, at each reactor scale, by using hydrodynamic correlations. The vertical variation of the wake velocity has been modeled as a function of the bubble fraction in the bed (δ) and the bubble velocity (u_b), according to the correlation suggested by Kunii and Levenspiel (Kunii and Levenspiel, 1991). Analogously, the bubble velocity can be related to bubble size and gas excess over the minimum fluidization (Equation 13), according to the Davidson and Harrison correlation (Davidson and Harrison, 1966).

$$u_1(z) = (1-\delta)\,u_b(z) = (1-\delta)[(u_{gas}(z) - u_{mf}) + 0.4\left(g\,d_b(z)\right)^{0.5}] \quad (13)$$

The bubble size profile, $d_b(z)$, has been modelled with the *JHM* model (Julián et al., 2014a), which takes into account the coupled effect of the section change and the additional gas feed for a *TS-TZFBR*. This model uses the correlation of Mori and Wen (Mori and Wen, 1975) for $d_b(z)$ within straight *TS-TZFBR* bed zones and a non-parametric expression derived from the mass balance to the gas phase within the tapered bed region affected by an additional gas inlet. The bubble fraction (δ) can be measured experimentally and the superficial gas velocity along the vertical bed position, $u_{gas}(z)$, is an input variable related to the *TS-TZFBR* geometry.

$$f_1 = \frac{\delta f_w}{\delta f_w + 1 - \delta} \quad (14)$$

Besides, a mass balance of the three-phase system allows the calculation of the upward solid fraction (f_1) as a function of the bubble wake fraction, f_w, and the experimental bubble fraction, δ (Equation 14). Several authors (Basesme and Levy, 1992; Kozanoglu and Levy, 1991; Rowe and Partridge, 1965; Sane et al., 1996) assume that the wake fraction in a bubble does not depend on the bubble size and that it represents, approximately, a 20% of bubble's volume. Thus, a constant f_w = 0.2 was considered.

Lastly, according to some existing correlations (Chiba and Kobayashi, 1970; Hull et al. 1999; Lim et al.1993), the wake-emulsion exchange coefficient (K_w) can be related to the relative gas velocity ($u_r = u_{gas}/u_{mf}$) and the bubble size. In this work, the correlation of Lim et al. (K. S. Lim et al., 1993) was used (Equations 15a and 15b) to model K_w.

$$K_w = \frac{7.5\ (u_r - 1)}{d_b} \quad for \quad u_r \leq 3 \tag{15a}$$

$$K_w = \frac{15}{d_b} \quad for \quad u_r > 3 \tag{15b}$$

5. Results and discussion

In this section, the most relevant results concerning the effect of scale on the hydrodynamic behavior of a *TS-TZFBR* will be shown.

5.1 Minimum fluidization velocity

Theoretically, the minimum fluidization velocity (u_{mf}) of a group of particles depends on their physical properties, i.e. size distribution, density, shape, but not on the bed height or the bed diameter. However, several authors (Ramos Caicedo et al., 2002; Sánchez-Delgado et al., 2011) have proven that the wall effect plays a significant role in the estimation of u_{mf}, especially working with pseudo-2D beds.

In this study, three different experimental series were conducted to evaluate the effect of bed height and reactor geometry on the minimum fluidization velocity of the used optical tracers. The reactor configurations tested were: the two pseudo-2D beds which have been described in Section 2.1, with the same depth (0.8 cm) and different width (4 and 8 cm, respectively), and a cylindrical reactor with a bed diameter of 2.6 cm. For each bed size, we tested three to four different bed heights ranging from 5 to 25 cm.

From the experimental results shown in Table 4 it can be observed that the reactor configuration does have an effect on the estimation of the minimum fluidization velocity. In particular, the lower the cross-sectional area-to-perimeter ratio (S_{bed}/L_{bed}), the higher is the variation of u_{mf} with the bed height. Indeed, a low S_{bed}/L_{bed} ratio enhances the wall effect on fluidization. The wall-particle interactions hinder particle movement at the wall boundaries. For this reason, higher u_{mf} values were found in reaction configurations which have low S_{bed}/L_{bed} rates. The effect of the bed height on u_{mf} became critical when using narrow vessels. For instance, the u_{mf} value increased by around 37% for a threefold increase in the bed height (from 6.2 cm to 18.7 cm) for a pseudo-2D configuration, w_{bed} = 4 cm. A similar bed height change in the cylindrical configuration results in just around a 5% variation of u_{mf}.

Considering that the minimum fluidization velocity is an intrinsic property of a group of particles with a certain size distribution and density, the selected u_{mf} for the particle tracers used was 11.0 cm/s. This u_{mf} corresponds to the experimental measurement in the cylindrical reactor (h_{bed} = 9 cm), in which wall effects are low compared to those of the tested pseudo-2D configurations. Although hydrodynamic tests were then conducted in pseudo-2D reactors, this u_{mf} value was used throughout the study for the calculations: determination of the relative gas velocity (u_{gas}/u_{mf}), implementation of the *JHM* model for bubble size modeling, etc.

5.2 Effect of scale on the axial mixing of solids

The axial mixing results of experiments conducted with optical tracers in scaled *TS-TZFBR* (*2x*) were compared to those obtained in a smaller reactor configuration (*1x*). The number of particles used at each scale differs. However, the same relative gas velocities and a similar front bed light excited-to-unexcited particles ratio were used in both cases. Figures 5.a and 5.b show axial tracer mixing profiles for relative gas velocities of 1.5 and 3.0 times u_{mf} at the greater reactor scale. As expected, the higher the inlet gas velocity, the faster is the axial mixing of solids. As an example, full solids mixing is obtained after 20 seconds on stream at u_r = 3.0 whereas poor axial tracer dispersion is measured after 40 seconds on stream at u_r = 1.5. This is illustrated by a quite homogeneous axial concentration profile in the first case and a gradual axial C_t decrease in the second. A qualitative comparison between the previous C_t profiles and these obtained in a smaller reactor scale (Julián et al. 2013) (Figures 5.c and 5.d) suggests that the experimental effect of the relative gas velocity is substantially higher than the effect of scale. Since the sole comparison of transient C_t profiles does not give a quantitative estimation of the extent of solids mixing, we will use the 'Mixing Index' (*MI*) concept (Grasa and Abanades, 2002b; Julián et al., 2013) to quantify the transient degree of axial mixing in a fluidized bed, as described in Section 2.1. Figure 6 illustrates the transient evolution of *MI* curves for both reactor scales at u_r= [1.5 – 3.0]. It is observed that the experimental axial mixing becomes faster at the *2x* reactor scale under the same gas velocities. The evaluation of the time derivative of the Mixing Index for the experiments at different bed sizes, $(dMI_{2x}/dt)/(dMI_{1x}/dt)$, reveals the effect of scale on the solids mixing rate. In this case, the average axial mixing rate increased by 29.7% using double-sized reactors at gas velocities u_r = 2.0 – 3.0. At very low velocities (u_r = 1.5), the discrepancies between the mixing rates at the different scales were even greater.

An explanation for that could be the effect of bed walls. As stated above, the lower the S_{bed}/L_{bed} ratio, the higher is the difference between the apparent minimum fluidization velocity (u_{mf}^*) for pseudo-2D beds and the intrinsic u_{mf} for a group of particles. Regarding Table 4 it can be inferred that $u_{mf,1x}^* > u_{mf,2x}^*$ and thus the apparent gas excess ($u_{gas} - u_{mf,i}^*$) for a given u_r regime would be higher in the case of the scaled reactor, promoting faster motion of solids.

Another reason could be the different average bubble size for a given u_r at each reactor scale, even if it is assumed that $u_{mf,1x}^* = u_{mf,2x}^* = u_{mf}$ (which is equivalent to assume that the gas excess would be constant between scales). However, the higher and wider the vessel, the higher is the probability of finding bigger bubbles (due to coalescence) at similar gas flow regimes. As bubbles promote the motion of solids and bigger bubbles drag up larger amounts of solids the solids mixing would be faster at a larger scale, as shown in Figure 6.

The *CCBM* model predictions are presented together with the experimental mixing curves. Parameters u_1, f_1 and K_w have been modeled as a function of fluidization (u_{gas}, u_{mf}) and bubble properties (u_b, d_b), as detailed in equations 13 to 15. The use of average values for the model parameters along the vertical bed position limits the predictability of the model. A quantitative comparison between experimental and modeled *MI* curves leads to significant discrepancies, especially concerning the results obtained for the biggest reactor size. Only the experimental

full mixing times and the effect of the inlet gas velocity on *MI* could be roughly predicted. Actually, the average relative error between the experimental and modeled *MI(t)* profiles along the first few seconds on stream rises up to 67% depending on the fluidization regime. This suggests that the model is unable to reproduce the transient evolution of the solids axial mixing using its actual formulation. Therefore, further model improvement is required in order to use it confidently for the prediction of the transient solids axial mixing in scaled TS-TZFBR. Basically, the improvement involves the consideration of the local variation of the parameter values along the vertical position in the bed, i.e. $u_1(z)$, $f_1(z)$ and $K_w(z)$, instead of using average values. The model re-formulation is out of the scope of this work and will be addressed in a further study.

The estimation of the mass exchange rate between bed zones (which is a key fluid dynamic parameter in a *TS-TZFBR*) from experimental solids mixing results is not very straight forward, although both magnitudes are intimately related. The determination of the average mass exchange requires detailed particle velocimetry studies whereas the solids mixing measurement gives a global insight into the dispersion rate of solids between bed zones. In parallel studies (Julián et al., 2014), *PIV/DIA* experiments have been conducted on purpose to measure the mass exchange rate through the bed zone boundaries in a *TS-TZFBR*. In any case, both techniques provide complimentary and valuable information to improve the reactor design.

5.3 Dense phase motion and solids hold-up in a scaled TS-TZFBR

In this section, the ability of the *TFM* to predict the experimental bed dynamics in a scaled *TS-TZFBR* is evaluated. In particular, the solids hold-up distribution (ε_s), velocity maps (v_z) and mass flux profiles (F_s) reported in previous experimental works using *PIV/DIA* (Julián et al., 2012, 2015) will be compared to these obtained in the simulations on scaled *TS-TZFBR* at several gas velocities.

Figure 7 shows the time-average simulated ε_s and v_z axial profiles at relative gas velocities in the range, u_r = (1.5 – 3.0). It is found that the higher u_r, the lower is the average ε_s, the higher the bed expansion and the higher v_z. In all cases the most densified region is found at the beginning of the tapered bed section. At this bed height, the solids velocity decreases locally due to the section enlargement. Above this position, the solids axial velocity is enhanced by the effect of the additional gas feed.

Together with simulation results, the experimental ε_s and v_z profiles measured by Julián et al. (Julián et al., 2015) for a scaled *TS-TZFBR* (α = 80º) at u_r = 3.0 (dashed lines) are presented. On the one hand, both the experimental solids hold-up and the bed expansion are qualitatively well described by the model. On the other hand, some discrepancy between the experimental and simulated solids velocity profiles is found at this fluidization regime: the model over predicts the solids velocity at the very bottom of the bed and underestimates it in the vicinity of the immersed gas inlet and the freeboard. Nevertheless, experimental average velocity results (especially the downflow values) are affected by particle raining which is inherent to *PIV* measurements on pseudo-2D beds. Since the v_z values do not provide any information on

the solids hold up, the sole comparison of experimental and simulated v_z profiles may drive to a wrong interpretation of the model predictability.

On this regard, the comparison of the time-average mass flux distributions (F_s) gives a more confident guess on the model validity. Figure 8 shows the radial distribution of experimental (Julián et al., 2015) and simulated F_s profiles at different axial locations. The time-average F_s distributions were obtained by coupling transient bed porosity and velocity results.

As it can be observed, the simulated radial F_s profiles agree qualitatively with experimental ones at every vertical position. For instance, at z = 12 cm there is a local increase on the solids flux in the upward direction, whereas at z = 18 cm a bimodal curve (regarding the positive mass flux) is found. This last local mass flux decrease at the bed center is related to the effect of the immersed distributor tube, which hinders the axial mass exchange. Additionally, the maximum net mass fluxes in the upward and downward directions are well predicted at every bed height, illustrating the suitability of the model for predicting the fluid dynamic behaviour of the scaled *TS-TZFBR*.

Figure 9 illustrates the evolution of the experimental and simulated time-average positive (upward) and negative (downward) mass flux along the vertical bed position at the operational conditions described above. The simulated profile suggests a slightly over prediction of the mass exchange within the lower bed zone and an underestimation of the axial mixing within the tapered bed zone. It is important to remark that the direct summation of axial positive and negative average F_s for an experiment is not representative of its mass balance, since the frequency of positive and negative mass flux occurrences is not taken into account. Therefore, the positive and negative curves do not need to be symmetric. As an example, for the experiment shown in Figure 9 the ratio of solids flowing in the upward direction against those flowing down within the lower bed zone is around 0.9 whereas upward-to-downward ratios within the tapered section are between 0.6 and 0.8. Actually, it has been found that the upward-to downward ratio increases with the gas flow rate in the tapered region over the immersed gas distributor location and decreases with u_{gas}/u_{mf} in the lower bed zone (Julián et al., 2014).

To illustrate the effect of scale on the experimental axial solids flux at different gas velocities, the Table 5 compares time-average absolute F_s values along the vertical bed position obtained at different gas flow rates (u_r = 1.0 – 3.0) for the tested reactor scales. Although F_s fluctuates substantially along the bed height, a correlation between gas velocity and axial solids flux can be found. The average mass flux variation with u_{gas} becomes quite similar at the two different reactor scales. However, at high gas velocities, F_s tends to be slightly higher at the biggest scale.

The experimental F_s profiles shown by *PIV/DIA* and the average absolute F_s values predicted by the *CCBM* model are in quantitative agreement. For such a comparison, the modeled average solids velocity in the upward direction, u_1, has been multiplied by the bed density and the average solids volume fraction within the bubble wake, which was assumed to be around 30%

lower than that in the emulsion phase, as measured by some authors (Almendros-Ibáñez et al., 2010).

5.4 Effect of scale on the defluidization angle, β

A conservative tapered section angle, α, to avoid defluidization effects over the *TS-TZFBR* section change height has been defined elsewhere (Julián et al., 2012, 2013, 2014a, 2014b, 2015) to be α = 80º with respect to the horizontal axis for this particle type. Defluidization tests performed in previous studies (Julián et al., 2013, 2014b) for *1x* reactor configurations revealed that, even in the worst fluidization regime scenario (inlet gas velocity as low as $u_r \sim$ 1.1), the defluidization angle within the tapered bed zone, β, would not be greater than 80º.

In this section, the effect of scale on the defluidization angle is presented and discussed. Figure 10 shows the evolution of the experimental and simulated β with respect to the fluidization regime at the two different reactor scales, with and without feeding gas by the immersed gas distributor. The experimental β was measured using a prescribed threshold intensity to track the banked zones of tracer particles. The simulated defluidized zone was defined as the region enclosed by the following limits in volume packing and solids velocity: ε_s = 0.65 and $v_z \leq$ 0.5 cm/s (Julián et al., 2014b).

The experimental results suggest that the reactor size has a noticeable effect on the defluidization angle, since the inclination of the banked region of particles over the section change increased from the 1x to the 2x reactor configurations (Figure 10). An exponential decay of the defluidization angle was found at the two reactor scales as a function of the relative gas velocity within the upper bed zone: $\beta_{2x} = 75.2 \cdot u_r^{-0.07}$ and $\beta_{1x} = 76.3 \cdot u_r^{-0.26}$. Therefore, the increase of the defluidization angle using a double-sized reactor could be estimated as $\beta_{2x}/\beta_{1x} \approx u_r^{0.25}$ for the Geldart-B particles used in this work. This suggests that $\beta_{2x} \approx \beta_{1x}$ at low relative gas velocities. Consequently, the prescribed α = 80º that was used as a conservative inclination for the tapered reactor region at a small scale becomes valid, as well, to avoid defluidization phenomena in a double-sized TS-TZFBR.

At each gas velocity, two different gas feed configurations were tested. The filled symbols represent defluidization experiments performed with two gas inlets whereas the empty symbols refer to experiments in which only the bottom gas distributor was used. As an example, the determination of β for a relative gas velocity, $u_{r,up}$ = 3.0, was carried out either feeding $u_{r,low}$ = 3.0 and $u_{r,up}$ = 3.0 or just feeding $u_{r,low}$ = 6.0, since the cross-sectional area in the upper zone was twice as large as that in the lower zone. The experimental findings showed, then, that the use of a single bottom inlet results in a lower β than using two inlets.

Although in both cases $u_{r,up}$ remained constant within the region of interest, the fluidization regimes became quite different. In the first case, the fluidization gas coming from the immersed T-shaped distributor flew up close to the distributor tube through the bed core. Therefore, its circulation path did not enhance movement of solids at the reactor walls. In the second case, the use of a gas velocity twice as high within the lower bed zone resulted in a more turbulent regime. Although $u_{r,up}$ was the same for both configurations, the more chaotic

bubble circulation of the second regime led to an enhanced mixing of solids at the bed walls, thus to lower β values. In general, the simulated β over-predicted the experimental measurements but followed the same qualitative trends related to the fluidization regime: the lower the gas flow rate, the higher is the simulated defluidization angle.

5.5 Effect of scale on the bubbling behavior

A critical comparison of the *TS-TZFBR* bubbling behavior between the two reactor scales under the same fluidization conditions is here presented. Figure 11 shows experimental, simulated and modeled $d_b(z)$ profiles at relative gas velocities, u_r = 1.5, 2.0 and 3.0 for both *2x* (Figure 11.a) and *1x* (Figure 11.b) bed sizes. The results shown in Figure 11.b were extracted from our previous studies (Julián et al., 2014a, 2014b). Experimental bubbling results were obtained using the method described in Section 2.2. Simulation profiles were determined using the Two-Fluid Model described in Section 3 under the assumption of constant viscosity for the solids phase (Patil et al., 2005; Pei et al., 2012; Upadhyay and Park, 2015; Yusuf et al., 2012) in order to speed up the model convergence and to reduce the computational cost of the simulations, allowing longer lasting ones. Simulated bubble data were averaged out of 10 seconds on stream. Modeled profiles refer to these obtained using the *JHM* correlation (Julián et al., 2014a) for *TS-TZFBR* reactors.

A rough comparison between Figures 11.a and 11.b shows that for each fluidization regime (u_r) the average bubble size becomes bigger at the largest reactor scale. Regarding the $d_b(z)$ within the lower *TS-TZFBR* bed zone, the bubble length becomes as big as the bed width (2 cm) for the small reactor scale at u_r = 3.0. This results in a slugging regime in which bubble growth is limited by the bed walls. In contrast, bubbles formed at u_r = 3.0 in the scaled reactor do not even represent half of the bed width (4 cm) being far from a slugging regime and from growth limitations.

As already discussed in the previous section, since the bed height is twice higher in the *2x* configuration, the double-sized reactor promotes the formation of bigger bubbles for a given fluidization regime. This is in agreement with the faster solids mixing rate observed for the scaled reactor in Figure 6. Regarding the correlation predictability, experimental bubble growing trends at both reactor scales are in qualitative agreement with the predictions of the non-parametric *JHM* model within the tested interval of gas velocities. Concretely, the axial-average relative error of the JHM predictions for the experimental $d_b(z)$ in the double-sized reactor ranges from 14.4% at u_r = 3.0 to 16.8% at u_r = 1.5. Likewise, *TFM* simulations were able to describe the $d_b(z)$ profiles satisfactorily for every tested operational condition. In this case, the relative prediction errors for the $d_b(z)$ profile ranged from 12.8% at u_r = 3.0 to 19.2% at u_r = 1.5.

Figure 12 shows a comparison between the experimental results for bubble size distribution (*BSD*), bubbling frequency and aspect ratio at the two different reactor scales. Regarding the *BSD* of different fluidization regimes at the two bed sizes (Figure 12.a), the probability of finding big bubbles (d_b > 3 cm) within the scaled reactor is substantially higher than in the small one, regardless of the inlet gas velocity. Besides, the probability of finding small bubbles (0 < d_b

< 2 cm) in the *1x* configuration is considerably higher than finding them in the *2x* reactor. On the other hand, the higher the inlet gas flow, the more frequent are the big bubbles as opposed to the small ones.

Figure 12.b illustrates the bubbling frequency in both reactor scales, i.e. the number of bubbles per area and time unit, under the same fluidization velocities. As it can be observed, the formation of bubbles in the lower bed zone of the small reactor is more frequent than in the scaled bed. This may be related to the gas distributor issues. Some centimeters above the distributor, just under the tapered bed zone, bubbles seem to coalesce into bigger bubbles, thus, reducing the number of bubbles per area unit within this region. The sharp decrease in the bubbling frequency that was measured in the vicinity of the bed section change in the small reactor has not been found in the scaled reactor. Coalescence within the lower bed zone of the *2x* reactor (where no slugs are formed) is not as favored as in the *1x*, in which fast bubbles coming from the immersed distributor find slow slugs, enhancing coalescence and thus reducing the number of bubbles per area unit. Nevertheless, the bubble frequency decreases above the immersed distributor and the tapered region in both reactor configurations, as usually occurs in a conventional straight fluidized bed.

Regarding the effect of the fluidization regime a higher gas excess results in a higher number of small bubbles close to the gas distributor. Since bubbles grow faster at higher gas velocities, the bubbling frequency decreases more significantly in such cases due to coalescence. For instance, in the vicinity of the immersed distributor, big bubbles coming from the lower bed zone may incorporate small new bubbles from the distributor at high u_r, having no effect on the effective bubbling frequency within this region. In contrast, low u_r may result in these small new bubbles from the immersed distributor being able to flow upwards as independent entities, resulting in a higher bubbling frequency. The effect of the addition of new bubbles coupled with the fluidization regime can be clearly observed in Figure 12.b, for the scale *2x* and at an axial bed location in the range: z = 12 – 17 cm.

Figure 12.c shows the effect of scale on the probability distribution of the bubble aspect ratio, which is here defined as the ratio between bubble height and width. Basically, the experimental measurements suggest that bubbles are mainly spherical, i.e. cylindrical in a pseudo-2D reactor configuration. The slight skewness of the *AR* curves towards *AR* values greater than 1 suggests that fast vertical bubbles predominate over slow flattened bubbles. Besides, a possible explanation for why the *probability density* curve of the small reactor tends more towards high *AR* values than that of the scaled reactor is that its narrow bed section limits bubble growth in the horizontal dimension and forces bubbles to adopt vertical ellipsoidal shapes. Regarding the effect of the superficial gas velocity on the bubble aspect ratio Figure 12.c shows that the higher the gas flow rate, the faster the bubbles and thus the more vertical they become.

Another interesting hydrodynamic characteristic of a fluidized bed regime is the average bubble hold-up, b_h. This b_h represents the time-averaged value of the fractions of the total fed gas that cross the bed instantaneously as gas bubbles. Closely related to b_h is the average bed height or vertical bed location at which the freeboard starts, z_{fb}. Assuming that the dense

phase porosity remains almost constant, the transient bubble hold-up would determine the instantaneous bed height. The average hold-up and freeboard location values, as well as their standard deviations, are listed in Table 6 for the different reactor scales and gas velocities tested, for both experiments and *TFM* simulations. The gas fraction present as bubbles varies experimentally between 10% and 25% with a standard deviation that ranges from 4% to 10%, depending on the fluidization regime, i.e. the greater the gas excess, the higher is the bubble hold-up and the broader the hold-up fluctuation. Simulations can predict the gas fraction in bubbles satisfactorily, especially at the highest gas velocities within the interval tested. The fluctuation range along the fluidization time is also in agreement with the experimental findings. Compared to the experimental and simulated b_h values in a small reactor, the results obtained in a scaled *2x* reactor are very similar at every fluidization regime. Although it has been shown that bigger bubbles are found in the larger reactor more frequently than in the smaller one (Figure 11), the volumetric gas flow rate is also higher in the *2x* configuration in order to fluidize it, because of its larger bed cross-section. As a result, the bubble hold-up remains almost constant between configurations, i.e. the effect of scale on b_h seems to be negligible.

Regarding the freeboard location, the simulations are able to predict both the average bed height and the fluctuation of the freeboard location reasonably well at each operational condition. The bed height increases regularly with the inlet gas velocity and, thus, with the bubble hold-up. The fluctuation amplitude of the bed height, given by the standard deviation, is higher in the larger reactor scale than in the smaller because bigger bubbles are formed.

In order to fully characterize the bubble hydrodynamics in a *TS-TZFBR*, figures 13 and 14 illustrate the effect of scale on the average bubble velocity profiles as a function of bubble size, $u_b(d_b^{0.5})$, and vertical bed position, $u_b(z)$, respectively. In Figure 13, experimental $u_b(d_b^{0.5})$ measurements are compared to the Davidson-Harrison (*DH*) model (Davidson and Harrison, 1966) predictions and the *TFM* simulation results for each fluidization regime and reactor configuration. The experimental average bubble velocities are in the range of those predicted by the simulations for both reactor scales. Besides, the classical *DH* model is able to describe qualitatively the motion of bubbles related to their size in a *TS-TZFBR*. However, the *DH* model clearly underestimates bubble velocities for big bubbles ($d_b^{0.5}$ > 1.5 $cm^{0.5}$) in the scaled *2x* reactor, while it correctly predicts bubble velocities for all sizes of bubbles in the small reactor. Of course, some experimental deviation of the model linearity was expected due to the unconventional *TS-TZFBR* configuration. Classical correlations for straight fluidized beds with a single bottom inlet suggest that bubble velocity is proportional to the square root of the equivalent bubble diameter. This may not be the case in a *TS-TZFBR*. Its special configuration may explain the systematic underestimation of u_b by the *DH* model for small (the addition of fast new bubbles) and mainly for big bubbles (high local gas flows within the tapered region), that is especially noticeable in the *2x* reactor configuration. The similarity between $u_b(d_b^{0.5})$ profiles at the tested reactor scales suggests that the effect of scale on the average bubble velocity vs. bubble size profile may be negligible when using the same particle type and fluidization gas velocities.

Figure 14 shows experimental, simulated (*TFM*) and modeled (*DH + JHM*) $u_b(z)$ profiles for different fluidization regimes and reactor configurations. Although $u_b(d_b^{0.5})$ coupled with $d_b(z)$ profiles are usually preferred to describe the hydrodynamic behavior of a conventional fluidized bed, the special geometry of the *TS-TZFBR* makes $u_b(z)$ profiles especially interesting for studying the motion of bubbles in the critical region of the reactor, in which both section enlargement and the addition of new small bubbles takes place. Apparently, the experimental average bubble velocity rises along the straight lower bed zone until reaching the tapered region. When bubbles enter the tapered section, they decrease their velocity as long as the cross-sectional area increases. The coupled effect of bubble growing and section enlarging results in an almost constant $u_b(z)$ along the tapered zone. Above this region, u_b rises significantly up to the freeboard. On the one hand, the coupled *DH + JHM* correlation is able to model the variation of u_b within the tapered bed region qualitatively. On the other hand, *TFM* simulations slightly over-predict the experimental $u_b(z)$ profiles. The over-prediction may be related to a number of factors, e.g. the monodispersity used to define simulated bed particles that would have underestimated u_{mf} and increased the simulated gas excess (u_{gas}-u_{mf}), leading to faster bubbles. Nevertheless, the *TFM* prediction of the *TS-TZFBR* bubbling behavior is quite satisfactory. Again, small $u_b(z)$ differences between reactor scales confirm the marginal effect of scale on bubble velocity profiles when using the same particle type (size distribution and density) in the different tests.

Conclusions

Non-intrusive imaging techniques and CFD simulations were employed to evaluate the effect of scale on the *pseudo-2D TS-TZFBR* fluid dynamics and to test the ability of the semi-empirical models *CCBM*, *JHM* and *TFM* to predict experimental bubble properties and solids motion at a larger reactor scale.

The slugging phenomena decreased due to the enlargement of the bed width and the experimental axial mixing increased by nearly 30% for double-sized TS-TZFBR in the range of gas velocities u_r = 2.0 – 3.0.

As a result, the classical CCBM algorithm was unable to predict the solids mixing rate in a scaled *TS-TZFBR*. Further model improvement is required to confidently estimate the transient axial solids mixing within this unconventional fluidized bed.

The *JHM* correlation was able to predict the bubble size profiles at both reactor scales with a relative error $\leq$ 17%. The simulation tool could predict the frequency and shape of bubbles as well as the bubble diameter and velocity profiles qualitatively at the two bed sizes. The *TFM* model estimation of the solids mass flux profiles compared well with the experimental *PIV*/*DIA* results obtained in a previous work using scaled *TS-TZFBR*.

The extent of the defluidized regions increased the with reactor size. The experimental defluidization angles at both reactor scales were correlated as a function of the fluidization gas velocity according to the expression: $\theta_{2x}(u_r) \approx \theta_{1x}(u_r) \cdot u_r^{0.25}$.

As a general conclusion the TFM, which was able to describe the bed behaviour at small scale, is also in agreement with the experimental behaviour at larger scale, while the CCBM was not so successful.

Acknowledgement

Financial support from MINECO, Spain (Project ENE2013-44350-R) is gratefully acknowledged. Financial aid for the maintenance of the consolidated research group CREG has been provided by the Fondo Social Europeo (FSE) through the Gobierno de Aragón (Aragón, Spain).

Notation

Acronyms

AR	Aspect Ratio, (-)
BSD	Bubble Size probability Distribution, (%)
CCBM	Counter-Current Back-Mixing Model
CFD	Computational Fluid Dynamics
DH	Davidson and Harrison Model
DIA	Digital Image Analysis
JHM	Julián-Herguido-Menéndez Model
MI	Mixing Index, (-)
PIV	Particle Image Velocimetry
TFM	Two-Fluid Model
TS-TZFBR	Two-Section Two-Zone Fluidized Bed Reactor
TZFBR	Two-Zone Fluidized Bed Reactor

Nomenclature

1x	Small scale reactor
2x	Scaled reactor
b_h	Bubble hold-up, (%)
C_D	Drag coefficient, (-)
C_1	Optical tracer concentration in the wake phase, (-)
C_2	Optical tracer concentration in the emulsion phase, (-)
C_∞	Optical tracer concentration at bed full mixing, (-)
C_t	Transient dimensionless tracer concentration, (-)
Δt	Time delay between subsequent frames, (ms)
d_b	Equivalent bubble diameter, (cm)
d_p	Particle diameter, (m)
e	Restitution coefficient, (-)
f_1	Solids fraction in the wake phase, (-)
F_s	Solids mass flux, (kg/m^2s)
g	Standard gravity, (m/s^2)
g_0	Radial distribution function, (-)
h_{bed}	Bed height, (cm)
I_t	Transient local bed pixel intensity, (-)
$I_{t=0,max}$	Maximum initial pixel intensity, (-)

K_w	Wake-emulsion mass transfer coefficient, (s^{-1})
K_{gs}	Interphase momentum exchange coefficient, (kg/m^3s)
L_{bed}	Bed perimeter, (cm)
P	Pressure, (Pa)
P_s	Solids pressure, (Pa)
Re_s	Reynolds number, (-)
S_{bed}	Bed cross-sectional area, (cm^2)
u_1	Upward velocity of the solids wake phase, (cm/s)
u_2	Downward velocity of the solids emulsion phase, (cm/s)
u_b	Bubble velocity, (cm/s)
u_{gas}	Superficial gas velocity, (cm/s)
u_{mf}	Minimum fluidization velocity, (cm/s)
u_{mf}^*	Apparent minimum fluidization velocity, (cm/s)
u_r	Relative gas velocity, (-)
$u_{r,low}$	Relative gas velocity within the lower bed zone, (-)
$u_{r,up}$	Relative gas velocity within the upper bed zone, (-)
v_z	Axial solids velocity, (cm/s)
w_{bed}	Bed width, (cm)
w_p	Bed weight, (g)
z	Vertical location in the TS-TZFBR, (cm)
z_{Fb}	Initial simulated fixed bed height, (cm)
z_{fb}	Average bed height in a fluidized bed regime, (cm)
z_{sc}	Vertical location of the section change in a TS-TZFBR, (cm)
z_{dis}	Vertical location of the immersed gas distributor, (cm)
z_{ilum}	Height of the initial light-excited bed region, (cm)
z_{max}	Maximum bed height in a fluidized bed regime, (cm)

Greek symbols

α	Tapered section angle in a TS-TZFBR, (^{o})
β	Defluidization angle, (^{o})
δ	Void fraction in the bed, (-)
ε	Volume fraction, (-)
θ	Granular temperature, (m^2/s^2)
λ	Bulk viscosity, (kg/(m·s))
μ	Shear viscosity, (kg/(m·s))
μ_{col}	Collisional shear viscosity, (kg/(m·s))
ν	Velocity, (m/s)
ρ	Density, (kg/m^3)
τ	Stress-strain tensor, (kg/ms^2)

Subscripts

i	Phase i, either fluid or solid
g	Gas phase
s	Solid phase

References

Abanades, J. C., Grasa, G. (2002). An extended version of the countercurrent back-mixing model suitable for solid mixing in two dimensional fluidized beds. *Fuel and Energ. Abstr. 43*, 282.

Ahuja, G. N., Patwardhan, A. W. (2008). CFD and experimental studies of solids hold-up distribution and circulation patterns in gas–solid fluidized beds. *Chem. Eng. J., 143*, 147-160.

Almendros-Ibáñez, J. A., Pallarès, D., Johnsson, F., Santana, D. (2010). Voidage distribution around bubbles in a fluidized bed: Influence on throughflow. *Powder Technol., 197*, 73-82.

ANSYS CFX-solver user's guide. (2009). *ANSYS Ltd.,*

Asegehegn, T. W., Schreiber, M., Krautz, H. J. (2011). Investigation of bubble behavior in fluidized beds with and without immersed horizontal tubes using a digital image analysis technique. *Powder Technol., 210*, 248-260.

Bahramian, A., Olazar, M., Ahmadi, G. (2013). Effect of slip boundary conditions on the simulation of microparticle velocity fields in a conical fluidized bed. *AIChE Journal, 59*, 4502-4518.

Basesme, E. A., Levy, E. K. (1992). Solids exchange between the bubble wake and the emulsion phase in a two-dimensional gas-fluidized bed. *Powder Technol., 72*, 45-50.

Busciglio, A., Vella, G., Micale, G., Rizzuti, L. (2008). Analysis of the bubbling behaviour of 2D gas solid fluidized beds part I. digital image analysis technique. *Chem. Eng. J., 140*, 398-413.

Chiba, T., Kobayashi, H. (1970). Gas exchange between the bubble and emulsion phases in gas-solid fluidized beds. *Chem. Eng. Sci., 25*(9), 1375-1385.

Cloete, S., Johansen, S. T., Amini, S. (2013). Investigation into the effect of simulating a 3D cylindrical fluidized bed reactor on a 2D plane. *Powder Technol., 239*, 21-35.

Cloete, S., Zaabout, A., Johansen, S. T., van Sint Annaland, M., Gallucci, F., Amini, S. (2013). The generality of the standard 2D TFM approach in predicting bubbling fluidized bed hydrodynamics. *Powder Technol., 235*, 735-746.

Davidson, J. F., Harrison, D. (1966). The behaviour of a continuously bubbling fluidised bed. *Chem. Eng. Sci., 21*, 731-738.

Di Maio, F. P., Di Renzo, A. (2013). Verification of scaling criteria for bubbling fluidized beds by DEM–CFD simulation. *Powder Technol., 248*, 161-171.

Froment, G. F. (2008). Kinetic modeling of hydrocarbon processing and the effect of catalyst deactivation by coke formation. *Catal.Rev.-Sci. Eng., 50*, 1-18.

Gimeno, M. P., Soler, J., Herguido, J., Menendez, M. (2010). Counteracting catalyst deactivation in methane aromatization with a two zone fluidized bed reactor. *Ind. Eng. Chem. Res., 49*, 996-1000.

Glicksman, L. R., Hyre, M. R., Farrell, P. A. (1994). Dynamic similarity in fluidization. *Int. J. Multiphase Flow, 20,* 331-386.

Glicksman, L. R. (1984). Scaling relationships for fluidized beds. *Chem. Eng. Sci., 39*, 1373-1379.

Grasa, G., Abanades, J. C. (2002). The use of two different models to describe the axial mixing of solids in fluidised beds. *Chem. Eng. Sci., 57*, 2791-2798.

Gwyn, J. E., Moser, J. H., Parker, W. A. (1970). A three-phase model for gas-fluidized beds. *Chem. Eng. Prog. Symp. Ser., 66*, 19-27.

Herguido, J., Menéndez, M., Santamaría, J. (2005). On the use of fluidized bed catalytic reactors where reduction and oxidation zones are present simultaneously. *Catal. Today, 100*, 181-189.

Hernández-Jiménez, F., García-Gutiérrez, L. M., Soria-Verdugo, A., Acosta-Iborra (2015), A. Fully coupled TFM-DEM simulations to study the motion of fuel particles in a fluidized bed. *Chem. Eng. Sci., 134*, 57-66.

Hernández-Jiménez, F., Gómez-García, A., Santana, D., Acosta-Iborra, A. (2013). Gas interchange between bubble and emulsion phases in a 2D fluidized bed as revealed by two-fluid model simulations. *Chem. Eng. J., 215–216*, 479-490.

Hernández-Jiménez, F., Sánchez-Delgado, S., Gómez-García, A., Acosta-Iborra, A. (2011). Comparison between two-fluid model simulations and particle image analysis & velocimetry (PIV) results for a two-dimensional gas–solid fluidized bed. *Chem. Eng. Sci., 66*, 3753-3772.

Hull, A. S., Chen, Z., Fritz, J. W., Agarwal, P. K. (1999). Influence of horizontal tube banks on the behavior of bubbling fluidized beds: 1. bubble hydrodynamics. *Powder Technol., 103*, 230-242.

Julián, I., Herguido, J., Menéndez, M. (2013). Particle mixing in a two-section two-zone fluidized bed reactor. experimental technique and counter-current back-mixing model validation. *Industrial & Engineering Chemistry Research, 52*, 13587-13596.

Julián, I., Herguido, J., Menéndez, M. (2014a). A non-parametric bubble size correlation for a two-section two-zone fluidized bed reactor (TS-TZFBR). *Powder Technol., 256,* 146-157.

Julián, I., Herguido, J., Menéndez, M. (2014b). CFD model prediction of the two-section two-zone fluidized bed reactor (TS-TZFBR) hydrodynamics. *Chem. Eng. J., 248*, 352-362.

Julián, I., Gallucci, F., van Sint Annaland, M., Herguido, J., Menéndez, M. (2012). Coupled PIV/DIA for fluid dynamics studies on a two-section two-zone fluidized bed reactor. *Chem. Eng. J., 207-208,* 122-132.

Julián, I., Gallucci, F., van Sint Annaland, M., Herguido, J., Menéndez, M. (2015). Hydrodynamic study of a two-section two-zone fluidized bed reactor with an immersed tube bank via PIV/DIA. *Chem. Eng. Sci., 134,* 238-250.

Knowlton, T. M., Karri, S. B. R., Issangya, A. (2005). Scale-up of fluidized-bed hydrodynamics. *Powder Technol., 150*, 72-77.

Kozanoglu, B., Levy, E. K. (1991). Wake fractions of small bubbles in gas fluidized beds. *Powder Technol., 68*, 285-286.

Kunii, D., Levenspiel, O. (1991). Fluidization engineering. *Butterworth-Heinemann,*

Levenspiel, O. (2008). Difficulties in trying to model and scale-up the bubbling fluidized bed (BFB) reactor. *Ind. Eng. Chem. Res., 47*, 273-277.

Li, T., Benyahia, S. (2013). Evaluation of wall boundary condition parameters for gas-solids fluidized bed simulations. *AIChE Journal, 59*, 3624-3632.

Lim, K. S., Gururajan, V. S., Agarwal, P. K. (1993). Mixing of homogeneous solids in bubbling fluidized beds: Theoretical modelling and experimental investigation using digital image analysis. *Chem. Eng. Sci., 48*, 2251-2265.

Lim, K., Zhu, J., Grace, J. (1995). Hydrodynamics of gas-solid fluidization. *Int. J. Multiphase Flow, 21*, 141-193.

Lobera, M. P., Téllez, C., Herguido, J., Menéndez, M. (2008). Transient kinetic modelling of propane dehydrogenation over a Pt–Sn–K/Al2O3 catalyst. *Applied Catal. A-Gen, 349*, 156-164.

Lun, C. K. K., Savage, S. B. (1986). The effects of an impact velocity dependent coefficient of restitution on stresses developed by sheared antigranulocytes-materials. *Acta Mechanica, 63*, 15-44.

Lun, C. K. K., Savage, S. B., Jeffrey, D. J., Chepurniy, N. (1984). Kinetic theories for granular flow - inelastic particles in couette-flow and slightly inelastic particles in a general flowfield. *J. Fluid Mech., 140*, 223-256.

Medrano, J. A., Julián, I., García, F., Li, K., Herguido, J., Menéndez, M. (2013). Two-zone fluidized bed reactor (TZFBR) with palladium membrane for catalytic propane

dehydrogenation: Experimental performance assessment. *Ind. Eng. Chem. Res., 52,* 3723-3731.

Mori, S., Wen, C. Y. (1975). Estimation of bubble diameter in gaseous fluidized-beds. *AIChE Journal, 21*, 109-115.

Patil, D. J., van Sint Annaland, M., Kuipers, J. A. M. (2005). Critical comparison of hydrodynamic models for gas–solid fluidized beds—Part I : Bubbling gas–solid fluidized beds operated with a jet. *Chem. Eng. Sci., 60*, 57-72.

Pei, P., Zhang, K., Wen, D. (2012). Comparative analysis of CFD models for jetting fluidized beds: The effect of inter-phase drag force. *Powder Technol., 221*, 114-122.

Pérez-Moreno, L., Soler, J., Herguido, J., Menendez, M. (2012). Stable steam reforming of ethanol in a two-zone fluidized-bed reactor. *Ind. Eng. Chem. Res., 51*, 8840-8848.

Pérez-Moreno, L., Soler, J., Herguido, J., Menéndez, M. (2013). Stable hydrogen production by methane steam reforming in a two-zone fluidized-bed reactor: Effect of the operating variables. *Int. J. Hydrogen Energy, 38*, 7830-7838.

Ramos Caicedo, G., García Ruiz, M., Prieto Marqués, J. J., Guardiola Soler, J. (2002). Minimum fluidization velocities for gas–solid 2D beds. *Chem. Eng. Proc.: Proc. Intensif., 41*, 761-764.

Rowe, P. N., Partridge, B. A. (1965). An X-ray study of bubbles in fluidised beds. *Transactions of the Institution of Chemical Engineers and the Chemical Engineer, 43*, T157.

Sánchez-Delgado, S., Almendros-Ibáñez, J. A., García-Hernando, N., Santana, D. (2011). On the minimum fluidization velocity in 2D fluidized beds. *Powder Technol., 207*, 145-153.

Sane, S., Haynes, H., Agarwal, P. (1996). An experimental and modelling investigation of gas mixing in bubbling fluidized beds. *Chem. Eng. Sci., 51*, 1133-1147.

Stankiewicz, A. I., Moulijn, J. A. (2000). Process intensification: Transforming chemical engineering. *Chem. Eng. Prog., 96,* 22-34.

Taghipour, F., Ellis, N., Wong, C. (2005). Experimental and computational study of gas-solid fluidized bed hydrodynamics. *Chem. Eng. Sci., 60*, 6857-6867.

Upadhyay, M., Park, J. (2015). CFD simulation via conventional two-fluid model of a circulating fluidized bed riser: Influence of models and model parameters on hydrodynamic behavior. *Powder Technol., 272*, 260-268.

Verma, V., Padding, J. T., Deen, N. G., Kuipers, J. A. M. (2014). Bubble formation at a central orifice in a gas–solid fluidized bed predicted by three-dimensional two-fluid model simulations. *Chem. Eng. J., 245*, 217-227.

Yusuf, R., Halvorsen, B., Melaaen, M. C. (2012). An experimental and computational study of wall to bed heat transfer in a bubbling gas–solid fluidized bed. *Int. J. Multiphase Flow, 42*, 9-23.

Table 1. Phosphor particle size distribution

Particle size distribution ($\overline{d_{p,s}} = 214\ \mu m$)	
Size (µm)	w/w (%)
400–320	2.3
320–250	44.2
250–200	20.4
200–150	21.7
150–100	11.4

Table 2. Set of closure equations for the TFM simulation of a fluidized bed

Interphase momentum exchange coefficient:	$\begin{cases} K_{gs} = 150\frac{\varepsilon_s(1-\varepsilon_g)\mu_g}{\varepsilon_g {d_p}^2} + 1.75\frac{\varepsilon_s\rho_g\lvert\vec{v}_s-\vec{v}_g\rvert}{d_p} & (\varepsilon_g \leq 0.8) \\ K_{gs} = \frac{3}{4}C_D\frac{\varepsilon_s\rho_g\lvert\vec{v}_s-\vec{v}_g\rvert}{d_p}{\varepsilon_g}^{-1.65} & (\varepsilon_g > 0.8) \end{cases}$
→ *Drag coefficient:*	$\begin{cases} C_D = \frac{24}{\varepsilon_g Re_s}\left[1+0.15(\varepsilon_g Re_s)^{0.687}\right] & (Re_s \leq 1000) \\ C_D = 0.44 & (Re_s > 1000) \end{cases}$
→ *Reynolds number (solids):*	$Re_s = \frac{d_p\rho_g\lvert\vec{v}_s-\vec{v}_g\rvert}{\mu_g}$
Solids stress-strain tensor:	$\bar{\bar{\tau}}_s = \varepsilon_s\mu_s\left(\nabla\vec{v_s} + \nabla\vec{v_s}^T\right) + \varepsilon_s(\lambda_s - \frac{2}{3}\mu_s)\nabla\cdot\vec{v_s}\bar{\bar{I}}$
→ *Solids bulk viscosity*:	$\lambda_s = \frac{4}{3}{\varepsilon_s}^2\rho_s d_p g_0(1+e)\left(\frac{\theta}{\pi}\right)^{1/2}$
→ *Solids shear viscosity*:	$\mu_s = \mu_{s,col} = \frac{4}{5}{\varepsilon_s}^2\rho_s d_p g_0(1+e)\left(\frac{\theta}{\pi}\right)$
→ *Radial distribution function*:	$g_0 = \left[1-(\frac{\varepsilon_s}{\varepsilon_{s,max}})^{1/3}\right]^{-1}$
→ *Algebraic equilibrium model (θ)*:	$\bar{\bar{\tau}}_s\,\nabla\vec{v_s} = \gamma_s$ *(Production = Dissipation)*
→ *Collisional dissipation of energy*:	$\gamma_s = \frac{12(1-e)^2 g_0}{d_p\sqrt{\pi}}\rho_s{\varepsilon_s}^2\theta^{3/2}$
Solids pressure:	$P_s = \varepsilon_s\rho_s\theta\left(1+2\,\varepsilon_s g_0(1+e)\right)$

Table 3. Model parameters used in the *CFD* simulation

Model parameter	Value
Reactor height (cm)	60
Particle density, ρ_s (kg/m^3)	2500
Particle diameter, d_p (μm)	200
Particles per cell unit, $d_p/cell$ (-)	≤ 5
Initial solids volume fraction, ε_{s0} (-)	0. 50
Initial fixed bed height, z_{Fb} (cm)	19
Maximum packing fraction, $\varepsilon_{s,m}$ (-)	0.65
Restitution coefficient, e (-)	0.90
Gas temperature (^{o}C)	25

Table 4. Minimum fluidization velocity as a function of reactor configuration

FBR config.	S_{bed}/L_{bed} (cm)	$H_{fix\text{-}bed}$ (cm)	w_p (g)	u_{mf} (cm/s)
2D (w_{bed} = 4.0 cm)	0.33	6.2	31.1	11.1
		11.6	58.7	12.1
		18.7	93.7	15.2
		26.8	135.3	15.6
2D (w_{bed} = 8.0 cm)	0.36	5.3	53.6	11.9
		9.4	95.6	12.8
		16.5	167.1	13.4
3D ($Ø_{bed}$ = 2.6 cm)	0.65	5.9	57.7	10.9
		9.0	87.6	11.0
		14.2	138.7	11.4

Table 5. Comparison between *PIV* results [9, 13] and *CCBM* model parameter values predicted by hydrodynamic correlations [11] at the two considered bed scales

Bed scale	u_r (-)	CCBM model parameters				PIV results
		f_1 (-)	k_w (s^{-1})	u_1 (cm/s)	$F_{s\,CCBM}$ (kg/m^2s)	$F_{s\,PIV}$ (kg/m^2s)
2x	1.5	0.02	7.1	4.7	37.6	-
	2.0	0.04	7.6	7.0	56.0	40 ± 21
	2.5	0.06	8.2	9.0	72.0	60 ± 23
	3.0	0.06	9.0	10.9	87.2	95 ± 37
1x	1.5	0.02	7.9	4.2	33.6	16 ± 11
	2.0	0.04	9.2	6.3	50.4	38 ± 21
	2.5	0.05	10.8	8.2	65.6	59 ± 34
	3.0	0.07	11.9	10.0	80.0	84 ± 45

Table 6. Effect of the relative gas velocity on the bubble hold-up and freeboard height ($z_{Fb,1x}$ = 15 cm, $z_{Fb,2x}$ = 28 cm)

Bed size (reactor scale)	Relative gas velocity, u_r (-)	Bubble hold-up, b_h (%)		Freeboard location, z_{fb} (cm)	
		Experimental	Simulation	Experimental	Simulation
2x	1.5	11 ± 4	8 ± 3	29 ± 1	29 ± 1
	2.0	18 ± 6	12 ± 5	31 ± 1	30 ± 1
	2.5	23 ± 8	20 ± 5	33 ± 2	32 ± 1
	3.0	24 ± 8	22 ± 7	34 ± 2	34 ± 1
1x	1.5	14 ± 6	8 ± 4	16 ± 1	18 ± 1
	2.0	18 ± 6	13 ± 5	20 ± 1	20 ± 1
	2.5	21 ± 8	20 ± 6	21 ± 1	21 ± 1
	3.0	26 ± 10	23 ± 8	22 ± 2	22 ± 1

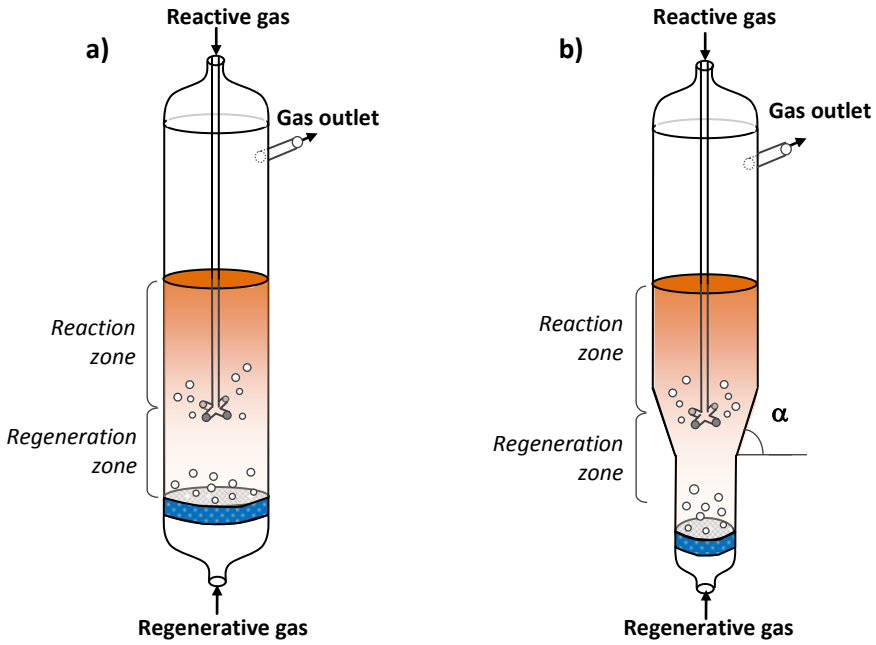
a)
Reactive gas
Gas outlet
Reaction zone
Regeneration zone
Regenerative gas
b)
Reactive gas
Gas outlet
Reaction zone
Regeneration zone
α
Regenerative gas

Figure 1.

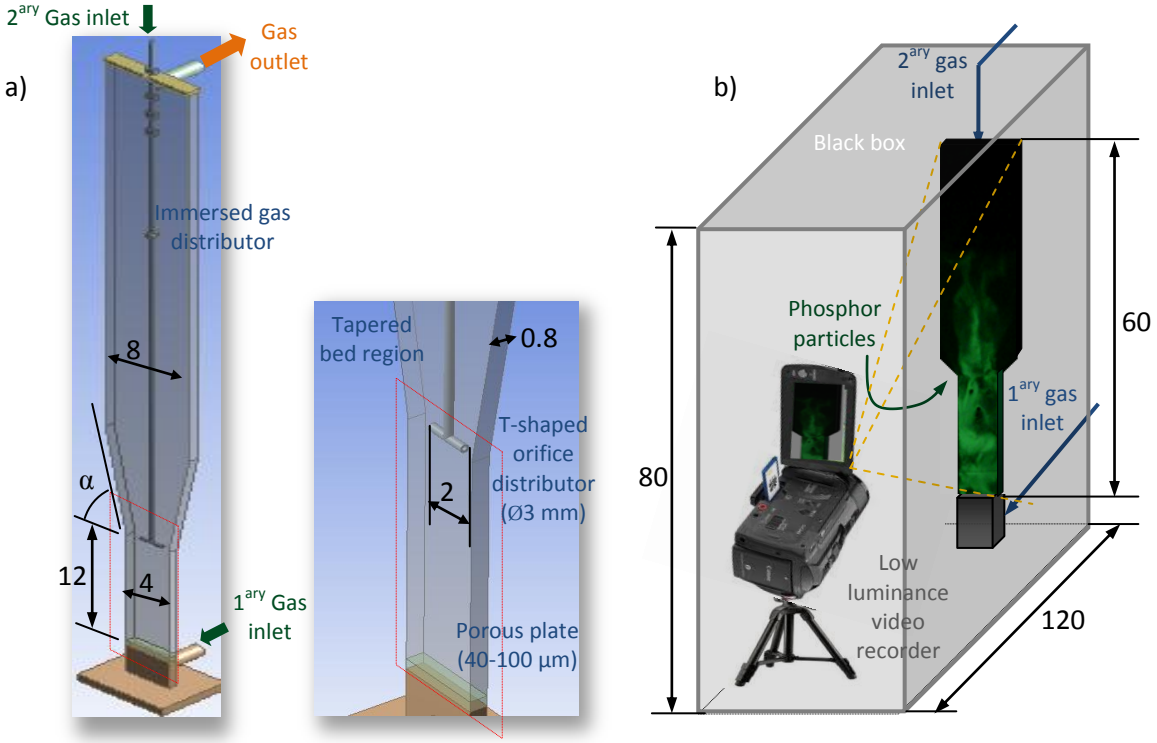
a)
2ary Gas inlet
Gas outlet
Immersed gas distributor
8
α
12
4
1ary Gas inlet
Tapered bed region
0.8
T-shaped orifice distributor (Ø3 mm)
2
Porous plate (40-100 µm)
b)
2ary gas inlet
Black box
Phosphor particles
1ary gas inlet
60
80
Low luminance video recorder
120

Figure 2.

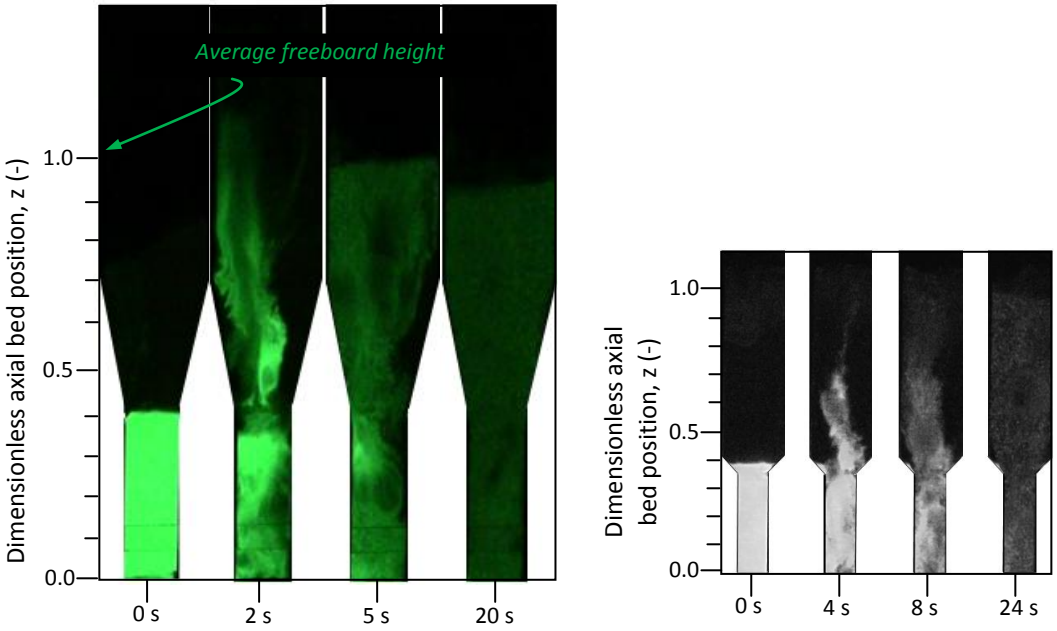
Average freeboard height
Dimensionless axial bed position, z (-)
1.0
0.5
0.0
0 s
2 s
5 s
20 s
Dimensionless axial bed position, z (-)
1.0
0.5
0.0
0 s
4 s
8 s
24 s

Figure 3.

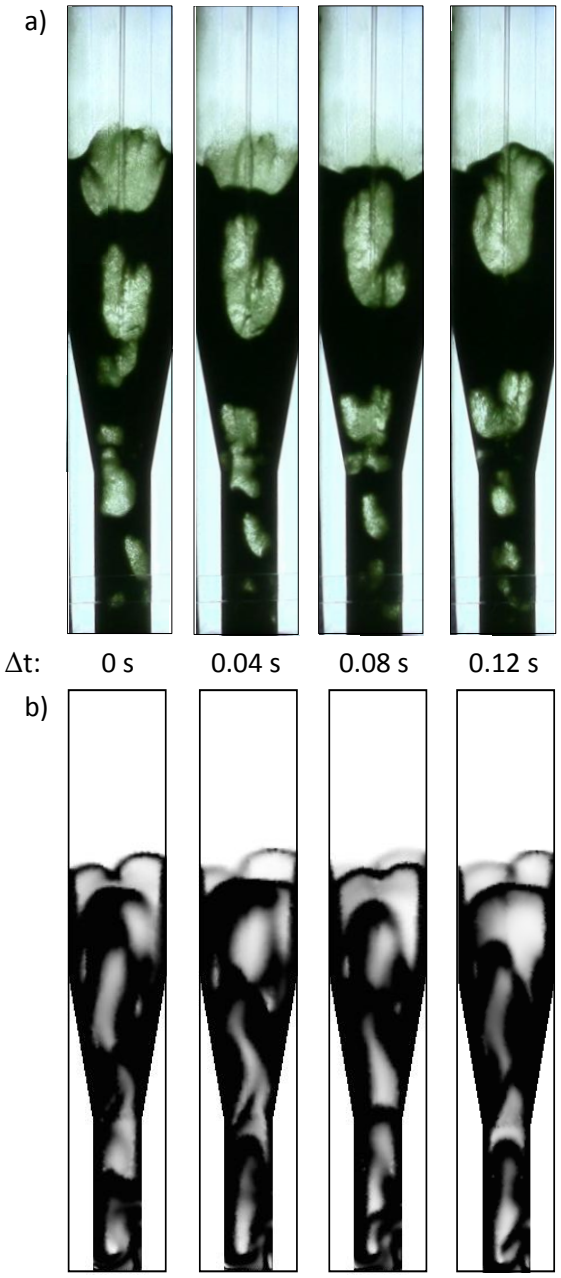

Figure 4.

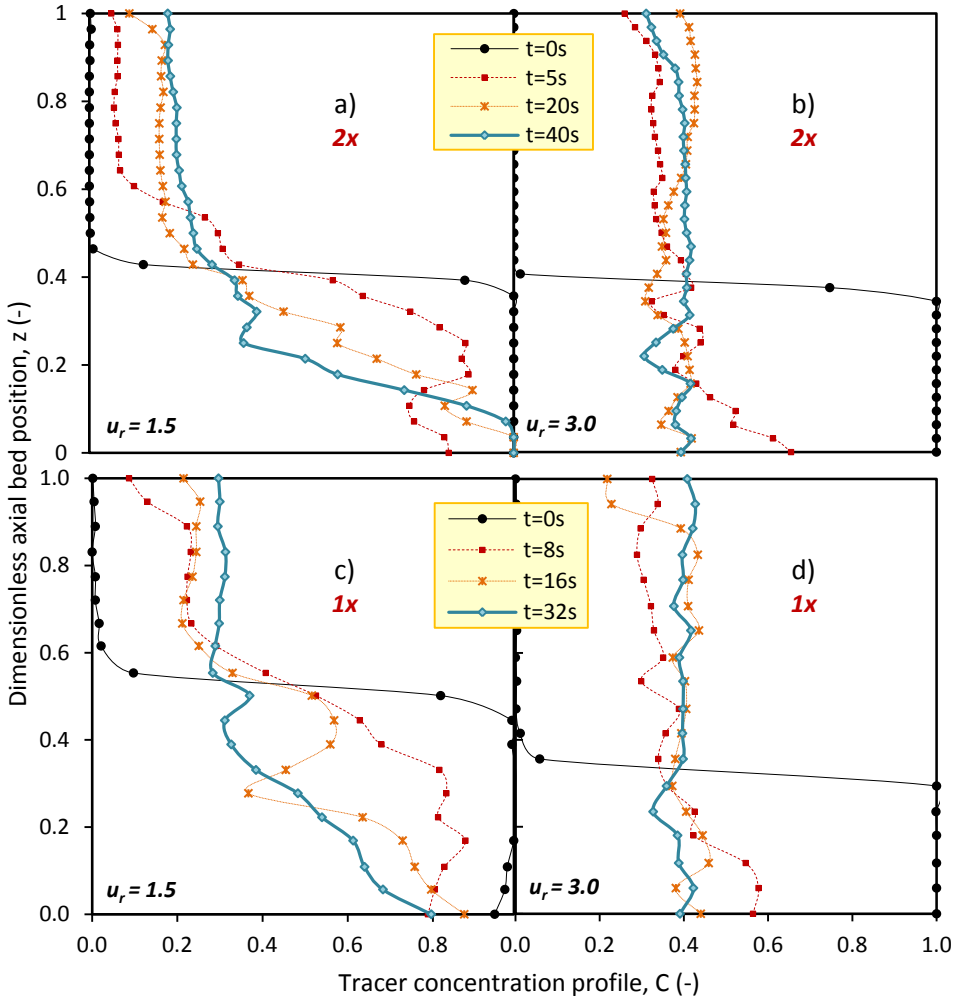
a)
2x
b)
2x
c)
1x
d)
1x
t=0s
t=5s
t=20s
t=40s
t=0s
t=8s
t=16s
t=32s
u_r = 1.5
u_r = 3.0
u_r = 1.5
u_r = 3.0
Dimensionless axial bed position, z (-)
Tracer concentration profile, C (-)
0
0.2
0.4
0.6
0.8
1
0.0
0.2
0.4
0.6
0.8
1.0

Figure 5.

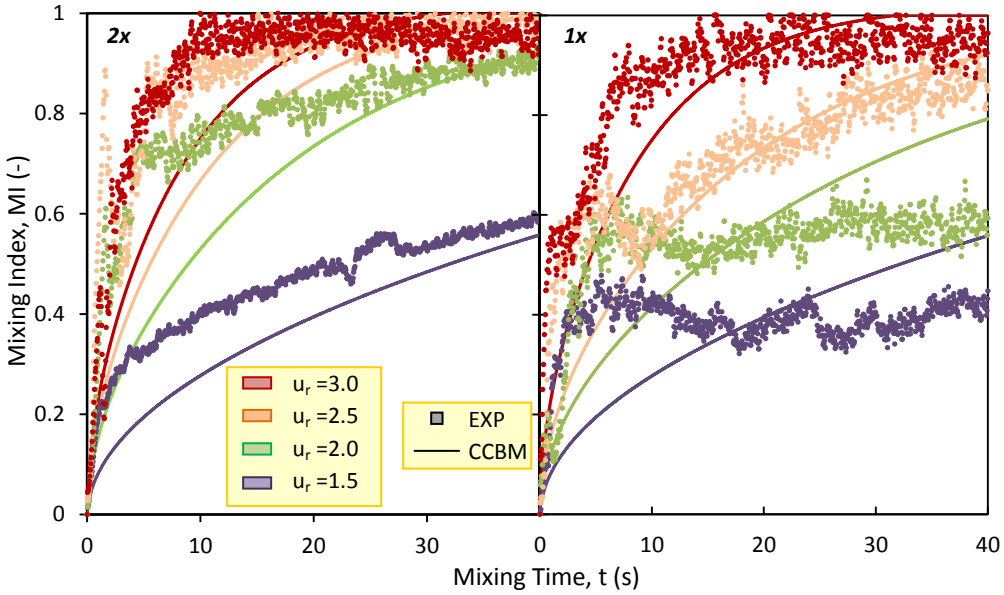
2x
1x
Mixing Index, MI (-)
Mixing Time, t (s)
0
0.2
0.4
0.6
0.8
1
0
10
20
30
40
u_r =3.0
u_r =2.5
u_r =2.0
u_r =1.5
EXP
CCBM

Figure 6.

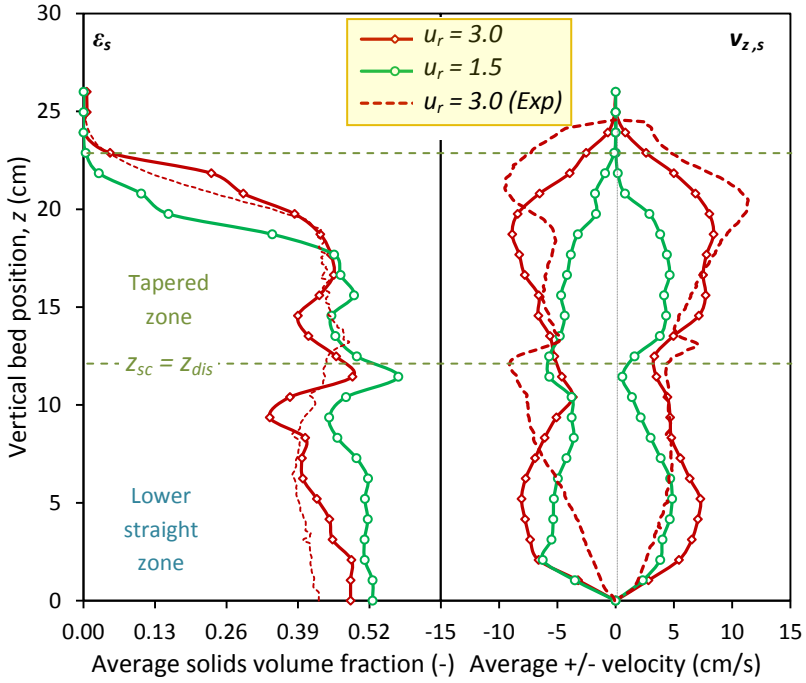
ε_s
$v_{z,s}$
u_r = 3.0
u_r = 1.5
u_r = 3.0 (Exp)
Tapered zone
$z_{sc} = z_{dis}$
Lower straight zone
Vertical bed position, z (cm)
Average solids volume fraction (-)
Average +/- velocity (cm/s)
0
5
10
15
20
25
30
0.00
0.13
0.26
0.39
0.52
-15
-10
-5
0
5
10
15

Figure 7.

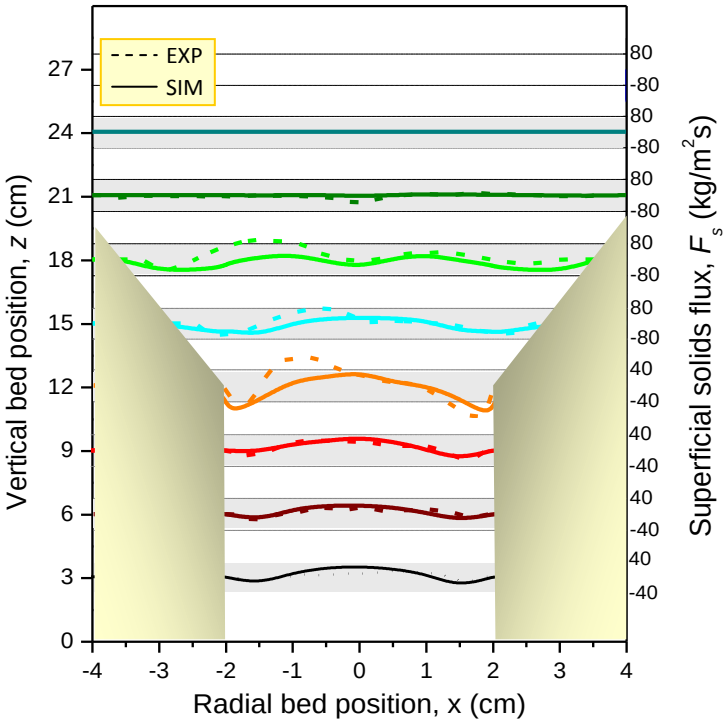
EXP
SIM
Vertical bed position, z (cm)
Radial bed position, x (cm)
Superficial solids flux, F_s (kg/m^{2}s)
0
3
6
9
12
15
18
21
24
27
-4
-3
-2
-1
0
1
2
3
4
80
-80
80
-80
80
-80
80
-80
80
-80
40
-40
40
-40
40
-40
40
-40

Figure 8.

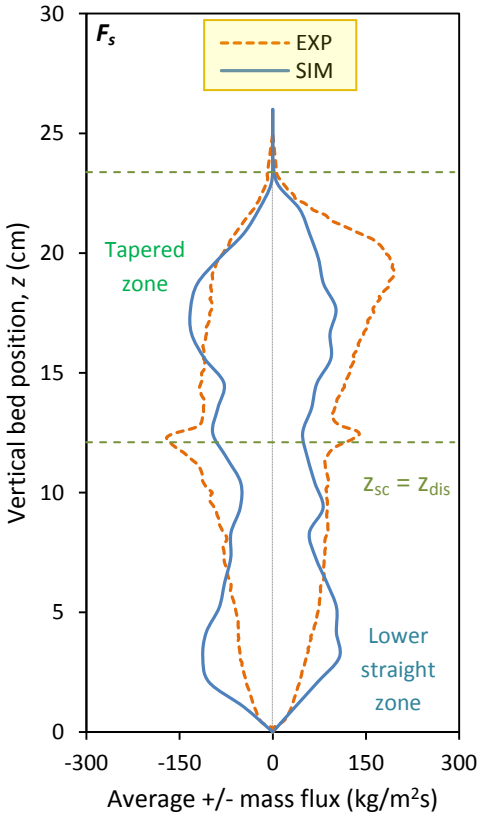
F_s
EXP
SIM
Tapered zone
$z_{sc} = z_{dis}$
Lower straight zone
Vertical bed position, z (cm)
Average +/- mass flux (kg/m²s)
30
25
20
15
10
5
0
-300
-150
0
150
300

Figure 9.

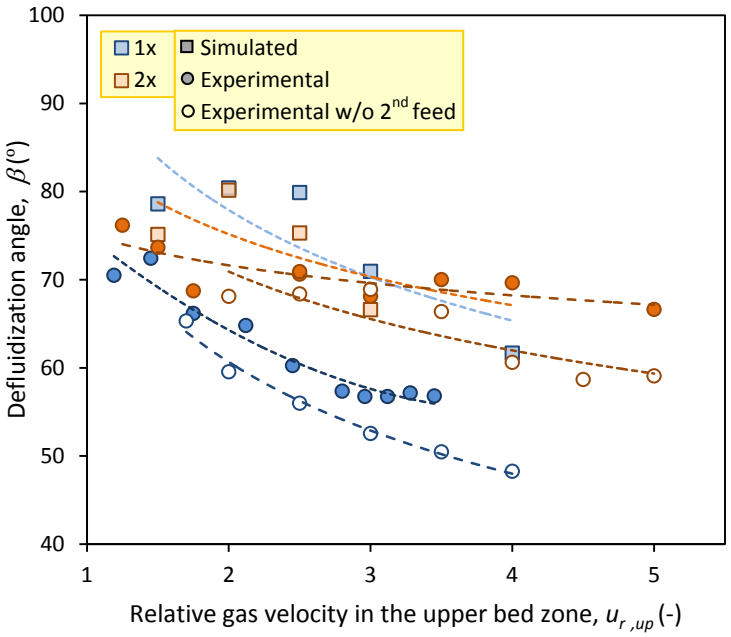
100
90
80
70
60
50
40
1
2
3
4
5
Defluidization angle, β (°)
Relative gas velocity in the upper bed zone, $u_{r,up}$ (-)
1x
2x
Simulated
Experimental
Experimental w/o 2nd feed

Figure 10.

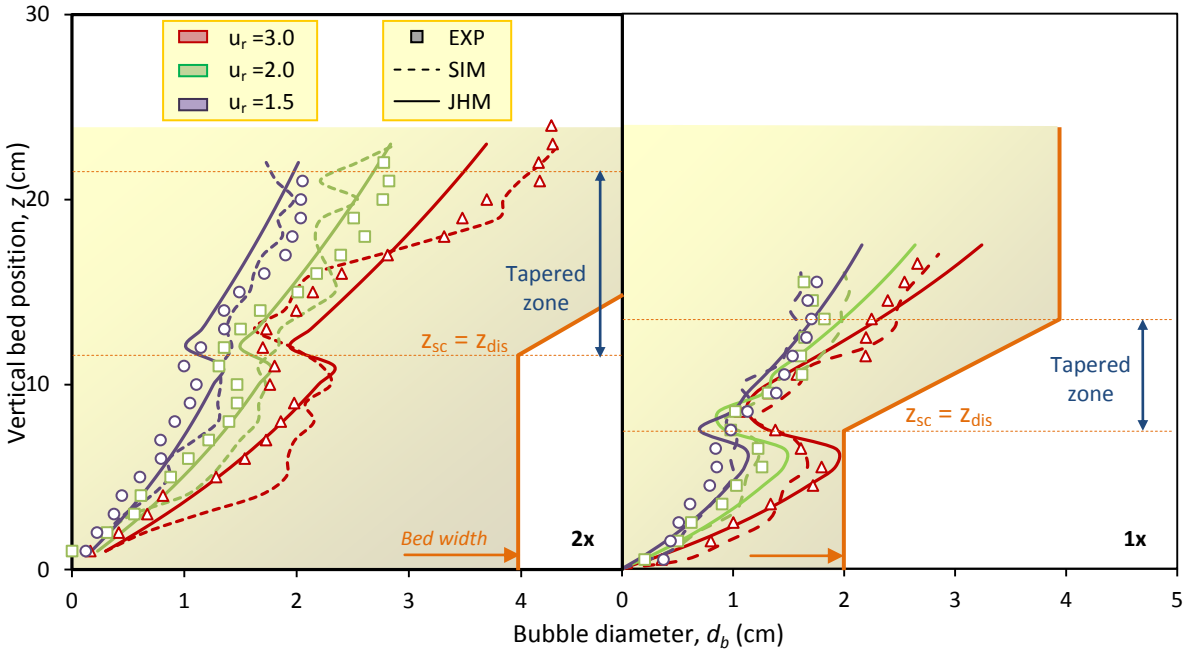
30
20
10
0
Vertical bed position, z (cm)
u_r =3.0
u_r =2.0
u_r =1.5
EXP
SIM
JHM
Tapered zone
Z_sc = Z_dis
Bed width
2x
Tapered zone
Z_sc = Z_dis
1x
0
1
2
3
4
0
1
2
3
4
5
Bubble diameter, d_b (cm)

Figure 11.

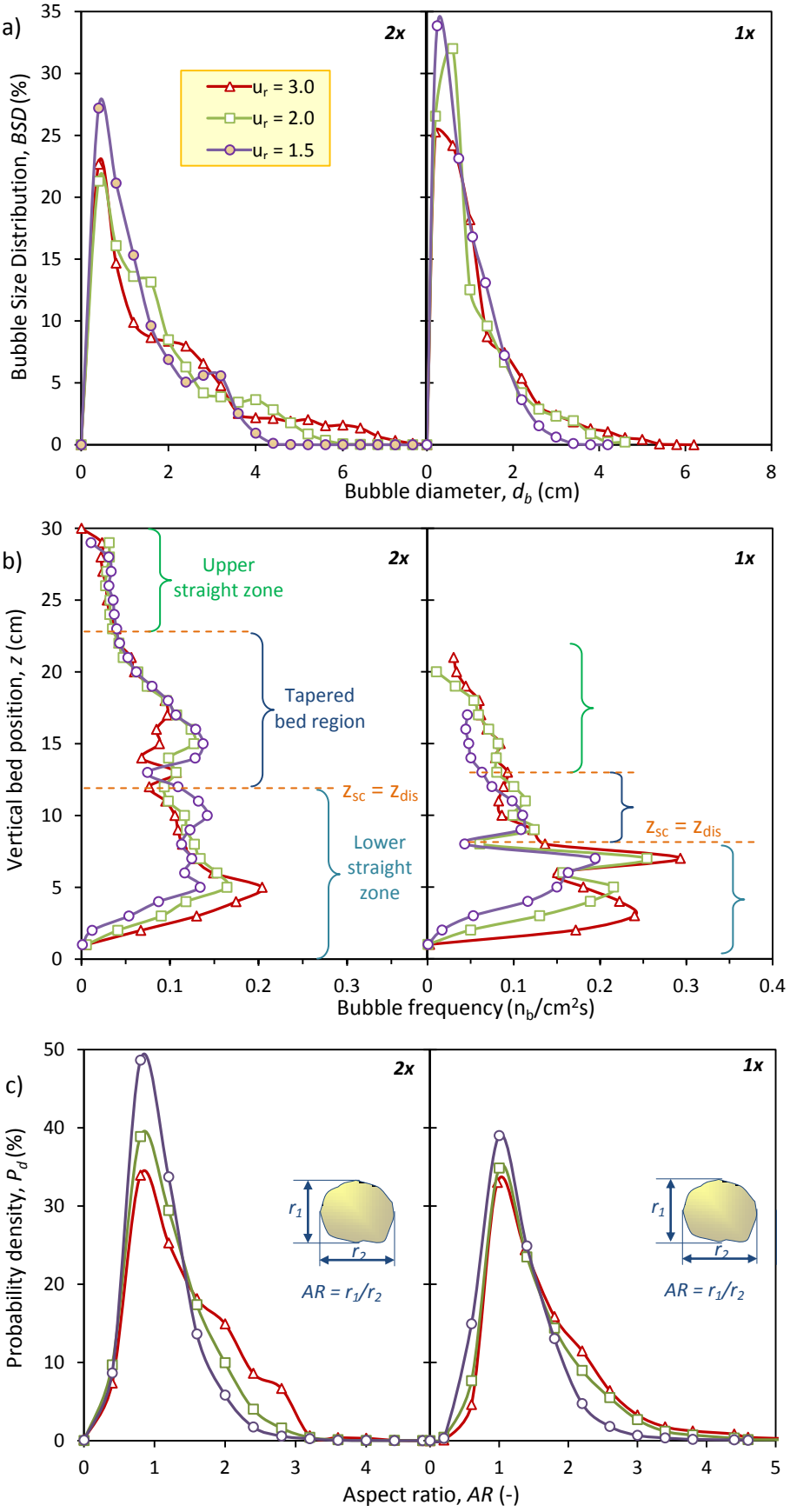
a)
2x
1x
u_r = 3.0
u_r = 2.0
u_r = 1.5
Bubble Size Distribution, BSD (%)
Bubble diameter, d_b (cm)
b)
Upper straight zone
Tapered bed region
$Z_{sc} = Z_{dis}$
Lower straight zone
Vertical bed position, z (cm)
Bubble frequency (n_b/cm^{2}s)
c)
r_1
r_2
$AR = r_1/r_2$
Probability density, P_d (%)
Aspect ratio, AR (-)

Figure 12.

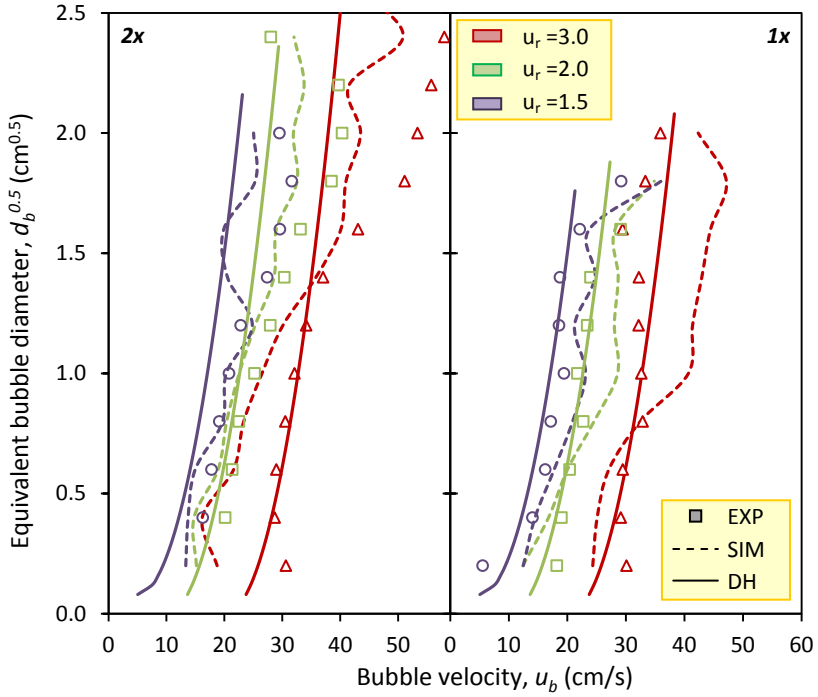
2x
1x
u_r =3.0
u_r =2.0
u_r =1.5
EXP
SIM
DH
Equivalent bubble diameter, $d_b^{0.5}$ (cm$^{0.5}$)
Bubble velocity, u_b (cm/s)
0.0
0.5
1.0
1.5
2.0
2.5
0
10
20
30
40
50
60

Figure 13.

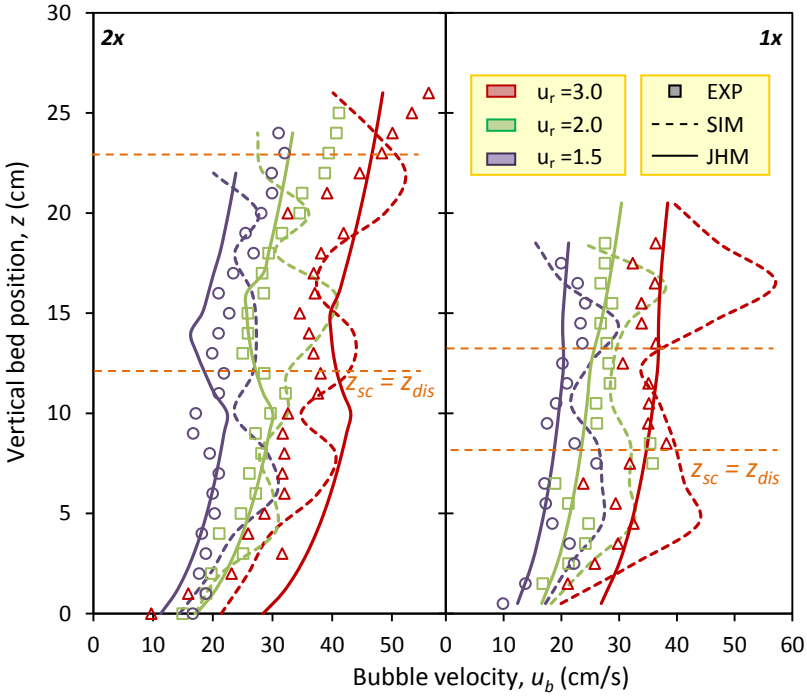
2x
1x
u_r =3.0
u_r =2.0
u_r =1.5
EXP
SIM
JHM
z_sc = z_dis
z_sc = z_dis
Vertical bed position, z (cm)
Bubble velocity, u_b (cm/s)
0
5
10
15
20
25
30
0
10
20
30
40
50
0
10
20
30
40
50
60

Figure 14.

Artículo VII

I. Julián, J. Herguido, M. Menéndez,
Gas permeation effect on the TS-TZFBR+MB fluid dynamics: a CFD simulation study,
Chem. Eng. J. (2015).

Gas permeation effect on the Two-Section Two-Zone Fluidized Bed Membrane Reactor (TS-TZFBMR) fluid dynamics: a CFD simulation study

I. Julián, J. Herguido, M. Menéndez
Catalysis, Molecular Separations and Reactor Engineering Group (CREG), Aragon Institute of Engineering Research (I3A), Universidad de Zaragoza, Mariano Esquillor s/n, 50018 Zaragoza, Spain; tel. +34 876555168, e-mail: ijulian@unizar.es

Abstract

Two-Fluid Model simulations were conducted using the commercial software Ansys CFX and Fluent to study the effect of the gas extraction on the fluid dynamic behaviour of a Membrane-assisted Two-Section Two-Zone Fluidized Bed Reactor (TS-TZFBMR). Simulated bubble properties and bed dynamics were analyzed and compared among different membrane reactor configurations, including reactor-wall (RWM) and immersed tubular (ITM) membranes, for their future use in catalytic reactions, e.g. alkane dehydrogenation or methane steam reforming. According to the solids hold-up distribution at different fluidization regimes and permeation fluxes, the ITM configuration is the most suitable to enhance the gas-particle contact and to favor the solids axial mixing for in-situ catalyst regeneration purposes. However, the RWM configuration provides a greater permeation area for selective gas removal and is preferred to enhance purification. It was found that relative permeation fluxes above 20% of the total fed gas have a significant impact on the fluid dynamic regime within the TS-TZFBMR, concerning the appearance of local defluidized regions, gas channeling and solids axial mixing.

Keywords: Two-Fluid Model, Membrane reactor, Two-Zone Fluidized Bed Reactor, fluid dynamics, gas permeation

1. Introduction

The Two-Zone Fluidized Bed Reactor (TZFBR) represents an effective solution to counteract catalyst deactivation in gas-solid catalytic reactions affected by coking in the presence of light hydrocarbon feedstock [1, 2]. The TZFBR performance has been successfully tested for a number of processes including alkane dehydrogenation, steam reforming and aromatization [3-5] among others. All these processes involve a fast decay of catalytic activity due to catalyst fouling by coke deposition after some minutes on stream. Separated inlets for the gaseous reactants and the oxidizer (or regenerative agent) provide two different atmospheres along the bed. This configuration allows performing simultaneous catalytic reaction and catalyst regeneration in a single unit (Figure 1.a). According to previous studies [3, 6], the following variables may play a role on the process efficiency in a TZFBR: catalyst activity, selectivity and flowability, reaction temperature, fluidization regime, reactant-to-oxidizer ratio, reactive-to-regenerative bed volume ratio, arrangement of gas distributors or residence time, among

others. On this regard, the steady-state operation can only be achieved if the catalytic reaction and regeneration reaction rates as well as the solids axial mixing rate between bed zones are of the same order. For this reason, the understanding of the fluid dynamic behaviour of the reactor becomes essential to improve its design.

Recently, a conical transition section between bed zones with different cross-sectional area was implemented in order to get a better fluid dynamic control within each bed zone separately, resulting in the so-called Two-Section Two-Zone Fluidized Bed Reactor (TS-TZFBR) [5]. This novel configuration added basically three new operational variables to be considered in the reactor design: the tapered section angle, the relative distance between the axial position of secondary gas distributor inlet and the bottom-end of the conical bed section and the relative gas velocity within both reactor zones having different cross-sections. The authors characterized the fluid dynamic performance of the novel TS-TZFBR configuration by means of imaging techniques [7-9] and CFD simulations [10]. As a result, a novel bubble size correlation for the TS-TZFBR was proposed accounting for the effect of these three variables [7]. Additionally, the phenomenological Counter-Current Back-Mixing model (CCBM) [9] and the more detailed Two-Fluid Model (TFM) simulations [10] were validated against experimental tracers mixing and PIV/DIA (Particle Image Velocimetry & Digital Image Analysis) measurements on pseudo-2D TS-TZFBR [6, 8]. The study of this novel reactor fluid dynamics comprised lab scale beds of different sizes without and with several arrangements of internals in their lower zone [8].

A step further in the reactor design is the coupling of perm-selective membranes into the TS-TZFBR to reduce the downstream separation costs and capital costs, while improving the yield and selectivity of the process by overcoming the equilibrium conversion [11].

It is well known that membrane reactors combine the separation properties of membranes with the advantages of fluidized beds and represent a very promising technology in the field of process integration and intensification. Fluidized bed membrane reactors become especially attractive to generate ultra-pure hydrogen from water-gas-shift [12] or methane steam reforming [13-16]. These reactor configurations can also enhance the reactant conversion by H_2 removal as in alkane dehydrogenation [17].

It is obvious that the gas extraction from the catalytic bed shrinks the gas excess over minimum fluidization conditions and, thus, modifies the bubble properties and the overall bed dynamics. Therefore, the purpose of the present work is to study the effect of the membrane reactor configuration and the extent of gas extraction on the Two-Section Two-Zone Fluidized Bed Reactor (TS-TZFBMR) fluid dynamics in order to identify operational limitations and improve the multifunctional reactor design.

The main limitations of the membrane-assisted fluidized bed reactors are identified as the low hydrogen permeation rate through the perm-selective membranes and the eventual poor bubble-to-emulsion mass transfer derived from the gas extraction [14, 18, 19].

The first limitation can be overcome either by increasing the permeation area per reactor volume unit or by decreasing the membrane thickness and thereby increasing the permeability [11]. On the one hand, the reduction of the membrane thickness may compromise its stability

(lifetime) and perm-selectivity. On the other hand, the installation of a greater membrane surface may drastically reduce the space between membranes where the catalyst is suspended eventually leading to the concept of "micro-structured" fluidized bed membrane reactor [20].

The second limitation requires a deeper analysis on the solids hold-up distribution and bubble dynamics as a function of the membrane location, extraction degree and fluidization regime. In a first step towards a proper fluid dynamic design of a TS-TZFBMR, Two-Fluid Model (TFM) CFD simulations were conducted to investigate the effect of the membrane arrangement and permeated gas extent on the reactor dynamics.

Among the available simulation models to predict the complex fluid dynamic behaviour of multiphase flows [21], the Eulerian-Eulerian or Two-Fluid Model is preferred for the simulation of large gas-solid fluidized beds thanks to its reasonable compromise between accuracy and computational cost [22-24]. On this regard, several authors have recently used the Eulerian approach to describe the tapered bed dynamics [25, 26] as well as the hydrodynamic behaviour of fluidized beds with multiple jets [27] or with permselective membranes [28, 29].

However, this is the first time in which the simultaneous effect of multiple gas inlets, local gas extraction and a tapered region was evaluated for predicting the TS-TZFBMR fluid dynamics. As a first approach, the gas permeation was simulated as a fixed outward directed gas flux through the porous membrane walls of the computational domain. Two different membrane reactor arrangements were tested varying the membrane location with respect to the fluidized bed. The first configuration depicts the membrane as an immersed permeable tube located at the bed center within the upper reactor zone (Figure 1.b). In the second, certain region of the lateral reactor walls was set as permeable (Figure 1.c).

The Two-Fluid Model simulations were carried out using two commercial CFD codes: Ansys Fluent 12.1 and Ansys CFX 12.1. Fluent is one of the most inclusive software offered to the CFD community because of its wide range of industrial applications [30] and it is among the most widely employed software to perform gas-solid fluidized bed simulations. CFX was also used by a number of researchers [31, 32] to model the fluidized bed dynamics. Given that every CFD model involves several assumptions and needs to be validated against experimental results [33], the strengths and weaknesses in the predictability of both commercial codes was evaluated. For this purpose the fluid dynamic predictions of the different TFM formulations were compared to the experimental results obtained using Particle Image Velocimetry and Digital Image Analysis techniques [6] in similar reactors.

2. Computational model

2.1 Numerical model

The Eulerian model used to perform the computational simulations considers both solid and gas phase as interpenetrating continua, where the volume of a phase cannot be occupied by others. Therefore, the concept of phase volume fraction is introduced. The model equations (eq. 1 to 3) consider mass and momentum conservation for each phase, *i* (gas or solid).

$$\frac{\partial}{\partial t}(\varepsilon_i \rho_i) + \nabla \cdot (\varepsilon_i \rho_i \, \vec{v}_i) = 0 \quad \text{(E.1)}$$

$$\frac{\partial}{\partial t}\left(\varepsilon_g \rho_g \, \vec{v}_g\right) + \nabla \cdot \left(\varepsilon_g \rho_g \, \vec{v}_g \vec{v}_g\right) = -\varepsilon_g \nabla P + \varepsilon_g \nabla \cdot \bar{\bar{\tau}}_g + \varepsilon_g \rho_g \bar{g} + K_{gs}(\vec{v}_g - \vec{v}_s) \quad \text{(E.2)}$$

$$\frac{\partial}{\partial t}(\varepsilon_s \rho_s \, \vec{v}_s) + \nabla \cdot (\varepsilon_s \rho_s \, \vec{v}_s \vec{v}_s) = -\varepsilon_s \nabla P - \nabla P_s + \varepsilon_s \nabla \cdot \bar{\bar{\tau}}_s + \varepsilon_s \rho_s \bar{g} + K_{gs}(\vec{v}_s - \vec{v}_g) \quad \text{(E.3)}$$

Essentially, both CFD codes employed in this work are suitable to simulate the TS-TZFBR fluid dynamics. Nevertheless, their spatial discretization methods (cell-centered for Fluent, vertex-centered for CFX), the available closure models and fluid dynamic parameters differ. For this reason, the choice of one or another depends on the required degree of detail, computational cost and numerical stability. On the one hand, the libraries of Fluent contain a greater number of models and parameters for the simulation of multiphase flows making this software more versatile. On the other hand, the CFX solver is faster and more stable [34, 35]. The model equations and discretization schemes used for Fluent and CFX are detailed below.

The left hand side of the momentum conservation equation represents the temporal and spatial transport terms. The right hand side represents the various interacting forces: buoyancy, pressure drop, viscous stress, gravity and interphase drag force. K_{gs} is the interphase momentum exchange coefficient whereas $\bar{\bar{\tau}}_i$ is the *i* phase stress-strain tensor.

The solution of this set of partial differential equations requires some closures to describe the interaction between phases. Concretely, the solid-fluid interphase momentum exchange coefficient was modeled with the Gidaspow drag function, that combines the equations of Ergun (equation 4) and Wen and Yu (equation 5) for the interphase drag force, where C_D was estimated using the Schiller-Naumann drag coefficient model (equation 6) and Re_s the particulate Reynolds number (equation 7). The interphase stress-strain tensor for the phase *i* (either gas or solid) was assumed to follow the Newtonian strain-rate relation, which depends on the bulk and shear viscosities (equation 8). Both the bulk (equation 9) and shear (equation 10) viscosities depend on the granular temperature (θ) and a collisional restitution coefficient (*e*). In this study, the restitution coefficient was set to *e* = 0.95. The angle of internal friction, φ, was set to 30º and the radial distribution function, g_0, (which measures the average distance between particles) was modeled according to the description of Lun and Savage [36]. To model the shear viscosity, Fluent uses the model of Gidaspow [37] to estimate the collisional (equation 11) and kinetic (equation 12) contributions plus the model of Schaefer [38] for the frictional viscosity (equation 13). However, Ansys CFX omits the frictional and kinetic contributions, thus calculating μ_s as the collisional viscosity given by the correlation of Gidaspow [37].

The granular temperature was determined algebraically under the assumption of local equilibrium in a transport equation model, i.e. energy production equals energy dissipation. This assumption is often used in dense, slow moving fluidized beds where the local generation and dissipation of granular temperature far outweigh the transport by convection and diffusion [39]. Lastly, the solids pressure was modeled according to the kinetic theory model of gases, being adapted to consider the inelastic collisions between particles (equation 14). The maximum solid packing, $\varepsilon_{s,m}$, was set to 0.65. A monodisperse 200 μm particle size distribution,

which agrees with the particle size used in the experimental works, was used in the simulations throughout the study. The model parameters are listed in Table 1.

$$\varepsilon_g \leq 0.8 \;\rightarrow\; K_{gs} = 150\frac{\varepsilon_s(1-\varepsilon_g)\mu_g}{\varepsilon_g {d_p}^2} + 1.75\frac{\varepsilon_s\rho_g|\vec{v}_s-\vec{v}_g|}{d_p} \tag{E.4}$$

$$\varepsilon_g > 0.8 \;\rightarrow\; K_{gs} = \frac{3}{4}C_D\frac{\varepsilon_s\rho_g|\vec{v}_s-\vec{v}_g|}{d_p}{\varepsilon_g}^{-1.65} \tag{E.5}$$

$$C_D = \begin{cases} \frac{24}{\varepsilon_g Re_s}\left[1+0.15(\varepsilon_g Re_s)^{0.687}\right] & Re_s \leq 1000 \\ 0.44 & Re_s > 1000 \end{cases} \tag{E.6}$$

$$Re_s = \frac{d_p\rho_g|\vec{v}_s-\vec{v}_g|}{\mu_g} \tag{E.7}$$

$$\bar{\bar{\tau}}_i = \varepsilon_i\mu_i\left(\nabla\vec{v_i}+\nabla\vec{v_i}^T\right)+\varepsilon_i\left(\lambda_i-\frac{2}{3}\mu_i\right)\nabla\cdot\vec{v_i}\bar{\bar{I}} \tag{E.8}$$

$$\lambda_s = \frac{4}{3}{\varepsilon_s}^2\rho_s d_p g_0(1+e)\left(\frac{\theta}{\pi}\right)^{1/2} \tag{E.9}$$

$$\mu_s = \mu_{s,col} + \mu_{s,fr} + \mu_{s,kin} \tag{E.10}$$

$$\mu_{s,col} = \frac{4}{5}{\varepsilon_s}^2\rho_s d_p g_0(1+e)\left(\frac{\theta}{\pi}\right)^{1/2} \tag{E.11}$$

$$\mu_{s,kin} = \frac{5\rho_s d_p\sqrt{\theta\pi}}{48 g_0(1+e)}\left[1+\frac{4}{5}g_0\varepsilon_s(1+e)\right]^2 \tag{E.12}$$

$$\mu_{s,fr} = \frac{P_s\,\sin\varphi}{2\sqrt{I_{2D}}} \tag{E.13}$$

$$P_s = \varepsilon_s\rho_s\theta\left(1+2\,\varepsilon_s g_0(1+e)\right) \tag{E.14}$$

The set of governing equations was solved using a finite volume method for the different TS-TZFBR geometries depicted in Figure 1, dividing the computational domain into control volumes. The pressure and velocity fields of the momentum equation were solved iteratively via a SIMPLE (*Semi Implicit Method for Pressure Linked Equations*) scheme. The convergence criterion was based on the residual error in the mass and momentum equations, which was set to 10^{-3}.

The numerical discretization of the model equations followed a first-order upwind scheme for the phase volumetric fractions and second-order upwind scheme for pressure and velocity fields. In Fluent, the cell-based spatial gradients were computed by the least-squares method. The discretization of the transient terms followed a first-order backward Euler (for improved numerical stability) in CFX, being second-order (for improved accuracy) in Fluent. An adaptive

time step (10^{-4} – $2 \cdot 10^{-4}$ seconds) was used to achieve a faster convergence in Ansys CFX whereas a constant time step of 10^{-4} seconds was employed in Fluent simulations.

2.2 Computational domain

The TFM simulations were conducted in two different pseudo-2D membrane-assisted TS-TZFBR configurations. Membranes for gas extraction were located either surrounding the immersed gas distributor tube (Figure 1.b) or at the lateral reactor walls (Figure 1.c). The simulated reactor domain mimicked half of the depth-wise experimental bed geometry. The total dimensions of the computational domain were: 30 x 4 x 0.4 (height x width x depth, in cm). The tapered angle that connects the TS-TZFBR straight bed zones was α = 60º, with respect to the horizontal axis. The width of the lower bed zone was 2 cm and its height was 8 cm. The immersed T-shaped gas distributor orifices ($ø_{orif}$ = 0.3 cm) were axially located at the bottom-end of the tapered bed region. Air was used as fluidization gas and the dense phase was described as a monodisperse distribution of spherical particles (d_p = 200 μm, ρ_{bulk} = 2.5 g/cm^3, $\varepsilon_{s,max}$ = 0.65, u_{mf} = 10.1 cm/s). Both simulated membranes were 6 centimeters high and their bottom-end was located at the upper straight bed zone, 2 centimeters above the tapered bed region. The reactor dimensions, detailed in Figure 1.a, mimic these used in previous experimental studies [6, 7, 9]. Mesh independence studies were conducted to find suitable conditions in terms of computational cost, numerical stability and reproducibility of hydrodynamic results. On this regard, the computational domain was finally discretized by more than 32000 hexahedra defining a structured mesh with an edge length in the range 0.10 – 0.12 cm (5 to 6 times the fluidized particle size).

2.3 Initial and boundary conditions

All simulations start off from a fixed bed with homogeneous solids volume fraction, being the same as the maximum bed packing measured experimentally.

A ‘bulk mass flow rate’ boundary condition was selected for the reactor gas inlets to avoid dense phase outflow. An ‘opening’ boundary was applied to the reactor outlet at the top of the domain. The opening condition refers to the unrestricted circulation of gas and dense phase (if it eventually reaches the top of the bed) through the boundary. The flow direction through inlets and outlets was defined as normal to the boundary surface.

At the reactor walls (front, rear and lateral bed walls, as well as the immersed T-shaped distributor wall) a fluid-dependant boundary was applied. The used no-slip condition for the gas phase is widely accepted and generally proposed. However, the proper selection of the particle-wall boundary condition is not so straightforward for Euler-Euler models and different formulations can be found in the open literature: no-slip [40], partial-slip [41-43] and free-slip [44, 45]. Although it seems that the partial-slip is the most realistic approach, the selection of an appropriated specularity coefficient is not trivial and needs to be done with care. Since the detailed analysis of the wall-particle friction is out of the scope of this work, a free-slip boundary condition was applied for the dense phase as a first approach.

Finally, a reverse 'bulk mass flow rate' boundary condition was applied to the simulated membranes. For simplicity the permeation rate was here described as the gas flow through the membranes, which represents a certain volumetric fraction of the total outlet gas flow.

2.4 Simulation case studies

Ten different operational conditions combining two inlet gas velocities (u_r = 1.5 and u_r = 2.5), two membrane configurations (ITM and RWM) and three permeation rates (0%, 20% and 50% with respect to the total inlet gas flow) have been tested to analyze the effect of gas permeation on the hydrodynamic performance of a TS-TZFBMR.

The selected relative gas velocities are in the range of the optimal u_r values obtained for alkane dehydrogenation in similar membrane-assisted TS-TZFBR facilities [3, 46]. On this regard, the simulated tapered angle was kept constant throughout the study (α = 60º) to mimic the reactor geometry used in these experimental studies.

On the contrary, the tested permeation rates are quite higher than these measured experimentally for H_2 removal through Pd-based membranes (~ 5%). The purposes of testing one order of magnitude greater permeation rates are: a) to enhance and make clear the effect (if any) of the gas removal on the TS-TZFBMR fluidization regime; b) to establish upper permeation limits for the applicability of previous hydrodynamic findings on membrane-assisted TS-TZFBR, e.g. the use of the JHM model for predicting the bubble size evolution (7).

3. Results

This section illustrates the main findings regarding the effect of the membrane-reactor arrangement, either ITM or RWM, and the permeation flux on the simulated TS-TZFBMR fluid dynamics. Bubble properties such as size and velocity profiles, radial distribution and aspect ratio will be analyzed and discussed. Analogously, transient average solids hold-up and axial velocity profiles will be compared in order to identify fluid dynamic limitations within the TS-TZFBMR. As a previous point, the ability of the commercial software CFX and Fluent to predict the experimental bubble characteristics and solids motion in a pseudo-2D TS-TZFBR without gas extraction will be tested.

3.1 Predictability of the experimental TS-TZFBR fluid dynamic behaviour

The simulated TS-TZFBR fluid dynamic results obtained by the commercial codes at several fluidization gas velocities were compared with the experimental PIV/DIA measurements from the authors in a previous study [6].

In Figure 2 the main experimental and simulated bubble characteristics obtained at relative gas velocities u_r = 1.5 and 2.5 are displayed. Figure 2.a illustrates the axial evolution of the equivalent bubble diameter whereas Figure 2.b shows the bubble size distribution at each regime. Both CFX and Fluent simulation results correspond to average bubble data over 8 seconds on stream while the experimental values were averaged out of 40 seconds on stream. Following the recommendations of some authors [23, 47-51], a solids volume fraction ε_s = 0.15 was used as a threshold value to identify bubble boundaries.

Although the variety of model closures and discretization schemes available in CFX is lower than in Fluent, the more unconstrained (and faster) TFM formulation used in CFX resulted in similar accuracy than that showed by Fluent to predict the experimental bubble characteristics. Concretely, the average relative error in the prediction of the experimental d_b along the bed height was: 8.8% and 11.2% for CFX and 4.8% and 8.7% for Fluent at u_r = 1.5 and 2.5, respectively. Due to the low discrepancies between the predictions of CFX and Fluent and the lower computational cost of the CFX code, CFX was selected to perform the statistical analysis on the simulated bubble hydrodynamics in a membrane-assisted TS-TZFBR, i.e. the TS-TZFBMR.

The model predictions of the experimental solids hold-up distribution and local solids motion are shown in Figure 3.a shows the axial evolution of the experimental and simulated solids volume fraction at two gas velocities. Figure 3.b illustrates the time-averaged solids velocity in the upward and downward directions along the vertical position in the bed measured at u_r = 2.5. In general, it is observed that CFX overestimates the experimental bed packing and, thus, predicts a lower fluidized bed height. On the contrary, Fluent underestimates the experimental solids hold-up along the bed at the different fluidization regimes, although it predicts both the total bed height and the axial evolution of the solids volume fraction qualitatively at the two gas velocities. The experimental solids motion depicts quasi-symmetric time-averaged upward and downward velocity profiles at u_r = 2.5. The axial solids velocity increases along the vertical axis within the straight bed zones whereas it decreases within the tapered bed region, following the same trend as that observed for the average bubble size depicted in Figure 2.a. Fluent is able to predict the axial solids velocity profile along the whole bed while CFX clearly overestimates the upward and downward particle velocities (given in absolute values) within the upper bed zone, i.e. z = 10 – 15 cm. This suggests that the more relaxed constraints used in the CFX model formulation with respect to these used in Fluent lead to a poor estimation of the solids motion and hold-up distribution in a TS-TZFBR. For this reason, Fluent was selected as the simulation tool to evaluate the detailed bed fluid dynamics in a TS-TZFBMR.

3.2 TS-TZFBMR Bubble properties

The measurement of the axial evolution of the equivalent bubble diameter, $d_b(z)$, allows quantifying the average bubble size decrease as a function of the permeation rate and membrane location. Figure 4.a shows that, under the same relative fluidization gas velocity (u_r = 2.5), the RWM configuration leads to a sharper bubble size shrinkage along the permeable region in comparison to that for an ITM bed. This trend has been observed regardless the inlet gas velocity and the degree of gas extraction (Figures 4.b and 4.c). Even for the limiting case, in which the mean gas velocity in the upper bed region over the membrane is below the minimum fluidization velocity (u_r = 1.5 and 50% of the total gas permeated), small bubbles are still detected in the ITM configuration whereas no bubbles are measured in the RWM simulated bed.

The bubble size probability distribution measured for the TS-TZFBR and the membrane-assisted ITM and RWM configurations at u_r = 2.5 and 20% extraction (Figure 5.a) illustrates that the use of a RWM arrangement leads to a substantial bubble size shrinkage with respect to the ITM configuration under the same gas flow conditions. However, the classical bubble velocity

correlation developed by Davidson and Harrison for straight fluidized beds gives a quite accurate prediction of the u_b evolution as a function of the bubble size within the TS-TZFBMR regardless the membrane configuration. Figure 5.b suggests that the multiple gas inlets, unconventional geometry and selective gas removal do not have a relevant impact on the $u_b(d_b^{0.5})$ function linearity. As a result, the membrane configuration that leads to the smallest bubbles leads analogously to the lowest solids axial mixing rates.

The discrepancy between the bubble size distribution profiles for ITM and RWM membrane-reactor configurations operating at same conditions motivated the study of further bubble properties such their radial distribution along the region of interest, i.e. the bed section affected by the membrane. The Figure 6 depicts the radial distribution of bubble centroids within different bed regions for TS-TZFBR and TS-TZFBMR (20% extraction) at u_r = 2.5. Figures 6.a to 6.c analyze the radial distribution within the bed region affected by the IT and RW membranes whereas Figures 6.d to 6.f illustrate the effect of the membrane configuration on the distribution of bubble centroids within the lower straight bed zone.

The tri-modal distribution of bubble centroids found in the upper bed region (Figures 6.a to 6.c) is caused by the three bubble sources acting at that height: the bubbles coming from the two orifices of the immersed gas distributor and those coming from the bottom distributor. In the case without gas extraction, the bubbles flow up basically through the bed center with a marginal radial dispersion related to the bubbles coming from the immersed distributor. The use of an ITM broadens the distribution of bubble centroids in the vicinity of the bed center and reduces the relative probability of the central peak against the side peaks. In case of lateral extraction (RWM), bubbles tend to flow towards the wall-membranes thus increasing the radial dispersion. As a result, the probability of finding bubbles within the bed annulus becomes greater than that of finding them along the bed core.

It has been found that the effect of the membrane arrangement and gas extraction on the bubble radial distribution within the lower bed zone (Figures 6.d. to 6.f) is almost negligible. Nevertheless, it can be observed that the central location of the gas extraction in the ITM arrangement tends to promote an enhanced flow of bubbles through the bed center in that bed region in comparison to that for the TS-TZFBR or RWM.

3.3 TS-TZFBMR solids hold-up and velocity distribution maps

For the considered membrane-assisted TS-TZFBR configurations, i.e. ITM and RWM, the time-averaged (Δt = 8 s) dense phase porosity and axial velocity maps have been obtained using Fluent software. The purpose is to study the spatial solids hold-up, the dense phase dynamics and the porosity and velocity fluctuation along the time on stream in order to detect operational problems such as channeling or defluidization, as a function of the fluidization regime and extent of gas permeated.

Figure 7 shows the solids-hold up distribution for different gas extraction rates (0%, 20% and 50%) and membrane configurations (ITM and RWM) at a fluidization regime u_r = 2.5. The gas extraction induces for the RWM configuration a greater radial porosity gradient between the lateral walls and the bed center, leading to a lower bed expansion (greater packing) and an

enhanced preferential path for the axial solids circulation through the bed center with respect to the ITM configuration. This finding, together with the previous results on the bubbling fluidization, confirms that the solid mixing is favored in the ITM membrane arrangement.

Although the RWM configuration allows greater permeation areas and, thus, enhanced extraction flow rates, this membrane arrangement would compromise the TS-TZFBMR mass and heat transfer requirements for the process integration. It has been shown that the RWM configuration worsens both the gas-solid contact (i.e. the catalytic conversion, when operating under reaction conditions) and the axial mixing (i.e. the in-situ catalyst regeneration, when operating under reaction conditions), while enhancing mass transfer limitations for the gas permeation as a result of the densely packed regions arose close to the reactor walls.

The analysis of the transient fluctuation of the bed properties, viz. local porosity and solids velocity, allowed the study of the defluidization or formation of dead-zones within the TS-TZFBMR tapered bed region. In this study the bed regions in which the time-averaged solids volume fraction (Figure 8.a) is greater than 0.62 and the axial velocity (Figure 8.c) is lower than 0.5 cm/s, being the porosity (Figure 8.b) and velocity fluctuation (Figure 8.d) lower than 0.05 and 0.03 cm/s respectively, are considered as banked or defluidized zones. Figure 8.e illustrates the defluidized zones detected on both sides of the tapered bed region for an ITM (20%) configuration at u_r = 2.5 as a convolution of the four previous restrictions. The so-called defluidization angle, β, indicates the slope of the defluidized region boundaries with respect to the horizontal position as it is shown in Figure 8.e.

In previous studies [6, 7, 9, 10], a conservative tapered section angle α = 80º was found as a suitable reactor wall inclination angle to avoid defluidization phenomena within a TS-TZFBR under every fluidization condition. However, the use of in-situ perm-selective membranes for gas removal (TS-TZFBMR) enhances defluidization and such conservative α value may be eventually exceeded at low fluidization regimes and high permeation rates, as it can be observed in Table 2.

4. Conclusions

Two commercial CFD codes, Fluent and CFX, were employed to simulate the effect of gas extraction and membrane arrangement on the TS-TZFBMR fluid dynamics. Fluent provided a substantially better prediction of the experimental solids motion and hold-up distribution. However, both codes were suitable to reproduce the experimental average bubble size profile qualitatively ($\sim$ 10% error in the worst scenario). According to the simulation results, the membrane arrangement does have an impact on the bubble characteristics: a 20% gas extraction rate reduced the average bubble size (within the bed region affected by the membrane) by 18% in the case of ITM and by 31% for the RWM configuration. The membrane location also affected the solids hold-up distribution: the RWM configuration led to densely packed regions and enhanced defluidization near the bed walls in comparison to that in the ITM arrangement.

Although the RWM configuration provides a greater permeation area for selective gas removal, the ITM arrangement favors the solids axial mixing, which in our case would be useful for process integration purposes. Therefore, a compromise between the permeation flow rates

and the membrane location needs to be reached in order to optimize the reactor performance.

Acknowledgements

Financial support from MINECO, Spain (Projects CTQ2010-15568 and ENE2013-44350-R) is gratefully acknowledged. Financial aid for the maintenance of the consolidated research group CREG has been provided by the Fondo Social Europeo (FSE) through the Gobierno de Aragón (Aragón, Spain).

Nomenclature

C_D	Interphase drag coefficient, (-)
CFD	Computational Fluid Dynamics
d_b	Equivalent bubble diameter, (cm)
d_p	Particle diameter, (m)
DIA	Digital Image Analysis
e	Restitution coefficient, (-)
g	Acceleration due to gravity, (m s^{-2})
g_0	Radial distribution function, (-)
$\bar{\bar{I}}$	Stress tensor, (-)
ITM	Internal tubular membrane
I_{2D}	Second invariant of the deviatory stress tensor, (-)
K	Bubble velocity coefficient, (-)
K_{gs}	Interphase momentum exchange coefficient, (kg $m^{-3}s^{-1}$)
P	Pressure, (Pa)
PIV	Particle Image Velocimetry
Re	Reynolds number, (-)
RWM	Reactor-wall membrane
TS-TZFBR	Two-Section Two Zone Fluidized Bed Reactor
TS-TZFBMR	Two-Section Two Zone Fluidized Bed Membrane Reactor
TZFBR	Two-Zone Fluidized Bed Reactor
u_b	Single bubble velocity, (cm s^{-1})
u_{br}	Bubbles velocity, (cm s^{-1})
u_{gas}	Gas velocity, (cm s^{-1})
u_{mf}	Minimum fluidization velocity, (cm s^{-1})
$u_{r,bottom}$	Relative velocity (u_{gas}/u_{mf}) within the lower bed section, (-)
$u_{r,top}$	Relative velocity (u_{gas}/u_{mf}) within the upper bed section, (-)
$\vec{v}$	Local velocity, (m s^{-1})
z_{dis}	immersed distributor axial location, (cm)
z_{sc}	TS-TZFBR section change axial location, (cm)

Greek symbols

α	Tapered section angle, (^{o})

β	Defluidization angle, (^{o})
γ_s	Collision dissipation energy, (kg m^{-1}s^{-3})
ε	Volume fraction, (-)
θ	Granular temperature, (m^{2}s^{-2})
λ	Bulk viscosity, (kg m^{-1}s^{-1})
μ	Shear viscosity, (kg m^{-1}s^{-1})
μ_{col}	Collisional shear viscosity, (kg m^{-1}s^{-1})
μ_{kin}	Kinematic shear viscosity, (kg m^{-1}s^{-1})
μ_{fr}	Frictional shear viscosity, (kg m^{-1}s^{-1})
ρ	Density, (kg m^{-3})
$\bar{\bar{\tau}}$	Stress-strain tensor, (kg m^{-1}s^{-2})
φ	Angle of internal friction in particle collisions, (^{o})
ω	Probability density of bubble size, (%)

Subscripts

i	Phase i, either fluid or solid
g	Fluid phase (gas)
s	Solid phase
m	maximum
0	initial

References

[1]. J. Herguido, M. Menéndez, J. Santamaría, On the use of fluidized bed catalytic reactors where reduction and oxidation zones are present simultaneously. Catal. Today. 100 (2005) 181-189.

[2] S. Parient, V. Belliere-Baca, S. Paul, N. Fatah, Process for obtaining acrolein by catalytic dehydration of glycerol or glycerin. US Patent: US 20130217909 A1 (2013)

[3]. J.A. Medrano, I. Julián, F. García-García, K. Li, J. Herguido, M. Menéndez, Two-Zone Fluidized Bed Reactor (TZFBR) with palladium membrane for catalytic propane dehydrogenation: experimental performance assessment. Ind. Eng. Chem. Res. 52 (2013) 3723-3731.

[4]. L. Pérez-Moreno, J. Soler, J. Herguido, M. Menéndez, Stable hydrogen production by methane steam reforming in a two-zone fluidized-bed reactor: Effect of the operating variables. Int. J. Hydrogen Energy. 38 (2013) 7830-7838.

[5]. M.P. Gimeno, J. Soler, J. Herguido, M. Menéndez, Counteracting catalyst deactivation in methane aromatization with a Two Zone Fluidized Bed Reactor. Ind. Eng. Chem. Res. 49 (2010) 996-1000.

[6]. I. Julián, F. Gallucci, M. van Sint Annaland, J. Herguido, M. Menéndez, Coupled PIV/DIA for fluid dynamics studies on a Two-Section Two-Zone Fluidized Bed Reactor. Chem. Eng. J. 207-208 (2012) 122-132.

[7]. I. Julián, J. Herguido, M. Menéndez, A non-parametric bubble size correlation for a Two-Section Two-Zone Fluidized Bed Reactor (TS-TZFBR). Powder Technol. 256 (2014) 146-157.

[8]. I. Julián, F. Gallucci, M. van Sint Annaland, J. Herguido, M. Menéndez, Hydrodynamic study of a Two-Section Two-Zone Fluidized Bed Reactor with an immersed tube bank via PIV/DIA. Chem. Eng. Sci. 134 (2015) 238-250.

[9]. I. Julián, J. Herguido, M. Menéndez, Particle mixing in a Two-Section Two-Zone Fluidized Bed Reactor. Experimental technique and Counter-Current Back-Mixing model validation. Ind. Eng. Chem. Res. 52 (2013) 13587-13596.

[10]. I. Julián, J. Herguido, M. Menéndez, CFD model prediction of the Two-Section Two-Zone Fluidized Bed Reactor (TS-TZFBR) hydrodynamics. Chem. Eng. J. 248 (2014) 352-362.

[11]. F. Gallucci, E. Fernandez, P. Corengia, M. van Sint Annaland, Recent advances on membranes and membrane reactors for hydrogen production. Chem. Eng. Sci. 92 (2013) 40-66.

[12]. A. Basile, L.A. Paturzo, F. Gallucci, Co-current and counter-current modes for water gas shift membrane reactor. Catal. Today. 82 (2003) 275-281.

[13]. A. Basile, F. Gallucci, L.A. Paturzo, dense Pd/Ag membrane reactor for methanol steam reforming: Experimental study. Catal. Today. 104 (2005) 244-250.

[14]. L. Tan, I. Roghair, M. van Sint Annaland, Simulation study on the effect of gas permeation on the hydrodynamic characteristics of membrane-assisted micro fluidized beds. Appl. Math. Model. 38 (2014) 4291-4307.

[15]. A. Adris, S. Elnashaie, R.A. Hughes, Fluidized-bed membrane reactor for the steam reforming of methane. Can. J. Chem. Eng. 69 (1991) 1061-1070.

[16]. F. Gallucci, M. van Sint Annaland, J.A.M. Kuipers, Autothermal reforming of methane with integrated CO_2 capture in a novel fluidized bed membrane reactor. Part 1: Experimental Demonstration. Top. Catal. 51 (2008) 133-145.

[17]. R. Dittmeyer, V. Höllein, K. Daub, Membrane reactors for hydrogenation and dehydrogenation processes based on supported palladium. J. Molec. Catal. A-Chem. 173 (2001) 135-184.

[18]. F. Gallucci, M. van Sint Annaland, J.A.M. Kuipers, Theoretical comparison of packed bed and fluidized bed membrane reactors for methane reforming. Int. J. Hydrogen Energy. 35 (2010) 7142-7150.

[19]. A. Mahecha-Botero, Z. Chen, J.R. Grace, S.S.E.H. Elnashaie, C.J. Lim, M. Rakib, I. Yasuda, Y. Shirasaki, Comparison of fluidized bed flow regimes for steam methane reforming in membrane reactors: A simulation study. Chem. Eng. Sci. 64 (2009) 3598-3613.

[20] T.Y.N. Dang, F. Gallucci, M. van Sint Annaland, Microstructured fluidized bed membrane reactors: solids circulation and densified zones distribution, Chem. Eng. J. 239 (2014) 42-52.

[21]. M.A. van der Hoef, M. Ye, M. van Sint Annaland, A.T. Andrews, S. Sundaresan, J.A.M. Kuipers, Multiscale modeling of gas-fluidized beds. Adv. Chem. Eng. 31 (2006) 65-149.

[22]. N. Herzog, M. Schreiber, C. Egbers, H.J. Krautz. A comparative study of different CFD-codes for numerical simulation of gas-solid fluidized bed hydrodynamics. Comput. Chem. Eng. 39 (2012) 41-46.

[23]. A. Busciglio, G. Vella, G. Micale, L. Rizzuti, Analysis of the bubbling behaviour of 2D gas solid fluidized beds Part II. Comparison between experiments and numerical simulations via Digital Image Analysis Technique. Chem. Eng. J. 148 (2009) 145-163.

[24]. V.V. Ranade, Computational flow modelling for Chemical Reactor Engineering. Academic Press, London. 2002.

[25]. D.C. Sau, K.C. Biswal. Computational fluid dynamics and experimental study of the hydrodynamics of a gas–solid tapered fluidized bed. Appl. Math. Model. 35 (2011) 2265-2278.

[26]. W. Duangkhamchan, F. Ronsse, F. Depypere, K. Dewettinck, J.G. Pieters, Comparison and evaluation of interphase momentum exchange models for simulation of the solids volume fraction in tapered fluidised beds. Chem. Eng. Sci. 65 (2010) 3100-3112.

[27]. P. Pei, K. Zhang, J. Ren, D. Wen, G. Wu, CFD simulation of a gas–solid fluidized bed with two vertical jets. Particuology. 8 (2010) 425-432.

[28]. J.A. Medrano, R.J.W. Voncken, I. Roghair, F. Gallucci, M. van Sint Annaland, On the effect of gas pockets surrounding membranes in fluidized bed membrane reactors: An experimental and numerical study. Chem. Eng. J. In press. DOI: 10.1016/j.cej.2015.04.007

[29]. J.F. de Jong, T.Y.N. Dang, M. van Sint Annaland, J.A.M. Kuipers, Comparison of a Discrete Particle Model and a Two-Fluid Model to experiments of a fluidized bed with flat membranes. Powder Technol. 230 (2012) 93-105.

[30]. M.J.H. Khan, M.A. Hussain, Z. Mansourpour, N. Mostoufi, N.M. Ghasem, E.C. Abdullah, CFD simulation of fluidized bed reactors for polyolefin production – A review. J. Ind. Eng. Chem. 20 (2014) 3919-3946.

[31]. P. Lettieri, G. Saccone, L. Cammarata, Predicting the transition from bubbling to slugging fluidization using Computational Fluid Dynamics. Chem. Eng. Res. Design. 82 (2004) 939-944.

[32]. L. Cammarata, P. Lettieri, G.D.M. Micale, D. Colman, 2D and 3D CFD simulations of bubbling fluidized beds using Eulerian-Eulerian models. Int. J. Chem. React. Eng. 1 (2003) A48.

[33]. J.R. Grace, F. Taghipour, Verification and validation of CFD models and dynamic similarity for fluidized beds. Powder Technol. 139 (2004) 99-110.

[34]. W. Jeong, J. Seong, Comparison of effects on technical variances of computational fluid dynamics (CFD) software based on finite element and finite volume methods. Int. J. Mech. Sci. 78 (2014) 19-26.

[35]. G.H. Lee, Y.S. Bang, S.W. Woo, D.H. Kim, M.K. Kang, Comparative study of commercial CFD software performance for prediction of reactor internal flow. Transactions of the KSME, B. 37 (2013) 1175-1183.

[36]. C.K.K. Lun, S.B. Savage, The effects of an impact velocity dependent coefficient of restitution on stresses developed by sheared antigranulocytes-materials. Acta Mech. 63 (1986) 15-44.

[37]. D. Gidaspow, Multiphase flow and fluidization: continuum and Kinetic Theory descriptions. Academic Press, San Diego. 1994.

[38]. D.G. Schaeffer, Instability in the evolution equations describing incompressible granular flow. J. Diff. Eq. 66 (1987) 19-50.

[39]. S. Cloete, A. Zaabout, S.T. Johansen, M. van Sint Annaland, F. Gallucci, S. Amini, The generality of the standard 2D TFM approach in predicting bubbling fluidized bed hydrodynamics. Powder Technol. 235 (2013) 735-46.

[40]. G.N. Ahuja, A.W. Patwardhan, CFD and experimental studies of solids hold-up distribution and circulation patterns in gas–solid fluidized beds. Chem. Eng. J. 143 (2008) 147-160.

[41]. F. Hernández-Jiménez, A. Gómez-García, D. Santana, A. Acosta-Iborra, Gas interchange between bubble and emulsion phases in a 2D fluidized bed as revealed by two-fluid model simulations. Chem. Eng. J. 215–216 (2013) 479-490.

[42]. V. Verma, J.T. Padding, N.G. Deen, J.A.M. Kuipers, Bubble formation at a central orifice in a gas–solid fluidized bed predicted by three-dimensional two-fluid model simulations. Chem. Eng. J. 245 (2014) 217-227.

[43]. S. Cloete, S.T. Johansen, S. Amini, Investigation into the effect of simulating a 3D cylindrical fluidized bed reactor on a 2D plane. Powder Technol. 239 (2013) 21-35.

[44]. A. Bahramian, M. Olazar, G. Ahmadi, Effect of slip boundary conditions on the simulation of microparticle velocity fields in a conical fluidized bed. AIChE J. 59 (2013) 4502-4518.

[45]. T. Li, S. Benyahia, Evaluation of wall boundary condition parameters for gas-solids fluidized bed simulations. AIChE J. 59 (2013) 3624-3632.

[46]. J.A. Medrano, I. Julián, J. Herguido, M. Menéndez, Pd-Ag membrane coupled to a Two-Zone Fluidized Bed Reactor (TZFBR) for propane dehydrogenation on a Pt-Sn/$MgAl_2O_4$ catalyst. Membranes. 3 (2013) 69-86.

[47]. D.J. Patil, M. van Sint Annaland, J.A.M. Kuipers, Critical comparison of hydrodynamic models for gas–solid fluidized beds—Part II: freely bubbling gas–solid fluidized beds. Chem. Eng. Sci. 60 (2005) 73-84.

[48]. T.W. Asegehegn, M. Schreiber, H.J. Krautz, Numerical simulation and experimental validation of bubble behavior in 2D gas-solid fluidized beds with immersed horizontal tubes. Chem. Eng. Sci. 66 (2011) 5410-5427.

[49]. R.P. Utikar, V.V. Ranade, Singlejet fluidized beds: Experiments and CFD simulations with glass and polypropylene particles RID A-5627-2009. Chem. Eng. Sci. 62 (2007) 167-183.

[50]. J.A.M. Kuipers, K.J. van Duin, F.P.H. van Beckum, W.P.M. van Swaaij, Computer-simulation of the hydrodynamics of a 2-Dimensional gas-fluidized bed. Comput. Chem. Eng. 17 (1993) 839-858.

[51]. J.A.M. Kuipers, K.J. van Duin, F.P.H. van Beckum, W.P.M. van Swaaij, A numerical-model of gas-fluidized beds. Chem. Eng. Sci. 47 (1992) 1913-1924.

Table 1. TFM model parameters

Model parameter	Value
Reactor height (cm)	30
Solids density, ρ_s (kg/m^3)	2500
Particle size, d_p (μm)	200
Particles per cell unit, $d_p/cell$ (-)	≤ 6
Maximum bed packing, $\varepsilon_{s,m}$ (-)	0.65
Restitution coefficient, e (-)	0.95
Angle of internal friction, φ (^{o})	30
Gas temperature, T (^{o}C)	25

Table 2. Defluidization angle, β, as a function of gas velocity and membrane configuration

ITM	**u_r = 1.5**	**u_r = 2.5**
0%	74.1 ± 0.4	69.7 ± 0.1
20%	74.4 ± 0.3	73.2 ± 1.2
50%	76.9 ± 0.3	73.6 ± 1.1
RWM	**u_r = 1.5**	**u_r = 2.5**
0%	74.1 ± 0.4	69.7 ± 0.1
20%	81.7 ± 1.0	79.0 ± 2.5
50%	82.6 ± 0.1	81.5 ± 0.4

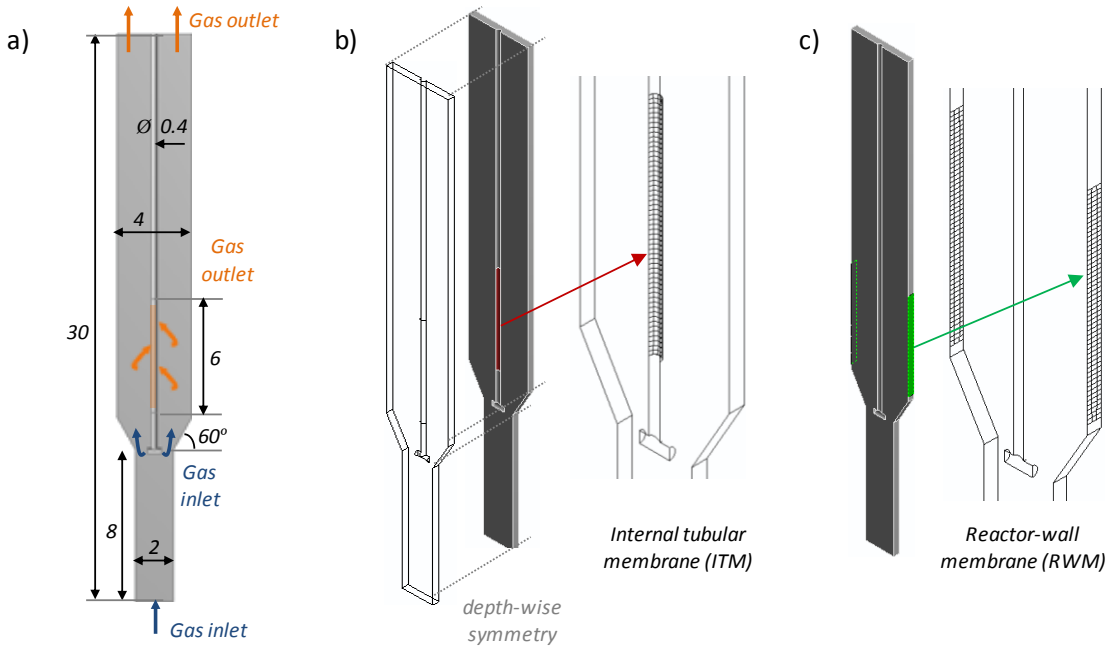

Figure 1. a) TS-TZFBR+M scheme, lengths in cm, b) ITM configuration, c) RWM configuration

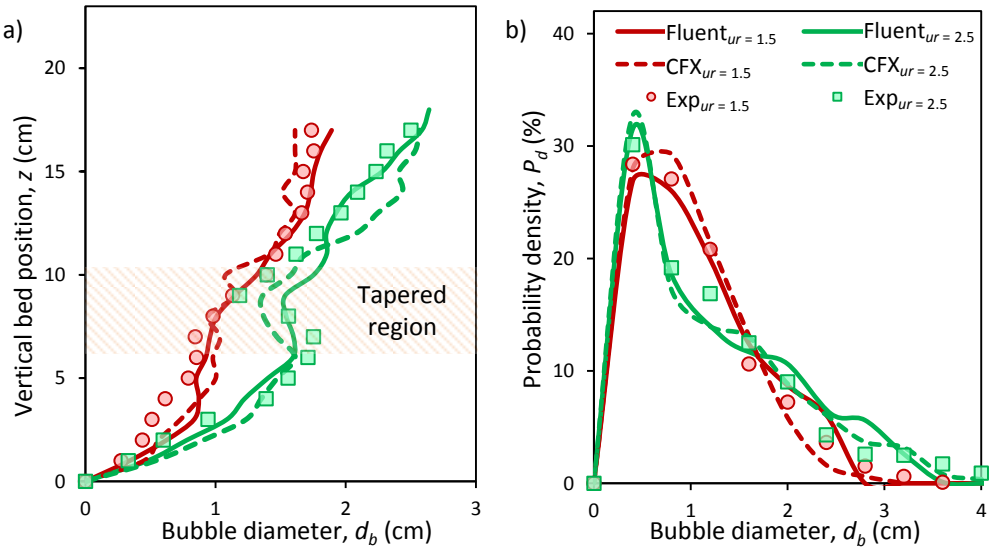

Figure 2. Comparison between experimental [6] and simulated (CFX and Fluent): a) axial equivalent bubble diameter profile, b) Bubble size distribution in a TS-TZFBR without gas extraction at relative gas velocities, u_r = 1.5 and 2.5

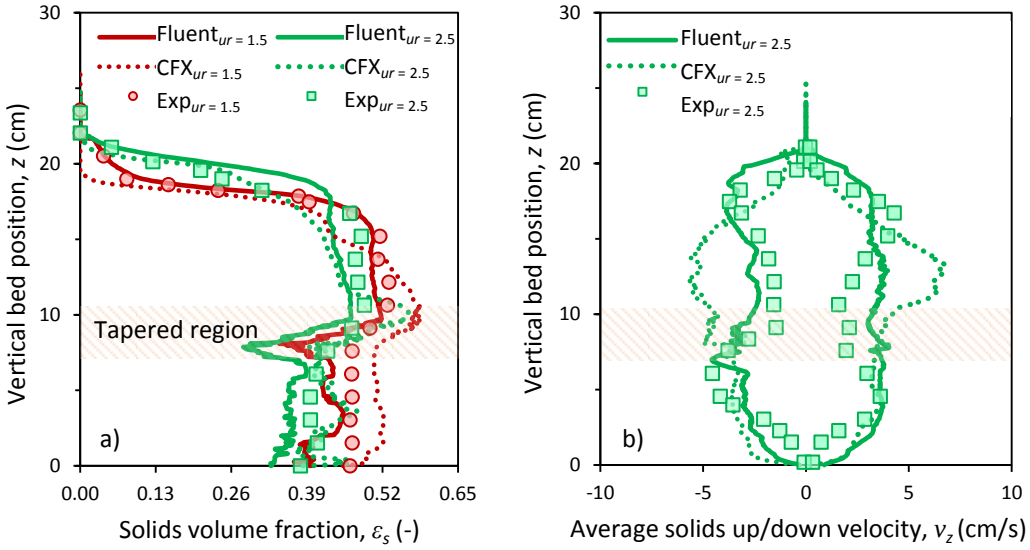

Figure 3. Comparison between experimental [6] and simulated (CFX and Fluent): a) solids hold-up, b) upward and downward solids velocity in a TS-TZFBR without gas extraction at u_r = 1.5 and 2.5

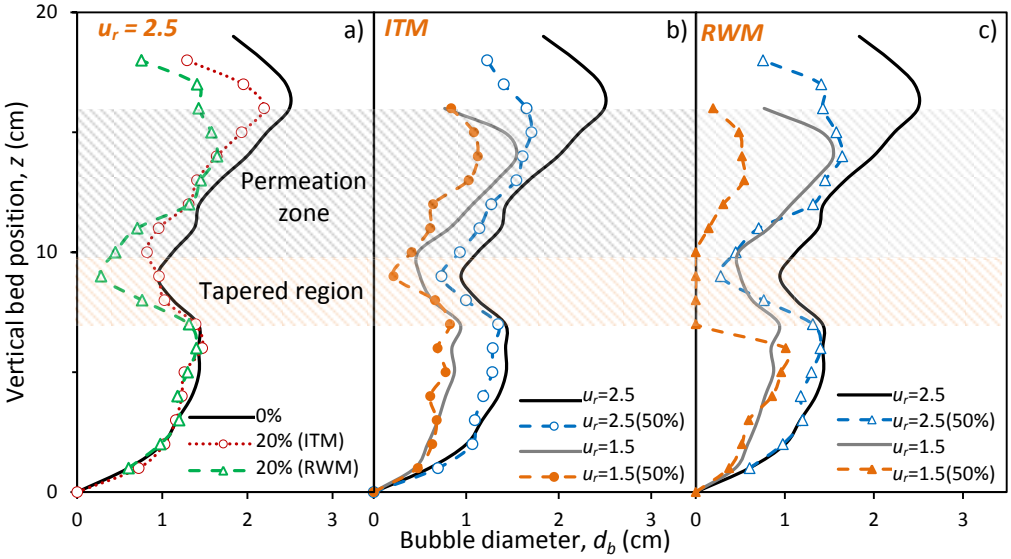

Figure 4. Axial evolution of the average equivalent bubble diameter. Effect of membrane configuration (a), gas velocity and permeation rate for tubular (b) and wall (c) membranes.

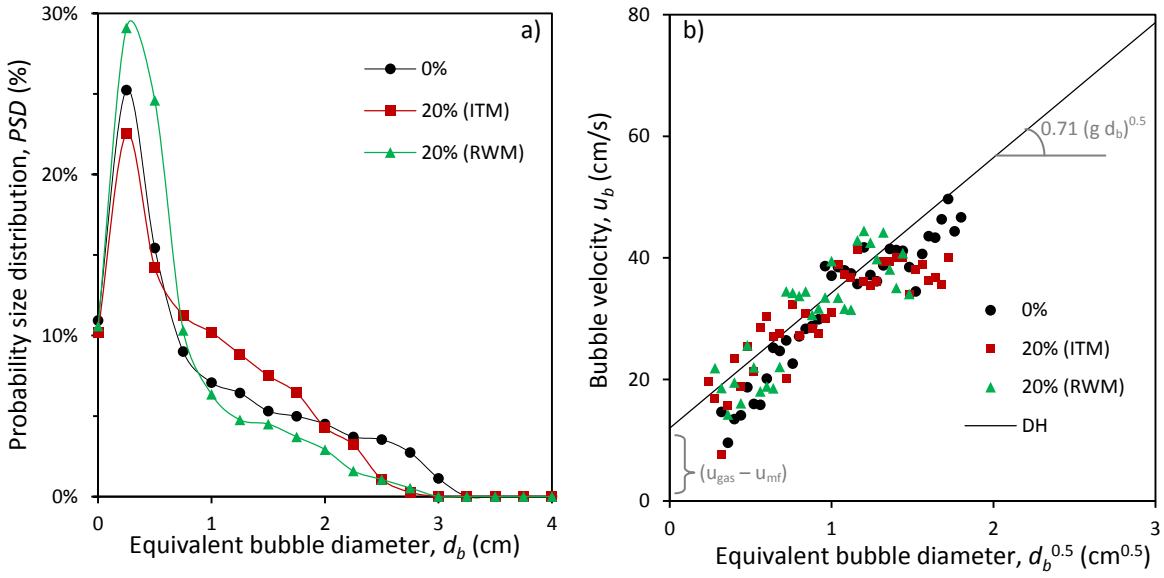

Figure 5. a) Simulated probability size distribution for different membrane-assisted TS-TZFBR configurations with and without gas extraction at u_r = 2.5. b) Time-averaged bubble velocity profiles for TS-TZFBR, TS-TZFBMR (ITM) and TS-TZFBMR (RWM) against the Davidson-Harrison $u_b(d_b^{0.5})$ correlation

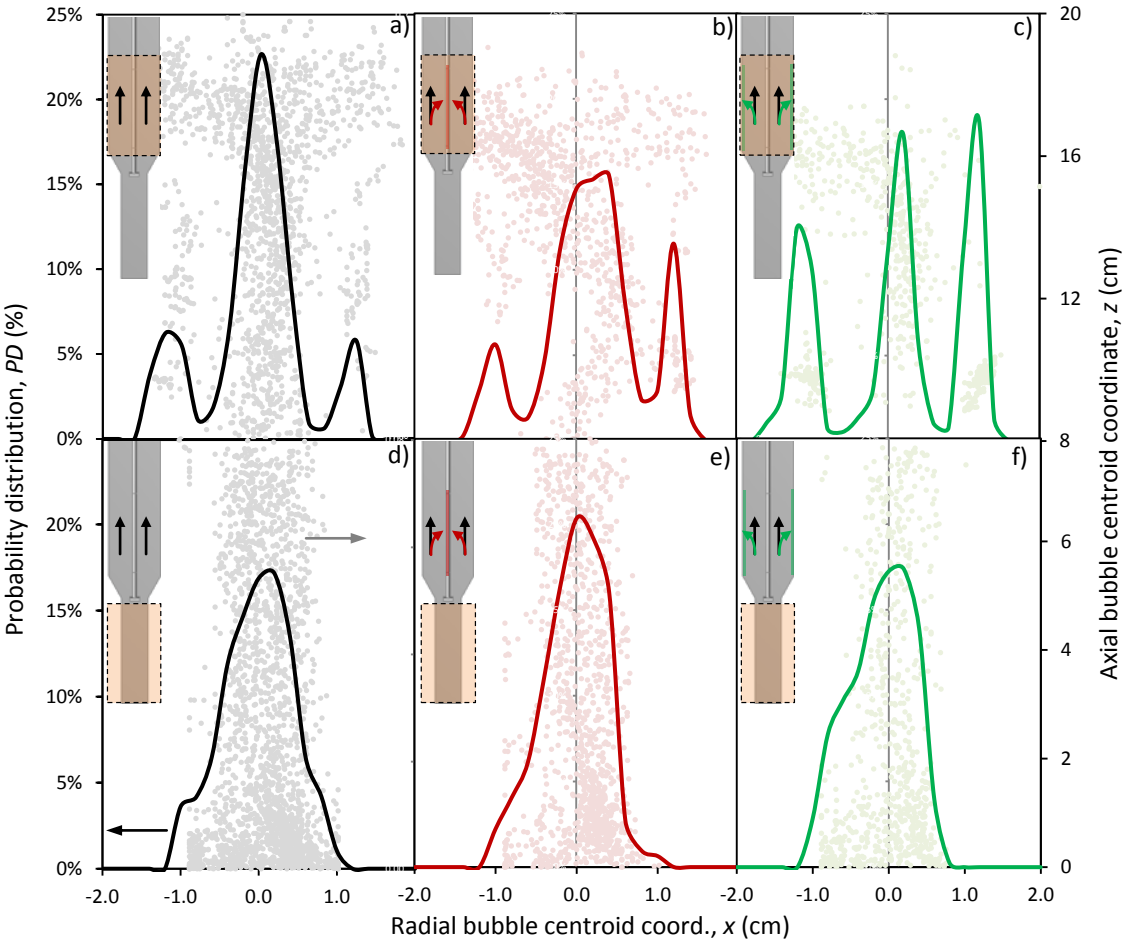

Figure 6. Effect of the membrane arrangement on the probability distribution of bubbles radial location within different bed regions: upper (a, b, c) and lower (d, e, f) bed zones for TS-TZFBR (a, d), TS-TZFBMR [ITM] (b, e) and TS-TZFBMR [RWM] (c, f). Fluidization regime: u_r = 2.5. Permeation rate: 20%.

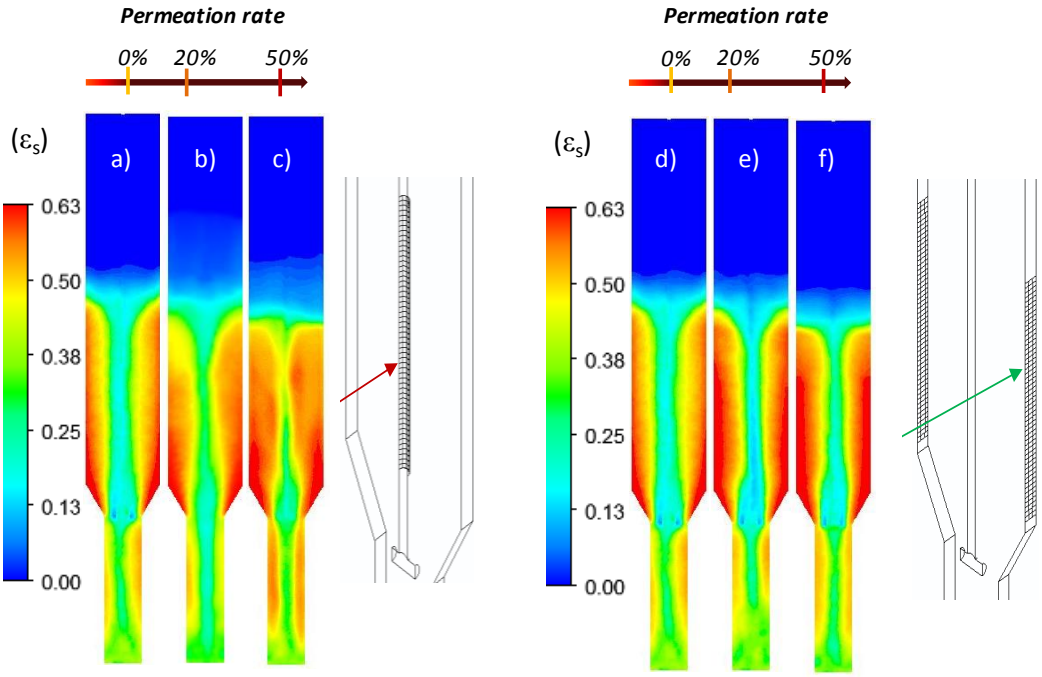

Figure 7. Time-averaged solids volume fraction (ε_s) distribution maps for ITM (a, b, c) and RWM (d, e, f) membrane-assisted TS-TZFBR configurations operated at 0%, 20% and 50% gas extraction rate, respectively. Inlet gas velocity: $u_{gas}/u_{mf} = 2.5$

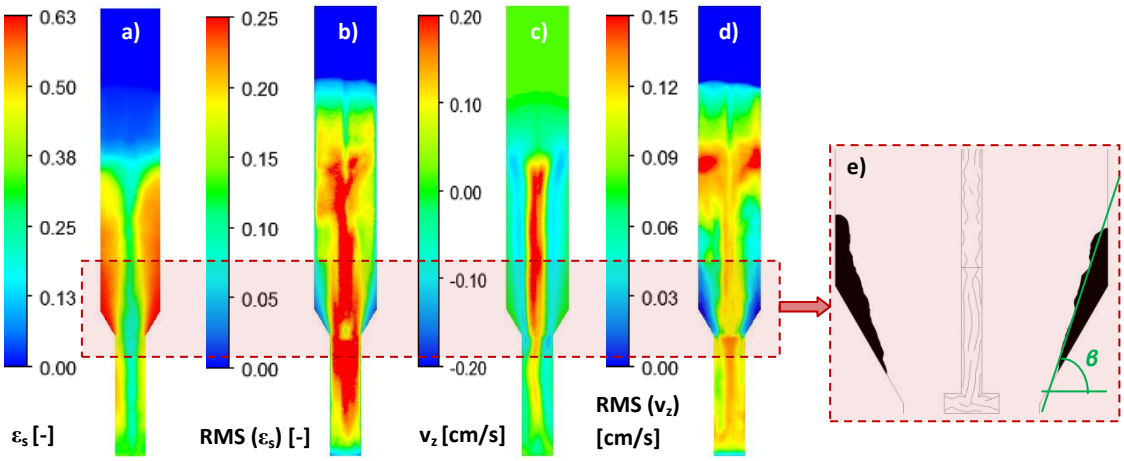

Figure 8. Time-averaged spatial distribution of: a) bed porosity, b) porosity fluctuation, c) axial solids velocity, d) axial velocity fluctuation, e) defluidized (or dead) bed regions. Operational conditions: TS-TZFBMR (ITM) at u_r = 2.5 and 20% permeation rate

Artículo VIII

I. Julián, D. González, J. Herguido, M. Menéndez,
On the use of α-shapes for the measurement of 3D bubbles in FBR from TFM simulations,
Powder Technol. (2015)

On the use of α-shapes for the measurement of 3D bubbles in fluidized beds from Two-Fluid Model simulations

Ignacio Julián[1], David González[2], Javier Herguido[1], Miguel Menéndez[1]

[1]*Catalysis, Molecular Separations and Reactor Engineering Group (CREG), Department of Chemical and Environmental Engineering*
[2]*Applied Mechanics and Bioengineering group (AMB), Department of Mechanical Engineering*

Aragon Institute of Engineering Research (I3A), Universidad de Zaragoza, 50018 Zaragoza, Spain

Abstract

A geometrical technique based on shape construction was employed to reconstruct the simulated domain of 3D bubbles in a gas-solid fluidized bed, from Two-Fluid Model (TFM) simulations. The Delaunay triangulation of the cloud of points that represent volume fraction iso-surfaces in transient TFM simulations was filtered by means of the so-called α-shapes, allowing a topologically accurate description of 3D bubbles within a fluidized bed. Consequently, individual 3D bubble properties such as size and velocity were measured. Simulated bubble characteristics were further compared to those measured on pseudo-2D bed facilities by image techniques in order to illustrate the effect of the bed geometry on the bubbling behaviour under mimicked operational conditions.

Keywords

Fluidized bed, bubble hydrodynamics, 3D bubble measurement, Delaunay triangulation, alpha-shape

1. Introduction

Fluidized beds provide an efficient mass and heat transfer due to their characteristic high fluid-solid contact area, high relative velocity between phases and high level of particulate mixing. For this reason, fluidization technology is widely used in industry for a number of physical and chemical processes involving catalytic reactions, mixing or drying [1]. Since the fluid dynamic performance of a fluidized bed determines its efficiency, it is essential to understand the behaviour of the multiphase flow in such a system. In particular, it is very important to analyze the bubbling regime within a fluidized bed, since bubbles promote solids axial mixing and determine mass and heat transfer limitations [1].

The complete understanding of the fluidization dynamics is very challenging. Many efforts have done in the last five decades in this field, both experimentally and with the aid of computational models. Reported experimental works are mainly focused on the fluid dynamic analysis of pseudo-2D beds by optical techniques (basically Particle Image Velocimetry (PIV) and Digital Image Analysis (DIA)), which are normally preferred due to their non-intrusiveness, ease of implementation and large amount of available data from visual access [2-4]. The main

drawback of these techniques is the need of visual access. Since dense gas-solid flows are typically opaque to visible light, this limits the use of the technique to 2D systems although most of the fluidized beds are cylindrically shaped [5]. To circumvent this limitation, some techniques were developed to characterize experimental 3D beds by means of non-intrusive tomography (electric capacitance tomography [6] or nuclear tomography [7]), particle tracking techniques [8-10], optical and capacitance probes [11, 12] or pressure transducers [13]. Excluding particle tracking techniques, which are developed to follow the motion of single particles, the above mentioned techniques allow the detection of local voidage in the bed, i.e. the measurement of the gas-solids distribution in 3D fluidized beds. In any case, the reconstruction of the experimentally measured signals into 3D bed porosity maps or bubbling characterization is quite troublesome [14].

On the other hand, simulation studies on bubbling characterization do not deal with the visual access, intrusiveness or data reconstruction issues but with the computational cost of the available literature models. Modeling of 3D fluidized beds can be used to provide instantaneous, whole-field information on the bubble behavior in geometries close to real ones, improving scale up advantages [15]. As a multiphase flow, the fluidized bed dynamics can be simulated basically according to three different models regarding the required degree of detail: direct numerical simulation, discrete particle model and continuum model based on the kinetic theory of granular flow [16]. Direct numerical simulation techniques, including Lattice-Boltzmann or Front-Tracking methods, reveal detailed gas-particles interactions [17] but they are nowadays limited to the study of very small beds with low number of particles due to their high computational cost. Discrete particle models, i.e. Eulerian-Lagrangian approach, provide relevant information about the particle-particle collisions and the solids mixing within the bed [18]. However, in spite of the increasing computational capacity over the last decade, they are still limited to the simulation of lab scale and medium-size fluidized beds. The continuum model, Eulerian-Eulerian or Two-Fluid Model depicts both gas and dense phase in the fluidized bed as interpenetrating continua, thus, reducing the computational cost and allowing the simulation of large scale structures for either pseudo-2D and 3D bed configurations [16].

The analysis of bubble hydrodynamics from transient Two-Fluid Model (TFM) results performed in 2D or pseudo-2D beds is well described by many authors in literature [19-23]. Basically, a prescribed threshold void fraction (normally in the range 0.70 – 0.85, according to several authors [19-21, 24-26]) is used to discriminate gas bubbles from the dense phase in the transient bed porosity maps. Image Processing algorithms binarize the obtained voidage maps to identify bubble contours and calculate bubble properties such: equivalent diameter, aspect ratio or bubble centroid location. By measuring the displacement of a single bubble centroid between subsequent frames, the bubble velocity is obtained.

However, the analysis of bubble characteristics from TFM simulations of 3D fluidized beds is not straightforward. Although commercial Computational Fluid Dynamic (CFD) codes are able to post-process transient results to show bubble contours by means of void fraction iso-surfaces, these software are not able to discriminate single gas bubbles. Therefore, bubble data such as size, aspect ratio or spatial location of the bubble centroid cannot be directly

extracted from simulation results. Some authors [15] use tomography techniques to get radial voidage maps at different bed heights and then carry out image reconstruction to estimate 3D bubble characteristics. Some others [27] couple porosity maps and bubble shape factors from single detached bubble simulations [28] to estimate the 3D bubble characteristics.

On the one hand, the latter technique requires some assumptions regarding bubble sphericity that may affect the accuracy of the results. On the other hand, the tomography reconstruction implies the concatenation of a series of two dimensional sliced images through the bed vertical axis to form transient 3D spatial images from which bubbles are identified. The 3D bubble volume estimation from 2D planar porosity maps is computationally expensive and the accuracy of the method depends on the number of sliced planes considered in the 3D image reconstruction [15].

Therefore, taking advantage of the characteristic fixed mesh which is used in the Two-Fluid Model formulation for the simulation of the fluidized bed dynamics, this work suggest a direct method to quantify 3D bubble properties from nodal results applying a geometric construction technique, the so-called α*-shape method* introduced by Edelsbrunner and Mücke (1994) [29]. The use of α-shapes allows a topological reconstruction of individual bubbles creating unconnected subdomains whose contours are the individual bubble boundaries. The accuracy of the bubble contour reconstruction depends on the computational mesh size, i.e. the distance between adjacent mesh nodes. The geometric reconstruction based on α-shapes, which is extensively applied in other fields such medical image analysis or molecular structure modeling, is here used for the first time (to the best of the authors' knowledge) to identify and measure gas bubbles in simulated 3D fluidized beds.

This study specifically focuses on the detection and measurement of 3D bubbles in a particular fluidized bed reactor configuration: the Two-Section Two-Zone Fluidized Bed Reactor (TS-TZFBR) showed in Figure 1.a. This reactor has been described elsewhere [30] as a potential tool for process intensification in the field of heterogeneous catalysis due to its ability to perform heterogeneous catalytic reactions and catalyst regeneration in a single vessel. Two separated gas inlets along the bed, through which the reactive and regenerative gas flows are fed, induce two bed zones with different atmospheres. The bed fluidization, i.e. the catalyst circulation, between the two zones allows the process integration [30]. The performance of this kind of reactor arrangement has been successfully tested in many processes such as: light alkane dehydrogenations, ethanol steam reforming or methane aromatization [31-33]. Its fluid dynamic characteristics have also been extensively studied both experimentally and with TFM simulations on pseudo-2D reactor geometries [24, 34-37]. In these studies, some relevant results regarding the most suitable reactor geometry to avoid defluidization phenomena were presented. Besides, in order to favor solids axial mixing and minimize mass transfer limitations an operational window for the inlet gas flow was defined. Nevertheless, all these studies were performed on pseudo-2D TS-TZFBR configurations.

Therefore, with the present work authors aim to study the potentials of the α-shapes method to identify and measure volumetric gas bubbles in simulated three-dimensional fluidized beds. As a first approach, a formulation of the TFM that was previously validated with experimental

data for pseudo-2D TS-TZFBR [23] has been used to perform the 3D fluid dynamic simulations. The model closures and parameter values were those previously adapted to the pseudo-2D system and might not give physical realistic predictions of a 3D TS-TZFBR bed, as already observed by some authors [38, 39]. The qualitative comparison of the model predictions on the bubbling characteristics performed in this work for both bed configurations aims to bring some light on the extrapolation of pseudo-2D bubble data to the real 3D column bubbling.

2. Simulations

Eulerian three-dimensional simulations were performed using commercial Ansys CFX 14.5 software. The Eulerian model that considers both solid and gas phase as interpenetrating continua introduces the concept of phase volume fraction [40]. The model equations consider mass and momentum conservation for each phase, *i* (gas or solid), Ec. 1 – 3.

$$\frac{\partial}{\partial t}(\varepsilon_i \rho_i) + \nabla \cdot (\varepsilon_i \rho_i \, \vec{v}_i) = 0 \tag{1}$$

$$\frac{\partial}{\partial t}\left(\varepsilon_g \rho_g \, \vec{v}_g\right) + \nabla \cdot \left(\varepsilon_g \rho_g \, \vec{v}_g \vec{v}_g\right) = -\varepsilon_g \nabla P + \varepsilon_g \nabla \cdot \bar{\bar{\tau}}_g + \varepsilon_g \rho_g \bar{g} + K_{gs}(\vec{v}_g - \vec{v}_s) \tag{2}$$

$$\frac{\partial}{\partial t}(\varepsilon_s \rho_s \, \vec{v}_s) + \nabla \cdot (\varepsilon_s \rho_s \, \vec{v}_s \vec{v}_s) = -\varepsilon_s \nabla P - \nabla P_s + \varepsilon_s \nabla \cdot \bar{\bar{\tau}}_s + \varepsilon_s \rho_s \bar{g} + K_{gs}(\vec{v}_s - \vec{v}_g) \tag{3}$$

The left hand side of the momentum conservation equation represents the temporal and spatial transport terms. The right hand side represents the various interacting forces: buoyancy, pressure drop, viscous stress, gravity and interphase drag force. K_{gs} is the interphase momentum exchange coefficient whereas $\bar{\bar{\tau}}_i$ is the *i* phase stress-strain tensor.

The solution of this set of partial differential equations requires some closures to describe the interaction between phases. In this study the computational model described in a previous work on pseudo-2D TS-TZFBR [24] was used to simulate the fluid dynamic behaviour of the 3D reactor configuration using the element-based finite volume method of Ansys CFX. Concretely, the solid-fluid interphase momentum exchange coefficient was modeled with the Gidaspow drag function [40], that combines the equations of Wen and Yu and Ergun for the interphase drag force, where C_D was estimated using the Schiller-Naumann drag coefficient model [41]. The interphase stress-strain tensor for the phase *i* (either gas or solid) was assumed to follow the Newtonian strain-rate relation, which depends on the bulk and shear viscosities. The shear viscosity was estimated as the sum of the collisional, frictional and kinematic contributions. Both the bulk and shear viscosities depend on the granular temperature and a collisional restitution coefficient [42]. In this study, the restitution coefficient was set to 0.95 for all simulations [24]. The angle of internal friction, φ, was set to 30º and the radial distribution function, g_0, (which measures the average distance between particles) was modeled according to the description of Lun and Savage [43]. The granular temperature was determined algebraically under the assumption of local equilibrium in a transport equation model, i.e. energy production equals energy dissipation. This assumption is often used in dense, slow moving fluidized beds where the local generation and dissipation of granular temperature far outweigh the transport by convection and diffusion [44]. Lastly, the solids pressure was modeled according to the kinetic theory model of gases [42], being adapted to consider the

inelastic collisions between particles. The maximum solid packing, $\varepsilon_{s,m}$, was set to 0.65. A monodisperse 200 μm particle size distribution, which agrees with the particle size used in previous experimental works, was used in the simulations throughout the study. The set of governing equations is detailed in Table 1.

2.1 Computational domain

The computational domain is presented in Figure 1.b. The three dimensional reactor is 50 cm high, having an external diameter of 8 cm in the upper region and 4 cm in the lower bed zone. The two cylindrical regions are connected by a tronco-conical section with an inclination of 80^o with respect to the horizontal axis. The narrower cylindrical section (i.e. 'regeneration zone') is 12 cm high. Additionally, the characteristic gas inlet through an intermediate bed height in a TS-TZFBR is simulated erecting a vertical tube wall (3 mm external diameter) having four cross-orifices for gas inlet in its bottom end. The length of each distributor blade is 1 cm and the diameter of the orifices is 3 mm. The internal gas inlet is located 12 cm above the bottom of the bed, thus, at the same height as the top end of the narrower bed cross-section. Both the tapered angle and the axial location of the immersed gas distributor have been described elsewhere [24, 36, 37] to be suitable to avoid defluidization effects and short-circuiting in the solids recirculation.

Mesh independence studies were conducted to find suitable conditions in terms of computational cost, numerical stability and reproducibility of hydrodynamic results. The domain was finally discretized by more than 10^5 nodes, with adaptive mesh size between 1 and 2.5 mm (Figure 1.c). CFD simulations were solved using a time step, $\Delta t = 10^{-4}$ s.

2.2 Boundary conditions and solver settings

The bulk mass flow rate was selected as the boundary condition for the reactor gas inlets to avoid dense phase outflow. An opening boundary was applied to the reactor outlet at the top of the domain. The opening condition refers to the unrestricted circulation of gas and dense phase (if it eventually reaches the top of the bed) through the boundary. The flow direction through inlets and outlets was defined as normal to the boundary surface and the relative pressure on the domain outlets was set to 0 Pa, i.e. $P = P_{atm}$. A no-slip condition was applied for the gas phase at the walls. Regarding the particle-wall interaction, the proper selection of the wall boundary condition for the solids phase is not straightforward for Euler-Euler models and different formulations can be found in the open literature: no-slip, partial-slip and free-slip, e.g. [44, 45] conditions. Although it seems that the partial-slip is the most realistic approach, the selection of a proper specularity coefficient is not trivial and needs to be done carefully. Since the detailed analysis of the wall-particle friction is out of the scope of this work, a no-slip boundary condition was applied for the gas dense phase as a first approach. The set of partial differential equations was solved using a SIMPLE scheme (Semi Implicit Method for Pressure Linked Equations) for pressure correction. In this algorithm, the velocity field is first predicted based on the pressure field from the previous iteration and then iteratively corrected using the mass and momentum equations to maintain incompressibility of

both phases [26]. A first order Backward Euler method was used for the discretization of the transient terms. The second order time discretization is usually preferred for accurate solution of fast-moving riser flows with the TFM but this is not the case for dense bubbling beds at low relative gas velocities, in which the majority of the bed moves relatively slowly [38, 46]. The numerical discretization of the system variables was done with an upwind scheme with convergence criteria based on a RMS residual target of 10^{-3}, as recommended from previous works [24]. CFD simulation parameters are listed in Table 2.

To obtain fully comparable results in terms of bed height fluctuation between pseudo-2D and 3D simulations, the total volume of the domain was initially filled with a 25% of solids, which settle in the absence of fluidization gas (sedimentation stage), following a previously described method [24].

3. Bubble discrimination

Transient TFM simulation results contain information about system variables, e.g. phase volume fraction, at every mesh node within the simulation domain. As an example, Figure 2.a illustrates the transient solids volume fraction map at a central xz plane of a 3D TFM simulation on a TS-TZFBR reactor configuration. The iso-surfaces tool, which is a common data visualization method available in the majority of CFD post-processing software, allows the visualization of regions with a constant property value within the computational domain. In order to identify bubble boundaries, a prescribed solids volume fraction $\varepsilon_s = 0.15$ was defined as a threshold value for the iso-surfaces method following the recommendations of some authors [19-21, 39]. Figures 2.b and 2.c. illustrate the bed regions detected as bubble contours after applying iso-surfaces threshold porosity. The domain defined by the iso-surfaces enclosed, then, a list of spatial coordinates of the mesh nodes (Figure 2.d) that accomplish the given restriction: $\varepsilon_s = 0.15$.

Once the list of bubble-boundary nodes was determined, a Delaunay triangulation algorithm was applied (using the Computational Geometry toolbox of Matlab R2010b) to connect every node by means of unique tetrahedral shapes. The algorithm itself did not discriminate nodes that belong to different bubbles. For this reason it was necessary to constrain node connections in order to identify 'false' connections and remove them, generating multiple domains: one for each bubble (Figure 2.e).

The filtration of the Delaunay triangulation was carried out using the α-shapes geometric method. To the best knowledge of the authors, this is the first time that this method was applied for bubble volume reconstruction in 3D fluidized bed simulations. Therefore, the description and validation of the method for the characterization of 3D bubbles in simulated gas-solid fluidized beds represents an innovative and major contribution of this work.

The α-shapes were firstly proposed by Edelsbrunner and Mücke [29] and deal with the elimination of all tetrahedra whose circumscribing radius, i.e. mesh size in finite element terminology, is greater than a prescribed level of detail for the geometry, α. Main drawbacks of the technique are the selection of a suitable α value and the fact that α-shapes only work well for a uniform concentration of points [47]. This is the case of the Eulerian approach, in which the nodes of the computational mesh remain fixed in the space along the time. Since the

distance between nodes in the fixed adaptive mesh used in this work ranges from 1 to 2.5 mm, the minimum α value that allows the discrimination of adjacent bubbles is the maximum distance between connected nodes in the mesh. In other words, all connections (from the Delaunay triangulation) made between nodes that are separated by a spatial distance greater than α = 2.5 mm are removed by the α-shape method. Analogously for a 3D grid, the volume of a regular tetrahedron with 2.5 mm long edges represents the threshold volume over which tetrahedra are removed from the Delaunay triangulation domain.

Otherwise, adjacent bubbles separated by less than 2.5 mm are computed as a single bubble. Although this may cause discrepancies in the analysis of bubble characteristics in bubble columns, where bubble clusters or swarms are formed under certain gas flow regimes, this should not represent an important issue in gas-solid fluidized beds at bubbling or slugging regimes. At these regimes, gas bubbles appear fairly isolated from each other and only coalescence and break up phenomena could compromise the accurate discretization of bubbles by the suggested α-shape method.

Once false node connections are removed, the volume and centroid (center of mass) of each isolated bubble domain can be calculated using equations 4 and 5. In equation 4, $v_{b,i}$ is the volume of the transient bubble *i* which is calculated as the sum of volumes of the "*T*" tetrahedra that form the bubble domain. *A*, *B*, *C* and *D* are the nodes of the tetrahedron "*t*" with spatial coordinates (*x*, *y*, *z*) as illustrated in Figure 3. In equation 5, $b_{CoM,i}$ is the center of mass of the bubble *i*, *N* is the number of nodes that form bubble *i* being $(n_x, n_y, n_z)_n$ the spatial coordinates of the node *n*.

$$v_{b,i} = \sum_{t=1}^{T} \left(\frac{1}{6} \begin{vmatrix} A_x & B_x & C_x \\ A_y & B_y & C_y \\ A_z & B_z & C_z \end{vmatrix} \right)_t = \sum_{t=1}^{T} \left(\frac{1}{6} \overline{AD} \cdot (\overline{BD} \times \overline{CD}) \right)_t \tag{4}$$

$$b_{CoM,i}(x,y,z) = \frac{1}{N} \left(\sum_{n=1}^{N} (n_x)_n \, , \sum_{n=1}^{N} \left(n_y \right)_n , \sum_{n=1}^{N} (n_z)_n \right) \tag{5}$$

The 3D equivalent bubble diameter (d_b) is determined as the diameter of the sphere that occupies the same volume as the bubble (equation 6), whereas the average equivalent bubble diameter at certain bed vertical position is calculated according to the equation 7. This expression, which has already been used in previous studies [24, 31, 35], weights bubble diameters proportionally to their size. The use of the weighted average d_b is motivated by the fact that big bubbles are more representative of the bubbling gas flow than small spurious bubbles. Moreover, from a fluid dynamic point of view, the larger bubbles have a greater influence on the mixing of solids in the fluidized bed than smaller ones.

$$d_{b(3D),i} = 2 \left(\frac{3}{4\pi} v_{b,i} \right)^{1/3} \tag{6}$$

$$\overline{d_b}(z) = \frac{\sum_{n=1}^{N} {d_{b,i}}^2(z)}{\sum_{n=1}^{N} d_{b,i}(z)} \tag{7}$$

The bubble velocity is calculated comparing bubble centroid locations between subsequent transient fluidization frames. A nearest-neighbour algorithm [48] is used to identify bubbles and track their displacement between shortly delayed simulation time steps, Δt = 10^{-2} s. Bubble data concerning volume, aspect ratio and centroid coordinates (*x, y, z*) are compared between consecutive transient results. The bubble identification is carried out by minimization of the global 'distance' between bubble data at the analyzed time steps under certain restrictions:

a) The axial coordinate of the bubble centroid at the previous time step cannot be greater than that at the later one, i.e. negative bubble velocities are not computed;

b) The equivalent diameter of an individual bubble cannot change in more than 20% between consecutive frames [49];

c) Each bubble data at the latter time step can have as maximum one correspondence to a bubble data at the previous time step. The determination of bubble velocity in case of bubble break-up or coalescence is, thus, avoided to prevent average u_b results to be influenced by wrong bubble tracking.

The statistical bubble size and velocity distribution in pseudo-2D and 3D fluidized beds is strongly dependant on the way to compute bubble data. In this work, several methods have been implemented to carry out a consistent comparison between bubbling results obtained for the two different reactor configurations. Concretely, two different approaches have been considered to compute the equivalent bubble diameter in pseudo-2D and 3D beds: the volumetric and the superficial formulation. As a result, four equivalent bubble diameters are considered:

1) 3D bed + volumetric formulation: equivalent diameter of the sphere that encloses the same volume as the bubble (equation 6).

2) 3D bed + superficial formulation: equivalent diameter of the circle that encloses the same area as that projected by the bubble through the plane that crosses the bed center axially (equation 8).

$$d_{b(area),i} = 2\left(\frac{A_{b,i}}{\pi}\right)^{1/2} \tag{8}$$

3) pseudo-2D + volumetric formulation: equivalent diameter of the cylinder that encloses the same volume as the bubble (equation 9).

$$d_{b(volume),i} = 2\left(\frac{3}{4\pi}A_{b,i}L_{bed}\right)^{1/3} \tag{9}$$

4) pseudo-2D + superficial formulation: equivalent diameter of the circle that encloses the same area as that projected in the front face of the bed (equation 8).

The suggested α-shapes method (Figure 2.e) applies only for the first case, i.e. the determination of the equivalent bubble diameter in 3D beds based on the gas volume enclosed by bubbles.

In the remaining cases, the equivalent bubble size can be determined using Digital Image Analysis (DIA) techniques. Such techniques discriminate gas bubbles from the emulsion phase

by means of pixel intensity in the solids volume fraction distribution maps and have been widely reported in literature [2-6]. Applied to 3D simulations, the DIA algorithm detected bubble contours in 2D void fraction maps traced through the 3D bed center (Figure 4.a). Similarly, the DIA processing of the facial transient porosity distribution was employed to determine planar bubble characteristics in the pseudo-2D bed. In both cases, the bubble size was determined from the equivalent diameter of a circle which surface had the same area as the projected bubble in the plane (Equation 8), as shown in Figure 4.b. Additionally, a formulation that takes into account the volume enclosed in pseudo-2D bubbles (Equation 9) was used to describe the equivalent bubble diameter as the diameter of a sphere that occupied the same volume as the projected bubble area (A_b) through the bed depth (L_{bed}), as shown in Figure 4.c. Concerning the statistical analysis of the bubble size profile along the vertical bed position, $d_b(z)$, the time-averaged axial distribution of the equivalent bubble diameter was obtained either by computing raw bubble data or just by using those bubbles that were identified at consecutive frames, i.e. bubbles whose rising velocity was determined from subsequent porosity maps. Therefore, spurious bubbles were filtered out from the bubble data statistics.

4. Results

In this section, the most relevant results regarding the use of α-shapes in bubble discrimination are presented. Besides, a critical comparison between the TFM simulation results of bubbling regimes obtained for 2D and 3D TS-TZFBR configurations is done, illustrating the role of the equivalent d_b definition on the bubble size profiles and further bubble characteristics. Pseudo-2D and 3D bubble measurements were carried out for a simulated Two-Section Two-Zone Fluidized Bed Reactor (Figure 1.b) at a relative gas velocity, $u_r = u_{gas}/u_{mf} = 2.5$ using Geldart-B particles ($d_p = 200$ μm, $\rho_p = 2.5$ g/cm^3) with $u_{mf} = 10.1$ cm/s.

4.1 Geometric 3D reconstruction of bubble topology

As it has been previously discussed, the accuracy of the geometric reconstruction of topological spaces based on α-shapes depends on the proper selection of a threshold α value to discriminate node connections in the 3D Delaunay triangulation mesh created from bubble contour nodes of CFD transient results. If a geometric reconstruction is not applied the triangulation method would connect every node under the Delaunay condition, leading to a unique mesh that does not discriminate individual bubbles. If α-shapes are applied, in principle the lower and more restrictive α value, the greater is the level of detail on individual bubble contours. Nevertheless, if the α threshold becomes lower than the edge length in the domain mesh, wrong topologies may be found. As an example, Figure 5 illustrates the effect of the α-shape value on the bubble contour detection for a transient simulated fluidization frame. Figure 5.a shows the iso-surface analysis performed to get the spatial coordinates of the bubble contour nodes. As already discussed, the iso-surface connects bed regions in which the solids volume fraction is 0.15 (or, analogously, the void fraction is 0.85). The planar iso-surface detected at the bed top represents the bed surface and, thus, it must be filtered out from the hydrodynamic analysis (Figure 5.a). From left to right, Figure 5.b shows the number and shape of the detected gas bubbles by the 3D geometry reconstruction algorithm with increasing α-

shape value. If the level of detail is greater than the mesh size, i.e. α < 0.25 cm, true node connections break leading to wrong bubble contour detection. In contrast, if α becomes higher than the mesh size the resolution of the method decreases resulting in bubble contour detection misleading.

The use of a fixed mesh along the time in the continuum Two-Fluid model simulations makes the selection of an appropriate α-shape value quite straightforward. This is not the case in meshless simulations of free surface flows, e.g. wave breaking [47], in which the selection of suitable α-shapes becomes troublesome.

4.2 Definition of 'equivalent bubble diameter'. Comparison between simulated bubble size profiles in pseudo-2D and 3D fluidized beds

Figures 6.a and 6.b show the evolution of the bubble size along the vertical bed position for the simulated 3D and pseudo-2D TS-TZFBR beds. Equations 6 and 8 have been used to calculate the equivalent diameter of raw bubbles from 3D reconstructed geometries and 2D projected areas, respectively. As can be observed in Figure 6.c, the time-averaged equivalent bubble diameter values are substantially greater in case of the pseudo-2D beds. This finding motivated the revision of the definition of 'equivalent bubble diameter'.

From the point of view of a pseudo-2D bed that aims to mimic a vertical slice of a cylindrical 3D bed through its bed center, the area-based bubble size of the 2D configuration should be compared with the planar projection of the 3D bed using Equation 8 to determine the equivalent bubble diameter.

From the point of view of the void volume enclosed by bubbles, the 3D bubble diameter measured by geometry reconstruction via α-shapes should be compared with the equivalent diameter of a sphere that occupies the same volume as that enclosed in the pseudo-2D bubble according to the definition given in Equation 9.

Figures 7.a and 7.b illustrate the comparison between time-averaged bubble size profiles obtained for 3D and pseudo-2D beds under the above considerations. For each case, the presented time-averaged d_b values have been calculated with respect to both the raw and the filtered bubble data.

Apparently, the effect of the spurious bubbles filtration on the computation of the time-averaged $d_b(z)$ profiles is negligible against the effect of the way to calculate d_b from simulation results. In general, the area-based definition of the bubble size leads to greater d_b values along the bed vertical position than the volume-based approach.

Image analysis from porosity maps (Figure 7.a) gives mimic $d_b(z)$ profiles for 2D and 3D configurations within the lower straight bed section. However, 2D simulations predict a substantial bubble size decrease along the tapered bed region and a fast bubble size growth within the upper straight bed zone, which are not observed in the porosity maps of the 3D configuration.

Regarding the volumetric formulation of the equivalent bubble diameter (Figure 7.b), the volume of bubbles from reconstructed 3D geometries is greater than that of pseudo-2D bubbles, with an average 23.2% overestimation on the equivalent bubble diameter. This

agrees with the fact that for a same gas excess velocity in both configurations, $u_{gas} - u_{mf}$, the bubbles in the 3D bed (which has a greater cross-sectional area than the pseudo-2D reactor) carry a greater amount of gas. Nevertheless, the shape of the volume-based $d_b(z)$ profiles for 2D and 3D configurations is very similar and the bubble growing and shrinking trends along the 3D TS-TZFBR are qualitatively well reproduced by the pseudo-2D bed.

Summarizing the previous results it has been found that 2D simulations (and experiments in pseudo-2D beds, by extension) give valuable insight into the 3D bubbling regime although they are not able to mimic the characteristics of real 3D bubbles. Neither image analysis (area-based) techniques nor the pseudo-2D volume-based definition of the equivalent d_b can exactly reproduce the 3D bubble characteristics obtained by geometric reconstruction of 3D Two-Fluid Model simulations. Nevertheless, this second approach provides a much better agreement between $d_b(z)$ profiles at both reactor configurations. As a result, the proposed reconstruction of 3D bubbles using α-shapes leads to a more reliable and accurate description of the bubbling behaviour than the use of image analysis, i.e. tomography techniques [15, 27] for TFM simulated 3D fluidized beds.

4.3 3D bubble characteristics in a Two-Section Two-Zone Fluidized Bed Reactor

For each transient result of both pseudo-2D and 3D bed simulations, five different bubble parameters have been collected: equivalent diameter (according to equations 6 to 9), centroid coordinates, aspect ratio, bubbles hold-up and bed height. Additionally, bubble velocity values have been determined comparing bubble data between consecutive frames by a nearest-neighbour algorithm. The collected data along the simulation time have been used to perform a statistical analysis on the bubbling behaviour in a TS-TZFBR.

4.3.1 Radial distribution of bubble location along the 3D bed

The determination of bubble centroid coordinates allowed the study of the spatial distribution of bubbles within the TS-TZFBR. Figure 8.a shows a 3D scattered plot of the bubble centroid spatial location for eight seconds of simulated fluidization (sampling time, $\Delta t = 0.01s$). Results suggest that at the very bottom of the bed a great number of bubbles were formed close to the gas distributor. The bubbles that were initially distributed along the whole bed cross section flow towards the bed center upwards, where the lower presence of centroid points illustrates the bubble coalescence phenomenon. At the bottom-end of the tapered bed region ($z = z_{dis} = z_{sc}$ = 12 cm), a high concentration of bubble centroids was found which is related to the incipient bubbles coming from the immersed gas distributor. As the bed cross-section area increases the number of bubbles decreased towards the freeboard, mainly due to coalescence and to the reduction of the gas excess over the minimum fluidization. The radial distribution map of bubble centroid location shown in Figure 8.b suggests that bubbles mainly flow up through the bed center and marginally close to the bed walls.

4.3.2 Bed expansion and void fraction in pseudo-2D and 3D TS-TZFBR configurations

Figure 9 shows the evolution of the bed height as well as the volume occupied by gas bubbles along the time on stream for the pseudo-2D and 3D bed configurations used in this

work. Figure 9.c illustrates the axial fluctuation with time of the free bed surface due to the bubbling regime. The transient simulated bed height has been here determined measuring the average vertical coordinate of the upper contour line in 2D bed images (Figure 9.a) and of the upper meshed iso-surface in the 3D bed (Figure 9.b).

The average bed height gives an idea on the bed expansion whereas the amplitude and frequency of the fluctuation are related to bubble size and bubbling frequency, respectively.

Simulation results suggest that the average bed height of the pseudo-2D bed is 7.2% greater than that of the 3D bed ($z_{fb(2D)}$ = 31.3 cm and $z_{fb(3D)}$ = 29.2 cm) under the same fluidization conditions, as already observed by some authors [50]. Due to the special TS-TZFBR geometry, the bed expansion cannot be directly determined from the average fluidized bed height data. A volumetric formulation of the bed expansion needs to be used instead. Since the initial fixed bed height is the same (z_0 = 24 cm) for both configurations, the average volumetric bed expansion becomes $B_{e(3D)}$ = 1.50 and $B_{e(2D)}$ = 1.48 for the 3D and pseudo-2D bed, respectively. The deviation of the bed expansion between configurations results, thus, in a negligible 1.5%.

The transient evolution of the total gas volume enclosed by bubbles for both pseudo-2D and 3D beds is shown in Figure 9.c. The time-average bubbles hold-up (b_h) differs in less than 7% between reactor configurations, being $b_{h(2D)}$ = 13.2 cm^3 and $b_{h(3D)}$ = 12.3 cm^3. Since the cross-sectional area of the pseudo-2D is lower than that of the 3D reactor, a similar bed volume increase by means of gas bubbles resulted in an increased bed height in the case of the narrower reactor, as already observed. Therefore, there is no evidence to attribute the different fluidized bed height to solids packing being different in both reactor configurations.

4.3.3 Size probability distribution and bubbles aspect ratio

Although the transient evolution of the bubbles hold-up becomes very similar between both bed arrangements at the same fluidization conditions, the bubble size and shape distributions may not follow the same trend necessarily.

To illustrate that, the Figure 10.a shows that the pseudo-2D bed leads to a broader size distribution than the 3D configuration. The increased probability to find either very small (d_b < 0.4 cm) or big bubbles (d_b > 4 cm) in the pseudo-2D bed is in agreement with the results presented in Figures 6 and 7: the pseudo-2D bed shows a sharper $d_b(z)$ profile as a result of very small bubbles close to the immersed gas distributor and quite big bubbles close to the freeboard with respect to the 3D bed.

The bubble shape distribution or 'bubble aspect ratio' (*AR*), which is defined here as the ratio between bubble height and width, is strongly related to bubble velocity. On this regard, we expect that faster bubbles tend to be sharp (i.e. high *AR*) whereas slower bubbles are more flattered (i.e. low *AR*) [19]. Assuming that bubbles are faster in a 3D configuration, according to the classical formulation of Davidson and Harrison [51] (DH) depicted in equation 10, lower bubble aspect ratios are expected for the pseudo-2D configuration. The results shown in Figure 10.b are in agreement with this assumption.

$$u_{br} = \left(u_{gas} - u_{mf}\right) + u_b = \left(u_{gas} - u_{mf}\right) + K\sqrt{g\, d_b}\,, \qquad K = \begin{cases} 0.4\ (2D) \\ 0.71\ (3D) \end{cases} \tag{10}$$

4.3.4 Bubbles motion

In a conventional fluidized bed, the bubble velocity is proportional to the square root of the equivalent bubble diameter (equation 10) and bubbles grow axially in the bed. In previous works [34, 37], the authors have shown that this is not the case in a TS-TZFBR in which a tapered region and an immersed gas jet modify the $d_b(z)$ and, thus, the $u_b(z)$ and $u_b(d_b^{0.5})$ profiles. A new $d_{b,TS\text{-}TZFBR}(z)$ correlation was developed [34] to account for the unconventional geometry of the reactor, i.e. the Julián-Herguido-Menéndez (JHM) model. This model, which couples the Mori and Wen $d_b(z)$ correlation [52] with the mass balance to the gas phase within the tapered bed region, is able to predict bubble size and velocity profiles in pseudo-2D TS-TZFBR.

Figure 11 shows a comparison between $u_b(z)$ and $u_b(d_b^{0.5})$ profiles at the two considered reactor configurations, as well as the prediction of the JHM+DH model for such velocity profiles. The TFM simulations were able to predict greater average bubble velocities in the 3D bed. Besides, the simulated average u_b values are in the range of these given by the semi-empirical correlations (JHM+DH) for both pseudo-2D and 3D bed.

It is important to remark that experimental measurements of 3D bubble properties are still not available in literature for TS-TZFBR configurations. Therefore, the computational formulation of the Two-Fluid Model used in this work cannot be validated against experimental data. However, to some extent the high agreement between the pseudo-2D and 3D $u_b(d_b)$ profiles in comparison to these predicted by the correlation of Davidson and Harrison (based on empirical values of the parameter K for their pseudo-2D and 3D measurements) suggests that the model is able to predict the experimental changes in the bubble properties as a function of the bed geometry.

5. Conclusions

In this work, an improved method to measure 3D bubbles from TFM simulations has been presented. The method deals with the volumetric discretization of connected bubble iso-contours by means of the so-called α-shapes. Compared to the tomographic techniques used in the open literature, this method provides a more reliable tool to analyze the bubble hydrodynamics in simulated 3D fluidized beds.

A critical comparison between the simulated bubble characteristics for a pseudo-2D and a 3D TS-TZFBR showed that the pseudo-2D bed gives a reasonably good estimation of the hydrodynamic behaviour in a 3D system. In particular the bed expansion, bubbles hold-up and bubble velocity profiles of the 3D TS-TZFBR could be directly estimated from pseudo-2D simulations.

Regarding the bubble size, the raw comparison between area-based $d_{b,pseudo\text{-}2D}(z)$ and volume-based $d_{b,3D}(z)$ profiles does not give a fair insight into the simulation model predictability and the validity of the α-shapes method. A volume-based formulation of the equivalent d_b for both pseudo-2D and 3D beds is preferred. This formulation accounts for the effective volume of gas enclosed by bubbles. Using the volume-based d_b definition the average $d_b(z)$ profiles compared qualitatively well between reactor configurations. Nevertheless, the average $d_{b,pseudo\text{-}2D}$

overestimated $d_{b,3D}$ by 23.2% within the tapered bed region. This reveals that the bed geometry effectively plays role in the fluid dynamic behaviour of the TS-TZFBR.

6. Acknowledgement

Financial support from MINECO, Spain (Project ENE2013-44350-R) is gratefully acknowledged. Financial aid for the maintenance of the consolidated research group CREG has been provided by the Fondo Social Europeo (FSE) through the Gobierno de Aragón (Aragón, Spain).

Nomenclature

AR	Bubble aspect ratio, (-)
b_d	Bubble population density, ($n_{bub.}/cm^2s$)
B_e	Bed expansion, (-)
b_h	Bubbles holdup, (%)
C_D	Interphase drag coefficient, (-)
CFD	Computational Fluid Dynamics
d_b	Equivalent bubble diameter, (cm)
d_p	Particle diameter, (m)
DIA	Digital Image Analysis
e	Restitution coefficient, (-)
g	Acceleration due to gravity, (m/s^2)
g_0	Radial distribution function, (-)
$\bar{\bar{I}}$	Stress tensor, (-)
I_{2D}	Second invariant of the deviatory stress tensor, (-)
K	Bubble velocity coefficient, (-)
K_{gs}	Interphase momentum exchange coefficient, (kg/m^3s)
P	Pressure, (Pa)
PIV	Particle Image Velocimetry
Re	Reynolds number, (-)
TS-TZFBR	Two-Section Two Zone Fluidized Bed Reactor
TZFBR	Two-Zone Fluidized Bed Reactor
u_b	Single bubble velocity, (cm/s)
u_{br}	Bubbles velocity, (cm/s)
u_{gas}	Gas velocity, (cm/s)
u_{mf}	Minimum fluidization velocity, (cm^3/cm^2s)
$u_{r,bottom}$	Relative velocity (u_{gas}/u_{mf}) within the lower bed section, (-)
$u_{r,top}$	Relative velocity (u_{gas}/u_{mf}) within the upper bed section, (-)
$\vec{v}$	Local velocity, (m/s)
z_{dis}	immersed distributor axial location, (cm)
z_{sc}	TS-TZFBR section change axial location, (cm)

Greek symbols

α	Level of detail for the geometry in the alpha-shapes method, (-)
β	Defluidization angle, (^{o})
γ	Tapered section angle, (^{o})

γ_s	Collision dissipation energy, (kg/(m·s^3))
ε	Volume fraction, (-)
θ	Granular temperature, (m^2/s^2)
λ	Bulk viscosity, (kg/(m·s))
μ	Shear viscosity, (kg/(m·s))
μ_{col}	Collisional shear viscosity, (kg/(m·s))
μ_{kin}	Kinematic shear viscosity, (kg/(m·s))
μ_{fr}	Frictional shear viscosity, (kg/(m·s))
ρ	Density, [kg/m^3]
$\bar{\bar{\tau}}$	Stress-strain tensor, (kg/(m·s^2))
φ	Angle of internal friction in particle collisions, (^{o})
ω	Probability density of bubble size, (%)

Subscripts

i	Phase i, either fluid or solid
g	Fluid phase (gas)
s	Solid phase
m	maximum
0	initial

References

[1] Kunii, D.; Levenspiel, O. Fluidization engineering. Butterworth-Heinemann 1991.

[2] Busciglio, A.; Vella, G.; Micale, G.; Rizzuti, L. Analysis of the bubbling behaviour of 2D gas solid fluidized beds part I. digital image analysis technique. Chem. Eng. J. 140 (2008) 398-413.

[3] Laverman, J. A.; Roghair, I.; van Sint Annaland, M.; Kuipers, J. A. M. Investigation into the hydrodynamics of gas-solid fluidized beds using particle image velocimetry coupled with digital image analysis. Can. J. Chem. Eng. 86 (2008) 523-535.

[4] de Jong, J.F.; Odu, S. O.; van Buijtenen, M. S.; Deen, N. G.; van Sint Annaland, M.; Kuipers, J. A. M. Development and validation of a novel digital image analysis method for fluidized bed particle image velocimetry. Powder Technol. 230 (2012) 193-202.

[5] van Ommen, J.R.; Mudde, R.F. Measuring the gas-solids distribution in fluidized beds-A review. Int. J. Chem. React. Eng. 6 (2008) R3.

[6] Dyakowski, T.; Jaworski, A. J. Application of non-invasive techniques for imaging fluidized beds — A review. In: Handbook of Conveying and Handling of particulate solids Elsevier Science B.V. 10 (2001) 807-823.

[7] Mudde, R. F. Time-resolved X-ray tomography of a fluidized bed. Powder Technol. 199 (2010) 55-59.

[8] Laverman, J. A.; Fan, X.; Ingram, A.; van Sint Annaland, M.; Parker, D. J.; Seville, J. P. K.; Kuipers, J. A. M. Experimental study on the influence of bed material on the scaling of solids circulation patterns in 3D bubbling gas–solid fluidized beds of glass and polyethylene using positron emission particle tracking. Powder Technol. 224 (2012) 297-305.

[9] Fraguío, M. S.; Cassanello, M. C.; Larachi, F.; Limtrakul, S.; Dudukovic, M. Classifying flow regimes in three-phase fluidized beds from CARPT experiments. Chem. Eng. Sci. 62 (2007) 7523-7529.

[10] T. Hensler, M. Tupy, T. Strer, T. Pöschel, K.E. Wirth, Positron emission particle tracking in fluidized beds with secondary gas injection, Powder Technol. 279 (2015) 113-122.

[11] He, C.; Bi, X. T.; Grace, J. R. Simultaneous measurements of particle charge density and bubble properties in gas-solid fluidized beds by dual-tip electrostatic probes. Chem. Eng. Sci. 123 (2015) 11-21.

[12] Rüdisüli, M.; Schildhauer, T. J.; Biollaz, S. M. A.; van Ommen J. R. Bubble characterization in a fluidized bed by means of optical probes. Int. J. Multiphase Flow 41 (2012) 56-67.

[13] Bi, H. T. A critical review of the complex pressure fluctuation phenomenon in gas–solids fluidized beds. Chem. Eng. Sci. 62 (2007) 3473-3493.

[14] Rüdisüli, M.; Schildhauer, T. J.; Biollaz, S. M. A.; Van Ommen, J. R. 18 - measurement, monitoring and control of fluidized bed combustion and gasification. In: Fabrizio Scala, editor. Fluidized bed technologies for near-zero emission combustion and gasification. Woodhead Publishing; 2013. .

[15] Sobrino, C.; Acosta-Iborra, A.; Izquierdo-Barrientos, M. A.; de Vega, M. Three-dimensional two-fluid modeling of a cylindrical fluidized bed and validation of the maximum entropy method to determine bubble properties. Chem. Eng. J. 262 (2015) 628-639.

[16] van der Hoef, M. A.; Ye, M.; van Sint Annaland, M.; Andrews, A. T.; Sundaresan, S.; Kuipers, J. A. M. Multiscale modeling of gas-fluidized beds. Advances in Chem. Eng. 31 (2006) 65-149.

[17] Wang, L.; Zhang, B.; Wang, X.; Ge, W.; Li, J. Lattice boltzmann based discrete simulation for gas–solid fluidization. Chem. Eng. Sci. 101 (2013) 228-239.

[18] Deen, N. G.; Van Sint Annaland, M.; Van der Hoef, M. A.; Kuipers, J. A. M. Review of discrete particle modeling of fluidized beds. Chem. Eng. Sci. 62 (2007) 28-44.

[19] Busciglio, A.; Vella, G.; Micale, G.; Rizzuti, L. Analysis of the bubbling behaviour of 2D gas solid fluidized beds part II. comparison between experiments and numerical simulations via digital image analysis technique. Chem. Eng. J. 148 (2009) 145-163.

[20] Hernández-Jiménez, F.; Sánchez-Delgado, S.; Gómez-García, A.; Acosta-Iborra, A. Comparison between two-fluid model simulations and particle image analysis & velocimetry (PIV) results for a two-dimensional gas–solid fluidized bed. Chem. Eng. Sci. 66 (2011) 3753-3772.

[21] Asegehegn, T. W.; Schreiber, M.; Krautz, H. J. Numerical simulation and experimental validation of bubble behavior in 2D gas-solid fluidized beds with immersed horizontal tubes. Chem. Eng. Sci. 66 (2011) 5410-5427.

[22] Shen, L.; Johnsson, F.; Leckner, B. Digital image analysis of hydrodynamics two-dimensional bubbling fluidized beds. Chem. Eng. Sci. 59 (2004) 2607-2617.

[23] Hulme, I.; Clavelle, E.; van der Lee, L.; Kantzas, A. CFD modeling and validation of bubble properties for a bubbling fluidized bed. Ind. Eng. Chem. Res. 44 (2005) 4254-4266.

[24] Julián, I.; Herguido, J.; Menéndez, M. CFD model prediction of the two-section two-zone fluidized bed reactor (TS-TZFBR) hydrodynamics. Chem. Eng. J. 248 (2014) 352-362.

[25] Patil, D. J.; van Sint Annaland, M.; Kuipers, J. A. M. Critical comparison of hydrodynamic models for gas–solid fluidized beds—Part II: Freely bubbling gas–solid fluidized beds. Chem. Eng. Sci. 60 (2005) 73-84.

[26] A. Bakshi, C. Altantzis, R.B. Bates, A. F. Ghoniem, Eulerian-Eulerian simulation of dense solid-gas cylindrical fluidized beds: Impact of wall boundary condition and drag model on fluidization, Powder Technol. 277 (2015) 47-62

[27] Verma, V.; Deen, N. G.; Padding, J. T.; Kuipers, J. A. M. Two-fluid modeling of three-dimensional cylindrical gas–solid fluidized beds using the kinetic theory of granular flow. Chem. Eng. Sci. 102 (2013) 227-245.

[28] Verma, V.; Padding, J. T.; Deen, N. G.; Kuipers, J. A. M. Bubble formation at a central orifice in a gas–solid fluidized bed predicted by three-dimensional two-fluid model simulations. Chem. Eng. J. 245 (2014) 217-227.

[29] Edelsbrunner, H.; Mucke, E.P.. 3-dimensional alpha-shapes. Acm Transactions on Graphics 13 (1994) 43-72.

[30] Herguido, J.; Menéndez, M.; Santamaría, J. On the use of fluidized bed catalytic reactors where reduction and oxidation zones are present simultaneously. Catal. Today 100 (2005) 181-189.

[31] Pérez-Moreno, L.; Soler, J.; Herguido, J.; Menéndez, M. Stable Steam Reforming of Ethanol in a Two-Zone Fluidized-Bed Reactor. Ind. Eng. Chem. Res. 51 (2012) 8840-8848.

[32] Medrano, J. A.; Julián, I.; García, F.; Li, K.; Herguido, J.; Menéndez, M. Two-Zone Fluidized Bed Reactor (TZFBR) with palladium membrane for catalytic propane dehydrogenation: experimental performance assessment. Ind. Eng. Chem. Res. 52 (2013) 3723-3731.

[33] Gimeno, M. P.; Soler, J.; Herguido, J.; Menendez, M. Counteracting Catalyst Deactivation in Methane Aromatization with a Two Zone Fluidized Bed Reactor. Ind. Eng. Chem. Res. 49 (2010) 996-1000.

[34] Julián, I.; Herguido, J.; Menéndez, M. A non-parametric bubble size correlation for a two-section two-zone fluidized bed reactor (TS-TZFBR). Powder Technol. 256 (2014) 146-157.

[35] Julián, I.; Gallucci, F.; van Sint Annaland, M.; Herguido, J.; Menéndez, M. Hydrodynamic study of a two-section two-zone fluidized bed reactor with an immersed tube bank via PIV/DIA. Chem. Eng. Sci. 134 (2015) 238-250.

[36] Julián, I.; Herguido, J.; Menéndez, M. Particle mixing in a two-section two-zone fluidized bed reactor. Experimental technique and counter-current back-mixing model validation. Ind. Eng. Chem. Res. 52 (2013) 13587-13596.

[37] Julián, I.; Gallucci, F.; van Sint Annaland, M.; Herguido, J.; Menéndez M. Coupled PIV/DIA for fluid dynamics studies on a two-section two-zone fluidized bed reactor. Chem. Eng. J. 207-208 (2012) 122-132.

[38] S. Cloete, S. T. Johansen, S. Amini, Investigation into the effect of simulating a 3D cylindrical fluidized bed on a 2D plane, Powder Technol. 239 (2013) 21-35.

[39] Cammarata, L.; Lettieri, P.; Micale, G. D. M.; Colman, D. 2D and 3D CFD simulations of bubbling fluidized beds using eulerian-eulerian models. Int. J. Chem. React. Eng. 1 (2003) A48.

[40] Gidaspow D. Multiphase flow and fluidization: Continuum and kinetic theory descriptions. Academic Press, San Diego 1994.

[41] L. Schiller, A. Naumann, A drag coefficient correlation, VDI Zeits 77 (1933) 318-320.

[42] C. K. K. Lun, S. B. Savage, D. J. Jeffrey, N. Chepurniy, Kinetic Theories for Granular Flow - Inelastic Particles in Couette-Flow and Slightly Inelastic Particles in a General Flowfield. J. Fluid Mech. 140 (1984) 223-256.

[43] C. K. K. Lun, S. B. Savage, The effects of an impact velocity dependent coefficient of restitution on stresses developed by sheared granular materials, Acta Mech. 63 (1986) 15–44.

[44] S. Cloete, A. Zaabout, S. T. Johansen, M. van Sint Annaland, F. Gallucci, S. Amini, The generality of the standard 2D TFM approach in predicting bubbling fluidized bed hydrodynamics, 235 (2013) 735-746.

[45] A. Bahramian, M. Olazar, G. Ahmadi, Effect of slip boundary conditions on the simulation of microparticle velocity fields in a conical fluidized bed, AIChE J., 59 (2013) 4502-4518.

[46] S. Cloete, S. Amini, S. T. Johansen, On the effect of cluster resolution in riser flows on momentum and reaction kinetic interaction, Powder Technol. 210 (2011) 6-17.

[47] Galavis, A.; González, D.; Alfaro, I.; Cueto, E. Improved boundary tracking in meshless simulations of free-surface flows. Comput. Mech. 42 (2008) 467-479.

[48] Patrick, E. A.; Fischer, F.P. A generalized k-nearest neighbor rule. Information and Control 16 (1970) 128-152.

[49] Asegehegn, T. W.; Schreiber, M.; Krautz, H. J. Investigation of bubble behavior in fluidized beds with and without immersed horizontal tubes using a digital image analysis technique. Powder Technol. 210 (2011) 5410-5427.

[50] Xie, N.; Battaglia, F.; Pannala, S. Effects of using two- versus three-dimensional computational modeling of fluidized beds: Part I, hydrodynamics. Powder Technol. 182 (2008) 1-13.

[51] Davidson, J.F.; Harrison, D. The behaviour of a continuously bubbling fluidised bed. Chem. Eng. Sci. 21 (1966) 731-738.

[52] Mori, S.; Wen, C.Y. Estimation of bubble diameter in gaseous fluidized-beds. AIChE J. 21 (1975) 109-115.

Table 1. Set of closure equations for the TFM simulation of the fluidized bed

Interphase momentum exchange coefficient:	$\begin{cases} K_{gs} = 150\frac{\varepsilon_s(1-\varepsilon_g)\mu_g}{\varepsilon_g {d_p}^2} + 1.75\frac{\varepsilon_s\rho_g\lvert\vec{v}_s-\vec{v}_g\rvert}{d_p} & (\varepsilon_g \leq 0.8) \\ K_{gs} = \frac{3}{4}C_D\frac{\varepsilon_s\rho_g\lvert\vec{v}_s-\vec{v}_g\rvert}{d_p}{\varepsilon_g}^{-1.65} & (\varepsilon_g > 0.8) \end{cases}$
→ *Drag coefficient:*	$\begin{cases} C_D = \frac{24}{\varepsilon_g Re_s}\left[1+0.15(\varepsilon_g Re_s)^{0.687}\right] & (Re_s \leq 1000) \\ C_D = 0.44 & (Re_s > 1000) \end{cases}$
→ *Reynolds number (solids):*	$Re_s = \frac{d_p\rho_g\lvert\vec{v}_s-\vec{v}_g\rvert}{\mu_g}$
Solids stress-strain tensor:	$\bar{\bar{\tau}}_s = \varepsilon_s\mu_s\left(\nabla\vec{v_s} + \nabla\vec{v_s}^T\right) + \varepsilon_s(\lambda_s - \frac{2}{3}\mu_s)\nabla\cdot\bar{v}_s\bar{\bar{I}}$
→ *Solids bulk viscosity*:	$\lambda_s = \frac{4}{3}{\varepsilon_s}^2\rho_s d_p g_0(1+e)\left(\frac{\theta}{\pi}\right)^{1/2}$
→ *Solids shear viscosity*:	$\mu_s = \mu_{s,col} + \mu_{s,fr} + \mu_{s,kin}$
→ *Collisional viscosity*:	$\mu_{s,col} = \frac{4}{5}{\varepsilon_s}^2\rho_s d_p g_0(1+e)\left(\frac{\theta}{\pi}\right)^{1/2}$
→ *Kinetic viscosity*:	$\mu_{s,kin} = \frac{5\rho_s d_p\sqrt{\theta\pi}}{48 g_0(1+e)}\left[1+\frac{4}{5}g_0\varepsilon_s(1+e)\right]^2$
→ *Frictional viscosity*:	$\mu_{s,fr} = \frac{P_s\sin\varphi}{2\sqrt{I_{2D}}}$
→ *Radial distribution function*:	$g_0 = \left[1-(\frac{\varepsilon_s}{\varepsilon_{s,m}})^{1/3}\right]^{-1}$
→ *Algebraic equilibrium model (θ)*:	$\bar{\bar{\tau}}_s\,\nabla\vec{v_s} = \gamma_s$ *(Production = Dissipation)*
→ *Collisional dissipation of energy*:	$\gamma_s = \frac{12(1-e^2)g_0}{d_p\sqrt{\pi}}\rho_s{\varepsilon_s}^2\theta^{3/2}$
Solids pressure:	$P_s = \varepsilon_s\rho_s\theta\left(1+2\,\varepsilon_s g_0(1+e)\right)$

Table 2. List of model parameters used in the *CFD* simulation

Model parameter	Value
Reactor height (cm)	50
Particle density, ρ_s (kg/m^3)	2500
Particle diameter, d_p (μm)	200
Mesh-to-particle size, (-)	≤ 12
Initial solids volume fraction, ε_{s0} (-)	0.25
Maximum packing fraction, $\varepsilon_{s,m}$ (-)	0.65
Restitution coefficient, e (-)	0.95
Gas temperature (^{o}C)	25

FIGURE CAPTIONS

Figure 1. a) Scheme of a 3D TS-TZFBR, b) Simulated TS-TZFBR dimensions (in centimeters), c) Domain mesh

Figure 2. a) 2D porosity distribution map, b) 3D bubble detection as threshold porosity iso-surface, c) Detail of detected 3D bubbles, d) Meshed bubble contours, e) Delaunay triangulation (tetrahedral)

Figure 3. Tetrahedron coordinates

Figure 4. Area-based equivalent bubble diameter for: a) 3D TS-TZFBR, b) pseudo-2D TS-TZFBR. c) Volume-based d_b for a pseudo-2D TS-TZFBR

Figure 5. a) Detected bubble contours as iso-surfaces with a solids volume fraction, $\varepsilon_s = 0.15$. b) Effect of the α-value on the bubbles discretization

Figure 6. Axial evolution of the equivalent bubble diameter in a TS-TZFBR at $u_{gas}/u_{mf} = 2.5$. a) volume-based d_b for a 3D TS-TZFBR, b) area-based d_b for a pseudo-2D TS-TZFBR, c) time-averaged $d_b(z)$ profiles for 3D and pseudo-2D configurations. Dots and circles represent raw and time-averaged $d_b(z)$ values, respectively

Figure 7. Comparison between time-averaged $d_b(z)$ profiles for 3D and pseudo-2D configurations using: a) an area-based d_b, b) a volume-based d_b

Figure 8. a) Spatial distribution of bubble centroids in the bed, b) Radial probability distribution of the bubble centroid location (PD_r)

Figure 9. Free bed surface detection for: a) pseudo-2D bed, b) 3D bed. c) Transient evolution of the free bed surface axial location and gas content in bubbles (or void bed volume)

Figure 10. Probability distribution of: a) bubble size, b) bubble aspect ratio for the pseudo-2D and 3D TS-TZFBR

Figure 11. Bubble velocity profiles: a) $u_b(z)$, b) $u_b(d_b^{0.5})$ for the pseudo-2D and 3D TS-TZFBR

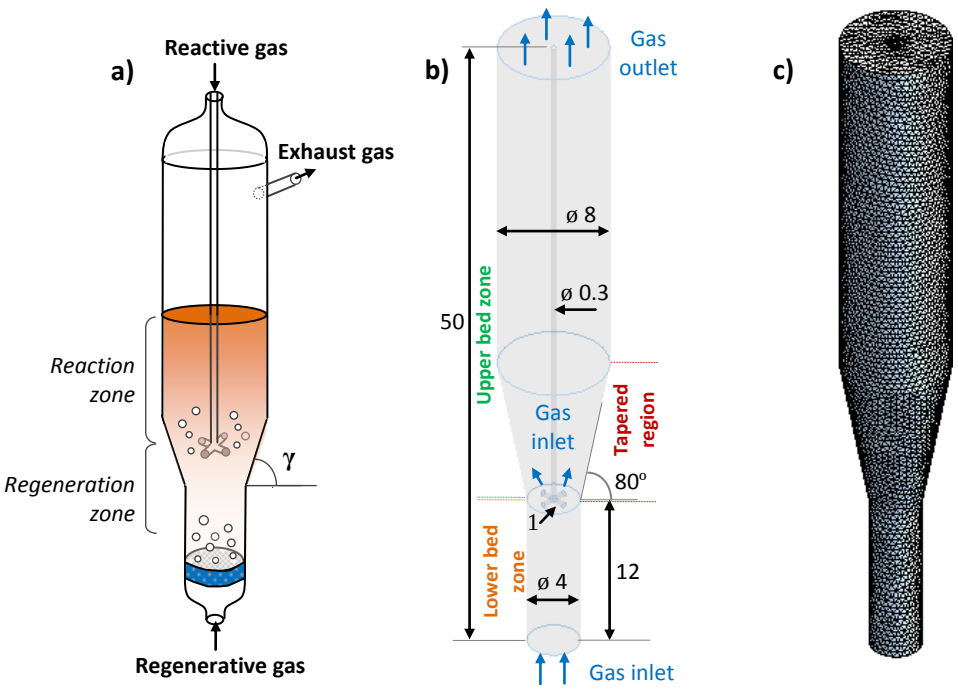
a)
Reactive gas
Exhaust gas
Reaction zone
Regeneration zone
γ
Regenerative gas
b)
Gas outlet
ø 8
ø 0.3
50
Upper bed zone
Gas inlet
Tapered region
80°
1
Lower bed zone
ø 4
12
Gas inlet
c)

Figure 1.

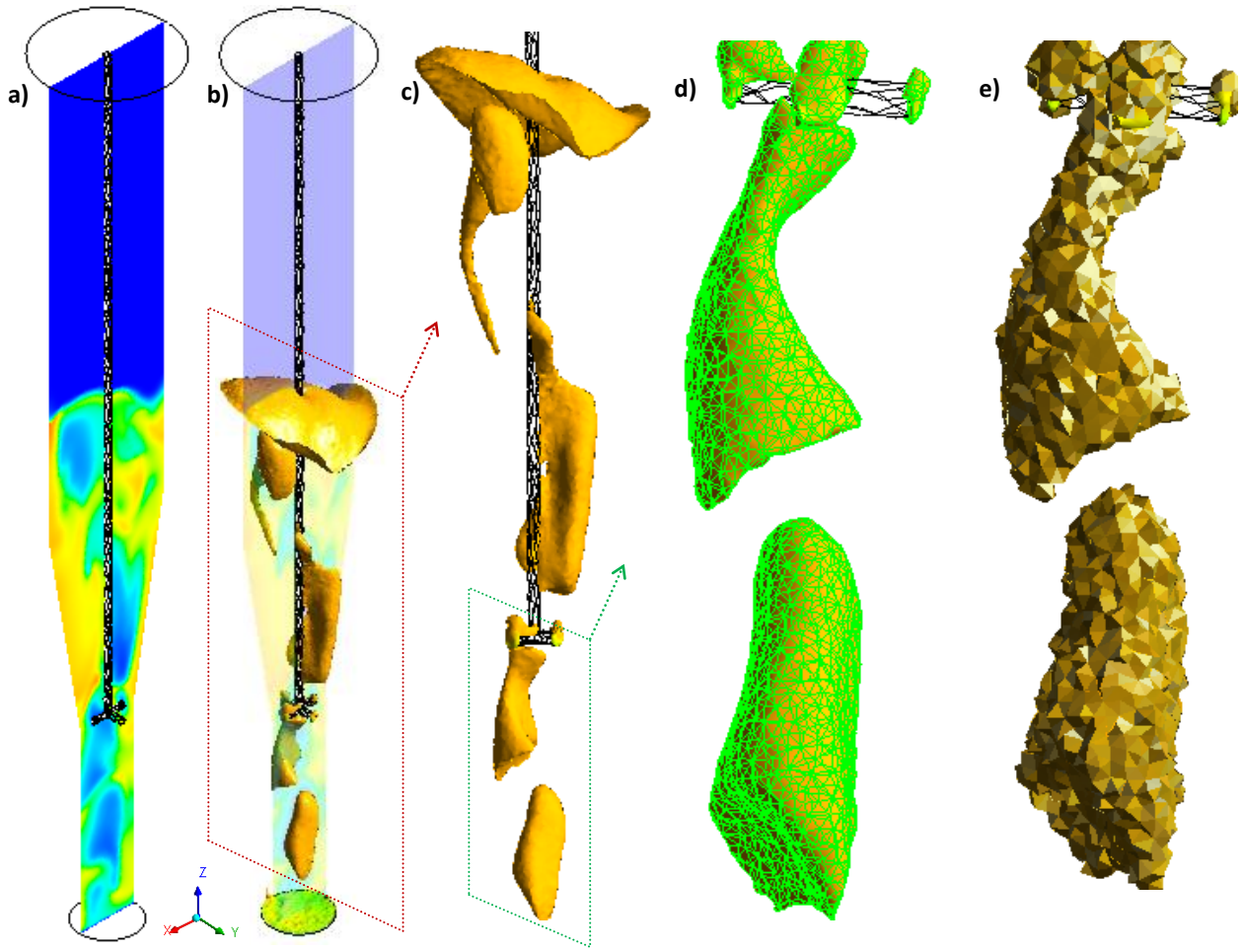

Figure 2.

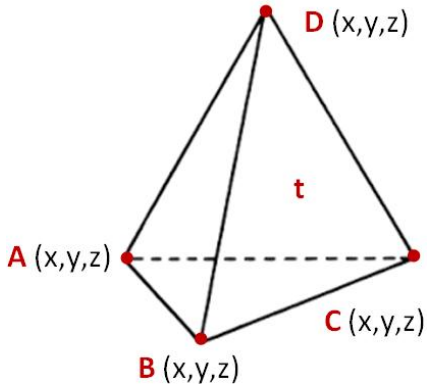

Figure 3.

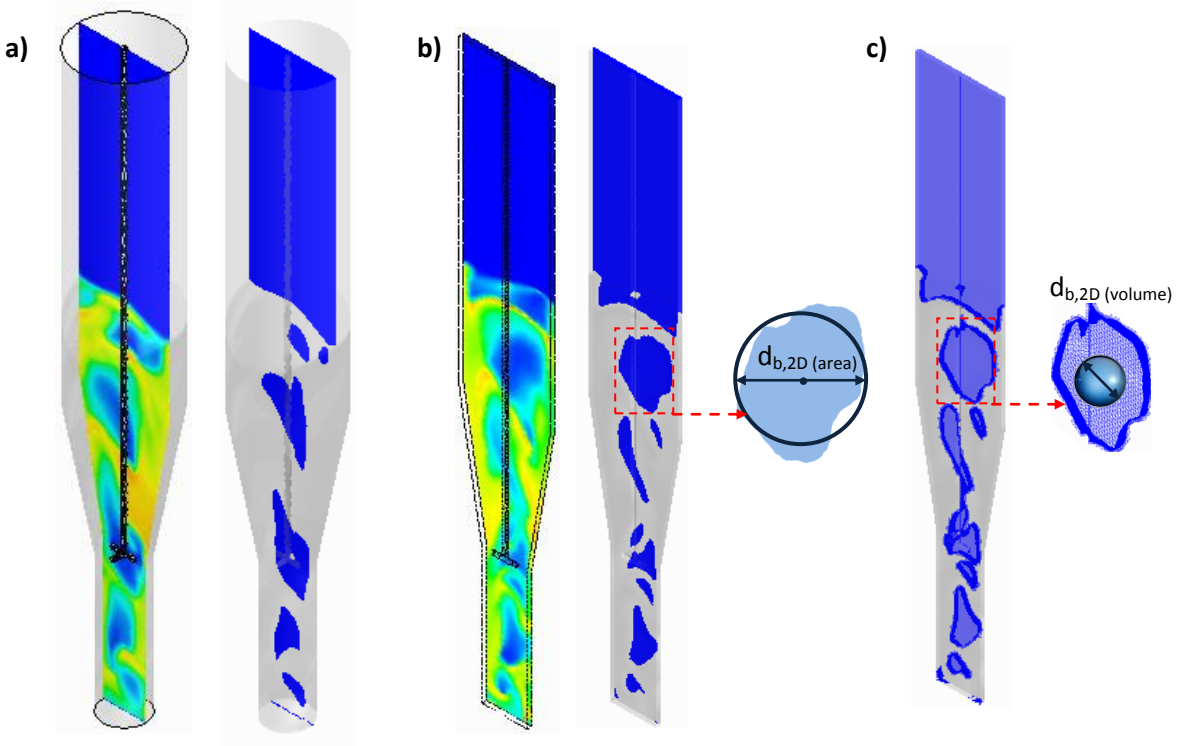

Figure 4.

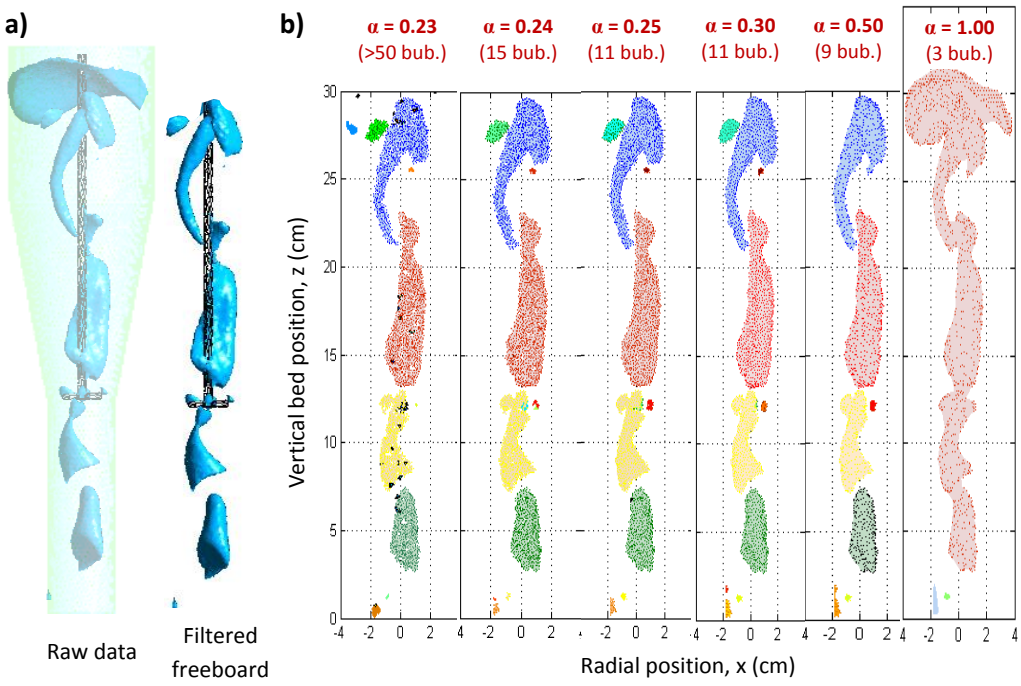
a)
b)
α = 0.23
(>50 bub.)
α = 0.24
(15 bub.)
α = 0.25
(11 bub.)
α = 0.30
(11 bub.)
α = 0.50
(9 bub.)
α = 1.00
(3 bub.)
Vertical bed position, z (cm)
Radial position, x (cm)
Raw data
Filtered freeboard
Iso-surfaces (εs = 0.15)
Triangulation + α-shape filtration

Figure 5.

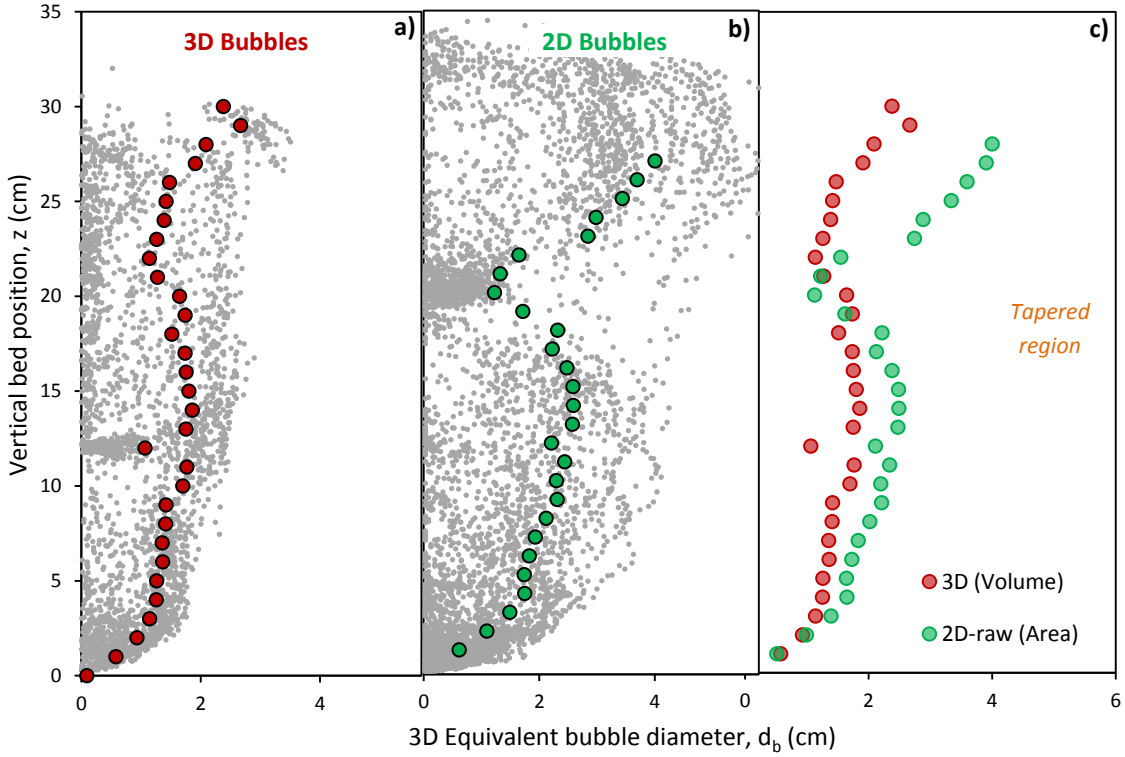
3D Bubbles
a)
2D Bubbles
b)
c)
Tapered region
3D (Volume)
2D-raw (Area)
Vertical bed position, z (cm)
3D Equivalent bubble diameter, d_b (cm)
0
5
10
15
20
25
30
35
0
2
4
6

Figure 6.

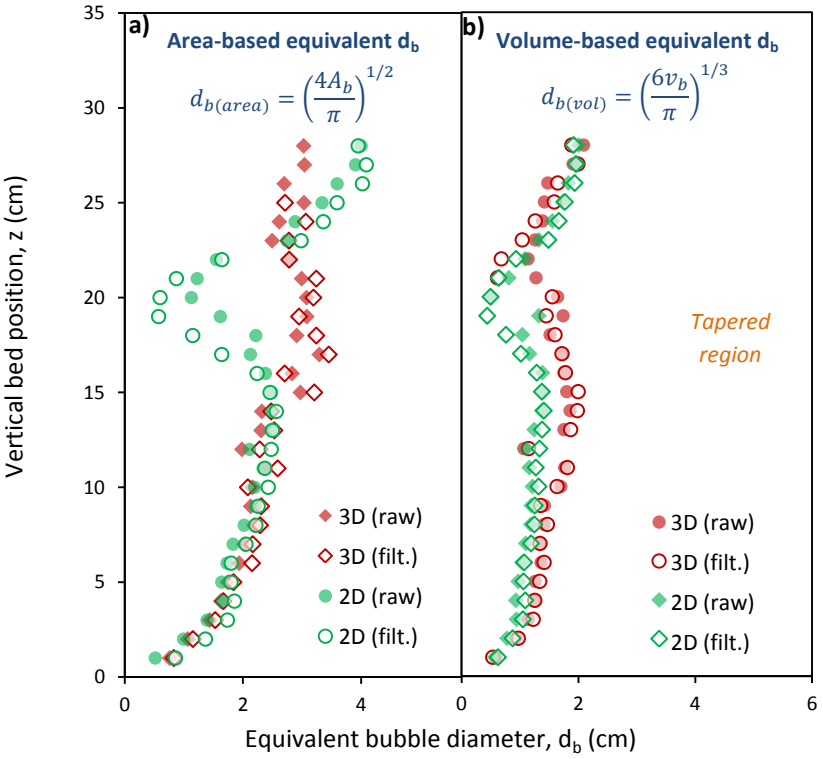
a)
Area-based equivalent d_b
$d_{b(area)} = \left(\frac{4A_b}{\pi}\right)^{1/2}$
b)
Volume-based equivalent d_b
$d_{b(vol)} = \left(\frac{6v_b}{\pi}\right)^{1/3}$
Tapered region
3D (raw)
3D (filt.)
2D (raw)
2D (filt.)
Vertical bed position, z (cm)
Equivalent bubble diameter, d_b (cm)
0
5
10
15
20
25
30
35
0
2
4
6

Figure 7.

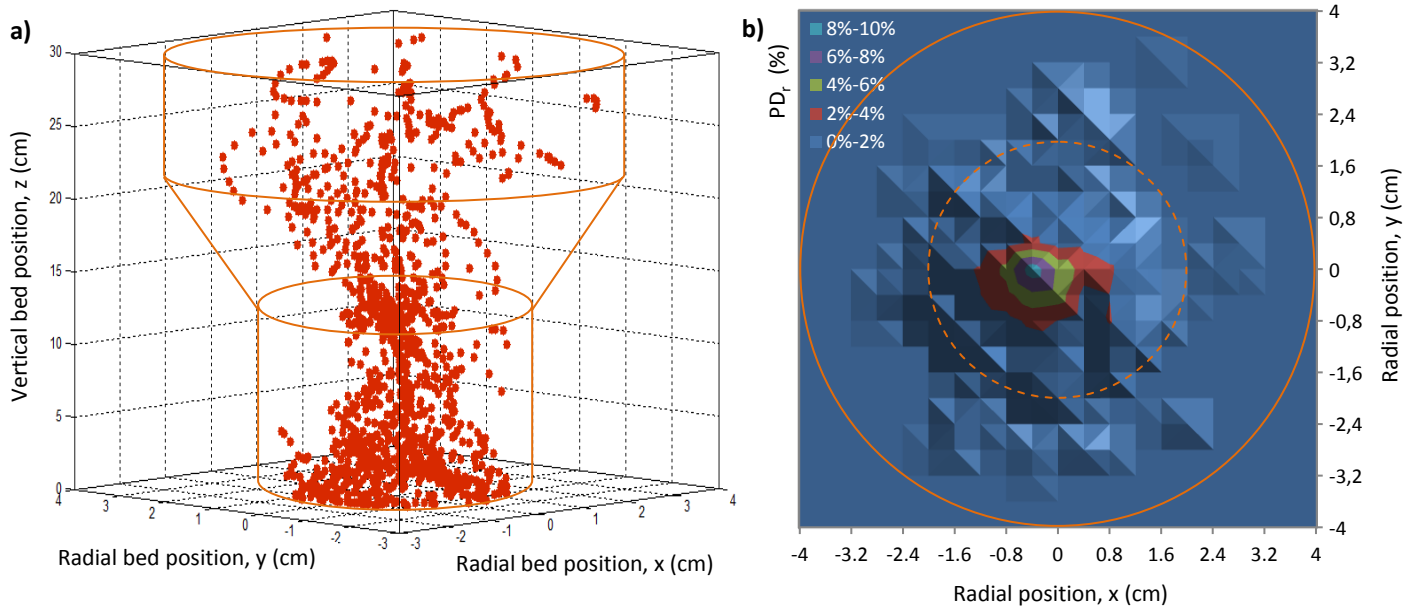
a)
Vertical bed position, z (cm)
Radial bed position, y (cm)
Radial bed position, x (cm)
b)
8%-10%
6%-8%
4%-6%
2%-4%
0%-2%
PDf (%)
Radial position, x (cm)
Radial position, y (cm)

Figure 8.

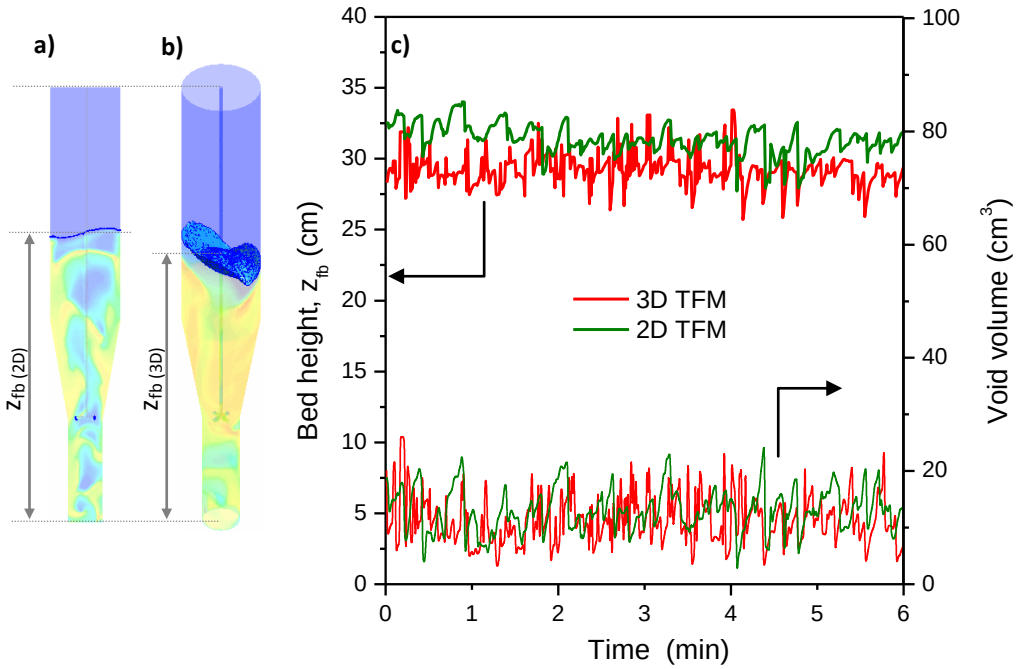
a)
b)
c)
$z_{fb\ (2D)}$
$z_{fb\ (3D)}$
Bed height, z_{fb} (cm)
Void volume (cm^3)
Time (min)
3D TFM
2D TFM
0
5
10
15
20
25
30
35
40
0
20
40
60
80
100
0
1
2
3
4
5
6

Figure 9.

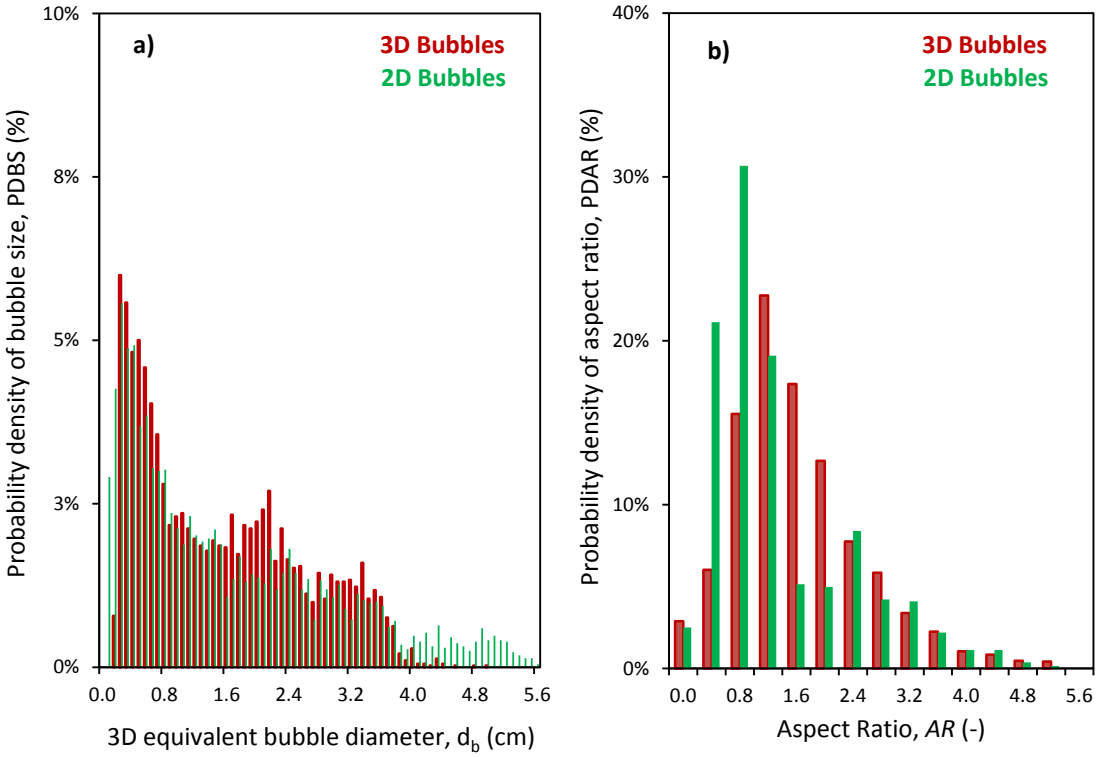
a)
3D Bubbles
2D Bubbles
Probability density of bubble size, PDBS (%)
10%
8%
5%
3%
0%
0.0
0.8
1.6
2.4
3.2
4.0
4.8
5.6
3D equivalent bubble diameter, d_b (cm)
b)
3D Bubbles
2D Bubbles
Probability density of aspect ratio, PDAR (%)
40%
30%
20%
10%
0%
0.0
0.8
1.6
2.4
3.2
4.0
4.8
5.6
Aspect Ratio, *AR* (-)

Figure 10.

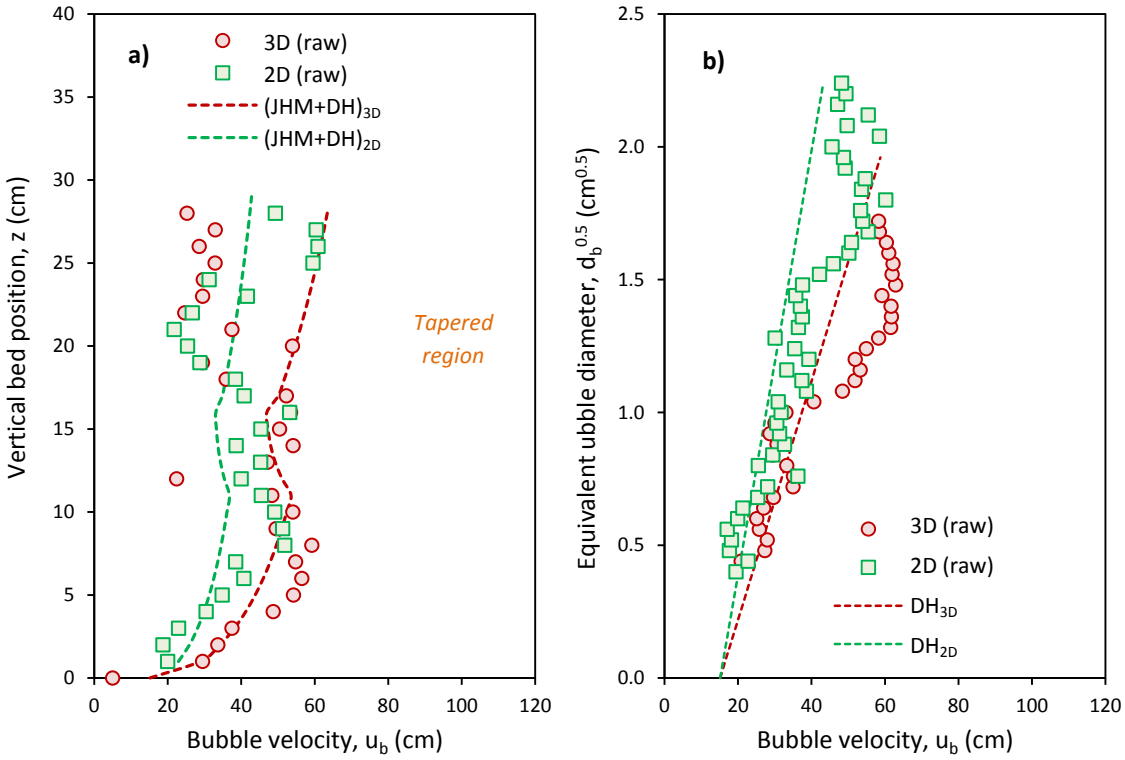
a)
3D (raw)
2D (raw)
(JHM+DH)3D
(JHM+DH)2D
Tapered region
Vertical bed position, z (cm)
Bubble velocity, ub (cm)
b)
3D (raw)
2D (raw)
DH3D
DH2D
Equivalent ubble diameter, db0.5 (cm0.5)
Bubble velocity, ub (cm)

Figure 11.

Artículo IX

J.A. Medrano, I. Julián, J. Herguido, M. Menéndez,
Pd-Ag membrane coupled to a TZFBR for propane dehydrogenation on Pt-Sn/$MgAl_2O_4$ catalyst,
Membranes 3 (2013) 69 – 86

Membranes **2013**, *3*, 69-86; doi:10.3390/membranes3020069

OPEN ACCESS

membranes

ISSN 2077-0375

www.mdpi.com/journal/membranes

Article

Pd-Ag Membrane Coupled to a Two-Zone Fluidized Bed Reactor (TZFBR) for Propane Dehydrogenation on a Pt-Sn/$MgAl_2O_4$ Catalyst

José-Antonio Medrano, Ignacio Julián, Javier Herguido and Miguel Menéndez *

Catalysis, Molecular Separations and Reactor Engineering Group (CREG), Aragón Institute for Engineering Research (I3A), University of Zaragoza, Zaragoza 50018, Spain;
E-Mails: 550765@unizar.es (J.-A.M.); ijulian@unizar.es (I.J.); jhergui@unizar.es (J.H.)

* Author to whom correspondence should be addressed; E-Mail: qtmiguel@unizar.es;
Tel.: +34-976-761-152; Fax: +34-976-762043.

Received: 27 February 2013; in revised form: 11 April 2013 / Accepted: 28 April 2013 / Published: 14 May 2013

Abstract: Several reactor configurations have been tested for catalytic propane dehydrogenation employing Pt-Sn/$MgAl_2O_4$ as a catalyst. Pd-Ag alloy membranes coupled to the multifunctional Two-Zone Fluidized Bed Reactor (TZFBR) provide an improvement in propane conversion by hydrogen removal from the reaction bed through the inorganic membrane in addition to *in situ* catalyst regeneration. Twofold process intensification is thereby achieved when compared to the use of traditional fluidized bed reactors (FBR), where coke formation and thermodynamic equilibrium represent important process limitations. Experiments were carried out at 500–575 °C and with catalyst mass to molar flow of fed propane ratios between 15.1 and 35.2 g min $mmol^{-1}$, employing three different reactor configurations: FBR, TZFBR and TZFBR + Membrane (TZFBR + MB). The results in the FBR showed catalyst deactivation, which was faster at high temperatures. In contrast, by employing the TZFBR with the optimum regenerative agent flow (diluted oxygen), the process activity was sustained throughout the time on stream. The TZFBR + MB showed promising results in catalytic propane dehydrogenation, displacing the reaction towards higher propylene production and giving the best results among the different reactor configurations studied. Furthermore, the results obtained in this study were better than those reported on conventional reactors.

Keywords: catalytic propane dehydrogenation; membrane reactor; Two Zone Fluidized Bed Reactor; Pd-Ag membrane

Nomenclature

dX/dt	propane conversion variation (min^{-1})
dY/dt	yield to propylene variation (min^{-1})
FBR	Fluidized Bed Reactor
$F_{C_3H_8}$	molar flow of propane (mmol min^{-1})
n	stabilization cycle number
$P_{permeate}$	pressure in the permeate side (mbar)
Q_{gas}	volumetric flow (mL_{STP} min^{-1})
$S_{C_3H_6}$	selectivity to propylene (%)
$S_{H_2/Ar}$	H_2 perm-selectivity: ratio of the permeation flux of pure H_2 to pure Ar
T_r	reaction temperature (°C)
TZFBR	Two-Zone Fluidized Bed Reactor
TS-TZFBR	Two-Section Two-Zone Fluidized Bed Reactor
TZFBR + MB	Two-Zone Fluidized Bed Reactor with Membrane
u_{mf}	minimum fluidization velocity (cm^3 cm^{-2} s^{-1})
$u_{r,react}$	relative velocity in the reaction zone (–)
$u_{r,regen}$	relative velocity in the regeneration zone (–)
u_r	relative velocity (–)
W_0	catalyst weight (g)
$X_{C_3H_8}^{eq.}$	propane conversion at equilibrium (%)
$X_{C_3H_8}$	propane conversion (%)
$Y_{C_3H_6}$	yield to propylene (%)
$Y_{C_3H_6}^*$	relative yield to propylene: $Y_{C_3H_6}/X_{C_3H_8}^{eq.}$ (–)
ΔP	partial pressure difference across the membrane (bar)
$\Delta Y_{C_3H_6}$	relative increase in yield to propylene from TZFBR to TZFBR + MB configurations (%)

1. Introduction

Nowadays, propylene is considered one of the most important basic products, especially in the plastics industry for polypropylene production. Propylene may be employed as a raw material for other interesting products, such as acrylonitrile, propylene oxide, different alcohols, cumene and acrylic acid. There are two main ways to produce propylene: as a byproduct in ethylene production and from off-gases in fluid catalytic cracking (FCC). Nevertheless, propylene consumption is increasing faster than ethylene consumption [1]. In addition, the increasing availability of natural gas, obtained by fracking, is reducing the use of naphtha as feedstock for ethylene production and this decreases the amount of propylene obtained by this process. Therefore, the development of on-purpose propylene

production technologies is of considerable interest. Current alternatives comprise metathesis of ethylene and butenes and alkanes dehydrogenation [2]. Catalytic propane dehydrogenation (PDH) represents one of the most promising on-purpose technologies. In the PDH process, propane can be directly transformed into propylene in the presence of a selective catalyst.

Propane dehydrogenation [Equation (1)] is a reaction limited by the thermodynamic equilibrium which main products are propylene and hydrogen. Hydrogen, as byproduct, is one of the most important energy vectors for the future [3]. Catalytic PDH is an endothermic reaction ($\Delta H_{298K} = -124$ kJ/mol) which is normally carried out at 500–600 °C and at atmospheric pressure, employing catalysts based on Pt [4,5] or Cr [6,7]. Under these operational conditions, undesirable secondary reactions take place [8,9], e.g., thermal cracking, propane hydrogenolysis or coke formation [Equations (2–4)]. Secondary reactions affect the selectivity to propylene and coke formation produces a carbon-thin layer over the catalyst active surface causing its deactivation [10,11]. As a result, the catalyst needs to be regenerated by removing the coke from its surface. Moreover, the extension of these secondary reactions increases at higher reaction temperatures, which implies an important drawback for this endothermic reaction.

$$C_3H_8 \longleftrightarrow C_3H_6 + H_2 \quad (1)$$

$$C_3H_8 \longrightarrow CH_4 + C_2H_4 \quad (2)$$

$$C_3H_8 + H_2 \longrightarrow CH_4 + C_2H_6 \quad (3)$$

$$C_3H_8 \longleftrightarrow 3CH_{0.5}\,(\text{coke}) + 3.25H_2 \quad (4)$$

Traditionally, industrial processes solve PDH limitations by employing serial reactors where reaction, purge and catalyst regeneration take place cyclically in a semi-continuous process. Other technologies co-feed propane and hydrogen mixtures in order to reduce coke deposition. As a result, lower yields to propylene are obtained.

With the aim of improving the yield to propylene and reducing the catalyst deactivation by coke deposition over the catalyst surface, several authors have proposed catalysts based on Pt alloyed with other elements such as Sn, Ga, or In [5,12,13]. Some authors have also proposed the use of Ce, K or Ni as catalyst promoters [10,14,15]. Zeolites have also been proposed as catalyst support [15,16]. In previous works by our group, Pt-Sn-K/γ-Al_2O_3 and Pt-Sn/$MgAl_2O_4$ catalysts were used to carry out PDH [17,18]. Pt-Sn-K/γ-Al_2O_3 showed higher coke formation than Pt-Sn catalyst supported on $MgAl_2O_4$ spinel, probably because of the low acidity of the latter support. The presence of Pt provided high catalytic activity towards olefins. Additionally, Sn as catalyst stabilizer improved the dehydrogenation-to-cracking ratio and reduced Pt sintering.

The TZFBR (Figure 1A) is an original reactor able to solve the limitation represented by coke formation in heterogeneous catalytic reactions [19]. This reactor has two different feed points placed at the bottom and at an intermediate point of the catalytic bed. This results in a system with two different atmospheres, *i.e.*, oxidative and reductive zones. The reactive agent (e.g., propane) is supplied in an intermediate position of the reactor. Therefore, the reaction of interest occurs in the upper zone of the fluidized bed or "reaction zone". An oxidant agent (e.g., oxygen diluted in an inert gas) is supplied through the feed point at the bottom of the bed. This oxidant removes by combustion the coke deposited over the catalyst coming from the upper bed zone. The catalytic surface, thus, recovers its

initial activity in the lower part of the reactor or "regeneration zone". The catalyst circulation characteristic of fluidized reactors [20] implies a continuous transference of catalytic solid between the reactive and regenerative bed zones. This process integration enables catalyst activity to be maintained throughout the time on stream. By extension, the TZFBR is here proposed as a compact multifunctional solution for carrying out this kind of catalytic reactions where the catalyst suffers from a rapid deactivation. The TZFBR system has already been tested in several catalytic dehydrogenations such as catalytic propane and butane dehydrogenation with different catalysts, as well as in other applications [8,21,22]. However, an adequate optimization of the TZFBR operational conditions is required in order to achieve a suitable reactor performance [17]. The oxidizing agent should not reach the "reaction zone" because in such an event it would interact with the reactive agent, resulting in an important selectivity loss. It is also important to avoid the oxidant flow supplied at the bottom of the reactor from being too low because in such event the catalyst would not be completely regenerated.

Figure 1. (**A**) Schematic drawing of the Two-Zone Fluidized Bed Reactor (TZFBR); and (**B**) of the Two-Section Two-Zone Fluidized Bed Reactor (TS-TZFBR) with a Pd-Ag membrane.

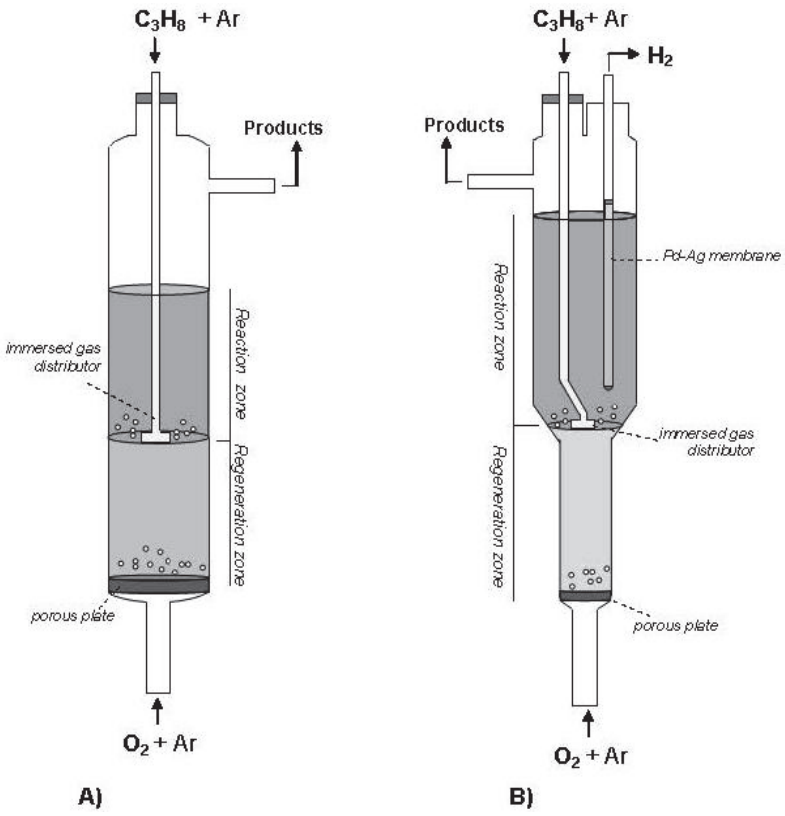

In this work, the use of an immersed Pd alloyed membrane coupled to a TZFBR represents two-fold process intensification. For this reason, operational conditions need to be even more carefully selected in order to get a proper performance of this novel membrane reactor concept.

Membrane reactors involve a multifunctional system, which is able to integrate a chemical reaction (e.g., oxidative reforming, hydrocarbon dehydrogenation, *etc.*) and a separation process through the membrane in the same unit [23,24]. Thus, membranes are not only considered as a separation system. Besides, they also influence the chemical reaction. The limitations of these reactors are related to the

adaptability between the membrane and the reaction [25]. Typical membrane reactors include Catalytic Membrane Reactors (CMR), Packed Bed Membrane Reactors (PBMR) and Fluidized Bed Membrane Reactors (FBMR), as described in recent reviews [26,27].

These reactors are often employed in reactions limited by the equilibrium conversion. Membrane reactors have two main applications: for product selective separation (extractive application) or reactive supply (distributive application) [25]. The most extensively studied processes within membrane reactor technology are based on inorganic Pd and Pd alloy membranes for selective H_2 removal in alkane dehydrogenations and catalytic reforming processes [28,29]. These processes are limited by the thermodynamic equilibrium, where a selective H_2 removal (H_2 is a product of the main reaction) implies an improvement in the yield of the process towards the product of interest. A limitation for the industrial implementation of these reactors is the considerable increase in coke deposition over the metal surface in reactions with hydrocarbons at high temperatures, such as dehydrogenation and reforming processes [30]. This deposition inhibits the H_2 separation through the membrane and causes an important decrease in the process conversion [18,31].

As a multi-purpose reactor, the TZFBR coupled with a Pd or Pd alloyed membrane reactor represents an appropriate system to overcome these limitations in a PDH process. Figure 1B shows a schematic drawing of the TZFBR with a Pd-Ag membrane (TZFBR + MB). This multifunctional reactor provides *in situ* catalyst regeneration due to the TZFBR configuration, and a displacement of the main reaction towards propylene production by the selective removal of H_2 in the "reaction zone", *i.e.*, molecular separation through the membrane. In the present work, a novel Two-Section configuration of the TZFBR has been employed (TS-TZFBR). In order to get a better control of the reactor fluid dynamics in each reactor zone, different bed sections between both zones have been implemented to provide low regenerative-to-reactive flows if required [18,32]. The tapered bed angle between zones was selected according to the recommendations from Julián *et al.* [20], in order to avoid defluidized catalytic regions within the upper bed section.

In a previous work, catalytic propane dehydrogenation was tested in the TS-TZFBR configuration with a hollow fiber palladium membrane employing Pt-Sn/$MgAl_2O_4$ as catalyst [17]. However, due to the limitations of hollow fiber Pd membranes, promising results were only obtained at low reaction temperatures. In the present study a commercial dense Pd-Ag membrane supported on porous stainless steel (*REB Research*®) is coupled to the TZFBR with the aim of testing catalytic propane dehydrogenation at higher reaction temperatures. The ability to work at higher temperatures has several process benefits such as increased propane conversion, and higher hydrogen permeation. Pd membranes supported on porous stainless steel have better mechanical resistance than Pd membranes supported on ceramic hollow fibers. Commercial tubular membranes used in this work have the following dimensions: 31.7 mm external diameter, 178 mm length and 76 μm thick Pd-Ag layer.

The effect of the different process intensifications for the catalytic PDH on Pt-Sn/$MgAl_2O_4$ will be presented step by step, using different reactor configurations: TZFBR without oxygen (acting as a traditional Fluidized Bed Reactor, FBR), TZFBR, and multifunctional TZFBR + MB. The purpose of the experimental series with the FBR at different reaction temperatures is to evaluate the catalyst deactivation by coke deposition. The decrease in conversion with time-on-stream is related to the amount of coke deposited over the catalyst. The goal of using a TS-TZFBR for PDH is to evaluate the reactor performance in terms of *in situ* catalyst regeneration and system stability. Finally, the

multifunctional TZFBR + MB is employed to illustrate the improvement in the yield to propylene by displacement of the reaction equilibrium towards products resulting from the selective hydrogen removal. This last study also deals with the PDH system stability along the time on stream and the ability of counteracting the catalyst deactivation.

2. Experimental Section

2.1. Catalyst Preparation

Pt-Sn/$MgAl_2O_4$ was prepared in two steps. Firstly, the catalyst support was synthesized by a sol-gel method. Secondly, catalytic active compounds (Pd and Sn) were deposited on the support by wet incipient impregnation.

Magnesium ($Mg(NO_3)_2{\cdot}6H_2O$, Aldrich, 99%) and aluminum ($Al(NO_3)_3{\cdot}9H_2O$, Aldrich, 99%) compounds were dissolved and reacted for 1 h at 50 °C and pH 9 while maintaining vigorous stirring. The resulting $MgAl_2O_4$ white gel was precipitated and aged at atmospheric conditions overnight. The gel was then filtered and dried at 120 °C overnight. Finally, the support was calcined in air in two consecutive steps: first, heating the gel at 350 °C for 2 h and then at 800 °C for 8 h (2 °C/min heating rate in both steps). The $MgAl_2O_4$ support was then sieved to 75–150 μm particle size and characterized by X-ray diffraction and BET specific surface area.

The second part of the catalyst preparation consisted of coating the support with the catalytic precursors. Tin and platinum precursors ($SnCl_2$, Aldrich, 98% and H_2PtCl_6, Aldrich, 8% dissolution in water) were deposited over the surface of the support by a wet incipient impregnation method in two consecutive steps. First, tin was impregnated during 6 h and dried at 120 °C overnight. Later, platinum was impregnated by the same method. Finally, the catalyst was calcined in air at 650 °C for 3 h (2 °C/min heating rate) and again sieved to 75–150 μm particle size.

With the aim of establishing suitable experimental conditions in the different fluidized reactors, the minimum fluidization velocity, u_{mf}, of the catalyst was measured. This test was carried out at 550 °C in a straight FBR with Ar, the inert gas employed during the present study, and a value of u_{mf} = 0.53 cm/s (*i.e.*, 0.163 cm^3(STP) cm^{-2} s^{-1}) was obtained.

Before carrying out the experimental study, the catalyst had to be stabilized to guarantee the reproducibility of the results. The catalyst stabilization consisted of three cyclical steps where the catalyst was first reduced with diluted H_2 during 2 h; then PDH was carried out in the presence of diluted C_3H_8 (2 h); and finally, coke deposited over the catalyst surface was removed with a stream of diluted oxygen. This cyclical process was repeated until two consecutive results were identical. The catalyst stabilization was carried out at 550 °C in a traditional fluidized bed reactor, where the conditions of the different streams in each step are summarized in Table 1.

Table 1. Experimental conditions during the stabilization cycles.

Variable	Reduction	Reaction	Regeneration
Feed composition	Ar:H_2 = 3:1	Ar:C_3H_8 = 1:1	Ar:O_2 = 20:1
u_r	3	3	3
Time (h)	2	2	Until CO and CO_2 signals not seen
W_0/F_{C3H8} (g min $mmol^{-1}$)	–	12.2	–

2.2. Materials Characterization

X-Ray diffraction data were obtained at 298 K in a "D-Max Rigaku" diffractometer with mobile anode. This works at 40 kV and 80 mA with a Cu anode and graphite monochromator to select a CuKα1.2 radiation. The diffraction angle during the measurements was varied between 10° and 90° with a 0.03° step. The BET specific surface of the catalyst was obtained in a "Micrometrics ASAP 2020".

Commercial Pd-Ag membranes were characterized by the permeation flux at different temperatures and pressures. These tests were carried out with the membrane inside the reactor, but without the presence of the catalytic bed. For this purpose, a constant flow rate of H_2 + Ar mixture was supplied at the bottom inlet of the reactor. When a pressure drop across the membrane was applied with a vacuum pump, hydrogen permeated selectively through the membrane. This resulted a reduced outlet gas flow in the reactor related to the removal of hydrogen through the membrane. Hydrogen permeation results were, therefore, obtained by difference between retentate side outlet flows with and without applying certain pressure drop. Membrane permeation studies were carried out employing different H_2/Ar ratios and temperatures. Finally, a closure test with pure Ar was carried out to verify the selectivity of the Pd alloy membrane. The retentate outflow measured in this test was the same with and without vacuum. This indicated that no Ar was flowing through the membrane, illustrating the membrane full selectivity towards hydrogen.

2.3. Reaction

Catalytic propane dehydrogenation was carried out in two different reactor facilities. A conventional FBR was first employed during the catalyst stabilization step. This reactor consisted of a 2.8 cm inner diameter quartz tube where the gases are fed at the bottom inlet of the reactor. The TZFBR + MB (Figure 1B) consisted of a quartz column with different sections in the reaction and the regeneration zones. The upper and lower inner diameters of the reactor were 3.0 and 1.8 cm, respectively, with a 60° angle (with respect to the horizontal position) in the transition between both zones. Having a different section in the lower zone provides better control of the fluid dynamic regime in both regions compared to a straight column reactor [31]. The oxidant agent (diluted oxygen) is fed through the bottom of a 40 μm porous quartz plate, which acts as gas distributor and catalytic bed support inside the reactor. Propane is fed at an intermediate point of the transition bed section. This reactive gas is fed through a 4-axis immersed gas distributor with 4 mm external diameter. The commercial Pd-Ag membrane was placed inside the reaction zone. The membrane consists of a dense layer of 1/8″ (3 mm) external diameter (0.03″ wall) and 5″ (12.7 cm) in length, sealed at one end and brazed to a stainless steel stub at the other. Its high mechanical resistance means that it can be immersed directly in the fluidized bed without an external membrane-shell for its protection, which was not the case in our previous works with Pd-membranes [17,18]. Both the commercial membrane and the propane distributor were connected to the top wall of the reactor.

Each reactive gas flow was controlled by a set of mass flow controllers. The furnace temperature control was carried out by an immersed thermocouple (Controller 3116, Eurotherm). Reaction products were analyzed by online gas chromatography (μGC-R3000, SRA Instruments) and a vacuum

pump (2P-3, Start) was employed to generate the vacuum inside the membrane for the hydrogen permeation.

A heating rate of 2 °C/min was employed to establish the reaction temperature, with the aim of avoiding membrane damage. Before the reaction started, the catalyst was activated for 2 h at 550 °C with hydrogen to reduce the platinum oxide species to Pt^0. Catalytic propane dehydrogenation was, then, carried out at different reaction temperatures between 500° and 575 °C and with different W_0/F_{C3H8} ratios (*i.e.*, ratio of catalyst mass to propane molar flow) between 15 and 35 g min mmol^{-1}, under the conditions described in the Table 2. A catalyst mass of 70 g was employed during the entire experimental series. After each experiment, the catalyst was fully regenerated with a diluted oxygen stream at 550 °C until CO and CO_2 signals were not detected by gas chromatography.

Table 2. Experimental series.

Variable	FBR (TZFBR without oxygen)	TZFBR	TZFBR + MB
T (°C)	500–575	500–575	500–575
$u_{r,regen}$ (–)	2.5	2.5	2.5
$u_{r,react}$ (–)	1.75	1.75	1.75
Oxygen (%)	–	1–5	1–5
W_0/F_{C3H8} (g min mmol^{-1})	21.1	15.1–35.2	15.1–35.2
ΔP (bar)	–	–	1.1

3. Results

Figure 2A shows that spinel $MgAl_2O_4$ was properly synthesized since the peaks in the X-Ray diffraction agree with its theoretical structural geometry. The adsorption isotherm represented in Figure 2B shows a typical type-4 adsorption curve, which is the characteristic isotherm of mesoporous solids. This is corroborated by the BJH analysis, where the average pore size obtained was 15.2 nm. The BET area shows high values (146 m^2 g^{-1}) with a suitable pore volume (0.61 cm^3 g^{-1}).

Figure 2. (**A**) XRD pattern; and (**B**) N_2 adsorption-desorption isotherms at 77 K for $MgAl_2O_4$ support.

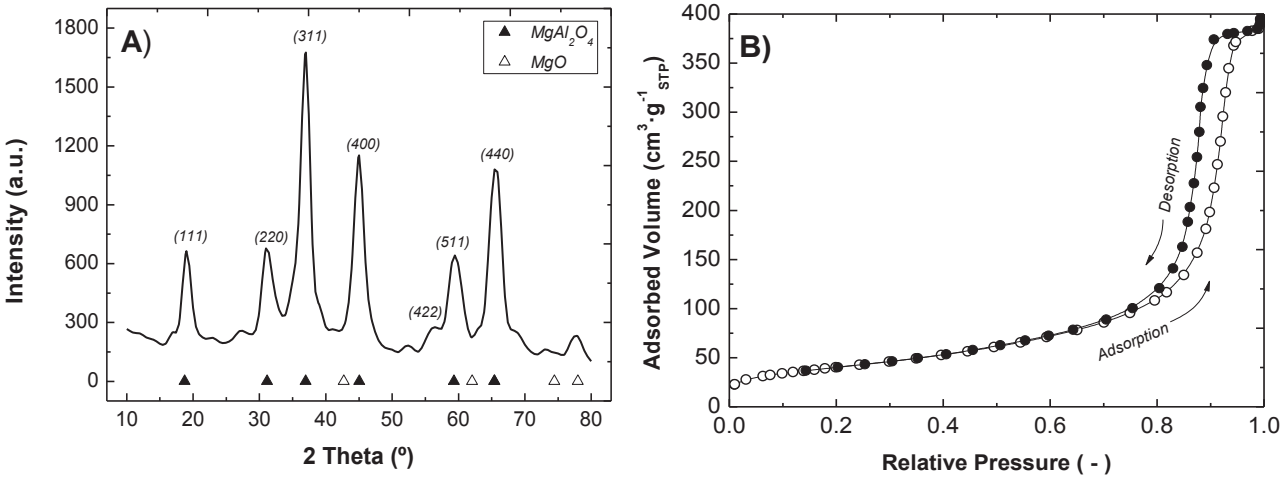

Consecutive stabilization cycles (reduction-reaction-regeneration) were carried out at 550 °C in a traditional fluidized bed reactor (FBR) until two consecutive cycles with similar results were obtained. The objective was to ensure PDH process reproducibility. Figure 3 shows curves of propane conversion (X_{C3H8}) and selectivity to propylene (S_{C3H6}) at different cycles, where the differences in performance between the first and the consecutive cycles are related to the catalyst stabilization process. It can be observed that results from the second and the third cycle were similar, indicating that a stable catalyst performance had been reached.

Figure 3. Propane conversion and selectivity to propylene for three stabilization (reduction + reaction + regeneration) cycles of the fresh Pt-Sn/$MgAl_2O_4$ catalyst.

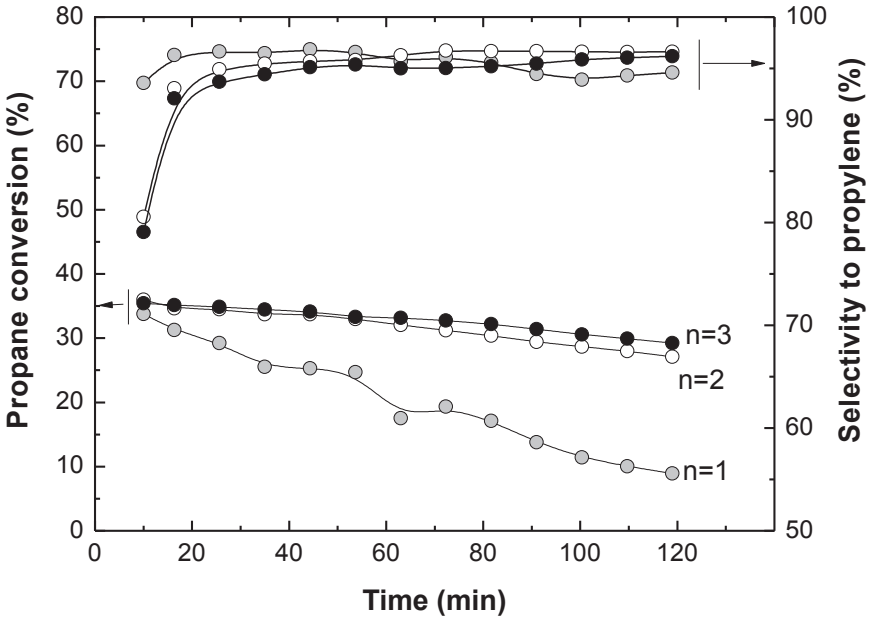

With the aim of studying the influence of the reaction temperature on the catalyst deactivation, different experiments were carried out in the TZFBR without feeding oxygen in the lower zone. The reactor performance was similar to that of a traditional fluidized bed reactor. With this reactor configuration, the final comparison between all configurations can be made more easily because the physical reactor is the same for all experiments.

The results for this experimental series in the TZFBR without oxygen being fed in the lower zone are shown in Figure 4. It can be seen that a high reaction temperature favors higher propane conversion, but lower selectivity to propylene. This is due to the secondary reactions such as cracking [Equations (2) and (3)] and coking [Equation (4)], which are favored at high temperatures. These results suggest that carrying out catalytic propane dehydrogenation in a traditional fluidized bed reactor is not efficient. The catalyst deactivation by coke deposition requires the use of a second reactor where the catalyst can be regenerated.

Figure 4. Propane conversion and selectivity to propylene for three stabilization (reduction + reaction + regeneration) cycles of the fresh Pt-Sn/$MgAl_2O_4$ catalyst.

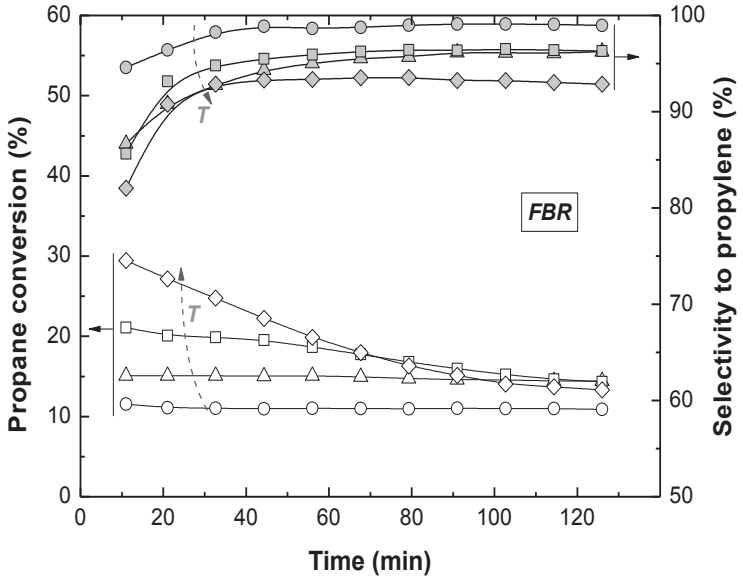

Figure 4 shows that catalyst deactivation was higher when the reaction temperature was increased. It was found that the average slope of the propane conversion along the time on stream was larger at higher temperatures. This means that coke was deposited faster at high temperatures, implying a quicker catalyst activity loss. This catalyst activity loss has been measured at each temperature as the slope (with the sign changed) in the linear regression of the experimental data ($-dX/dt$). This slope at each reaction temperature is represented in Figure 5. The amount of coke deposited over the catalyst was determined during the regeneration step. Results show that the higher the reaction temperature, the higher the amount of coke deposited, as can also be seen in Figure 5. This confirms that the catalyst deactivation rate and the amount of coke formed in the reaction are linearly related.

Figure 5. Propane conversion decay in the TZFBR without oxygen (measured as $-dX_{C3H8}/dt$), and amount of coke formed during reaction, both as a function of the temperature. Lines present as a visual help only.

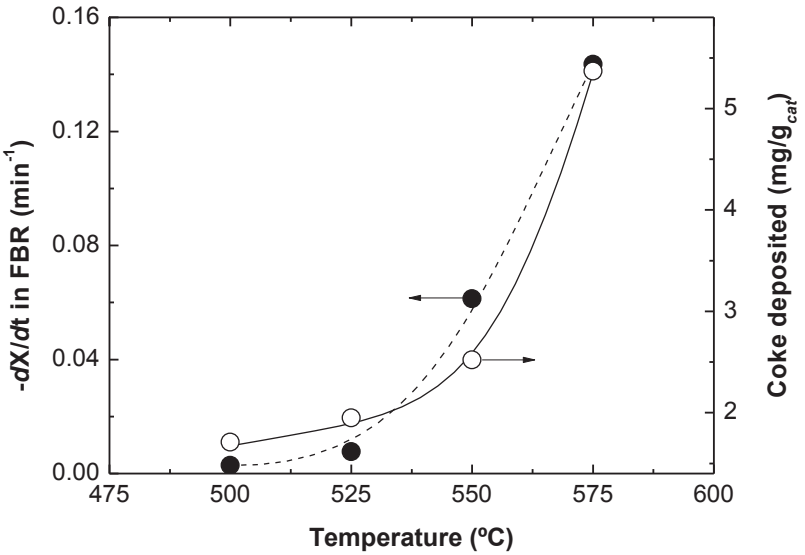

After proceeding with the experimental series in the multifunctional reactor, the results of the membrane characterization are shown in Figure 6.

Figure 6. H_2 permeating flux *vs.* Sieverts' driving force for Pd-Ag membrane at different temperatures (550–575 °C), Q_{gas} = 200 mL_{STP} min^{-1}, $P_{permeate}$ = 1 mbar.

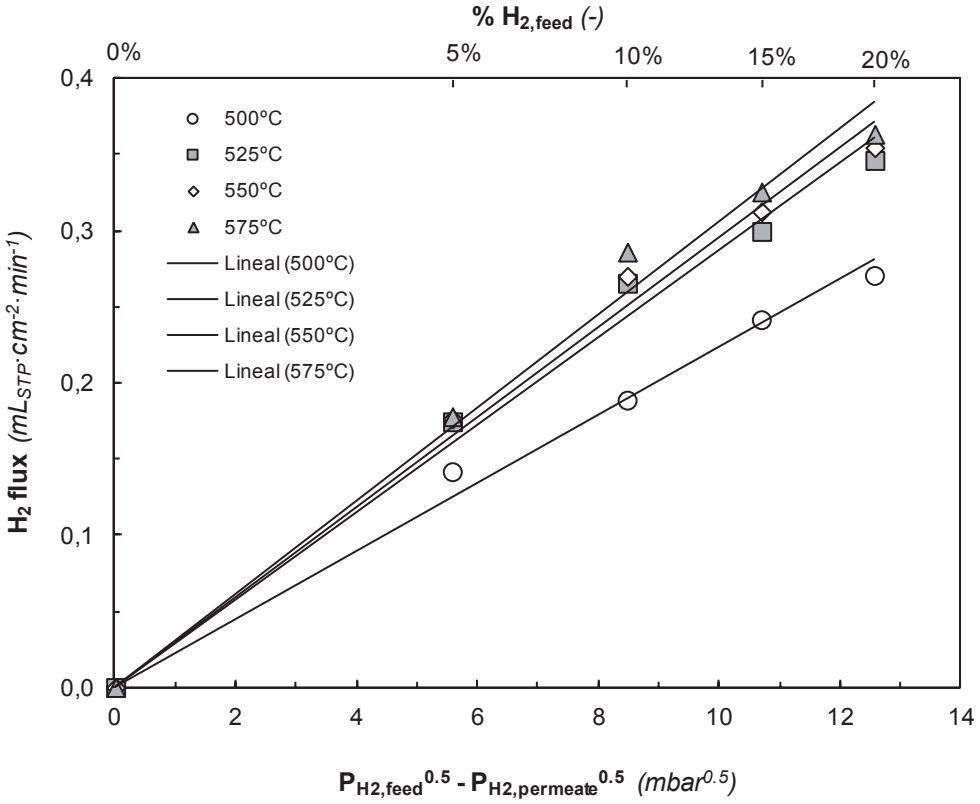

Inert gas did not permeate through the Pd-Ag layer under the conditions studied with a gas stream of pure Ar. This implies that the membrane consists of a defect-free continuous alloy layer and infinite H_2 perm-selectivity ($S_{H2/Ar} = \infty$). Permeation tests as those shown in Figure 6 were carried out before and after a number of experimental series in PDH reactive conditions, showing similar hydrogen permeation and selectivity. This result confirms good membrane stability. The almost linear H_2 permeation trend against the square root of the pressure drop indicates that H_2 permeation takes place via metallic diffusion, where the permeating flux is a function of the Sieverts' driving force. Moreover, the permeation flux is also affected by the temperature. Hydrogen permeation increases linearly with the difference of the square root of the H_2 partial pressure at both sides of the membrane, which implies that the permeation is controlled by proton diffusion through the Pd alloy membrane. Besides, higher temperatures provide higher hydrogen fluxes because the diffusion is favored.

Reactions in the TZFBR and in the TZFBR + MB were carried out consecutively, without catalyst regeneration in between. Firstly, the TZFBR + MB unit was used as a conventional TZFBR in which no pressure drop was applied across the Pd-Ag membrane. Once PDH achieved a steady state in this reactor configuration, the vacuum pump was connected. The system behaved then as a membrane reactor and hydrogen could be removed. As a result, the effect of the Pd-Ag membrane on the steady state operation of the conventional TZFBR could be analyzed in a single experiment and reactor unit by just switching on/off the vacuum pump. Figure 7 shows the evolution of propane conversion and

selectivity to propylene at several reaction temperatures for the first 2 h, when the system operated as TZFBR. The system reached a steady state catalytic activity at all reaction temperatures due to the *in situ* catalyst regeneration. Oxygen requirements at each temperature correspond with an optimum value, enough to counteract the catalyst deactivation but not so large that oxygen can reach the reaction zone. This optimum was determined in a previous work [17] for each temperature, being roughly 1%, 2%, 3%, and 5% (expressed as the percentage of oxygen fed in the regeneration zone relative to the total gas fed to the reactor) for 500, 525, 550, and 575 °C, respectively. After 2 h of reaction, the vacuum pump was turned on and hydrogen was selectively removed from the reaction zone through the Pd-Ag membrane, modifying the conversion reached. The new equilibrium was reached faster than in the previous configuration, obtaining constant values for selectivity to propylene and propane conversion from the first analysis (Figure 8). This was because the new stationary state was close to the previous one attained in the TZFBR configuration. An improvement in the yield to propylene was observed at all the reaction temperatures. Furthermore, the yield to propylene remained constant because of the performance of the multifunctional reactor, where catalyst is regenerated in the lower zone. This represents a substantial improvement of the system compared to membrane reactors, which provide higher coke formation in dehydrogenation reactions ending up with catalyst deactivation and a significant decrease in the process yield. In all cases the TZFBR + MB has shown an improvement in the results in relation to the TZFBR, with ΔY_{C3H6} = 2.54%, 1.97%, 1.88%, and 1.83% at 500, 525, 550, and 575 °C, respectively. Better relative improvements were obtained at low temperatures. This implies that the increase in the propane dehydrogenation rate by raising the temperature is greater than the increase in the hydrogen permeation flux through the membrane by the same factor.

Figure 7. Propane conversion and propylene selectivity at different reaction temperatures (○ 500 °C; Δ 525 °C; □ and × 550 °C; ◊ 575 °C) in the TZFBR, working at the optimum oxygen percentage. Operating conditions are similar to Figure 4.

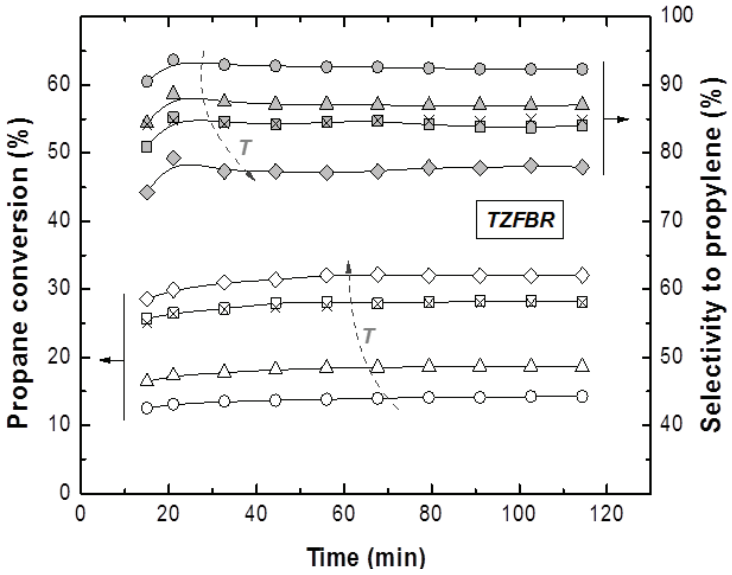

Figure 8. Propane conversion and propylene selectivity at different reaction temperatures (○ 500 °C; Δ 525 °C; □ and × 550 °C; ◊ 575 °C) in the Membrane (TZFBR + MB), working at the optimum oxygen percentage. Other operating conditions are similar to Figure 4.

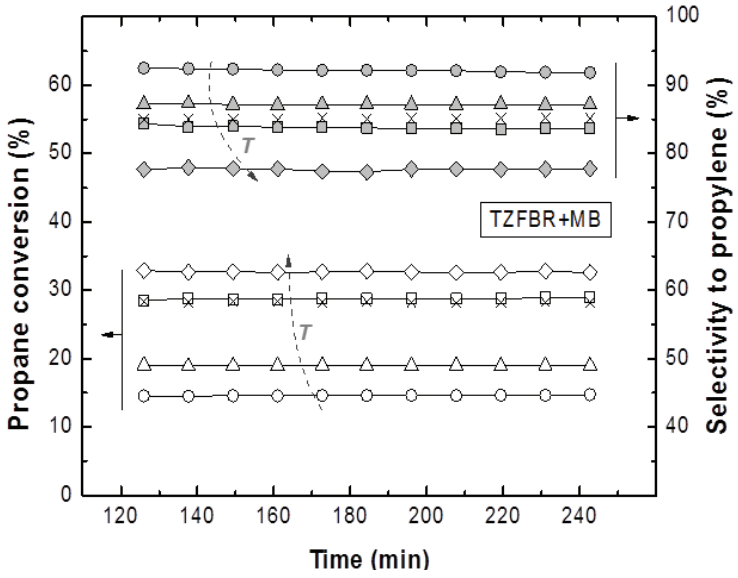

Comparative results between the three different reactor configurations at different reaction temperatures are shown in Figure 9. In all cases, the TZFBR + MB was found to be the best reactor configuration for catalytic PDH, followed by the TZFBR configuration. Both enabled the catalyst activity to be maintained during the reaction time, due to the multifunctional performance of the reactor. In contrast, the TZFBR working without oxidant (a configuration similar to a traditional FBR) showed the worst results, suffering catalyst deactivation at all reaction temperatures.

Figure 9. Yield to propylene with different reactor configurations and temperatures. Operating conditions as in Figure 4 (FBR), Figure 7 (TZFBR), and Figure 8 (TZFBR + MB).

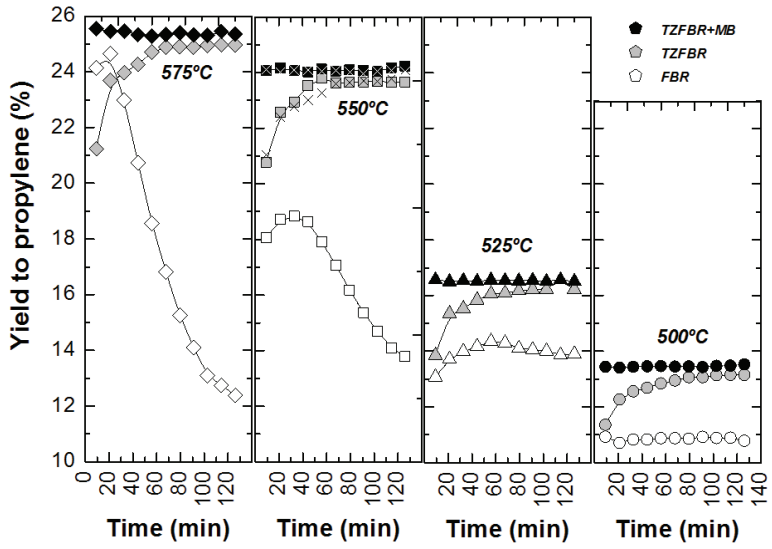

In order to assess the reproducibility of the results in the TZFBR and TZFBR + MB configurations, several repeated but not consecutive experiments were carried out under identical operating conditions.

As an example, for the repeated run at 550 °C, conversion, selectivity, and yield to propylene are presented in Figures 7–9 (× symbols), showing excellent agreement with those previously obtained at that temperature.

The effect of modifying the W_0/F_{C3H8} ratio in both the TZFBR and the TZFBR + MB configurations was analyzed by means of a series of experiments carried out at constant temperature (T = 550 °C) and constant catalyst load (W_0 = 70 g). Different propane flow rates were used for this purpose, with different percentages of propane in the total gas fed to the reactor. As expected, the higher the residence time in the reaction zone (*i.e.*, high W_0/F_{C3H8}), the higher the conversion achieved. However, significant differences in selectivity to propylene were not obtained. As a result, the yield to propylene increased with W_0/F_{C3H8}, being always higher for the TZFBR + MB configuration as can be seen in Figure 10. In these results, a better relative improvement was observed for low W_0/F_{C3H8} ratios. In fact, ΔY_{C3H6} = 2.69%, 1.85%, and 1.12% at 15.1, 21.1, and 35.2 g min mmol^{-1}, respectively. It can be assumed that lower propane conversions and higher hydrogen partial pressures were achieved by working with low W_0/F_{C3H8} ratios (*i.e.*, high propane percentages in the total gas feed to the reactor), making the hydrogen removal effect of the membrane more relevant.

Figure 10. Yield to propylene with different W_0/F_{C3H8} ratios for TZFBR and TZFBR + MB configurations. T = 550 °C; W_0 = 70 g; $u_{r,regen}$ = 1.75; $u_{r,react}$ = 2.5; O_2 percentage = 3%; C_3H_8 percentage = 30% (W_0/F_{C3H8} = 15.1 g min mmol^{-1}), 50% (W_0/F_{C3H8} = 21.1 g min mmol^{-1}), and 70% (W_0/F_{C3H8} = 35.2 g min mmol^{-1}).

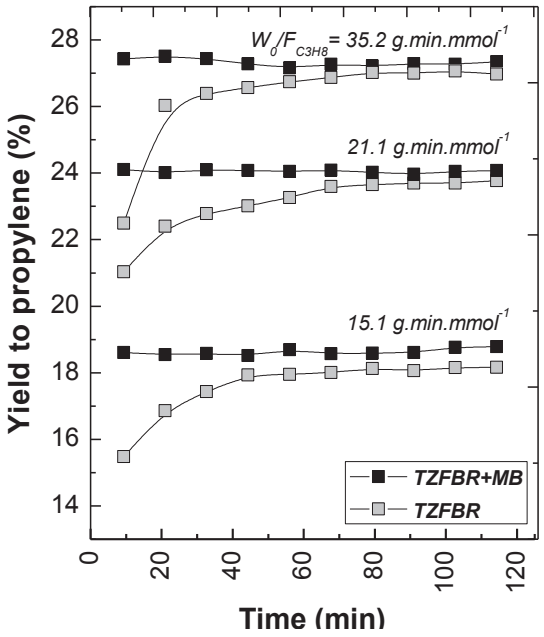

Finally, the results obtained in the TZFBR and TZFBR + MB multifunctional reactors are compared with previously published results for catalytic propane dehydrogenation with different reactor configurations (Figure 11) [13,16,33–37]. Results obtained at different operating conditions were normalized by dividing the experimental propane conversion by the equilibrium conversion in each case.

Figure 11 shows that the yield to propylene divided by the equilibrium conversion of propane in a conventional reactor (Y^*_{C3H6}) obtained with the TZFBR + MB was higher than with other reactor configurations published in the literature. Moreover, literature results correspond to instantaneous

values during the experiments where catalyst deactivation was taking place. By contrast, the values obtained with both the TZFBR and the TZFBR + MB correspond to a steady state during the time on stream, because coke deposition over the catalyst surface was counteracted *in situ* by coke removal in the lower zone of the multifunctional reactor.

Figure 11. Selectivity *vs.* (conversion/equilibrium conversion) for TZFBR and TZFBR + MB runs from Figure 8 and comparison with results from the literature: ★ Jablonsky *et al.*, 1999 [13], ☆ Assabumrungrat *et al.*, 2000 [33], ▽ Salmones *et al.*, 2002 [34], ■ Schäfer *et al.*, 2003 [35], □ Nawaz *et al.*, 2009 [16], ▲ Chen *et al.*, 2010 [36], △ Wang *et al.*, 2012 [37], ○ TZFBR (Figure 7), ● TZFBR + MB (Figure 8). Diverse operating conditions. Lines in graph represent constant values of Y^*_{C3H6} (*i.e.*, ratio "yield to C_3H_6/equilibrium conversion of C_3H_8").

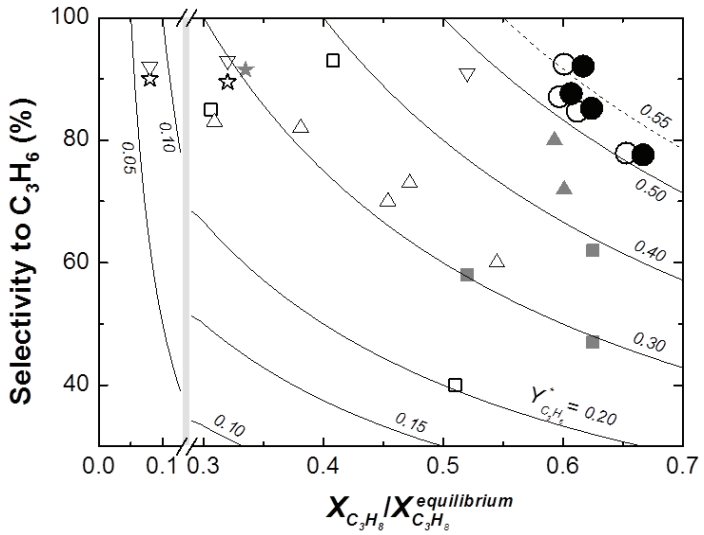

4. Conclusions

Different reactor configurations have been tested for catalytic propane dehydrogenation under different operational conditions employing Pt-Sn/$MgAl_2O_4$ as a catalyst. This catalyst showed good performance for the reaction studied, with a lower coking tendency than the Pt-Sn/γ-Al_2O_3 used in previous works. Results obtained using the FBR configuration (*i.e.*, without supplying oxygen in the lower zone of the bed) at different reaction temperatures confirmed that coke formation (and its deposition over the surface of the catalyst) causes significant catalyst deactivation and a continuous decrease in the yield to propylene during the reaction. The TZFBR is an interesting multifunctional reactor in which catalyst can be continuously regenerated due to the presence of two different atmospheres (zones) inside the catalytic bed. When the amount of oxygen fed is optimal, a steady state can be achieved at different reaction temperatures. In addition, coupling a selective Pd-Ag membrane with the TZFBR produces a novel tri-functional reactor, which enables a twofold process intensification for catalytic propane dehydrogenation.

A commercial Pd alloyed membrane has shown high selectivity to hydrogen. The use of a membrane coupled in the reaction zone of the TZFBR has improved the equilibrium limited process by displacement of the main reaction towards the products. Furthermore, the yield to propylene achieved

a constant value due to the suitable optimization of the reactor in its regeneration zone. The best results for catalytic propane dehydrogenation were obtained in the TZFBR + MB. The improvement of the membrane reactor compared to the TZFBR was better at low reaction temperatures and at low catalyst load to molar flow of fed propane ratios, according to the higher relative increase in propylene yield. A standardized comparison has shown that the multifunctional reactor provided better propylene yield than other reactor configurations reported in the literature.

Future work will focus on increasing the ratio of the permeation flux through the membrane to hydrogen produced by the reaction, with the aim of achieving a higher conversion increase. We suggest two main alternatives: to increase the membrane surface (coupling more than one membrane to the TZFBR) or to design a novel TZFBR with smaller total flows through the catalytic bed. Working with a lower total feed would mean the removal of a larger percentage of the formed hydrogen.

Acknowledgments

Financial support from the Spanish Ministry of Economy and Competitiveness (project CTQ2010-15568) is gratefully acknowledged. Financial aid for the maintenance of the consolidated research group CREG has been provided by the Fondo Social Europeo (FSE) through the Gobierno de Aragón (Aragón, Spain).

References

1. Cavani, F.; Ballarini, N.; Cericola, A. Oxidative dehydrogenation of ethane and propane: How far from commercial implementation? *Catal. Today* **2007**, *127*, 113–131.
2. Corma, A.; Melo, F.V.; Sauvanaud, L.; Ortega, F. Light cracked naphtha processing: Controlling chemistry for maximum propylene production. *Catal. Today* **2005**, *107–108*, 699–706.
3. Das, D.; Veziroglu, T.N. Hydrogen production by biological processes: A survey of literature. *Int. J. Hydrog. Energy* **2011**, *26*, 13–28.
4. Barias, O.; Holmen, A.; Blekkan, E. Propane dehydrogenation over supported Pt and Pt-Sn catalysts: Catalyst preparation, characterization, and activity measurements. *J. Catal.* **1996**, *158*, 1–12.
5. Kumar, M.S.; Chen, D.; Holmen, A.; Walmsley, J.C. Dehydrogenation of propane over Pt-SBA-15 and Pt–Sn–SBA-15: Effect of Sn on the dispersion of Pt and catalytic behavior. *Catal. Today* **2009**, *142*, 17–23.
6. Gascón, J.; Téllez, C.; Herguido, J.; Menéndez, M. Propane dehydrogenation over a Cr_2O_3/Al_2O_3 catalyst: Transient kinetic modeling of propene and coke formation. *Appl. Catal. A Gen.* **2003**, *248*, 105–116.
7. Derossi, S.; Ferraris, G.; Fremiotti, S.; Garrone, E.; Ghiotti, G.; Campa, M.C.; Indovina, V. Propane dehydrogenation on chromia/silica and chromia/alumina catalysts. *J. Catal.* **1994**, *148*, 36–46.
8. Gascón, J.; Téllez, C.; Herguido, J.; Menéndez, M. A Two-Zone Fluidized Bed Reactor for catalytic propane dehydrogenation. *Chem. Eng. J.* **2005**, *106*, 91–96.
9. Li, Q.; Sui, Z.; Zhou, X.; Chen, D. Kinetics of propane dehydrogenation over $Pt–Sn/Al_2O_3$ catalyst. *Appl. Catal. A Gen.* **2011**, *398*, 18–26.

10. Lobera, M.P.; Téllez, C.; Herguido, J.; Menéndez, M. Transient kinetic modelling of propane dehydrogenation over a Pt–Sn–K/Al_2O_3 catalyst. *Appl. Catal. A Gen.* **2008**, *349*, 156–164.
11. Larsson, M.; Hultén, M.; Blekkan, E.A.; Andersson, B. The effect of reaction conditions and time on stream on the coke formed during propane dehydrogenation. *J. Catal.* **1996**, *164*, 44–53.
12. Barias, O.A.; Holmen, A.; Blekkan, E.A. Propane dehydrogenation over supported platinum catalysts: Effect of tin as a promoter. *Catal. Today* **1995**, *24*, 361–364.
13. Jablonski, E.L.; Castro, A.A.; Scelza, O.A.; de Miguel, S.R. Effect of Ga addition to Pt/Al_2O_3 on the activity, selectivity and deactivation in the propane dehydrogenation. *Appl. Catal. A Gen.* **1999**, *183*, 189–198.
14. Yu, C.; Ge, Q.; Xu, H.; Li, W. Effects of Ce addition on the Pt-Sn/γ-Al_2O_3 catalyst for propane dehydrogenation to propylene. *Appl. Catal. A Gen.* **2006**, *315*, 58–67.
15. Zhang, Y.; Zhou, Y.; Liu, H.; Wang, Y.; Xu, Y.; Wu, P. Effect of La addition on catalytic performance of PtSnNa/ZSM-5 catalyst for propane dehydrogenation. *Appl. Catal. A Gen.* **2007**, *333*, 202–210.
16. Nawaz, Z.; Tang, X.; Zhang, Q.; Wang, D.; Fei, W. SAPO-34 supported Pt-Sn-based novel catalyst for propane dehydrogenation to propylene. *Catal. Comm.* **2009**, *10*, 1925–1930.
17. Medrano, J.A.; Julián, I.; García-García, F.; Li, K.; Herguido, J.; Menéndez, M. Two-Zone Fluidized Bed Reactor (TZFBR) with palladium membrane for catalytic propane dehydrogenation: Experimental performance assessment. *Ind. Eng. Chem. Res.* **2013**, *52*, 3723–3731.
18. Gimeno, M.P.; Wu, Z.T.; Soler, J.; Herguido, J.; Li, K.; Menéndez, M. Combination of a Two-Zone Fluidized Bed Reactor with a Pd hollow fibre membrane for catalytic alkane dehydrogenation. *Chem. Eng. J.* **2009**, *155*, 298–303.
19. Herguido, J.; Menéndez, M.; Santamaría, J. On the use of fluidized bed catalytic reactors where reduction and oxidation zones are present simultaneously. *Catal. Today* **2005**, *100*, 181–189.
20. Julián, I.; Gallucci, G.; van Sint Annaland, M.; Herguido, J.; Menéndez, M. Coupled PIV/DIA for fluid dynamics studies on a Two-Section Two-Zone Fluidized Bed Reactor. *Chem. Eng. J.* **2012**, *207–208*, 122–132.
21. Lobera, M.P.; Tellez, C.; Herguido, J.; Menéndez, M. Pt-Sn/$MgAl_2O_4$ as *n*-Butane Dehydrogenation Catalyst in a Two-Zone Fluidized-Bed Reactor. *Ind. Eng. Chem. Res.* **2009**, *48*, 6573–6578.
22. Gascón, J.; Téllez, C.; Herguido, J.; Menéndez, M. Fluidized bed reactors with two-zones for maleic anhydride production: Different configurations and effect of scale. *Ind. Eng. Chem. Res.* **2005**, *44*, 8945–8951.
23. Shu, J.; Grandjean, B.P.A.; Vanneste, A.; Kaliaguine, S. Catalytic palladium-based membrane reactors—A review. *Can. J. Chem. Eng.* **1991**, *69*, 1036–1060.
24. Paturzo, L.; Basile, A.; Drioli, E. High temperature membrane reactors and integrated membrane operations. *Rev. Chem. Eng.* **2002**, *18*, 511–551.
25. Armor, J.N. Applications of catalytic inorganic membrane reactors to refinery products. *J. Membr. Sci.* **1998**, *147*, 217–233.
26. Gallucci, F.; Fernandez, E.; Corengia, P.; van Sint Annaland, M. Recent advances on membranes and membrane reactors for hydrogen production. *Chem. Eng. Sci.* **2013**, *92*, 40–66.

27. Coronas, J.; Santamaría, J. Catalytic reactors based on porous ceramic membranes. *Catal. Today* **1999**, *51*, 377–389.
28. Dittmeyer, R.; Höllein, V.; Daub, K. Membrane reactors for hydrogenation and dehydrogenation processes based on supported palladium. *J. Mol. Catal. A Chem.* **2001**, *173*,135–184.
29. Gallucci, F.; Paturzo, L.; Fama, A.; Basile, A. Experimental study of the methane steam reforming reaction in a dense Pd/Ag membrane reactor. *Ind. Eng. Chem. Res.* **2004**, *43*, 928–933.
30. Collins, J.; Schwartz, R.W.; Sehgal, R.; Ward, T.L.; Brinker, C.J.; Hagen, G.P.; Udovich, C.A. Catalytic dehydrogenation of propane in hydrogen permselective membrane reactors. *Ind. Eng. Chem. Res.* **1996**, *35*, 4398–4405.
31. Gbenedio, E.; Wu, Z.; Hatim, I.; Kingsbury, B.F.K.; Li, K. A multifunctional Pd/alumina hollow fibre membrane reactor for propane dehydrogenation. *Catal. Today* **2010**, *156*, 93–99.
32. Menéndez, M.; Herguido, J.; Téllez, C.; Soler, J.; Gimeno, M.P. Two Zone Fluidized Bed Reactor. PCT Appl. Pat. ES2009/070241, 19 June 2008.
33. Assabumrungrat, S.; Jhoraleecharnchai, W.; Praserthdam, P.; Goto, S. Kinetics for dehydrogenation of propane on Pt-Sn-K/gamma-Al_2O_3 catalyst. *J. Chem. Eng. Jpn.* **2000**, *33*, 529–532.
34. Salmones, J.; Wang, J.-A.; Galicia, J.A.; Aguilar-Rios, G. H_2 reduction behaviors and catalytic performance of bimetallic tin-modified platinum catalysts for propane dehydrogenation. *J. Mol. Catal. A Chem.* **2002**, *184*, 203–213.
35. Schäfer, R.; Noack, M.; Kölsch, P.; Stöhr, M.; Caro, J. Comparison of different catalysts in the membrane-supported dehydrogenation of propane. *Catal. Today* **2003**, *82*, 15–23.
36. Chen, M.; Xu, J.; Cao, Y.; He, H.Y.; Fan, F.N.; Zhuang, J.H. Dehydrogenation of propane over In_2O_3–Al_2O_3 mixed oxide in the presence of carbon dioxide. *J. Catal.* **2010**, *272*, 101–108.
37. Wang, J.; Zhang, F.; Hua, W.; Yue, Y.; Gao, Z. Dehydrogenation of propane over MWW-type zeolites supported gallium oxide. *Catal. Commun.* **2012**, *18*, 63–67.

Artículo X

J.A. Medrano, I. Julián, F. García, K. Li, J. Herguido, M. Menéndez,
TZFBR with palladium membrane for catalytic PDH: experimental performance assessment,
Ind. Eng. Chem. Res. 52 (2013) 3723 – 3731

I&EC research
Industrial & Engineering Chemistry Research

Article

pubs.acs.org/IECR

Two-Zone Fluidized Bed Reactor (TZFBR) with Palladium Membrane for Catalytic Propane Dehydrogenation: Experimental Performance Assessment

J. A. Medrano,[†] I. Julian,[†] F. R. García-García,[‡] K. Li,[‡] J. Herguido,*[,†] and M. Menendez[†]

[†]Aragon Institute for Engineering Research (I3A), University of Zaragoza, 50018 Spain

[‡]Department of Chemical Engineering, Imperial College, London, SW7 2AZ U.K.

ABSTRACT: Catalytic propane dehydrogenation has been tested on different reactor configurations employing Pt−Sn/$MgAl_2O_4$ as a catalyst. Hollow fiber palladium membranes coupled to the two-zone fluidized bed reactor (TZFBR) combine the possibility of improving propane conversion by hydrogen removal from the reaction bed through the membrane with in situ catalyst regeneration in the lower section of the TZFBR. Experiments have been carried out at different reaction temperatures and time on stream. In addition, the optimum regenerative agent flow fraction (diluted oxygen) to be fed into the TZFBR has been determined at the reaction temperatures between 500 °C and 600 °C to get a constant catalytic activity without net deactivation. Moreover, the TZFBR with palladium membranes has been successfully tested, displacing the reaction equilibrium towards the production of propylene, and still keeping steady state in the catalytic propane dehydrogenation. These results were better than those reported in the literature for conventional reactors.

1. INTRODUCTION

Membrane reactors are among the technologies in the frame of chemical process intensification. This kind of system enables a chemical reaction (oxidative reforming, steam reforming, etc.) to be performed in a single unit and product separation through a membrane.[1] In this case, membranes are not only considered as separators but also have a direct influence on the chemical reaction.[2−4] Main limitations of these reactors are related to the adaptation between the membrane and the reactor as well as chemical and physical membrane resistance. Membranes employed in these reactors are classified in two generic types according to its composition: organic and inorganic membranes. Inorganic membranes represent the most studied ones in catalytic processes since organic membranes are not able to work at harsh conditions. Inorganic membranes usually have a high thermal stability and high chemical and physical resistance, which allow them to work at high temperatures.[5] Membrane reactors are, then, commonly employed to carry out chemical reactions limited by the thermodynamic equilibrium or reactions with low kinetic rates.[6,7] In fact, membrane separation capability is used to improve catalytic processes in two ways: by providing a selective product separation (extractive application) or by adding a reactant selectively (distributive application).[8] The removal of one of the main reaction products, in reactions limited by the thermodynamic equilibrium, modifies this equilibrium towards the products production.

Among the inorganic membranes, Pd-based dense membranes are the most employed ones in membrane reactors for hydrogen production.[9] Their ability to selectively remove high-purity hydrogen makes the Pd membrane interesting to be used in such reactions limited by the thermodynamic equilibrium, increasing their conversion and yield, thanks to the reaction displacement to more product formation. However, the high membrane cost represents an important limitation to implant it in industrial processes. The high price of both substrates and Pd, $27.5/g ($780/oz), is the bottleneck in employing membrane reactors for large-scale or distributed applications. Nevertheless, substrates are significantly more expensive than Pd; for example, medium quality porous stainless steel supports (PSS) are expensive, i.e. $100 per tube with dimensions of OD = 1 in. (2.54 cm) and L = 6 in.(15.24 cm), which is around 70% of the total price of the system since the Pd cost for a 5 μm Pd membrane over these PSS is about $20.[10] Another important process limitation is that the selective H_2 removal increases the coke formation in catalytic hydrocarbon conversion at high temperature. Therefore, the H_2 removal leads to a faster catalyst deactivation, being an important problem because it implies a catalyst deactivation with a critical yield process decrease.[11,12]

Currently, most propylene is obtained as ethylene byproduct. The propylene consumption is increasing faster than ethylene consumption; therefore, new ways to produce propylene must be developed. Catalytic propane dehydrogenation is one of the most promising paths to produce propylene. This process implies an endothermic reaction (ΔH_{298K} = −124 kJ/mol) limited by the thermodynamic equilibrium[13] where hydrogen is one of the reaction products (eq 1). According to its characteristics, this catalytic propane dehydrogenation is a suitable heterogeneous catalytic reaction where a membrane reactor can be implemented. This catalytic process is generally carried out with chromium[14,15] or platinum[16] catalysts supported on alumina at 500−600 °C at atmospheric pressure. Different systems and catalyst modifications have been studied by several authors, who found important process limitations.[17,18] One of them is the presence of undesired secondary

Received: November 19, 2012
Revised: January 28, 2013
Accepted: February 20, 2013
Published: February 20, 2013

reactions (eqs 2 and 3) that cause selectivity loss. Another important limitation is the coke formation reaction (eq 4).

$$C_3H_8 \rightarrow C_3H_6 + H_2 \quad (1)$$

$$C_3H_8 \rightarrow CH_4 + C_2H_4 \quad (2)$$

$$C_3H_8 + H_2 \rightarrow CH_4 + C_2H_6 \quad (3)$$

$$C_3H_8 \rightarrow 3CH_{0.5} + 3.25H_2 \quad (4)$$

This coke is deposited over the catalyst surface, inhibiting its activity and producing a severe and continuous yield decrease. However, the catalytic propane dehydrogenation is an already implemented process at industrial scale. As an example, BASF built a 350 kt/year plant in Tarragona (Spain) in 2004 based on the Oleflex process. In addition, the rise of shale gas has favored the use of propane as raw material, and several companies (Dow, Formosa Plastics, Enterprise Products) have announced new plants for 600−700 kt/year each.[19] The process limitations are currently faced by employing serial systems where catalytic reaction and catalyst regeneration take place in different batch reactors that provide a semicontinuous propylene production. Other industrial configurations consist of supplying hydrogen with propane feed with an aim of reducing coke formation in reaction but reaching lower yield to propylene. In the past few years, some authors tested catalysts based on gallium species[20] and several promoters such as Ce, K, La, or Na[16,21−23] to reduce the coke formation. Supports based on zeolites have also been used in catalytic propane dehydrogenation.[24]

The use of a two-zone fluidized bed reactor (TZFBR) has been proposed to carry out continuous catalyst regeneration (Figure 1). The TZFBR has been tested in several catalytic dehydrogenations, such as propane and butane catalytic dehydrogenation employing different catalysts, as well as other kinds of applications.[17,25,26] This novel reactor represents a useful system to be applied for such heterogeneous catalytic processes where the catalyst is deactivated by coke deposition or even for a red-ox process. The reactor configuration consists of two gas feed points that generate two different atmospheres inside the reactor. A reactive agent, e.g. propane, is fed at an intermediate point of a fluidized bed, creating the reaction zone in the upper part of the bed. Simultaneously an oxidant agent, e.g. diluted oxygen, is fed at the bottom of the bed, creating the regeneration zone. The characteristic bubbling regime in fluidized bed reactors provides the catalyst circulation between both zones. Therefore, the catalyst, which is deactivated by coke deposition in the reaction zone, flows down to the regeneration zone where coke combustion takes place. Due to the bed fluidization, the regenerated catalyst comes up to the reaction zone and it may react again with the same activity, resulting in a steady state system in only one unit.[27] To achieve a maximum yield at steady state, the TZFBR needs an exhaustive optimization of its operational conditions. On one hand, the system has to be operated in such conditions that the oxidizing agent does not reach the upper zone and does not interact with the reactive gas, avoiding an important selectivity loss. On the other hand, if the oxidant flow fed is lower than the optimum required, catalysts will not be completely regenerated, and coke would be accumulated over the catalyst surface leading to an important activity process decrease.

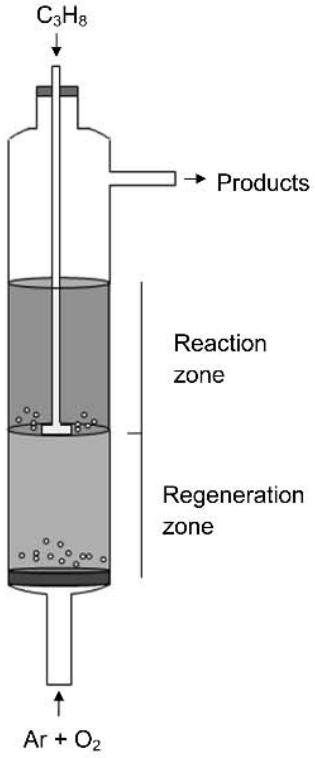

Figure 1. Schematic drawing of the TZFBR.

Palladium membranes coupled to the TZFBR represents a multifunctional membrane reactor for the catalytic propane dehydrogenation. The TZFBR could provide a constant process activity, whereas the dense Pd membrane could enhance the process yield to propylene via H_2 removal. To reduce membrane costs, a thin palladium layer can be supported over porous alumina hollow fibers showing the highest surface area/volume value in selective-hydrogen-removal membranes. In addition, the fabrication process of asymmetric ceramic composite tubes is expensive due to the multiple fabrication steps. However, a more economical fabrication process can be achieved by using a phase inversion technique, in which the multiple fabrication steps are combined into a single step. As already discussed, the hydrogen removal through these membranes increases the catalyst deactivation rate by coke deposition, but the TZFBR could solve this limitation thanks to continuous catalyst regeneration. Although the use of membranes in fluidized bed reactors, as a way to increase the conversion, has been described by several groups,[28,29] the combination of reaction, regeneration, and separation in a single unit is highly novel. In a previous study,[11] catalytic propane dehydrogenation was tested in the TZFBR with a palladium membrane employing a Pt−Sn−K/γ−Al_2O_3 catalyst. That study showed that the coke formation was higher than expected at working experimental conditions and good results could not be obtained, which suggested the use of other kind of catalysts with a lower trend to coke formation.

In the present study a Pt−Sn/$MgAl_2O_4$ catalyst has been tested in the TZFBR with a hollow fiber palladium membrane. This catalyst shows low coke deposition because of the low support acidity and an improved yield to olefins in previously tested dehydrogenation reactions, e.g. n-butane dehydrogenation.[30] With this catalyst, cracking and coking reactions are hindered. Therefore, the oxidant requirements in the TZFBR will be lower, providing high propylene selectivity. By this way, the limitation found in the previous study could be solved. In

this study, a novel two-section TZFBR configuration (TS-TZFBR) has been employed (Figure 2). Different bed sections

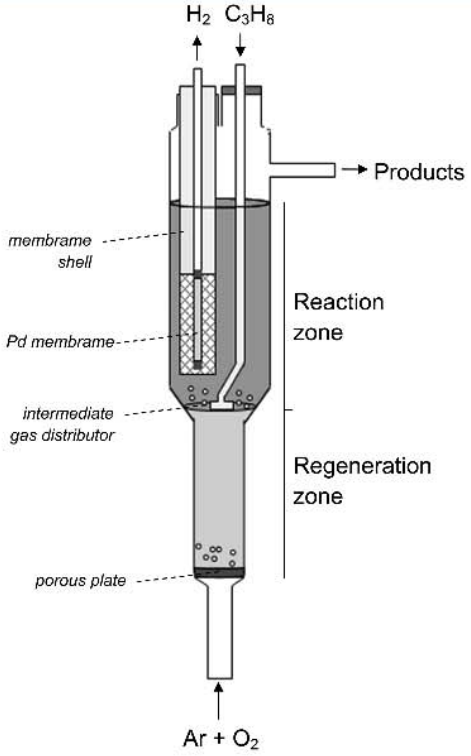

Figure 2. Schematic drawing of the TZFBR with two sections and membrane.

between both reactor zones have been implemented to allow a better control of the fluid-dynamic regime in each reactor zone, allowing low regenerating flows when required.[31,32] In the present work, the catalytic propane dehydrogenation is going to be tested for the propylene production on a TS-TZFBR with coupled dense Pd membrane. This multifunctional reactor could provide very important process intensification, where three different operations could take place: reaction, regeneration, and molecular separation. To illustrate the process improvement, the catalytic propane dehydrogenation has been carried out in different reactor configurations: traditional fluidized bed reactor (FBR), TZFBR, and the proposed coupled TS-TZFBR with palladium membrane.

2. EXPERIMENTAL SECTION

2.1. Catalyst Preparation. Pt−Sn/$MgAl_2O_4$ was prepared by incipient impregnation of platinum and tin compounds after synthesizing the catalytic support by a sol−gel method.[30] First of all, magnesium ($Mg(NO_3)_2{\cdot}6H_2O$, Aldrich, 99%) and aluminum ($Al(NO_3)_3{\cdot}9H_2O$, Aldrich, 99%) compounds were dissolved and reaction took place at 50 °C and pH 9, maintaining a vigorous stirring during 1 h. After that, the white-gel $MgAl_2O_4$ formed was precipitated and aged at atmospheric conditions for 8 h. Next, the white-gel was filtrated and neutralized in a vacuum system and dried at 120 °C all night. Finally, it was calcined with the following steps: the gel was first heated at 350 °C for 2 h and then at 800 °C for 8 h. Before impregnating the catalyst, the obtained catalytic support was sieved to 75−150 μm particle size. Once sieved, the $MgAl_2O_4$ particles were characterized by X-ray diffraction (XRD) and Brunauer−Emmett−Teller (BET) techniques in order to analyze their structure, specific external surface, and pore size distribution.

In the second part of catalyst preparation, the support was coated by tin and platinum precursors ($SnCl_2$, Aldrich, 98% and H_2PtCl_6, Aldrich, 8% dissolution in water) following an incipient impregnation method in two consecutive steps. First, tin is impregnated over the support for 6 h and dried at 120 °C for the whole night. After that, platinum is impregnated in the same way. Finally, the catalyst was calcined in air at 650 °C for 3 h (2 °C/min heating rate) and sieved, again, to 75−150 μm particle size.

Before proceeding with the experimental analysis, the Pt−Sn/$MgAl_2O_4$ catalyst has been further characterized by determining its minimum fluidization velocity, u_{mf}. The minimum fluidization velocity test was carried out with Ar at 550 °C in a traditional fluidized bed reactor, obtaining u_{mf} = 0.53 cm/s (i.e., 0.175 cm^3 STP/cm^2.s.).

Besides, several stabilization cycles (reduction, reaction, and regeneration of the fresh catalyst) have been performed to ensure the reproducibility of the Pt−Sn/$MgAl_2O_4$ catalytic activity. These cycles have been carried out in a traditional fluidized bed reactor configuration at 550 °C using reactive gas diluted in Ar. In a cycle, the volumetric percentage of reactive gas used was 25% hydrogen, 50% propane, and 5% oxygen for reduction, reaction, and regeneration steps, respectively.

2.2. Membrane Preparation. Palladium membranes have been developed by a direct deposition on a porous alumina hollow fiber. This support consists of a unique asymmetric alumina structure which was prepared via phase-inversion/sintering technique.[33] The preparation of the spinning suspension was previously described elsewhere.[13] After 2 h degassing under vacuum, the suspension was pressurized at 50−140 kPag (7−20 psig) using nitrogen and extruded through a tube in orifice spinneret with 1.2 mm inner diameter and 3.0 mm outer diameter. Fibers were coagulated by deionized water after extruding and sintered to obtain the final hollow fiber in a three-step process. First, fibers are heated at 600 °C during 2 h with 2 °C/min heating rate, then heated at 1000 °C during 2 h with a 5 °C/min heating rate, and finally, fibers were sintered during 4 h at 1450 °C. One side of the final hollow fiber is then sealed with glaze, whereas the other end remains opened. Moreover, the external hollow fiber surface was also sealed with glaze excepting the last 6 cm close to the sealed end where palladium will be coated.

Palladium deposition on the asymmetric hollow fiber was carried out by an electroless plating process.[34] Before coating, the hollow fiber surface was cleaned using deionized water and activated by six consecutive immersions in tin chloride ($SnCl_2$−HCl, 1 g/L, pH 2)) and palladium chloride ($PdCl_2$−HCl, 1 g/L, pH 2) solutions at atmospheric temperature. As a result, the surface color of the Al_2O_3 hollow fiber changed from white to dark brown. The aim of this process was to enhance the uniformity of palladium coating. Between each immersion, the support was cleaned with 0.1 M HCl. Finally, the hollow fiber surface was coated in the palladium bath (Table 1). The Pd membranes were dried in an oven at 120 °C for 2 h. The uniformity of the Pd coating was checked by SEM images at different positions.

2.3. Reaction. Catalytic propane dehydrogenation has been tested with three different reactors: a traditional fluidized bed reactor (FBR), a TZFBR, and a TZFBR with palladium

Table 1. Coating Bath Composition of Electroless Plating

compound	bath
temperature (°C)	60
pH	10−11
$V_{(solution)}/V_{(plating\ area)}$ (mL/cm^2)	~ 3.7
$Pd(NH_3)_4Cl_2{\cdot}H_2O$ (g/L)	4
$Na_2EDTA{\cdot}2H_2O$ (g/L)	40.1
NH_4OH (28%) (mL/L)	198
N_2H_4 (1 M) (mL/L)	5.6

membrane. The FBR consisted of a 3 cm inner diameter quartz column, where the reactive propane flow was fed at the bottom inlet of the reactor. The TZFBR with membrane configuration is shown in the Figure 2. It consisted of a quartz column with a variable cross-sectional area between the regeneration and the reaction zones. The lower and the upper reactor cross sections were 1.8 and 3 cm inner diameter, respectively, and the transition region between them formed a 60° angle with respect to the horizontal position. This configuration improves the control of the fluid dynamic regime in both reactor regions separately, with respect to the original straight-column TZFBR (Figure 1).[25,31] The oxidizer agent, i.e. diluted oxygen, enters the bed through a bottom porous quartz plate distributor. This porous plate acts as catalyst bed support as well. The reactive gas, i.e. propane, was fed through an immersed four-orifices gas distributor (4 mm external diameter), which was located at an intermediate point of the transition bed section. A palladium membrane, located within the reactive bed section, is placed inside a porous ceramic (2 μm pore size) α-alumina tubular membrane with 8 mm inner diameter. The use of an external shell provided better mechanical resistance to the palladium membrane and avoids erosive effects on the thin Pd layer due to catalyst particles circulation in the fluidized bed. Both the propane distributor and the Pd membrane were connected to the reactor top.

Before reaction begins, the catalytic bed was heated to reaction temperature at 2 °C/min heating rate to avoid membrane damages and is activated (reducing PtO species to Pt^0) at 550 °C with hydrogen according to the conditions shown in Table 2. A series of experiments has been performed

Table 2. Experimental Conditions

	reduction	reaction	regeneration
feed composition	Ar:H_2 = 3:1	Ar:C_3H_8 = 1:1	Ar:O_2 = 20:1
u_r	2	2.5	2
time (h)	2	1.5	until no-CO and no-CO_2 signal
$W_0/F_{C_3H_8}$ (g min mmol^{-1})	38	22	200

to evaluate the effect of the reaction temperature and the optimum percentage of oxygen in the regeneration flow in order to achieve a constant catalytic activity. For this purpose, the catalytic propane dehydrogenation was carried out at different temperatures between 500 and 600 °C with 72 g of catalyst in each case. After each reactive experiment, the catalyst was fully regenerated with an oxygen flow at 550 °C until no-CO and no-CO_2 signal was detected by online gas chromatography. Table 3 shows the working conditions for each experimental series.

Each reactive gas flow was controlled by a set of digital mass flow controllers. The furnace temperature control was carried

Table 3. Experimental Series

	FBR	TZFBR	TZFBR+MB
T (°C)	500−600	500−600	500−550
$u_{r,regen}$		2.5	2.5
$u_{r,react}$	2.5	1.75	1.75
oxygen (%)		0.5−12	0.5−10
$W_0/F_{C_3H_8}$ (g min mmol^{-1})	22	22	22
ΔP (bar)			1.1

out by an immersed thermocouple (Controller 3116, Eurotherm). Reaction gas products were analyzed by online gas chromatography (μGC-R3000, SRA Instruments), and a vacuum pump (2P-3, Start) is employed to generate the pressure drop (driving force) between both membrane sides for the hydrogen permeation.

2.4. Materials Characterization. XRD data were obtained at 298 K in a "D-Max Rigaku" difractometer with a mobile anode. The difractometer works at 40 kV and 80 mA with a Cu anode and graphite monochromator to select CuKα1.2 radiation. Experimental measurements have been carried out varying the diffraction angle between 10° and 90° with a 0.03° step.

The BET specific surface of the catalyst has been obtained in a Micrometrics ASAP 2020.

Permeation tests across the Pd membranes were carried out at different temperatures. For this purpose, the Pd membrane was assembled in the reactor shown in Figure 2, but working without the catalytic bed and with the propane inlet pipe previously sealed. A constant flow rate of pure Ar or H_2 + Ar was fed at the bottom inlet of the reactor using digital mass flow controllers. Then, a pressure drop across the membrane was established with the vacuum pump in the hydrogen exit pipe. Subsequently the nonpermeated flow was measured at the products exit pipe of the reactor using a flow meter at atmospheric pressure. Several gas flow rates with different H_2/Ar ratios were tested.

3. RESULTS

The results of solid characterization tests have shown that $MgAl_2O_4$ was correctly synthesized. Different X-ray diffraction peaks (Figure 3a) agree with the structural geometry of the $MgAl_2O_4$ spinel. The adsorption isotherm (Figure 3b) shows a typical type-4 adsorption curve, which is characteristic of mesoporous solids. From the BJH analysis an average pore size of 7.2 nm was obtained. The BET area was 123 m^2/g, and the pore volume 0.26 cm^3/g.

Figure 4 shows an example of how catalytic activity achieves a reproducible behavior after several reduction−reaction−regeneration cycles in a FBR at 550 °C with the conditions shown in Table 2. For the experimental conditions used in the study reported in the Figure 4, it can be seen that both curves of propane conversion ($X_{C_3H_8}$) and curves of selectivity to propylene ($S_{C_3H_6}$), were reproducible from the sixth cycle (n = 6) onward. It seems that in the first reduction−reaction−regeneration cycles those active sites with more tendency to coke formation are transformed into weaker active sites, thus reducing the overall tendency to coke formation and improving the propylene selectivity. Accordingly, for further reaction studies a solid with $n \geq 6$, i.e. a stabilized catalyst, was always used to load the reactor schematized in Figure 2.

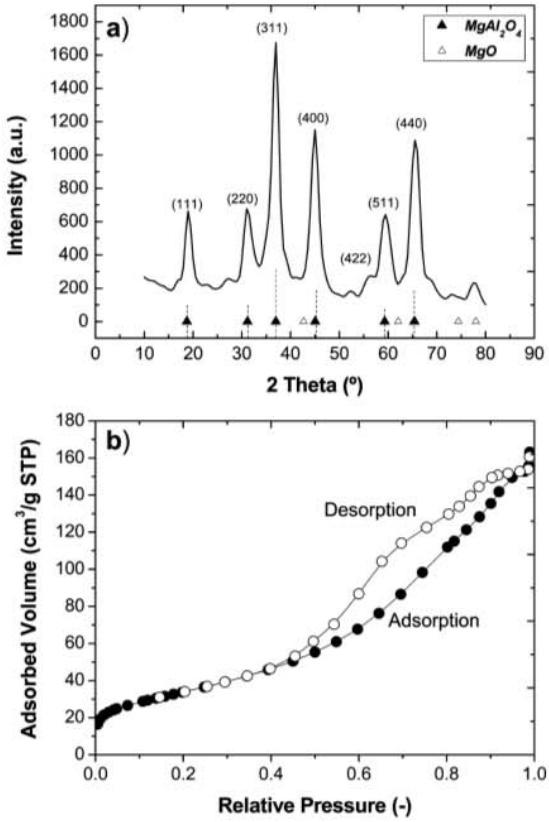

Figure 3. XRD pattern (a) and N_2 adsorption−desorption isotherms at 77 K (b) for $MgAl_2O_4$.

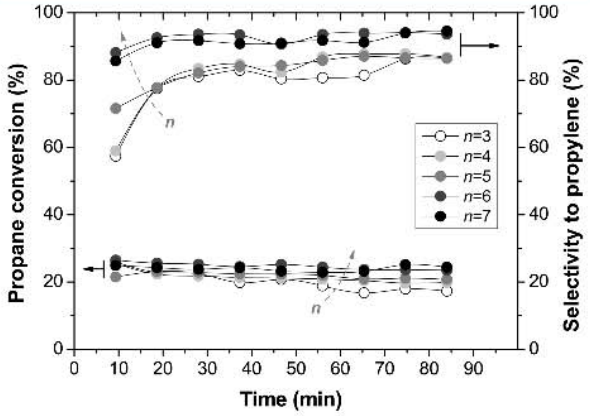

Figure 4. Propane conversion and selectivity to propylene after n stabilization (reduction + reaction + regeneration) cycles of the fresh $Pt-Sn/MgAl_2O_4$ catalyst. T = 550 °C.

A first study was carried out in the FBR configuration in order to evaluate the reaction temperature influence on the catalyst deactivation and on the evolution of the yield to propylene, the product of interest. The propane conversion obtained (Figure 5) was higher when reaction temperature increased, due to the endothermic character of the dehydrogenation reaction. However, the selectivity to propylene decreases at higher temperatures because of the presence of competitive cracking and coke-formation reactions. Moreover, it can be observed how it was impossible to reach a steady state operation with a constant catalytic activity in this kind of

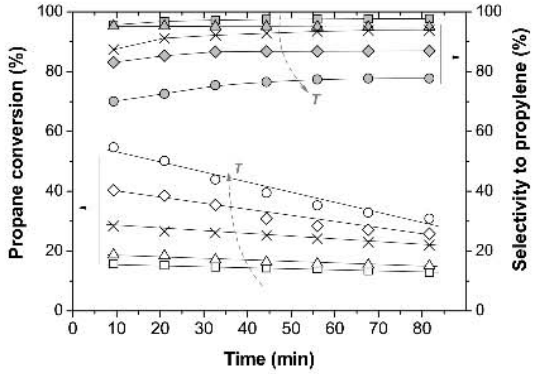

Figure 5. Propane conversion and selectivity to propylene at different reaction temperatures (□, 500 °C; Δ, 525 °C; ×, 550 °C; ◊, 575 °C; ○, 600 °C) in FBR configuration. C_3H_8/Ar = 50/50, W_0 = 72 g, $W_0/F_{C_3H_8}$ = 22 g min $mmol^{-1}$, u_r =2.5.

traditional fluidized bed reactor. In this case, the process yield to propylene decreased along the time on stream. As a conclusion, the catalyst must be regenerated after only 1 h of chemical reaction time in order not to lose catalytic activity due to coke deposition.

As can be observed in Figure 5, the higher the reaction temperature, the faster the catalyst deactivation and the sharper the propane conversion decrease. This deactivation rate can be measured by the rate of the conversion change ($-dX/dt$) for each reaction temperature (Figure 6). According to the results

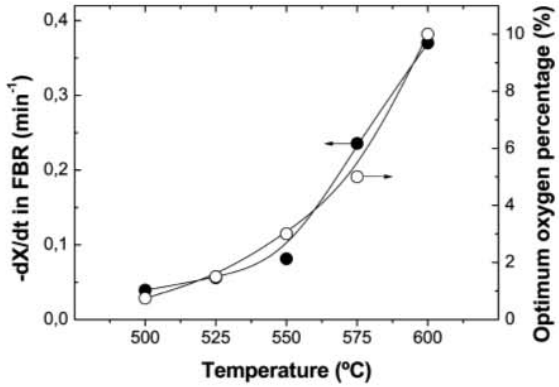

Figure 6. Propane conversion decay in FBR (measured as $-dX_{C_3H_8}/dt$) and O_2 optimum percentage needed in the feeding stream of TZFBR, both as a function of the temperature (remaining experimental conditions as in Figure 5). Lines only as a visual help.

presented in Figure 6, the deactivation rate increases exponentially with the reaction temperature. Back to Figure 5, it can be observed how the selectivity to propylene increases quickly during the first reaction minutes. The explanation is that when reaction begins, propane reacts with fully active catalytic particles. It leads to massive coke generation (higher at higher temperatures). After a few reaction minutes, the catalyst active sites are partially covered by coke, and the coke deposition rate decreases. For this reason, the selectivity to propylene tends to increase in such deactivation conditions.

As a solution to counteract the catalyst deactivation, the TZFBR may provide steady state operation with a constant activity for catalytic propane dehydrogenation. It can be done by adjusting the amount of oxygen to be introduced through

the regeneration bed section in order to burn the coke formed within the reaction zone. On the one hand, if the oxygen feed in the regeneration zone is too low, the rate of coke removal would be lower than the rate of coke formation, and the catalyst will be deactivated or will achieve a steady state with low activity. On the other hand, if the oxygen feed is too high, some oxygen could reach the reaction zone. It would lead to undesirable propane combustion and would entail an important propylene selectivity decrease. In this scenario, the catalyst could be overoxidized because of the lower hydrogen production that would impede the catalyst active sites reduction. Thus, the catalyst would be kept deactivated. Figure 7 shows several experiments performed at the same temperature T = 550 °C with different oxygen percentage fed on the regeneration zone (relative to the total gas feed into the reactor, i.e. reaction plus regeneration zones). In case of adding a 3% of oxygen, it allows constant yield to propylene along the reaction time-on-stream, indicating the optimum value of oxidant reactive to be fed into the TZFBR. Figure 8 shows the optimum oxygen inlet percentage on the regeneration zone at different reaction temperatures after analyzing the yield to propylene at several oxygen percentages at each reaction temperature. This figure represents the rate of propylene yield decrease (dY/dt) for several oxygen percentages at each temperature. In this case, the higher the reaction temperature, the higher the need of regenerative oxygen supply. This result can be explained by the fact that high temperatures favor secondary reactions like thermal cracking and coke formation. Consequently the higher the temperature, the faster the deactivation (see Figure 6, or data corresponding to a value of 0% O_2 inlet in Figure 8). The optimum oxygen percentage at different reaction temperatures has been plotted in Figure 6, showing that there is a logical correlation between the degree of deactivation in FBR configuration and the requirement of oxidant gas supply to continuously regenerate the catalyst in TZFBR configuration. The energy balances at adiabatic conditions for the TZFBR system working with the optimum oxygen percentage reveal autothermal functioning of the process when the temperature is about 550 °C (3% O_2) or higher (>3% O_2). This implies that in such conditions the amount of coke combustion is sufficient to supply the energy for the endothermic propane dehydrogenation.

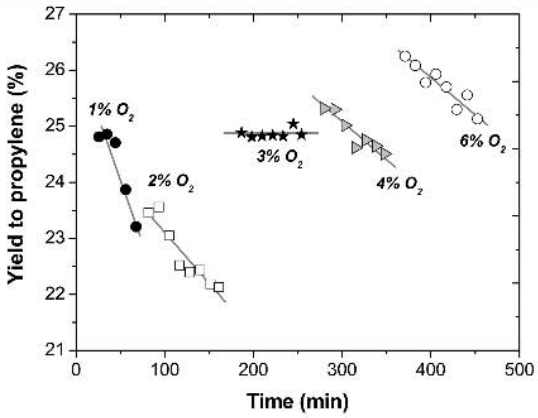

Figure 7. Yield to propylene at 550 °C in the TZFBR configuration for different oxidant percentages fed. $C_3H_8/(Ar + O_2)$ = 50/50, W_0 = 72 g, $W_0/F_{C_3H_8}$ = 22 g min mmol^{-1}, $u_{r,regen}$ =2.5, $u_{r,react}$ = 1.75.

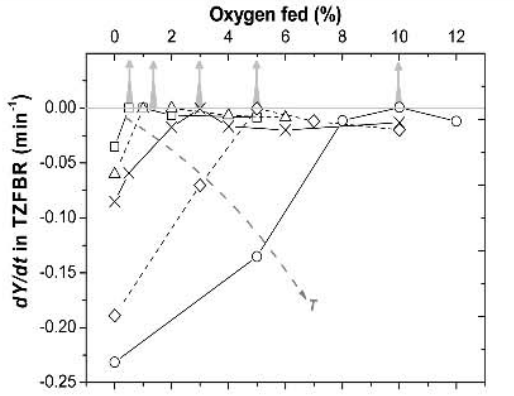

Figure 8. Determination of oxygen optimum percentage at different reaction temperatures (□, 500 °C; Δ, 525 °C; ×, 550 °C; ◊, 575 °C; ○, 600 °C) in the TZFBR. Remaining operating conditions as in Figure 7.

After determining the optimum oxygen flows in each case, several experiments at different reaction temperatures were carried out in order to confirm the good performance of the TZFBR. Figure 9 represents the propane conversion and the propylene selectivity for the catalytic propane dehydrogenation at different reaction temperatures employing the optimum conditions established before. Propylene selectivity is lower than 100% because part of the propane is converted to cracking products (eqs 2 and 3) and coke formed (eq 4) is transformed into CO_x. Under these conditions it was possible to reach steady state behavior for each reaction temperature. In this case, the catalyst was perfectly regenerated in situ, and it maintained the same activity along the time. This performance implies an important process intensification for the analyzed catalytic propane dehydrogenation.

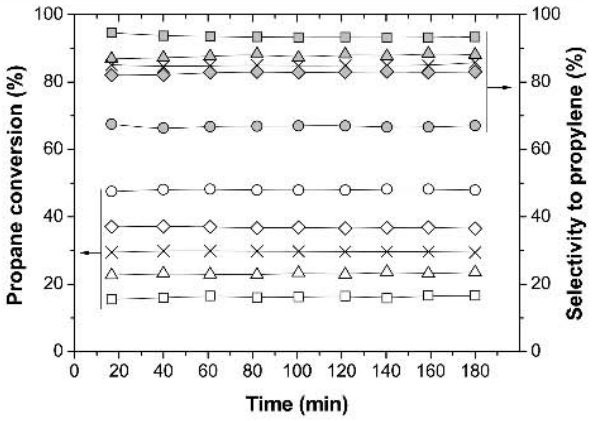

Figure 9. Propane conversion and selectivity to propylene at different reaction temperatures (□, 500 °C; Δ, 525 °C; ×, 550 °C; ◊, 575 °C; ○, 600 °C) in the TZFBR, working at the optimum oxygen percentage for each temperature (Figure 6). Remaining conditions as in Figure 7.

The next stage in the process intensification consists in introducing the hollow fiber palladium selective membrane inside the reactor. One limitation of this kind of membrane is its maximum work temperature, around 600 °C, in order not to damage the thin Pd layer. In this regard, gas did not permeate through the Pd membrane under the conditions studied in

permeation tests when pure Ar is used as gas stream. This indicates that the Pd membrane consists of a defect-free continuous film with an infinite H_2 perm-selectivity ($S_{H_2/Ar} = \infty$). Thus, H_2 permeation takes place via metallic diffusion.[35] Figure 10 shows that the H_2 permeation flux increases linearly

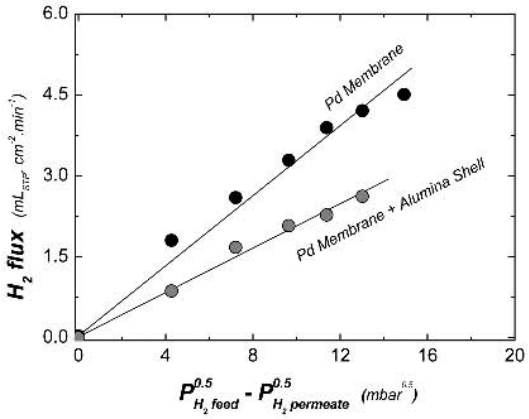

Figure 10. H_2 permeating flux vs Sieverts' driving force for Pd membrane with and without α-alumina shell. T = 550 °C, Q_{gas}= 200 mL (STP) min^{-1}, $P_{permeate}$ = 8 mbar.

with the difference of the square root of the H_2 partial pressure at both sides of the membrane, according to Sieverts' law, indicating that hydrogen permeation is controlled by metallic diffusion through the Pd bulk membrane and not by other steps such as dissociative adsorption or associative desorption. As it can be seen in Figure 10, a H_2 permeation of 2.5 mL (STP) cm^{-2} min^{-1} was obtained working at 550 °C and a $\Delta P^{0.5}$ of around 7.5 mbar$^{0.5}$, which is expected to be the pressure gradient in reaction experiments. However, the use as external shell of a porous α-alumina tube leads to a decrease in the hydrogen flux (around 1.7 mL (STP) cm^{-2} min^{-1} at $\Delta P^{0.5}$ = 7.5 mbar$^{0.5}$).

Figure 11 shows the evolution of the yield to propylene with different reactor configurations at a reaction temperature of 500 °C. The novel TZFBR with membrane presents the highest values of yield to propylene with respect to the TZFBR and FBR. In the multifunctional reactor, a part of the produced hydrogen is removed from the catalytic system through the Pd membrane, producing a conversion increase compared to

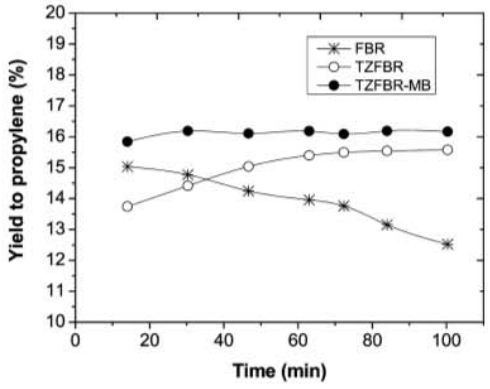

Figure 11. Yield to propylene with different reactor configurations at 500 °C.

thermodynamic equilibrium in a conventional reactor. With this hydrogen removal, a higher coke formation takes place. This issue is counteracted, in this case, by adjusting the oxygen feed on the regeneration zone to allow the complete catalyst regeneration, making process stability possible. At the same time, the TZFBR configuration shows good result in the catalytic propane dehydrogenation as well, especially for the process stability with high yield to propylene values. On the other hand, FBR presents the worst result in the comparative figure with an important process yield decrease because of the lack of regenerative oxygen on this traditional reactor. This figure shows the process intensification evolution with each reactor. The first intensification occurs when TZFBR is employed replacing the FBR. In this case the process achieves a steady state performance in comparison with the unstable FBR. The second one is possible when a palladium membrane is coupled with the TZFBR to get the coupled TZFBR with membrane. At this moment, when hydrogen is removed from the bed reaction, propane conversion increases, and stability is possible by continuous regeneration. The selectivities to each product with respect to the total products (propylene, C_2 hydrocarbons, methane, and CO_x) obtained in the experiments of Figure 11 are shown in Table 4. For TZFBR and

Table 4. Selectivities to Di erent Products for the Experiments of Figure 11

	$S_{C_3H_6}$	S_{C_2}	S_{CH_4}	S_{CO_x}
FBR[a]	97.8	0.8	1.3	0.1
TZFBR	91.0	3.1	3.5	2.4
TZFBR+MB	90.3	3.0	4.0	2.7

[a] t = 100 min.

TZFBR+MB configurations these selectivities correspond to a stationary state. For FBR configuration no stationary state is achieved, so the values in Table 4 correspond to the final state attained (i.e., t = 100 min in Figure 11). No net coke generation can be assumed in TZFBR and TZFBR+MB configurations working at steady state. However, in conventional FBR there is a continuous coke generation. As an example, the selectivity to coke with respect to the propane reacted, calculated assuming carbon mass balance closure, was 5.2% in the aforementioned final state (t = 100 min) for FBR run in Figure 11.

Finally, a comparison of obtained results in TZFBR and TZFBR+MB (Figure 11) with previously published results on propane dehydrogenation in other reacting configurations[12,20,36−41] is shown in Figure 12. To compare the data regardless of the operating conditions, the results were standardized with the equilibrium conversion for a traditional reactor, accounting for the different temperatures and propane dilutions in each study. Therefore, Figure 12 shows propene selectivity versus conversion/equilibrium conversion (at operating conditions). It may be seen that a higher yield to propylene related to equilibrium conversion of propane in a conventional reactor (Y^*_{C3H6}) is obtained with the TZFBR and especially with TZFBR+MB of Pd than with other reacting configuration used in literature. Moreover, it is worth remembering that the literature values shown in Figure 12 are instantaneous results in experiments with catalyst deactivation whereas the values obtained with both the TZFBR and the TZFBR+MB reactor configurations correspond to the steady state when the coke formation is

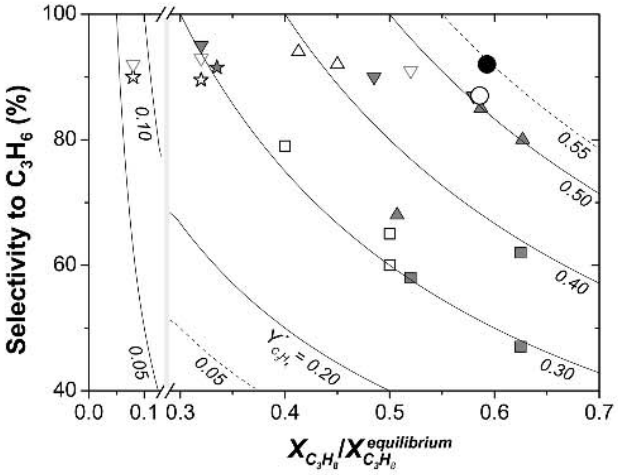

Figure 12. Selectivity vs (conversion/equilibrium conversion) for TZFBR and TZFBR+MB runs from Figure 11 and comparison with results from the literature: , Jablonsky et al. (1999);[20] , Assabumrungrat et al. (2000);[36] ▼, Hullmann et al. (2002);[37] ▽, Salmones et al. (2002);[38] ■, Schafer et al. (2003);[12] □, Putra et al. (2011);[39] ▲, Fattahi et al. (2011);[40] Δ, Botavina et al. (2011);[41] ○, TZFBR (Figure 11); ●, TZFBR+MB (Figure 11). Diverse operating conditions. Lines in graph represent constant values of $Y^*_{C_3H_6}$ (i.e. ratio 'yield to C_3H_6/equilibrium conversion of C_3H_8').

counteracted continuously by the regeneration in the lower zone of the bed.

4. CONCLUSIONS

Catalytic propane dehydrogenation has been tested with different reactors at several reaction temperatures with a Pt−Sn/$MgAl_2O_4$ catalyst. The coke formation during reaction with FBR highly influences the process, because it is impossible to maintain propane conversion along the time on the stream and the catalyst must be regenerated. Then, it is not possible to reach a steady state with this reaction system under these experimental conditions. The TZFBR allows working in a continuous way with only one reactor due to the presence of two different atmospheres inside the reactor, where catalyst can circulate between both zones. By this way deactivated catalyst can be regenerated in situ, preserving its activity during the reaction time. The amount of regenerative agent, oxygen, must be optimized for each reaction temperature, which was found to be higher at high temperatures. Finally, the use of a TZFBR with hollow fiber palladium membrane presents good results in the catalytic propane dehydrogenation, where process yield is improved with respect to other reactor configurations. Also, catalyst activity can be maintained. With this 2-fold process configuration, intensification is achieved in regard to FBR, and better results of yield to propylene than those reported in the literature for conventional reactors were obtained. The advantage of using Pt−Sn/$MgAl_2O_4$, instead of Pt−Sn−K/γ−Al_2O_3 as in previous study, comes from its lower coking tendency. The limitation is the operation range of palladium membranes, which is different from the desirable reaction temperature range of the catalytic propane dehydrogenation. New palladium alloy membranes are needed to meet both operation requirements, with the aim of testing TZFBR with membranes at high temperatures.

AUTHOR INFORMATION

Corresponding Author

*E-mail: jhergui@unizar.es.

Notes

The authors declare no competing financial interest.

ACKNOWLEDGMENTS

Financial support of the Spanish Ministry of Economy and Competitiveness (project CTQ2010-15568) is gratefully acknowledged. Financial aid for the maintenance of the consolidated research group CREG has been provided by the Fondo Social Europeo (FSE) and the Gobierno de Aragon (Aragon, Spain).

NOMENCLATURE

dX/dt = propane conversion variation rate [min^{-1}]
dY/dt = yield to propylene variation rate [min^{-1}]
FBR = fluidized bed reactor
$F_{C_3H_8}$ = molar flow of propane [mmol min^{-1}]
n = stabilization cycle number
$P_{permeate}$ = pressure in the permeate side [mbar]
Q_{gas} = volumetric flow [mL_{STP} min^{-1}]
$S_{C_3H_6}$ = selectivity to propylene [%]
$S_{H_2/Ar}$ = H_2 perm-selectivity; ratio of the permeation flux of pure H_2 to pure Ar
T_r = reaction temperature [°C]
TZFBR = two-zone fluidized bed reactor
TZFBR+MB = two-zone fluidized bed reactor with membrane
u_{mf} = minimum fluidization velocity [cm^3 cm^{-2} s^{-1}]
$u_{r,react}$ = relative velocity in the reaction zone
$u_{r,regen}$ = relative velocity in the regeneration zone
u_r = relative velocity ($u_r = u/u_{mf}$)
W_0 = catalyst weight [g]
$X^{eq}_{C_3H_8}$ = propane conversion at equilibrium [%]
$X_{C_3H_8}$ = propane conversion [%]
$Y_{C_3H_6}$ = yield to propylene [%]
$Y^*_{C_3H_6}$ = relative yield to propylene: $Y_{C_3H_6}/X^{eq}_{C_3H_8}$
ΔP = partial pressure difference across the membrane [bar]

REFERENCES

(1) Shu, J.; Grandjean, B. P. A.; Vanneste, A.; Kaliaguine, S. Catalytic palladium-based membrane reactors - a review. *Can. J. Chem. Eng.* **1991**, *69*, 1036−1060.

(2) Paturzo, L.; Basile, A.; Drioli, E. High temperature membrane reactors and integrated membrane operations. *Rev. Chem. Eng.* **2002**, *18*, 511−551.

(3) Gallucci, F.; Paturzo, L.; Fama, A.; Basile, A. Experimental study of the methane steam reforming reaction in a dense Pd/Ag membrane reactor. *Ind. Eng. Chem. Res.* **2004**, *43*, 928−933.

(4) Armor, J. N. Applications of catalytic inorganic membrane reactors to refinery products. *J. Membr. Sci.* **1998**, *147*, 217−233.

(5) Lin, Y. S. Microporous and dense inorganic membranes: current status and prospective. *Sep. Purif. Technol.* **2001**, *25*, 39−55.

(6) Marigliano, G.; Barbieri, G.; Drioli, E. Equilibrium conversion for a Pd-based membrane reactor. Dependence on the temperature and pressure. *Chem. Eng. Process.* **2003**, *42*, 231−236.

(7) Weyten, H.; Luyten, J.; Keizer, K.; Willems, L.; Leysen, R. Membrane performance: the key issues for dehydrogenation reactions in a catalytic membrane reactor. *Catal. Today* **2000**, *56*, 3−11.

(8) Coronas, J.; Santamaría, J. Catalytic reactors based on porous ceramic membranes. *Catal. Today* **1999**, *51*, 377−389.

(9) Lu, G. Q.; Diniz da Costa, J. C.; Duke, M.; Giessler, S.; Socolow, R.; Williams, R. H.; Kreutz, T. Inorganic membranes for hydrogen

production and purification: A critical review and perspective. *J. Colloid Interface Sci.* **2007**, *314*, 589−603.
(10) Ma, Y. H. Pd-based hydrogen separation membranes - status and perspective. Proceedings of the 9th International Conference on Inorganic Membranes (ICIM9), Lillehammer, Norway, June 25−29, 2006; Bredesen, R., Raeder, H., Eds.; *SINTEF*: Lillehammer, 2006, 28−37.
(11) Gimeno, M. P.; Wu, Z. T.; Soler, J.; Herguido, J.; Li, K.; Menendez, M. Combination of a Two-Zone Fluidized Bed Reactor with a Pd hollow fibre membrane for catalytic alkane dehydrogenation. *Chem. Eng. J.* **2009**, *155*, 298−303.
(12) Schäfer, R.; Noack, M.; Kölsch, P.; Stöhr, M.; Caro, J. Comparison of different catalysts in the membrane-supported dehydrogenation of propane. *Catal. Today* **2003**, *82*, 15−23.
(13) Gbenedio, E.; Wu, Z.; Hatim, I.; Kingsbury, B. F. K.; Li, K. A multifunctional Pd/alumina hollow fibre membrane reactor for propane dehydrogenation. *Catal. Today* **2010**, *156*, 93−99.
(14) XSuzuki, K.; Kaneko, Y. Dehydrogenation of propane over chromia-alumina-potassium oxide catalyst. *J. Catal.* **1977**, *47*, 239−248.
(15) Gascon, J.; Tellez, C.; Herguido, J.; Menendez, M. Propane dehydrogenation over a Cr_2O_3/Al_2O_3 catalyst: transient kinetic modeling of propene and coke formation. *Appl. Catal., A* **2003**, *248*, 105−116.
(16) Barias, O.; Holmen, A.; Blekkan, E. Propane dehydrogenation over supported Pt and Pt-Sn catalysts: Catalyst preparation, characterization, and activity measurements. *J. Catal.* **1996**, *158*, 1−12.
(17) Gascon, J.; Tellez, C.; Herguido, J.; Menendez, M. A two-zone fluidized bed reactor for catalytic propane dehydrogenation. *Chem. Eng. J.* **2005**, *106*, 91−96.
(18) Li, Q.; Sui, Z.; Zhou, X.; Chen, D. Kinetics of propane dehydrogenation over $Pt−Sn/Al_2O_3$ catalyst. *Appl. Catal., A* **2011**, *398*, 18−26.
(19) Greenwood, A. Tight US propylene may lead to two more PDH plants, in http://www.icis.com/, dated June/29/2012, checked at January/23/2013.
(20) Jablonski, E. L.; Castro, A. A.; Scelza, O. A.; de Miguel, S. R. Effect of Ga addition to Pt/Al_2O_3 on the activity, selectivity and deactivation in the propane dehydrogenation. *Appl. Catal., A* **1999**, *183*, 189−198.
(21) Zhang, S.; Zhou, Y.; Zhang, Y.; Huang, L. Effect of K Addition on catalytic performance of PtSn/ZSM-5 catalyst for propane dehydrogenation. *Catal. Lett.* **2010**, *135*, 76−82.
(22) Zhang, Y.; Zhou, Y.; Liu, H.; Wang, Y.; Xu, Y.; Wu, P. Effect of La addition on catalytic performance of PtSnNa/ZSM-5 catalyst for propane dehydrogenation. *Appl. Catal., A* **2007**, *333*, 202−210.
(23) Zhang, Y.; Zhou, Y. M.; Qiu, A. D.; Wang, Y.; Wu, P. Effect of Na addition on catalytic performance of PtSn/ZSM-5 catalyst for propane dehydrogenation. *Acta Phys. -Chim. Sin.* **2006**, *22*, 672−678.
(24) Nawaz, Z.; Tang, X.; Zhang, Q.; Wang, D.; Fei, W. SAPO-34 supported Pt-Sn-based novel catalyst for propane dehydrogenation to propylene. *Catal. Commun.* **2009**, *10*, 1925−1930.
(25) Julian, L.; Gallucci, F.; van Sint Annaland, M.; Herguido, J.; Menendez, M. Coupled PIV/DIA for fluid dynamics studies on a Two-Section Two-Zone Fluidized Bed Reactor. *Chem. Eng. J.* **2012**, *207−208*, 122−132.
(26) Rubio, O.; Herguido, J.; Menendez, M. Two-zone fluidized bed reactor for simultaneous reaction and catalyst reoxidation: influence of reactor size. *Appl. Catal., A* **2004**, *272*, 321−327.
(27) Herguido, J.; Menendez, M.; Santamaría, J. On the use of fluidized bed catalytic reactors where reduction and oxidation zones are present simultaneously. *Catal. Today* **2005**, *100*, 181−189.
(28) Vigneault, S. S.; Elnashaie, S.S.E:H.; Grace, J. R. Simulation of a compact multichannel membrane reactor for the production of pure hydrogen via steam methane reforming. *Chem. Eng. Technol.* **2012**, *35*, 1520−1533.
(29) Gallucci, F.; van Sint Annaland, M.; Kuipers, J. A. M. Pure hydrogen production via autothermal reforming of ethanol in a fluidized bed membrane reactor: A simulation study. *Int. J. Hydrogen Energy.* **2010**, *35*, 1659−1668.
(30) Armendariz, H.; Guzman, A.; Toledo, J. A.; Llanos, M. E.; Vazquez, A.; Aguilar-Rios, G. Isopentane dehydrogenation on Pt-Sn catalysts supported on Al-Mg-O mixed oxides: effect of Al/Mg atomic ratio. *Appl. Catal., A* **2001**, *211*, 69−80.
(31) Menendez, M.; Herguido, J.; Tellez, C.; Soler, J.; Gimeno, M. P. Two zone fluidized bed reactor. PCT Application ES2009/070241, June 19, 2008.
(32) Gimeno, M. P.; Soler, J.; Herguido, J.; Menendez, M. Counteracting catalyst deactivation in methane aromatization with a Two Zone Fluidized Bed Reactor. *Ind. Eng. Chem. Res.* **2010**, *49*, 996−1000.
(33) Tan, X.; Liu, S.; Li, K. Preparation and characterization of inorganic hollow fiber membranes. *J. Membr. Sci.* **2001**, *188*, 87−95.
(34) Paglieri, S. N.; Way, J. D. Innovations in palladium membrane research. *Separ. Purif. Methods* **2002**, *31*, 1−169.
(35) García-García, F. R.; Torrente-Murciano, L.; Chadwick, D.; Li, K. Hollow fibre membrane reactors for high H_2 yields in the WGS reaction. *J. Membr. Sci.* **2012**, *405−406*, 30−37.
(36) Assabumrungrat, S.; Jhoraleecharnchai, W.; Praserthdam, P.; Goto, S. Kinetics for dehydrogenation of propane on Pt-Sn-K/gamma-Al_2O_3 catalyst. *J. Chem. Eng. Jpn.* **2000**, *33*, 529−532.
(37) Hullmann, D.; Wendt, G.; Singliar, U.; Ziegenbalg, G. Propane dehydrogenation over supported platinum silicon nitride catalysts. *Appl. Catal., A* **2002**, *225*, 261−270.
(38) Salmones, J.; Wang, J.; Galicia, J. A.; Aguilar-Rios, G. H_2 reduction behaviors and catalytic performance of bimetallic tin-modified platinum catalysts for propane dehydrogenation. *J. Mol. Catal. A: Chem.* **2002**, *184*, 203−213.
(39) Putra, M. D.; Al-Zahrani, S. M.; Abasaeed, A. E. Oxidative dehydrogenation of propane to propylene over Al_2O_3-supported Sr−V−Mo catalysts. *Catal. Commun.* **2011**, *14*, 107−110.
(40) Fattahi, M.; Khorasheh, F.; Sahebdelfar, S.; Zangeneh, F.; Ganji, K.; Saeedizad, M. The effect of oxygenate additives on the performance of $Pt−Sn/\gamma$ - Al_2O_3 catalyst in the propane dehydrogenation process. *Sci. Iran.* **2011**, *18*, 1377−1383.
(41) Botavina, M. A.; Evangelisti, C.; Agafonov, Yu.A.; Gaidai, N. A.; Panziera, N.; Lapidus, A. L.; Martra, G. CrO_x/SiO_2 catalysts prepared by metal vapour synthesis: Physical−chemical characterisation and functional testing in oxidative dehydrogenation of propane. *Chem. Eng. J.* **2011**, *166*, 1132−1138.

Artículo XI

H. Montesinos, I. Julián, J. Herguido, M. Menéndez,
Effect of the presence of light HC mixtures on H_2 permeation through Pd-Ag membranes,
Int. J. Hydrogen. Energ. 40 (2015) 3462-3471

Available online at www.sciencedirect.com

ScienceDirect

journal homepage: www.elsevier.com/locate/he

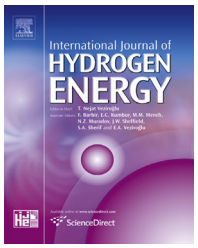

Effect of the presence of light hydrocarbon mixtures on hydrogen permeance through Pd–Ag alloyed membranes

Hector Montesinos, Ignacio Julián, Javier Herguido, Miguel Menéndez *

Catalysis, Molecular Separations and Reactor Engineering Group (CREG), Aragón Institute of Engineering Research (I3A), University of Zaragoza, Spain

ARTICLE INFO

Article history:
Received 1 July 2014
Received in revised form
30 October 2014
Accepted 8 November 2014
Available online 8 December 2014

Keywords:
Hydrogen permeation
Pd membranes
Membrane reactors
Propane dehydrogenation

ABSTRACT

The production of light olefins by alkane dehydrogenation is limited by the thermodynamic equilibrium. The use of membrane reactors for this process enhances alkane conversion by a selective removal of hydrogen from the reaction media. This hydrogen removal results in an equilibrium shift towards the production of olefins. However, hydrogen permeance through Pd-based membranes may be affected by the presence of light olefins. This work evaluates the effect of the composition of propane/propylene mixtures on the hydrogen permeation through Pd–Ag alloyed membranes for propane dehydrogenation. It has been observed that the transient hydrogen permeation decreases in the presence of C_3 species due to coke deposition over the Pd–Ag layer. The permeation decrease has been characterized and quantified as a function of propane/propylene contents in the feed gas and of operation temperature.

Introduction

Membrane reactors (*MR*) allow simultaneous reaction and separation in a single unit. The potential advantages of *MR* are the reduction of downstream separation costs, the reduction of capital costs and the improvement of yield and selectivity in reactions limited by the thermodynamic equilibrium [1]. Among the most extensively investigated *MR* configurations are those that use inorganic membranes, essentially based on palladium or alloyed Pd thin layers, for hydrogen production or extraction. The use of *MR* has been increasingly applied to water-gas-shift (e.g. Ref. [2]) or steam reforming (e.g. Ref. [3]) processes for hydrogen production. In contrast, alkane dehydrogenations are processes where hydrogen extraction promotes equilibrium shift effects [4]. The success of a Pd-based *MR* depends on the membrane production method and the reactor configuration. The first factor concerns perm-selectivity enhancement, while the second addresses the reduction of mass and heat transfer limitations [1].

An example of a chemical process where hydrogen is selectively removed from the system is propane dehydrogenation, e.g. Refs. [4–6]. In a recent work, Medrano et al., 2013 [7] used a novel *MR* concept to produce propylene by catalytic propane dehydrogenation (*PDH*) in the presence of Pt–Sn catalyst supported on $MgAl_2O_4$ spinel. The main drawbacks of the reaction were its high endothermicity, equilibrium limited conversion, side-reactions and tendency

* *Corresponding author*. Tel.: +34 976761152; fax: +34 976762043.
E-mail address: qtmiguel@unizar.es (M. Menéndez).
http://dx.doi.org/10.1016/j.ijhydene.2014.11.054

to produce coke deposition over the catalyst surface [8]. The combined effect of a low acidity support with a highly selective catalyst, together with the use of a novel auto-regenerative reactor concept coupled to a Pd–Ag membrane, resulted in a successful performance of *PDH* with an increased conversion rate and steady-state operation at the usual reaction temperatures.

The above-mentioned novel auto-regenerative reactor concept, i.e. the Two-Zone Fluidized Bed Reactor (*TZFBR*), consisted of a catalytic gas–solid fluidized bed with two gas injection points [9]. Propane was fed through an immersed gas distributor, whereas an oxidizer (diluted O_2) was fed through a distributor located at the bottom of the bed. The catalytic *PDH* took place within the upper region of the bed leading to coke deposition over the catalyst as a byproduct. Oxygen was used to burn coke deposits and to regenerate the catalyst within the lower bed zone [8,10]. The characteristic axial mixing of solids that takes place in a fluidized bed allowed the steady-state operation to be maintained without net catalyst deactivation under certain operation conditions [8]. The TZFBR was designed according to the recommendations of Julián et al. [11,12] for improving hydrodynamic reactor performance and axial mixing. Additionally, a Pd–Ag membrane immersed in the upper bed zone was used to enhance propane conversion by removing H_2 selectively from the reactive atmosphere, thus shifting the reaction equilibrium towards propylene production. Nevertheless, the increase in the yield to propylene due to the equilibrium shift was not consistent with the permeation capacity of the membrane at similar H_2 pressure drop conditions. Membrane characterization tests showed higher hydrogen permeation with H_2/Ar feeds than at reactive conditions, i.e. H_2 in a mixture of alkanes (C_1–C_3) and light olefins, with the same H_2 molar fraction in the feed gas [7]. These results motivated the present study.

Several authors have recently studied the effect of CH_4 and CO contents, i.e. syngas compositions, on the performance of Pd-based membranes [13–16]. Analogously, many efforts have been made to develop Pd-alloyed membranes to minimize the effect of H_2S poisoning [17–20]. However, the effect of light olefins on hydrogen permeation for *PDH* processes in *MR* has not been studied in depth. Some authors describe the effect of the Pd membrane support [4,21] or membrane composition [22] on the *PDH* equilibrium shift. Others focus on Pd membrane fabrication to enhance hydrogen permeation for application in *PDH* process [6] or on process conditions [23]. However, only a few authors have reported Pd-based membrane coking by propylene decomposition under usual *PDH* operation conditions ($T \sim 550\ ^\circ C$) and showed a comprehensive study on membrane deactivation due to Pd–C formation and coke deposition in the presence of C_3H_6/H_2 mixtures [24,25].

This work analyzes the effect of propylene (the main reaction product) and propane (the main reactive agent) contents on the hydrogen permeation through commercial dense Pd–Ag membranes supported on porous stainless steel, provided by *REB Research*®, at reactive *PDH* conditions. For this purpose, a number of previous characterization tests were required to determine the characteristic permeation curve as a function of pressure drop for the commercial membranes at different temperatures.

According to Sieverts' law, the solubility of a diatomic gas in metal is proportional to the square root of the partial pressure of the gas in thermodynamic equilibrium. Therefore, hydrogen permeation through Pd-based membranes should follow a linear trend against the difference of $P_{H_2}^{0.5}$ on both sides of the membrane (equation (1)). Sieverts' law is frequently referred to Richardson's equation (equation (2)), which considers a general value *n* for the exponent of the pressure drop expression. Some authors, e.g. Ref. [26], suggest that the exponent of Richardson's equation may vary between 0.5 and 0.86 depending on the sorbent metal characteristics. Chen and cols. [27] suggest that *n* may even reach values close to one depending on the permeation temperature, thickness of the metal layer and magnitude of the H_2 pressure drop. Indeed, the square-root law may only be applied to evaluate and predict the hydrogen permeation flux when the lattice diffusion of hydrogen is the controlling step while at the same time the Pd–H system is "infinitely diluted" (very low H_2 concentration at the Pd lattice) [28]. In practice, H_2 solubility and diffusivity in the metal lattice are determined by the hydrogen concentration [28,29] and, thus, Richardson's coefficient differs from 0.5 even in the case of using thick Pd layers.

$$N_{H_2} = P_{H_2}^0 \exp\left(\frac{-E_a}{RT}\right)\left(P_{H_2,F}^{1/2} - P_{H_2,P}^{1/2}\right) = K\left(P_{H_2,F}^{0.5} - P_{H_2,P}^{0.5}\right) \quad (1)$$

$$N_{H_2} = K\left(P_{H_2,ext}^{n} - P_{H_2,P}^{n}\right) \quad (2)$$

Therefore, the experimental Richardson's coefficient for the commercial Pd–Ag membranes has here been estimated as the *n*-value that maximizes the linear regression between the H_2 permeation flux and the hydrogen pressure drop between the membrane sides.

Once the membrane permeability was characterized for H_2/Ar feed gas mixtures, diluted propane and propylene contents were then introduced into the membrane system. A comprehensive set of feed gas compositions and temperatures has been tested to evaluate the coupled effect of temperature, driving force and the presence of hydrocarbon species on the Pd–Ag membrane performance.

Experimental set-up

The experimental set-up essentially consisted of four gas feed lines, a heated quartz vessel where the Pd–Ag membranes were located, a vacuum pump to establish a pressure drop for hydrogen extraction, an in-line gas chromatograph and a flow meter to measure both the molar composition and the volumetric flow of the retentate gas, respectively. A scheme of the experimental set-up is shown in Fig. 1.

Four different gas lines, viz. propylene, hydrogen, inert gas for dilution (argon) and oxygen for membrane regeneration, were driven to the inlet at the bottom of the reactor. The flow of each compound in the feed gas was controlled by digital mass flow meters (*Alicat Scientific*). A 3-way valve was placed before the vessel entrance in order to measure the inlet gas pressure with a pressure transducer (*Digitron P445*). A temperature controller (*Eurotherm 3116*) attached to a thermocouple, which was located inside the vessel, was connected to

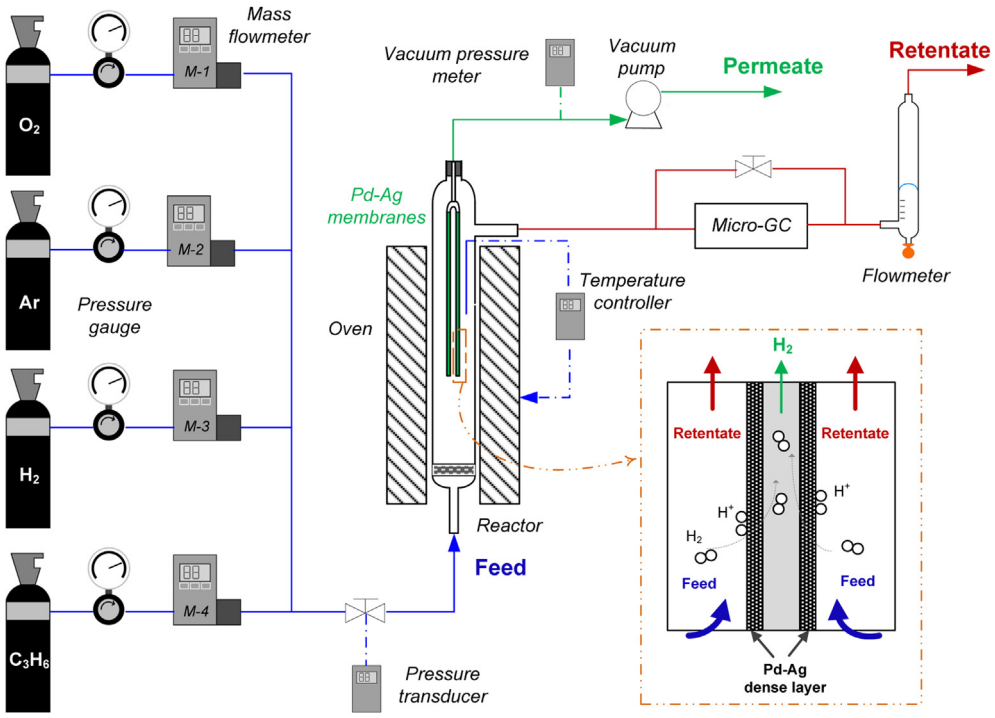

Fig. 1 – Experimental set-up for hydrogen permeation tests.

an electrical furnace surrounding the reactor. Two commercial dense Pd–Ag membranes supported on porous stainless steel (*REB Research*®) were attached to the top-end of the reactor. The two tubular membranes used in this work were 178 mm long with an external diameter of 3.17 mm and a Pd–Ag layer thickness of 76 μm. The total permeation area was 30.4 cm^2. The thickness of the membrane ensures 100% selectivity to hydrogen and allows its use in a fluidized bed reactor without protective shell against attrition. The bottom-end of the membrane was sealed whereas the top-end consists of a standard 3/16 stainless steel tube for connection to a vacuum pump (*Telstar 2P-3*). The deposition of the Pd-(23%–25%)Ag [30] membrane layer on the porous metal support reinforced with Inconel® was accomplished by electroless or electrolytic plating using a proprietary technique [31]. The two membranes were bridged through their upper part as shown in Fig. 1.

The vacuum pump worked at its maximum flow, providing quite a low pressure (P_v ~ 3 mbar) depending on the atmospheric pressure fluctuations, i.e. the vacuum pressure was not controlled. A vacuum pressure meter measured the transient vacuum pressure in the permeate line.

The volumetric composition of the retentate gas was measured by gas chromatography using a micro-GC (R3000, SRA Instruments®). The volumetric retentate flow at room conditions was measured by an on-line bubble flow meter.

Hydrogen permeation tests

First, H_2/Ar mixtures were fed at typical *PHD* process temperatures (T ~ 550 °C) to obtain the H_2 permeation curve as a function of pressure drop on both sides of the membrane. The inlet gas was fed at atmospheric pressure in every experiment. This means that the hydrogen dilution factor determined the H_2 partial pressure on the feed side ($P_{H_2,F}$) in each case. The experimental series are summarized in Table 1.

The characteristic Richardson's equation coefficient for the considered Pd/Ag membranes was estimated with respect to different approximations for the partial pressure of hydrogen on the external side of the membrane ($P_{H_2,ext}$). Due to the reactor configuration and membrane geometry, there was a hydrogen partial pressure gradient at the membranes' outer wall from the bottom to the top. As can be observed in Fig. 2,

Table 1 – Experimental permeation series.

$H_{2,F}$ (%)	$C_3H_{6,F}$ (%)	$C_3H_{8,F}$ (%)	Temperature (°C)	Inlet gas flow (mL_{STP}/min)
Determination of H_2 permeation curve vs. pressure drop at different temperatures (n-value)				
2.4%	0	0	500–550–575–600	410
5.9%	0	0		425
11.1%	0	0		450
15.8%	0	0		475
19.9%	0	0		500
Determination of membranes performance in the presence of C_3 hydrocarbons				
19.0%	0	0	500–550–575–600	530
19.0%	19.0%	0		530
19.0%	9.5%	0		530
19.0%	3.8%	0		530
19.0%	0	3.8%		530
9.5%	9.5%	0	550	1060
19.0%	19.0%	0	550	105

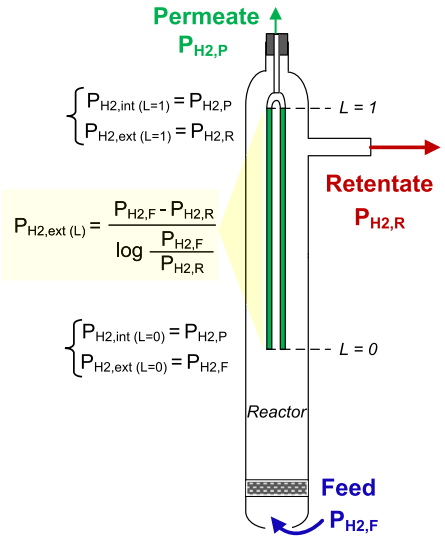

Fig. 2 – Diagram of hydrogen partial pressures involved in the system.

the partial pressure of hydrogen at the very bottom of the membrane corresponds to the composition of the feed gas ($P_{H_2,L=0} = P_{H_2,F}$) whereas the H_2 pressure at the top corresponds to the hydrogen partial pressure in the retentate gas flow ($P_{H_2,L=1} = P_{H_2,R}$). Here, ΔP_{H_2} was estimated under the assumption of constant pressure of hydrogen in the permeate ($P_{H_2,ext}$) along the membrane length. Taking into account that the driving force for gas permeation is the gas pressure drop (ΔP_{gas}) between both sides of the membrane, four different approximations were tested. Firstly, it was assumed that $P_{H_2,ext}$ would correspond to $P_{H_2,F}$. The "maximal pressure drop" assumption is often used in works with hollow fiber membrane configurations, e.g. Ref. [28]. Secondly, the approximation $P_{H_2,ext} \approx P_{H_2,R}$ was tested. This second definition is also commonly used by several authors when using hollow fibers, e.g. Refs. [32,33]. $P_{H_2,ext}$ was further estimated as the arithmetic mean between the feed and retentate partial pressure of hydrogen. Finally, a logarithmic mean between these two pressures was applied to estimate the hydrogen permeation driving force.

In a second step, the effect of the operation temperature on H_2 permeation was measured. The performance of the commercial Pd/Ag was evaluated within the temperature range $T = 500\ ^\circ C$–$600\ ^\circ C$, which is frequently used in *PHD* processes and usually leads to moderate conversions with relatively low catalyst coking and propane cracking rates [8].

Finally, the effect of a *PDH* reactive atmosphere (C_3 mixture) on hydrogen permeation and membrane performance was evaluated. For this purpose, $H_2/C_3H_6/C_3H_8/Ar$ mixtures were fed at reactive temperatures to the empty reactor vessel, i.e. without using a catalytic bed for propylene conversion. Tested feed gas compositions include C_3H_6:H_2 = 1:1, 1:2 and 1:5, as well as C_3H_8:H_2 = 1:5. Different inert gas flows were used for dilution. The detailed experimental series is shown in Table 1.

Experimental results

In this section, results concerning the characterization of commercial Pd/Ag membranes to be used in *PDH* with hydrogen recovery will be discussed. Firstly, their characteristic Richardson's equation coefficient will be determined together with the most suitable definition of the hydrogen pressure drop for this singular reactor configuration. Next, the effect of the *PDH* operation temperature on H_2 permeation will be discussed. Furthermore, it will be illustrated that the presence of light hydrocarbons affects membrane performance and that H_2 permeation changes over time on stream under reactive conditions. A rough estimation of the catalytic activity of the Pd/Ag membrane layer for *PDH* and propylene hydrogenation (*PH*) will be presented. Finally, the '*membrane efficiency*' under different operation conditions will be quantified and discussed.

Hydrogen pressure drop definition. Richardson's coefficient determination

Four different pressure drop definitions have been suggested in Section 3 to evaluate the H_2 permeation curve under the assumption of constant hydrogen partial pressure on the outer walls of the membrane ($P_{H_2,ext}$). In the following discussion, "A" represents $P_{H_2,ext} \approx P_{H_2,F}$. "R" represents $P_{H_2,ext} \approx P_{H_2,R}$. The expression "$m$(A,R)" means $P_{H_2,ext} \approx (P_{H_2,F} + P_{H_2,R})/2$, whereas "log m(A,R)" refers to $P_{H_2,ext} \approx (P_{H_2,F} - P_{H_2,R})/\log(P_{H_2,F}/P_{H_2,R})$.

A multivariable optimization procedure has been carried out to determine both the most suitable pressure drop definition and the Richardson's equation coefficient n that minimize regression residuals for the different permeation curves.

Fig. 3 shows the effect of different n-values in the linear fitting between H_2 permeation at 550 °C and the hydrogen pressure drop, $\Delta P_{H_2}^n$ being calculated with the "log m(A,R)" expression. Fig. 4 shows the fitting quality of the four

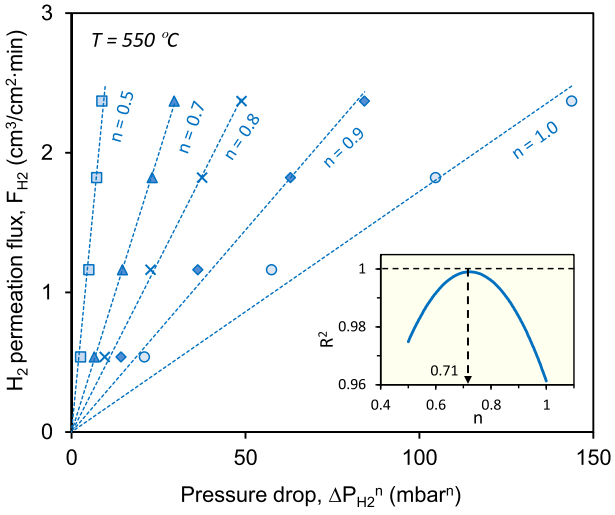

Fig. 3 – H_2 permeation flux at $T = 550\ ^\circ C$ for different Richardson equation coefficient values (n) being $\Delta P_{H_2} = P_{H_2,ext} - P_{H_2,P}$, where $P_{H_2,ext} = (P_{H_2,F} - P_{H_2,R})/\log(P_{H_2,F}/P_{H_2,R})$.

suggested pressure drop definitions for a Richardson's exponent of $n = 0.71$.

In Fig. 3 it can be observed that $n = 0.71$ leads to the best linear regression ($R^2 = 0.9993$) compared to other n-values tested in the range suggested by Deveau et al. [26], from 0.5 (dissociative chemisorption control) to 1.0 (ordinary diffusion control). The optimal value 0.71 maximizes the regression coefficient for every tested condition, including permeation tests at different temperatures in the range of those prescribed elsewhere [7,8] for suitable PDH operation in fluidized bed membrane reactors. According to some authors [33], the high n-value that may frequently be found in this kind of membranes could be explained by: a) the formation of segregated silver on the Pd–Ag surface at higher temperature that would result in a H_2 adsorption retardation on the Pd surface [34,35]; b) the formation of Pd–Al bonds at the interface between the dense layer and the alumina support that would decrease the reaction rate for H_2 transportation through the membrane [36].

In Fig. 4, the evaluation of the four proposed definitions for the average $\Delta P_{H_2}^{0.71}$ along the membrane length suggests that the approximation $P_{H_2,ext} \approx P_{H_2,R}$ may not be suitable for describing the linearity between the H_2 permeation and its pressure drop between the membrane sides. On the other hand, the expressions "A", "m(A,R)", "log m(A,R)" lead to quite high linear correlations. The pressure drop based on the logarithmic mean between $P_{H_2,F}$ and $P_{H_2,R}$ for the calculation of the $P_{H_2,ext}$ has been selected, from among the different assumptions as the most representative of the experimental conditions.

Effect of temperature on H_2 permeation

It is well known that temperature has an effect on the permeation of diatomic gases through metallic surfaces. According to Sieverts' law (equation (1)), gas permeation is favored at high temperatures. Focusing the research on the application of Pd/Ag alloyed membranes in *PDH* for hydrogen recovery and dehydrogenation equilibrium shift, the performance of these membranes has been analyzed in a range of temperatures that represents a suitable operation window for *PDH*, i.e. 500 °C–600 °C. H_2 permeation results at different temperatures and pressure drops are presented in Fig. 5. The results show that the H_2 permeation flux slightly increases with an increase of 50 °C in temperature, from 550 °C to 600 °C. The small improvement in hydrogen removal at 600 °C would not on its own justify the use of such an operation temperature in PDH processes, since the enhancement of catalyst coking and side-reactions plays an important role at these high temperatures. Moreover, operation temperatures above 600 °C may compromise the Pd–Ag membrane thermal stability. Although these membranes could work at 700 °C or even higher temperatures according to the manufacturer, the maximum working temperature without damage depends on the applied pressure drop on both sides of the membrane. To illustrate this, the maximum reported temperature at which similar membranes have been tested without deteriorating the perm-selectivity to hydrogen along the time on stream is 650 °C [37,38].

Concerning the effect of temperature on the Richardson's coefficient for a linear regression between permeation flux and pressure drop, it can be observed that n remains almost constant within the temperature range 550 °C–600 °C whereas it peaks up to 1 at lower temperatures (500 °C). Some authors, e.g. Refs. [33,39], found that the operation temperature has an effect on the n-value. On the one hand, Maneerung et al. [33] suggest that at high temperatures ($T \geq 400$ °C) silver may segregate towards the Pd–Ag surface retarding hydrogen adsorption on the Pd surface, thus leading to an increase of n with temperature. On the other hand, Guazzone et al. [39] found that n decreases with temperature for Pd membranes in the range 250 °C–400 °C and remains almost constant

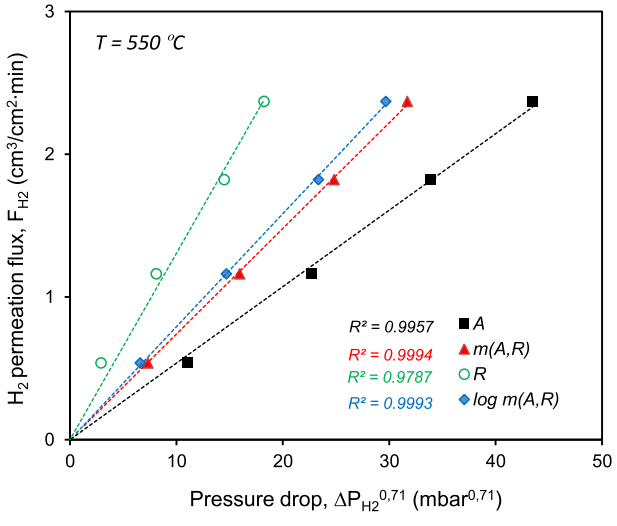

Fig. 4 – H_2 permeation flux at $T = 550$ °C for different pressure drop formulations. $\Delta P_{H_2} = P_{H_2,ext} - P_{H_2,P}$, being P_{ext} equal to $P_{H_2,F}[A]$, $(P_{H_2,F} + P_{H_2,R})/2[m(A,R)]$, $P_{H_2,R}[R]$, $(P_{H_2,F} - P_{H_2,R})/\log(P_{H_2,F}/P_{H_2,R})$ [log m(A,R)], respectively.

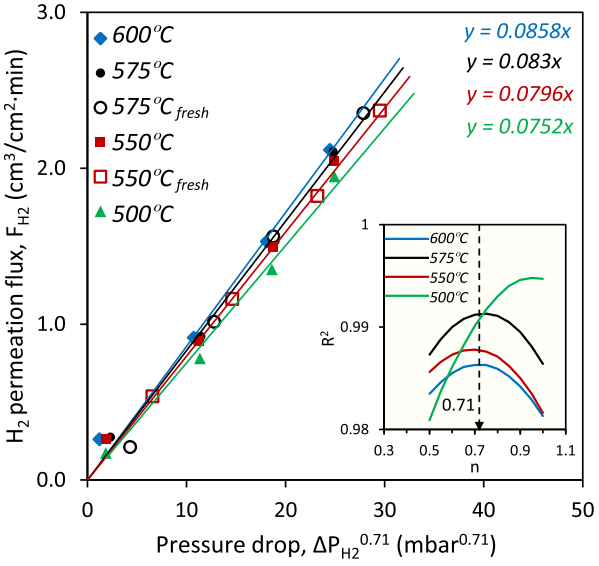

Fig. 5 – Effect of operation temperature on the H_2 permeation flux through commercial Pd/Ag membranes, before ("*fresh*") and after regeneration with diluted O_2.

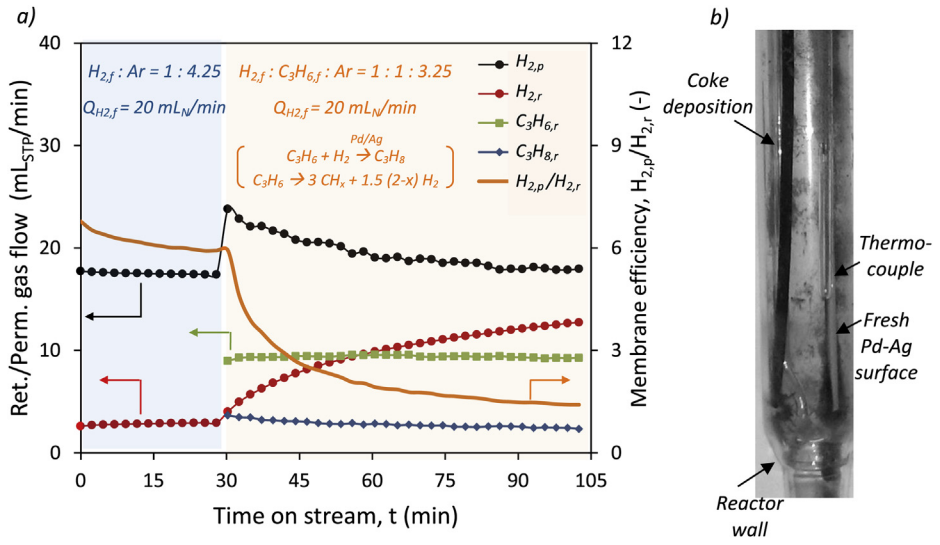

Fig. 6 – a) Effect of propylene co-feed (C_3H_6:H_2:Ar = 1:1:3.25) on membrane performance at T = 550 °C. Pd–Ag surface as catalyst for propylene hydrogenation and coke deposition; b) Comparison between fresh and used membrane after a C_3H_6/H_2 co-feed test.

between 400 and 500 °C. In the present study, the *n*-values that led to the best linear regression between pressure drop and hydrogen permeation at 500 °C, 550 °C, 575 °C and 600 °C are, respectively: 0.99, 0.71, 0.74 and 0.71. This illustrates that *n* remains almost constant in the range 550 °C–600 °C, whereas it peaks up to almost 1 at the lowest tested temperature, as stated above. The evolution of the linear regression coefficient (R^2) against *n* for the different temperatures is shown in Fig. 5. Substantial *n*-value differences may be expected when modifying the Pd-alloy layer thickness, since this determines the hydrogen dissociation-to-diffusion ratio [39], but not for the range of temperatures tested in this work. The unexpected $n = 0.99$ at 500 °C would suggest that hydrogen bulk diffusion through the dense Pd–Ag layer would be the rate determining step in comparison to the H_2 dissociative chemisorption over the membrane surface.

Effect of propylene co-feed on H_2 permeation

Prior studies [25] suggested that propylene decomposition may occur over Pd surfaces at high temperatures leading to Pd–C species formation, coke deposition and a decrease in H_2 permeability. This section will illustrate the transient carbon deposition over the Pd/Ag layer that takes place when co-feeding propylene and hydrogen to the membrane reactor. The tested C_3H_6:H_2 = 1:1 ratio in the feed gas is of interest to the authors since it represents the stoichiometric gas production in a real PDH process. In order to show the effect of co-existing C_3H_6 on the membrane performance, transient H_2 permeation results have been collected in two consecutive steps: firstly feeding diluted hydrogen in a mixture H_2:Ar = 1:4.25 and, secondly, co-feeding C_3H_6 in the following proportions: H_2:C_3H_6:Ar = 1:1:3.25. Fig. 6(a) illustrates the hydrogen permeation decrease and, analogously, the H_2 retentate increase at the time that propylene is fed to the system. The transient hydrogen permeation increase at the very beginning of the second step is due to the fact that propylene decomposition leads not only to carbon deposition on the membrane surface but also to hydrogen generation. Therefore, the pressure drop increases and both permeate and retentate H_2 fluxes become higher than in the previous step. As long as Pd carbides are formed and coke deposits cover the Pd/Ag layer, hydrogen permeation decreases and the H_2 retentate flow increases. The analysis of the '*membrane efficiency*' (*ME*) defined as the quotient between permeate and retentate hydrogen volumetric flows, i.e. $ME = F_{H_2,P}/F_{H_2,R}$, reveals a transient *ME* decrease during the time on stream in the presence of propylene as a result of membrane coking. Similarly, it has been found that *ME* decreases in the presence of H_2/Ar mixtures during the operation time. This slight decrease in *ME* may be related to concentration polarization phenomena, which are widely reported in the literature for similar membrane configurations (e.g. Refs. [40,41]). Nevertheless, the effect of concentration polarization may be neglected against coking in terms of membrane efficiency as shown in Fig. 6(a). By co-feeding propylene (C_3H_6:H_2:Ar = 1:1:3.25), *ME* drops to half of its initial value in about 15 min.

At the same time that propylene decomposition occurs, propylene hydrogenation takes place producing propane. To some extent, propane generation implies hydrogen consumption. However, membrane coking becomes favored in the test conditions and this results in hydrogen production. A global mass balance to hydrogen reveals a net H_2 accumulation in the system (around 15% of the hydrogen supplied) as hydrogenated carbon, CH_x. The transient C_3H_8 generation slightly decreases during the time on stream due to its decomposition and the enhanced trend to coke deposition of the reactive propylene. Nevertheless, the C_3H_6 conversion remains almost constant over the testing time. Fig. 6 b shows a comparison between a fresh Pd/Ag layer and a coked membrane surface after a C_3H_6/H_2 co-feeding test. Membrane coking is almost completely reversible. Regeneration of the membranes was carried out by feeding diluted O_2 in an inert gas (e.g. O_2:Ar = 1:20) until no CO_x signal was detected by gas

chromatography. The carbon deposits were burned away and the membrane surface recovered its initial permeability without being damaged. Hydrogen permeation fluxes before ("*fresh*") and after membrane coking and regeneration at 550 °C and 575 °C are compared in Fig. 5. It was observed that the permeability of the Pd–Ag layer was not significantly affected by the formation of superficial Pd carbides and the subsequent burning of carbonaceous species.

Fig. 7 shows the transient C_3H_6 conversion, together with its selectivity to hydrogenation (towards C_3H_8 production) and to decomposition. As already discussed, the decomposition of C_3 species occurs to a greater extent than C_3H_6 hydrogenation. This trend is enhanced over the permeation time, maybe due to an increase of propane decomposition. The same figure shows the cumulative coke deposition mass over the time on stream. The mass of coke deposit has been estimated considering a CH formulation for the carbonaceous species. As can be observed, the coke deposition increases in an almost linear fashion. This would suggest that the membrane layer is still not saturated. Otherwise, fresh propylene would not interact with the metal surface and decomposition would not take place, thus reducing the coking rate.

Effect of feed gas composition and temperature on membrane efficiency

The membrane efficiency (*ME*), as defined in the previous section, allows the transient membranes performance to be analyzed in terms of instantaneous permeate and retentate H_2 volumetric flows. Of course, *ME* depends on the applied H_2 pressure drop on both sides of the membrane. In this study, in which gas mixtures are fed at atmospheric pressure and the driving force is provided by a vacuum pump connected to the permeate side, the hydrogen partial pressure in the feed gas ($P_{H_2,F}$) can be expressed in terms of H_2 concentration in the feed mixture. Five different H_2/Ar mixtures at four different temperatures have been tested to analyze the influence of the composition and operation temperature on the steady-state *ME*, thus neglecting concentration polarization effects. Experimental $ME = f(T,\%H_{2,F})$ results are shown in Fig. 8. For each test, the steady-state membrane efficiency represents the average *ME* during one hour on stream. The relative *ME* values presented in Fig. 8 refer to the membrane efficiency of the reference case, $ME_{550\,°C,19\%}$. This experiment was carried out at 550 °C, feeding a gas mixture of H_2:Ar = 1:4.25. The results illustrate that the higher the H_2 concentration in the feed gas, the higher the membrane efficiency. Similarly, it is shown that the higher the operation temperature, the higher the permeate-to-retentate ratio, as expected. The steady-state *ME* peaks at around 10% from 550 °C to 600 °C, as a general trend, which may be of interest for any eventual use of Pd–Ag membranes for PDH.

Fig. 9 shows the transient relative membrane efficiency, defined as $ME_t/ME_{t=0}$, at a certain operation temperature (T = 550 °C) and different hydrocarbon concentrations in the feed gas, having 19% $H_{2,F}$ in all cases. It can be observed that the feed gas free of C_3 species maintains a constant relative *ME* during the time on stream. The slight transient decrease in *ME* may be related to concentration polarization effects, as already discussed. Nevertheless, these effects can be considered negligible against membrane surface coking as is clearly observed in Fig. 9. The increase in the propylene content in the feed gas leads to a faster *ME* decrease in similar driving force conditions for H_2 permeation. Indeed, in the case of C_3H_6:H_2 = 1:1 (19% C_3H_6) *ME* drops to half of its initial value in less than 15 min, as already discussed in relation to Fig. 6.

Compared to propylene, the effect of propane co-feed on the membrane performance is less critical, as shown in Fig. 9. The initial *ME* decrease in the presence of propane mimics the decrease experienced while co-feeding propylene. Firstly, most active Pd sites for C_3H_8 decomposition are covered, leading to a ~10% decrease in *ME*. After some time on stream,

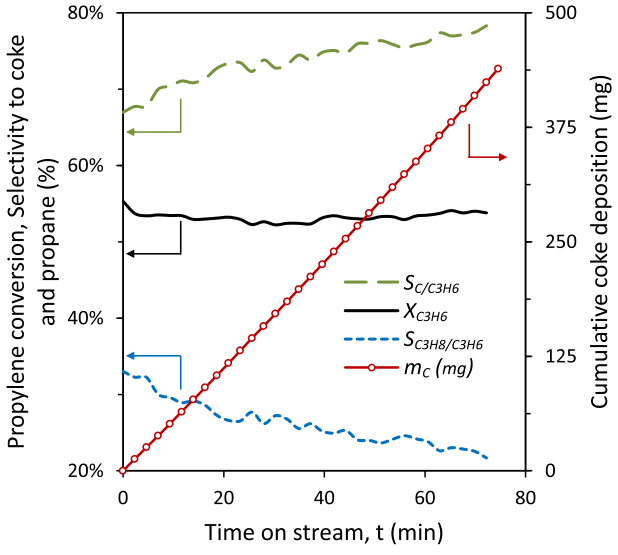

Fig. 7 – Transient evolution of Pd/Ag membrane coking in the presence of C_3 mixtures at T = 550 °C.

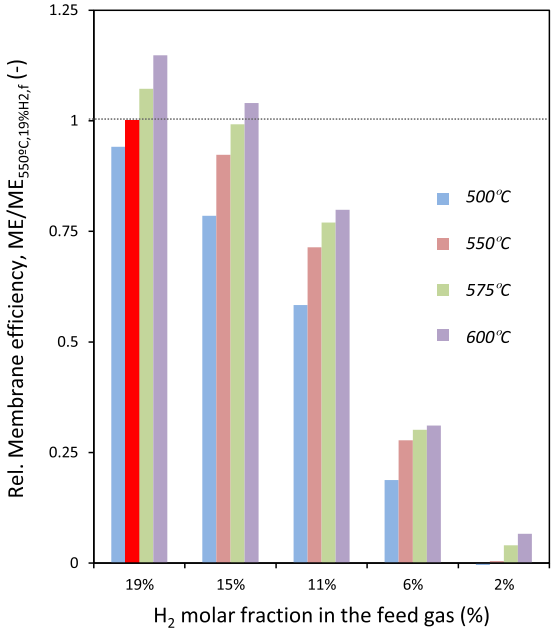

Fig. 8 – Steady-state relative membrane efficiency ($ME_r = ME/ME_{550\,°C,19\%H_2}$) as a function of operation temperature and H_2/Ar feed composition.

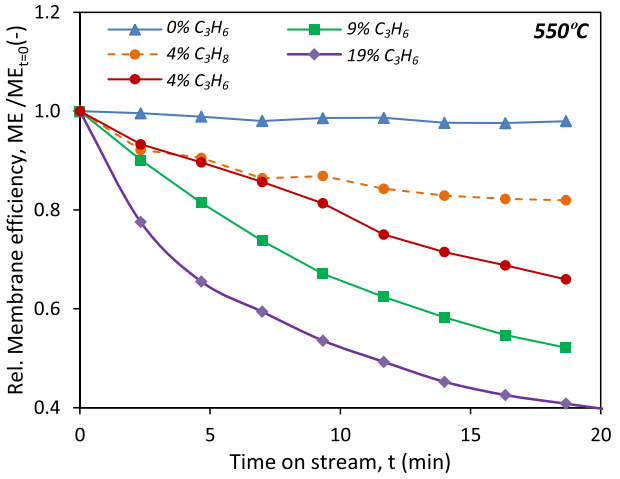

Fig. 9 – Transient relative membrane efficiency ($ME_t = ME(t)/ME_{t=0}$) as a function of propylene content in the feed gas. Operation temperature: $T = 550$ °C.

the C_3H_8 tendency to coke formation diminishes severely, thus, showing an almost constant *ME*. This suggests that propane would behave as an inert species for H_2 permeation inhibition after covering the most active membrane surface sites. On the other hand, the presence of propylene leads to a continuous decrease in membrane performance during the time on stream. The olefin's C=C double bond may explain why propylene becomes more reactive than propane and has a greater tendency to decompose into highly dehydrogenated species, i.e. coke, in the presence of the Pd/Ag membrane layer.

Regarding the coupled effect of temperature and propylene contents in the feed gas, Fig. 10 shows that high temperatures favor hydrocarbon decomposition and thus membrane fouling by coke deposition. It can be observed that the relative *ME* decrease at 600 °C as against 550 °C for a feed gas mixture containing C_3H_6:H_2 = 1:5 is already significant. In the context of a *PDH* process in membrane reactors, this result illustrates that working at 600 °C or higher temperatures is not recommended since coking effects become so significant that the membrane performance severely decreases. The observed membrane fouling may play a role in the poor equilibrium-shifting performance of the Pd–Ag membranes illustrated in previous works on *PDH* processes with in-situ H_2 separation [7,8].

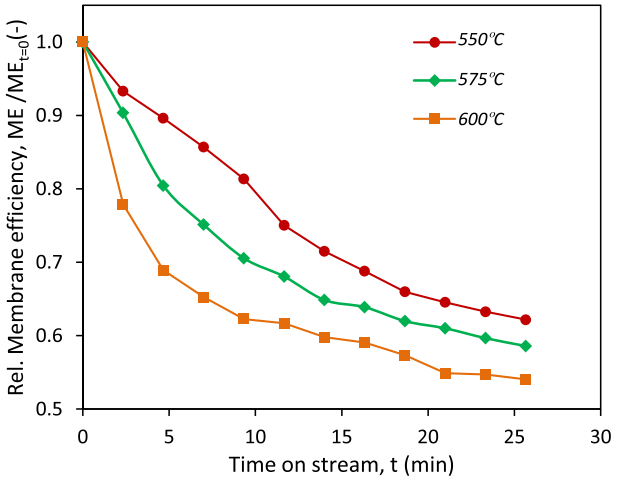

Fig. 10 – Transient relative membrane efficiency ($ME_t = ME(t)/ME_{t=0}$) as a function of operation temperature. Propylene-to-hydrogen ratio in the feed gas: C_3H_6:H_2 = 1:5.

Conclusions

Commercial Pd/Ag alloyed membranes have been characterized for hydrogen separation in a *PDH* process, studying the effect of the H_2 pressure drop, the temperature and the co-existence of C_3 hydrocarbons on the permeation rates. Due to the tubular configuration of the membranes, the driving force for hydrogen permeation has been estimated considering a logarithmic mean of the hydrogen feed and retentate pressures for the external partial pressure, $P_{H_2,ext}$. A Richardson's equation coefficient $n = 0.71$ was found as the optimal value to describe the linear trend between H_2 permeation and its driving force. The effect of temperature on the permeation flux was found to be negligible in the range of usual *PDH* operation conditions (T = 550 °C–575 °C). However, the co-feeding of propylene to the separation system resulted in a significant transient decrease in H_2 permeation due to the propylene decomposition. Carbon deposits covered the Pd/Ag membrane layer leading to a worsening in the membrane performance. The coking was, however, reversible and it did not affect H_2 permeation in the absence of C_3 species after regeneration of the membranes with diluted oxygen.

Acknowledgments

Financial support from MINECO, Spain (Projects CTQ2010-15568 and ENE2013-444350-R) is gratefully acknowledged. Financial aid for the maintenance of the consolidated research group CREG has been provided by the Fondo Social Europeo (FSE) through the Gobierno de Aragón (Aragón, Spain).

Nomenclature

Acronyms and abbreviations

A	hydrogen feed pressure, mbar
log *m*(A,R)	H_2 logarithmic mean pressure between feed and retentate, mbar
m(A,R)	H_2 mean partial pressure between feed and retentate, mbar
MR	membrane reactor
ME	membrane efficiency, $F_{H_2,P}/F_{H_2,R}$, –
ME_r	steady-state relative membrane efficiency, $ME/ME_{T(°C),\%H_{2,F}}$, –
ME_t	transient relative membrane efficiency, $ME(t)/ME_{t=0}$, –
PDH	propane dehydrogenation
PH	propylene hydrogenation
R	hydrogen retentate pressure, mbar
TZFBR	Two-Zone Fluidized Bed Reactor

Parameters

E_a	activation energy, J/mol
F_{H_2}	hydrogen volumetric flow, cm^3_{STP}/min
F_i	volumetric flow of species I, cm^3_{STP}/min
n	Richardson's equation coefficient
N_{H_2}	hydrogen permeation flux, $cm^3_{STP}/cm^2 \cdot min$
ΔP_{H_2}	hydrogen pressure drop or driving force, mbar
P^0	pre-exponential permeability coefficient, $mol/m \cdot min \cdot mbar^n$
$P_{H_2,ext}$	hydrogen partial pressure on the external membrane side, mbar
$P_{H_2,F}$	hydrogen partial pressure in the feed gas, mbar
$P_{H_2,L=0}$	external hydrogen partial pressure at the membrane bottom, mbar
$P_{H_2,L=1}$	external hydrogen partial pressure at the membrane top, mbar
$P_{H_2,P}$	hydrogen partial pressure in the permeate gas, mbar
$P_{H_2,R}$	hydrogen partial pressure in the retentate gas, mbar
P_v	vacuum pressure, mbar
R	Ideal gas constant, J/mol·K
T	Temperature, K

REFERENCES

[1] Gallucci F, Fernandez E, Corengia P, van Sint Annaland M. Recent advances on membranes and membrane reactors for hydrogen production. Chem Eng Sci 2013;92:40–66.

[2] Basile A, Paturzo L, Gallucci F. Co-current and counter-current modes for water gas shift membrane reactor. Catal Today 2003;82:275–81.

[3] Basile A, Gallucci F, Paturzo L. A dense Pd/Ag membrane reactor for methanol steam reforming: experimental study. Catal Today 2005;104:244–50.

[4] Dittmeyer R, Höllein V, Daub K. Membrane reactors for hydrogenation and dehydrogenation processes based on supported palladium. J Mol Catal A Chem 2001;173:135–84.

[5] Ziaka ZD, Minet RG, Tsotsis TT. A high temperature catalytic membrane reactor for propane dehydrogenation. J Memb Sci 1993;77:221–32.

[6] Gbenedio E, Wu Z, Hatim I, Kingsbury BFK, Li K. A multifunctional Pd/alumina hollow fibre membrane reactor for propane dehydrogenation. Catal Today 2010;156:93–9.

[7] Medrano JA, Julián I, Herguido J, Menéndez M. Pd-ag membrane coupled to a two-zone fluidized bed reactor (TZFBR) for propane dehydrogenation on a pt-Sn/$MgAl_2O_4$ catalyst. Membranes 2013;3:69–86.

[8] Medrano JA, Julián I, García F, Li K, Herguido J, Menéndez M. Two-zone fluidized bed reactor (TZFBR) with palladium membrane for catalytic propane dehydrogenation: experimental performance assessment. Ind Eng Chem Res 2013;52:3723–31.

[9] Herguido J, Menéndez M, Santamaría J. On the use of fluidized bed catalytic reactors where reduction and oxidation zones are present simultaneously. Catal Today 2005;100:181–9.

[10] Gascón J, Téllez C, Herguido J, Menéndez M. A two-zone fluidized bed reactor for catalytic propane dehydrogenation. Chem Eng J 2005;106:91–6.

[11] Julián I, Herguido J, Menéndez M. Particle mixing in a two-section two-zone fluidized bed reactor. Experimental technique and counter-current back-mixing model validation. Ind Eng Chem Res 2013;52:13587–96.

[12] Julián I, Gallucci F, van Sint Annaland M, Herguido J, Menéndez M. Coupled PIV/DIA for fluid dynamics studies on a two-section two-zone fluidized bed reactor. Chem Eng J 2012;207–208:122–32.

[13] Miguel CV, Mendes A, Tosti S, Madeira LM. Effect of CO and CO_2 on H_2 permeation through finger-like Pd–Ag membranes. Int J Hydrogen Energy 2012;37:12680–7.

[14] Li H, Goldbach A, Li W, Xu H. PdC formation in ultra-thin pd membranes during separation of H_2/CO mixtures. J Memb Sci 2007;299:130–7.

[15] Flanagan TB, Wang D, Shanahan K. The effect of CO on hydrogen permeation through Pd and through internally oxidized and un-oxidized pd alloy membranes. Sep Purif Technol 2011;79:385–92.

[16] Mejdell AL, Jøndahl M, Peters TA, Bredesen R, Venvik HJ. Effects of CO and CO_2 on hydrogen permeation through a ~3 μm Pd/Ag 23 wt.% membrane employed in a microchannel membrane configuration. Sep Purif Technol 2009;68:178–84.

[17] Peters TA, Kaleta T, Stange M, Bredesen R. Hydrogen transport through a selection of thin pd-alloy membranes: membrane stability, H_2S inhibition, and flux recovery in hydrogen and simulated WGS mixtures. Catal Today 2012;193:8–19.

[18] Braun F, Tarditi AM, Miller JB, Cornaglia LM. Pd-based binary and ternary alloy membranes: morphological and perm-selective characterization in the presence of H_2S. J Memb Sci 2014;450:299–307.

[19] Peters TA, Kaleta T, Stange M, Bredesen R. Development of ternary Pd–Ag–TM alloy membranes with improved sulphur tolerance. J Memb Sci 2013;429:448–58.

[20] Braun F, Miller JB, Gellman AJ, Tarditi AM, Fleutot B, Kondratyuk P, et al. PdAgAu alloy with high resistance to corrosion by H_2S. Int J Hydrogen Energy 2012;37:18547–55.

[21] Quicker P, Höllein V, Dittmeyer R. Catalytic dehydrogenation of hydrocarbons in palladium composite membrane reactors. Catal Today 2000;56:21–34.

[22] Yildirim Y, Gobina E, Hughes R. An experimental evaluation of high-temperature composite membrane systems for propane dehydrogenation. J Memb Sci 1997;135:107–15.

[23] Gimeno MP, Wu ZT, Soler J, Herguido J, Li K, Menéndez M. Combination of a two-zone fluidized bed reactor with a Pd hollow fibre membrane for catalytic alkane dehydrogenation. Chem Eng J 2009;155:298–303.

[24] Collins JP, Schwartz RW, Sehgal R, Ward TL, Brinker CJ, Hagen GP, et al. Catalytic dehydrogenation of propane in hydrogen permselective membrane reactors. Ind Eng Chem Res 1996;35:4398.

[25] Jung SH, Kusakabe K, Morooka S, Kim S. Effects of co-existing hydrocarbons on hydrogen permeation through a palladium membrane. J Membr Sci 2000;170:53–60.

[26] Deveau ND, Ma YH, Datta R. Beyond sieverts' law: a comprehensive microkinetic model of hydrogen permeation in dense metal membranes. J Membr Sci 2013;437:298–311.

[27] Chen W, Hsu P, Lin B. Hydrogen permeation dynamics across a palladium membrane in a varying pressure environment. Int J Hydrogen Energy 2010;6(35):5410–8.

[28] Caravella A, Hara S, Sun Y, Drioli E, Barbieri G. Coupled influence of non-ideal diffusion and multilayer asymmetric porous supports on sieverts law pressure exponent for hydrogen permeation in composite pd-based membranes. Int J Hydrogen Energy 2014;39:2201–14.

[29] Flanagan TB, Wang D, Shanahan KL. Diffusion of H through Pd membranes: effects of non-ideality. J Membr Sci 2007;306:66–74.

[30] Buxbaum RE. Apparatus and methods for gas extraction. US5913987 Patent. 1999.

[31] Buxbaum RE, Hsu PC. Method for plating Palladium. US5149420 Patent. 1992.
[32] Chen W, Hsia M, Lin Y, Chi Y, Yang C. Hydrogen permeation and recovery from H_2–N_2 gas mixtures by Pd membranes with high permeance. Int J Hydrogen Energy 2013;38:14730–42.
[33] Maneerung T, Hidajat K, Kawi S. Ultra-thin (<1 μm) internally-coated Pd–Ag alloy hollow fiber membrane with superior thermal stability and durability for high temperature H_2 separation. J Membr Sci 2014;452:127–42.
[34] Shu J, Grandjean BPA, Ghali E, Kaliaguine S. Simultaneous deposition of Pd and Ag on porous stainless steel by electroless plating. J Membr Sci 1993;77:181–95.
[35] Bosko ML, Miller JB, Lombardo EA, Gellman AJ, Cornaglia LM. Surface characterization of Pd–Ag composite membranes after annealing at various temperatures. J Membr Sci 2011;369:267–76.
[36] Zhang K, Wei X, Rui Z, Li Y, Lin YS. Effect of metal-support interface on hydrogen permeation through palladium membranes. AIChE J 2009;55:630–9.
[37] Roses L, Gallucci F, Manzolini G, van Sint Annaland M. Experimental study of steam methane reforming in a Pd-based fluidized bed membrane reactor. Chem Eng J 2013;222:307–20.
[38] Gallucci F, van Sint Annaland M, Kuipers JAM. Autothermal reforming of methane with integrated CO_2 capture in a novel fluidized bed membrane reactor. Part I: experimental demonstration. Top Catal 2008;51:133–45.
[39] Guazzone F, Engwall EE, Ma YH. Effects of surface activity, defects and mass transfer on hydrogen permeance and n-value in composite palladium-porous stainless steel membranes. Catal Today 2006;118:24–31.
[40] Caravella A, Barbieri G, Drioli E. Concentration polarization analysis in self-supported Pd-based membranes. Sep Purif Technol 2009;66:613–24.
[41] Chen W, Hsia M, Chi Y, Lin Y, Yang C. Polarization phenomena of hydrogen-rich gas in high-permeance pd and Pd–Cu membrane tubes. Appl Energy 2014;113:41–50.